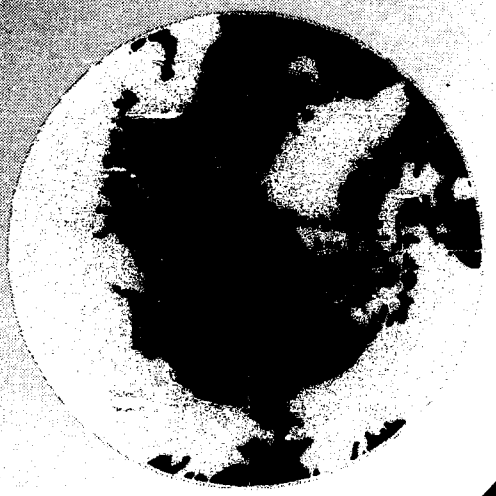
AD-A253 027

ARO 27859.1-GS-CF

...ational Conference ... Role of the Polar ...ions in Global Change

Vol. I

DTIC
ELECTE
APR 20 1992
S D



This document has been approved for public release and sale; its distribution is unlimited.

...d a Conference
...-13, 1990 at the
...aska Fairbanks

MASTER COPY · KEEP THIS COPY FOR REPRODUCTION PURPOSES

REPORT DOCUMENTATION PAGE

Form Approved
OMB No. 0704-0188

Public reporting burden for this collection of information is estimated to average 1 hour per response, including the time for reviewing instructions, searching existing data sources, gathering and maintaining the data needed, and completing and reviewing the collection of information. Send comments regarding this burden estimate or any other aspect of this collection of information, including suggestions for reducing this burden, to Washington Headquarters Services, Directorate for Information Operations and Reports, 1215 Jefferson Davis Highway, Suite 1204, Arlington, VA 22202-4302, and to the Office of Management and Budget, Paperwork Reduction Project (0704-0188), Washington, DC 20503.

1. AGENCY USE ONLY (Leave blank)	2. REPORT DATE	3. REPORT TYPE AND DATES COVERED
	March 1992	Final 1 May 1990-30 April 1991

4. TITLE AND SUBTITLE
International Conference on the Role of the Polar Regions in Global Change Volume I

5. FUNDING NUMBERS
DAAL03-90-G-0126

6. AUTHOR(S)
Gunter Weller (principal investigator on project)

7. PERFORMING ORGANIZATION NAME(S) AND ADDRESS(ES)
University of Alaska Geophysical Institute
Fairbanks, AK 99775-0800

8. PERFORMING ORGANIZATION REPORT NUMBER

9. SPONSORING/MONITORING AGENCY NAME(S) AND ADDRESS(ES)
U. S. Army Research Office
P. O. Box 12211
Research Triangle Park, NC 27709-2211

10. SPONSORING/MONITORING AGENCY REPORT NUMBER
ARO 27859.1-GS-CF

11. SUPPLEMENTARY NOTES
The view, opinions and/or findings contained in this report are those of the author(s) and should not be construed as an official Department of the Army position, policy, or decision, unless so designated by other documentation.

12a. DISTRIBUTION/AVAILABILITY STATEMENT
Approved for public release; distribution unlimited.

12b. DISTRIBUTION CODE

13. ABSTRACT *(Maximum 200 words)*

The International Conference on the Role of the Polar Regions in Global Change took place on the campus of the University of Alaska Fairbanks on June 11–15, 1990. It was co-sponsored by several national and international scientific organizations, as listed on the preceding page. The host institutions were the Geophysical Institute and the Center for Global Change and Arctic System Research, both at the University of Alaska Fairbanks.

The goal of the conference was to define and summarize the state of knowledge on the role of the polar regions in global change, and to identify gaps in knowledge. To this purpose experts in a wide variety of relevant disciplines were invited to present papers and hold panel discussions. While there are numerous conferences on global change, this conference dealt specifically with the polar regions which occupy key positions in the global system.

continued on reverse side

14. SUBJECT TERMS	15. NUMBER OF PAGES
Conference, Global Change, Polar Regions, Global System	362
	16. PRICE CODE

17. SECURITY CLASSIFICATION OF REPORT	18. SECURITY CLASSIFICATION OF THIS PAGE	19. SECURITY CLASSIFICATION OF ABSTRACT	20. LIMITATION OF ABSTRACT
UNCLASSIFIED	UNCLASSIFIED	UNCLASSIFIED	UL

Over 400 scientists from 15 different countries attended and presented 200 papers on research in the Arctic and Antarctic. The papers were distributed among seven major themes and sessions, each having about three invited papers, a dozen contributed papers, and 15–20 poster papers. These papers, or their abstracts, are contained in the two proceedings volumes. In publishing the papers we did not distinguish between invited, contributed, or poster papers, but gave them all equal weight. On the final day of the conference three panels met to discuss problems and priorities in polar research. A summary of their recommendations follows the final section of papers.

International Conference on the Role of the Polar Regions in Global Change: Proceedings of a Conference Held June 11-15, 1990 at the University of Alaska Fairbanks

Volume I

Accesion For
NTIS CRA&I
DTIC TAB
Unannounced
Justification
By
Distribution /
Availability Codes
Dist
A-1
Avail
COPY INSPECTED 4

Edited by

Gunter Weller
Cindy L. Wilson
Barbara A. B. Severin

Published by

Geophysical Institute
University of Alaska Fairbanks

and

Center for Global Change and Arctic System Research
University of Alaska Fairbanks
Fairbanks, Alaska 99775

92-09872

December, 1991

92 4 17 031

ISBN 0-915360-08-X (Volume I)
ISBN 0-915360-10-1 (2-Volume Set)

International Organizing Committee

G. E. Weller, Chair
University of Alaska Fairbanks, USA

E. P. Borisenkov
Main Geophysical Observatory, USSR

W. F. Budd
University of Melbourne, Australia

D. Elliot
Ohio State University, USA

A. L. Gordon
Columbia University, USA

G. Hempel
Alfred Wegener Institut, FRG

A. W. Johnson
San Diego State University, USA

K. Ya. Kondratyev
Institute for Lake Research, USSR

C. Lorius
CNRS, LGGE, Grenoble, France

M. F. Meier
University of Colorado, USA

L. M. Proenza
University of Alaska Fairbanks, USA

E. F. Roots
Environment Canada, Canada

N. Untersteiner
University of Washington, USA

O. R. Young
Dartmouth College, USA

Local Organizing Committee
(All University of Alaska Fairbanks)

C. Wilson, Conference Coordinator
Geophysical Institute

S. Akasofu
Director, Geophysical Institute

V. Alexander
Director, Institute of Marine Science

N. Bachner
Conferences and Special Events

C. Benson
Geophysical Institute

D. Hopkins
Geology/Geophysics Dept.

M. O. Jeffries
Geophysical Institute

G. Juday
Forest Sciences Division

D. Klein
Biology/Wildlife Dept.

S. MacLean
Institute of Arctic Biology

L. L. McCauley
Center for Global Change and Arctic System Research

G. McBeath
Political Science/Justice Dept.

J. McBeath
Plant and Animal Sciences Div.

C. Naske
History Dept.

S. Oien
Conferences and Special Events

W. Reeburgh
Institute of Marine Science

T. Royer
Institute of Marine Science

G. Shaw
Geophysical Institute

C. Slaughter
Institute of Northern Forestry

W. Weeks
Geophysical Institute

F. Williamson
Director, Inst. of Arctic Biology

J. Zarling
Director, Institute of Northern Engineering

Financial Sponsors of the Conference

Army Research Office
BP Exploration
Cold Regions Research and Engineering Laboratory
Dept. of Energy, CO_2 Program
Dept. of Energy, Ecological Research Program
National Aeronautics and Space Administration
National Oceanic and Atmospheric Administration
National Park Service
National Science Foundation
North Slope Borough
Office of Naval Research
U.S. Geological Survey

Conference Cosponsors

American Association for the Advancement of Science
American Geophysical Union
American Meteorological Society
Arctic Institute of North America
Arctic Research Commission of the U.S.
Arctic Research Consortium of the United States
Center for Global Change and Arctic System Research, University of Alaska Fairbanks
Geophysical Institute, University of Alaska Fairbanks
International Glaciological Society
Oceanography Society
Scientific Committee on Antarctic Research, ICSU

PREFACE

The International Conference on the Role of the Polar Regions in Global Change took place on the campus of the University of Alaska Fairbanks on June 11–15, 1990. It was co-sponsored by several national and international scientific organizations, as listed on the preceding page. The host institutions were the Geophysical Institute and the Center for Global Change and Arctic System Research, both at the University of Alaska Fairbanks.

The goal of the conference was to define and summarize the state of knowledge on the role of the polar regions in global change, and to identify gaps in knowledge. To this purpose experts in a wide variety of relevant disciplines were invited to present papers and hold panel discussions. While there are numerous conferences on global change, this conference dealt specifically with the polar regions which occupy key positions in the global system.

Over 400 scientists from 15 different countries attended and presented 200 papers on research in the Arctic and Antarctic. The papers were distributed among seven major themes and sessions, each having about three invited papers, a dozen contributed papers, and 15–20 poster papers. These papers, or their abstracts, are contained in the two proceedings volumes. In publishing the papers we did not distinguish between invited, contributed, or poster papers, but gave them all equal weight. On the final day of the conference three panels met to discuss problems and priorities in polar research. A summary of their recommendations follows the final section of papers.

Our goal has been to produce an interesting and readable overview of the conference, and we hope you enjoy the result.

Gunter Weller
Cindy L. Wilson
Barbara A. B. Severin

Editors

TABLE OF CONTENTS

Volume I:

Section A: *Detection and Monitoring of Change* 1

Polar Regions and Global Change: the Role of Remote Sensing
K. Y. Kondratyev 3

Variations in Sea Ice Thickness in the Polar Regions
P. Wadhams 4

Detection of High Latitude Atmospheric Circulation Changes Using Satellite Data
J. Turner 14

***Strengths and Weaknesses of* Sea Ice as a Potential Early Indicator of Climate Change**
C. L. Parkinson 17

Variability of Antarctic Sea Ice
H. J. Zwally, J. C. Comiso, and J. E. Walsh 22

Sea Ice Variability in the Nordic Seas
T. Vinje 23

Variations of Extent, Area, and Open Water of the Polar Sea Ice Covers: 1978–1987
P. Gloersen and W. J. Campbell 28

Multi-Year Elevation Changes Near the West Margin of the Greenland Ice Sheet from Satellite Radar Altimetry
C. S. Lingle, A. C. Brenner, H. J. Zwally, and J. P. DiMarzio 35

Properties of the Antarctic Ice Sheet Derived from Passive Microwave Data
K. C. Jezek and D. Cavalieri 43

Satellite Monitoring of Areal Changes in the Glacier Component of the Earth's Cryosphere
R. S. Williams, Jr. and J. G. Ferrigno 44

Monitoring for Global Change in Alaska Research Natural Areas
G. P. Juday 45

Baseline Studies for Monitoring Global Climatic Change in the Arctic Environment; A Remote Sensing–Spatial Data Base Approach
M. B. Shasby and E. F. Binnian 46

Radar Sensing of Polar Regions
G. I. Belchansky and A. P. Pichugin 47

The Polar Automatic Weather Station Project of the University of Wisconsin
C. R. Stearns and G. A. Weidner 58

Detection of Temperature and Sea Ice Extent Changes in the Antarctic and Southern Ocean
T. H. Jacka and W. F. Budd 63

Interannual Variability of Monthly Sea Ice Distributions in the North Polar Region
C. L. Parkinson 71

Contour Mapping of Arctic Basin Ice Roughness Parameters
A. S. McLaren, R. H. Bourke, and R. L. S. Weaver 79

Generation of Sea Ice Geophysical Flux Estimates Utilizing a Multisensor Data Processor in Preparation for the RADARSAT and EOS Eras
B. Holt, R. Kwok, F. Carsey, and J. Curlander 80

A Review of the Antarctic Region Ice Phenomenon Based on Satellite Images
L. Hus 87

Recent Changes in the Coastal Regions of Antarctica Documented by Landsat Images
J. G. Ferrigno, R. S. Williams, Jr., B. K. Lucchitta, and B. F. Molnia 88

One Glacier's Retreat, a Global Warming does not Make: An Argument for Systematic Monitoring of North American Glaciers
B. F. Molnia 89

Evaluation of Dynamics of Polar Regions Landscapes on The Basis of Remote Sensing Information
L. S. Garagula and V. E. Roujansky 90

Taiga Forest Stands and SAR: Monitoring for Subarctic Global Change
J. Way, R. Kwok, L. Viereck, C. Slaughter, C. Dobson, K. McDonald, and N. Christensen 93

Contamination of U.S. Arctic Ecosystems by Long-range Transport Of Atmospheric Contaminants
J. Ford and D. H. Landers 102

Arctic Environmental Data Directory
D. R. Posson and M. O. Jones 106

Data for Polar Regions Research
R. L. Jenne 107

Interactive Information System: Database Elaboration for Biodiversity Research
G. I. Belchansky, V. G. Petrosyan, and E. N. Boukvareva 112
A Comprehensive Collection of Arctic Meteorological Soundings for Use in Climate Studies
J. D. Kahl, P. J. Sheridan, and R. C. Schnell 119
Development of Sea Ice Data Sets from Passive Microwave Satellite Data: Preliminary Lessons
R. L. Weaver, V. J. Troisi, and C. S. Hanson 120
Contribution of the Argos System for the Study of the Polar Regions
J.-L. H. Bessis 126
Quick-Look Satellite Imagery for Alaska: A Tool for Environmental Monitoring
T. George, G. Reynolds, K. Dean, and J. Miller 133
Measuring Sea Ice Deformation with Imaging RADAR Satellites
C. Olmsted 141

Section B: *Climate Variability and Climate Forcing* 147

How Climate Changes
J. O. Fletcher 149
High Latitude Climate Forcing by 18.6-Year Lunar Tidal Fluctuations
T. C. Royer 150
Cloud Radiation Interaction and the Earth's Climate: Relevance to the Climate of the Arctic
G. L. Stephens 151
Polar Forcing of Natural Variability of the Atmospheric Climate
G. V. Alekseyev 158
Interannual Changes in Northern Hemispheric Tropospheric Temperatures, 1960-1989
G. A. Herbert 159
Interannual Variability of the January Meridional Heat Transport by Planetary Waves in the Northern Latitudes
K. Higuchi, C. A. Lin, A. Shabbar, and J. L. Knox 164
Low-Frequency Variability of Polar Atmosphere due to Blocking Formations: A Numerical Experiment of Blocking
H. L. Tanaka 170
Trends in Global and Polar Cloudiness from Satellite Data
I. I. Mokhov 176
Cloud Radiative Effects and Associated Changes in Tropospheric Temperatures and Winds at the South Pole During Austral Winter
R. S. Stone and J. D. Kahl 184
Precipitation Trends over Polar Ice Sheets from Atmospheric Moisture Fluxes
D. H. Bromwich 190
On the Relationship Between Antarctic Katabatic Winds and Large-Scale Tropospheric Circulation
T. R. Parish 191
Plateau Weather
U. Radok and G. Wendler 192
On the Effect of Global Warming on the Snowmelt in an Arctic Permafrost Area
K. Kodama, D. Kobayashi, N. Ishikawa, and G. Wakahama 199
Impacts of Projected Global Warming: A Research Proposal for the Mackenzie Basin
S. J. Cohen and J. B. Maxwell 200
Allowance for the Relaxation Effects in Global Processes of Heat Transfer
N. Yu. Doronin and G. A. Zablotsky 205
Problems With the Use of Climatological Data to Detect Climatic Change at High Latitudes
S. A. Bowling 206
A Winter Season Synoptic Climatology of Alaska: 1956-1986
M. F. Milkovich 210
A Two-Year Record of the Climate on the Greenland Crest from an Automatic Weather Station
G. A. Weidner and C. R. Stearns 220
Snow Temperature Profiles and Heat Fluxes Measured on the Greenland Crest by an Automatic Weather Station
C. R. Stearns and G. A. Weidner 223
Studies of -40°C Isothermal Layers at High Latitudes
R. E. Stewart and C. A. Lin 227
Variations in Cloudiness, Temperature and Satellite-Derived Outgoing Longwave Radiation for Alaska
G. Wendler 231
Study of the Influence of Gravity Flows on the Antarctic Circulation Using Simulations with the French General Circulation Model
P. Pettré and M. Déqué 236
Climate Impacts of the Boundary Layer Circulation over Antarctica
D. H. Bromwich 237

The Surface Condition on the Antarctic Ice Sheet
K. Seko, T. Furukawa, and O. Watanabe 238
Study on Characteristics and Evolution of the High Asia Cryosphere and Its Effects on Natural Environments of the Earth
Xie Zichu and Cheng Guodong 243

Section C: *Ocean–Sea Ice–Atmosphere Interactions and Processes* 245

Arctic Sea Ice Balance and Climate
N. Untersteiner 247
Sea Ice and the Arctic Ocean: Issues in Climate and Hydrology
K. Aagaard and E. C. Carmack 248
The Southern Ocean: Its Involvement in Global Change
A. Gordon 249
Model Studies of the Effects of Global Warming and Antarctic Sea Ice Changes on Antarctic and Global Climates
I. Simmonds and W. F. Budd 256
Antarctic Sea Ice and Temperature Variations
J. E. Walsh, H. J. Zwally, and J. W. Weatherly 263
The Role of the Southern Ocean/Sea Ice Interaction in Global Climate Change
D. G. Martinson 269
Antarctic Sea Ice: Its Development and Basic Properties
M. A. Lange 275
Greenland Sea Ice Anomalies During 1901–1984 and their Relation to an Interdecadal Arctic Climate Cycle
L. A. Mysak, D. K. Manak, and R. F. Marsden 284
Seasonal Mean Ice Motion in the Arctic Basin
R. Colony 290
A Coupled, Zonally Averaged Atmosphere–Ocean Model: Variability of the Thermohaline Circulation
T. F. Stocker, D. G. Wright, and L. A. Mysak 291
Tidal Water and Ice Dynamics in the Arctic Ocean
A. Yu. Proshutinsky 296
Laboratory Studies of Exchange Between a Polar and a Subpolar Basin
K. L. Hunkins 304
Mathematical Modeling in Studies of Arctic Ocean Circulation
N. Y. Doronin and A. Y. Proshutinsky 310
Air–Sea Interaction and Penetrating Winter Convection in the Greenland Sea
G. V. Alekseyev 317
Multiyear Variability of Atmospheric Circulation Shifts Over the North Pacific and a Method to Forecast Ice Cover on the Okhotsk and Bering Seas
A. M. Polyakova 318
Sea Surface Temperature Anomalies in the North Pacific, Their Connection With Atmospheric Processes in Transitional Seasons and Ice Variability in the Bering and Okhotsk Seas
K. A. Rogachev and A. F. Lomakin 319
A Statistical Study of Atmosphere–Sea Ice Interactions in the Southern Ocean
E. Breitenberger and G. Wendler 320
The Impact of Snow and Sea Ice Variations on Global Climate Change
T. S. Ledley 321
Energy Exchange Over Antarctic Sea Ice in Late Winter
G. König-Langlo, B. Ivanov, and A. Zachek 325
The Partition of Thermal Energy in the Summertime Sea Ice–Ocean System
M. Steele 330
Ice Thickness and Vertical Heat Flux in the Arctic Ocean
J. S. Wettlaufer and N. Untersteiner 331
Perennial Water Stratification and the Role of Basal Freshwater Flow in the Mass Balance of the Ward Hunt Ice Shelf, Canadian High Arctic
M. O. Jeffries 332
The Influence of the Hydrologic Cycle on the Extent of Sea Ice with Climatic Implications
K. G. Dean, J. P. Gosink, T. Weingartner, and D. Musgrave 338
Water Mass Formation at High Latitudes
S. Hakkinen and G. L. Mellor 339
Tracing Upper Waters in the Arctic Ocean
E. P. Jones and L. G. Anderson 340
The Arctic Ocean Eigen Oscillations
A. Yu. Proshutinsky and I. V. Polyakov 347

Transport of Atmospheric CO_2 to the Bottom Water of the Weddell Sea
L. G. Anderson 355
On Small Climatic Effects of Air Invasion in Polar Regions: The Influence on Atmospheric Pressure and Heat Flux
I. P. Semiletov 356
Determination of Net Atmospheric Heat Transfer, Ice Production, and Salt Rejection from the Chukchi Polynya Using AVHRR Thermal Imagery
J. E. Groves and W. J. Stringer 357

Volume II:

Section D: *Effects on Biota and Biological Feedbacks* 367

Effects of Global Change on Net Ecosystem Carbon Flux of Arctic Tussock Tundra
W. C. Oechel 369
The Role of Tundra and Taiga Systems in the Global Methane Budget
W. S. Reeburgh and S. C. Whalen 370
The Influence of Sea Ice on the Structure and Function of Southern Ocean Ecosystems
C. W. Sullivan 371
Methane Emissions from Alaska Arctic Tundra in Response to Climatic Change
G. P. Livingston and L. A. Morrissey 372
The Toolik Lake Project: Terrestrial and Freshwater Research on Change in the Arctic
J. E. Hobbie, B. J. Peterson, G. R. Shaver, and W. J. O'Brien 378
Paleolimnologic Evidence of High Arctic Late Quaternary Paleoenvironmental Change: Truelove Lowland, Devon Island, N.W.T., Canada
R. H. King, I. R. Smith, and R. B. Young 384
Effect of Global Climate Change on Forest Productivity: Control Through Forest Floor Chemistry
K. Van Cleve, J. Yarie, and E. Vance 390
The Sensitivity of Ecosystem CO_2 Flux in the Boreal Forests of Interior Alaska to Climatic Parameters
G. B. Bonan 391
Evolutionary History of Polar Regions
J. A. Crame 396
Possible Impacts of Ozone Depletion on Trophic Interactions and Biogenic Vertical Carbon Flux in the Southern Ocean
H. J. Marchant and A. T. Davidson 397
Relationships Between Whale Hunting, Human Social Organization, and Subsistence Economies in Coastal Areas of Northwest Alaska during Late Prehistoric Times
R. K. Harritt 401
The Effect of Climatic Change on Farming and Soil Erosion in Southern Greenland During the Last Thousand Years
B. H. Jakobsen 406
Climate and Landscape Perestroykas
S. A. Zimov and V. I. Chuprynin 411
Trajectory Analysis of the Atmospheric Carbon Dioxide Bimodal Distribution in the Arctic
K. Higuchi and N. B. A. Trivett 412
Winter CO_2 Flux from Ecosystems in Northeast Asia
S. A. Zimov, G. M. Zimova, U. V. Voropaev, Z. V. Voropaeva, S. P. Davydov, A. I. Davydova, S. F. Prosyannikov, and O. V. Prosyannikova 416
Peat Accumulation Rates in Arctic Alaska: Responding to Recent Climatic Change?
D. M. Schell and B. Barnett 417
Microbial Mineralization in Soils and Plant Material from Antarctica
M. Bölter 418
Effects of Point Source Atmospheric Pollution on Boreal Forest Vegetation of Northwestern Siberia
T. M. Vlasova, B. I. Kovalev, and A. N. Filipchuk 423
The Natural Background Disturbance in the Soviet Far East
V. P. Karakin and A. S. Sheinhouse 429
Sexual Reproduction of *Arctophila fulva* and Seasonal Temperature, Arctic Coastal Plain, Alaska
J. D. McKendrick 430
In the Footsteps of Robert Marshall: Proposed Research of White Spruce Growth and Movement at the Tree Limit, Central Brooks Range, Alaska
T. D. Droessler 431
USDA Forest Service Global Change Research: Monitored Ecosystems, Northern Linkages
D. V. Sandberg and C. W. Slaughter 435

Changes in the Source/Sink Relationships of the Alaskan Boreal Forest as a Result of Climatic Warming
J. Yarie and K. Van Cleve 436
Holocene Meltwater Variations Recorded in Antarctic Coastal Marine Benthic Assemblages
P. A. Berkman 440
EPOS—A New Approach to International Cooperation
G. Hempel 450
Estimation of Matter Fluxes in the River–Sea and Ocean–Atmosphere Systems for Okhotsk and Bering Seas
V. V. Anikiev, A. V. Alekseev, A. N. Medvedev, and E. M. Shymilin 451
Investigations of Scales of Changeability of Biogeochemical Processes on the Okhotsk Sea Shelf
V. V. Anikiev, O. V. Dudachev, T. A. Zadonskaya, A. P. Nedashkovski, A. V. Pervushin, S. G. Sagalaev, D. A. Choclov, and V. V. Yarosh 452
Long-term Monitoring of Airborne Pollen in Alaska and the Yukon: Possible Implications for Global Change
Anderson, J. H. 453
Potential Effects of Global Warming on Calving Caribou
W. G. Eastland and R. G. White 460
Growing Season Length and Climatic Variation in Alaska
B. S. Sharratt 465
Ecological Aspects in Construction of West Siberian Oil Field Surface Facilities
I. D. Sevortzov and P. N. Crushin 468
The Effects of Geographical Latitude on the Dynamics of Medical Data
I. V. Naborov and T. K. Breus 469
The Commons Game: A Lesson in Resources Management
C. A. Kirts and M. A. Tumeo 470

Section E: ***Ice Sheet, Glacier and Permafrost Responses and Feedbacks*** **.....475**

State and Dynamics of Snow and Ice Resources in the Arctic Region Derived from Data in the World Atlas of Snow and Ice Resources
V. M. Kotlyakov and N. N. Dreyer 477
Mass Balance of Antarctica and Sea Level Change
C. R. Bentley and M. B. Giovinetto 481
The Impact of Global Warming on the Antarctic Mass Balance and Global Sea Level
W. F. Budd and I. Simmonds 489
The Greenland Ice Sheet Contribution to Sea Level Changes During the Last 150,000 Years
A. Letréguilly, N. Reeh, and P. Huybrechts 495
A Post-Cromerian Rise in Sea Level
E. Olausson 496
Meltwater Runoff Lag from Arctic Glaciers and Ice Caps During Global Warming
W. T. Pfeffer, M. F. Meier, and T. H. Illangasekare 499
Measurement Error and Climate Change Implications of Glacier Mass Balance Records from Western Canada
M. M. Brugman 500
Ice Front Fluctuations of the Shirase Glacier, East Antarctica
F. Nishio 501
Changes in Ice Cover Thickness and Lake Level of Lake Hoare, Antarctica
R. A. Wharton, Jr., G. D. Clow, C. P. McKay, D. T. Andersen, and G. M. Simmons 502
Thermal and Hydrologic Responses of an Arctic Watershed to Climatic Warming
L. D. Hinzman and D. L. Kane 503
Contemporary Climate Change in the Mackenzie Valley, N.W.T. and the Impact upon Permafrost
A. Judge, A. Hedley, M. Burgess, and K. MacInnes 504
Response of Permafrost to Changes in Paleoclimate
T. E. Osterkamp, J. P. Gosink, T. Fei, and T. Zhang 505
The Antarctic Glacial Geologic Record and GCM Modeling: A Test
D. H. Bromwich, D. H. Elliot, D. Harwood, and P.-N. Webb 508
A Search for Short-Term Variations in the Flow of Ice Stream B, Antarctica
W. D. Harrison, K. A. Echelmeyer, and N. Humphrey 517
The Velocity Field of Antarctic Outlet Glaciers
B. K. Lucchitta, J. G. Ferrigno, T. R. MacDonald, and R. S. Williams, Jr. 518
Glacier Terminus Fluctuations in the Wrangell and Chugach Mountains Resulting from Non-Climatic Controls
M. Sturm, D. K. Hall, C. S. Benson, and W. O. Field 519
Radar Mapping of Malaspina Glacier, Alaska, with Applications for Global Change Investigations
J. E. Jones and B. F. Molnia 524
Climate-Related Research in Svalbard
K. Sand, J. O. Hagen, K. Repp, and E. Berntsen 525

Application of Aerial Photographs to Registration of Dynamic Phenomena in Polar Environment
K. Furmanczyk and J. Prais 532
Inversion of Borehole Temperature Data for Recent Climatic Changes: Examples from the Alaskan Arctic and Antarctica
G. D. Clow, A. H. Lachenbruch, and C. P. McKay 533
Climate Change and Permafrost Distribution in the Soviet Arctic
O. A. Anisimov and F. E. Nelson 534
Permafrozen Temperature Regime Affected by Climate Variability
P. A. Yanitsky 535
Computer Simulation of the Retrospective and Perspective Geocryological Situations in the Polar Regions
L. S. Garagula, V. E. Romanovsky, and N. V. Seregina 536
Paleotemperature Reconstruction for Freeze-Thaw Processes During the Late Pleistocene Through the Holocene
V. E. Romanovsky, L. N. Maximova, and N. V. Seregina 537
Freezing and Thawing of Soils Under the Influence of 300- and 90-Year Periods of Temperature Fluctuation
V. E. Romanovsky, L. S. Garagula, and N. V. Seregina 543
Microbiological Weathering of Silicates in Permafrost
T. P. Kolchugina and S. P. Fedosova 549
Anthropogenic Structures in the Geosystems (Landscapes) of the Permafrost Zone
V. P. Antonov-Druzhinin 552
Engineering-Geological Monitoring Within the Soviet Global Change Program (the Northern Regions of Western Siberia)
G. I. Pushko 553

Section F: *Paleoenvironmental Studies* 555

Palynological Data as Tools for Interpreting Past Climates: Some Examples from Northern North America
P. M. Anderson 557
High-Latitude Tree-Ring Data: Records of Climatic Change and Ecological Response
L. J. Graumlich 565
Polar Ice Cores: Climatic and Environmental Records
C. Lorius 570
Canadian Ice Caps as Sources of Environmental Data
R. M. Koerner, B. T. Alt, J. C. Bourgeois, and D. A. Fisher 576
A Two-Million-Year-Old Insect Fauna from North Greenland Indicating Boreal Conditions at the Plio-Pleistocene Boundary
J. Böcher 582
Late Quaternary and Paleoclimatology from Sediment Cores of the Eastern Arctic Ocean
U. Pagels and S. Köhler 585
The Record of Global Change in Circum-Antarctic Marine Sediments
P. F. Barker, C. J. Pudsey, and R. D. Larter 586
Eolian Sediments in Arctic Alaska as Sources of Paleoenvironmental Data
L. D. Carter 593
Paleoclimatic Significance of High Latitude Loess Deposits
J. E. Begét 594
Global Change and Thermal History as Recorded by Northern North American Tree-Ring Data
G. C. Jacoby and R. D. D'Arrigo 599
Spatial and Temporal Characteristics of the Little Ice Age: The Antarctic Ice Core Record
E. Mosley-Thompson and L. G. Thompson 606
Paleoenvironmental Data from Less-Investigated Polar Regions
R. Vaikmäe 611
Little Ice Age Glaciation in Alaska: A Record of Recent Global Climatic Change
P. E. Calkin and G. C. Wiles 617
The Greenland Ice Sheet Margin as a Source of Paleoenvironmental Data
N. Reeh, H. Oerter, A. Letréguilly, and H. Miller 626
The History of the Climate of the Northern Polar Region in the Holocene and Recent Millennia from Proxy and Historical Data
E. P. Borisenkov and V. M. Pasetsky 627
Two Late Quaternary Pollen Records from the Upper Kolyma Region, Soviet Northeast: A Preliminary Report
P. M. Anderson, L. B. Brubaker, A. A. Andreev, B. I. Chernenky, I. N. Federova, L. N. Kotova, A. V. Lozhkin, A. I. Polujan, L. G. Rovako, P. A. Colinvaux, W. R. Eisner, D. M. Hopkins, and M. C. Miller 628
Vegetation, Climate, and Lake Formation During Interglacial Periods in Northeast Interior Alaska
M. E. Edwards 633

Deglaciation and Latest Pleistocene and Early Holocene Glacier Readvances on the Alaska Peninsula: Records of Rapid Climate Change Due to Transient Changes in Solar Intensity and Atmospheric CO_2 Content?
D. Pinney and J. E. Begét 634

An Algorithm of Approximate Paleotemperature Calculation of the Earth Surface by Temperature Measurements in Deep Boreholes
N. A. Baranova and S. F. Khroutsky 641

Arctic Environments and Global Change: Evidence in Deep Permafrost Temperatures, Canadian Arctic Archipelago
A. Taylor 642

Glacial Marine Sediments from the Antarctic Peninsula: A Record of Climate Change and Glacial Fluctuations During the Late Holocene
E. W. Domack and L. Burkley 643

Project CELIA: Climate and Environment of the Last Interglacial (Isotope Stage 5) in Arctic and Subarctic North America
J. Brigham-Grette, M. Edwards, S. Funder, J. Kutzbach, L. Maher, J. V. Matthews, Jr., G. H. Miller, A. Morgan, N. W. Rutter, C. Schweger, C. Tarnocai, J.-S. Vincent, A. de Vernal 644

A Proxy Late Holocene Climatic Record Deduced from Northwest Alaska Beach Ridges
O. K. Mason and J. W. Jordan 649

Holocene Loess and Paleosols in Central Alaska: A Proxy Record of Holocene Climate Change
N. H. Bigelow and J. E. Begét 658

Comparisons of Late Quaternary Climatic Development Between the Arctic and Antarctic Through Calcareous Nannofossils
G. Gard and J. A. Crux 663

Japanese Ice Core Studies in the Polar Regions
O. Watanabe, Y. Fujii, F. Nishio, H. Narita, M. Nakawo, and H. Shoji 664

On the Development in Elaboration of Polar Ice Core Gas Content Analysis
I. P. Semiletov 665

Evolution of Southern Indian Ocean Surface and Deep Waters During the Paleogene as Inferred from Foraminiferal Stable Isotope Ratios
E. Barrera and B. T. Huber 666

Surface Currents in the Arctic Ocean During the Last 250 ka: Composition of Ice-Rafted Detritus (IRD) as a Key for Ice Drift Directions
M. Kubisch and R. F. Spielhagen 667

Sediment-Laden Sea Ice in the Arctic Ocean: Implications for Climate, Environment and Sedimentation
I. R. Wollenburg, S. L. Pfirman, and M. A. Lange 668

Environmental Marine Geology of the Arctic Ocean
P. J. Mudie 669

Section G: *Aerosols/Trace Gases* 671

Chemical Changes in the Arctic Troposphere at Polar Sunrise
L. A. Barrie 673

Arctic Haze and Air Pollution
J. M. Pacyna and G. E. Shaw 674

A Polar Climate Iteration?
A. W. Hogan, D. Riley, B. B. Murphey, S. C. Barnard, and J. A. Samson 681

The Role of the Polar Regions in the Global Carbon Cycle and Related Climatic Changes
E. P. Borisenkov 687

The Influence of Arctic Haze and Radiatively Active Trace Gases on the Arctic Climate
J.-P. Blanchet 693

AGASP-III, Polar Lows and CEAREX Norwegian Arctic Flight Program, Spring 1989
R. C. Schnell, P. J. Sheridan, and J. D. Kahl 694

Comparison of Measurements of Aerosol Black Carbon at Barrow, Alaska, and Wrangel Island, USSR: An Approach to Estimating the Deposition of Soot to Snow and Ice Surfaces
A. D. A. Hansen, R. C. Schnell, J. D. Kahl, B. A. Bodhaine, and V. N. Kapustin 695

A Review of Arctic Gas Hydrates as a Source of Methane in Global Change
K. A. Kvenvolden 696

Methane and Nitrous Oxide in Arctic Permafrost
R. A. Rasmussen and M. A. K. Khalil 702

Depletion in Antarctic Ozone and Associated Climatic Change
M. Lal 703

Contamination of the Arctic Air During the Megahaze Vent in Late Winter, 1986
M. DjupstrHom, J. M. Pacyna, G. E. Shaw, J. W. Winchester, and S.-M. Li 707

Individual Particle Analysis of the Springtime Arctic Aerosol, 1983–1989
P. J. Sheridan, R. C. Schnell, and J. D. Kahl 708

Deposition of Metals from the Atmosphere at the North Pole Compared to Background Regions of the Northwestern U.S.S.R.
V. N. Adamenko, K. Ya. Kondratyev, and S. A. Sinyakov 716

Seasonal Change and Chemical State of Polar Stratospheric Aerosols
Y. Iwasaka, M. Hayashi, A. Nomura, Y. Kondoh, S. Koga, M. Yamato, P. Aimedieu, and W. A. Matthews 720

Tropospheric Nitrogen Oxide Measurements at Barrow, Alaska
D. A. Jaffe and R. E. Honrath 730

Observations of Ozone and Related Quantities by the Japanese Antarctic Research Expedition
H. Kanzawa and S. Kawaguchi 735

Ozone Evolution Peculiarities in the Polar Regions: Analysis of Observational Data and Results of Modeling
I. I. Mokhov 736

Uncertainties in Total Ozone Amounts Inferred from Zenith Sky Observations: Implications for Ozone Trend Analyses
K. Stamnes, S. Pegau, and J. Frederick 741

Permafrost-Associated Gas Hydrates of Northern Alaska: A Possible Source of Atmospheric Methane
T. S. Collett 742

The Role of Natural Gas Hydrates in Global Changes
Y. F. Makogon 743

Volcanic Eruption Events and the Variations in Surface Air Temperature over High Latitude Regions
J. Pengqun 744

Satellite and Slow-Scan Television Observations of the Rise and Dispersion of Ash-Rich Eruption Clouds from Redoubt Volcano, Alaska
J. Kienle, A. W. Woods, S. A. Estes, K. Ahlnaes, K. Dean, and H. Tanaka 748

Bromine and Surface Ozone Atmospheric Chemistry at Barrow, Alaska During Spring 1989
W. T. Sturges, R. C. Schnell, and S. Landsberger 751

PANEL DISCUSSIONS: Summary and Recommendations **757**

PHOTO COLLAGE **762**

ADDRESSES OF PRIMARY AUTHORS **765**

AUTHOR INDEX **773**

Section A:

Detection and Monitoring of Change

Chaired by

R. Thomas
NASA Headquarters
U.S.A.

P. Wadhams
Scott Polar Research Institute
England

Polar Regions and Global Change: the Role of Remote Sensing

K. Ya. Kondratyev
The U.S.S.R. Academy Institute for Lake Research, Leningrad, U.S.S.R.

ABSTRACT

The fashionable notion of the Arctic as a weather kitchen, which existed during the 1930s, has since been forgotten. It is true, however, that the role of polar regions as sinks of energy for the climatic system, areas of specific cloud–radiation interaction as well as unique interaction between photochemistry, polar stratospheric clouds (PSC), dynamics, solar activity (the Antarctic ozone hole), etc. has been broadly recognized. It is equally true that polar regions are highly sensitive in ecological respects, including the impact of greenhouse gases and the early warning of global climate change at high latitudes. This is why the environmental monitoring of polar regions is of particular importance and where satellite remote sensing can undoubtedly play a decisive role.

The following areas of remote sensing application are discussed in the paper: (i) cloud cover properties (including PSCs) as well as interaction between extended cloudiness and radiation; (ii) Arctic haze phenomenon; (iii) Antarctic ozone hole; (iv) polar ice cover dynamics; (v) high-latitude biosphere dynamics. A special value of combined in situ and satellite observations, such as those during the Soviet–American Bering Sea Experiment is emphasized.

AD-P007 260

Variations in Sea Ice Thickness in the Polar Regions

Peter Wadhams
Scott Polar Research Institute, University of Cambridge, England

92-17942

ABSTRACT

An overview paper is presented on the evidence for variations in sea ice thickness in the polar regions. Most ice thickness data in the Arctic come from upward-looking sonar profiling by submarines. The available dataset is large, but the sampling has been necessarily unsystematic, so that only very few cases exist of directly comparable profiles from different years or seasons in the same location. Comparisons made so far are reviewed. They show that large fluctuations of mean ice thickness can occur over significant areas (15% over 300,000 km^2) but that these are associated strongly with variability in the field of ice motion in regions upstream of land boundaries, where ice deformation is usually an important contributor to the mean draft. Comparisons made in the Trans Polar Drift Stream far from land boundaries show a remarkable consistency in mean draft between seasons and years. In the Antarctic ice thickness data are much sparser, and most have been obtained by direct drilling. Most of the available winter data come from only two cruises, the 1986 and 1989 Weddell Sea cruises of F.S. *Polarstern*. They show that first-year ice, which comprises most of the ice in the Antarctic, is remarkably thin, with a mean thickness of about 60 cm when undeformed. Second-year ice, found in the western Weddell Sea, is much thicker (1.17 m mean thickness when undeformed). Pressure ridging adds about 42% to the mean drafts due to undeformed ice alone, but most ridges are very shallow (less than 5 m deep). There is no evidence of temporal variations between the two cruises, although winter ice extent in the Atlantic sector was much greater in the second year.

INTRODUCTION

Do we have any evidence that the mean thickness of sea ice is changing in the Arctic or Antarctic? The question is an important one because most recent numerical models of the response of the global climate to an increase in atmospheric CO_2 predict that a warming will occur which is greatest in the polar regions, and especially in the Arctic. Examples are the model of Hansen et al. [1988], where it is predicted that over 60 years mean annual temperatures will rise by 3–5°C in the Arctic and in parts of the Antarctic (Weddell and Ross Sea regions); and the model of Stouffer et al. [1989] in which over the same period a 3–4°C rise is predicted for the Arctic but only 0.5–1.5°C for the Antarctic. The large disagreement in Antarctic predictions is a product of the different way in which oceanic heat transport is treated in the two models, and reflects the pitfalls inherent in making model predictions at our current state of knowledge of climatic processes. The good agreement in the Arctic occurs because land processes dominate at high northern latitudes.

The two main physical mechanisms invoked for an enhanced Arctic warming are the stability of the Arctic atmosphere, so that warming is concentrated within a thinner layer of troposphere than at lower latitudes; and the ice–albedo feedback effect. The latter effect occurs because if ice or snow cover retreats as a consequence of warming, an area with an albedo of about 0.9 (fresh snow) to 0.4–0.6 (summer sea ice surface) is replaced by land terrain or water (0.15 or less), thus enhancing the fraction of radiation absorbed. The albedo feedback effect is expected to be stronger in the Arctic because of the scope for radical change in the extent of

snow cover on land. Snow extent at present varies from 48 x 10^6 km^2 in winter to 4 x 10^6 km^2 in summer (largely the Greenland and other permanent ice caps), compared to an annual sea ice extent variation of 15 x 10^6 km^2 in winter to 8 x 10^6 km^2 in summer. The considerable scope for snow-line retreat is not shared by the Antarctic, where the land mass is permanently ice-covered and only the sea ice cover can participate in ice–albedo feedback.

Thus, despite many unknowns (such as the effect of cloudiness changes which may accompany changes in sea ice extent) there is a reasonable physical basis for the view that, in the Arctic, global warming will be greatly enhanced relative to low latitudes, and may therefore be detectable at an early stage in the form of snow line retreat, permafrost melt, sea ice retreat and sea ice thinning. In the Antarctic enhanced warming is predicted by some models and would also result in the retreat and thinning of sea ice.

It is therefore important that we seek evidence of presently occurring changes in cryospheric parameters. In the case of sea ice, extent is comparatively easy to measure from satellite imagery, and so in this paper we concentrate on thickness, which is a much more difficult quantity to monitor synoptically.

PRESENT KNOWLEDGE OF SEA ICE THICKNESS IN THE ARCTIC

The first systematic measurements of ice thickness in the Arctic were made by Nansen [1898], who drilled through undeformed ice during the drift of *Fram*. Many subsequent drilling campaigns have followed. Rothrock [1986] showed that a reasonable estimate of mean thickness can be obtained from a few hundred holes, so long as these are drilled in a completely random fashion, while Eicken and Lange [1989] obtained a reasonable approximation to an Arctic ice thickness distribution in this way. In general, however, we have to conclude that although drilling may yield a usable estimate of local ice thickness characteristics, to obtain data on a regional or basin-wide scale with a sufficient sampling density it is necessary to use a remote sensing technique from above or below.

To date, almost all the usable data from which we can deduce ice thickness distributions over the Arctic come from surveys by military submarines using upward-looking sonar. The sonar measures range to the ice underside, which is converted into draft using a sea level datum obtained either from the profile itself (by interpolation between water openings) or from an independent pressure gauge. Draft distribution can then be converted into thickness distribution by use of an appropriate isostatic factor, a reasonable figure for the Arctic being 1.12. Corrections have to be applied for beamwidth effects; these have been discussed by Wadhams [1981]. Mean ice drafts are usually derived by averaging profile data over 50–100-km track lengths; this results in a mean draft with a standard error of 0.05–0.06 m on statistical grounds alone [Wadhams and Horne, 1980]. The reliance on submarines has caused the survey coverage of the Arctic to be unsystematic both in time and space, with limited opportunities for direct comparisons between datasets obtained along identical tracks.

It should be noted that several other techniques hold promise for more systematic monitoring of Arctic ice thickness in the future. *Laser profiling* measures ice freeboard, but in a recent laser–sonar experiment [Wadhams, 1990b; Comiso et al., 1991] it was found that an excellent correlation between freeboard and draft probability density functions was obtained, with an appropriate isostatic factor, suggesting that laser profiling alone can be an adequate thickness monitoring technique. *Upward sonar* has been mounted on fixed moorings [Vinje, 1989], yielding valuable time series information in critical regions such as Fram Strait, which defines the ice outflow from the Arctic Basin. Sonar could also be mounted on autonomous underwater vehicles or on neutrally buoyant floats. *Acoustic tomography*, although designed to measure ocean structure, should also yield a signal due to an ice cover, from which the modal draft may be obtained [Guoliang and Wadhams, 1989]. Results from a 1988–1989 Greenland Sea experiment are now being analyzed. *Electromagnetic techniques* are difficult to apply, because of scattering and attenuation from the brine content of the sea ice, but some success has been obtained by impulse radar at about 100 MHz and by induction methods from the air [Holladay et al., 1990]. Finally, *satellite sensors* such as passive microwave and synthetic aperture radar may yield useful information by empirical correlations with sonar data, while satellite-borne radar altimetry holds promise despite difficulty in interpretation of the location of the reflecting horizon in sea ice.

The results of several specific regional studies of ice thickness distribution have been reported, covering many parts of the Arctic Basin, Beaufort Sea, Northwest Passage, Davis Strait and Greenland Sea [e.g., Kozo and Tucker, 1974; Williams et al., 1975; Wadhams and Horne, 1980; Wadhams, 1981, 1983, 1989a, 1990a; McLaren et al., 1984; Wadhams et al., 1985; McLaren, 1989]. An attempt to merge these and other results, including semi-quantitative data from cruise reports, into a systematic set of seasonal mean thickness contours was made by Bourke and Garrett [1987]. Their maps show that the main pattern of thickness variation comprises a thickening across the Arctic Basin starting from the seas north of the USSR, where the mean thickness is only about 2 m and where most ice is first-year, and progressing to the parts of the Canada Basin and Eurasian Basin lying north of Greenland and the Canadian Archipelago, where mean thicknesses may reach 6–7 m. This is partly an effect of increasing age of the ice as one moves downstream in the Trans Polar Drift Stream (the mean reaches about 4.5 m at the pole itself) or in the Beaufort Gyre where ice can circulate for many years; and partly an effect of the buildup of ridging as the ice approaches a fixed downstream land boundary. This pattern fits the predictions of the ice dynamics model of Hibler [1980] with good agreement.

LIKELY EFFECTS OF WARMING ON ICE THICKNESS

The simplest effect of warming is likely to be on the thickness of fast ice, which grows in fjords, bays and inlets in the Arctic, along the open coast in shallow water, and in channels of restricted dimensions. Because this type of ice generally forms in shallow water, oceanic heat flux is small or non-existent, and the thickness of the ice is determined almost entirely by air temperature history (modified by the thickness of the snow cover, which alters the growth rate). Empirical relationships have been successfully developed

relating thickness achieved to the number of degree days of freezing since the beginning of winter [e.g., Bilello, 1961]. We can easily see from such curves that if the average daily air temperature increases by a known amount, the ultimate ice thickness will diminish by a calculable amount, and the ice-free season will lengthen. Using this technique, Wadhams [1989b] predicted that in the Northwest Passage and Northern Sea Route an air temperature rise of 8°C (equivalent to about a century of warming) will lead to a decline in the winter fast ice thickness from 1.8–2.5 m (depending on snow thickness) to 1.4–1.8 m and an increase in the ice-free season from 41 days to 100 days. This effect would be of great value to the extension of the navigation season in the Soviet Northern Sea Route and the Northwest Passage.

In moving ice the effect is much more difficult to predict. Presumably the thickness of undeformed (i.e., thermodynamically grown) sea ice will decrease, but a large part of the ice in the Arctic is in the form of ridging, and ridging may occur more readily in thinner ice. It is reasonable to expect an overall thinning and retreat, but it is not a simple matter to predict magnitudes.

EVIDENCE OF CHANGES IN MEAN ICE THICKNESS

In order to assess reliably whether ice thickness changes are occurring in the Arctic it is necessary to obtain area-averaged observations of mean ice thickness over the same region using the same equipment at different seasons or in different years. Ideally the region should be as large as possible, to allow us to assess whether changes are basin-wide or simply regional. Also the measurements should be repeated annually in order to distinguish between a fluctuation and a trend. Because of the unsystematic nature of Arctic submarine deployments this goal has not yet been achieved, but a number of comparisons between pairs of datasets have been carried out.

McLaren [1989] compared data from two U.S. Navy submarine transects of the Arctic Ocean in August 1958 and August 1970, stretching from Bering Strait to the North Pole and down to Fram Strait. He found similar conditions prevailing in each year in the Eurasian Basin and North Pole area, but significantly milder conditions in the Canada Basin in 1970. Since the two cruises employed different sonar systems, it is difficult to assess the significance of the result. If valid, it is possibly due to anomalous cyclonic activity as observed in the region in recent summers [Serreze et al., 1989]. Another possibility is that since August is the month of greatest ice retreat in the Beaufort Sea, the difference is simply due to differences between the extent to which the ice retreated in the Chukchi and southern Beaufort Seas during the respective summers. The extent and duration of the open water season in the Beaufort Sea is known to have a high interannual variation, and an unusually open southern Beaufort Sea would lead to more open conditions within the

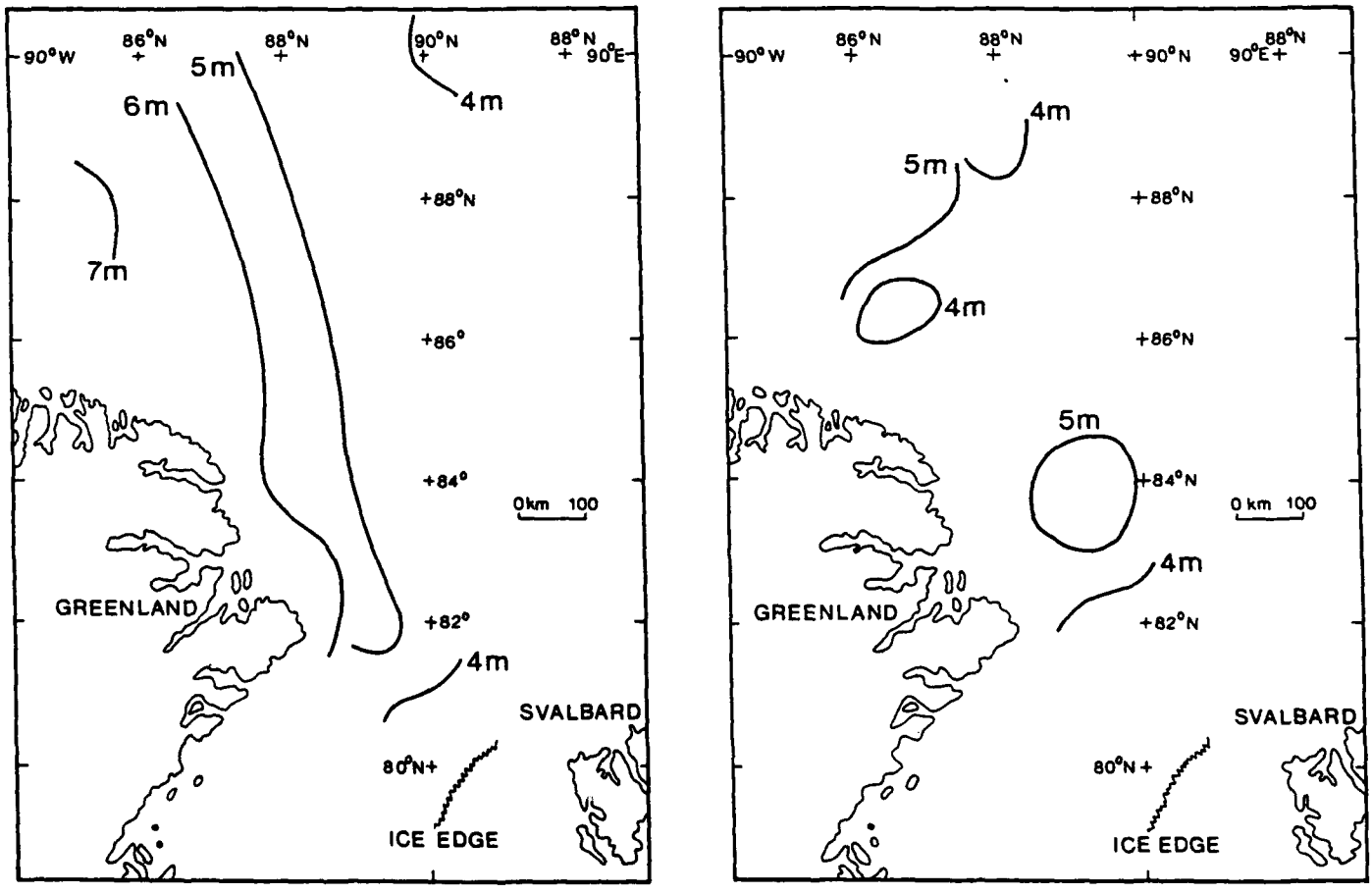


Figure 1. (a) Contour map of mean ice drafts from submarine cruise of October 1976. (b) Contour map of mean drafts from cruise of May 1987 [after Wadhams, 1990a].

	N–S transect		E–W transect	
	1976	1987	1976	1987
Mean draft (m)	6.09	5.31	6.32	4.07
Ice < 2 m draft (%)	11.6	16.7	7.9	29.9
Ice 2-5 m draft (%)	48.7	38.6	46.5	39.6
Ice > 5 m draft (%)	39.7	44.7	46.0	30.5
Refrozen leads (%)	4.0	7.9	3.7	15.6

Table 1. Comparisons of ice statistics from 1976 and 1987 datasets.

pack itself.

Wadhams [1989a] compared mean ice thicknesses for a region of the Eurasian Basin lying north of Fram Strait, from British Navy cruises carried out in October 1976, April–May 1979 and June–July 1985. All three datasets were recorded using similar sonar equipment. I found that a box extending from 83°30'N to 84°30'N and from 0° to 10°E had an especially high track density from the three cruises (400 km in 1976, 400 km in 1979, and 1800 km in 1985), and this was selected for the comparison. It is a region far from any downstream boundary, and represents typical conditions in the Trans Polar Drift Stream prior to the acceleration and narrowing of the ice stream which occurs as it prepares to enter Fram Strait. The mean thicknesses from the three cruises were remarkably similar: 4.60 m in 1976, 4.75 m in 1979, and 4.85 m in 1985. It should be remembered that these datasets were recorded in different seasons as well as different years.

More recently I was able to compare data from a triangular region extending from north of Greenland to the North Pole, and recorded along almost identical tracks in October 1976 and May 1987 [Wadhams, 1990a]. Mean drafts were computed over 50-km sections, and each value was positioned at the centroid of the section concerned; the results were contoured to give the maps shown in Figure 1. There was a decrease of 15% in mean draft averaged over the whole area (300,000 km^2), from 5.337 m in 1976 to 4.548 m in 1987. Profiles along individual matching track lines (Figure 2) show that the decrease was concentrated in the region south of 88°N and between 30° and 50°W. From Figure 1 it appears that the buildup of pressure ridging which gave the high mean drafts near the Greenland coast in 1976 was simply absent in 1987, but in fact the situation is not that simple. I compared the probability density functions of ice thickness from the pairs of profiles shown in Figure 2 (strictly, two 300-km sections from the southern part of the N–S transect and two 200-km sections from 40–50°W in the E–W transect). The results are shown in Table 1. In 1987 there was more ice present in the form of young ice in refrozen leads (coherent stretches of ice with draft less than 1 m) and as first-year ice (draft less than 2 m). There was less multi-year ice (interpreted as ice 2- to 5-m thick) and less ridging (ice more than 5 m thick) in 1987 in the E–W transect, although slightly more ridged ice in the N–S transect. The main contribution to the loss of volume appears to be, then, the replacement of multi-year and ridged ice by young and first-year ice.

To determine how this may have occurred I examined the tracks of drifting buoys from the Arctic Ocean Buoy Program [Colony and Rigor, 1989; R. L. Colony, personal communication]. Four buoys were in the region during the months prior to the 1987 cruise (Figure 3). The three in the westernmost positions, corresponding to a portion of the Beaufort Gyre, remained almost stationary during the period January–May 1987, while buoy 1897, in the Trans Polar Drift Stream, moved towards Fram Strait at an average speed of 2 km per day. The result of this anomalous halting of the motion of part of the Beaufort Gyre would be a divergence within the experimental region, as the Trans Polar Drift Stream ice continued its motion towards the southeast. This would lead to the opening up of the pack, creating areas of young and first-year ice. Thus the indications are

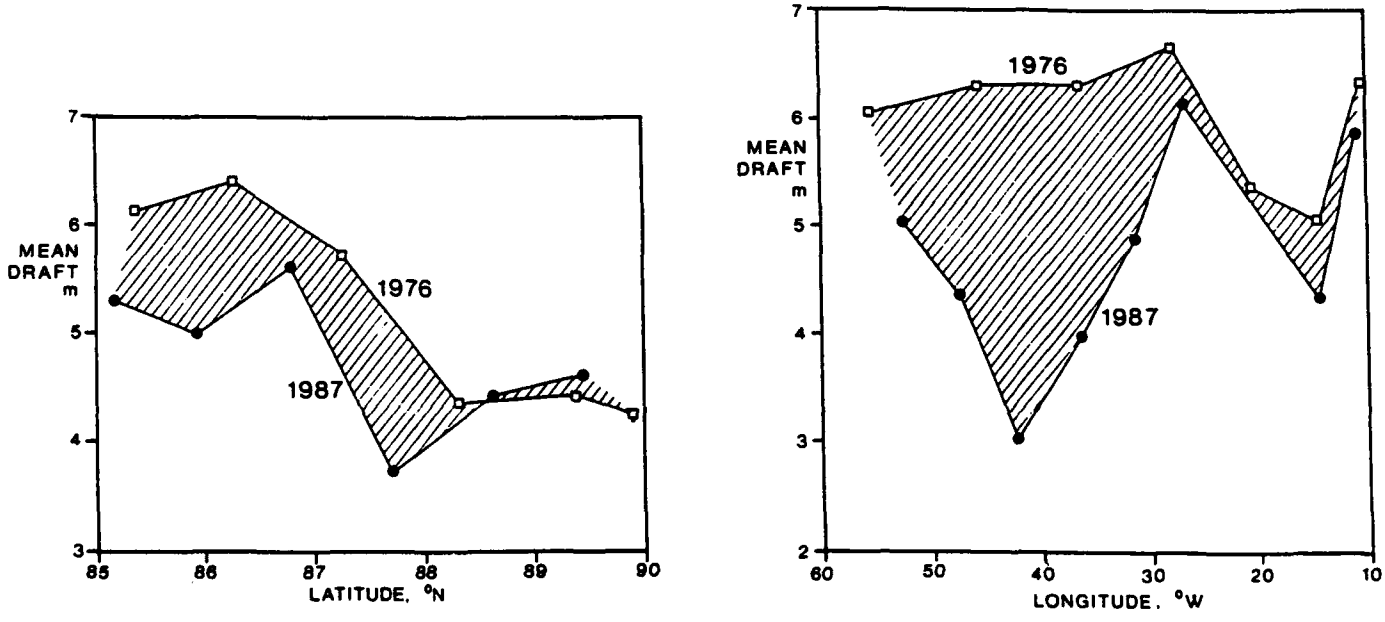


Figure 2. (a) Comparison of mean ice drafts from 1976 and 1987 along a N–S transect from North Pole to 85°N. (b) Comparison for transect across north of Greenland from 60°W to 10°W.

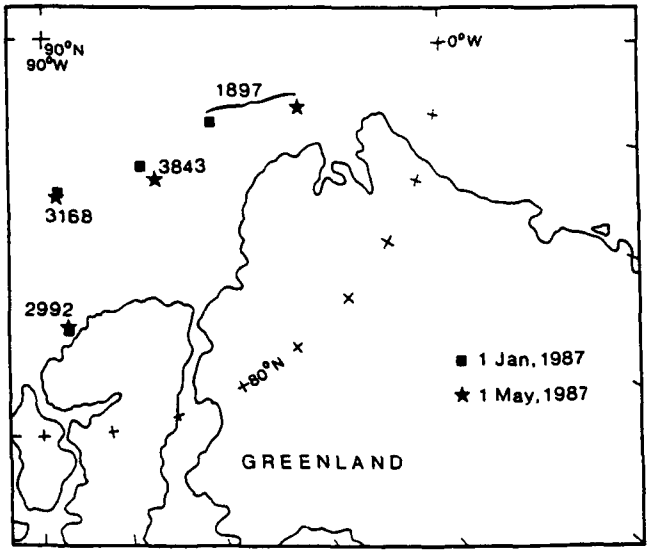


Figure 3. Positions of drifting buoys north of Greenland on 1 January and 1 May 1987.

that it is an ice motion anomaly rather than, or as well as, an ice growth anomaly that is responsible for the observed decrease in mean ice draft. This supposition is supported by modeling results from J. Walsh [personal communication], who ran the Hibler ice model using daily wind forcing and monthly thermodynamic forcing, both varying interannually. He found that the simulated thicknesses showed negative anomalies in this region in May 1987 and positive anomalies in October 1976.

Further observations are clearly necessary from other years (past, recent and future), and a closer study should be made of pressure fields over the Arctic and the variations that they may be capable of creating in the geographical distribution of mean ice drafts. One of the surprising aspects of the results described above is that the buildup of mean ice draft towards Greenland was thought to be a very stable aspect of the ice climatology of the Arctic, appearing consistently in the model predictions of Hibler [1980] and in the tentative seasonal climatology of Bourke and Garrett [1987]. It appears that the ice cover, like the ocean, possesses a weather as well as a climate, and it is vital that sufficient data be examined to resolve details of this weather such that the underlying trend in basin-wide mean ice thickness, if any, can be revealed. In this respect the author is now examining more recent datasets.

A final regional comparison which the 1987 dataset has made possible occurs in the region immediately north of Fram Strait, between 82°N and 80°N (Figure 4). Here I was able to compare data from the four years 1976, 1979, 1985 and 1987. This is a region which is ice-covered in most years, and where mixing occurs between the various ice streams preparing to enter Fram Strait, notably the streams of old, deformed ice moving south from the North Pole region and southeast from the region north of Greenland; and the stream of younger, less heavily deformed ice moving southwest from the seas north of the USSR. Figure 4 shows all available mean drafts from 50-km sections [from Wadhams, 1981, 1983, 1989a and current analyses]. There is very good consistency among these four datasets, regardless of year or season of generation; fluctuations appear to be random in character, and where centroids from different experiments lie close to one another, the mean drafts are usually similar. Only the 1976 data points appear somewhat thicker than their neighbors.

From the data comparisons made so far in the Arctic, we can thus draw the following tentative conclusions:

(1) Ice reaching Fram Strait via the Trans Polar Drift Stream along routes where it is not heavily influenced by a

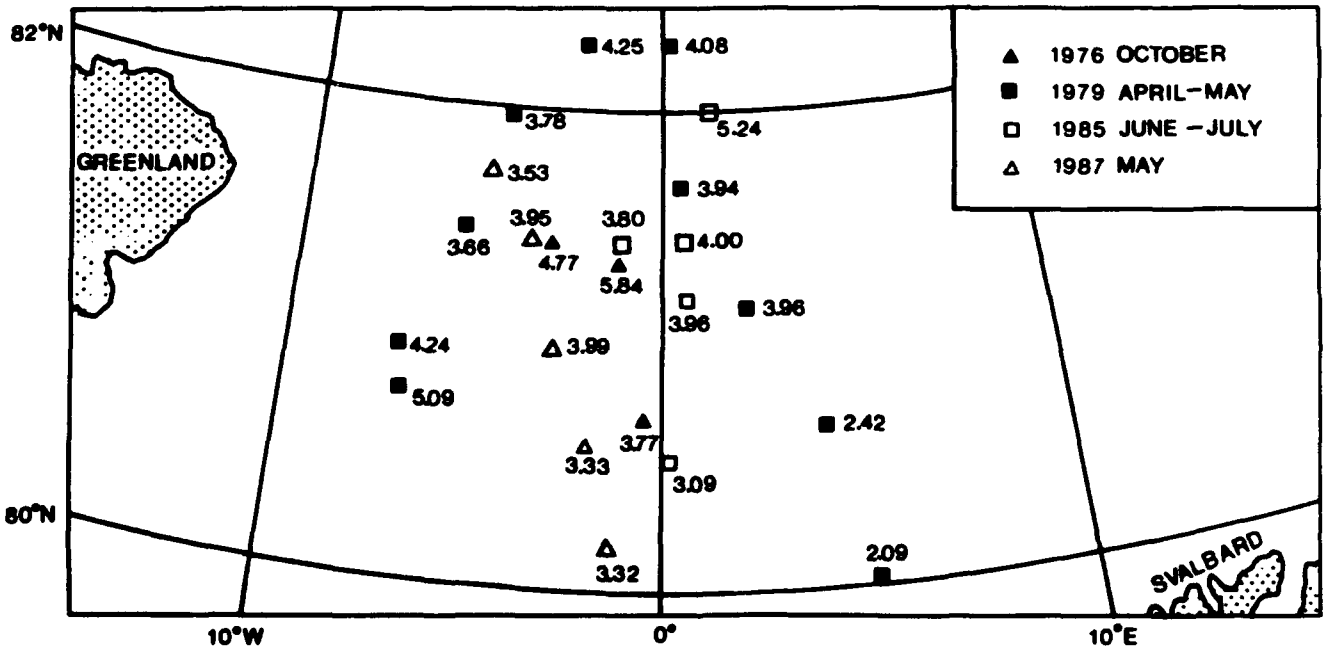


Figure 4. A comparison of mean ice drafts near the entrance to Fram Strait obtained from cruises in 1976, 1979, 1985 and 1987.

downstream land boundary shows great consistency in its mean thickness from season to season and from year to year, at latitudes from 84°30'N to 80°N and longitudes in the vicinity of 0°.

(2) Ice upstream of the land boundary of Greenland can show great changes in its mean ice draft, but it is possible to ascribe these to anomalies in the balance between pressure ridge formation through convergence (the normal source of a high ice draft in the region) and open water formation through divergence (the anomalous situation). A deeper knowledge of wind field anomalies is needed to understand these changes fully, together with more adequate datasets.

(3) Ice in the Canada Basin in summer also appears to show great variability in mean ice draft, but here there is a free boundary with ice-free marginal seas, permitting relaxation of the ice cover into a less concentrated state under certain wind conditions.

We cannot yet conclude that there is conclusive evidence of systematic thermodynamic thinning of the sea ice cover, as would be caused by the impact of the greenhouse effect.

ICE THICKNESS IN THE ANTARCTIC

Sea ice thickness data from the Antarctic are much sparser than from the Arctic. There has been no opportunity to carry out submarine sonar profiling, and almost all available data come from drilling. The only profiling data of any kind are airborne laser profiles of the upper surface [Weeks et al., 1989] and some limited thickness profiling by impulse radar from a helicopter [Wadhams et al., 1987]. Laser data are valuable in delineating the occurrence of pressure ridging and in assessing its likely contribution to the overall thickness distribution, but cannot be used reliably to infer ice thickness directly by isostasy, largely because of the effect of the thick and variable snow cover. In the Arctic, on the other hand, it has been shown in laser–sonar comparisons that laser data can indeed be used to give a good estimate of the ice thickness distribution [Comiso et al., 1991]. The usefulness of impulse radar in the Antarctic is limited by the fact that the first-year ice is thin and has a high salinity, and by the unconsolidated nature of ridges, which present misleading water horizons to the electromagnetic radiation; thus, such radar has only been used as an auxiliary to drilling efforts [Wadhams et al., 1987].

The first drilling measurements of Antarctic sea ice thickness were from shore stations, and tended to give an unrealistically high estimate of typical thicknesses, since coastal waters offer lower average air temperatures from continental influence, a lower oceanic heat flux, and the possibility of surface water modification (e.g., supercooling) following residence under nearby ice shelves. The first measurements from within the pack ice itself were made in summer [Ackley, 1979] and demonstrated the typical multi-year ice thicknesses in the western Weddell Sea.

It is the winter pack which is of real global importance, however. The annual variation in sea ice area in the Antarctic is from 4×10^6 km^2 in February to 20×10^6 km^2 in September [Zwally et al., 1983], and so it is of the greatest importance to know the thickness of the ice which covers such a vast area of ocean for part of the year. The first penetration of the pack during Antarctic spring was the cruise of the *Mikhail Somov* in October–November 1981, which reached 62.5°S in the eastern Weddell Sea [Ackley et al., 1982], but it was not until 1986 that the first deep penetration into the circumpolar Antarctic pack during early winter, the time of ice edge advance, took place. This was the Winter Weddell Sea Project (WWSP) cruise of F.S. *Polarstern*, during which systematic ice thickness measurements were made throughout the eastern part of the Weddell–Enderby Basin, from the ice edge to the coast, covering Maud Rise and representing a typical cross-section of the first year circumpolar Antarctic pack during the season of advance [Wadhams et al., 1987; Lange et al., 1989]. A second winter cruise was carried out in 1989: the Winter Weddell Gyre Study (WWGS) of Alfred Wegener Institute involved a crossing of the Weddell Sea from the tip of the Antarctic Peninsula to Kap Norvegia in the east during September–October, and thus allowed the multi-year ice regime of the western Weddell Sea to be studied in midwinter [Wadhams and Crane, 1991]. During the later part of this cruise, and in collaborative work carried out by *Akademik Fedorov*, ice conditions were studied in the same region of the eastern Weddell Sea as was covered by *Polarstern* in 1986, permitting the first interannual comparison of ice thicknesses in the same region of the seasonal pack to be carried out.

Ice thickness measurements in both cruises were made by drilling holes at 1-m intervals along lines of about 100 holes. Typically, during a daily ice station, two such lines would be laid out at right angles to one another, with an attempt at a random choice of location so that ridges were properly represented in the results. Clearly very thin ice and open water could not be sampled, but their contribution to the overall PDF was estimated from the results of aerial photography and video recording. Ice thickness, snow thickness and freeboard (hence ice draft) were measured in each hole. Cores were taken at each site to examine ice composition and character.

In the 1986 experiment our first discovery was a new mechanism for the formation of ice at the advancing edge, the so-called pancake–frazil cycle [Lange et al., 1989]. We found that the ice which first forms at such an edge, in a region of high turbulence and wave activity, does so in the form of frazil ice, a suspension of small ice crystals in water. As the suspension thickens, it congeals into small cakes called pancakes, probably by wave-induced compression as described by Martin and Kauffman [1981]. At the ice margin the pancakes are only a few centimeters in diameter, but with increasing penetration into the pack they grow to reach 3–5 m in diameter and about 50 cm in thickness. The growth occurs by accretion from the frazil, facilitated by the continued presence of an open water surface which allows latent heat to be dissipated. The pancakes begin to freeze together in groups as one proceeds further from the margin, but it required (in the 1986 experiment) some 270 km of penetration before the wave field was damped down sufficiently to permit the pancakes to freeze together fully, the frazil acting as "glue." The final product was an ice type, consolidated pancake, in which the typical thickness was that of one of the original pancakes (50–60 cm), but with a rough bottom caused by rafting of two or three pancakes over one another at the time of freeze-up (Figure 5a). It was found that the closure of the sea surface cut down the subsequent growth rate to a very low value (estimated at 0.4 cm per day) so that across the entire remainder of the pack to the coast the mean thickness increased by only a few centi-

meters. Within this first-year pack ice new smoother ice would form by freezing in the calm waters of polynyas. Ridging was scarce, except very close to the coast where episodes of wind-induced shoreward motion would have led to the observed increase. Most ridges were also very shallow, less than 6 m in draft. Examination of the structure of ridges showed that they are formed by the buckling of the floe itself, rather than the crushing of refrozen leads between thicker floes. Thus a compressive stress can be relieved by the creation of a number of small ridges rather than one large ridge.

The end product of these processes was an ice thickness distribution shown in Figure 6 [after Wadhams et al., 1987]. Note the peak at the very low value of 50–60 cm, with a peak in snow cover thickness at 14–16 cm. The snow cover was sufficient to push the ice surface below water level in some 17% of holes drilled, and this leads to water infiltration into the snow layer and the possibility of formation of a new type of ice, snow-ice, at the boundary between ice and overlying snow. The mechanism of formation of most of the ice out of frazil and pancake explains earlier structural observations [Gow et al., 1982] which showed most of the thickness of ice cores from the Antarctic to be composed of small randomly oriented frazil-like crystals, rather than the long columnar crystals characteristic of freezing onto the bottom.

It is reasonable to suppose that these mechanisms are typical of the entire circumpolar advancing ice edge in winter (neglecting embayments such as the Ross and Weddell Seas). This implies that the first-year ice, which makes up the bulk of the winter pack, has a low mean draft of less than 1 m.

Multi-year ice was virtually absent in the region covered by the 1986 cruise. Only a small number of thick "islands" were seen (up to 11 m thick), which are thought to be very old fast ice broken out from sites along ice shelf fronts. Only in 1989 were we able to sample both first- and multi-year ice in an intimate combination, in the western Weddell Sea. The Weddell Gyre carries ice from the eastern Weddell Sea deep into high southern latitudes in the southern Weddell Sea off the Filchner–Ronne Ice Shelf, and then northward up the eastern side of the Peninsula. This journey takes about 18 months, and so permits much of the ice to mature into multi-year (strictly, second-year) ice. Such ice was seen only west of 40°W in our crossing of the Weddell Sea, the zone which experiences the northward drift regime.

Class	Holes		Mean thickness Snow	Ice	Draft	Total
Undeformed First-year	2034	Mean	0.16	0.60	0.60	0.76
		St Dev	0.10	0.21	0.20	0.25
Deformed First-year	2195	Mean	0.23	1.03	1.00	1.26
		St Dev	0.17	0.60	0.55	0.64
Undeformed Multi-year	349	Mean	0.63	1.17	1.25	1.80
		St Dev	0.18	0.35	0.36	0.45
Deformed Multi-year	282	Mean	0.79	2.51	2.48	3.30
		St Dev	0.23	1.08	1.05	1.09
All ice	5339	Mean	0.26	0.97	0.96	1.23
		St Dev	0.23	0.73	0.70	0.86

Table 2. Mean ice thicknesses for different categories of ice floe drilled during 1989 Winter Weddell Gyre Study (courtesy of M. A. Lange).

Multi-year ice could be identified by its structure in cores, and by the very thick snow cover which it acquires, which is almost always sufficient to depress the ice surface below the waterline [Figure 5b]. Ice profile lines were divided into four types on the basis of this identification: undeformed first-year ice; first-year ice profiles containing deformed ice; undeformed multi-year ice; and multi-year profiles containing deformed ice. Table 2 shows the mean thickness results from these classes. It can be seen that:

(1) The mean thickness of undeformed multi-year ice (1.17 m) is about double that of first-year ice (0.60 m), indicating conditions in the southern Weddell Sea which permit much more rapid growth for an existing ice sheet than those experienced in the eastern Weddell Sea in 1986;

(2) The mean thickness of first-year ice throughout the Wed-

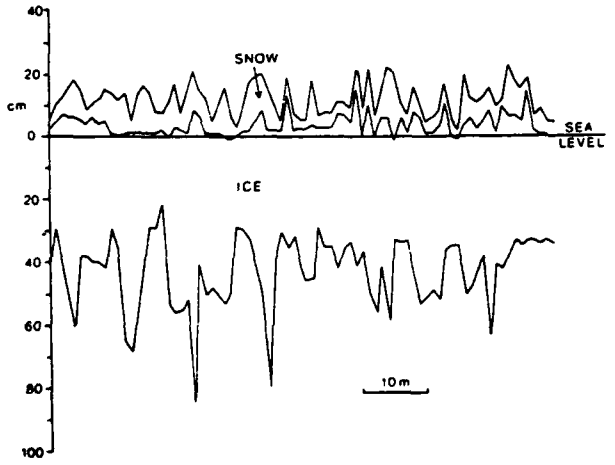


Figure 5. (a) A profile of first-year Antarctic sea ice of the consolidated pancake type, obtained from eastern Weddell Sea during 1986 *Polarstern* cruise. (b) A profile of multi-year ice obtained in western Weddell Sea during 1989 *Polarstern* cruise.

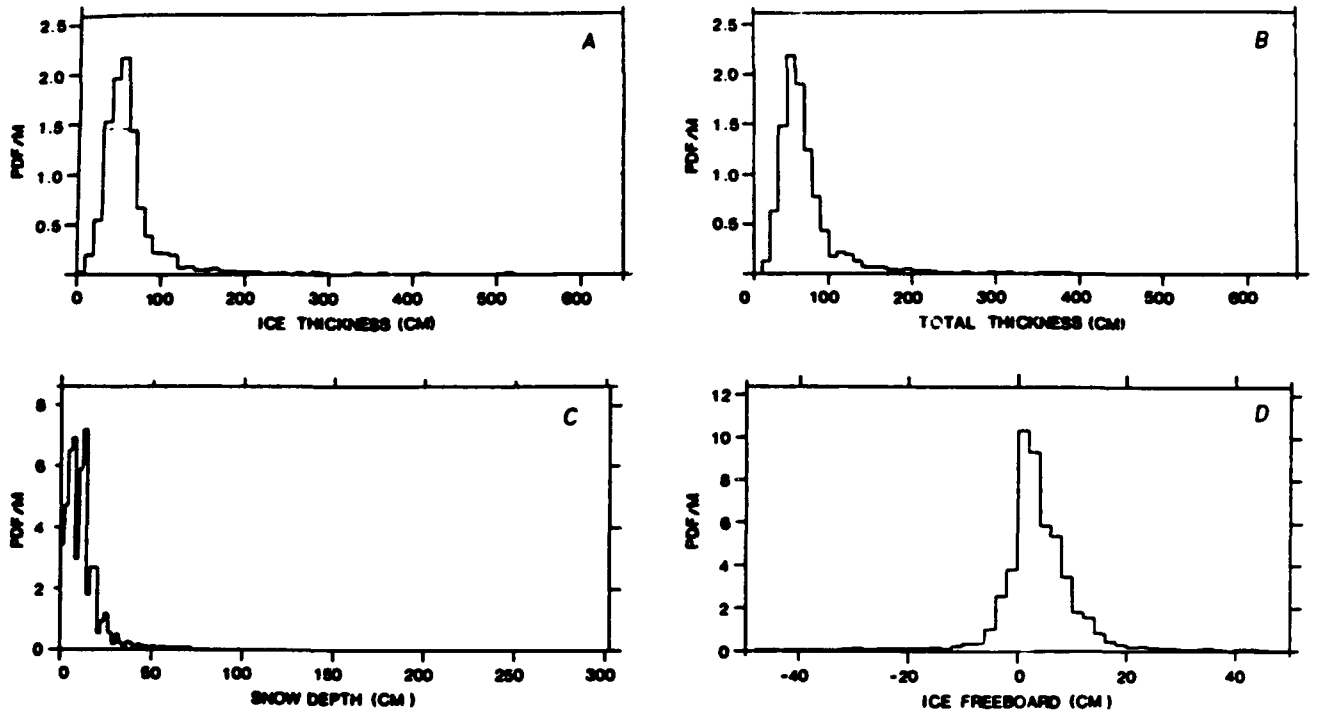


Figure 6. Probability density functions of first-year Antarctic ice thickness in eastern Weddell Sea, obtained during 1986 cruise [after Wadhams et al., 1987].

dell Sea is very similar to the thickness observed in 1986 in the Maud Rise area;
(3) The presence of ridging roughly doubles the mean draft of the 100-m floe sections in which it occurs (0.60 to 1.03 m in first-year; 1.17 to 2.51 m in multi-year); and
(4) Snow is very much deeper on multi-year ice (0.63–0.79 m) than on first-year (0.16 –0.23 m).
These classifications were carried out, and the table constructed, by M. A. Lange, and will form part of a forthcoming paper by Lange, Wadhams and Ackley.

If we consider only those ice stations in the passage northward out of the eastern Weddell Sea, i.e., the region covered in the 1986 results, we find mean ice thicknesses as shown in Figure 7. The results have been plotted over similar data from 1986. At first sight it appears that the thicknesses tend to be greater in 1989, but a number of factors should be noted. First, the 1986 plot was made to examine the thicknesses reached by the natural growth process; profiles consisting largely of ridging were excluded, and those with some ridging were represented with brackets around them, while in 1989 all profiles from the region are included. Second, the 1986 northward decline in mean thickness in the latitude range 62° to 58° represented the approach to a stationary, but compact, ice edge. In 1989 the ice edge lay much further north (the last ice was seen at 53°44'S), although its outer regions were diffuse and composed of wide bands, characteristic of off-ice winds. Consolidated pack ice could be studied as far north as 57°, at which point Figure 7 shows that there were some signs of melting (stations 4 and 5 relative to stations 1–3). The five ice stations north of 62° in which undeformed ice was profiled can therefore be seen as reproducing the trend of ice thickness against latitude seen in 1986, but with a bodily northward shift of about 3°.

We conclude that there is no evidence of a change in the thickness to which first-year ice grows by congelation in the eastern Weddell Sea between the 1986 and 1989 winters. The difference lay in the fact that the ice edge at this longitude lay much further north in 1989.

Thus, from the limited data available so far (4441 holes in 1986 and 5339 in 1989) we cannot detect a change in the thickness of Antarctic sea ice. The datasets are much too sparse, however, and meaningful results must await the development of a profiling method, from above or below, which will generate genuinely synoptic maps of mean thickness.

THE STABILITY OF ANTARCTIC SEA ICE

First-year Antarctic sea ice probably comprises at least 80% of the total Antarctic sea ice area in winter, and yet is very thin. This immediately suggests that it may be unstable under warming, and that one consequence of global warming may therefore be a radical reduction in Antarctic sea ice extent. Clearly there are regions in which instability may occur. The Weddell Polynya is a large region of open water which appeared in the middle of the winter pack, over Maud Rise, during the 1970s [Zwally et al., 1983] but has not recurred. Gordon and Huber [1990] postulate that oceanic heat flux can be higher over Maud Rise because of the influence of the bottom topography on the depth of the thermocline, causing it to become more shallow. A recent model by Martinson [1990] suggests, however, that over the Antarctic Ocean as a whole the winter sea ice cover may be quite stable. A typical predicted effect of greenhouse warming is

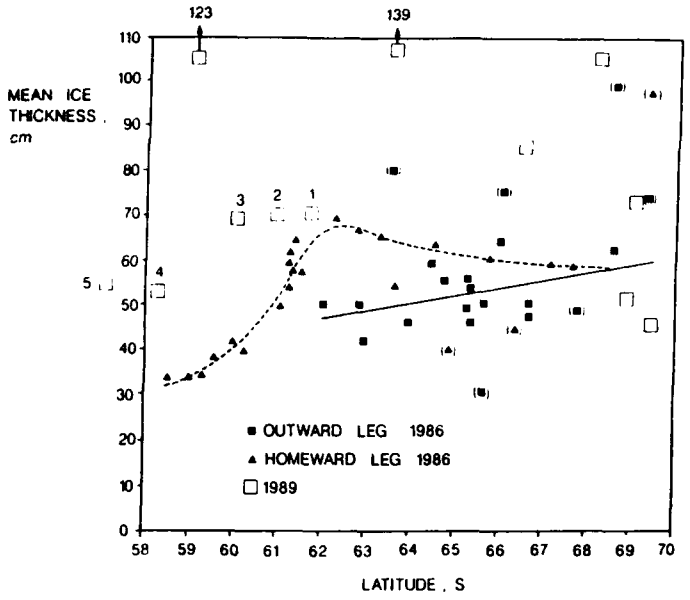


Figure 7. Mean ice thicknesses from ice stations in eastern Weddell Sea occupied during winter of 1989, compared with mean thicknesses from the same region obtained in winter 1986.

an increase in air temperature accompanied by a decrease in the vigor of the atmospheric circulation, which would lead to less divergence and less opening of leads. Martinson showed that a complex set of feedback mechanisms exists, involving the fractional area of open water, the salinity of the upper layer, and the depth of the thermocline. Variations in the input parameters as expected from global warming would not necessarily lead to disappearance of the ice but rather to adjustments in ice concentration and upper ocean structure. A winter sea ice cover, however thin, may therefore be a resilient feature of the Antarctic Ocean.

GENERAL CONCLUSIONS AND RESEARCH PRIORITIES

Models of global warming agree in predicting a greatly enhanced rate of temperature rise in the Arctic, and some models also predict enhanced warming in the Antarctic. This warming should manifest itself by a decrease in the area and the mean thickness of the sea ice cover. We may expect the thickness of fast ice to diminish as the most direct response to warming, and this would have important favorable economic consequences. The areal extent of moving pack ice is not coupled to air temperatures in such a simple way, and no predictions of the extent of retreat, or of the reduction in mean ice thickness, have yet been made.

Experimentally, the monitoring of ice extent is very reliable using satellites, and there is no evidence of any strong trend in sea ice area on a hemispheric scale. The monitoring of sea ice thickness on a scale sufficient to detect synoptic trends is extremely difficult. In the Arctic we have a large but unsystematic set of submarine sonar profiles which show, where comparisons are possible, that the mean ice thickness in the Trans Polar Drift Stream far from coasts is very stable, but that large fluctuations can occur in the mean thickness upstream of the Greenland land boundary (where heavy deformation usually takes place) and possibly also in the Canada Basin in summer. Further datasets, systematically collected from year to year within similar regions of the Arctic, are required to tell us whether these fluctuations represent only the range of normal variability or do represent the beginning of a trend.

In the Antarctic, ice thickness monitoring is in its infancy, and only two systematic datasets from winter exist, both representing drilling results. No evidence of thickness changes can be seen in them.

To achieve the level of reliability in synoptic monitoring that we seek, it is necessary to consider new methods of data gathering. The possibilities which have been summarized all have the advantage that they can be applied to the Antarctic where military activity is not allowed.

ACKNOWLEDGMENTS

I am grateful for the continuing support of the Office of Naval Research, Arctic Program, for the submarine work described in this paper; to Flag Officer Submarines, Royal Navy, Northwood, for access to submarines and submarine data; and of the Natural Environment Research Council for the Antarctic sea ice work.

REFERENCES

Ackley, S. F., Mass-balance aspects of Weddell Sea pack ice, *J. Glaciol., 24*, 391–405, 1979.

Ackley, S. F., S. J. Smith, and D. B. Clarke, Observations of pack ice properties in the Weddell Sea, *Antarct. J. U.S., 17*, 105–106, 1982.

Bilello, M. A., Formation, growth and decay of sea ice, *Arctic, 14*, 3–24, 1961.

Bourke, R. H., and R. P. Garrett, Sea ice thickness distribution in the Arctic Ocean, *Cold Regions Sci. & Technol., 13*, 259–280, 1987.

Colony, R. L., and I. Rigor, Arctic Ocean Buoy Program Data Report for 1 January 1986–31 December 1986, *Tech. Memo APL-UW TM 6-89*, Applied Physics Lab., U. Washington, Seattle, 1989.

Comiso, J. C., P. Wadhams, W. B. Krabill, R. N. Swift, J. P. Crawford, and W. B. Tucker III, Top/bottom multisensor remote sensing of Arctic sea ice, *J. Geophys. Res.*, 1991, In press.

Eicken, H., and M. A. Lange, Sea ice thickness data: the many vs the few, *Geophys. Res. Lett., 16*, 495–498, 1989.

Gordon, A. L., and B. A. Huber, Southern Ocean winter mixed layer, *J. Geophys. Res., 95*, 11655–11672, 1990.

Gow, A. J., S. F. Ackley, W. F. Weeks, and J. W. Govoni, Physical and structural characteristics of Antarctic sea ice, *Ann. Glaciol., 3*, 113–117, 1982.

Guoliang, J., and P. Wadhams, Travel time changes in a tomography array caused by a sea ice cover, *Prog. Oceanogr., 22*, 249–275, 1989.

Hansen, J., I. Fung, A. Lacis, D. Rind, S. Lebedeff, R. Ruedy, and G. Russell, Global climate changes as forecast by Goddard Institute for Space Studies three-dimensional model, *J. Geophys. Res., 93*, 9341–9364, 1988.

Hibler, W. D., III, Modeling a variable thickness sea ice cover, *Mon. Wea. Rev., 108*, 1943–1973, 1980.

Holladay, J. S., J. R. Rossiter, and A. Kovacs, Airborne measurement of sea ice thickness using electromagnetic induction sounding, *Proc. 9th Intl. Conf. Offshore Mech. Arctic Engng.*, edited by O. A. Ayorinde, N. K. Sinha, and D. S. Sodhi, pp. 309–315, Am. Soc. Mech. Engrs., 1990.

Kozo, T. L., and W. B. Tucker, III , Sea ice bottomside features in the Denmark Strait, *J. Geophys. Res., 79*, 4505–4511, 1974.

Lange, M. A., S. F. Ackley, P. Wadhams, G. S. Dieckmann, and H. Eicken, Development of sea ice in the Weddell Sea, *Ann. Glaciol., 12*, 92–96, 1989.

McLaren, A. S., The under-ice thickness distribution of the Arctic Basin as recorded in 1958 and 1970, *J. Geophys. Res., 94*, 4971–4983, 1989.

McLaren, A. S., P. Wadhams, and R. Weintraub, The sea ice topography of M'Clure Strait in winter and summer of 1960 from submarine profiles, *Arctic, 37*, 110–120, 1984.

Martin, S., and P. Kauffman, A field and laboratory study of wave damping by grease ice, *J. Glaciol., 27*, 283–313, 1981.

Martinson, D. G., Evolution of the Southern Ocean winter mixed layer and sea ice: open ocean deepwater formation and ventilation, *J. Geophys. Res., 95*, 11641–11654, 1990.

Nansen, F., *Farthest North*, George Newnes, London, *1*, 299, 1898.

Rothrock, D. A., Ice thickness distribution—measurement and theory, in *The Geophysics of Sea Ice*, edited by N. Untersteiner, pp. 551–575, Plenum, New York, 1986.

Serreze, M. C., R. G. Barry, and A. S. McLaren, Seasonal variations in sea ice motion and effects on sea ice concentration in the Canada Basin, *J. Geophys. Res., 95*, 10955–10970, 1989.

Stouffer, R. J., S. Manabe, and K. Bryan, Interhemispheric asymmetry in climate response to a gradual increase of atmospheric CO_2, *Nature, 342*, 660–662, 1989.

Vinje, T., An upward looking sonar ice draft series, *POAC-89, Proc. 10th Intl. Conf. Port & Ocean Engng. under Arctic Condns.*, edited by K. B. E. Axelsson and L. A. Fransson, *1*, pp. 178–187, Tekniska Hogskolan i Lulea, 1989.

Wadhams, P., Sea-ice topography of the Arctic Ocean in the region 70°W to 25°E, *Phil. Trans. Roy. Soc., A302*, 45–85, 1981.

Wadhams, P., Sea ice thickness distribution in Fram Strait, *Nature, 305*, 108–111, 1983.

Wadhams, P., Sea-ice thickness distribution in the Trans Polar Drift Stream, *Rapp. P.-v. Reun. Cons. int. Explor. Mer, 188*, 59–65, 1989a.

Wadhams, P., Sea ice and economic development in the Arctic Ocean—a glaciologist's experience, in *Arctic Technology and Economy. Present situation and problems, future issues*, pp. 1–23, Bureau Veritas, Paris, 1989b.

Wadhams, P., Evidence for thinning of the Arctic ice cover north of Greenland, *Nature, 345*, 795–797, 1990a.

Wadhams, P., Ice thickness distribution in the Arctic Ocean, in *Ice Technology for Polar Operations*, edited by T. K. S. Murthy, J. G. Paren, W. M. Sackinger, and P. Wadhams, pp. 3–20, Computational Mechanics Publns., Southampton, 1990b.

Wadhams, P., and D. R. Crane, SPRI participation in the Winter Weddell Gyre Study 1989, *Polar Record*, 1991, In press.

Wadhams, P., and R. J. Horne, An analysis of ice profiles obtained by submarine sonar in the Beaufort Sea, *J. Glaciol., 25*, 401–424, 1980.

Wadhams, P., A. S. McLaren, and R. Weintraub, Ice thickness distribution in Davis Strait in February from submarine sonar profiles, *J. Geophys. Res., 90*, 1069–1077, 1985.

Wadhams, P., M. A. Lange, and S. F. Ackley, The ice thickness distribution across the Atlantic sector of the Antarctic Ocean in midwinter, *J. Geophys. Res., 92*, 14535–14552, 1987.

Weeks, W. F., S. F. Ackley, and J. Govoni, Sea ice ridging in the Ross Sea, Antarctica, as compared with sites in the Arctic, *J. Geophys. Res., 94*, 4984–4988, 1989.

Williams, E., C. W. M. Swithinbank, and G. de Q. Robin, A submarine sonar study of Arctic pack ice, *J. Glaciol., 15*, 349–362, 1975.

Zwally, H. J., J. C. Comiso, C. L. Parkinson, W. J. Campbell, F. D. Carsey, and P. Gloersen, Antarctic Sea Ice 1973–1976: Satellite Passive-microwave Observations, *Rept. SP-459*, 206 pp., NASA, Washington, DC, 1983.

AD-P007 261

Detection of High Latitude Atmospheric Circulation Changes Using Satellite Data

J. Turner
British Antarctic Survey, Cambridge, UK

92-17943

ABSTRACT

Satellite remote sensing data can provide valuable information on the broad-scale circulation of the polar regions and help in understanding changes on a range of time scales. Early results with sounder data have suggested that they can be used to accurately monitor tropospheric temperature changes, although further work is needed to fully interpret these data in the polar regions. Determining the movement of baroclinic zones and the associated synoptic and mesoscale disturbances is possible using sounder data and imagery, respectively. However, tracking of weather systems currently requires considerable manual processing. The production of a cloud climatology of the polar regions can be achieved using automatic processing of imagery and the resulting analysis could be important as an indicator of increasing moisture levels if a significant high latitude warming occurs.

INTRODUCTION

The monitoring of global surface and upper-air temperatures is now one of the most important tasks facing meteorologists because of the possible impact of "greenhouse" gas emission on the global climate system. Recent research [Stouffer et al., 1989] has shown that the greatest effect of any global warming could be felt in the polar regions of the northern hemisphere with a consequent dramatic impact on the oceanographic/cryospheric/atmospheric system. Unfortunately, the polar regions have the poorest distribution of conventional meteorological observing stations of any area of the world. The record of temperature measurements from these stations is essential for monitoring changes at single sites. In regions where there are many surface stations it is possible to analyze the records of many stations together to show regional and global changes. However, in data-sparse regions such as the polar regions, and in particular Antarctica, such composites are unrealistic and it is difficult to demonstrate the causes of the changes through alterations in the general circulation. Satellite observing systems on polar orbiting satellites give very good spatial coverage of the high latitude areas, but currently suffer from problems of accuracy which limit their usefulness for determining small trends. In the following sections the value of the various forms of satellite data available over the polar regions in studies of global change is considered and strategies for using these data in future programs are recommended.

CURRENTLY AVAILABLE SATELLITE DATA

High resolution imagery. Since the 1970s high resolution (1 km) imagery has been available from the Advanced Very High Resolution Radiometer (AVHRR) on the TIROS-N/NOAA series of polar orbiting satellites [Schwalb, 1982]. A global dataset of the five-channel imagery, but at a degraded resolution of 4 km, has been maintained by NOAA/NESDIS since 1979. Direct reception of the full, 1-km-resolution imagery at high latitude receiving stations is now taking place [Anonymous, 1988]. However, there is little coordination of the reception and no central archive of data. AVHRR data have a high, 0.1 K, radiometric accuracy with good onboard calibration. The corrections necessary for tropospheric water vapor and other radiatively active gases are small in polar regions and so AVHRR can provide accurate ice, cloud top and sea surface temperatures.

Sounder data. The TIROS-N series satellites carry three sounding instruments: the High Resolution Infrared Radiation Sounder (HIRS), the Microwave Sounder Unit (MSU),

and the Stratospheric Sounder Unit (SSU). These are collectively known as the TIROS Operational Vertical Sounder (TOVS) and are capable of providing temperature profiles from the surface to the middle stratosphere, and humidity data in the troposphere [Smith et al., 1979]. Although soundings can be produced with a horizontal resolution of 80 km the vertical resolution of the retrievals is relatively poor and more indicative of broad atmospheric layers of the order of 100–200 mb deep. Global TOVS data are available at NOAA/NESDIS and are increasingly available on the meteorological data networks for use in forecasting.

Passive microwave. The launch of the Special Sensor Microwave/Imager (SSM/I) on the U.S. Defense Meteorological Satellite Program (DMSP) F8 satellite provided useful passive microwave data for meteorological studies. The passive microwave data provide useful information on sea ice extent [Comiso, 1986] and on precipitation [Katsaros et al., 1989; Spencer et al., 1989]. The 85 GHz channel in particular has a horizontal resolution of 12.5 km which is high enough to provide data on individual precipitation systems.

PRESENT STUDIES USING SATELLITE DATA

The location of atmospheric systems. Tracking of synoptic-scale weather systems from high latitude imagery has been carried out periodically since the early 1970s [Streten and Troup, 1973]. The first studies were concerned with identifying the locations of cyclogenetic regions and determining the main tracks of depressions. As no accurate, automatic method is available for analyzing imagery and producing climatological tracks, the manual analysis of imagery is very labor-intensive.

Cloud climatology. The International Satellite Cloud Climatology Project (ISCCP) was established as a project of the World Climate Research program with the aim of producing the first global datasets of mean cloud cover and cloud properties [World Climate Programme, 1987]. The project used five years of data from the geostationary and polar-orbiting satellites beginning in 1983 and has already presented some initial results. Although useful results were obtained for the tropics and mid-latitude areas the problems of detecting cloud over ice and snow led to less accurate results in the polar regions. For this reason a special study group [World Climate Programme, 1987] has been established to consider new methods for the detection of cloud in the polar regions and to re-analyze the high latitude data.

FUTURE OPTIONS

Detection of tropospheric temperature changes. Spencer and Christy [1990] presented a method of detecting trends in global tropospheric temperatures using channel 2 brightness temperatures from the MSU. Although their analysis was global the method is perhaps one of the best current options for detecting the first indications of broadscale warming in the polar regions. Unfortunately the MSU is an old instrument and has a number of shortcomings including high noise levels, broad weighting functions and a different response over land and sea areas. With the introduction of the Advanced Microwave Sounder Unit (AMSU) [see Foot, 1990] in the mid 1990s these difficulties will be overcome and channels with strong atmospheric signals largely independent of the surface conditions will become available. Analysis of the AMSU brightness temperatures and integration with the existing series of MSU observations will be a high priority.

Monitoring of synoptic and mesoscale weather systems. Recent research has shown the diversity of weather systems occurring in the polar regions [Businger and Reed, 1989; Heinemann, 1990]. Although the role of these vortices in the general circulation is still unclear, theoretical studies of the Antarctic [James, 1989] have suggested that the mesocyclones occurring in the coastal region may be important in maintaining the katabatic drainage flow which dominates the low-level flow over the continent. In parallel with these theoretical investigations, observational studies using satellite data will be able to determine the interactions between the synoptic and mesoscale systems and the possible role in the larger scale circulation. The prospects for automatically tracking depressions in imagery and producing climatological fields of cyclogenesis and depression movement are not good. For the foreseeable future these tasks will require considerable manual effort as the cloud signals in the imagery are so variable. However, work carried out so far, such as that by Carleton and Carpenter [1989], has helped understand the interaction between atmospheric systems and sea ice which need to be continued over the coming decades. The monitoring of baroclinic zones in thickness fields produced from TOVS radiances is a far simpler task and one which can be carried out automatically.

Clouds and radiation studies. ISCCP showed that automatic analysis of satellite imagery could provide valuable data on cloud extent in remote regions. As the representation of clouds is one of the weakest features of the current generation of atmospheric models these datasets will be extremely important in validating the representation of moisture processes and the parameterization of cloud. They also, however, provide a means of monitoring the interannual variability of cloud and give the only means possible of detecting long-term trends in cloud cover. As the extent of polar cloud plays a major role in regulating the input of shortwave radiation and the emission to space of terrestrial radiation, it is an important factor in the high latitude climate signal and may also provide an early indicator of increasing high latitude moisture.

Precipitation. Direct measurement of precipitation in the polar regions is difficult because of blowing snow and the contribution from the formation of rime. Yet a knowledge of precipitation over the Antarctic is vital for mass balance studies concerned with the growth and decay of the ice sheets. New microwave instruments have recently allowed the production of the first satellite-derived fields of precipitation by detecting the unpolarized, atmospheric signal from the areas of precipitation [Katsaros et al., 1989; Spencer et al., 1989]. Unfortunately the method is only applicable over the ice-free ocean areas, and ice-free land areas in the case of the Spencer et al. method. The atmospheric signal has so far not been identified over land or sea ice. Nevertheless, the data can provide very useful information on precipitation over areas such as the Norwegian and Barents sea in winter and around the coast of the Antarctic in summer. Zwally [1977] has used the microwave emissivity of the snow surface to determine the accumulation rate over the Antarctic continent, although this method has never been fully validated.

CONCLUSIONS

Although atmospheric models are the main tool used in climate change studies, parallel work with observational data is essential to try and detect the first indications of the predicted global warming. In-situ observations from the polar regions provide the most accurate data but with so few observing sites they are not representative of the whole continent and often only show regional signals. As satellite data become more accurate and our ability to generate geophysical information in the polar regions improves, so we will be able to use these data to complement the in-situ observations and set these data in their wider context.

REFERENCES

Anonymous, McMurdo Station gets a satellite-image processing system, *Antarct. J. U.S.*, *23*, 8–9, 1988.

Businger, S., and Reed, R. J., Polar lows, in *Polar and Arctic Lows*, edited by P. F. Twitchell, E. A. Rasmussen, and K. L. Davidson, pp. 3–45, A Deepak Publishing, Hampton, Virginia, 1989.

Carleton, A. M., and D. A. Carpenter, Polar Lows, in *Polar and Arctic Lows*, edited by P. F. Twitchell, E. A. Rasmussen, and K. L. Davidson, pp. 401–413, A Deepak Publishing, Hampton, Virginia, 1989.

Comiso, J. C., Characteristics of Arctic winter sea ice from satellite multispectral microwave observations, *J. Geophys. Res.*, *91*, 975–994, 1986.

Foot, J. S., AMSU-B and the meteorological office's supporting scientific programme, *Fifth Conference on Satellite Meteorology and Oceanography*, pp. 449–450, AMS, London, 1990.

Heinemann, G., Mesoscale vortices in the Weddell Sea region (Antarctica), *Mon. Wea. Rev.*, *118*, 779–793, 1990.

James, I. N., The Antarctic drainage flow: implications for hemispheric flow on the Southern Hemisphere, *Antarctic Science*, *1*, 279–290, 1989.

Katsaros, K. B., I. Bhatti, L. A. McMurdie, and G. W. Petty, Identification of atmospheric fronts over the ocean with microwave measurements of water vapor and rain, *Weather and Forecasting*, *4*, 449–460, 1989.

Schwalb, A., Modified version of the TIROS-N/NOAA A-G satellite series (NOAA E-J)—Advanced TIROS-N (ATN), *NOAA tech memo NESS 116*, 23, 1982.

Smith, W. L., H. M. Woolf, C. M. Hayden, D. Q. Wark, and L. M. McMillin, The TIROS-N operational vertical sounder, *Bull. Amer. Meteorol. Soc.*, *60*, 1177–1187, 1979.

Spencer, R. W., and J. R. Christy, Precise monitoring of global temperature trends from satellites, *Science*, *247*, 1558–1562, 1990.

Spencer, R. W., H. M. Goodman, and R. E. Hood, Precipitation retrieval over land and ocean with the SSM/I: identification and characteristics of the scattering signal, *J. Atmos. Ocean Tech.*, *6*, 254–273, 1989.

Stouffer, R. J., S. Manabe, and K. Bryan, Interhemispheric asymmetry in climate response to a gradual increase in atmospheric CO_2, *Nature*, *342*, 660–662, 1989.

Streten, N. A., and A J. Troup, A synoptic climatology of satellite observed cloud vortices over the Southern Hemisphere, *Quart. J. Roy. Met. Soc.*, *99*, 56–72, 1973.

World Climate Programme, *Report of the International Satellite Cloud Climatology Project (ISCCP) Workshop on Cloud Algorithms in the Polar Regions*, edited by E. Raschke, Tokyo, Japan 19–21 August 1986, 1987.

Zwally, H. J., Microwave emissivity and accumulation rates of polar firn, *J. Glaciol.*, *18*, 195–215, 1977.

AD-P007 262

92-17944

Strengths and Weaknesses of Sea Ice as a Potential Early Indicator of Climate Change

Claire L. Parkinson
Oceans and Ice Branch, Goddard Space Flight Center, Greenbelt, Maryland, U.S.A.

ABSTRACT

Sea ice is examined for its potential as an early indicator of climate change by considering how well it satisfies four criteria listed as desired characteristics for potential early indicators. Results of numerical modeling studies in the 1970s and 1980s suggested that sea ice satisfies the first characteristic, that the variable be expected to exhibit a large climate signal, very well; but these results have recently been updated in a way that decreases the success of sea ice in satisfying this particular property. Sea ice satisfies the second characteristic, that it be routinely measurable on a global basis, exceptionally well through satellite passive-microwave observations, and at the moment this is the core of its strength as a potential early indicator. However, the absence of a solid pre-satellite database considerably hinders how well sea ice satisfies the third characteristic, that it have low enough and known natural variability to allow a climate signal to be distinguished from the background noise, and how well it can be known to satisfy the final characteristic, that changes in it should not significantly lag changes in other climate variables. The conclusion reached is that although changes in the sea ice cover, when analyzed in conjunction with changes in other variables, will provide important information on climate change, sea ice is unlikely any time in the near future to be a definitive early indicator of climate change when considered by itself. There remain too many uncertainties regarding the natural variability of sea ice, the full interplay of the various positive and negative feedbacks involving sea ice, and the precise sequences in which past climatic changes have occurred.

INTRODUCTION

Four desirable characteristics of a variable which would combine to make it a likely early indicator of climate change are: (1) the variable should be expected, from physical theory and/or modeling, to exhibit a large climate signal; (2) it should be readily measurable on a global basis through routine observations; (3) it should have low enough and known natural variability to allow a climate signal to be distinguished from the background noise; and (4) changes in it should be expected to lead (or at least not significantly lag) changes in other climate variables. Sea ice is considered here for its potential as an early climate-change indicator by examining it in the context of each of these four characteristics. The arguments given are specifically for the spatial distribution and areal extent of sea ice, rather than for other aspects of the sea ice cover, although some of the points made apply more generally. For instance, in the cases of the discussions of characteristics 1 and 4, similar arguments to those made here would also apply to sea ice thickness, which is another sea ice variable of importance to global climate.

EXPECTATION OF A LARGE SIGNAL

Results from several major general circulation models (GCMs) in the 1970s and 1980s indicated that the polar regions should have a particularly high sensitivity to the anticipated greenhouse-gas-induced global warming [e.g., Manabe and Wetherald, 1975; Manabe and Stouffer, 1980;

Hansen et al., 1984; Washington and Meehl, 1984; Wetherald and Manabe, 1986]. In fact, such indications are among the major reasons why the polar regions have been given increased attention in discussions of climate change over the past decade. Furthermore, a first-order expectation of amplified polar warming could be readily argued even prior to the GCM results, on the basis of simple positive feedback mechanisms involving the polar sea ice cover. Among the strongest and best known of these is the ice–albedo–temperature feedback whereby higher temperatures lead to reduced ice extents, which result in a lowering of the surface albedo and thereby lead to additional warming [Kellogg, 1975; Crowley and North, 1991].

Sea ice models simulate a sizable response of the sea ice cover to the level of polar surface air temperature increases calculated by GCMs in the 1970s and early 1980s for the condition of a doubling of atmospheric carbon dioxide (CO_2). For instance, a prescribed 5 K warming in the Arctic led to a simulated seasonal disappearance of the Arctic ice pack in August and September [Parkinson and Kellogg, 1979], and a 5 K warming in the Antarctic led to a halving of the wintertime ice extents in the southern ocean [Parkinson and Bindschadler, 1984]. Such results signify a very strong climate signal from the sea ice cover, especially when placed in the context of paleoclimatic studies that suggest that the Arctic has not experienced ice-free conditions at any time during the past million years [Lamb, 1977]. However, the large sea ice signal is in response to the anticipated large temperature signal in the polar regions, and this latter signal is being called into question by more recent GCM simulations.

Polar results in at least two major GCMs have altered dramatically upon the incorporation of more detailed ocean calculations and the change from simulating the consequences of an instantaneous doubling of CO_2 to simulating the consequences of a more realistic gradual increase (1% per year) in CO_2. This is true for models from both the National Center for Atmospheric Research (NCAR) in Boulder, Colorado, and the Geophysical Fluid Dynamics Laboratory (GFDL) at Princeton University. In the NCAR case, results from an updated version of the model used by Washington and Meehl [1984] show, for the December–January–February season in the final five years of a 30-year simulation, only a slight warming (0–1 K) over most of the southern ocean and in fact a cooling over most of the Arctic Ocean and some of its peripheral seas. The warming and cooling are for the surface air temperatures simulated in the case with increasing CO_2 versus those simulated in the control case with constant CO_2. The Arctic cooling is particularly strong in the area of the Greenland and Norwegian Seas, where it peaks at over 6 K [Figure 30a in Washington and Meehl, 1989], and it naturally leads to a local advance rather than retreat of the sea ice cover [Figure 32b in Washington and Meehl, 1989]. In the case of the GFDL results, averages for the final decade of a 70-year simulation with gradually increasing CO_2 show a warming in the Arctic (compared to the control case with constant CO_2) but a prominent cooling of up to 4 K in the Ross Sea of the southern ocean [Figure 3 in Stouffer et al., 1989]. In fact, on the basis of zonally averaged surface air temperatures, the Stouffer et al. results show the southern ocean region to be the least sensitive of all to the gradual CO_2 increases [Figure 2 in Stouffer et al., 1989], suggesting that this region would be particularly poor for observing an early climate signal.

The reduced sensitivity of the polar regions in the updated models versus the earlier models can be explained at least in part on the basis of the effect of ocean currents on the sea ice simulations in the respective GCMs. As described and shown by Spelman and Manabe [1984], when ocean currents are added to a GCM, the poleward heat transport produced by the currents decreases the amount of sea ice in the control case, thereby reducing the area available for sea ice reductions from the control case to the CO_2-perturbed case. Through the albedo effect, this tends to lessen the sensitivity of the simulated polar temperatures to increased CO_2 [Spelman and Manabe, 1984]. The sequence is illustrated well by the case of the models of Washington and Meehl [1984, 1989]. The earlier model, which did not have horizontal transport within the oceans and hence did not advect warm water into the polar regions, simulated considerably too much sea ice in the control case; the more complete model allowed ocean transport and consequently simulated a much lesser sea ice cover in the control case. The change in the sea ice simulation for the control lessened the overall albedo decrease from the control to the case with increased CO_2, contributing directly to the simulated reduced sensitivity of polar surface air temperatures [Washington and Meehl, 1989].

As with the earlier GCM simulations, the Washington and Meehl [1989] and Stouffer et al. [1989] results are of course not definitive, and it remains possible that the polar regions will show larger climate-change signals than other regions. In fact, too little sea ice is simulated in the control case of Washington and Meehl [1989], especially in winter, so that a greater response to increased CO_2 could be expected if the control were improved. Also, inadequate resolution and physics in the ocean formulations used by Washington and Meehl [1989] and Stouffer et al. [1989] could be worsening the atmospheric results over those obtained with atmospheric GCMs prior to ocean coupling, so that the resultant simulations should not necessarily be accepted as improvements over results from earlier versions of the same models. Nonetheless, the newer results do at a very minimum at least lessen the confidence with which it can be stated that the polar regions should exhibit particularly large climate signals for the specific case of CO_2-induced global warming.

ROUTINE GLOBAL MEASUREMENTS

Regarding the desired characteristic that a variable be readily measurable on a global basis through routine observations, sea ice fares far better than most other climate variables. Although many aspects of the ice cover (such as ice thickness) are not yet obtainable either routinely or on even close to a global basis, and other aspects (such as distinctions among new ice, first-year ice, second-year ice, and other ice types) are not obtainable on a routine, global basis without large error bars, this is not true of the overall global distribution of the sea ice cover. Spatial sea ice distributions, and through them areally integrated sea ice extents, are obtainable routinely and globally through satellite passive-microwave observations.

The value of satellite passive-microwave observations in sea ice studies derives from the large contrast in microwave

emissivities between ice and water. For instance, at a 1.55 cm wavelength, the wavelength used by the first major satellite passive-microwave imager, the Nimbus 5 Electrically Scanning Microwave Radiometer (ESMR), the emissivity of water near the freezing point is approximately 0.44 whereas the emissivity of sea ice varies from about 0.80 to about 0.97. Although the large range in ice emissivities complicates the determination of ice types and ice concentrations from the microwave data, the large contrast between the emissivities of ice and water enables the data to be used to distinguish ice from water and thereby to determine the overall distribution of the sea ice cover. Furthermore, the emission of microwave radiation does not depend upon solar lighting, and at many microwave wavelengths atmospheric interference is not a major problem. Hence microwave observations provide an all-weather, all-season means of obtaining global sea ice distributions. Satellite microwave instruments have provided data with spatial resolutions on the order of 30 kilometers and temporal resolutions on the order of 1–3 days, the former being adequate for climate studies and the latter far exceeding climate-study requirements. Thus the technology exists, through satellite passive-microwave observations, for routinely measuring global sea ice distributions. Details on the microwave properties of sea ice and the derivation of sea ice parameters from satellite passive-microwave data can be found in Zwally et al. [1983a], Parkinson et al. [1987], and Gloersen et al. [1991].

Complementing the existence of the technology for obtaining routine sea ice measurements, there is a corresponding commitment of the research community and funding agencies, with a result that the satellite passive-microwave record has an established baseline and is expected to continue indefinitely into the future. The existent record comes largely from three data sets, the first covering most of the four-year period from January 1973 through December 1976, the second covering almost the entire nine-year period from the end of October 1978 through August 1987, and the third covering the period from late June 1987 to the present. The 1973–1976 data are from the single-channel Nimbus 5 ESMR and are presented and analyzed in Zwally et al. [1983a] and Parkinson et al. [1987] for the Antarctic and Arctic respectively; the 1978–1987 data are from the 10-channel Nimbus 7 Scanning Multichannel Microwave Radiometer (SMMR) and are presented and analyzed in Gloersen et al. [1991]; and the data since 1987 are from the 9-channel Defense Meteorological Satellite Program (DMSP) Special Sensor Microwave Imager (SSMI). Unfortunately, in contrast to the ESMR, neither the SMMR nor the SSMI provides truly global data coverage, as the specific satellite orbits prevent coverage poleward of 84° latitude in the case of the SMMR and poleward of 87.6° in the case of the SSMI. On the positive side, however, the multichannel nature of the SMMR and SSMI allows improved calculations of ice concentrations over those calculated from single-channel instruments and presents the possibility of distinguishing different ice types [e.g., Cavalieri et al., 1984]. A sequence of at least 10 SSMIs is planned, with the hope that no major gaps will occur in the data record. As with all data records, these will require care in ensuring proper calibrations and the elimination of instrument drift [e.g., Gloersen et al., 1991], but assuming that such care is provided, then when major changes occur in the sea ice cover these should be readily determined through the satellite passive-microwave observations.

NATURAL VARIABILITY

Regarding the desired characteristic that to be an early indicator a variable should have low enough and known natural variability to allow a climate signal to be distinguished from the background noise, sea ice does not fare nearly as well as it does regarding the characteristic that it be readily measurable. Sea ice has considerable variability, and this is compounded by the fact that the extent of the variability is not known. Both points are informatively illustrated by the case of southern ocean sea ice extents in the 1970s and 1980s. A marked decrease of about 18% occurred in the annually averaged southern ocean sea ice extents from 1973 to 1977 [Kukla and Gavin, 1981], and this decrease was briefly heralded as possible geophysical evidence of a CO_2 warming of the atmosphere. However, the premature nature of this speculation became apparent when the ice cover rebounded in the late 1970s and early 1980s, with ice extents in 1981 within about 5% of those in 1973 [Chiu, 1983; Zwally et al., 1983b]. The 18% decrease that had seemed so large initially, now appears to be within the natural variability of the ice cover.

In the northern hemisphere, overall ice extents over the course of the satellite passive-microwave record have not shown nearly as large an interannual variability as in the southern hemisphere, but have shown significant regional variability. Annually averaged northern hemisphere ice coverage varied over the course of the ESMR/SMMR record by less than 8%, from a minimum of approximately 11.9×10^6 km^2 in 1974 to a maximum of approximately 12.8×10^6 km^2 in 1982. In fact, considering the two records separately (recognizing that the ESMR and SMMR data sets are not entirely compatible, being from two significantly different instruments), the variation is only 3% in each case, from approximately 11.9×10^6 km^2 in 1974 to approximately 12.2×10^6 km^2 in 1975 for the four-year ESMR record, and from approximately 12.4×10^6 km^2 in 1984 to approximately 12.8×10^6 km^2 in 1982 for the nine-year SMMR record [Parkinson and Cavalieri, 1989]. However, interannual variability on a regional scale over the same period was quite large, for instance with maximum monthly averaged winter ice extents in the Sea of Okhotsk varying over the nine years of the SMMR data set by a factor of 2, from 0.6×10^6 km^2 in 1984 to 1.2×10^6 km^2 in 1979, and November monthly averaged ice extents in Hudson Bay varying even more, from 0.5×10^6 km^2 in 1981 to 1.2×10^6 km^2 in 1986 [Parkinson and Cavalieri, 1989].

The small amount of interannual variability in the sea ice extent of the north polar region as a whole seems to favor the use of this variable for monitoring purposes, as it suggests a low noise level and thereby a high likelihood that future decreases (or increases) in the ice cover could be identified as a climate signal, distinguishable from the background noise. Unfortunately, the brevity of the existent data record again presents a problem. Certainly an 18% decrease in annually averaged north polar ice extents over a few years would appear significant following the stability of the ice extents over the SMMR years (with only a 3% variation in the annual averages); yet it is important to remember the

18% decrease that occurred in the southern ocean in the 1970s and the fact that this decrease was apparently not a climate signal, in view of the subsequent southern ocean ice extent increases. Furthermore, the southern ocean ice extent was stable during the nine-year SMMR period, just as the northern hemisphere ice extent was [Gloersen et al., 1991]. There is no immediate reason to discard the possibility that the ice covers of both hemispheres undergo periods of rapid change intermingled with periods of seeming stability and that a longer data set might show 18% or greater decreases to occur as naturally in the northern hemisphere as in the southern hemisphere. The available data sets are simply too short at the present time to determine what level of fluctuation should be considered part of the natural variability.

LEAD/LAG EXPECTATIONS

The issue of whether sea ice leads or lags other climate variables is an issue hindered even more by inadequate data sets than the issue of the natural variability of sea ice. Certainly on a seasonal basis sea ice lags many variables, with surface air temperature being one primary one that it lags significantly. For instance, maximum ice extents in both the Arctic and Antarctic occur about a month after minimum surface air temperatures, and minimum ice extents occur about a month after maximum surface air temperatures [Parkinson et al., 1987, and Zwally et al., 1983a, for the Arctic and Antarctic respectively]. However, seasonal lagging does not imply climatic lagging, and whether or not on a climate time scale changes in sea ice tend to lead or lag changes in other variables remains uncertain. In fact, the data to settle this issue might not even exist. Satellite data do not cover nearly a long enough time period; pre-satellite historical data are very incomplete for many variables, sea ice included; and dating of paleoclimatic data tends to have error bars far broader than would allow the determination of leads or lags of the order of relevance here (years to decades). Resolution of the lead/lag issue will presumably involve a combination of modeling and improved historical and paleoclimatic data sets, improved both in terms of increased spatial coverage and in terms of more precise dating.

SUMMARY AND CONCLUSIONS

This study provides a mixed picture of the likelihood that sea ice will emerge as an early indicator of climate change, with its strongest attribute being the ease with which changes in the global sea ice cover can be observed, and several of its weakest attributes centering on the lack of a solid pre-satellite sea ice database. The first of four criteria listed for a potential early indicator is that the variable be expected to exhibit a large climate signal. This expectation seemed to be met by the results of numerical modeling studies in the 1970s and 1980s, but two updated GCM studies in 1989 considerably weakened this expectation by suggesting that the polar regions might not show as straightforward and anomalously high a sensitivity to, for instance, atmospheric CO_2 increases as had formerly been simulated. This issue is therefore more questionable than might have been the case prior to 1989.

The strongest point in favor of sea ice as a potential early indicator of climate change is that the sea ice cover is being routinely monitored on a global basis with a technology (satellite passive-microwave imagery) that provides adequate spatial and temporal resolutions for climate studies. Hence as changes occur in the global sea ice distributions these can be readily determined. However, the fact that sea ice has high interannual variability, at least on a regional basis, combined with the uncertainty in the extent of the variability, due to the brevity of the global sea ice record, tends to lessen its potential as an early indicator. This follows because of the difficulty of knowing how much the ice cover must change before a climate signal can with confidence be said to have emerged above the background noise; standard deviations can be calculated for the satellite passive-microwave sea ice data and statistical tests can be applied, but these data go back only to 1972. Another complicating factor concerns the issue of leads and lags. However well measured a variable is and however large its eventual signal, it will not be an early indicator of climate change if its changes significantly lag those in other well-measured variables. Historical studies are incomplete and present varied results on the lead/lag issue.

To encapsulate the preceding comments, sea ice can be informally "graded" regarding each of the four desired characteristics listed in the Introduction for potential early indicators of climate change. Based on the arguments presented and with some regard for other potential early indicators, such as continental snow cover, permafrost, sea surface temperature, surface air temperature, coral growth, cloud cover, and desertification, sea ice can be given a hesitant "good/fair" for the expectation of a large climate signal, an "excellent" for being routinely measurable on a global basis, a "poor" for the amount and uncertainty of its natural variability, and a question mark, or "incomplete," for whether or not its climatic changes will significantly lag those of other climate variables. To reiterate a point made earlier, this grading is basically for sea ice distributions (and extents, calculated from the distributions) as a climate variable and not for other aspects of the sea ice cover. For sea ice thicknesses, although the expectation of a large climate signal might be high, the potential as an early indicator would be seriously hurt by the limited amount of information on past sea ice thicknesses and by the fact that ice thicknesses at present are not easily measured and certainly are not obtainable on a global basis.

It is very unlikely that any climate variable will satisfy all four desired characteristics for potential early indicators well. It is much more likely that as climate change occurs it will be best identified not by an individual variable but by a suite of variables. As an important component of the climate system, sea ice should certainly be considered among the large complement of variables which together present the ever-altering picture of global change. This is especially true in view of the fact that global sea ice distributions are being so well determined from satellite observations, so that major changes in the ice cover can be identified with much greater certainty than can changes in many other climate variables.

ACKNOWLEDGMENTS

The author very much appreciates constructive scientific comments received from John Walsh, plus research funding received from the Oceanic Processes Branch at NASA Headquarters.

REFERENCES

Cavalieri, D. J., P. Gloersen, and W. J. Campbell, Determination of sea ice parameters with the Nimbus 7 SMMR, *J. Geophys. Res.*, *89*, 5355–5369, 1984.z

Chiu, L. S., Variation of Antarctic sea ice: An update, *Mon. Wea. Rev.*, *111*, 578–580, 1983.

Crowley, T. J., and G. R. North, *Paleoclimatology*, 339 pp., Oxford University Press, New York, 1991.

Gloersen, P., W. J. Campbell, D. J. Cavalieri, J. C. Comiso, C. L. Parkinson, and H. J. Zwally, *Arctic and Antarctic Sea Ice, 1978–1987: Satellite Passive-Microwave Observations and Analysis*, National Aeronautics and Space Administration, Washington, DC, 1991, In press.

Hansen, J., A. Lacis, D. Rind, G. Russell, P. Stone, I. Fung, R. Ruedy, and J. Lerner, Climate sensitivity: Analysis of feedback mechanisms, in *Climate Processes and Climate Sensitivity*, edited by J. E. Hansen and T. Takahashi, pp. 130–163, American Geophysical Union, Washington, DC, 1984.

Kellogg, W. W., Climatic feedback mechanisms involving the polar regions, in *Climate of the Arctic*, edited by G. Weller and S. A. Bowling, pp. 111–116, Geophysical Institute, University of Alaska, Fairbanks, 1975.

Kukla, G., and J. Gavin, Summer ice and carbon dioxide, *Science*, *214*, 497–503, 1981.

Lamb, H. H., *Climate: Present, Past and Future, vol. 2, Climatic History and the Future*, 835 pp., Methuen & Company, London, 1977.

Manabe, S., and R. J. Stouffer, Sensitivity of a global climate model to an increase of CO_2 concentration in the atmosphere, *J. Geophys. Res.*, *85*, 5529–5554, 1980.

Manabe, S., and R. T. Wetherald, The effects of doubling the CO_2 concentration on the climate of a general circulation model, *J. Atmos. Sci.*, *32*, 3–15, 1975.

Parkinson, C. L., and R. A. Bindschadler, Response of Antarctic sea ice to uniform atmospheric temperature increases, in *Climate Processes and Climate Sensitivity*, edited by J. E. Hansen and T. Takahashi, pp. 254–264, American Geophysical Union, Washington, DC, 1984.

Parkinson, C. L., and D. J. Cavalieri, Arctic sea ice 1973–1987: Seasonal, regional, and interannual variability, *J. Geophys. Res.*, *94*, 14499–14523, 1989.

Parkinson, C. L., and W. W. Kellogg, Arctic sea ice decay simulated for a CO_2-induced temperature rise, *Climatic Change*, *2*, 149–162, 1979.

Parkinson, C. L., J. C. Comiso, H. J. Zwally, D. J. Cavalieri, P. Gloersen, and W. J. Campbell, Arctic Sea Ice, 1973–1976: Satellite Passive-Microwave Observations, *NASA SP-489*, 296 pp., National Aeronautics and Space Administration, Washington, DC, 1987.

Spelman, M. J., and S. Manabe, Influence of oceanic heat transport upon the sensitivity of a model climate, *J. Geophys. Res.*, *89*, 571–586, 1984.

Stouffer, R. J., S. Manabe, and K. Bryan, Interhemispheric asymmetry in climate response to a gradual increase of atmospheric CO_2, *Nature*, *342*, 660–662, 1989.

Washington, W. M., and G. A. Meehl, Seasonal cycle experiment on the climate sensitivity due to a doubling of CO_2 with an atmospheric general circulation model coupled to a simple mixed-layer ocean model, *J. Geophys. Res.*, *89*, 9475–9503, 1984.

Washington, W. M., and G. A. Meehl, Climate sensitivity due to increased CO_2: experiments with a coupled atmospheric and ocean general circulation model, *Climate Dynamics*, 4, 1–38, 1989.

Wetherald, R. T., and S. Manabe, An investigation of cloud cover change in response to thermal forcing, *Climatic Change*, *8*, 5–23, 1986.

Zwally, H. J., J. C. Comiso, C. L. Parkinson, W. J. Campbell, F. D. Carsey, and P. Gloersen, Antarctic Sea Ice, 1973–1976: Satellite Passive-Microwave Observations, *NASA SP-459*, 206 pp., National Aeronautics and Space Administration, Washington, DC, 1983a.

Zwally, H. J., C. L. Parkinson, and J. C. Comiso, Variability of Antarctic sea ice and changes in carbon dioxide, *Science*, *220*, 1005–1012, 1983b.

Variability of Antarctic Sea Ice

H. J. Zwally and J. C. Comiso
Oceans and Ice Branch, NASA Goddard Space Flight Center, Greenbelt, Maryland, U.S.A.

J. E. Walsh
Department of Atmospheric Sciences, University of Illinois, Urbana, Illinois, U.S.A.

ABSTRACT

Previous analysis of the Antarctic sea ice cover, as observed by satellite passive-microwave sensors beginning in 1973, showed significant inter-annual variations in the ice extent and the open water within the ice pack, but no significant long-term trend. In this paper, ice maps using several parameter-extraction algorithms and recalibrated Nimbus-7 SMMR data are compared with the Navy–NOAA ice maps, showing significant quantitative differences and the need to use a consistently calibrated and analyzed data set. Regional inter-annual variations in the sea ice area continue to be as large as 30%, compared to about 10% in the overall coverage. For periods of 3–5 years, more ice area in winter appears to be associated with less ice in summer. For longer periods, the changes are similar in all seasons. However, the overall change in ice extent over 15 years is not considered to be significant. Similarly, there is no significant change in the amount of open water within the ice pack.

AD-P007 263

92-17945

Sea Ice Variability in the Nordic Seas

Torgny Vinje
Norwegian Polar Research Institute, Oslo Lufthavn, Norway

ABSTRACT

The variability of ice distribution in the Nordic Seas is considered for the period 1966–1988. The average maximum extension is found to be nearly constant for the whole area, except for the Iceland Sea where there is a reduction of about 33%. The average minimum extension shows a reduction between 13% and 40%, except for the Greenland Sea where the changes are insignificant. The largest reductions in the minimum extension are observed in the Barents and the Iceland Seas. Although these calculations are based on regression analysis, rendering the best estimate of the observed changes, the variability is so large that the series becomes too short for statistically significant conclusions. A comparison with older data shows that the average minimum extension of the ice in the Barents Sea has decreased drastically since the turn of the century.

Estimations made for the Barents Sea suggest that the average increase over the last two decades of the area being melted from the end of April to the end of August may be caused by either a decrease in the ice thickness of about 17% or an increase of the heat input of about 20%, or a combination of these effects.

INTRODUCTION

The Nordic Seas lie in the area with the broadest opening into the Arctic Ocean and where therefore low-pressure systems may move farther north than anywhere else without being affected noticeably by continents. Apart from atmospheric effects, the heat budget of the area is dominated by the world's most concentrated meridional exchanges of water and ice. The variability in both oceanic and atmospheric fluxes is mirrored in the high variability of ice extent in the region. While the maximum extension of the ice cover mainly is determined by the distribution of cold and warm water masses, the minimum extension is determined mainly by meteorological factors, such as the track of the cyclones, circulation intensity, and particularly the radiative effects on ice and open water in the ice fields. As the distribution of cold and warm water masses as well as the boundary conditions for the various Nordic Seas are so individually different, it is natural to consider the various seas separately. Because of the interaction with the Arctic Ocean, adjacent parts of this ocean have also been added to the Kara Sea, the Barents Sea and the Greenland Sea when evaluating the temporal trends of the ice distribution (Figure 1).

BOUNDARY CONDITIONS AND TEMPORAL TRENDS

The Barents Sea and Adjacent Part of the Arctic Ocean

The western part of the Barents Sea shows the lowest variability in the maximum extension (Figure 2). This is due to the well-defined shelf break which here separates the warmer and colder water masses more distinctly. The extreme high variability observed in the eastern part can to a large extent be ascribed to the lack of a shelf break in this area. This entails that the ice conditions in the eastern part should be controlled to a higher degree by the changing effects of the atmospheric circulation and corresponding changes in the oceanic heat fluxes.

During the freezing season, winds from the east reduce the influx of warmer water from the Norwegian Sea and force the ice fields to expand westward due to cooling and wind drift, while the opposite will take place when the Barents Sea Low is active. Then we may observe open water far to the north along the western coast of Novaja Zemlya in the middle of winter.

The Barents Sea is on an average an ice source for the

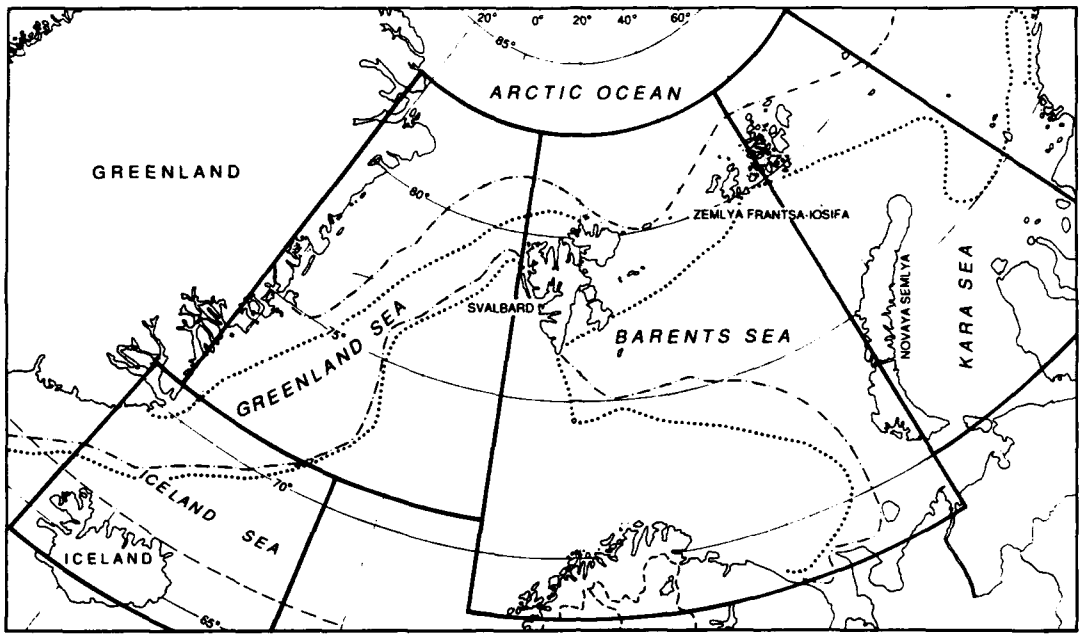


Figure 1. The different areas considered for the estimation of changes in the average maximum and minimum extensions of the ice.

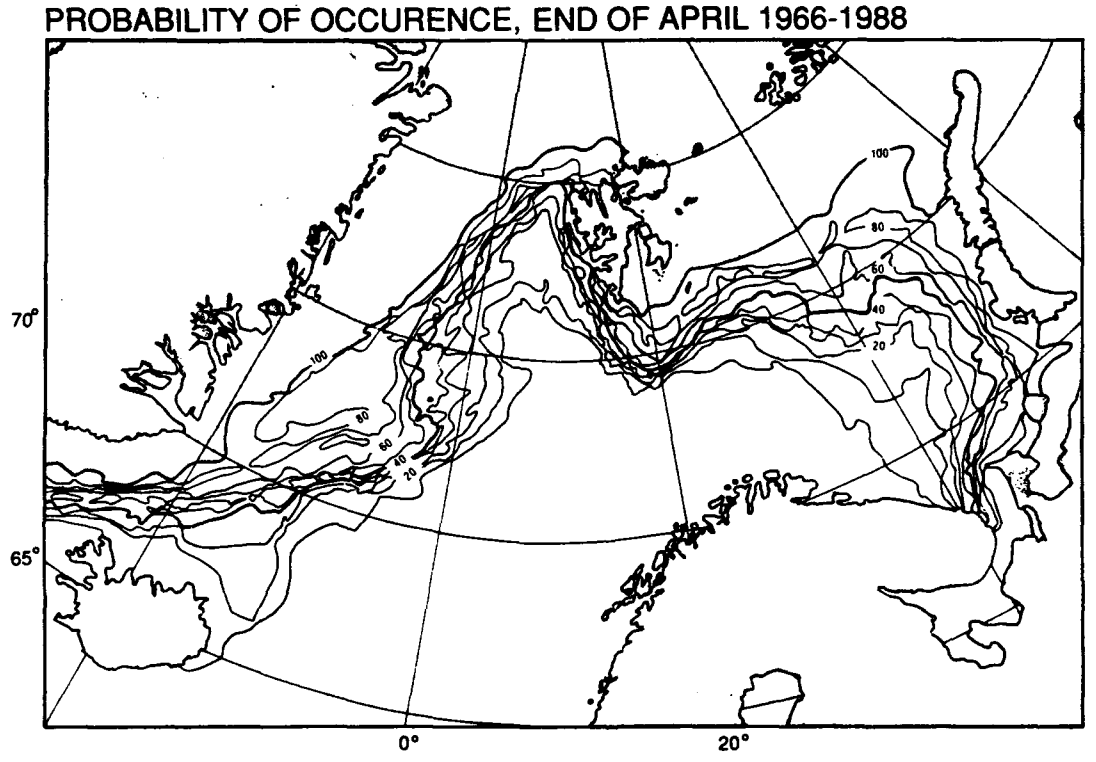


Figure 2. The frequency distribution of ice occurrence in the Nordic Seas at the end of April, 1966–1988, based on weekly ice maps edited by the Norwegian Meteorological Institute, the UK Meteorological Office, the Navy–NOAA Joint Ice Center, the Icelandic Meteorological Institute, and aircraft, field observations and early satellite information collected by the Norwegian Polar Research Institute. About 1200 weekly ice maps have been line digitized with regard to concentration after being quality controlled and adjusted from an inter-comparison of the above maps and observations. The pixel size is about 6 km^2 in the Svalbard area increasing to about 12 km^2 at 65°N.

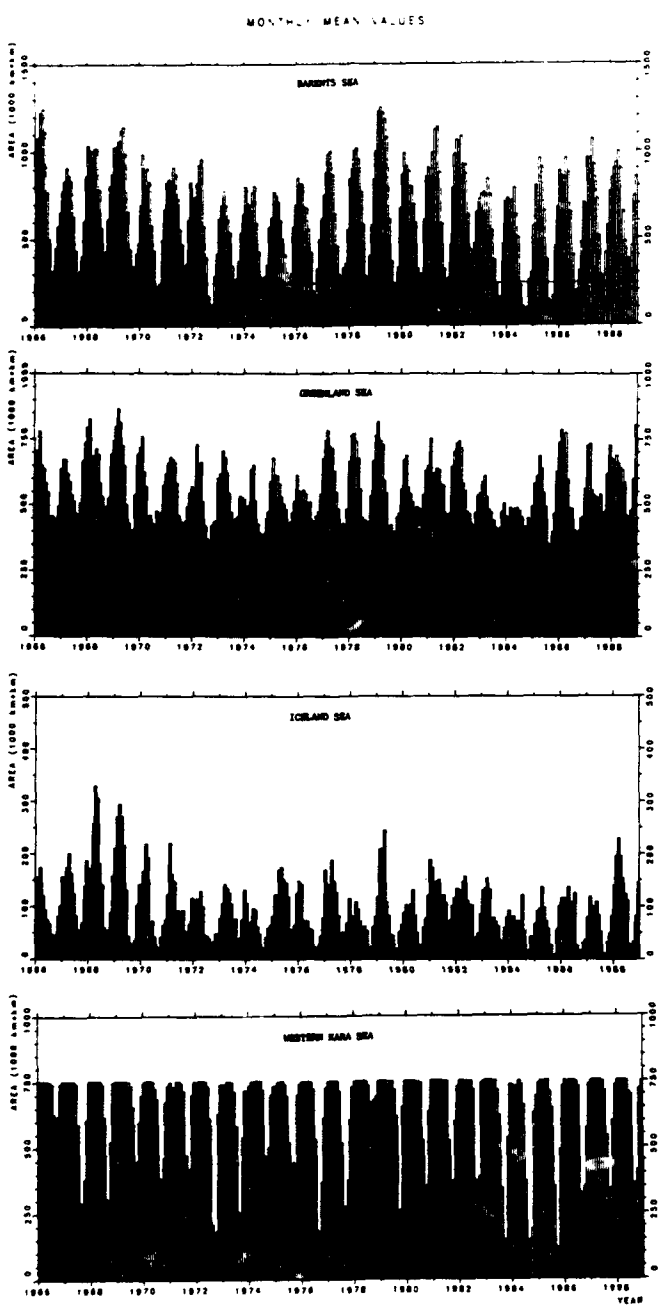


Figure 3. Monthly mean ice extent given in km² for the different Nordic Seas. The horizontal line above the time axis indicates the area of the adjacent part of the Arctic Ocean that has been included for the calculations of the change in the average maximum and minimum extensions. The data base is the same as for Figure 2.

Arctic Ocean and an ice sink for the Kara Sea [Zacharov, 1976]. There is, however, a seasonal variation, indicating a reversed ice exchange between the mentioned seas during the warmer season. Assuming the ice thickness to be 2 m, the annual average net influx from the Kara Sea will amount to about 500 km³ and the net export to the Arctic Ocean will be an order of magnitude less [Vinje, 1988].

The maximum and minimum extensions of the ice generally occur at the end of April and August, respectively (Figure 3). There is a great interannual variability with an indication of a decadal periodicity in the maximum ice

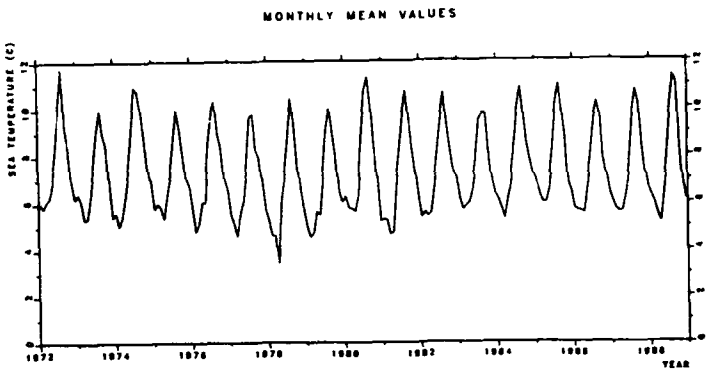


Figure 4. Monthly mean sea surface temperatures in the Norwegian Sea east of 5°W between 65 and 70°N as averaged from the weekly ice maps edited by the Norwegian Meteorological Institute.

extension in the Barents Sea. A decadal variation is also suggested for the Barents and Kara Sea region jointly by a comprehensive investigation made for the whole Arctic by Mysak and Manak [1989]. Although we consider a smaller area (the Barents Sea), there is a fair correspondence between the occurrences of maximum and minimum ice extensions in both investigations.

A branch of warmer water from the Norwegian Sea flows into the southern part of the Barents Sea. Helland-Hansen and Nansen [1909] found that climatic variations in the Barents Sea were lagged one year with respect to the Lofoten oceanographic section. A similar correspondence may be detected when comparing Figure 3 with the surface temperatures in the Norwegian Sea, west of Lofoten (65–70°N) (Figure 4). The comparison indicates a negative correlation between the ice extension in the Barents Sea and the surface temperature in the Norwegian Sea, with a minimum temperature in 1978 corresponding to a maximum sea ice extension one year later in the Barents Sea. Although 1979 was an unusual year, with a deviation in the atmospheric circulation strongly favoring ice formation in this area [Vinje, 1980], the present comparison indicates that amplifying signals affecting the ice conditions here may also be advected from the south as suggested by, e.g., Helland-Hansen and Nansen [1909].

The observation series of minimum extension based on weekly ice maps indicates an average reduction of about 40% over the last 23 years in the Barents Sea and the adjacent part of the Arctic Ocean (Figure 5, lower part). This is in contrast to the average maximum extension which shows no significant change over the same period (Figure 5, upper part). Although these calculations are based on a regression analysis rendering the best estimate of the observed change in the average extension, the variability is so large that the series becomes too short for statistically significant conclusions. For example, a maximum of 16% of the variance can be explained by the time variable for the regressions considered above. This should be kept in mind also when considering the observed average changes for the other Nordic Seas.

According to the monthly average ice borders given in the Yearbooks of The Danish Meteorological Institute [Loeng and Vinje, 1979], a reduction of the ice extent at the end of the melting season is a continuation of a trend

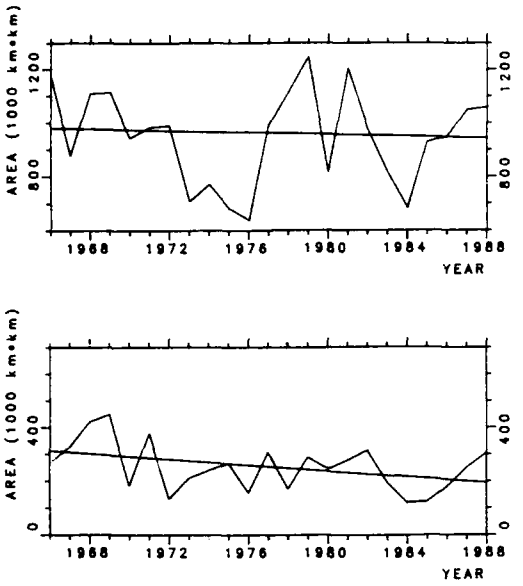


Figure 5. The maximum and minimum extensions of sea ice in the Barents Sea and adjacent part of the Arctic Ocean at the end of April and August, 1966–1988, with regression lines.

extending back to the turn of the century. The most rapid decrease in the Barents Sea proper was observed during the first three decades of this century, from about 270,000 km^2 in 1898–1922 to about 110,000 km^2 in 1929–1939, with a slower reduction from the latter period to 1966 when the average minimum area was reduced to about 80,000 km^2. Today the average minimum ice border in this region has withdrawn from the Barents Sea into the Arctic Ocean.

This long-term trend is now the subject of a special investigation using the individual, older observations to obtain a better temporal resolution of the ice extension. The weekly changes are so large, particularly during the melting season, that important signals may be masked when considering only monthly averages.

It is of interest to estimate the order of magnitude of the changes in two of the parameters that could cause the indicated temporal trend. We have the following relationship

$$Q_1/(\Delta A_1 H_1)_{1966} = Q_2/(\Delta A_2 H_2)_{1988}$$

where Q is the heat quantity needed to melt a volume of ice given by the area ΔA and the average ice thickness H.

The long-term maximum average is about 950,000 km^2, while the minimum average has decreased from 320,000 to 195,000 km^2 from 1966 to 1988. This gives

$$\Delta A_1/\Delta A_2 = 1.2 \text{ and } H_1/H_2 = 1.2\, Q_1/Q_2$$

Then, if the ice thickness is unchanged with time due to unaltered freezing, the heat needed to melt the ice would have to be increased by 20% to account for the change in the melted area. If, on the other hand, the heat input needed to melt the ice is unchanged with time, the ice thickness would have to be decreased by 17% to balance the increase in the melted area. This would imply a decrease in the ice thickness of 0.25 m over the 23-year period, provided an initial ice thickness of about 1.5 m in 1966.

On the basis of the observed average reduction in the ice fields, the above estimations should give the order of magnitude for the possible extreme changes of the two parameters to which the indicated change in the ice extension could be attributed. It is more likely to assume that a small change in both parameters may take place. Then, for example, if a 10% reduction in the ice thickness has taken place, this would balance with an increase of the heat input of only 8%. This shows that relatively small variations in the ice thickness due to a small variation in the freezing, and a small increase in the heat input that melts the ice, may result in a large variation in the ice extension. The calculations made above suggest a percentage accuracy with which the parameters in question should be measured to provide reliable results for detailed budget studies.

The Iceland Sea

The ice conditions in the Iceland Sea are determined by the influx of multi-year ice from the Greenland Sea as well as local ice formation in the East Iceland Current extending southeastward from the East Greenland Current. When the Icelandic Low is in position, the southern area of the sea will generally be kept free of ice by easterly winds. However, when the atmospheric circulation becomes anticyclonic, during blocking situations, the surface layers of this cold current are speeded up together with colder air influx from the northwest. The improvement of the ice conditions north of Iceland since the extreme year of 1968 corresponds to a change in the deviation from the long-term monthly mean at Reykjavik of about 7 hPa in May 1968 to about -7 hPa in May 1971 according to air pressure maps. The variable influence of the atmospheric forcing field over the Iceland Sea makes the ice conditions here very variable (Figure 2).

Both the average minimum and maximum extensions show a decrease in this area for the last 23 years, amounting to about 40% and 33%, respectively. Maximum extensions were observed in 1968 (320,000 km^2) and in 1979 (240,000 km^2). The sea ice disappeared completely in this area during September 1985 and 1986 (Figure 3).

The Western Kara Sea and Adjacent Part of the Arctic Ocean

The Kara Sea is relatively shallow. It is bounded by islands and the mainland, and the ice drift is mainly determined by the atmospheric stress field. The ice cover consists of first-year ice or summered-over multi-year ice formed locally.

Also in this area the observations show a temporal reduction of the average minimum extension, amounting to about 13% for the last 23 years. The Western Kara Sea has been covered with ice at the end of the freezing season for the whole period considered (Figures 2 and 3).

The Greenland Sea and Adjacent Part of the Arctic Ocean

The ice fields in the Greenland Sea are dominated by the large influx of multi-year ice from the Arctic Ocean through Fram Strait. The influx past the 80th parallel amounts, on average, to 4500 km^3 of ice per year [Vinje and Finnekåsa, 1986], equalling a fresh water supply of the same magnitude as the Amazon. Measurements by an upward-looking sonar of the ice thickness distribution over a year at 75°N suggest a net annual reduction of this ice flux of about 30% between

the two latitudes [Vinje, 1990]. This indicates that a net amount of about 1350 km^3 of ice is melted annually in the mentioned area. If this meltwater were equally distributed in the Greenland Sea between 75 and 80°N, it would correspond to a 3-m-thick fresh water layer. The melting of sea ice represents accordingly a potential for a marked effect on the stability of the water masses in this important convective area.

The most dominant ice feature in the Greenland Sea during the freezing season is the ice promontory called Odden, observed to extend for shorter or longer periods northeastward from Jan Mayen over the Mohn Ridge. The most extreme and persistent development of this feature seems to take place when we have an intensified atmospheric cyclonic circulation in the area which corresponds to that in the ocean. This was the case in March 1970, 1979 [Vinje, 1980] and also in 1989 when the monthly deviation from the long-term mean atmospheric pressure was -14 hPa for the mentioned month. Otherwise Odden may develop temporarily between passages of lows which disintegrate and melt the ice in the promontory. The variability of the ice extension in this area is therefore particularly high (Figure 2).

The observation series shows no significant reduction in either the average minimum or the average maximum ice extent in the Greenland Sea during the 23-year period. This is in contrast to what we have found for the other Nordic Seas where marked changes were observed for both or one of the averaged extensions. This difference might be due to the fact that the Greenland Sea is the only Nordic Sea that is dominated by ice import from the Arctic Ocean. If, for example, there occurs an overall reduction in the ice thickness due to increased melting or reduced freezing, this would be reflected more by a reduction in the ice extent in the other areas where the ice is markedly thinner. In this connection it may be noted that a marked average reduction in the average minimum extent is observed in the bordering Icelandic Sea for the period in question.

ACKNOWLEDGMENTS

Thanks are extended to G. Kjærnli for having made the quality control of the great number of ice maps that have formed the basis for the digitized data set and to Å. S. Johnsen for the performance of the statistical calculations. The work was carried out under a contract with the Operators Committee Nord of the oil companies. Norsk Polarinstitutt Contribution No. 274.

REFERENCES

Helland-Hansen, B., and F. Nansen, The Norwegian Sea, *Fiskeridirektoratetets Skrifter, Serie Hav Unders.* 2(2), 360 pp., 1909.

Mysak, A. L., and D. K. Manak, Arctic sea-ice extent and anomalies, 1953–1984, *Atmosphere-Ocean*, 27, 376–405, 1989.

Loeng, H., and T. Vinje, On the sea ice conditions in the Greenland and Barents Sea, *Proceedings of the 5th International Conference on Port and Ocean Engineering Under Arctic Conditions*, Vol. 1, The Norwegian Institute of Technology, Trondheim, 1979.

Vinje, T., On the extreme sea ice conditions observed in the Greenland and Barents Seas in 1979, *Norsk Polarinstitutt Årbok 1979*, 59–65, 1980.

Vinje, T., Dynamics and morphology of the Barents Sea ice fields, *Proceedings of the 9th Conference of Port and Ocean Engineering under Arctic Conditions*, Vol. 1, pp. 263–268, University of Alaska Fairbanks, 1988.

Vinje, T., An upward looking sonar ice draft series, *The 10th International Conference on Port and Ocean Engineering under Arctic Conditions*, Vol. 3, pp. 178–183, Tekniska Høgskolan, Luleå, Sweden, 1990.

Vinje, T., and Ø. Finnekåsa, The ice transport through the Fram Strait, *Norsk Polarinstitutt Skrifter 186*, 39 pp., Oslo, 1986.

Zacharov, V. F., Cooling of the Arctic and the ice cover of the Arctic Seas (Trsl: Norsk Polarinstitutt), *AANI Trudy 337*, 96 pp., Gidrometeoizdat, Leningrad, 1976.

AD-P007 264

Variations of Extent, Area, and Open Water of the Polar Sea Ice Covers: 1978–1987

Per Gloersen
Laboratory for Oceans, NASA Goddard Space Flight Center, Greenbelt, Maryland, U.S.A.

William J. Campbell
Ice and Climate Project, U.S. Geological Survey, University of Puget Sound, Tacoma, Washington, U.S.A.

92-17946

ABSTRACT

The Scanning Multichannel Microwave Radiometer (SMMR) which operated onboard the Nimbus-7 satellite from October 1978 to August 1987 obtained sequential synoptic observations of the entire Arctic and Antarctic sea ice covers every 2 days through the clouds during night and day. It is a unique almost decade-long data set of the large-scale behavior of sea ice on earth. This paper presents the results of an analysis of SMMR observations of the Arctic, Antarctic, and global sea ice area, extent, and open water within the ice pack. These data are corrected for instrumental drift and errors due to variations in the ecliptic angle. Also presented is an analysis based on a combination of Fourier and ordinary least-squares regression techniques which yields their interannual variations and trends. In the power spectra of the Arctic and Antarctic sea ice areas and extents, the largest peaks are the dominant annual cycles, the second and third harmonics which are distinct, and the fourth and fifth which are identifiable. In order to remove the seasonal cycle, the first five harmonics are subtracted from the area and extent data, obtaining the residuals from which the trends are determined. During this 9-year period, the Arctic ice cover has negative trends of $1.9 \pm 1.3\%$ for the extent and $1.6 \pm 1.6\%$ for the area, with confidence levels of 95% as defined by the two-sigma criterion. During this time, the Antarctic ice cover is trendless both in extent and area. However, the global trend is $-1.0 \pm 0.7\%$ at the 95% confidence level. In the Arctic, the average seasonal range of open water area is from a minimum of 1.6 to a maximum of 3.2 million square kilometers. At the time of maximum ice extent, the amount of open water is typically 10%. In the Antarctic, the average seasonal range of open water area ranges from a minimum of 1.5 to a maximum of 4.5 million square kilometers. At the time of maximum ice extent, the amount of open water is typically 25%. The residuals and trends of the open water variations in the ice packs are discussed.

INTRODUCTION

The Scanning Multichannel Microwave Radiometer (SMMR) which operated onboard the Nimbus-7 satellite from October 1978 to August 1987, the longest period of observation ever accomplished by a satellite-borne passive microwave instrument, obtained sequential synoptic observations of the entire Arctic and Antarctic sea ice covers every 2 days through the clouds during night and day. It is a unique almost decade-long data set of the large-scale behavior of sea ice on earth. These data are presently being recorded onto CD-ROMs in a series of 12 disks, which will be available before the end of calendar 1991 from the National Snow and Ice Data Center in Boulder.

In a recent paper [Gloersen and Campbell, 1988], the nearly 9-year span of SMMR observations, uncorrected for instrument drift and errors due to variations in the ecliptic

angle, were used to derive variations of the Arctic and Antarctic sea ice extents and areas, and their sum, the global sea ice extents and areas. The ice extent is the total area enclosed by the ice perimeter or edge including areas of open water in polynyas and leads. Therefore, the sea ice area is the extent less the area of the open water. The initial regression analysis of these uncorrected data [Gloersen and Campbell, 1988] indicated that trends of -4% in the maxima of the annual ice extents and -5% in the minima occur in the Arctic over the 8.8-year span. The goodness-of-fit parameters (R^2) are 0.4 and 0.1, respectively. The trend in the Antarctic ice extent maxima was reported as -3% (R^2=0.1). However, there was noted a statistically more significant trend of -5% (R^2=0.8) in the maxima of the sum of the two polar packs, which is termed the global ice extent.

The key question posed by this earlier paper, and left unanswered, was: if the global ice extent maxima show a significant negative 8.8-year trend, what occurs within the separate Arctic and Antarctic sea ice extent curves, the sources of this trend, beyond what occurs at their annual extrema, which represent but a small sample of the total SMMR data set? This question led to the surmise that the trends of the individual annual ice extents can only be discerned by analyzing the complete every-two-day ice extent data. Perhaps the answer lies in the shape of the individual annual ice extent oscillations.

This paper presents the entire set of the 8.8-year SMMR Arctic, Antarctic, and global sea ice extent, ice area, and area of interior open water observations which have been calculated from radiances corrected for instrumental drift [Gloersen et al., 1991] and errors dependent on ecliptic angle [Francis, 1987; Gloersen et al., 1991]. These data are presently being prepared at NASA/Goddard for inscription onto a set of 12 CD-ROMs, which is scheduled to be available from the National Snow and Ice Data Center in Boulder late in 1991. Also presented are the results of an analysis, based on a combination of Fourier and ordinary least squares regression analyses, which determines their interannual variations and trends. The global sea ice coverage is obtained by summing the Arctic and Antarctic results. The phasing of global coverage is an important consideration for global atmospheric and oceanic circulation models. Among other things, variations in global sea ice coverage translate into variations in the global oceanic albedo.

OBSERVATIONS

Since the earlier publication [Gloersen and Campbell, 1988], there has been additional analysis of the SMMR instrument drift and instrument errors due, among other things, to unequal solar heating over the course of an orbit [Gloersen et al., 1991]. The drift analysis includes first removing the annual and semiannual cycles from the average oceanic radiances poleward of 50°N and 50°S to the ice edges. Second, the ascending and descending portions of the orbital data are averaged separately in each hemisphere in order to observe the seasonal variations of solar effects on the instrument [Gloersen et al., 1991]. This procedure for removing the annual and semiannual cycles also removes the 9-year means, and upon comparison the four results for the ascending and descending, north and south polar averages are found to be nearly identical. The radiation reference used for the detection and subsequent correction of SMMR instrument drift in the horizontally and vertically polarized components of the 0.8- and 1.7-cm wavelengths (37 and 18 GHz) channels utilized in the sea ice concentration calculations is an average of the polar ocean radiances between the 50° parallels and the ice edges [Gloersen et al., 1991]. Briefly, the instrument drifts are determined on the premise that the averaged polar oceanic radiances are invariant with time, and so the observed drift in these oceanic radiances constitutes instrument drift. Since the SMMR radiometers are of the Dicke type, no drifts are expected when observing targets radiometrically equivalent to the internal warm references, and none are observed in these channels. The actual correction for drift is scaled according to the relative position of the observed radiance between the oceanic and warm reference values. (Note that the space horn reference antennae do not detect instrument errors occurring between the microwave antenna/reference switches and the main antenna dish.)

The SMMR radiances used in this analysis are corrected for these drifts and for variations with ecliptic angle [Francis, 1987; Gloersen et al., 1991]. Further, we use the 15% ice concentration isopleth as the ice edge in addition to a weather filter [Cavalieri et al., 1984; Gloersen and Cavalieri, 1986] to reduce false ice signatures over the oceans due to storm effects. We decided to use the 15% isopleth for the ice edge in line with similar analyses with the Nimbus-5 microwave data [Zwally et al., 1983; Parkinson et al., 1987]. In the earlier SMMR study [Gloersen and Campbell, 1988], only the weather filter was used, which places the ice edge between the 8% and 12% ice concentration isopleths, depending on ice type. As a final correction, we discovered that the Arctic land mask used earlier [Gloersen and Campbell, 1988] for the mapping of the SMMR images was too large, which leads to an overestimation of the land area, and a consequent underestimation of the oceanic area. Accordingly, we revised the logic for developing the land mask used here. In so doing, we have also improved the area calculations with the proper use of both the equatorial and polar earth radii rather than just the equatorial radius as was done in the previous studies with the Nimbus-5 data. The net result of all of these corrections is that the magnitude of the SMMR ice extent variations shown in Figure 1 is about 7% greater in the Arctic and about the same in the Antarctic than those reported earlier [Gloersen and Campbell, 1988]. The Nimbus-5 Arctic sea ice extent data [Parkinson et al., 1987] should be about 1% greater.

The Arctic, Antarctic, and global ice extent and area variations shown in Figures 1 and 2 are determined with the entire corrected SMMR data set of the polar ice covers. On the average, this occurs every other calendar day, but there are brief periods of every-day operation or no operation occurring in less than 1% of the data set. An uneven data set is not suitable for the Fourier analysis used here, and so an evenly spaced time series of alternate days was produced by removal of extra days and interpolation to fill a few gaps.

An ordinary least squares regression analysis of the Arctic and Antarctic ice extent cycle curves shown in Figure 1 results in a preliminary determination of their trends. These observations cover a period with a fractional number of seasonal cycles. The Arctic ones start when the pack is rapidly growing towards its 1979 maximum extent and ends near its 1987 minimum. The Antarctic ones start soon after the pack

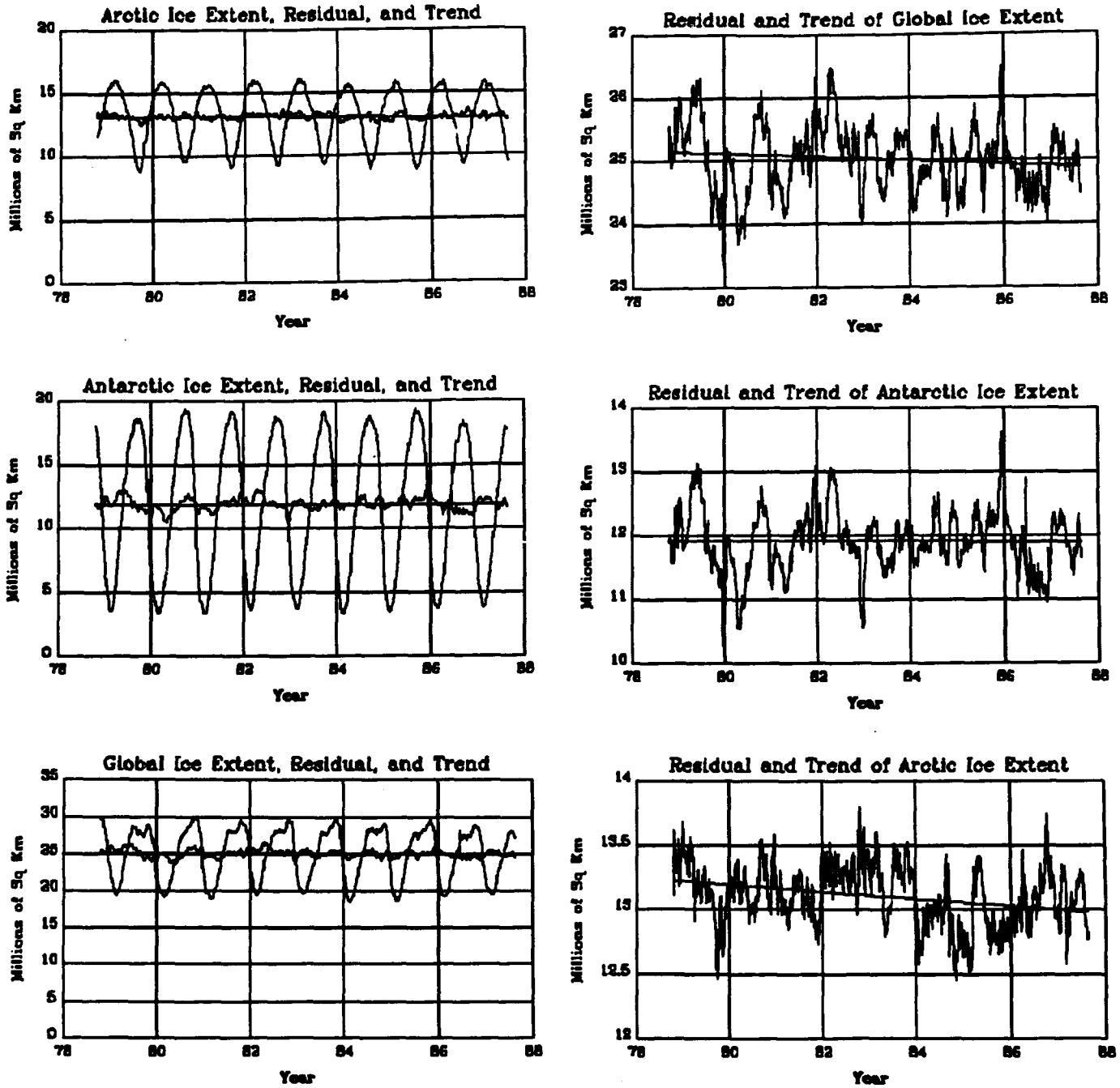


Figure 1. The areas enclosed by the margin of the sea ice covers (extents), the residuals after removal of the first five harmonics of the seasonal cycles, and the trends for the Arctic, Antarctic, and their sum (global) from October 25, 1978 to August 20, 1987. The extents were determined from the vertically polarized radiances at wavelengths of 0.8 and 1.7 cm obtained by the Scanning Multichannel Microwave Radiometer (SMMR) on board the Nimbus-7 spacecraft. The radiances were corrected for instrumental long-term drift and variations and systematic variations over the course of an orbit. The residuals and trends are also shown to the right of the figure on an expanded scale.

attains its 1978 maximum extent and ends just before its 1987 maximum. The following trends are so obtained: -2.6 ± 1.3% in the Arctic and -1.4 ± 1.5% in the Antarctic. The error estimates are based on twice the standard deviations of the slopes, which means that if the data were normally distributed, then there would be a 95% probability that the slopes would lie within those limits. However, a histogram analysis shows that these data are not normally distributed due to the large amplitudes of the seasonal cycles. In order to remove the bias to the trend due to a fractional number of seasonal cycles and to produce a normally distributed data set, we developed a procedure for removing the seasonal cycle, or deseasoning the observations, as described later.

Variations of the Arctic and Antarctic sea ice areas and extents for the 8.8-year SMMR record are summed to provide the global curves shown in Figures 1 and 2. An impor-

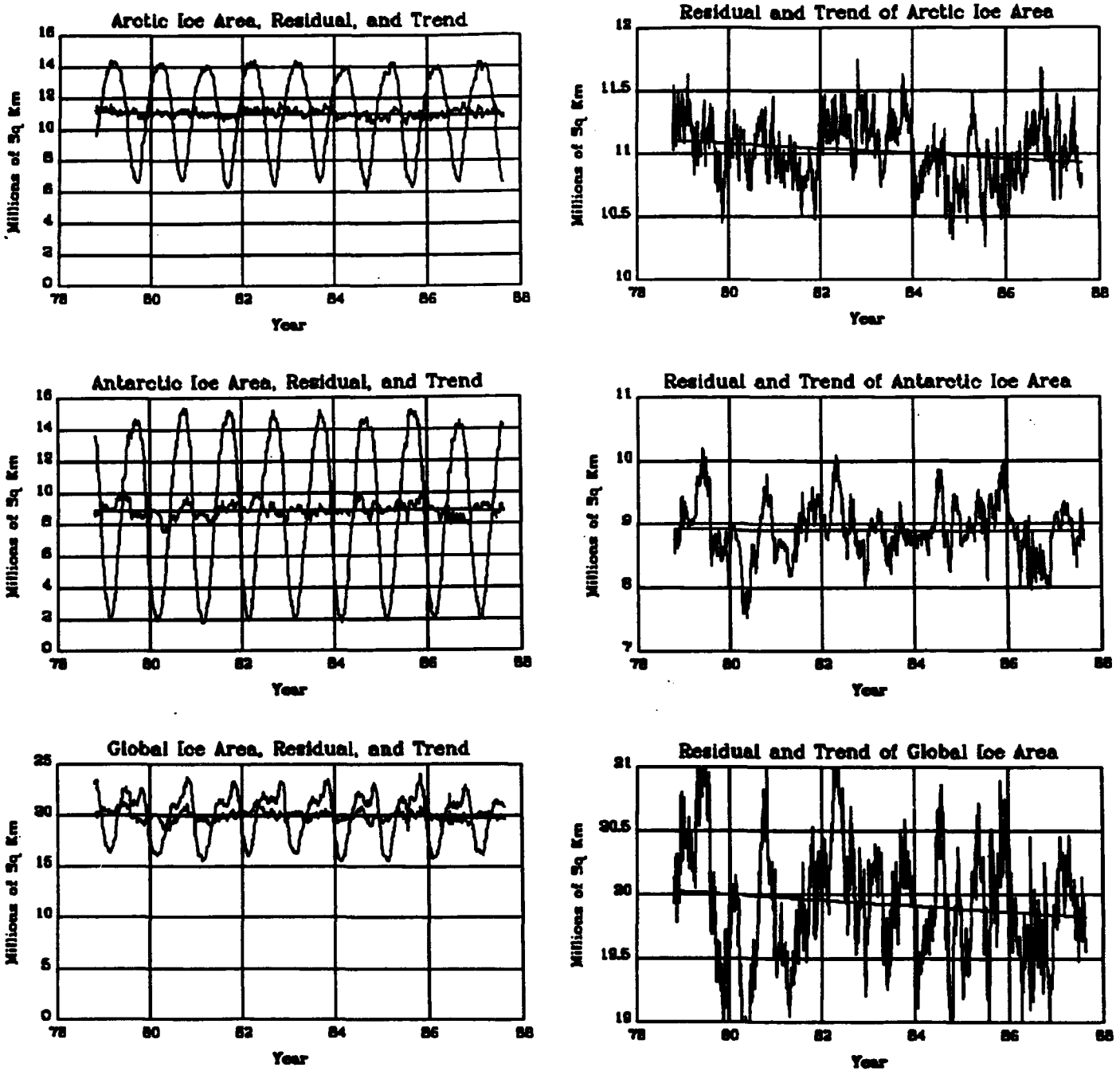


Figure 2. Same as Figure 1, except for the areal coverage by sea ice (sea ice area).

tant observation to be made from the global ice area and extent oscillations is that they vary annually by as much as 35%, representing a substantial annual variation in the amount of latent heat stored in the global oceans.

REMOVAL OF ANNUAL CYCLE

The earlier procedures used for trend analysis of the extrema of the sea ice extents or their annual averages [Zwally et al., 1983; Parkinson et al., 1987; Gloersen and Campbell, 1988] suffer from some inadequacies. Annually averaged data or data limited to the vicinity of extrema result in very few points and, when subjected to trend analysis, yield unacceptably wide 95% confidence limits. On the other hand, a histogram of the detrended entire Arctic ice extent data set (Figure 1) or, more properly, eight of the 8.8 years of the data (to find the trend through a whole number of annual cycles) shows these data to be not normally distributed due to the large amplitudes of the seasonal cycles. The trend of data so distributed has questionable statistical significance [Davis, 1973]. In order to remove the bias to the trend due to a fractional number of seasonal cycles and to produce a normally distributed data set, a procedure is used to remove the seasonal cycle.

Power spectra obtained from the Fast Fourier Transform (FFT) of the corrected SMMR time series of Arctic and Antarctic sea ice extents and areas show five identifiable har-

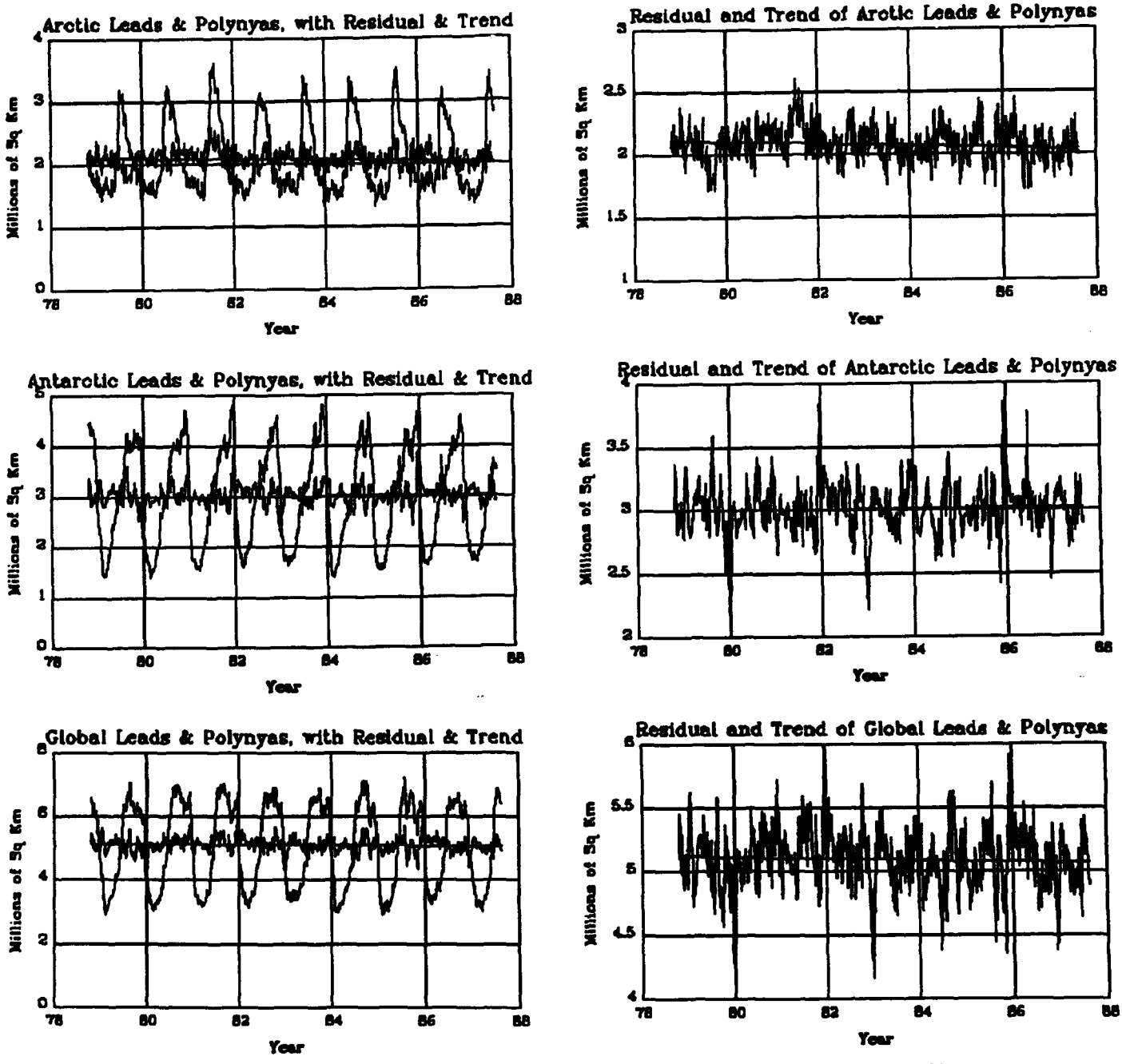


Figure 3. Same as Figure 1, except for the area of leads and polynyas (open water within the pack).

monics of the annual cycle resulting from the shapes of the seasonal ice extent oscillations. The seasonal oscillations are removed by subtracting all five of these harmonics of the annual cycle. To improve the precision of the procedure, the amplitudes and phases of the five harmonics of the Arctic and Antarctic annual cycles are determined by means of multiple linear regression, using the individual sines and cosines of each harmonic as the independent variables, rather than utilizing the amplitudes of the five harmonics in the complex FFT. The coefficients of multiple regression (R^2) for the fit of the five-harmonic seasonal cycle to the data are 0.98 and 0.99 for the Arctic extent and area, and 0.96 and 0.99 for the Antarctic. The residuals (anomalies) of the polar ice extents and areas with the seasonal cycles removed are also shown in Figures 1 and 2, with the linear trend lines of the anomalies superimposed. It is tempting to contemplate also removing the multiple-year cycles remaining in the residuals, but, unlike the seasonal cycle (as synthesized by the sum of the first five harmonics of the annual cycle), their periods are also unknowns as well as their amplitudes and phases and so synthesizing and removing them would lead to controversial results.

SEASONAL CYCLES OF THE OPEN WATER AREAS WITHIN THE ICE PACKS

The sea ice area curves (Figure 2) are subtracted from the sea ice extent curves (Figure 1) to produce curves of open water within the polar packs, which we designate as leads

and polynyas (Figure 3). It should be noted that this difference also includes contributions from various forms of new ice of short persistence which are characterized by lower radiances than thicker first-year ice, in some instances because of a thin moisture layer on a highly saline surface [Ramseier et al., 1975]. The seasonal variation in the areas of leads and polynyas on the global scale (Figure 3) is dramatic, with a range of about 75%. Since there is a 2–3 order-of-magnitude difference in the rate of sensible heat exchange between the atmosphere and the global surface depending on whether that surface is ice or water [Badgley, 1966], annual fluctuations of this magnitude are expected to play a significant role in weather patterns associated with the sea ice canopies and the oceans bordering them.

The open water peaks within the Antarctic ice pack occur during the times of maximum ice extent during the late austral winter and spring. Maximum open water occurs in the austral spring, consisting of approximately 18% of the area enclosed by the ice boundary.

The open water peaks in the Arctic occur in the late spring to early summer and are approximately 25% of the total ice area at that time. At the time of maximum ice extent, the amount of open water within the Arctic pack decreases to 9%.

ANOMALIES AND TRENDS OF THE ICE EXTENTS, AREAS, AND OPEN WATER

The Arctic ice extent anomalies (Figure 1) are normally distributed and ordinary least squares analysis [Davis, 1973] produces a trend of -1.9 ± 1.3% at a confidence level of 95% (the limits being two standard deviations) over the nearly 9-year SMMR record. The anomalies of the Antarctic sea ice extents show a trend of -0.1 ± 1.4% at a 95% confidence level. While the Antarctic residuals are also normally distributed, this trend is statistically insignificant. The anomalies of their sum, the global sea ice extents, have a trend of -1.0 ± 0.7% at the 95% confidence level. This trend has slightly narrower 95% confidence limits than the Arctic by itself, probably because of the tendency of the differing periods of the Arctic and Antarctic undulations in the residuals to cancel each other in their sum.

It is interesting to examine the undulations of the Arctic and Antarctic ice extent anomalies about their trend lines (Figure 1). The FFT power spectrum of the Arctic residual indicates the period of that undulation is about 4 years. The spectrum of the Antarctic residual gives two main peaks, one at a period of about 1.2 years and another slightly higher peak at about 3 years. The superposition of these nearly equal-amplitude oscillations makes it difficult to ascertain a correlation between these oscillations in the residuals of the Antarctic ice extent and the 5-year oscillation in sea surface temperatures observed [Reynolds et al., 1989] in the southern hemisphere, peaking in January 1983 and 1988.

The procedures discussed in the preceding section are applied also to the Arctic and Antarctic sea ice areas. The results are that the trend of the Arctic sea ice area anomaly (Figure 2) over the 8.8-year SMMR record is -1.6% ± 1.6%, at a confidence level of 95%. As with the extent, the trend in Antarctic sea ice area anomaly is insignificant. The global area anomaly (the sum of the Arctic and Antarctic anomalies) also has a significant trend, -1.0 ± 0.9% at the 95% confidence level.

The procedure for removing the average seasonal cycle from the ice area and extent anomalies is difficult to apply to their difference, the polynyas and leads, because too many Fourier components are required to obtain a good seasonal average. Therefore, as in the case of the global areas and extents, the anomalies of the polynyas and leads were obtained from a combination of the area and extent results (Figure 3). Application of ordinary least squares analysis to the residuals does not lead to significant trends in the areas of the leads and polynyas for the 8.8 SMMR years.

DISCUSSION

A number of studies have suggested that changes in the global average air temperature might be detectable by observing changes in the extents of the polar sea ice covers [Sissla et al., 1972; Streten, 1973; Budd, 1975; Kukla and Gavin, 1981; Carsey, 1982; Zwally et al., 1983; Parkinson et al., 1987]. After the Nimbus-7 SMMR observations are corrected for instrument drift and variations with ecliptic angle, they give us a unique look at the variations of these extents every 2 days for almost a decade. It is the most accurate and comprehensive such record ever obtained. The trends of the residuals obtained from the Arctic (-1.9 ± 1.3%) and the global (-1.0 ± 0.7%) sea ice extents may be signals of climate change. The large amounts of open water within both polar packs during all seasons, much larger than has been assumed before passive microwave observations occurred, must have strong influences on regional and global climates, yet to be studied.

We wish to emphasize that the near-decade of SMMR observations is not sufficiently long to establish clearly a climate trend. When these findings are combined with records of significant changes of other large-scale phenomena which have occurred during the same decade, the ensemble presents a possible case for global warming. Studies of changes of the global atmospheric air temperature [Hansen and Lebedeff, 1988; Jones et al., 1988] have found that a dramatic increase commenced in 1974 and persisted until the 1980s, which became the distinctly warmest period in the hundred-odd-year record. A warming of the Alaskan Arctic permafrost, typically 2°–4°C, commenced during this century, and during the SMMR period the average increase was 0.5°C [Lachenbruck et al., 1988]. A decrease in the extent of the Arctic sea ice cover is a plausible and possible cause for this permafrost warming. On the other hand, there has been no evidence of warming in oceanic surface temperatures in the northern hemisphere during this period [Badgley, 1966]. We do not know the causes of these significant decreases in Arctic sea ice extents, nor do we know why no corresponding decrease occurred in the Antarctic.

We do know that sea ice exists in those parts of the earth where global warming is expected to be the greatest. We also know that its insulating effect between polar atmospheres and oceans and its albedo undergo pronounced seasonal variations due to large open water effects. It is important that the recent Arctic decline and open water effects be considered in the context of predicted global change.

REFERENCES

Badgley, F. I., Heat budget of the Arctic Ocean, in *Proc. Symp. on the Arctic Heat Budget and Atmospheric Circulation*, edited by J. O. Fletcher, pp. 267–277, *Report No. RM-5233-NSF*, 1966.

Budd, W. F., Antarctic sea ice variations from satellite sensing in relation to climate, *J. Glaciol., 15*, 417–426, 1975.

Carsey, F. D., Arctic sea ice distribution at end of summer 1973–1976 from satellite microwave data, *J. Geophys. Res., 87*, 5809–5835, 1982.

Cavalieri, D. J., P. Gloersen, and W. J. Campbell, Determination of sea ice parameters with the Nimbus-7 SMMR, *J. Geophys. Res., 89*, 5355–5369, 1984.

Davis, J. C, *Statistics and Data Analysis in Geology*, John Wiley & Sons, New York, 1973.

Francis, E. A., Calibration of the Nimbus-7 Scanning Multichannel Microwave Radiometer (SMMR), 1979–1984, M.S. Thesis, 248 pp., Oregon State University, 1987.

Gloersen, P., and W. J. Campbell, Variations in the Arctic, Antarctic, and global sea ice covers during 1978–1987 as observed with the Nimbus 7 Scanning Multichannel Microwave Radiometer, *J. Geophys. Res., 93*, 10666–10674, 1988.

Gloersen, P., and D. J. Cavalieri, Reduction of weather effects in the calculation of sea ice concentration from microwave radiances, *J. Geophys. Res., 91*, 3913–3919, 1986.

Gloersen, P., W. J. Campbell, D. J. Cavalieri, J. C. Comiso, C. L. Parkinson, and H. J. Zwally, Arctic and Antarctic Sea Ice, 1978–1987: Satellite Passive Microwave Observations and Analysis, *NASA SP-_____*, 1991, In press.

Hansen, J., and S. Lebedeff, Global surface air temperatures: Update through 1987, *Geophys. Res. Lett., 15*, 323–326, 1988.

Jones, P. D., T. M. L. Wigley, C. K. Folland, D. E. Parker, J. K. Angell, S. Lebedeff, and J. E. Hansen, Evidence for global warming in the past decade, *Nature, 332*, 790, 1988.

Kukla, G., and J. Gavin, Summer ice and carbon monoxide, *Science, 215*, 497–503, 1981.

Lachenbruck, A. H., T. T. Cladouhos, and R. W. Saltuls, Permafrost temperature and the changing climate, in *Permafrost 3*, edited by K. Senneset, pp. 9–17, Tapir Publ., Trondheim, Norway, 1988.

Parkinson, C. L., J. C. Comiso, H. J. Zwally, D. J. Cavalieri, P. Gloersen, and W. J. Campbell, Arctic Sea Ice, 1973–1976: Satellite Passive-Microwave Observations, *NASA SP-489*, 296 pp., National Aeronautics and Space Administration, Washington, DC, 1987.

Ramseier, R. O., P. Gloersen, W. J. Campbell, T. C. Chang, Mesoscale description for the principal Bering Sea Experiment, in *Proceedings of the Final Symposium on the Results of the Joint Soviet–American Expedition*, Leningrad, May 12–17, 1974, edited by K. Ya. Kondratyev, Yu. I. Rabinovich, and W. Nordberg, pp. 234–269, Gidrometeoizdat, Leningrad, 1975. (Republished as *USSR/USA Bering Sea Experiment* by A. A. Balkema, Rotterdam, 307 pp., 1982.)

Reynolds, W. R., C. K. Folland, and D. E. Parker, Biases in satellite-derived sea surface temperature data, *Nature, 341*, 728–731, 1989.

Sissla, J. F., R. R. Sabatini, and H. J. Ackerman, Nimbus satellite data for polar ice survey, *Polar Rec., 16*, 367–373, 1972.

Streten, N. A., Satellite observations of the summer decay of the Antarctic sea ice, *Arch. Meteorol. Geophys. Bioklimatol. Ser. A, 22*, 129–134, 1973.

Zwally, H. J., J. C. Comiso, C. L. Parkinson, W. J. Campbell, F. D. Carsey, and P. Gloersen, Antarctic Sea Ice, 1973–1976: Satellite Passive-Microwave Observations, *NASA SP-459*, 206 pp., National Aeronautics and Space Administration, Washington, DC, 1983.

AD-P007 265

92-17947

Multi-Year Elevation Changes Near the West Margin of the Greenland Ice Sheet from Satellite Radar Altimetry

Craig S. Lingle
Geophysical Institute, University of Alaska Fairbanks, Fairbanks, Alaska, U.S.A.

Anita C. Brenner
ST Systems Corporation, Lanham, Maryland, U.S.A.

H. Jay Zwally
NASA Goddard Space Flight Center, Oceans and Ice Branch, Greenbelt, Maryland, U.S.A.

John P. DiMarzio
ST Systems Corporation, Lanham, Maryland, U.S.A.

ABSTRACT

Mean changes in the surface elevation near the west margin of the Greenland ice sheet are measured using Seasat altimetry and altimetry from the Geosat Exact Repeat Mission (ERM). The Seasat data extend from early July through early October 1978. The ERM data extend from winter 1986-87 through fall 1988. Both seasonal and multi-year changes are measured using altimetry referenced to GEM T2 orbits. The possible effects of orbit error are minimized by adjusting the orbits into a common ocean surface. Seasonal mean changes in the surface height are recognizable during the Geosat ERM. The multi-year measurements indicate the surface was lower by 0.4 ± 0.4 m on average in late summer 1987 than in late summer 1978. The surface was lower by 0.2 ± 0.5 m on average in late summer 1988 than in late summer 1978. As a control case, the computations are also carried out using altimetry referenced to orbits not adjusted into a common ocean surface.

INTRODUCTION

After the last glacial maximum about 18,000 years before present (B.P.), the western margin of the Greenland ice sheet retreated from its position near the coast to near its present position [Weidick, 1984]. In a summary of marginal fluctuations inferred from geologic evidence, Weidick [1984] states that this occurred between ≥10,000 and 8000–6000 B.P., and that minor re-advances and retreats have occurred since then. A gap in the record, about which little is known, occurred between 6000 B.P. and the Little Ice Age due to destruction of proglacial deposits during re-advances. The Little Ice Age occurred between about 450 and 150 years ago [Grove, 1988]. An advance occurred in the 1880s, during the last neoglacial maximum, and a minor readvance occurred around 1920. According to Weidick [1984] the margin has been retreating since then, although the rate of retreat has slowed during recent decades. Continuous advance in some sectors, since at least the early part of the 20th century, has been superimposed on the general pattern of retreat.

More recent interest in the ablation area of West Greenland [e.g., Braithwaite and Olesen, 1989; Lingle et al., 1990] has resulted from the possibility that increased melting of the Greenland ice sheet may contribute to the increasing rate of sea level rise expected during the next century due to climatic warming, which is predicted because of increasing CO_2 and trace greenhouse gases. The National Research Council [1985] estimated that this ice sheet may account for 10–26 cm of sea level rise by A.D. 2100 [Bindschadler, 1985]. In contrast, the Intergovernmental Panel on Climatic

Change [IPCC, 1990] Report on Sea Level Rise estimates that the Greenland ice sheet may contribute 0.5–3.7 cm to rising sea level by A.D. 2030 [Warrick and Oerlemans, 1990]. If extrapolated, the latter estimate suggests a contribution of roughly 5.4 ± 4.1 cm from this source by A.D. 2100. The substantial difference between the NRC and IPCC estimates is a reflection of current uncertainty regarding the overall mass balance of the Greenland ice sheet.

The only direct measurement of a multi-year mean change in the surface elevation of a large area of the Greenland ice sheet (the southern half, approximately) has been made by Zwally et al. [1989], using satellite radar altimetry. They found that during the 7-year interval between Seasat and the Geosat Geodetic Mission (GM), there was a mean increase in the surface height equivalent to a linear rate of increase of 20 ± 6 cm yr^{-1}. Most of the measurements used in this determination were over the central regions of the ice sheet, due to relatively poor altimeter tracking near the margins. Zwally [1989] pointed out that this is equivalent to a sea level lowering of 0.2–0.4 mm yr^{-1}, depending on whether the increase of the surface height is short-term, consisting mostly of increased snow depth, or long-term, consisting mostly of increased ice thickness. (See also Douglas et al. [1990] and Zwally et al. [1990a].) The GM consisted of the initial 18 months following the spring 1985 launch of Geosat. Subsequently Geosat was maneuvered into an orbit geometry closely following the previous Seasat ground tracks in order to carry out the Exact Repeat Mission (ERM), which started in fall 1987 [e.g., Douglas and Cheney, 1990].

Seasonal mean changes in the surface height of the West Greenland ablation area were measured by Lingle et al. [1990], using altimetry from the Geosat GM. Here we extend that study, by measuring multi-year mean changes in the surface height throughout a larger area that includes the ablation area and extends farther up the ice sheet to about the 2000-m contour (Figure 1). Elevation differences are measured at orbit crossover points during the Geosat ERM, and also between Seasat and the ERM. A crossover point is a location where an orbit ascending in latitude is later crossed by an orbit descending in latitude, or the reverse, so two measurements of the surface height, separated by a time interval, are obtained at approximately the same location. Seasonal and multi-year mean changes in elevation are estimated by averaging the crossover differences throughout the region.

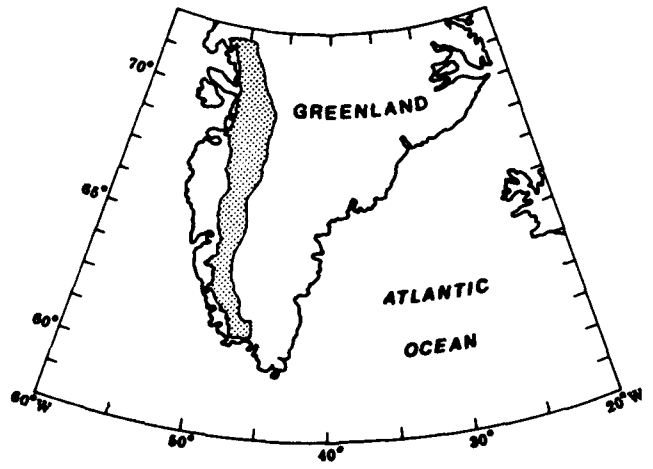


Figure 1. The stippled area is the measurement region, which includes the ablation area of the western Greenland ice sheet and extends up to the 2000-m elevation contour, approximately, and to Lat. 72°N.

ORBITS AND ORBIT ADJUSTMENT

Precision orbit determination is a fundamental aspect of altimetry, because the position of the satellite must be accurately known at the time of each measurement. Precision orbits are computed by iterating to a self-consistent solution among the observations from the tracking stations, which are widely separated on the earth's surface, and the equation of motion for the satellite, which must be satisfied everywhere. The numerical solutions of the equation of motion require an accurate model of the gravitational potential field, and nonconservative forces, primarily air drag and radiation pressure due to the solar wind and radiation upwelling from the earth's surface, must be taken into account [see, e.g., Stewart, 1985, pp. 260–309]. Precision orbits for the Geosat ERM have been computed by Haines et al. [1990] and Shum et al. [1990].

The most accurate model of the gravitational potential field (based entirely on satellite tracking observations) available at the time of this study was the Goddard Earth Model T2, or GEM T2 [Marsh et al., 1989]. This model was employed for re-computation by Haines [1991] of the Seasat orbits used in this study, as well as for computation of the Geosat ERM orbits [Haines et al., 1990]. The Greenland altimeter measurements employed here, which were obtained by two different satellites, are thus with respect to orbits computed using the same gravity model. The radial (vertical) precision of the GEM T2 Geosat ERM orbits is estimated to be about 0.35 m RMS [ibid].

Radial orbit error tends to result primarily from inaccuracies in the spherical harmonic expansions used to represent the gravitational potential field, i.e., the gravitational field is not equally well represented everywhere, and from errors in the estimates of air drag and radiation pressure, which must be made from other models. Radial orbit errors tend to be spatially well correlated, so it is necessary to be cognizant of the possibility that an apparent change through time in the height of a surface in a particular region, such as western Greenland, may be an expression of time-dependent orbit error. Although the 0.35 m RMS radial precision of the Geosat ERM orbits is excellent, time-dependent orbit error in particular regions can be larger than this.

The possibility of orbit error is taken into account by adjusting the Seasat and Geosat ERM orbits crossing Greenland into a common ocean surface, which is the Seasat/Geos-3 mean surface derived from the global Seasat and Geos-3 altimetric data sets [Marsh et al., 1986, 1990]. Short-arc adjustments are used; that is, the orbits are adjusted into the ocean surface immediately on either side of Greenland. A detailed description of the method is given by Zwally et al. [1990b]. Briefly, for each arc the differences (residuals) are computed between the ocean elevations derived from the data along that arc, and the smoothed Seasat/Geos-3 ocean elevations along the same arc, on both sides of Greenland. The residuals are plotted versus time for satellite travel

along the arc, and a least-squares straight-line fit is performed. The corrections for the ice sheet measurements along the arc are then obtained by evaluating the linear function at the corresponding times. The underlying assumption is that if the orbit error were zero, the ocean surface measured along the arc would differ only negligibly from the mean ocean surface along the same arc.

It is important to note that this strategy cannot be expected to remove all traces of orbit error because the ocean surface is not static. Adjustment inaccuracy for an individual pass can be introduced, for example, by inadequately modeled ocean tides at the time of the pass, by changes in the height of the sea surface caused by mesoscale changes in atmospheric pressure, and possibly by seasonal to multi-year changes in the steric height and dynamic topography. It is assumed here, however, that on the whole this orbit adjustment procedure is sufficient to eliminate any apparent long-term trend that might otherwise appear as an artifact of time-dependent orbit error.

DATA

The Seasat and Geosat ERM altimeter data from the Greenland ice sheet were corrected for tracking errors, atmospheric effects, and solid earth tides as described by Martin et al. [1983] and Zwally et al. [1983]. These corrections were carried out prior to the orbit adjustment procedure described above. Data from the region of interest near the western margin of the ice sheet were selected using the mask shown in Figure 1. The lower elevation limit for acceptable data was specified, as a function of latitude, far enough up-glacier from the ice sheet margin to exclude waveforms back-scattered from coastal rocks and nunataks. The upper elevation limit coincides, approximately, with the 2000-m elevation contour.

MEASUREMENT NOISE AND CROSSOVER ERROR

The measurement noise levels in Geosat GM altimetry were estimated and mapped by Lingle et al. [1990] as a function of position throughout the West Greenland ablation area, using semivariogram methods. GM altimetry noise levels were similarly estimated and mapped by Lingle and Brenner [1989] within a series of 100 km x 100 km area blocks extending along the EGIG line [see, e.g., Seckel, 1977] from the ablation area to the central ice divide. These results, which are assumed to be characteristic of the Geosat ERM data (acquired by the same instrument on board the same satellite), indicate that average measurement noise levels near the west margin of the ice sheet, up to about the 2000-m contour, are about 10 m. The standard error of a Geosat ERM crossover difference is taken to be $\sqrt{2}$ (10) m or 14.1 m.

The Seasat and Geosat altimeters were generally similar in design, although improvements were incorporated in the Geosat version [MacArthur et al., 1987]. The Geosat altimeter yielded an instrument-induced along-track noise level of about 3 cm RMS over the oceans, compared to 5 cm RMS for Seasat (for 1 per second data in each case), but additional noise due to oceanographic effects caused both altimeters to have an average noise level, integrated over all frequencies, of about 8 cm RMS [Sailor and LeShack, 1987]. Over the ice sheets, the factors primarily responsible for high noise levels in the data are backscatter from off-nadir undulations and points upslope from nadir, and these factors were the same for both Seasat and Geosat. The Geosat measurement noise levels estimated and mapped by Lingle et al. [1990] and Lingle and Brenner [1989] (for 10 per second data) are therefore assumed to be characteristic of the Seasat altimetry.

The Seasat altimeter yielded less continuous data over the Greenland ice sheet due to a tracker that was less responsive over sloping and undulating surfaces. Consequently most of the valid Seasat–Geosat crossover differences are from the subregion of the area shown in Figure 1 that is above the ablation area, where the ice sheet topography is less rugged. The results of Lingle and Brenner [1989] suggest that in the 1300–2000 m elevation range, the average altimetry noise level is roughly 7 m. The standard error of a Seasat–Geosat ERM crossover difference is taken to be $\sqrt{2}$ (7) m or 9.9 m.

SEASONAL ELEVATION CHANGES, 1987–1988

Seasonal mean changes are first computed during the Geosat ERM by dividing the ERM into 91-day "seasons," with late summer defined to coincide with the Seasat time frame (July 10 through October 9). This definition fixes the times of the other seasons. The first season having data of sufficient quality to yield enough crossover differences for statistically valid averaging is late winter 1986-87 (i.e., January 8 through April 9, 1987). Subsequent seasonal mean changes in the surface height are computed with respect to that season. The method, which is described in detail by Lingle et al. [1990, pp. 160–161], is an adaptation of the methods of crossover analysis developed by Zwally et al. [1989]. The method includes cancellation of the ascending versus descending orbit bias [see Lingle et al., 1990, equation (6)]. The method used here differs from that described by Lingle et al. [1990], however, in that each crossover difference is not weighted in proportion to the inverse square of the measurement noise level in the local neighborhood of the crossover point. Rather, a representative noise level for the entire region shown in Figure 1 is estimated, as described above, and unweighted averaging of the crossover differences is employed. An edit level of 15 m is used to define acceptable Geosat ERM–Geosat ERM crossover differences.

The seasonal mean fluctuations in the surface height during 1987-88 (the Geosat ERM) are shown in Figure 2, starting in late winter 1986-87. The standard errors of the mean ranged from ±0.3 to ±0.5 m for the computed changes relative to late winter 1986-87. The error limits shown in Figure 2 are larger than that, however, because the larger errors associated with the crossover differences between Seasat and the Geosat ERM are taken into account, as described in the next section.

Figure 2 shows that during the Geosat ERM the surface was highest on average during late winter, which includes part of spring, the time of maximum snow depth. In both 1987 and 1988 the surface was slightly lower on average during late spring, which includes part of summer, when melting was presumably in progress. During both years the surface height was lowest during late summer, when maximum surface lowering due to ablation is expected. The mean decrease in the surface height from late winter to late

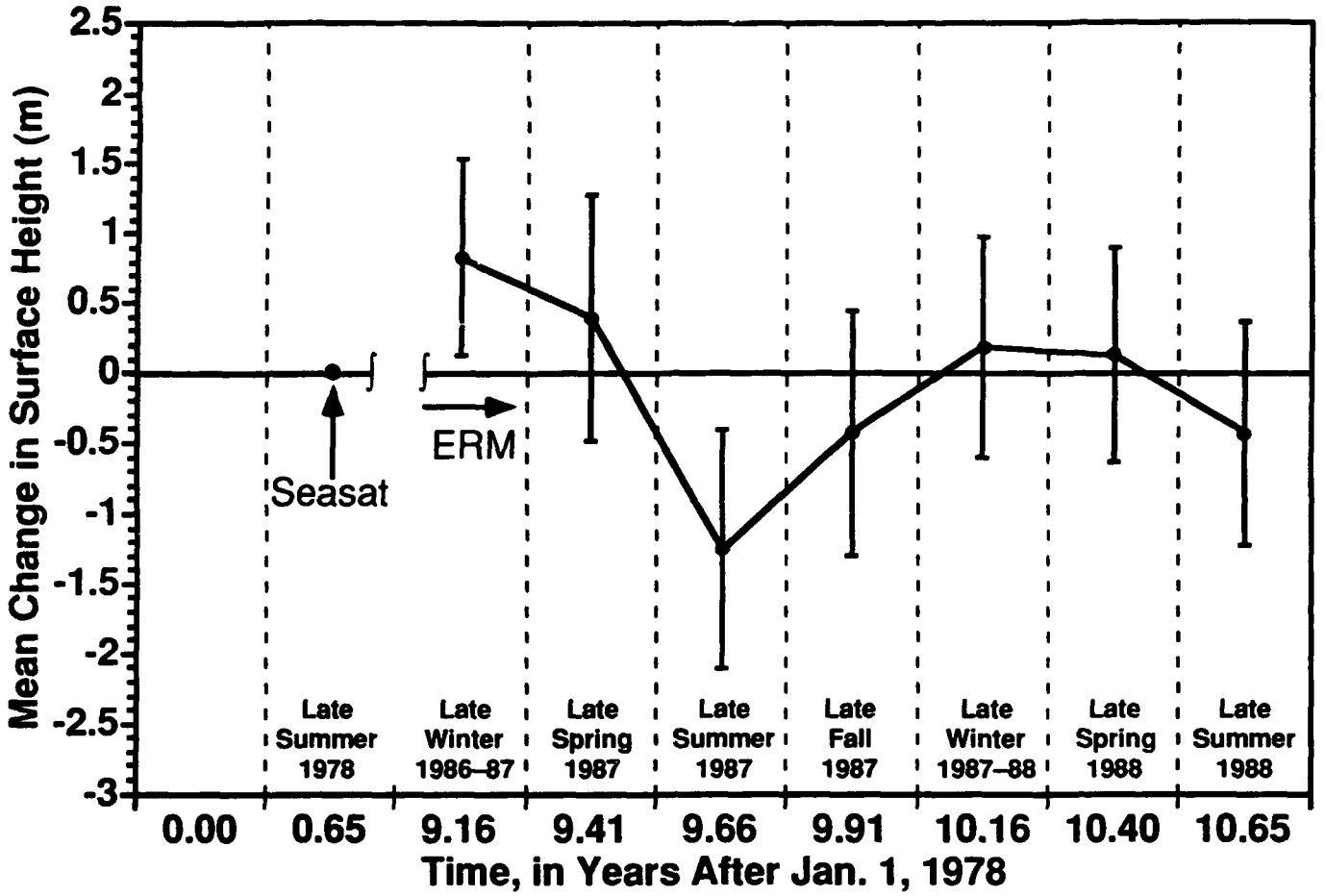


Figure 2. Mean changes in surface elevation near the west margin of the Greenland ice sheet, within the area shown in Figure 1, between late summer 1978 (Seasat) and 1987-88 (the Geosat ERM). Changes were computed using orbits adjusted into the Seasat/Geos-3 mean ocean surface. This figure corresponds to case 1 in Table 1. (Cases 1–4 in Table 1 are used to derive the mean height changes quoted in the abstract and conclusions, as described in the text.) Each error bar represents one standard deviation of the mean for the change computed with respect to the Seasat surface, which is the datum.

summer in 1987 was 2.1 ± 0.7 m. Between late winter and late summer in 1988, the mean decrease in the surface height was 0.6 ± 0.5 m.

MULTI-YEAR ELEVATION CHANGES, 1978 TO 1988

Multi-year mean changes in elevation near the west margin of the Greenland ice sheet are computed by defining the Seasat time frame, late summer 1978, as the initial season. Mean elevation changes between Seasat and the successive seasons of the Geosat ERM were first computed as described by Lingle et al. [1990], with the difference that there is an 8.5-year time gap between late summer 1978 and late winter 1987 (the first season of usable ERM data). Otherwise the method used was as described above, with unweighted averaging of crossover differences employed and a representative standard error assigned to all crossover differences.

The results showed a seasonal cycle during the Geosat ERM relative to late summer 1978, but were less than satisfactory because the discontinuous nature of the Seasat data, combined with data of varying spatial continuity during the Geosat ERM, resulted in two seasons (late fall 1987 and late winter 1987-88) having insufficient valid crossover differences for a statistically meaningful measurement of mean elevation change. (An edit level of 30 m is used to define acceptable Seasat–Geosat ERM crossover differences.) These results are not shown.

An alternative method is adopted instead, consisting of computation of the mean elevation change between Seasat and the first 91-day season of the Geosat ERM having useable data (late winter 1986-87). Subsequent elevation changes are determined by "adding-on" the time series of subsequent seasonal changes during the Geosat ERM, determined as described above. This method does not decrease the standard error of the mean for the Geosat ERM seasonal changes computed relative to the surface during the Seasat time frame, because the error of each change relative to the initial Geosat ERM season is combined with the additional (larger) error of the computed change between the surface during the Seasat time frame and the surface during the initial season of the Geosat ERM. This approach does, however, give a clearer and more continuous picture of the mean changes in the surface height during the Geosat ERM relative to the surface during the earlier Seasat time frame. The results are shown in Figure 2.

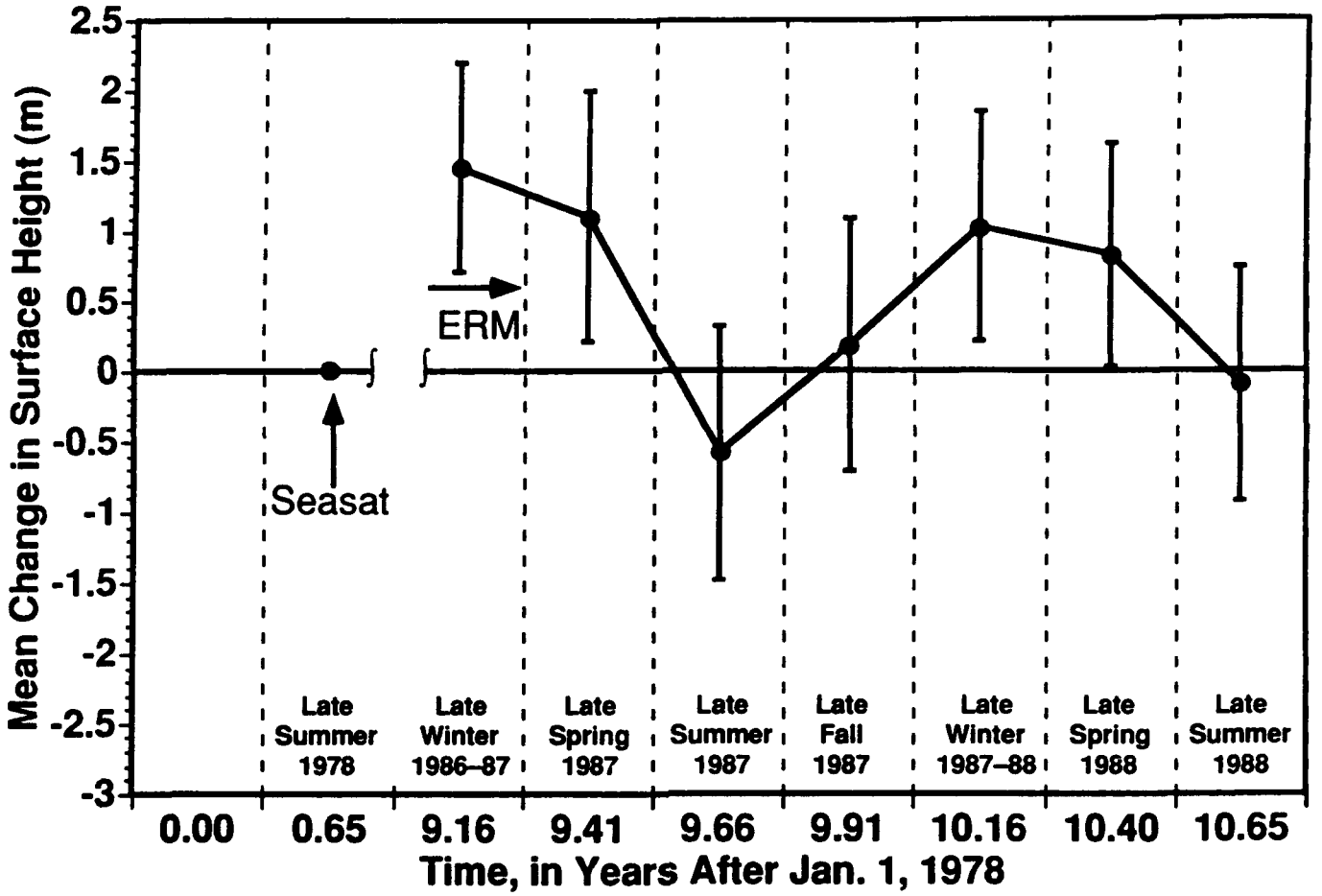


Figure 3. Control case: mean changes in surface elevation near the west margin of the Greenland ice sheet, within the area shown in Figure 1, computed using orbits *not* adjusted into the Seasat/Geos-3 mean ocean surface. The computation is otherwise identical to that shown in Figure 2. These results are analogous to case 1 in Table 1. (The mean height changes quoted in the abstract and conclusions are computed using adjusted orbits, and are derived from cases 1–4 in Table 1, as described in the text.)

CONTROL CASE: MULTI-YEAR ELEVATION CHANGES, 1978 TO 1988, COMPUTED WITHOUT ORBIT ADJUSTMENTS

Figure 3 shows the results of the crossover analysis described above, carried out using altimetry referenced to GEM T2 orbits that were not adjusted into the Seasat/Geos-3 mean ocean surface. Comparison of Figure 3 to Figure 2 shows that the effect of orbit adjustment is to cause a slight downward shift of the curve showing seasonal mean changes in the surface height during the Geosat ERM, relative to the Seasat surface. Otherwise, the curve showing seasonal mean changes during the Geosat ERM is quite similar. Figure 3 suggests that there may have been a negative mean change in the surface height between late summer 1978 and the same season in 1987, but the standard error of the mean overlaps zero. The mean change in the surface height between late summer 1978 and the same season in 1988 is near zero (in Figure 3).

ALTERNATIVE COMPUTATIONS OF LATE SUMMER CHANGES

In this paper, the primary focus is on determination of mean changes in the surface height between late summer 1978 and the same season in 1987 and 1988. This change can be determined in four ways, referred to below as cases 1 through 4, by making use of the different Geosat ERM seasons having sufficient crossovers with the Seasat orbits for valid averaging. Seasat and Geosat ERM orbits that were adjusted into the Seasat/Geos-3 mean ocean surface are employed in all of these cases. Case 1 is described above. In case 2, the Seasat orbits are crossed with the Geosat ERM orbits of late spring 1987, in order to fix the curve showing the ERM seasonal changes (analogous to Figure 2) relative to the mean surface height during the Seasat time frame (the datum in Figure 2). The heights of the late summer 1987 and 1988 surfaces are then calculated relative to late spring 1987, and corrected for the height change between late summer 1978 and late spring 1987.

In case 3, the Seasat orbits are crossed directly with the Geosat ERM orbits of late summer 1987, and with the ERM orbits of late summer 1988. In case 4, the Seasat orbits are crossed with the Geosat ERM orbits of late spring 1988, in order to fix the curve showing the ERM seasonal changes (also analogous to Figure 2) relative to the mean surface height during the Seasat time frame (the datum in Figure 2). The remainder of the calculation is analogous to case 2. The results of the 4 cases are shown in Table 1.

Table 1 shows that although the four cases yield differing results, the error bars overlap. The results are thus self-consistent to within one standard deviation of the mean. The mean change in the surface height between late summer 1978 and late summer 1987 is taken as the unbiased

Case	Late Summer 1978 to Late Summer 1987 (m)	Late Summer 1978 to Late Summer 1988 (m)
1	-1.26 ± 0.85	-0.43 ± 0.80
2	-1.16 ± 1.02	-0.33 ± 0.98
3	0.14 ± 0.78	-1.66 ± 1.08
4	0.24 ± 0.87	1.07 ± 0.82

Table 1. Alternative calculations of mean changes in surface height, late summer to late summer (adjusted orbits).

weighted average of the four cases, with each case weighted in proportion to the inverse square of its standard error. The result is -0.43 ± 0.44 m. The mean change in the surface height between late summer 1978 and late summer 1988, determined in the same way, is -0.18 ± 0.45 m.

DISCUSSION: VARIABLE PENETRATION DEPTH

Ridley and Partington [1988] found that the effect of surface and volume scattering can cause error in the measured range to the snow surface of as much as 1.1 to 3.3 m, depending on the ratio of surface to volume scattering, if the return wave forms are retracked using an assumption that the snow surface lies at the location on the leading slope of half the peak power. That is, the apparent surface measured by the altimeter is lower by an amount that depends on the predominance of volume scattering. These authors also state [Ridley and Partington, 1988, p. 621] that "the error is much smaller if the Martin et al. (1983) method of retracking is used, as the function fitted to the return is sensitive to the inflection point."

The method of Martin et al. [1983] was used to retrack the altimeter waveforms used to derive the elevation measurements employed in this study, as noted in the section on data.

Suppose, however, that surface scattering predominates in summer, when melting and refreezing tend to result in formation of a surface crust on snow, and in exposed bare ice in the ablation area, and that volume scattering predominates is winter, when lower temperatures tend to result in a dry snow surface. Then the seasonal mean changes in the surface height measured by the altimeter would be minimized, since the penetration depth would be maximum during late winter and spring, when the surface is highest, and minimal during late summer when the surface is lowest. The measured seasonal mean changes shown in Figures 2 and 3 and in Lingle et al. [1990] are not overly small, however, relative to the changes one would expect from the ablation rates measured by Braithwaite and Olesen [1989], and the accumulation rates mapped by Radok et al. [1982] (with the exception, perhaps, of the measured mean change between late spring 1988 and late summer 1988, shown in Figure 2). The results of this study and of Lingle et al. [1990] suggest, therefore, that seasonal changes in penetration depth do not preclude measurement of seasonal mean changes in the surface height with altimetry, when the crossover differences are averaged over a suitably large region. The central focus of this study—measurement of mean changes between 1978 and 1987-88—should be unaffected by seasonal variations in penetration depth, in any case, because the mean changes in surface height are measured between the same season (late summer) in each year.

COMPARISON TO FIELD MEASUREMENTS AND OTHER WORK

The multi-year mean changes in the surface height computed in this study can be compared to mean changes in the surface height measured by optical leveling on the lower EGIG line within the ablation area at about Lat 69.5°N. Bauer et al. [1968] found the surface lowered at a mean rate of 0.3 m yr^{-1} between 1948 and 1959. Seckel [1977] found the surface lowered at a mean rate of 0.24 m yr^{-1} between 1959 and 1968. (These results are also summarized by Reeh [1985].) Over an area including the lower EGIG line and measuring about 22 km parallel to the ice sheet margin by 6 km perpendicular to the margin, Thomson et al. [1986] measured a mean surface lowering of 14 m between 1959 and 1982 using photogrammetric methods, which is equivalent to a mean lowering rate of 0.61 m yr^{-1}. A 0.24–0.61 m yr^{-1} mean rate of surface lowering during the 9–10 year measurement period considered here would be significantly greater than the error range shown in Figures 2 and 3, and should thus be recognizable in the altimeter data. If the ablation area of West Greenland is thinning, however, the rate of thinning should decrease upglacier from the margin because of the parabolic nature of ice sheet profiles [Paterson, 1981]. The EGIG optical leveling results, in fact, show thickening of the inland ice sheet above the equilibrium line [Reeh, 1985]. The results of this study are determined using altimeter crossover differences from both below and above the equilibrium line, with most being from higher elevations (up to about 2000 m). Thus, if the ice sheet is still thinning close to the western margin, while thickening above the equilibrium line, as determined by earlier field workers, this may be consistent with the near-zero mean change determined in this study using crossover differences averaged over the whole area (Figure 1).

If there was a linear mean decrease of the surface height between late summer 1978 and the same season in 1987, the results obtained here indicate the rate of surface lowering would have been 0.05 ± 0.05 m yr^{-1}. Between late summer 1978 and the same season in 1988, however, the assumption of a linear mean decrease leads to a conclusion that the surface lowered at a mean rate of 0.02 ± 0.05 m yr^{-1}. The error bars for these two cases overlap, but the difference, and the seasonal mean changes shown in Figures 2 and 3, indicate that the interannual variability is significant and a uniform rate of surface lowering during the 9 to 10 year measurement period is unlikely.

The seasonal mean elevation changes in the West Greenland ablation area measured by Lingle et al. [1990] suggest an increasing trend for the surface height during the Geosat GM. Zwally et al. [1989] and Zwally [1989] measured an increased surface height in all elevation intervals between Seasat and the Geosat GM (1978 to 1985-86), as well as during the Geosat GM, including the 700–1200-m interval, which generally coincides with the ablation area. However, the results obtained in this study (Figures 2 and 3) suggest,

if anything, a decreasing trend for the surface height superimposed on the seasonal mean changes during the Geosat ERM, while the Seasat to Geosat ERM measurements show no statistically significant mean change in the surface height between late summer 1978 and the same season in 1987 and 1988, throughout the area shown in Figure 1. These apparent discrepancies may be related to short-term variability.

CONCLUSIONS

The results of this analysis indicate that the surface of the Greenland ice sheet near the western margin, throughout the region including the ablation area and extending up to about the 2000-m elevation contour and to Lat. 72°N (Figure 1), was lower by 0.4 ± 0.4 m on average in late summer 1987 than in late summer 1978. The surface was lower by 0.2 ± 0.5 m on average in late summer 1988 than in late summer 1978. This result was obtained from unbiased weighted averaging of the four sets of results shown in Table 1, of which case 1 (only) is shown in Figure 2. The possible effects of time-dependent orbit error were minimized by adjusting the GEM T2 Seasat and Geosat ERM orbits into the Seasat/Geos-3 mean ocean surface [Marsh et al., 1986, 1990].

The mean changes in elevation between late summer 1978 and the same season in 1987 and 1988 were also computed using altimetry referenced to GEM T2 orbits that were not adjusted into the Seasat/Geos-3 mean ocean surface. The results, shown in Figure 3, are analogous to Figure 2 and case 1 in Table 1. These results also indicate no statistically significant mean change in the surface height during the 9–10 year measurement interval.

ACKNOWLEDGMENTS

This study was partially supported by the NASA Interdisciplinary Research Program in the Earth Sciences, Project on Detection of Changes and Identification of Forcings Due to the Greenhouse Effect in the Climate System. We thank R. H. Thomas for providing additional support from the NASA Polar Research Program. Support was also provided by a National Research Council Resident Research Associateship to C. S. Lingle at the Oceans and Ice Branch, NASA Goddard Space Flight Center, and by the Alaska SAR Facility at the University of Alaska Fairbanks. Thanks are extended to R. A. Bindschadler and R. H. Thomas for comments that improved the manuscript, to C. G. Rapley and an anonymous referee for constructive critical reviews, to S. Fiegles, T. Seiss, and D. Coccia for digitizing, plotting and drafting the area shown in Figure 1, and to D. Sandberg for preparing Figures 2 and 3.

REFERENCES

Bauer, A., A. Ambach, and O. Schimpp, Mouvement et variation d'altitude de la zone d'ablation ouest de l'Indlandsis du Groenland entre 1948 et 1959, *Meddelelser om Grønland, 174*, 1968.

Bindschadler, R. A., Contribution of the Greenland ice cap to changing sea level: Present and future, in *Glaciers, Ice Sheets, and Sea Level: Effect of a CO_2-Induced Climatic Change*, pp. 258–266, National Academy Press, Washington, DC, 1985.

Braithwaite, R. J., and O. B. Olesen, Detection of climate signal by inter-stake correlations of annual ablation data Qamanarssup Sermia, West Greenland, *J. Glaciol., 35*, 253–259, 1989.

Douglas, B. C., and R. E. Cheney, Geosat: Beginning a new era in satellite oceanography, *J. Geophys. Res., 95*, 2833–2836, 1990.

Douglas, B. C., R. E. Cheney, L. Miller, R. W. Agreen, W. E. Carter, and D. S. Robertson, Greenland ice sheet: Is it growing or shrinking?, *Science, 248*, 288, 1990.

Grove, J. M., *The Little Ice Age*, Methuen, London, 498 pp., 1988.

Haines, B. J., Evaluation of Seasat-Geosat orbits and altimetry, with application to long-term sea level changes in the North Pacific, Ph.D. Thesis, University of Colorado, May 1991.

Haines, B. J., G. H. Born, G. W. Rosborough, J. G. Marsh, and R. G. Williamson, Precise orbit computation for the Geosat Exact Repeat Mission, *J. Geophys. Res., 95*, 2871–2885, 1990.

Intergovernmental Panel on Climatic Change, *Climate Change: The IPCC Scientific Assessment*, edited by J. T. Houghton, G. J. Jenkins, and J. J. Ephraums, 365 pp., Cambridge University Press, New York, 1990.

Lingle, C. S., and A. C. Brenner, Radar altimetry, measurement noise, and elevation changes in the ablation area of the West Greenland ice sheet, unpublished poster session presented at AGU Chapman Conference on Long-Term Sea Level Changes, Snowbird, Utah, 17–20 April 1989.

Lingle, C. S., A. C. Brenner, and H. J. Zwally, Satellite altimetry, semivariograms, and seasonal elevation changes in the ablation zone of West Greenland, *Ann. Glaciol., 14*, 158–163, 1990.

MacArthur, J. L., P. C. Marth, Jr., and J. G. Wall, The Geosat radar altimeter, *Johns Hopkins APL Technical Digest, 8*, 176–181, 1987.

Marsh, J. G., et al., The GEM T2 Gravitational Model, *NASA Tech. Memo. 100746*, 94 pp., Sept. 1989.

Marsh, J. G., A. C. Brenner, B. D. Beckley, and T. V. Martin, Global mean sea surface based upon the Seasat altimeter data, *J. Geophys. Res., 91*, 3501–3506, 1986.

Marsh, J. G., C. J. Koblinsky, H. J. Zwally, A. C. Brenner, and B. D. Beckley, Global mean sea surface based upon Geos-3 and Seasat altimeter data, *EOS, Transactions, American Geophysical Union, 71*, 1266, 23 October 1990.

Martin, T. V., H. J. Zwally, A. C. Brenner, and R. A. Bindschadler, Analysis and retracking of continental ice sheet radar altimeter waveforms, *J. Geophys. Res.*, 88, 1608–1616, 1983.

National Research Council, *Glaciers, Ice Sheets, and Sea Level, Effect of a CO_2-Induced Climatic Change*, National Academy Press, Washington, DC, 1985. (Available as *Department of Energy Report DOE/ER/60235-1*, from National Technical Information Service, U.S. Department of Commerce, Springfield, Virginia 22161, U.S.A.)

Paterson, W. S. B., *The Physics of Glaciers*, Pergamon, New York, 1981.

Radok, U., R. G. Barry, D. Jenssen, R. A. Keen, G. N. Kiladis, and B. McInnes, *Climatic and Physical Characteristics of the Greenland Ice Sheet*, report available from Cooperative Institute for Research in Environmental Sciences, University of Colorado, Boulder, CO 80309, U.S.A., 1982.

Reeh, N., Greenland ice-sheet mass balance and sea-level change, in *Glaciers, Ice Sheets and Sea Level: Effect of a CO_2-Induced Climatic Change*, pp. 155–171, National Academy Press, Washington, DC, 1985.

Ridley, J. K., and K. C. Partington, A model of satellite radar altimeter return from ice sheets, *Int. J. Remote Sensing, 9*, 601–624, 1988.

Sailor, R. V., and A. R. LeSchack, Preliminary determination of the Geosat radar altimeter noise spectrum, *Johns Hopkins APL Technical Digest, 8*, 182–183, 1987.

Seckel, H., Hohenanderungen im Gronlandischen Inlandeis zwischen 1959 and 1968, *Meddelelser om Grønland, 187*, 1977.

Shum, C. K., D. N. Yuan, J. C. Ries, J. C. Smith, B. E. Schutz, and B. D. Tapley, Precise orbit determination for the Geosat Exact Repeat Mission, *J. Geophys. Res., 95*, 2887–2898, 1990.

Stewart, R. H., *Methods of Satellite Oceanography*, 360 pp., University of California Press, Berkeley, California, 1985.

Thomsen, H. H., L. Thorning, and R. J. Braithwaite, Vurdering af de gletscher-hydrologiske forfold pa Inlandsisen ved Paakitsup Akuliarusursua, Ilulissat/Jakobshavn, *Gronl. Geol. Undersogelse Arbejdsnotat*, 1986.

Warrick, R. A., and J. Oerlemans, Sea level rise, in *Climate Change, the IPCC Scientific Assessment*, edited by J. T. Houghton, G. J. Jenkins, and J. J. Ephraums, pp. 257–281, Cambridge University Press, New York, 1990.

Weidick, A., Studies of glacier behaviour and glacier mass balance in Greenland—A review, *Geografiska Annaler, 66*, 183–195, 1984.

Zwally, H. J., Growth of Greenland ice sheet: Interpretation, *Science, 246*, 1589–1591, 1989.

Zwally, H. J., R. A. Bindschadler, A. C. Brenner, T. V. Martin, and R. H. Thomas, Surface elevation contours of Greenland and Antarctic ice sheets, *J. Geophys. Res., 88*, 1589–1596, 1983.

Zwally, H. J., A. C. Brenner, J. A. Major, R. A. Bindschadler, and J. G. Marsh, Growth of Greenland ice sheet: Measurement, *Science, 246*, 1587–1589, 1989.

Zwally, H. J., A. C. Brenner, J. A. Major, R. A. Bindschadler, and J. G. Marsh, Greenland ice sheet: Is it growing or shrinking? Reply, *Science, 248*, 288–289, 1990a.

Zwally, H. J., A. C. Brenner, J. A. Major, T. V. Martin, and R. A. Bindschadler, Satellite radar altimetry over ice. Vol. 1. Processing and corrections of Seasat altimetry over Greenland, *NASA Reference Publication 1233, Vol. 1*, 1990b.

Properties of the Antarctic Ice Sheet Derived from Passive Microwave Data

Kenneth C. Jezek
Byrd Polar Research Center, The Ohio State University, Columbus, Ohio, U.S.A.

Donald Cavalieri
Goddard Space Flight Center, Greenbelt, Maryland, U.S.A.

ABSTRACT

The goal of this work is to investigate new techniques for separating the geophysical signals of changing physical temperature and changing electrical properties of polar firn from observed brightness temperature data. In turn, we seek to exploit these techniques for monitoring spatial and temporal variations in the near-surface temperature regime of the ice sheet and their associated impacts on ice sheet accumulation and ablation.

In this paper, we briefly summarize our approach to detecting relative changes in the near-surface temperature field of the Antarctic Ice Sheet. Essentially, antarctic brightness temperatures (Tb) compiled from the NASA Scanning Multichannel Microwave Radiometer data set are segmented by different glacial regimes. Tb time series for each sector are compared. Because we can show that temporal variations in Tb are dominated by changes in physical temperature, we can infer meaningful differences in relative physical temperature between regimes. Together with identifying expected seasonal trends in near-surface temperature, this analysis highlights more subtle variations such as the anomalously cold winter temperatures in 1982 over East Antarctica followed one year later by a cold winter in West Antarctic.

Variations in electrical properties of antarctic firn are investigated using the polarization ratio (defined as the difference of the vertical and horizontal channels of a single frequency divided by the sum of the same channels). We show that in the annual mean, the polarization is largely independent of physical temperature. We go on to show that very low polarization ratios of mean monthly data are probably due to the presence of free-water in the firn. Monthly mean values of polarization for each January in the SMMR data set are presented and discussed in this context.

Satellite Monitoring of Areal Changes in the Glacier Component of the Earth's Cryosphere

R. S. Williams, Jr. and J. G. Ferrigno
U.S. Geological Survey, Reston, Virginia, U.S.A.

ABSTRACT

One of the major expected environmental impacts of the predicted global climate warming on the geosphere and biosphere is accelerated melting of glacier ice (net loss of global glacier volume) and a concomitant rise in sea level. The cryosphere (glacier ice, floating ice [sea, lake, and river]), snow cover, ground ice, permafrost) is the most sensitive component of the geosphere to seasonal and longer term changes in global surface temperature. During the past two decades, satellite sensors have recorded changes in the areal extent of sea ice, snow cover, and glaciers. Satellite sensing technology is the only practical way of continuing such regional and global documentation of change in these three components of the cryosphere. Within the last 18,000 years, the geologic record shows that sea level has been as much as 100 m lower; during the peak of the last inter-glacial (about 125,000 years ago), sea level was about 6 to 8 m higher than at present. Key unanswered questions in the context of present day global change are: (1) how would the ice sheets in Greenland and Antarctica, which contain an estimated 99.3 percent of global ice volume, respond to global warming?, and (2) which glacierized region(s), the polar (Antarctica and Greenland) or sub-polar (ice caps, ice fields, and other glaciers), will be the most likely contribute to any future rise of sea level?

To begin answering these questions, the U.S. Geological Survey began, in 1978, an international project in which Landsat images are used to document the areal extent of glacier ice on our planet during the mid-1970s. Two of eleven chapters of U.S. Geological Survey Professional Paper 1386, Satellite Image Atlas of Glaciers of the World, have been published. On the basis of Landsat images and other sources of data, accurate glacier areas are now available for Antarctica, Greenland, and 14 other glacierized regions. The baseline reference study of the areal extent of glaciers during the mid-1970s will serve as the basis for comparison of future variations in glacier area and termini in response to climate change.

Monitoring for Global Change in Alaska Research Natural Areas

G. P. Juday
School of Agriculture and Land Resources Management, University of Alaska Fairbanks, Fairbanks, Alaska, U.S.A.

ABSTRACT

The prospect of a significant shift in climatic equilibria and changes in atmospheric composition raises concerns about the potential decline of important natural resources and threats to the survival of the complete range of natural diversity. Three elements are needed in any program with a focus on such concerns: (1) a network of sites containing examples of all or most of the diversity; (2) testable hypotheses of mechanisms by which global change effects will occur in real ecosystems; and (3) a monitoring program robust enough to detect the changes at the sites. With such a program, hypotheses of global change effects can be accepted, rejected, or modified.

The Alaska Research Natural Area (RNA) network has been selected to encompass natural diversity. It contains sites and some modest data sets that offer insights into possible effects and outcomes of global warming. Geothermally heated soils at Clear Creek Hot Springs and Big Windy Hot Springs RNAs offer a possible model of forest growth under a warmer climate. On the other hand, a warmer climate may allow greater winter survival of forest insects and increase in forest mortality, similar to that which killed 19% of the trees in a forest reference monitoring plot in 1989 in a mature white spruce stand in the Bonanza Creek Long-Term Ecological Research site. Grassland meadows dominated by *Carex obtusata* and *Calamagrostis purpurascens* at Volkmar Bluffs RNA may expand across the forested landscape with a warmer and drier climate, especially if accompanied by a higher fire frequency, a model of forest replacement that could become widespread across much of the interior Alaska. Glacier recession at Schwan Glacier Terminus, Columbia Glacier, and Hugh Miller Inlet RNAs provide insights into forest succession in coastal Alaska. Isolated mountain alpine features at Mount Prindle and Limestone Jags RNAs could be entirely displaced by an upward shift of vegetation zone with climatic warming.

Even if global warming proves to be modest, the program of selecting and monitoring natural diversity according to global change hypotheses is justified because it will contribute greatly to an improved understanding of functioning and linkages among earth systems and because widespread, human-caused reductions in biological diversity have already occurred and are accelerating.

Baseline Studies for Monitoring Global Climatic Change in the Arctic Environment; A Remote Sensing-Spatial Data Base Approach

M. B. Shasby and E. F. Binnian
U.S. Geological Survey/EROS Field Office, Anchorage, Alaska, U.S.A.

ABSTRACT

The U.S. Geological Survey's National Mapping Division has initiated research to establish a long-term monitoring program based on remotely sensed and other digital spatial earth science data bases. Six to eight specific eco-physiographic provinces in Alaska will be identified and studied in support of global climate change research in Arctic regions. A study site in the Colville River delta region has been selected for developing a demonstration/pilot data base, which will serve as a conceptual model for the other eco-physiographic regions yet to be identified. Regional data sets assembled to date include a complete Alaskan coastline digitized from 1:250,000 scale USGS map sheets, a state-wide mosaic of digital elevation model data at 0.5-km resolution, and a digitized version of the physiographic divisions of Alaska. The monitoring program focuses on the compilation and integration of digital spatial data bases for scientific investigations of earth system processes. Research elements associated with the climate change study include the spatial integration of widely varying sources of earth science data and multi-platform, multi-temporal sources of remotely sensed data. Selection of the monitoring sites follow criteria established by the International Geosphere–Biosphere Program and will occur through a series of inter-agency workshops. The integrated digital spatial data bases for the defined monitoring sites will provide a working tool for researchers to examine global climate change over the past 20 years, as well as provide a basis for future comparative studies.

AD-P007 266

92-17948

Radar Sensing of Polar Regions

G. I. Belchansky and A. P. Pichugin
Institute of Animal Evolutionary Morphology and Ecology, U.S.S.R. Academy of Sciences, Moscow, U.S.S.R.

ABSTRACT

In order to monitor ecological conditions, study the processes of energy and mass transfer, and predict climate in polar regions it is necessary to introduce modern means of remote sensing. This paper considers potential applications and presents results of remote sensing of the ocean surface, ice, and soil–vegetation ground cover in polar regions obtained by satellite and aircraft side-looking radar. Unlike optical systems, surface studies using radar systems are not limited by illumination, or restricted by clouds and fog. Interpretation of radar data was based on comparisons between the coefficients of inverse diffusion and direct measurements made at test sites.

The structure of ocean waves is reflected in radar images, revealing processes such as surface currents, internal waves, eddies, and frontal zones. Control data have shown economic disasters such as oil spills and drifting pollutants from coastal cities into the sea. Prospects are presented for using radar sensing for resolving a number of scientific and practical problems for the study of ice in the Arctic Basin. Radar methods also permit the characterization of soil–vegetation ground cover. In regions intensively used for agriculture, geochemical processes taking place under the earth and on its surface affect the soil structure and dielectric permeability at the surface level, and are evident in radar images. Results are presented of studies aimed at tracking the processes of spring thaw, areas subject to thermal erosion, floods, and vegetation condition.

INTRODUCTION

The present-day stage in the development of mankind is characterized by serious contradictions between society and nature. Ever growing is the pollution of the atmosphere, hydrosphere and lithosphere; ever decreasing is the biological productivity of soils; ever aggravating is the quality of foodstuffs; ever growing is the incidence of human diseases, likewise the social tension.

If the negative trends remain, the biosphere may lose its stability: due to the degradation of the living cover, its climate-regulating capacity becomes disturbed, the greenhouse effect, resulting in hard-to-predict climatic changes, is further developing; the ozone layer is getting destroyed, the biological diversity is undergoing calamitous reduction.

Polar regions play an important role in physical–chemical processes occurring in the atmosphere. The ecosystems of the polar regions are very sensitive to changes in the natural and anthropogenic environmental factors. That is why it is so vital to intensify multidisciplinary investigations of polar regions by using modern information technology.

Particularly essential in this technology are methods of aerospace remote sensing. At present, most widely used are the optical systems working in the visible and the near-infrared spectra of electromagnetic waves. However, these methods have a number of drawbacks (the data depend on the illumination of the surface under examination; no information can be obtained in cloudy weather or in mists, etc.) which hinder any application of such methods in polar regions.

The above drawbacks are not observed in modern radar systems working in the microwave range. Therefore such systems can be well employed for studies of polar regions.

The efficiency of radar systems is greatly governed by the further advance in the procession technology.

This paper presents the results of investigations of polar regions by using radar complexes of remote sensing. Some of the results are based on the data obtained by a side-looking radar (SLR) installed on the satellite "Cosmos-1500" and "Ocean" series. The main characteristics of this system are as follows: the distance to the earth's surface is 640–660 km; the orbital inclination is 82.6°; the radiation frequency is 9510 MH; the radiation polarization and the intake polarization is vertical; the diagram width of the directional antenna in terms of the level is 3 db, of the azimuth -0.15°, the angle of the place -30°, the range of incidence angles within which the surface is observed is 20 to 47°; the shift of the beginning of the survey in relation to the surface of the data unit is 850 km; the width of the survey band is 400 to 500 km; the average resolution within the survey band is 0.8 x 1.5 km. To accelerate the transmission of data to the earth the received signal is processed right on board. To this end, one uses the continuous calibration of the radar potential provided by introducing some part of the transmitter's power to the reception tract; the data are processed preliminarily by correcting the range of remoteness of the received signals so to preclude any geometric distortions of information due to the earth's curvature; the dispersion of noise fluctuation is reduced to improve the discernibility of images and to heighten the ratio between the signal and noise. Such data processing helps forming the line-structure of the information frame to transmit the radio images to the users along standard radio lines within the ranges of 137 MH and 465 MG which are widely employed for transmission of optical data [Pichugin et al., 1984a].

Some of the results below were obtained from the data gathered by a side-looking airborne radar (SLAR) which had similar characteristics. The difference was only in a higher resolution (30–50 m) and a wider band of survey which was 10 to 15 km. The SLAR data were also processed and registered on magnetic tape on board in terms of real time.

Further in the text, the potentials of radar sensing of environmental objects are considered in the light of Figure 1, and provide the general features of the main objects of the investigations and parameters under study.

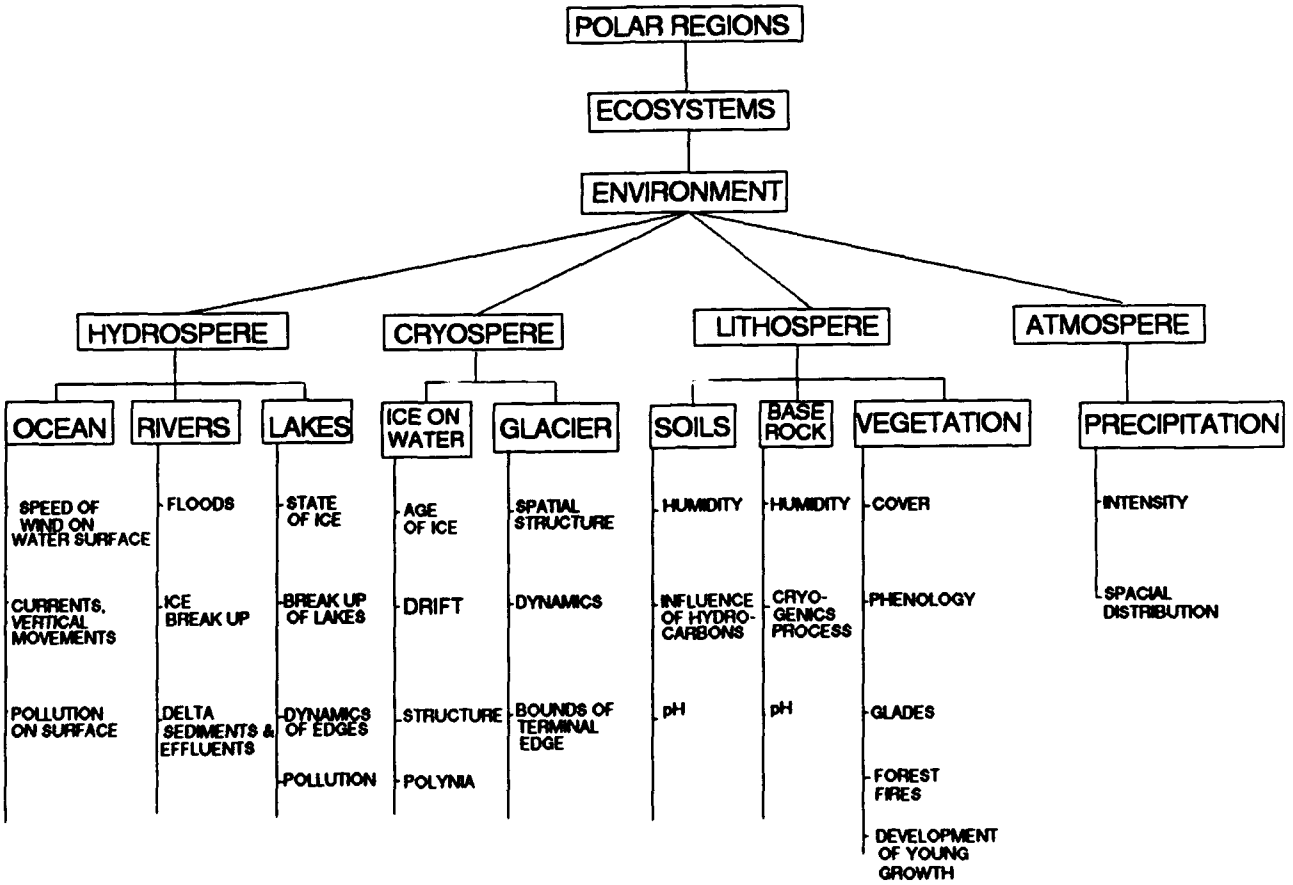


Figure 1. Objects of studies and parameters under measurement.

RADAR REMOTE SENSING OF OPEN WATER

Determination of the Vector of the Driving Wind Velocity

The scattering of radio waves in the 1 cm range is rather selective and is due to the waves of ripples varying in length (the gravitation–capillary components of the agitation spectrum) [Bass et al., 1968]. In its turn, the spectral density of the ripples depends on the wind velocity W. In this way, the value of the specific effective area of scattering (SEAS) δ also depends on the wind velocity. Inasmuch as large gravitation waves are clear proof of anisotropy, the signal scattered over the ripples is modulated by the inclinations of these waves; the maximum difference in the levels of reflections is manifested in the directions to the wind and orthogonally to the wind. By using the dependencies δ between the velocity of the driving wind, W, and the direction of the surface radiation in relation to the direction of movement of large waves φ, presented in Figure 2, one can, in principle, determine the vector of the driving wind velocity [Chan and Fung, 1977].

To define the driving wind velocity by means of SLR of the satellites "Cosmos-1500" and "Ocean," the image is filtered, the space window being 5 x 5 km, 10 x 10 km or 20 x 20 km so to additionally reduce the dispersion of fluctuations and heighten the accuracy of the SEAS definition. The optimal parameters of the filter are chosen with regard to the spatial structure of the image. After that one calculates the values of δ with accounts of the through calibration of receiving–transmitting tract of the radar [Pichugin et al., 1984b]. Since the water surface gets irradiated only in one direction, additional information is used to specify the orientation of the driving wind. To this end, one considers the peculiar dislocation of clouds in the optical images, the shading behind islands and the coastline, as well as data from ships. Then, taking into account the direction of the driving wind, the measured values of δ are corrected. After that, the radiation angle θ regarding the earth's curvature is found for each section of the surface. By graphs like those in Figure 2 one finds the module of the wind velocity [Kalmykov et al., 1985]. Figure 3 shows an example of such data procession; the circumferences demonstrate the data of meteorological measurements.

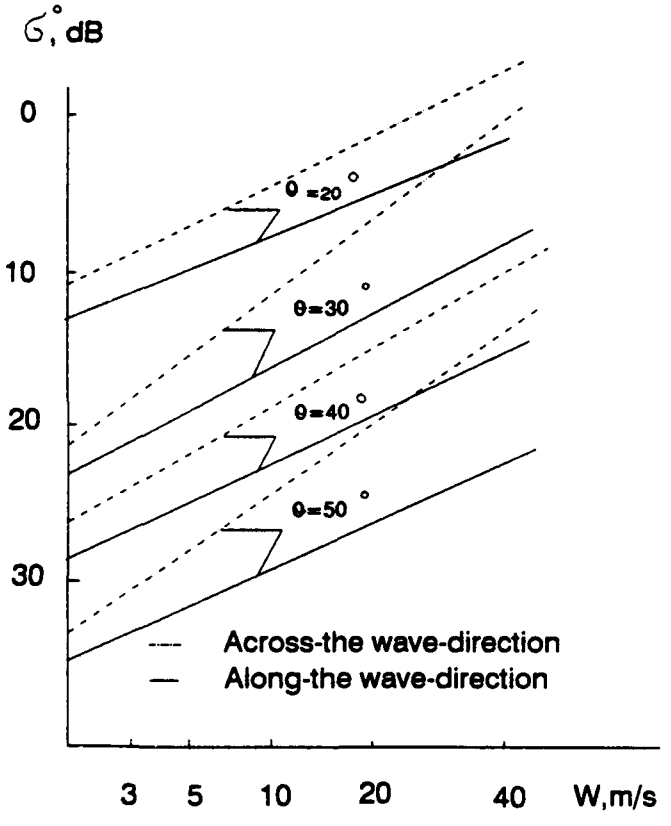


Figure 2. Relationship between specific effective area of scattering (SEAS) and the wind velocity W with radiation of the surface directed towards the wave and along the wave for radiation angles θ of 30° and of 40°.



Figure 3. Definition of the vector of driving wind velocity by using a radar image, the region of the Bering Sea and of the Sea of Okhotsk. The circles show the data from ship measurements.

Observation of Pollution

Radio images of water surfaces reveal different heterogeneities caused by numerous processes in the atmosphere, on the surface and in the aqueous medium. Examples of such heterogeneities are presented in Figures 4–7. There is a special kind of heterogeneity due to oil pollution of the water surface. An oil film drastically diminishes the spectral density of the scattering ripples, which is manifested in the reflected signal [Krishen, 1973]. The reflected signal can decrease in an oil spot down to 20 db, permitting reliable detection of oil pollution irrespective of the weather conditions [Kalmykov et al., 1982].



Figure 4. Radar image of earth surface during the flood of the Amur River.

RADAR REMOTE SENSING OF RIVERS

Among the tasks of hydrology is thestudy of the regime of flood plain submersion during river floods. High river inundations during river floods elevate the water table in the watershed swamps; such river floods are responsible for the formation of flood plain swamp massives and their recurrent flooding. River inundations render specific effects upon various ecological processes. Therefore it is very important to apply radar sensing to investigate the river inundation dynamics.

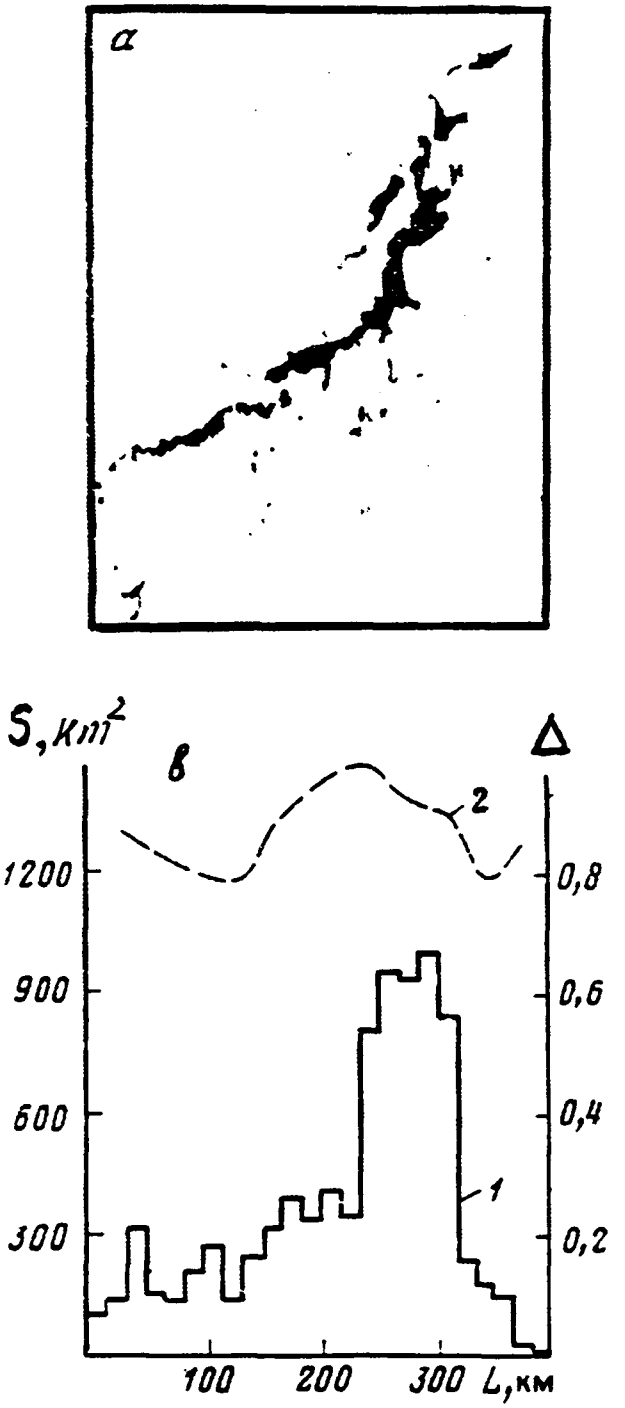


Figure 5. Results of the procession of the marked fragment from Figure 4: (a) the flooded floodplain of the Amur; (b) distribution of the area of flooded sections S (1) and of the relative land area covered with water (2) along distance L in the floodplain of the Amur.

Figure 4 shows a radio image obtained on the Amur River during its flood when practically all of the Low Amur lowland was flooded. The water-covered sections of the surface look darker in the radio image than the neighboring dry surface, i.e., the intensity of scattering on the water-covered areas is lower. This can be attributed to the differences in the SEAS value δ which determines the intensity of the reflected signal for the earth's surface and for water. For instance, within the microwave range of radio waves the SEAS of dry land with the radiation angles θ over 15° is, as a rule, higher than that of the water surface. One element of resolution of the radar may embrace both the elevated sections of the surface not flooded with water and the flooded lowlands. Therefore the intensity of the signal scattered over partially flooded sections of the earth's surface acquires some intermediate value between the minimum one, which corresponds to the water surface of the river, and the maximum one, which characterizes the reflection from the dry land. The radio image can be conventionally distinguished for three zones of brightness (Figure 4). The darkest sections correspond to the maximum flooding in the flood plain of the Amur River, the lighter areas to the partial flooding of the Low Amur lowland, and the bright sections of the image correspond to the dry earth's surface without flooding.



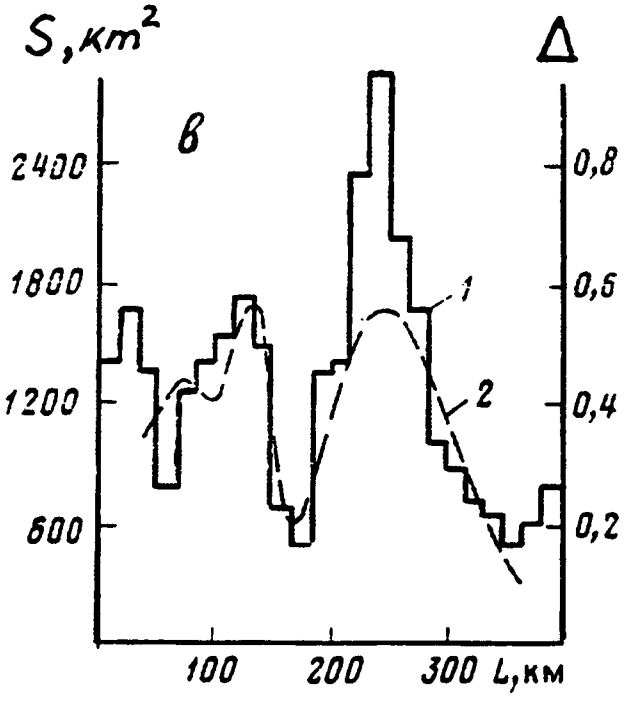


Figure 6. Results of procession of the marked fragment from Fig. 4: (a) flooded Low Amur Lowland; (b) distribution of area of flooded sections S "(1) and of relative land area covered with water (2) along distance L in the Low Amur Lowland.

Among the tasks of river inundation control is to define the area of the territory involved in flooding. To automatically compute these areas, after the initial image is filtered, one specifies sections with different extents of flooding. It should be mentioned that the threshold brightness is to be chosen as a function of actual results of observations, since different territories of the earth's surface, which can be involved in river inundations, reveal their own scattering properties. A correct choice of the value of threshold brightness governs the accuracy of the estimation of the flooded areas. Figure 5 presents some results of processing a fragment from Figure 4 [Pichugin, 1985]. The dark sections show the flood plain of the Amur River and the adjacent lakes. The area S of the flooded sections was found in windows about 17 km wide and in heights equal to the vertical of the fragment (about 540 km). The results of the computations are presented in Figure 5b as the distribution of the area of the flooded flood plain of the Amur River (curve 1) at the distance L. Less exposed to the impact of flooding is the lowland adjacent to the Amur flood plain. Figure 6a shows the entire area of flooding for the same fragment of the radio image. The calculation of the flooded area was made in the same windows of 17 x 540 km but the area of the flooded flood plain was subtracted. The distribution S over the distance L is described in Figure 6b by curve 1. When studying, predicting and regulating the water level during river inundations, timely determination of the relative area completely covered with water within the region of flooding is very important. Figures 5b and 6b present the results of computations as the distributions of relative areas over the distance L, Δ = SW/S (where SW is the area of

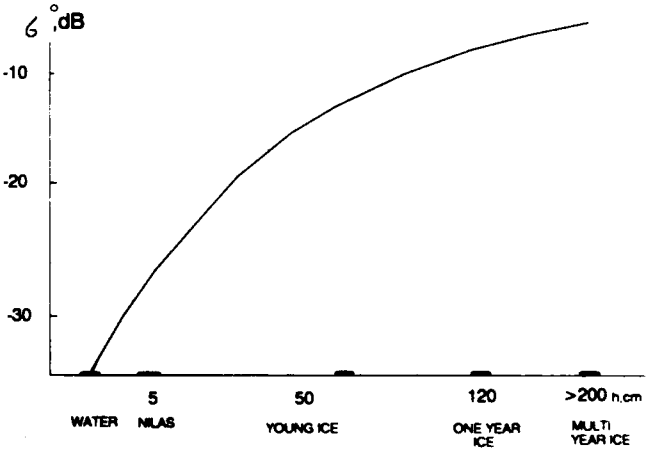


Figure 7. Specific Effective Area of Scattering (SEAS) δ as a function of the age of ice.

water surface in the section under analysis), which correspond to the floodplain of the Amur River and of the Low Amur lowland. As follows from the distribution Δ (L), the percent of complete flooding in the Amur flood plain is very great: in this region 80–99% of the area was covered by water. Much lower is the percent of flooding in the Low Amur lowland where less than 60% of dry land was covered by water.

RADAR REMOTE SENSING OF ICE COVER

An important object to study in polar regions is the ice cover whose basic parameters can be effectively measured by radar sensing. Such parameters include: the ice cover structure; the age of ice and the ice thickness associated with the ice age; the sea–ice boundary and its variability in time; etc. This information can be derived by SLR sensing in any weather condition, irrespective of illumination. However, it is very difficult to elaborate a model of radar reflection from the ice cover. There are certain difficulties in using electrodynamic approaches, because the ice covers are very complicated. In addition, the problem becomes even more difficult to tackle because the conditions of ice generation are extremely diversified and they affect the process of scattering. Therefore the methods for ice cover sensing and for processing the information on such investigations are based on summarized experimental data [Ostott et al., 1982] on the function of the age (thickness) of ice H, the radio wave length λ, radiation angle θ, polarization, etc. Ostott et al. [1982] and some others show that the value δ within the 1 cm range increases with the age of ice and practically does not depend on polarization. Figure 7 shows the relationship between the value δ and the age of the ice. As one can see, reflections from water differ from those from the ice by their lower values of δ. Old ice, as a rule, reflects much more strongly than other structures. However, smoothed old ice may in summer slightly decrease its value of δ. It is worth mentioning that while in the 1 cm range the contrast between the young and old ice is quite marked, in the decimeter range this difference is practically negligible; there can be differences only between reflections from water and from ice, without any age gradations [Efimov et al., 1985].

Some of the Results of Ice Cover Studies Obtained from the SLR Data of Satellite "Cosmos-1500"

Figure 8 shows radio images of the ice situation in the region of Wrangel Island obtained on 20.10.1983 (a) and 23.10.1983 (b). In the Strait of Long there is perennial ice, while in the northern part of the Strait, within the southern margins of Wrangel Island, the ice is thin and there is water. One can see the dark canals in the perennial ice. These are canals with clean water or thin ice, which are typically 3 to 5 km in width and are sufficiently stable. Taking into account the operative value of such information, it is of great importance for the studies of ecosystems in the polar regions. Figure 8a shows the image of a perennial ice floe and an ice window to the west of Wrangel Island. There is no ice window in the image presented in Figure 8b, which testifies to considerable shifts of ice occurring in this region.

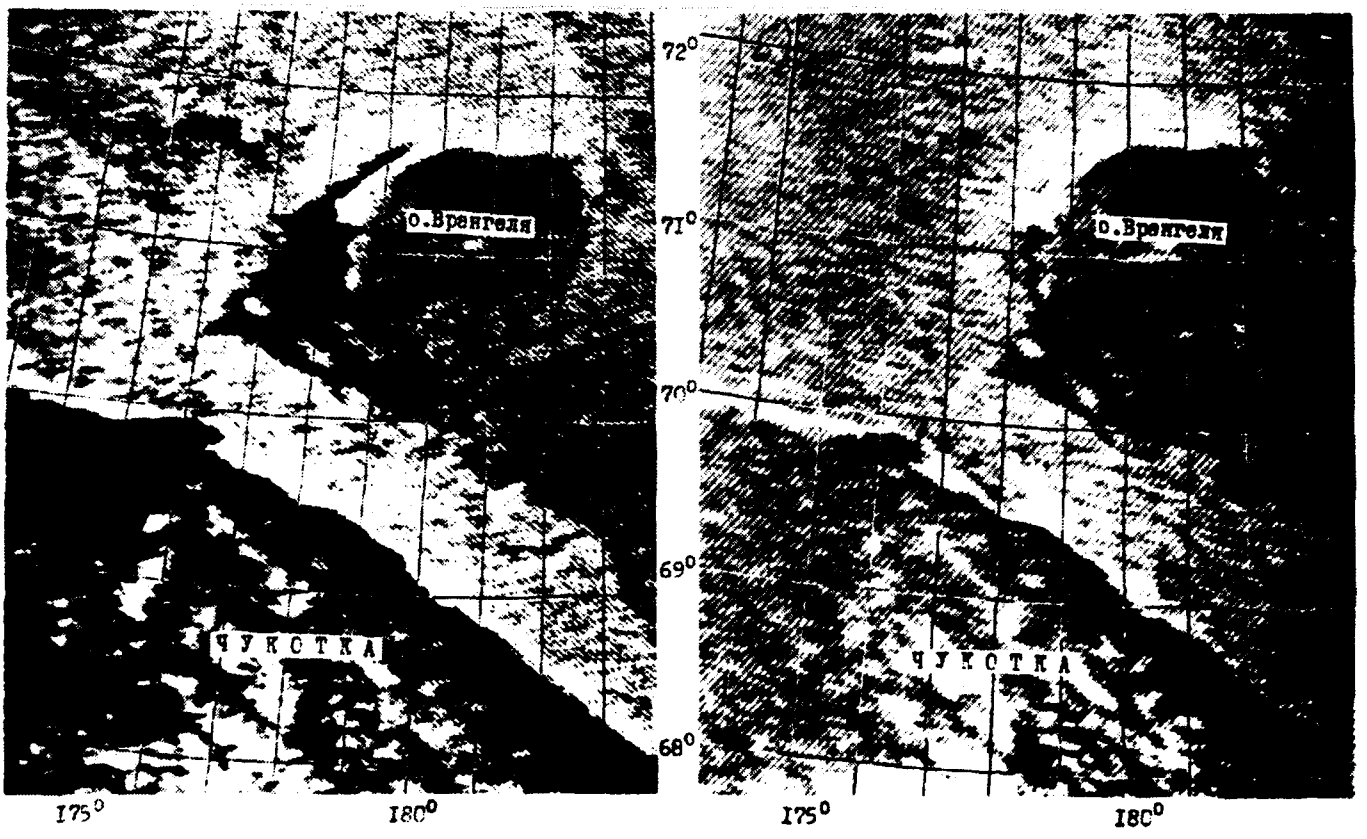


Figure 8. Radar image of the ice situation in the region of Wrangel Island: (a) 20.10.1983; (b) 23.10.1983.

Other studies of radio images of the Kara Sea and of the regions with pack ice near the North Pole reveal the boundary of perennial ice whose dynamics are easy to trace. The processing of images has demonstrated that the contrast between perennial and annual ice equals 3–5 db. The number of age gradations of the ice cover, which can be reliably identified by radar survey, equals 4–5 db. Today the data obtained by "Ocean" side-looking radar are used for operative descriptions of the ice cover situation in the Arctic and Antarctic.

Results of Radar Sensing of Continental Ice

Individual radio images were used to compile radar map-composites of Antarctica and Greenland. These maps reveal several regions which drastically differ from one another by the intensity of the radar signal. The lightest is the margin zone of the continental ice cover affected by the summer melting of ice revealed in the structure of ice. Further to the center of the glaciers there are areas covered with a poorly scattering layer of refined snow which resists melting. Besides, in the inner regions of Antarctica and Greenland there are meso-scale heterogeneities of different brightness and of diverse configuration. Quite possibly the structure of the images repeats the relief under the ice, but this hypothesis should be thoroughly verified. The shelf glaciers are characterized by a more homogeneous grey background of the images. Radar sensing from outer space involving the hard-to-access glaciers of Antarctica and Greenland is a new source of unique information which can be used to resolve vital problems of glaciology and geophysics.

RADAR REMOTE SENSING OF SOILS

Among the serious problems in the studies of polar regions is the control of melting of soils and grounds permafrost terrain. In December 1983, under conditions similar to the above, a series of radar surveys from the satellite "Cosmos-1500" involved some agrarian regions in the southern Ukraine. Figure 9 shows radio images of these regions obtained from 5.12.1983 to 29.12.1983. The radio image in Figure 9a demonstrates the homogeneous shade of brightness, and was made before any atmospheric precipitation. The images in Figure 9b–d were made during the period of rain and snow. The vast land areas in the images presented in Figure 9b–d are of greater brightness because they are associated with the zones of precipitation (the greater brightness of different sections in the images of the Black Sea in Figure 9b,d is due to another effect discussed above, namely the accelerated velocity of the driving wind). It is also necessary to mention that the more intensive signals scattered from some sections of land demonstrated in Figure 9b–d are due to the changes in the reflection characteristics of the earth surface and not to the scattering from rain drops. When precipitation is less than 10 mm h^{-1} (in the survey series under consideration the intensity of precipitation was registered to be up to 1 mm h^{-1}) their impact upon the intensity of the signal is negligibly low [Spiridonov and Pichugin, 1984].

The territory of the southern Ukraine examined here is of plain topography. The soil cover of the regions under study is represented by chernozem loamy soils which are everywhere plowed. There are practically no natural forests or steppe vegetation. In view of this, to describe these sections of the earth surface a model of surface with complicated roughness was applied. Within the framework of this model the radar contrasts $\Delta\delta_c=\delta_a/\delta_n$ were calculated (where the indexes a, n correspond to the abnormal and normal conditions of radiation in the reflection parameters of the territories in question) as a function of the humidity V for sandy and clay soils at different angles of radiation θ. These relationships are presented in Figure 10. Curves 1 and 2 in this figure characterize the sandy soil, while curves 5 and 6 are the clay soil. In terms of the territories of the Ukraine under consideration, their soils are chiefly composed of mixtures of sand and clay particles. The most applicable characterization of these soils are curves 3 and 4, revealing the 1:1 ratio between these components of the Ukrainian soils. Curves 1, 3, and 5 in Figure 10 are compiled for the radiation angle θ equalling 40, while curves 2, 4, and 6 are for the θ equalling 20.

To quantify the reflection characteristics of the territories under examination, the images in Figure 9 presented numerically were supplied to a computer for further processing. Then, using the interactive regime of processing, sections of equal brightness were outlined and the reflected signals were averaged within the territories so identified. After that, the radar contrasts in abnormal sections of the images were found as presented in Figure 9b–d, and compared with the respective sections of the test image in Figure 9a. The values of contrasts K measured in this way were correlated with the amount of precipitation; these values are presented in Figure 11. One group of experimental points (the light circles) corresponds to the meteorological conditions when atmospheric precipitation as rain falls upon the frozen soil (the conditions in the polar regions); the other group of experimental points (the dark circles) characterize the change in the contrast due to precipitation falling on the dry sun-heated soil.

As one can see from Figure 11, when rain falls on frozen soil, the contrast increases considerably and reaches 8.5 db with precipitation of 4 to 6 mm. In such a case the soil moisture may approach 100%, which corresponds to the maximum contrast in relation to the dry soil, as shown in Figure 10 (about 12 db, curves 3 and 4). Then, as follows from Figure 10 (curves 3 and 4) the soil moisture in the frozen soil makes up 3 to 6% (with regard to dispersion of values K in Figure 11). With increased precipitation, and positive air temperature gradually melting the soil, water penetrates through its lower layers, and the water content in the surface of the soil decreases. As a result, the radar contrasts at θ>6 mm are getting weaker. When the frozen soil was completely melted, the drizzling precipitation did not exceed 1 mm h^{-1}. Combined with the positive air temperature, these conditions of soil moisture exchange maintained the soil moisture at a certain stable level. Because of this, the contrasts were practically independent of the quantity of precipitation if it was above 8 mm.

When rain falls on sun-heated soil, the contrast is gradually augmented and reaches 3 to 4 db when the level of precipitations equals 4 mm. With further rise in precipitation, the contrast does not change and remains within the same limit of 3 db<K<4 db. As one can see from Figure 10, such values of the contrast correspond to the increase in the moisture of the soil surface layer up to 20–40%.

Thus, the results presented here suggest that it is possible

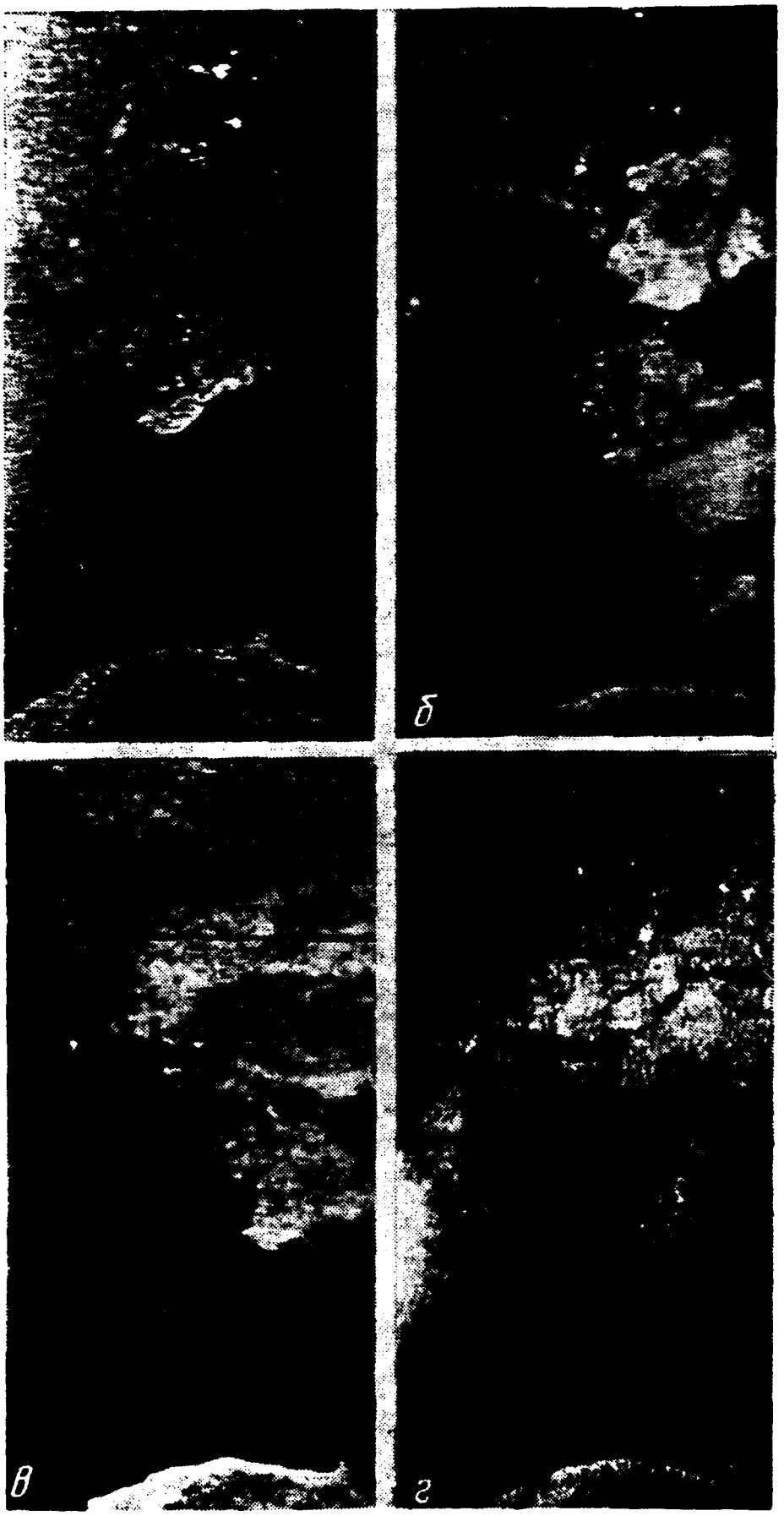


Figure 9. Radar images of the southern Ukraine: (a) 5.12.1983; (b) 7.12.1983; (c) 8.12.1983; (d) 28.12.1983.

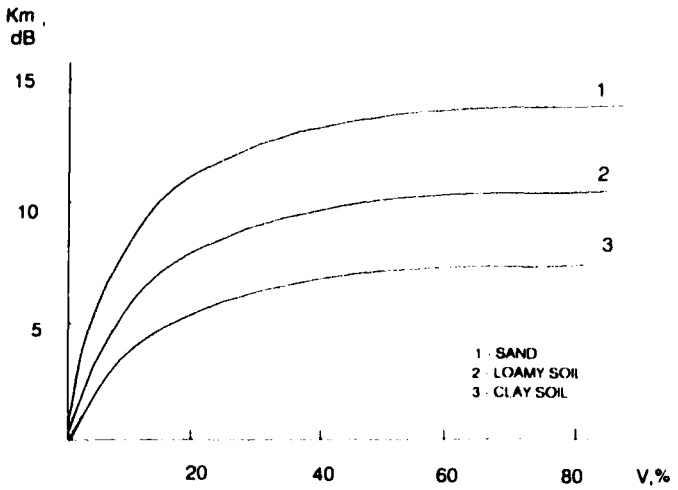


Figure 10. Calculated relationships between the radar contrast K and the soil moisture of the surface soil layer V for sand (1, 2), loamy soils (3, 4) and clay (5, 6) with radiation angles θ of 40° (1, 3, 5) and of 20° (2, 4, 6).

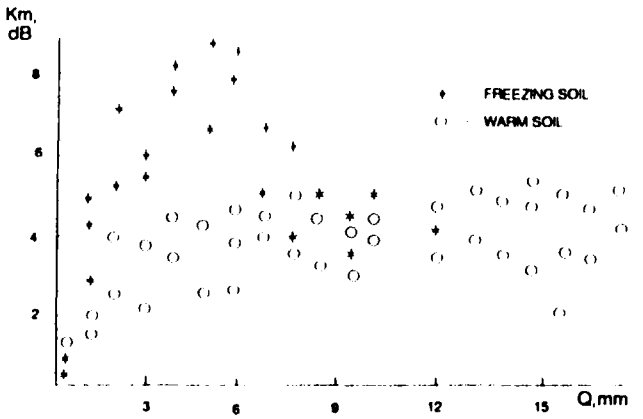


Figure 11. Experimental relationships between the radar contrast K and the amount of precipitation Q: (1) precipitation falling on frozen soil; (2) precipitation falling on melted soil.

to obtain integral data on the spatial distribution of soil moisture in the surface layer of soils over vast territories, these data being obtained by means of space SLR. The experimental evidence derived for the two cases of agrometeorogical conditions (precipitation on frozen and on warm soil) have principal differences, permitting control of such conditions by regular observations within the given region.

RADAR REMOTE SENSING OF ANTHROPOGENIC IMPACT ON THE ENVIRONMENT

In many cases the lithosphere may act as an indicator of the nature and degree of anthropogenic impact on the environment. Such impact is manifested as soil cover degradation due to the effects of products resulting from biochemical oxidation of technogenic components, abnormal accumulation of heavy metals, etc. To be able to reveal the mechanism of the functioning and stability of soil ecosystems under conditions of technogenic halos of hydrocarbons, which are inevitable with the existing technologies

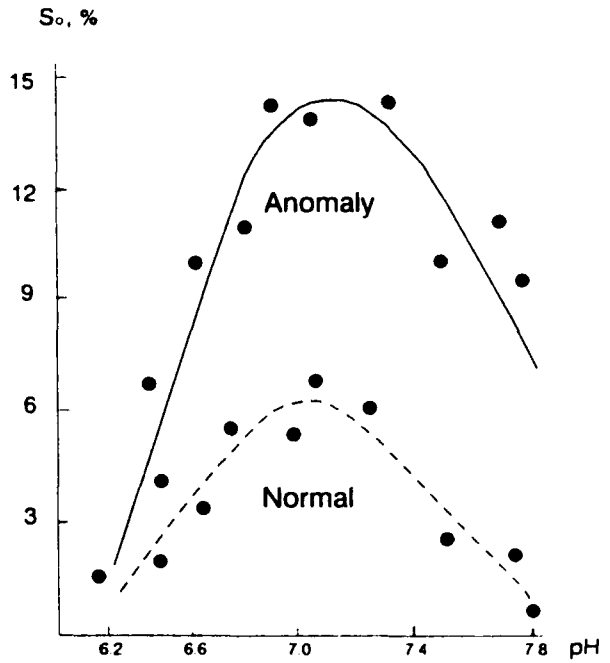


Figure 12. Relationship between the relative area S_r and pH in the gas-bearing (1) and base (2) sections.

of prospecting and exploitation of oil and gas deposits, special ecological–geochemical studies were made in the territory of the Ukraine–largest Shebelin deposit of condensed gas. The studies included a litho–gas–biochemical survey of soils and subsoil layers, a chemical, a granulometric, an ionmetric analysis of soil samples from the arable layer; soil surfaces were also photographed. The latter operation was performed with the view of assessing the amount of soil aggregates and their dimensions (the results of calculations based on the photographs are presented in values of the relative areas S_r occupied by soil aggregates with their cross-section over 1 cm^2 [Belchansky et al., 1990].

The litho–gas–biochemical survey showed the principle gas–biochemical indices to be very different than the base sections (Table 1). For example, the concentrations of CH_4, of heavy hydrocarbons of CO_2, and the intensity of the growth of bacteria oxidizing hydrocarbons contained by soil, were found to be 2 to 7 times higher in places of hydrocarbon leaching as compared with the areas which were previously known to be free from any technogenic hydrocarbons (the relations between the values of these parameters within the zone of technogenic impact and those in the base section are tabled as coefficients of contrast). The abnormal concentrations of CO_2, and the obvious deficit of nitrogen and oxygen in the gas phase of closed pores of soil, directly point to the active process of oxidation of technogenic hydrocarbons by specific hydrocarbon-oxidizing microflora. The growth of this microflora, combined with the increasing concentration of hydrocarbons, results in the alteration of the aggregate composition of the arable soil layer. For instance, as observed in the Shebalin deposit, in places of hydrocarbon leaching the soil aggregates were evidently of larger size though the geochemical changes in the humus horizon of soil were not profound.

Indices	Units of measurement	Base Sections: Average values	Base Sections: Ratios of phases	Technogenic Sections: Average values	Technogenic Sections: Ratios of phases	Coefficients of contrast
CH_4	10^{-3} volume-tric %%	14.70 11.90	1.24	82.5 51.3	1.61	5.6 4.3
heavy hydrocarbons	10^{-3} vol.%%	0.50 0.35	1.43	1.6 0.8	2.00	3.2 2.3
N	vol.%%	79.50 82.20	0.96	65.0 86.7	0.75	0.8 1.1
0_2	vol.%%	16.90 17.00	1.00	9.9 10.7	0.93	0.6 0.6
$C0_2$	vol.%%	3.50 0.60	5.80	24.3 2.4	10.00	6.9 4.0
hydrocarbon-oxidizing bacteria	conventional units	61.20		248.1		4.1

Table 1. Gas-biochemical parameters of soils in the base and technogenic sections of the Shebelin deposit (June, 1983). The numerator of the fractions shows the indices of gases of sorbed phase, the denominator of the free phase.

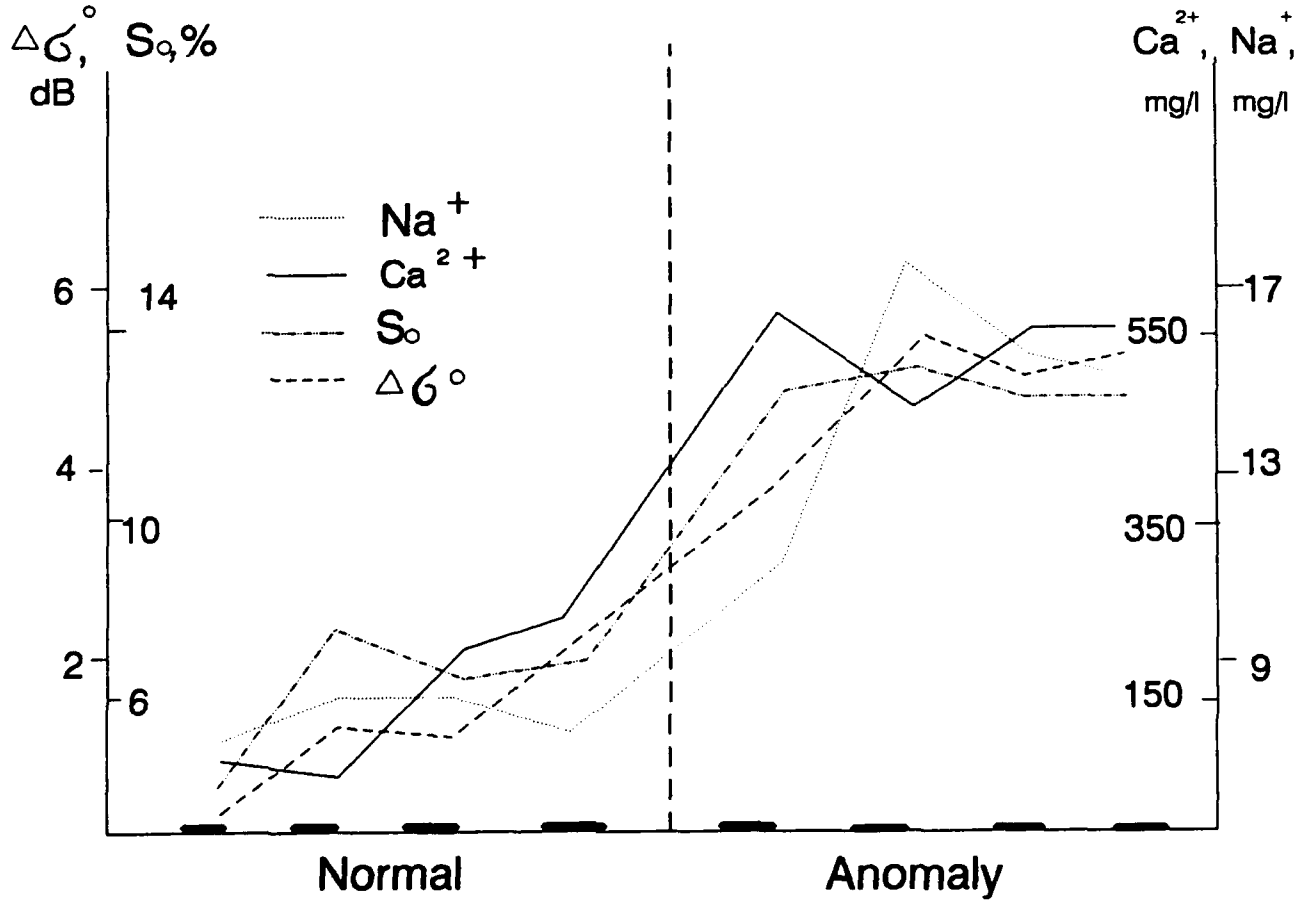


Figure 13. Relationship between physical–chemical parameters and radar contrasts for average and anomalous conditions.

The aggregation of soil was revealed to be associated only with concentrations of CO_2, Fe_2O_3, Al_2O_3, and the alkaline-oxidation conditions [Belchansky et al., 1990].

The above experiments demonstrated the relative area of soil aggregates S_r to be very sensitive to the changes in pH (Figure 12). The curves describing the relationships S_r(pH) in oil- and gas-bearing sections and in the base sections are similar: the maximum values are characteristic of weakly alkaline, almost neutral, conditions. However, these curves are slightly different; in the zone of hydrocarbon migration; the value of S_r is obviously higher than that in the neighboring base sections.

In this way, soils that are in the path of technogenic hydrocarbon migration and serve as the substrate for intensive growth of hydrocarbon-oxidizing microflora are subjected to transformations at all stages. The most essential among them, at least in terms of soil fertility, is the pelletization of the arable layer, the disturbance in the saltwater regime, and the changes in the mechanical properties of soils. An important feature which demonstrates that technogenic hydrocarbons arrive in the soil profile is an increase in the content of large soil aggregates in the arable layer.

The results discussed above allow elaboration of complex methods of remote geochemical sensing of soil covers under conditions of anthropogenic loads. For instance, to indicate technogenic atmospheric changes (acid rains, etc.) or changes beneath the surface soil layer (zones of hydrocarbon migration), which are responsible for the variations in the described physical–chemical parameters of the arable layer, we regard as the most promising method that of radar sensing. This can be attributed to the fact that in radar sensing the main scatters are the rough points of the surface which in size equal (within the order) the length of the radio wave. Inasmuch as the abnormal processes discussed are manifested in the changing content of soil aggregates with the size of 1 to 10 cm, it is possible to expect that the maximum sensitivity of these phenomena during their radar sensing will be found within the 1 cm band of radio waves. Thus, a quantitative analysis of the results of the SLAR survey of the territory of the Shebelin deposit of condensed gas and of the nonproductive area adjacent to it showed these structures to be of great radar contrast. The intensity of the reflected signal within the section under comparison is higher in the productive area than beyond this area by 4 db on the average, varying from 2 to 5 db (Figure 13). As one can see from Figure 13, there is a high spatial correlation between the basic physical–chemical parameters of the territories under study and the radar contrasts in the same areas.

In these experiments the comparison involved sections with close values of soil moisture, pH and agrotechnical treatment of the arable layer. The sections embraced harrowed plowed areas and plowed lands with winter cereal sprouts, their projected covering under 5%. The soil moisture in the upper soil layer was 19–25%.

Thus, the revealed characters of the eco–geochemical transformations of soils due to anthropogenic loads may be used to assess the impact of these loads upon the environment. Remote methods of geochemical sensing seem to be very promising for such purposes [Belchansky and Vostokova, 1977; Belchansky and Sazonov, 1982; Belchansky et al., 1990].

ACKNOWLEDGMENTS

We gratefully appreciate the professional help offered by Dr. David Douglas (Alaska Fish and Wildlife Research Center, U.S. Fish and Wildlife Service) on every step of preparation of this report. Many thanks for his help.

REFERENCES

Bass, F. G., et al., Very high frequency radiowave scattering by a disturbed sea surface, *IEEE Trans., AP-16*, 554–559, 1968.

Belchansky, G. I., and N. V. Sazonov, Sistema kompleksnoi obrabotky aerokosmitcheskoi informatcii, *Issledovanie Zemli iz Kosmosa*, *5*, 76–83, 1982.

Belchansky, G. I., and E. A. Vostokova, Detection of underground water and related phenomena by means of space photographs, *Proceeding of Commission in Data Sensing Processing*, Canada, 1977.

Belchansky, G. I., A. I. Vasilev, N. E. Zhurabel, and A. P. Pichugin, Priznaki ecologo-geohemicheskoy transformatsii pochv pod vozdeystviem uglevodorodnikh gazov i ikh distantcionnaia irdicatcia, *Doklady AN SSSR, seria geofizika, Tou N313*, *5*, 1082–1085, 1990.

Chan, H. L., and A. K. Fung, A theory of sea scatter at large incident angles, *J. Geophys. Res.*, *82*, 3439–3444, 1977.

Efimov, V. B., et al., Issledovanie ledovykh pokrovov radiofizicheskimi sredstvami s aerokosmicheskikh nositelei, *Izvestia AN SSSR. Fizika atmosfery i okeana*, *21*, 512–519, 1985.

Kalmykov, A. I., A. P. Pichugin, Yu. A. Sinitsyn, and V. P. Shestopalov, Some features of radar monitoring of the oceanic surface from aerospace platforms, *Int. J. Remote Sensing*, *3*, 311–325, 1982.

Kalmykov, A. I., A. P. Pichugin, and V. N. Tsymbal, Opredelenie polia privodnogo vetra radiolokatsioonoy sistemoy bakavogo abzora ISZ "Kosmos-1500," *Issledovanie Zemli iz Kosmosa*, *4*, 65–77, 1985.

Krishen, K., Detection of oil spills using a 13.3 GHz radar scatterometr, *J. Geophys. Res.*, *78*, 1952–1963,1973.

Ostott, R. G., R. K. Moore, S. Gogineni, and C. Delker, Four years of low-altitude sea ice broad-band backscatter measurements, *IEEE, OE-7*, 44–50, 1982.

Pichugin, A. P., et al., Operativnaya obrabotka radiolokatcionnoi informatcii na bortu ISZ "Kosmos-1500," *Issledovanie Zemli iz Kosmosa*, *5*, 93–102, 1984a.

Pichugin, A. P., et al., Osobennosti tsifrovoy obrabotki radioizobrajeniy, poluchennykh RLS-BO ISZ "Kosmos-1500," *Issledovanie Zemli iz Kosmosa*, *6*, 82–90, 1984b.

Pichugin, A. P., Radiolokatsionnye nablydeniya razlivov rek s ISZ "Kosmos-1500," *Issledovanie Zemli iz Kosmosa*, *5*, 61–66, 1985.

Spiridonov, Yu. G. and A. P. Pichugin, Vliyanie meteouslovii na kharakteristiki radiolokatsionnykh izobrazhenii zemnoi poverkhnosti iz kosmosa, *Issledovanie Zemli iz Kosmosa*, *6*, 21–27, 1984.

92-17949

AD-P007 267

The Polar Automatic Weather Station Project of the University of Wisconsin

Charles R. Stearns and George A. Weidner
Department of Meteorology, University of Wisconsin-Madison, Madison, Wisconsin, U.S.A.

ABSTRACT

The polar automatic weather station (AWS) of the University of Wisconsin is a battery-powered, solar panel–charged, computer-controlled unit that measures wind speed, wind direction, air temperature, air pressure, vertical temperature difference, and relative humidity. The nominal height of the measurements is three to five meters at the time of installation. The data are transmitted to polar-orbiting satellites equipped with the ARGOS data collection system. The sensors are measured at ten-minute intervals and three to five values of each sensor are transmitted at 200-second intervals. More than 100 values at ten-minute intervals are recorded in 24 hours. Thirty-four AWS units are installed in Antarctica and four AWS units are installed on the Greenland Crest. Up to 28 of the 38 AWS units are received by the Global Telecommunications System at six-hour intervals.

INTRODUCTION

The National Science Foundation Division of Polar Programs (DPP) polar automatic weather station project places automatic weather station (AWS) units in remote areas of Antarctica and Greenland in support of meteorological research and operations. The AWS data are collected by the ARGOS Data Collection System on board the National Oceanographic and Atmospheric Administration (NOAA) series of polar-orbiting satellites.

Antarctica is a continent 97% covered with ice with an area of 15×10^6 km^2 and covers 1.3% of the earth's surface. The average elevation of Antarctica is 2300 m with an average annual temperature of -35°C, making it the highest and coldest continent on earth. The operation of manned stations for collecting meteorological data is extremely difficult and expensive. Out of approximately 30 stations operating the entire year in Antarctica only two or three are located in the interior of the continent, with the remaining stations located along the coast, usually in sheltered locations.

Greenland is an island about 80% ice covered with an area of 2.2×10^6 km^2. The average elevation of Greenland is about 1200 m. Greenland has three interior and 19 coastal stations that collect meteorological data. Occasional camps have collected meteorological data for one-year periods on the crest of Greenland at an elevation of 3200 m. The Greenland interior is as difficult as the Antarctic interior for the maintenance of manned stations for meteorological observations.

The installation of the ARGOS system on polar-orbiting satellites made possible the collection of data from remote locations on a very reliable real-time basis. The development of low-power computer components allowed the design of low-power automatic weather stations capable of operating in the extreme climates of Greenland and Antarctica.

AWS SYSTEM

The AWS unit was developed by the Radio Science Laboratory at Stanford University under the direction of Prof. Alan Peterson. The basic AWS units measure air temperature, wind speed, and wind direction at a nominal height of three meters above the surface, and air pressure at the electronics enclosure. Some AWS units may measure relative humidity at three meters, air temperature difference between three meters and 0.5 meters above the surface, snow temperature difference at several levels, and solar radiation. Table 1 gives the sensors and the resolution for the AWS measurements.

The AWS is controlled by a microcomputer which updates the data at a nominal 10-minute interval. At 200-second intervals three to five data points for each sensor are transmitted to the ARGOS-equipped polar-orbiting

Variable	Sensor	Resolution
Air pressure	Parascientific model 215	0.05 mb
Air temperature	Platinum resistance thermometer	0.125°C
Wind speed	Belfort aerovane model 123	0.25 m/s
Wind direction	" " " "	2°
Relative humidity	Vaisala HMP-31UT	1%
Solar radiation	Kipp and Zonen solarimeter	8 W m^{-2}
Temp. differences air and snow	two thermocouple junctions	0.05°C

Table 1. Meteorological variable, sensor, and resolution for the polar automatic weather stations. The pressure sensor drifts less than 0.2 mb in one year.

satellites. Power is provided by six to twelve 40 ampere-hour gel-cell batteries charged by solar panels. Twelve batteries are used at the South Pole and six batteries are used at latitudes of 60°S to 70°S and nine batteries between 70°S and 85°S. The AWS unit at Whitlock Site on Franklin Island has operated on batteries for more than seven years.

Table 2 gives the unit's latitude, longitude, and elevation past and present, and the start and stop date for each location for all DPP polar AWS units. The AWS units are grouped together based on the area and usually are related to a single meteorological experiment in the area. The stop date may be the last month that the AWS unit provided data or the month that the site was no longer operational. The data are not always continuous, as the units occasionally

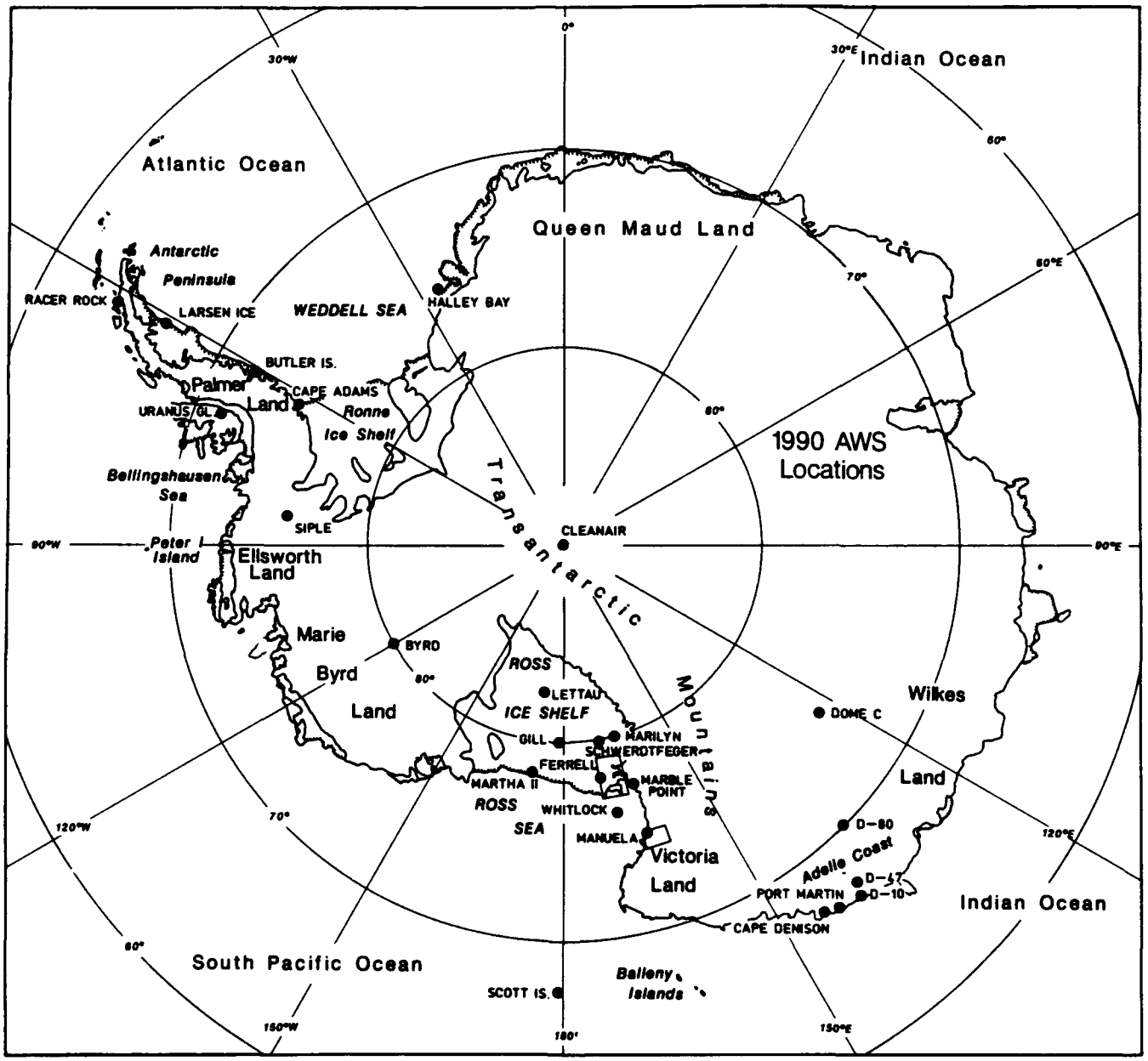


Figure 1. Map of Antarctica showing the locations of the AWS units for 1990. The units in the rectangle about Manuela Site are shown in Figure 2 and the units in the rectangle at Ferrell Site are shown in Figure 3.

Site	Lat. (deg)	Long. (deg)	Elev. (m)	Date Start	Stop
		Adelie Coast			
D-10	66.70°S	139.80°E	240	Feb 80	
D-17	66.70°S	139.70°E	438	Jan 80	Jun 80
D-47	67.38°S	138.72°E	1560	Jan 83	
D-57	68.18°S	137.52°E	2105	Jan 81	Dec 88
D-80	70.02°S	134.72°E	2500	Nov 84	
Dome C	74.50°S	123.00°E	3280	Feb 80	
Port Martin	66.82°S	141.39°E	39	Jan 90	
Cape Denison	67.02°S	142.68°E	31	Jan 90	
		Stations			
Byrd Station	80.00°S	120.00°W	1530	Feb 80	
Siple Station	75.90°S	83.92°W	1054	Dec 87	
		Ross Island Region			
Marble Point	77.43°S	163.75°E	120	Feb 80	
Manning	78.77°S	166.85°E	66	Dec 80	Jan 86
Ferrell	78.02°S	170.80°E	45	Dec 80	
Asgard	77.60°S	160.10°E	1750	Feb 80	Dec 82
Meeley	78.52°S	170.18°E	49	Dec 80	Jan 86
Jimmy	77.87°S	166.81°E	202	Dec 81	
Laurie	77.55°S	170.09°E	23	Dec 81	Jan 86
Nancy	77.91°S	168.17°E	25	Jan 83	Nov 83
Katie	77.70°S	167.70°E	40	Feb 83	Jan 86
Fogle	77.82°S	166.75°E	202	Jan 84	Jan 85
Tiffany	78.00°S	168.20°E	25	Jan 84	Jan 86
Pegasus	77.97°S	166.49°E	10	Jan 89	Nov 89
Pegasus North	77.95°S	166.51°E	10	Jan 90	
Mount Erebus	77.53°S	167.15°E	3700	Nov 89	
		Ocean Islands			
Whitlock	76.24°S	168.70°E	275	Jan 82	
Buckle Island	66.87°S	163.24°E	520	Feb 87	Oct 88
Scott Island	67.37°S	179.97°W	30	Dec 87	
		Ross Ice Shelf			
Marilyn	79.98°S	165.03°E	75	Jan 84	
Martha I	78.31°S	172.50°W	42	Feb 84	Jan 87
Schwerdtfeger	79.94°S	169.83°E	60	Jan 85	
Gill	80.00°S	179.00°W	55	Jan 85	
Bowers	85.20°S	163.40°E	2090	Jan 86	Jan 87
Elaine	83.15°S	174.46°E	60	Jan 86	Jan 89
Lettau	82.59°S	174.27°W	55	Jan 86	
Martha II	78.38°S	173.42°W	18	Feb 87	
		Reeves Glacier			
Manuela	74.92°S	163.60°E	80	Feb 84	
Shristi	74.72°S	161.58°W	1200	Dec 87	
Sushila	74.41°S	161.28°E	1431	Jan 88	
Sandra	74.51°S	160.42°E	1525	Jan 88	
Lynn	74.23°S	160.29°E	1772	Jan 88	
Pat	74.90°S	163.10°E	30	Jan 89	
		Antarctic Peninsula			
Larsen Ice Shelf	66.97°S	60.55°W	17	Oct 85	
Butler Island	72.20°S	60.34°W	91	Mar 86	
Dolleman Island	70.58°S	60.92°W	396	Feb 86	Jun 88
Uranus	71.43°S	68.93°W	780	Mar 86	
Cape Adams	75.01°S	62.53°W	?	Jan 89	
Racer Rock	64.16°S	61.54°W	17	Nov 89	
Halley Bay	75.50°S	26.65°W	52	Mar 90	
		South Pole Station			
Clean Air	90.00°S		2835	Jan 86	
Allison	89.88°S	60.00°W	2835	Jan 86	Jan 88
Patrick	89.88°S	45.00°E	2835	Jan 86	Jan 88
		Greenland Ice Cap			
Cathy	72.3 °N	38.0 °W	3210	May 87	May 89
GISP2	72.58°N	38.46°W	3205	Jun 89	
GRIP	72.57°N	37.62°W	3230	Jun 89	
Kenton	72.36°N	38.80°W	3185	Jun 89	
Barber	71.68°N	38.20°W	3170	Jul 90	
Klinck	72.35°N	40.50°W	3100	Aug 90	

Table 2. AWS locations from 1980 to 1990: If the site does not have a stop date then the AWS unit is at the site in 1990.

stop and cannot be repaired or replaced until the next field season. Figure 1 is a map of Antarctica showing the locations of the widely dispersed AWS units. Figure 2 is a map of the area near Terra Nova Bay, Antarctica showing the locations of the AWS units for the study of the katabatic winds down the Reeves Glacier. Figure 3 shows the locations of the AWS units around Ross Island, Antarctica. Figure 4 is a map of the Greenland Crest showing the AWS locations including Cathy site which is no longer in operation.

AWS APPLICATIONS

The AWS units are located in arrays for meteorological experiments and at other sites for operational purposes. Any one AWS unit may contribute to several experiments and all contribute to operational purposes especially for preparing weather forecasts for aircraft flights to and from New Zealand and within Antarctica. The Polar AWS units support the following research and operational areas:

- •Barrier wind flow along the Antarctic Peninsula and the Transantarctic Mountains;
- •Katabatic wind flow down the slope to the Adelie Coast, Reeves Glacier, Byrd Glacier, and Beardmore Glacier;
- •Mesoscale circulation and the sensible and latent heat fluxes on the Ross Ice Shelf;
- •Climatology of Byrd, Siple, and Dome C stations;
- •Oceanography in the Ross Sea;
- •Climate and meteorology of the Greenland Crest in support of ice core studies;
- •Meteorological support for air operations at McMurdo, Antarctica and the Greenland Crest; and
- •Monitoring for possible station locations and aircraft landing sites.

Stearns and Wendler [1988] present a review of some of the results from the AWS units in Antarctica.

Site	Lat. (deg)	Long. (deg)	Elev. (m)
Antarctica			
Adelie Coast			
Cape Jules?	67.0 °S	144.0 °E	
Ross Sea			
Beaufort Island	77. °S	167. °E	
Granite Harbor	77. °S	162. °E	
Buckle Island	66.87°S	163.24°E	
Ross Ice Shelf			
Cape Crozier	77.55°S	170.09°E	
Minna Bluff	78.5 °S	166.5 °E	
Minna Bluff East	78.5 °S	168. °E	
Ice Shelf Edge	78. °S	177.5 °E	
Byrd Neve	80.5 °S	152. °E	
Pegasus South	77.98°S	166.55°E	
Elaine	83.15°S	174.46°E	
Greenland Summit			
Summit East	72.3 °N	35.0 °W	3100
Summit North	73.4 °N	37.72°W	3100

Table 3. Locations Planned for 1991. The exact locations, ARGOS identification number, elevations, and start date will not be known until the units are actually installed.

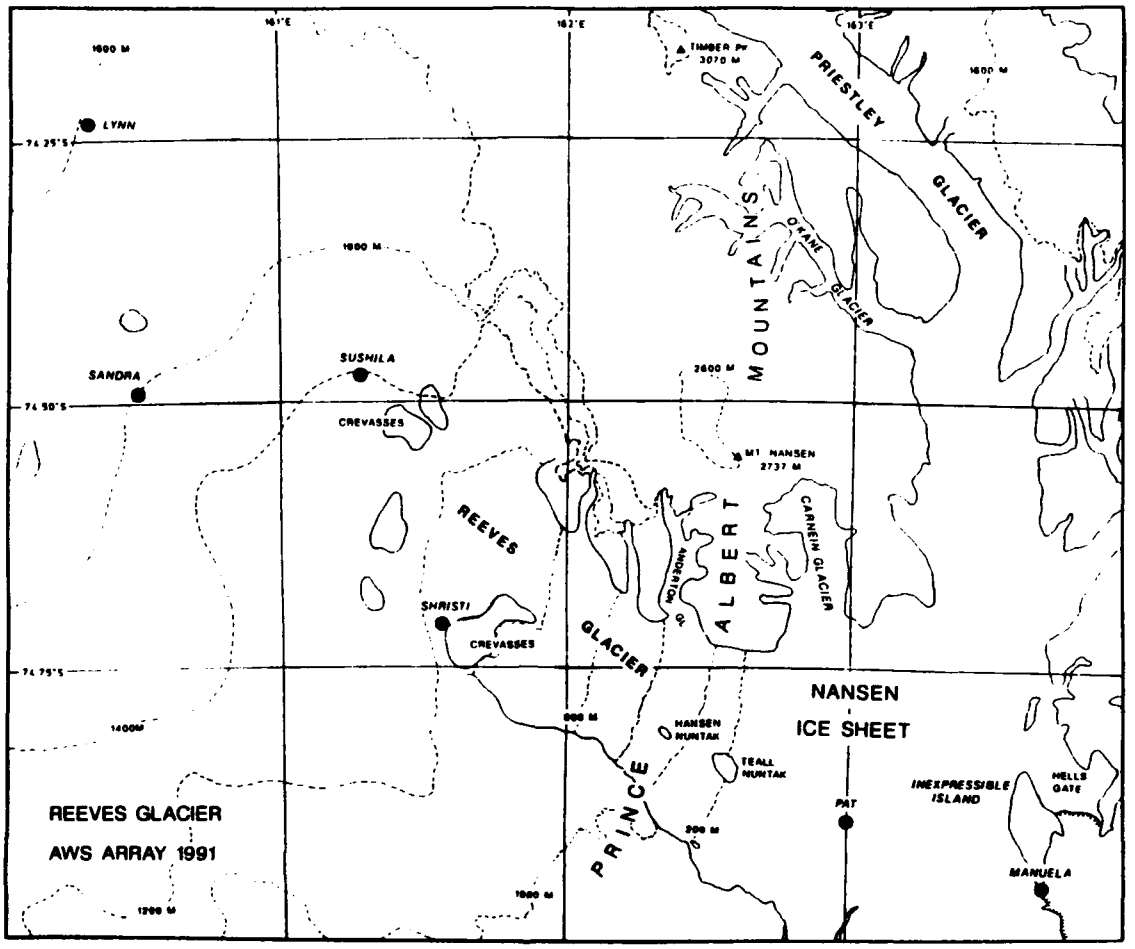


Figure 2. Map of the locations of AWS units in the Reeves Glacier area of Antarctica including Manuela Site.

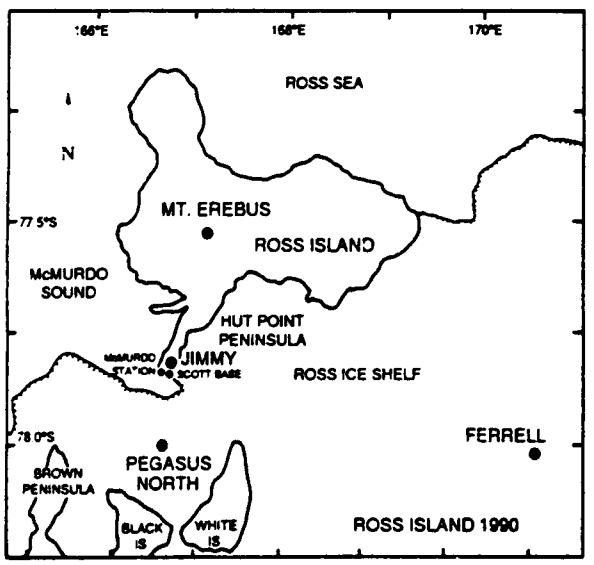


Figure 3. Map of the Ross Island area of Antarctica showing the locations of Ferrell, Jimmy, and Pegasus Sites.

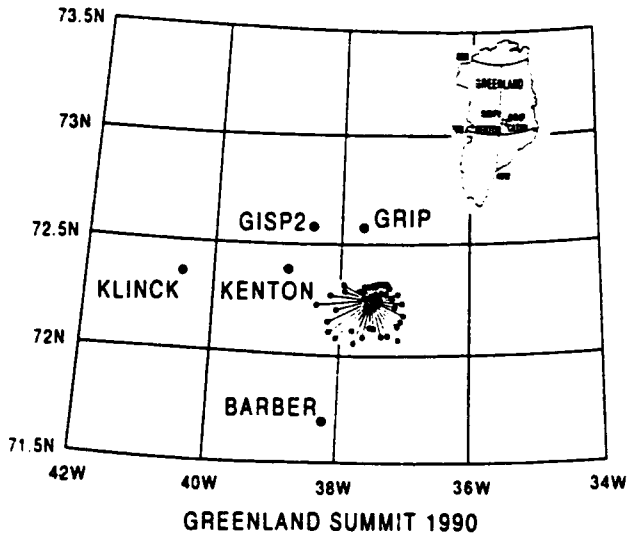


Figure 4. Map of Greenland showing the locations of GRIP, GISP2, Kenton, Barber, and Klinck sites. The May 1987 to June 1989 wind direction frequency rose is shown for Cathy site which was south of GRIP site and east of Kenton site. The map insert shows the locations of GISP2, GRIP, and Kenton on Greenland.

AWS DATA

The data are available on paper as values taken every three hours of wind speed, wind direction, air temperature, and pressure for each month including a monthly summary. The three-hourly data are available on 5.25- and 3.5-inch magnetic disks in IBM format and include any additional data that may be available such as the vertical air temperature difference and relative humidity. The complete data set is available on magnetic tape. AWS data from 28 sites are entered into the Global Telecommunications System every six hours.

FUTURE PLANS

Table 3 gives the AWS sites planned for 1991 in Antarctica and Greenland. The Antarctic units should be installed between November 1990 and February 1991. The Greenland units should be installed during July 1991. After an experiment is completed the AWS units will be removed, repaired, modified, and relocated for another experiment.

ACKNOWLEDGMENTS

The AWS program is supported by National Science Foundation Division of Polar Program grants 8606385, 8818171, and 8821894. The British Antarctic Survey installs and services the AWS units in the Antarctic Peninsula area. Expeditions Polaires Francaises installs and services the AWS units from D-10 to D-80.

REFERENCE

Stearns, C. R., and G. Wendler, Research results from Antarctic automatic weather stations, *Rev. Geophys.*, *26*, 45–61, 1988.

AD-P007 268

92-17950

Detection of Temperature and Sea Ice Extent Changes in the Antarctic and Southern Ocean

T. H. Jacka
Australian Antarctic Division, Kingston, Australia

W. F. Budd
Meteorology Department, The University of Melbourne, Parkville, Australia

ABSTRACT

Some global climate models indicate that future global warming from increased atmospheric concentrations of greenhouse gases may be greatest in the polar regions, over areas where the sea ice cover is reduced. The reduction of sea ice area in the models also gives rise to a strong positive feedback to the warming. From the increase of atmospheric greenhouse gas concentration to date and the results of transient climate models, an estimate of the expected change in the Antarctic temperatures and sea ice extent can be made.

The existing data for observed changes in temperatures of the Antarctic and Southern Ocean (extending back to ~1956 and ~1945 respectively) are analyzed along with the data of sea ice cover (commencing in 1973) to examine the extent to which the anticipated warming trends and sea ice decrease are being realized.

In spite of high temporal and spatial variability, the data does support small significant trends of temperature increase and sea ice cover decrease compatible in magnitude to those expected as a consequence of atmospheric greenhouse gas increase.

The seasonal cycle shows a delayed period of autumn–winter sea ice growth with a longer period of open water. This supports a mechanism for positive feedback between decreasing sea ice cover and increasing temperature.

INTRODUCTION

Results of several numerical modeling studies of the effects of increased atmospheric greenhouse gas concentrations on climate [e.g., Manabe and Wetherald, 1975, 1980; Manabe and Stouffer, 1979; Dickinson et al., 1987] have suggested that changes in climatic parameters could be greatest in the polar regions, where feedback mechanisms operate between the climate and the sea ice. Several studies have thus been carried out on relationships between sea ice extent and other climate characteristics [e.g., Schwerdtfeger and Kachelhoffer, 1973; Streten and Pike, 1980; Cavalieri and Parkinson, 1981].

In particular, many of the climate models aimed at studying greenhouse effects predict increased surface air temperatures, amplified in the polar regions as a consequence of the effect on the climate of changing sea ice extent, concentration, and thickness. This suggests that as an early warning indicator of the onset of a detectable warming from the increasing atmospheric greenhouse gas concentrations, the monitoring of surface air temperatures in the Antarctic region would be worthwhile. This task has been tackled by Budd [1975], Jacka et al. [1984] and Jones and Limbert [1987].

At the same time, the monitoring of Antarctic sea ice extents would also seem worthwhile, is practicable, and has been tackled by several workers [e.g., Zwally et al., 1983].

This paper updates previous reports [Budd, 1975, 1980; Jacka, 1981, 1990] based on climate monitoring projects which have been described in detail by Jacka [1983], Jacka et al. [1984] and Cook et al. [1991].

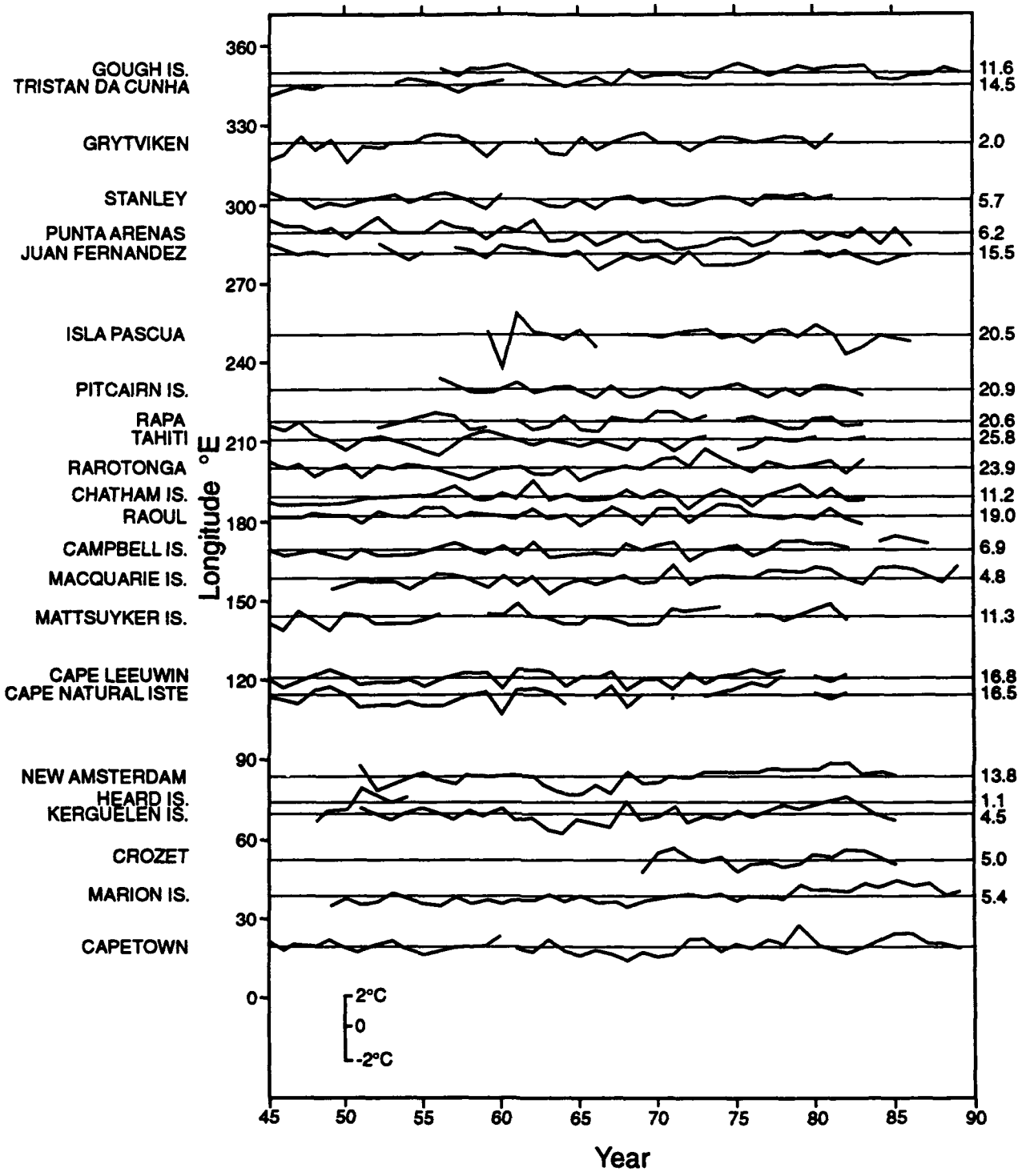


Figure 1. Mean annual surface air temperatures for Southern Ocean and South Pacific Ocean stations. The time series are plotted as anomalies about a zero line. The long-term mean temperature for each station is indicated in the right-hand margin. Data are plotted approximately according to station longitude (°E), indicated on the left-hand axis.

Climatic data for these monitoring projects are collected from several publications emanating from countries responsible for the operation of the various meteorological stations. Examples of these publications include *Antarctic Journal of the United States*, the *Japanese Antarctic Bulletin*, *Information Bulletin of the Soviet Antarctic Expeditions*, the Australian *ANARE News*, New Zealand's *Meteorological Observations* published annually, and the monthly climate data summary from South Africa. In addition, *Monthly Climatic Data of the World* and *Climate Monitor* include summaries for several Antarctic and Southern Ocean stations. Finally and where necessary, data are obtained by personal communication with observers at the stations themselves.

Sea ice extent data from the U.S. Navy/NOAA Joint Ice Center weekly maps are monitored on a monthly basis.

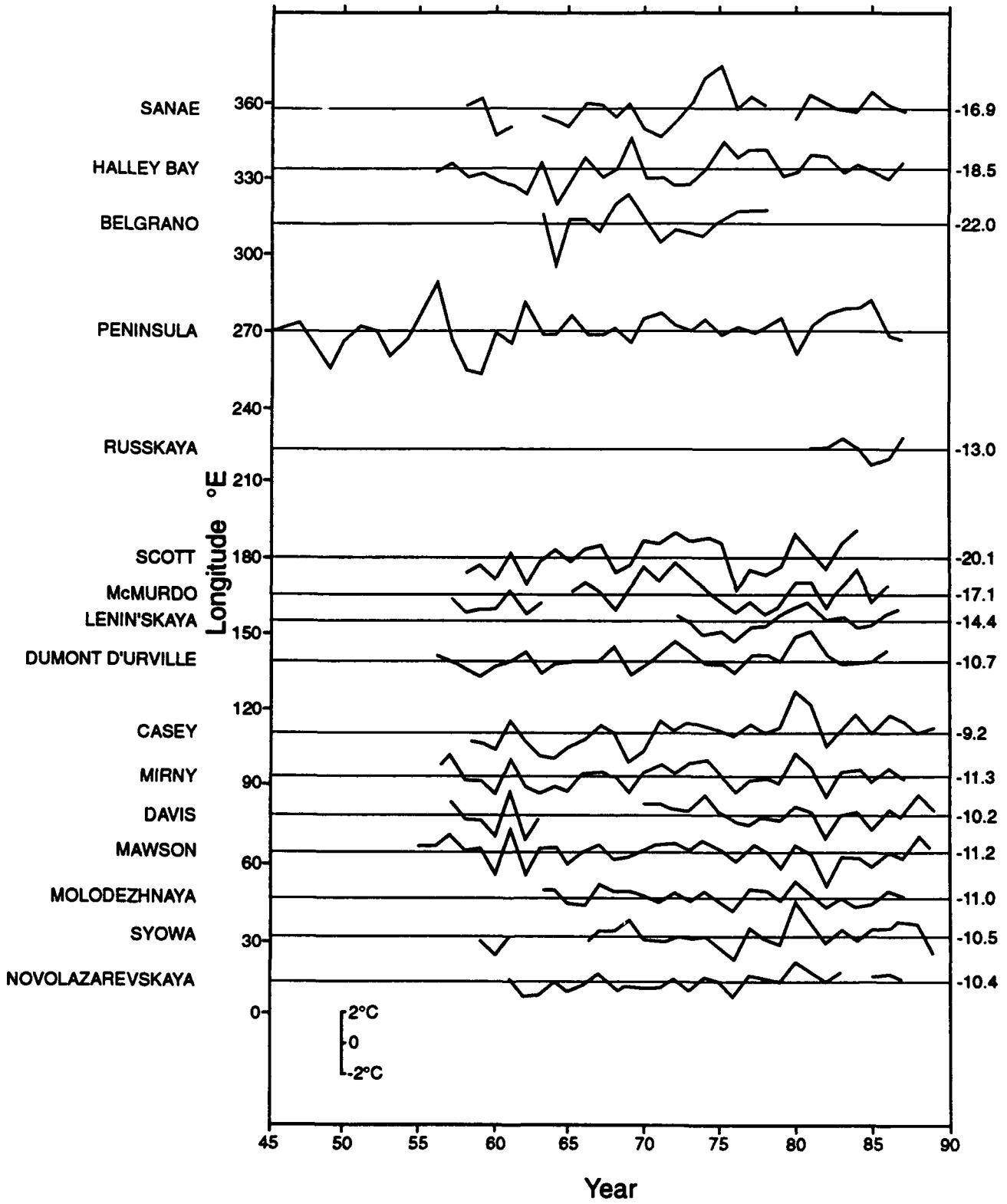


Figure 2. Mean annual surface air temperatures for coastal Antarctic stations. The time series are plotted as anomalies about a zero line. The long-term mean temperature for each station is indicated in the right hand margin. Data are plotted approximately according to station longitude (°E), indicated on the left-hand axis.

Computer-linked digitization of these maps is of the northern ice limit at each 10° of longitude. The Joint Ice Center maps have been available in the current format since January, 1973 and are compiled from various sources [Godin, 1979].

The data banks described above, and upon which this paper is based, are now available to interested researchers on 3.5-inch diskettes (IBM or Apple Macintosh) by contacting the authors [see Jacka, 1990 for further details].

For now, three topics are addressed. First, what techniques can be used to detect (a) a warming trend in the Antarctic and Southern Ocean, and (b) a trend to less extensive sea ice extent? Second, what is the relationship between these trends, and third, are the trends compatible with those expected to result from increased atmospheric concentrations of greenhouse gases?

In order to examine the results in relation to possible greenhouse warming, the following numerical values may provide a useful reference. The ice core data [Pearman et al., 1986] indicate that the pre-industrial level of atmospheric CO_2 at about the middle of the last century was 280 ppm compared with about 350 ppm at present (1990). This suggests that if there were no thermal lags in the system, expected changes could be equivalent to those at about one quarter of the way towards a CO_2 doubling from 280 to 560 ppm or the equivalent in terms of other greenhouse gases. Any thermal delays would make this an upper limit.

A typical global average temperature increase for the equilibrium greenhouse doubling, according to the IPCC report [Houghton et al., 1990], is about 3°C. In the region near the Antarctic sea ice the changes obtained from many of the models have been about double this amount. The anticipated trends over the past century might therefore be expected to be about one quarter of these increases, i.e., up to 0.75°C north of the sea ice and 1.5°C further south.

In most of the model results a reduction in maximum sea ice latitudinal extent is also obtained. A typical reduction for the equilibrium CO_2 doubling scenario is about 6°lat. within an annual amplitude of 8°lat. One quarter of the 6°lat. would be 1.5°lat. which could be expected if the changes are on schedule without lags. These values can be used for reference to those obtained by our analysis of the data.

DETECTION OF TEMPERATURE CHANGES

Mean annual surface air temperature data are shown in Figures 1 and 2 for Southern Ocean and South Pacific Ocean stations and for coastal Antarctic stations respectively. Within each figure, the data are arranged approximately according to station longitude, facilitating both temporal and spatial examination of trends. Figure 2 includes one station, "Peninsula," for which data were compiled by calculating the mean annual temperature anomalies across all Antarctic Peninsula stations. It should be noted that because of the sparse coverage of islands in the Southern Ocean, Figure 1 includes data from islands in the South Pacific and from locations at the southern extremities of the continents.

Examination of the data sets on the spatial domain shows clearly that neighboring stations exhibit similar trends. It is interesting to note in addition for the coastal Antarctic station data, that in some years (1980 is a good example) East Antarctic stations exhibit high temperatures, while West Antarctic stations exhibit low temperatures, and vice versa in other years (e.g., 1962). To examine the extent of this phenomena in more detail, an array of correlation coefficients was calculated by comparing annual mean temperatures from each Antarctic station with every other Antarctic station. Figure 3 shows longitudinal difference between the stations as a function of correlation coefficient. The data of Figure 3 have themselves a correlation coefficient of -0.66, significant at the 99% confidence interval. Note that while temperatures from stations close together are well correlated, there is also some tendency for stations on opposite sides of the continent to be negatively correlated.

On the time domain of Figures 1 and 2, it is seen that most station data exhibit warming trends. These trends are greater for the Antarctic stations than for the ocean stations. They are, however, small in comparison with the interannual variability of the data (particularly for the Antarctic stations) and thus the statistical significance of the trends, especially for stations with only a few years of data, is difficult to establish. The significance of the trends is made clear by the analysis shown in Figure 4.

The histograms of Figure 4 show the frequencies of stations with annual mean temperature data exhibiting different linear regression line slopes. Regression slopes were calculated over various time periods, viz. (for Southern Ocean stations) 1949 to 1958, 1949 to 1968, 1949 to 1978 and 1949 to 1988, and (for coastal Antarctic stations) 1959 to 1968, 1959 to 1978 and 1959 to 1988, so that each histogram includes a further 10 years of data than the one above.

For the 1949 to 1958 Southern Ocean station data, the distribution of frequencies about a near-zero regression line slope is similar to that expected for a random sample of data exhibiting no trend. With the addition of a further 10 years of data, a slight tendency to higher frequencies near zero slope is exhibited. The 1949 to 1978 data shows a clearly skewed distribution with reduced range and a mean slope indicating slight warming. Finally, this distribution is strengthened by the addition of data to 1988. The mean of the regression slopes for the ocean station temperature data over the period 1949 to 1988 is ~0.8°C/100 years. The confidence that can be placed on this warming extent is strengthened by the consistency of stations exhibiting a

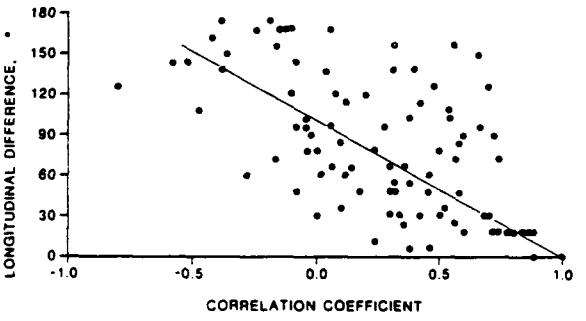


Figure 3. By comparing annual mean temperatures from each Antarctic station with every other Antarctic station, an array of correlation coefficients is formed. The plot shows longitudinal difference between stations as a function of correlation coefficient. The plotted data have correlation coefficient -0.66, significant at the 99% confidence interval.

warming trend and by the closer approach to this figure with the addition of further data. Those stations showing negative trends are primarily located in the South Pacific, north of the circumpolar ocean flow.

The histograms for the Antarctic data show trends similar to the ocean data. However, because not as many years of data are available for the Antarctic stations and because the Antarctic data exhibit higher interannual variability, the convergence of the trend is not as clear as for the ocean data. It should be noted that only two of the fifteen Antarctic stations exhibit a cooling. These two stations, Mawson and Molodezhnaya, are neighboring stations which may be affected by increased air flow from the cold interior, as indicated by the gridded analysis of station seasonal pressure anomalies plotted by Jones and Wigley [1988]. For the Antarctic stations, the mean of the slopes of regression lines through the data sets indicates a warming of ~2.8°C/100 years. This figure cannot be designated the same degree of confidence as the ocean data warming rate; however it is clear that there is a warming trend for the Antarctic stations and that it is higher than that exhibited by the Southern Ocean stations. The clear movement of the histograms to the positive side over time provides confidence in the significance of the trends.

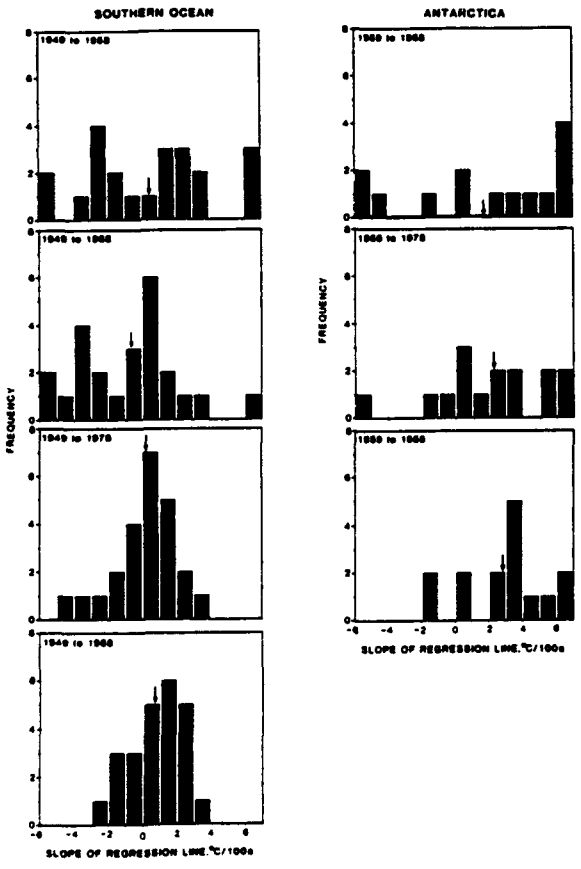


Figure 4. Histograms showing the frequency of stations with annual mean temperature data exhibiting different linear regression line slopes. Data periods examined are (for Southern Ocean stations) 1949 to 1958, 1949 to 1968, 1949 to 1978 and 1949 to 1988, and (for Antarctic stations) 1959 to 1968, 1959 to 1978 and 1959 to 1988. The mean regression slope in each histogram is indicated by an arrow.

DETECTION OF SEA ICE EXTENT CHANGES

Figure 5 is a presentation of annual mean sea ice extent at each 10° of longitude, plotted in a format similar to the temperature data of Figures 1 and 2. On the spatial domain, it is seen that in some years, there are large areas of reduced sea ice extent (e.g., 310 to 360° longitude in 1977) and in others, of increased extent (e.g., 30 to 60° longitude in 1976; 280 to 310° longitude in 1987). In addition, note that on occasions, the same trend reversal between East and West Antarctica noted for the temperature data, also occurs for the sea ice extent data (e.g., for 1980, a marked reduction in extent at longitudes 170 through 240°, yet substantially increased extent at longitudes 300 through 330°).

On the time domain, it is clear from the results shown in Figures 5 to 8 that the annual variations in sea ice are greater than any long-term trend, but that at most longitudes, although the mean changes from 1975 on are small, a decrease in ice extent from the early 1970s is evident. In addition, the few data from Cook's expeditions of 1772 to 1775 [Herdman, 1959; Rubin, 1982] and from the *Discovery* expeditions in the 1930s [Mackintosh and Herdman, 1940] indicate that for the summer months, there is evidence of a decrease in sea ice extent over this longer period prior to the start of the satellite data.

Calculations of slopes of linear regression fits through each curve of Figure 5 reveal that 26 of the 36 curves exhibit a trend to reduced sea ice. The mean of the slopes indicates a reduction in sea ice extent of 1.9°lat./100 years. For the ice extent there are too few years of good quality data to carry out a progressive trend analysis; however the consistency of the trend to reduced ice extent around the continent gives support to the confidence of the above figure.

In order to examine changes in the ice edge on a seasonal basis, Figure 6 is a plot of the mean ice edge latitude for each month of the year from data averaged over the four-year periods at the beginning and end of the series, viz. 1973 to 1976 and 1986 to 1989. The mean decrease in sea ice extent between these two periods is clearly illustrated and the plots show that there is less ice during the time of minimum extent and throughout the growth period for the later four-year period. The greatest reduction is during the months August through October, the time of maximum ice extent. It can be seen that at maximum extent, the mean sea ice extent has reduced by ~0.6°lat. (i.e., a total area reduction around the continent of ~2.3 x 106 km2) over the observation period. There has been a reduction in the duration of the mean ice cover of about 2 weeks over most of the sea ice area and at the current maximum ice latitude (i.e., at ~61°S), a reduction of about 2 months. This can be observed in Figure 6, and is compatible with the observation by Gloersen and Campbell [1988] of a later occurrence of the maximum ice extent. During the period of sea ice decay, November through January, the ice extent is unchanged over the observation period.

RELATIONS BETWEEN SEA ICE AND TEMPERATURE CHANGES

Since some climate models have predicted greater warming in polar regions due to feedback mechanisms as a consequence of reduced sea ice extent, it is useful to examine these two parameters together and to establish some

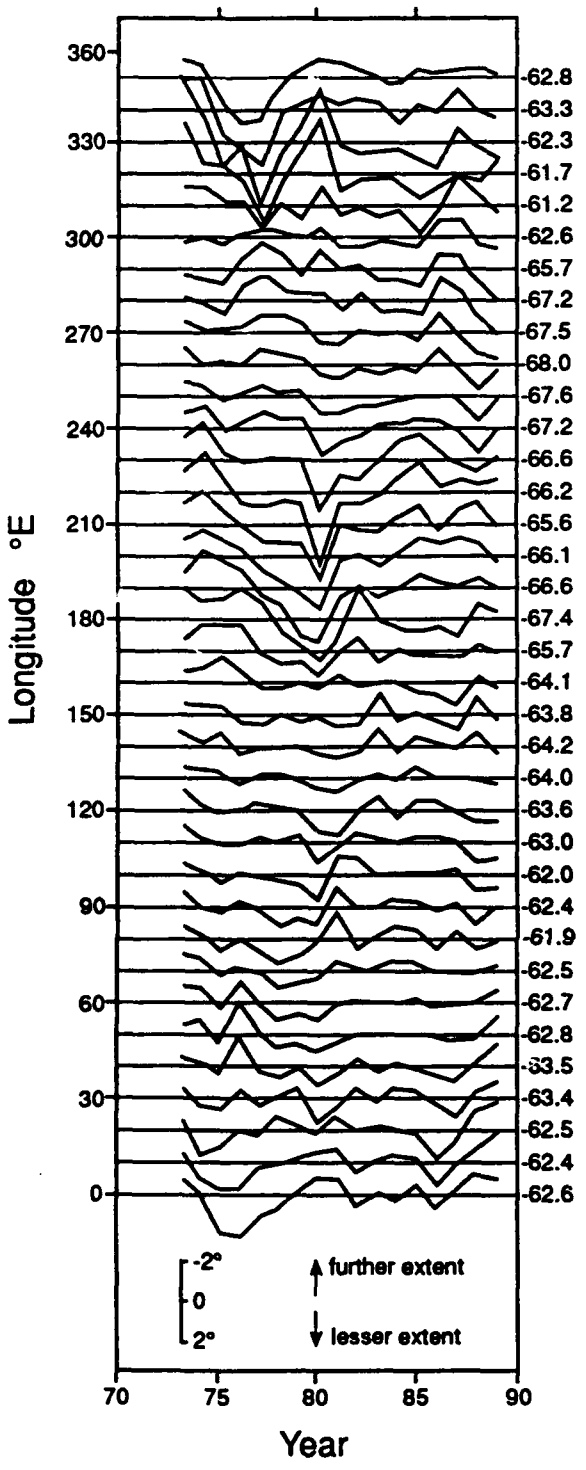


Figure 5. Mean annual sea ice extent at each 10° of longitude, plotted in the same format as the temperature data of Figures 1 and 2. The long-term (1973-1989) mean latitude of the ice edge is indicated in the right margin.

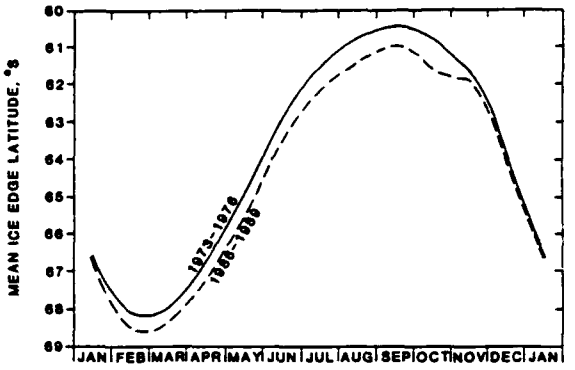


Figure 6. The mean (across 36 x 10° longitudes) annual sea ice cycle is plotted for the 4-year periods 1973 to 1976 and 1986 to 1989.

relationship between warming rate and ice extent. Figure 7 shows time series of the mean across all longitudes of the annual temperature anomalies for the Southern and South Pacific Ocean stations and for the coastal Antarctic stations, along with the mean annual latitude anomalies for the sea ice extent. Comparison, for the period 1973 to 1989, of these data sets reveals that for a few selected years (e.g., 1980) particularly high Antarctic temperatures and high Southern Ocean temperatures occurred along with reduced sea ice extent. Comparisons over the whole record (1973 to 1989) do not result in high correlations. The slopes of linear regressions through these mean anomaly curves do, as expected, indicate higher temperatures and reduced sea ice extent. For the data from 1973 to 1989, the sea ice extent has reduced by ~1.9°lat./100 years while coastal Antarctic temperatures have increased by ~1.3°C/100 years. Assuming that these phenomena are dependent, a long-term change of ~1.5°lat./°C is implied. [cf. Budd, 1975 who found for data at Laurie Island involving ice duration, an inferred relation between sea ice and temperature fluctuations of ~2.0°lat./°C].

It has already been observed that most of the Southern Ocean island stations exhibit a warming trend, that all but two neighboring coastal Antarctic stations exhibit a warming trend and that the sea ice extent exhibits a reduction at twenty-six of the thirty-six 10° longitudinal increments.

To examine the geographical distribution of the trends further, in Figure 8 the slopes of regression lines through the annual mean temperature data for each station are plotted for coastal Antarctic stations about the inner circle, and for Southern Ocean and South Pacific Ocean island stations, about the outer circle. In addition, the slope of regression lines through the annual mean sea ice extent data at each 10° of longitude is plotted about the middle circle. Some interesting features can be seen from the diagram. All of the Southern Ocean stations exhibit a warming trend while the more northerly South Pacific Ocean stations generally exhibit a cooling trend. For the Antarctic stations, as already noted, only Mawson and Molodezhnaya exhibit a cooling trend. These Pacific Ocean islands are under the influence of the westerly flowing tropical water in the northern branch of the South Pacific Ocean gyre which could exhibit a cooling from reduced circulation as described for a future warming by Simmonds and Budd [this volume].

The sea ice extent curve is particularly interesting. While the total sea ice extent shows a trend to less ice, the curve exhibits a (weak) four-wave pattern, with each of the regions of increasing extent located 10 to 30° to the east of due north of the major ice shelves. The regions where the sea ice is slightly more extensive are in the northern parts of the Ross and Weddell gyres. This could also result from a reduction in the ice drift from reduced Westerly winds.

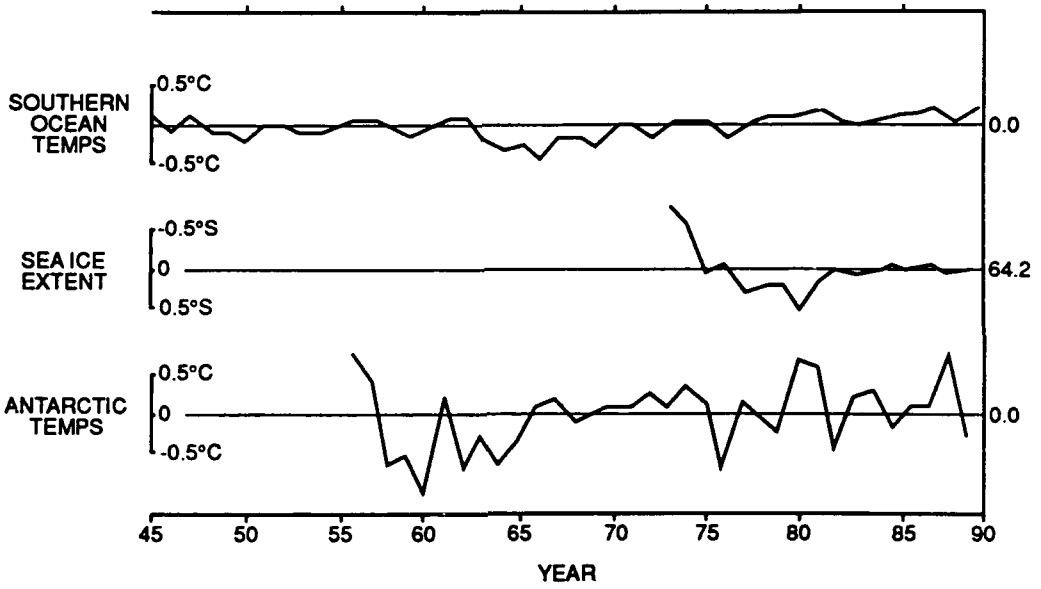


Figure 7. Means across all longitudes of (a) Southern and South Pacific Ocean mean temperature anomaly, (b) annual sea ice extent, and (c) coastal antarctic station mean temperature anomaly.

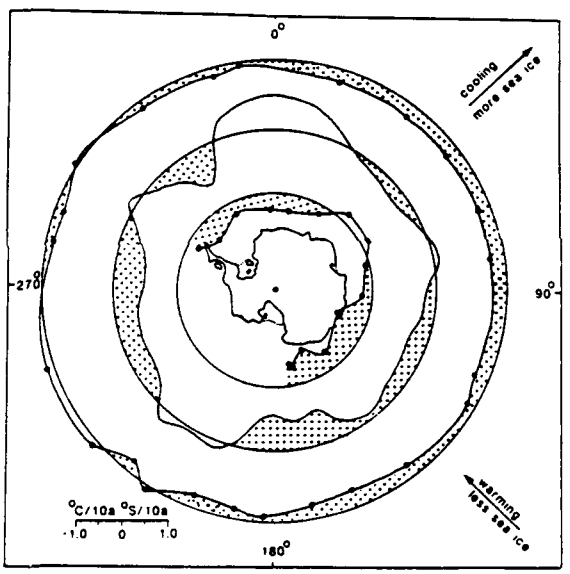


Figure 8. The slope of regression lines through the annual mean temperature data for each station is plotted for Antarctica about the inner circle; and for the Southern Ocean and Pacific Ocean islands, about the outer circle. Also, the slope of regression lines through the annual mean sea ice extent data at each 10° of longitude is plotted about the middle circle. Areas exhibiting a warming effect, and areas exhibiting a reduced sea ice extent, are indicated by shading.

Jacka [1981] found that the sea ice extent was best correlated with annual mean temperature if an eastward shift of the sea ice of ~30° was imposed. Lemke et al. [1980] related sea ice drift to the west-to-east–flowing circumpolar current.

CONCLUSIONS AND FUTURE RESEARCH

The results indicate a trend to higher temperatures in the south polar regions. With the addition of further data, the significance and uniformity of the trend is increasing. The warming rate is consistent with that expected from the increased concentration of greenhouse gases in the atmosphere. Further, as expected from the effect of feedback mechanisms between higher temperatures and reduced sea ice coverage, the warming rate appears to be higher for the Antarctic stations than for the Southern Ocean stations, and higher for the Southern Ocean stations than for the South Pacific Ocean stations. The sea ice extent results indicate a reduction, also of about the magnitude expected from the effects of greenhouse warming.

To more accurately determine the temperature trends, the sea ice trends, the relations between these two climatic parameters, and the influence on them of increasing greenhouse gas concentrations, monitoring projects need to continue. With more years of data, the significance of the trends will become clearer. For the temperature monitoring, more climate stations are required. In particular, the West Antarctic coast between the Ross Ice Shelf and the Antarctic Peninsula is data sparse. Significantly, this same sector of the Southern Ocean has no climate stations. The inclusion of South Pacific Ocean stations in this project was made specifically to partially overcome this problem. Plans to deploy automatic weather stations at several sites in Antarctica and the Southern Ocean [Stearns and Weidner, this volume], particularly in the Pacific Ocean sector, are encouraging. However, until automatic weather stations have operated continuously for at least five years they are of little assistance for climate monitoring. Fortunately, these stations are now reliable enough to do this and one or two can now be utilized for this purpose.

Sea ice monitoring also needs to continue. Recent studies [e.g., Ackley and Smith, 1983; Jacka et al., 1987; Allison, 1989; Brandt et al., 1990] have shown that the Antarctic sea ice area includes large areas of very thin ice and of open water. For future studies, therefore, it will be necessary to examine not just the northern ice limit, but to also include monitoring of ice concentration and thickness. Ice concentration can be estimated by remote sensing from satellites. For now, however, the measurement of ice thickness

requires expeditions into the sea ice zone and the development of special devices such as upward-looking sonar. Future expeditions to the Antarctic sea ice zone, particularly during winter and spring, along with further drifting buoy and automatic weather station deployment, will provide data for more precise monitoring of these climatic parameters.

REFERENCES

Ackley, S. F., and S. J. Smith, Ice observations. Reports of the US-USSR Weddell-Polynya Expedition, October–November 1981, *5*, *CRREL Special Report* 83-2, 1983.

Allison, I., Pack-ice drift off East Antarctica and some implications, *Ann. Glaciol.*, *12*, 1–8, 1989.

Brandt, R., I. Allison, and S. Warren, Albedo of young and first-year Antarctic ice, *Ann. Glaciol.*, *14*, 331, 1990.

Budd, W. F., Antarctic sea ice variations from satellite sensing in relation to climate, *J. Glaciol.*, *15*, 417–427, 1975.

Budd, W. F., The importance of the Antarctic region for studies of the atmospheric carbon dioxide concentration, in *Carbon Dioxide and Climate: Australian Research*, Edited by G. I. Pearman, pp. 115–128, Australian Academy of Science, Canberra, 1980.

Cavalieri, D. J., and C. L. Parkinson, Large scale variations in observed Antarctic sea ice extent and associated atmospheric circulation, *Mon. Wea. Rev.*, *109*, 2323–2336, 1981.

Cook, B. J., L. Christou, and T. H. Jacka, Antarctic climate monitoring: mean monthly and annual surface pressure data, in *Australian Glaciological Research, 1984–1986*, Edited by T. H. Jacka, *ANARE Research Notes*, 1991, In press.

Dickinson, R. E., G. A. Meehl, and W. M. Washington, Ice-albedo feedback in a CO_2 doubling simulation, *Climatic Change*, *10*, 241–248, 1987.

Gloersen, P., and W. J. Campbell, Variations in the Arctic, Antarctic and global sea ice covers during 1978–1987 as observed with the Nimbus 7 scanning multichannel microwave radiometer, *J. Geophys. Res.*, *93*, 10666–10674, 1988.

Godin, R. H., Data sources and sea ice products of Fleet Weather Facility/Joint Ice Center, Suitland, *Glaciological Data Report GD-5*. Workshop on snow cover and sea ice data, pp. 29–35, 1979.

Herdman, H. F. P., Early discoveries, XII - some notes on sea ice observed by Captain James Cook, R.N., during his circumnavigation of Antarctica, 1772–1775, *J. Glaciol.*, *3*, 534–541, 1959.

Houghton, J. T., G. J. Jenkins, and J. J. Ephraums (Eds.), *Climate Change. The IPCC Scientific Assessment*, 365 pp., Cambridge University Press, 1990.

Jacka, T. H., Antarctic temperature and sea ice extent studies, in *Antarctica: Weather and Climate*, preprint volume of conference sponsored by Royal Meteorological Society Australian Branch, edited by N. W. Young, pp. 88–97, 1981.

Jacka, T. H., A computer data base for Antarctic sea ice extent, *ANARE Research Notes 13*, 54 pp., Australian Antarctic Division, 1983.

Jacka, T. H., Antarctic and Southern Ocean sea ice and climate trends, *Ann. Glaciol.*, *14*, 127–130, 1990.

Jacka, T. H., L. Christou, and B. J. Cook, A data bank of mean monthly and annual surface temperatures for Antarctica, the Southern Ocean and South Pacific Ocean, *ANARE Research Notes 22*, 97 pp., 1984.

Jacka, T. H., I. Allison, R. Thwaites, and J. C. Wilson, Characteristics of the seasonal sea ice of East Antarctica and comparisons with satellite observations, *Ann. Glaciol.*, *9*, 85–91, 1987.

Jones, P. D., and D. W. S. Limbert, A data bank of Antarctic surface temperature and pressure data, *Report TR038* prepared for United States Department of Energy, 52 pp., 1987.

Jones, P. D., and T. M. L. Wigley, Antarctic gridded sea level pressure data: an analysis and reconstruction back to 1957, *J. Climate*, *1*, 1199–1220, 1988.

Lemke, P., E. W. Trinkl, and K. Hasselmann, Stochastic dynamic analysis of polar sea ice variability, *J. Phys. Oceanogr.*, *10*, 2100–2120, 1980.

Mackintosh, N. A., and H. F. P. Herdman, Distribution of pack-ice in the Southern Ocean, *Discovery Reports*, *19*, 285–296, 1940.

Manabe, S., and R. J. Stouffer, A CO_2-climate sensitivity study with a mathematical model of the global climate, *Nature*, *282*, 491–493, 1979.

Manabe, S., and R. T. Wetherald, The effects of doubling the CO_2 concentration on the climate of a general circulation model, *J. Atmos. Sci.*, *32*, 3–15, 1975.

Manabe, S., and R. T. Wetherald, On the distribution of climate change resulting from an increase in CO_2 content of the atmosphere, *J. Atmos. Sci.*, *37*, 99–118, 1980.

Pearman, G. I., D. Etheridge, F. deSilva, and P. J. Fraser, Evidence of changing concentrations of CO_2, N_2O and CH_4 from air bubbles in antarctic ice, *Nature*, *320*, 248–250, 1986.

Rubin, M. J., James Cook's scientific program in the Southern Ocean, 1772–1775, *Polar Record*, *21*, 33–49, 1982.

Schwerdtfeger, W., and S. J. Kachelhoffer, The frequency of cyclonic vortices over the Southern Ocean in relation to the extension of the pack belt, *Ant. J. of the U.S.*, *8*, 234, 1973.

Simmonds, I., and W. F. Budd, Model studies of the effects of global warming and Antarctic sea ice changes on Antarctic and global climates, *This volume*.

Stearns, C. R., and G. A. Weidner, The polar automatic weather station project of the University of Wisconsin, *This volume*.

Streten, N. A., and D. J. Pike, Characteristics of the broad-scale Antarctic sea ice extent and the associated atmospheric circulation, 1972–1977, *Archiv. Met. Geophys. Biokl.*, *29*, 279–299, 1980.

Zwally, H. J., J. C. Comiso, C. L. Parkinson, W. J. Campbell, F. D. Carsey, and P. Gloersen, Antarctic sea ice, 1973–1976: satellite passive-microwave observations, *National Aeronautics and Space Administration (SP-459)*, Washington, DC, 1983.

AD-P007 269

92-17951

Interannual Variability of Monthly Sea Ice Distributions in the North Polar Region

Claire L. Parkinson
Oceans and Ice Branch, NASA Goddard Space Flight Center, Greenbelt, Maryland, U.S.A.

ABSTRACT

Passive-microwave data from the Nimbus 5 and Nimbus 7 satellites have been used to determine and map, by month, the interannual variability of the spatial distribution of north polar sea ice over the period 1973–1987. Results are illustrated for the months of January and July, during the winter ice growth and summer ice decay seasons, respectively. In January, the greatest interannual variability in the distribution of the ice occurs in the Sea of Okhotsk, whereas the portions of the ice edge exhibiting the least interannual variability lie in the southern Greenland Sea and immediately to the southwest of Svalbard. In July, spatial variability is high in Hudson Bay, Baffin Bay, the southern Kara Sea, and the northern Barents Sea. The monthly maps are meant to allow ready comparison with past and future sea ice distributions and aid in the assessment of whether specific changes are climatically important.

INTRODUCTION

When examined regionally, sea ice distributions often exhibit a high level of interannual variability. For instance, over the eight-year period 1979–1986, November monthly average sea ice extents in Hudson Bay varied from 0.5×10^6 km^2 in 1981 to 1.2×10^6 km^2 in 1986, January ice extents in the Sea of Okhotsk varied from 0.5×10^6 km^2 in 1984 to 1.2×10^6 km^2 in 1979, and March ice extents in Baffin Bay/Davis Strait varied from 1.1×10^6 km^2 in 1981 to 1.7×10^6 km^2 in 1983 [Parkinson and Cavalieri, 1989]. The high regional variability, with monthly average extents in one year sometimes exceeding double those in other years, opens abundant possibilities for incautiously making misleading inferences of climate change from selectively chosen data. At the same time, however, the known high interannual variability, coupled with the lack of a long-term global sea ice data base, can lead overly cautious scientists to despair of ever interpreting any change in the ice cover as climatologically significant. Yet there are aspects of the ice cover that show a high level of consistency from year to year and for which noticeable future changes could indeed be significant from a climatological viewpoint. For instance, over the same 1979–1986 period used to illustrate high variability in certain months and regions, there was no variability in January, February, or March ice extents in Hudson Bay, as ice extended over the entire bay in each year [Parkinson and Cavalieri, 1989; "ice extent" is defined here, and elsewhere, as the areal coverage of ice with concentration $\geq 15\%$]. Also, for the north polar region as a whole, the maximum monthly average ice extents for each of the eight years varied by only 4%, from 14.9×10^6 km^2 in March 1984 to 15.5×10^6 km^2 in March 1979 [Parkinson and Cavalieri, 1989].

Clearly proper interpretation of the climatological significance of a given change in the ice cover and of whether a 10% change or a 20% change or even a 100% change is significant requires knowledge of past changes and preferably a long sequence of past changes. It is unfortunately not possible at the present time, for either the northern or the southern hemisphere, to obtain a consistent sea ice data base covering 30 or more years, as is standard for many so-called "climatological" data bases for other variables. However, the technology exists, through satellite passive-microwave observations, for such data sets to be obtained eventually. Furthermore, the existent satellite passive-microwave record now spans most of the period since 1972 and is thus long enough to make it worthwhile to present in concise form the interannual variability revealed by it. Consequently, the data from two major satellite passive-microwave imagers have been used to generate maps depicting the interannual variability of monthly sea ice distributions in the north polar region over the period covered by the two data sets,

including most of 1973–1987. The maps are illustrated here for the months of January and July and are meant to serve as a baseline for comparison with future sea ice distributions.

DATA SOURCES

The sea ice data used for this study are derived from radiometric data of two satellite passive-microwave instruments, the single-channel Electrically Scanning Microwave Radiometer (ESMR) on the Nimbus 5 satellite and the Scanning Multichannel Microwave Radiometer (SMMR) on the Nimbus 7 satellite. The ESMR was operational for most of the period 1973–1976, and the SMMR was operational from October 1978 through August 1987.

The Nimbus 5 ESMR recorded horizontally polarized radiation at a wavelength of 1.55 cm, a wavelength at which the emissivity of sea ice differs considerably from that of open water, thereby allowing the determination of approximate sea ice concentrations. The emissivity of ice at 1.55 cm varies with ice type but generally falls between 0.80 and 0.98, whereas the emissivity of open water is much lower, being approximately 0.44. In regions of predominantly one ice type, the algorithm used to derive sea ice concentrations from the ESMR data is based in large part on a simple linear interpolation between the 0.44 emissivity of open water and the appropriate emissivity for the single ice type. In the case of first-year ice, with an emissivity of approximately 0.92, these calculated ice concentrations are estimated to have an accuracy (versus the actual ice concentrations) of ±15% [Zwally et al., 1983]. In regions with mixtures of ice types, a similar algorithm is used but the contrast in emissivities between ice types hinders the unambiguous determination of ice concentration from the single-channel ESMR data, so that the estimated accuracy worsens to ±25% [Parkinson et al., 1987]. The worsened accuracy in these regions is not a major problem for the current study, because only the overall distributions of the ice are considered, not the specific concentrations within the ice pack. The reader is referred to Parkinson et al. [1987] for more details on the Arctic ESMR data and the associated calculations of sea ice concentrations. The ESMR transmitted good quality data for the north polar region for most of the four-year period from the launch of Nimbus 5 in December 1972 through the end of October 1976, allowing the calculation of monthly averages for each month from January 1973 through October 1976 except March, April, May, and August of 1973, and June, July, and August of 1975. The data have a spatial resolution of approximately 30 km.

The Nimbus 7 SMMR was a 10-channel instrument that recorded both vertically and horizontally polarized radiation at each of five wavelengths: 0.81, 1.4, 1.7, 2.8, and 4.6 cm. Because of the multichannel nature of the instrument, ice concentrations can be calculated from the SMMR data with less ambiguity than is inherent in the calculations from the single-channel ESMR data. Cavalieri et al. [1984] have taken advantage of the multichannel nature of the SMMR to calculate sea ice concentrations from a polarization ratio involving the two 1.7 cm channels and a gradient ratio involving the vertically polarized 0.81 cm and 1.7 cm channels. The resulting ice concentrations have a 60 km spatial resolution and are estimated, based on the variability of the observed brightness temperatures over one annual cycle, to have a precision of 5–9% [Cavalieri et al., 1984]. Cavalieri et al. [1984] do not estimate the accuracy of the derived ice concentrations, but later comparisons of the SMMR values with independently derived ice concentrations suggest that the 5–9% estimate for ice-concentration precision is a good estimate for ice-concentration accuracy as well [P. Gloersen, personal communication, 1991]. Although other sea ice algorithms have also been developed for the SMMR data, the SMMR sea ice concentrations used here are derived from the Cavalieri et al. (1984) algorithm. The SMMR data were collected on an every-other-day basis for most of the period from the launch of Nimbus 7 in October 1978 through late August 1987, and monthly averages are available for every month November 1978–August 1987. The SMMR data have been mapped to the 30 km grid of the ESMR data.

RESULTS

The ESMR and SMMR data have been used to generate monthly maps of the range of sea ice distributions existent in the north polar region over the period of the two data sets. In addition, more detailed monthly maps have been generated showing, for each 30 x 30 km grid element, the number of years with sea ice in the particular month. The two sets of maps are illustrated here for the winter month of January (Figures 1–2) and the summer month of July (Figures 3–4). The reader is referred to Parkinson [1991] for the full set of 12 monthly maps of the range of sea ice distributions and for the September and March maps of the number of years with ice. The latter two months are typically the months of ice extent minimum and maximum in the north polar region, with January and July being months generally still experiencing net ice-cover growth and decay, respectively.

[To assist in the proper interpretation of Figures 1–4, a few general comments will be made regarding, first, the defining threshold for ice concentrations used in generating the figures and, second, the spurious indications of ice around much of the land/sea boundary, for instance along the southern and western coasts of Europe. A threshold of 30% ice concentration was used in determining the sea ice distributions. This 30% threshold matches the ice concentration isopleth found, in a study of coincident SMMR and aircraft observations in the Greenland Sea, to be the SMMR-derived isopleth that best correlates with the ice edge position for diffuse ice edges [Campbell et al., 1987]. The 30% threshold also eliminates almost all atmospheric interference, making it a reasonable choice for defining the ice edge for Figures 1–4. The pervasive indication of ice along warm-water coasts (Figures 1–4) occurs in grid elements having both land and ocean within the relevant field of view of the satellite sensor. Such grid elements have brightness temperatures which combine high values for land with low values for ocean, resulting in intermediate values suggestive of fractional sea ice coverage. This land contamination of the data is a problem common to all passive-microwave data sets and necessitates added caution in the calculation and interpretation of ice extents. Basically, however, when a study concentrates on spatial images, as here, the land contamination problem can be more easily identified and ignored.]

The results for January and July are summarized in Figures 1–4. In January, the greatest interannual variability in the distribution of the ice occurs in the Sea of Okhotsk (Figure 1), where in some years the sea is almost completely ice covered and in other years ice exists only in the



Figure 1. Spatial variability in January monthly averaged sea ice distributions over the 13 Januarys of the ESMR/SMMR sea ice record (January 1973-76 and 1979-87). White signifies sea ice coverage with concentration ≥ 30% in each January of the ESMR and SMMR data sets; green signifies January sea ice coverage in some years but not others; and blue signifies no January sea ice (with concentration ≥ 30%) in any of the ESMR/SMMR years. *Note: Color reprints are available from the author.*

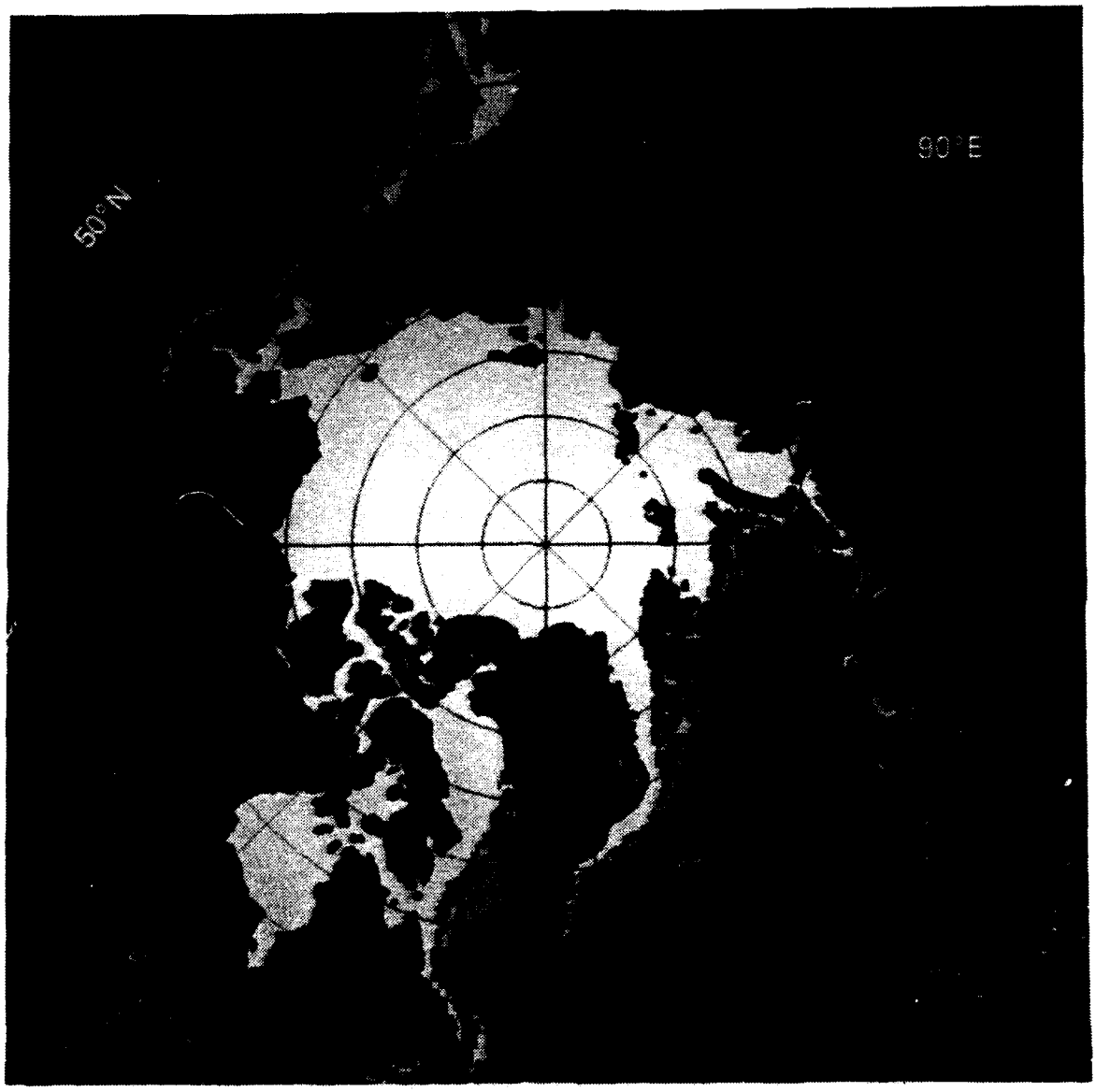


Figure 2. Frequency of January sea ice occurrence, on a monthly average basis, over the 13 Januarys of the ESMR/SMMR record.

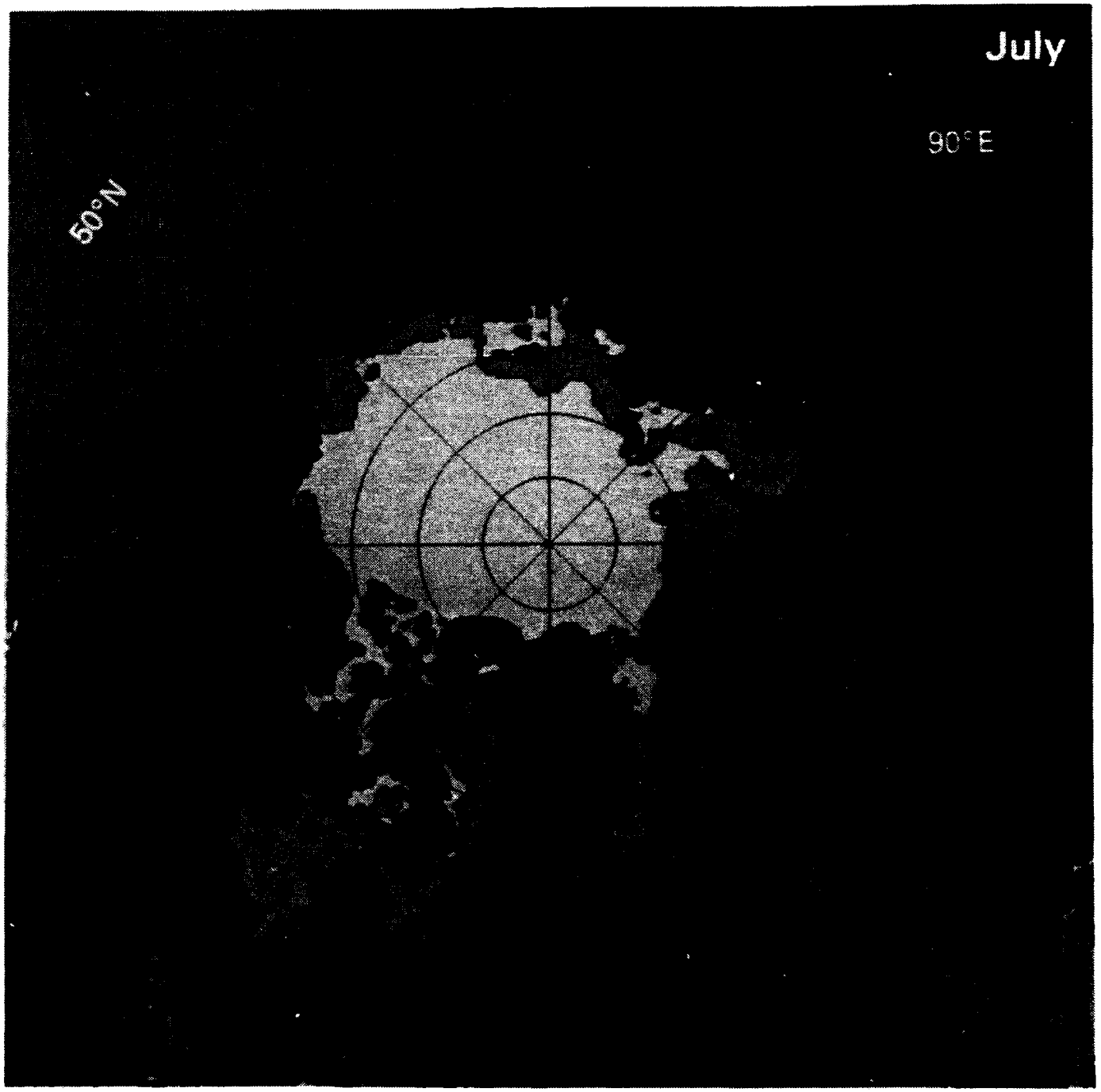


Figure 3. Same as Figure 1, but for the 12 Julys of the ESMR/SMMR record (July 1973-1974, 1976, and 1979-1987).

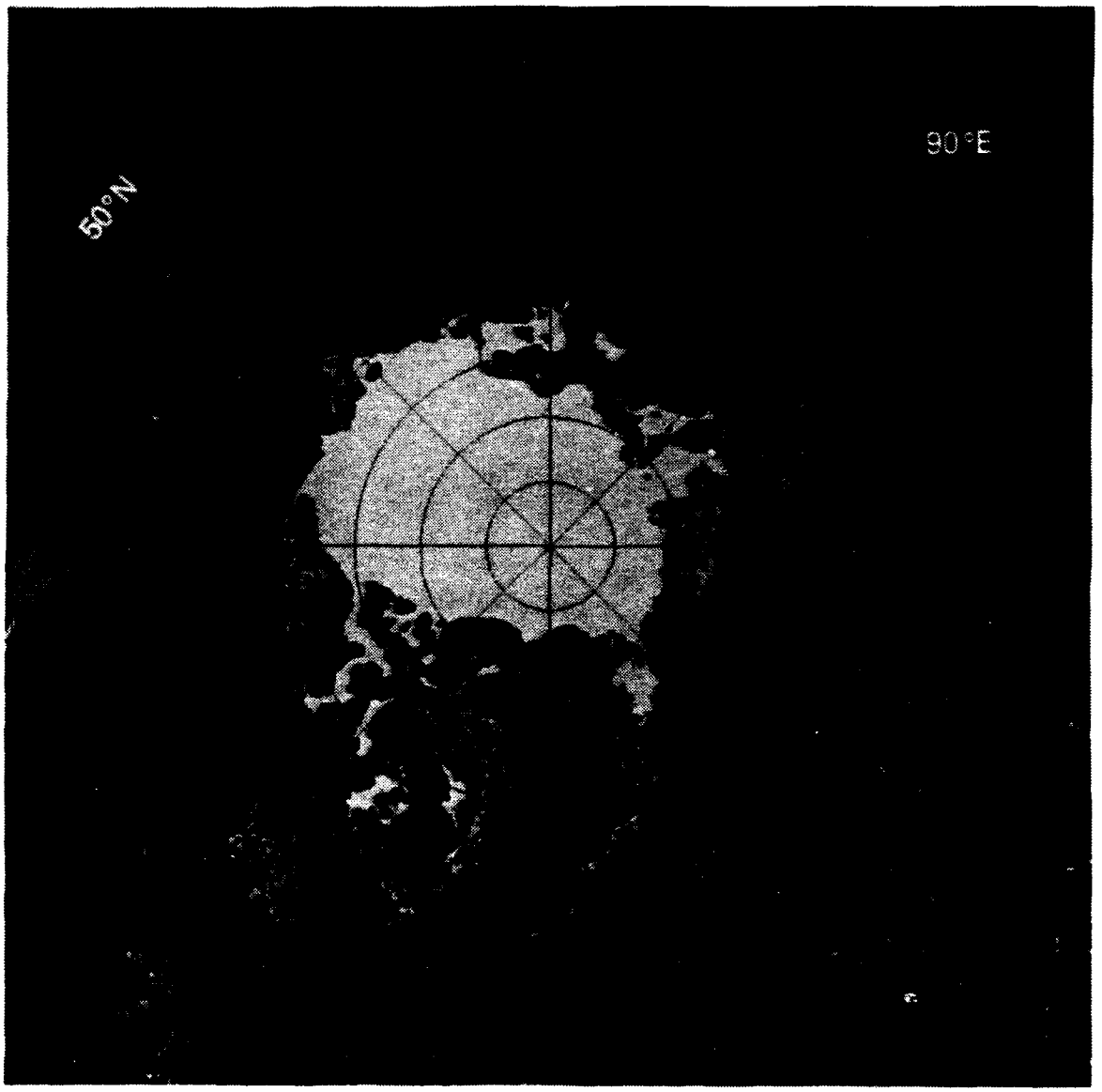


Figure 4. Frequency of July sea ice occurrence, on a monthly average basis, over the 12 Julys of the ESMR/SMMR record.

westernmost and northernmost portions. Examination of the sequence of Januarys [e.g., Parkinson and Cavalieri, 1989] shows that this variability results from large fluctuations in the ice cover from year to year and not from a consistent or even near-consistent trend toward either increasing or decreasing ice coverage over the ESMR/SMMR period. The high interannual variability suggests that the Sea of Okhotsk in January would be a particularly poor selection of place and time to seek evidence of future climate change, although indeed if the entire sea were to be free of ice in January, this might signify something significant.

The portions of the ice edge exhibiting the least interannual variability in January lie in the southern Greenland Sea (latitudes 59°–67°N) and immediately to the southwest of Svalbard (Figure 1). The consistency in these two locations contrasts not only with the high variability in the Sea of Okhotsk but also with the sizeable spatial variability existent along the entire remaining ocean-bound edge of the ice pack. However, within the ice pack there is also a great deal of consistency, ice existing in each ESMR/SMMR January throughout the Canadian Archipelago, Hudson Bay, northern Baffin Bay, the Kara Sea, and the entire Arctic Ocean with the exception of a small area just north of Svalbard (Figure 1). The appearance in future January averages of sizeable areas of open water in any of these latter regions would show a definite change from the ice coverage existent in the ESMR/SMMR years.

Taking the Sea of Okhotsk as an example, details provided in the January frequency map (Figure 2) include that in all years except one there was a large region of open water in the southeast portion of the sea and that the coastal polynyas indicated in Figure 1 in the northwest were rare, occurring in each instance in only one of the 13 January averages for the ESMR/SMMR years.

In July, spatial variability is high in Hudson Bay, Baffin Bay, the southern Kara Sea, and the northern Barents Sea (Figure 3). In fact, even though in some years much of Hudson Bay remains ice covered in July, in some years the bay is free of ice altogether, a point that is also true of the southern Kara Sea, the northern Barents Sea, and the northern and eastern portions of Baffin Bay. Nonetheless, there remain areas even in these seas and bays where consistency exists for each of the ESMR and SMMR Julys, and hence future changes from that consistency could signify important changes in the sea ice distributions. For instance, in northern Baffin Bay a sizeable open water region (actually an enlarged North Water polynya) existed in all 12 Julys, as did a wide band of open water along much of the west coast of Greenland (Figures 3 and 4). A failure of the band of open water to appear west of Greenland would signify colder conditions than usual, with a likely cause being a weakened West Greenland Current, as the warm north-flowing waters of the West Greenland Current are a major cause of the open water in this vicinity. In contrast, a completely open Kara Sea (extending northeast to Severnaya Zemlya) in future July monthly averages would signify warmer conditions than those existent during the ESMR/SMMR years. As an isolated occurrence, such an opening might reflect temporary shifts in currents or winds, but as part of a more general pattern of reduced ice extents it might be indicative of a widespread warming.

In the Arctic Ocean in July, many of the ESMR/SMMR years had a sizeable region of open water off the northern Canadian coast just east of Alaska, but the ice cover consistently continued to reach the north coast of Alaska itself (Figures 3 and 4). Ice also consistently remained south of the islands Severnaya Zemlya and Novosibirskiye Ostrova, in spite of occasional occurrences of open water to the east and west and, in the case of Novosibirskiye Ostrova, to the north as well, although indeed open water existed immediately to the east of Novosibirskiye Ostrova in only one year (Figure 4).

The January and July results highlighted here show comparable overall levels of monthly average ice distribution variability (as defined by the areal extent of green in Figures 1 and 3) to the levels found in each of the other months [Parkinson, 1991], although the annual cycle of variability varies significantly from region to region. For the Sea of Okhotsk, its January variability (Figure 1) exceeds its variability in any other month; and for Hudson Bay, its July variability (Figure 3) is exceeded only by its variability in November and greatly exceeds its variability in the remaining 10 months. In contrast, for the Canadian Archipelago and the Arctic Ocean, their January and July variabilities are well below their variabilities in September, the month of minimum ice coverage overall; and for the Bering Sea, its highest variability is in April, at the start of the ice-decay season [Parkinson, 1991].

CONCLUSIONS

The combination of high interannual variability in portions of the sea ice cover and the lack of a long-term global sea ice data base makes it difficult to place observed interannual changes in a climatological context. The ESMR/SMMR satellite passive-microwave record is still too short for the desired climatological data base, but the 13-year record is a major advance over what was available previously and it provides valuable information on interannual variability. Consequently, the ESMR and SMMR data have been used to map the interannual range in monthly sea ice distributions and the frequency of ice coverage, as illustrated in Figures 1–4 for January and July. These maps reveal spatial details on the interannual variability in the positioning of the sea ice edge, showing regional differences within a month and temporal differences between months. Future noticeable changes in regions exhibiting only slight variability, such as along the southeast coast of Greenland in January (Figure 1), could be more significant than comparable changes in regions showing great variability, such as the eastern Sea of Okhotsk in January (Figure 1). By allowing ready comparisons with January and July ice edge positionings at other times, the summary information provided in Figures 1–4 on the range and frequency of January and July ice edge positionings over the ESMR/SMMR years can assist in interpreting past and future changes in the ice cover and assessing whether those changes reflect normal interannual variability or are more likely due to climate change. Justification of claims of future climate change in sea ice distributions will be easier if there are sizeable areas in which the new distributions fall outside the range of distributions obtained during the ESMR and SMMR years.

Additional details on this study, and a full set of 12 monthly maps for the range of sea ice distributions over the years of the ESMR/SMMR record, can be found in Parkinson [1991]. Maps of sea ice concentrations for each month of the ESMR data set are available in Parkinson et al. [1987] and for each month of the SMMR data set will be available in Gloersen et al. [1991].

ACKNOWLEDGMENTS

The author very much appreciates the constructive comments of Norbert Untersteiner and an anonymous reviewer, plus the help of Jamila Saleh in the generation of the figures, and the funding support of the Oceanic Processes Branch at NASA Headquarters.

REFERENCES

Campbell, W. J., P. Gloersen, E. G. Josberger, O. M. Johannessen, P. S. Guest, N. Mognard, R. Shuchman, B. A. Burns, N. Lannelongue, and K. L. Davidson, Variations of mesoscale and large-scale sea ice morphology in the 1984 Marginal Ice Zone Experiment as observed by microwave remote sensing, *J. Geophys. Res.*, *92*, 6805-6824, 1987.

Cavalieri, D. J., P. Gloersen, and W. J. Campbell, Determination of sea ice parameters with the Nimbus 7 SMMR, *J. Geophys. Res.*, *89*, 5355-5369, 1984.

Gloersen, P., W. J. Campbell, D. J. Cavalieri, J. C. Comiso, C. L. Parkinson, and H. J. Zwally, *Arctic and Antarctic Sea Ice, 1978-1987: Satellite Passive-Microwave Observations and Analysis*, National Aeronautics and Space Administration, Washington, DC, 1991, In press.

Parkinson, C. L., Interannual variability of the spatial distribution of sea ice in the north polar region, *J. Geophys. Res.*, *96*, 4791-4801, 1991.

Parkinson, C. L., and D. J. Cavalieri, Arctic sea ice 1973-1987: Seasonal, regional, and interannual variability, *J. Geophys. Res.*, *94*, 14499-14523, 1989.

Parkinson, C. L., J. C. Comiso, H. J. Zwally, D. J. Cavalieri, P. Gloersen, and W. J. Campbell, *Arctic Sea Ice, 1973-1976: Satellite Passive-Microwave Observations*, NASA SP-489, National Aeronautics and Space Administration, Washington, DC, 296 pp., 1987.

Zwally, H. J., J. C. Comiso, C. L. Parkinson, W. J. Campbell, F. D. Carsey, and P. Gloersen, *Antarctic Sea Ice, 1973-1976: Satellite Passive-Microwave Observations*, NASA SP-459, National Aeronautics and Space Administration, Washington, DC, 206 pp., 1983.

Note: Color reprints are available from the author.

Contour Mapping of Arctic Basin Ice Roughness Parameters

A. S. McLaren
CIRES, University of Colorado, Boulder, Colorado, U.S.A.

R. H. Bourke
Department of Oceanography, Naval Postgraduate School, Monterey, California, U.S.A.

R. L. S. Weaver
CIRES, University of Colorado, Boulder, Colorado, U.S.A.

ABSTRACT

The U.S. Navy has recently developed an underwater acoustic propagation loss model suitable for use in ice-covered seas. The under-ice scattering component of this model requires a spatially varying input data base of ice roughness characteristics to support both empirically- and theoretically derived scattering loss algorithms. The empirical algorithms characterize the under-ice roughness by the standard deviation of the mean ice draft. The theoretical algorithms are based upon keel characteristics, namely the mean deep draft keel and the number of deep draft keels per unit distance.

We have attempted to construct a data base of these parameters for the Arctic Ocean based upon analysis of under-ice thickness distribution data acquired from inverted echo-sounder data from submarines transmitting under the ice. From the voyages of 13 submarines, which traversed virtually all regions of the Arctic Ocean during all seasons, a suite of ice thickness statistics have been calculated for 50-km segments along each submarine track. Contour maps of the roughness parameters were constructed. Not surprisingly they show that the roughest ice and the greatest number of deep draft ice keels are found off the north coasts of the Canadian Archipelago and Greenland due to ice convergence on these land barriers. A linear regression demonstrates that the ice roughness, characterized by the standard deviation, increases with increasing ice thickness at a rate of about 0.5.

Similar maps based on further analysis of all submarine-collected under-ice thickness distribution data on a year by year basis could be invaluable in the determination and monitoring of geographically specific and basin-wide sea ice changes. Such maps could be of considerable significance in the determination of the role of the polar regions in global change.

92-17952



AD-P007 270



Generation of Sea Ice Geophysical Flux Estimates Utilizing a Multisensor Data Processor in Preparation for the RADARSAT and EOS Eras

Benjamin Holt, Ron Kwok, Frank Carsey, and John Curlander
Jet Propulsion Laboratory, California Institute of Technology, Pasadena, California, U.S.A.

ABSTRACT

A geophysical processor for deriving sea ice type and ice motion information from sequential SAR image data has been designed and is in implementation phase for use with ERS-1 SAR data at the Alaska SAR Facility (ASF). This SAR ice data processor, called the ASF Geophysical Processing System, or ASF-GPS, will be in place for launch in May 1991. Descriptions of the salient aspects of ASF-GPS and its current status are presented.

The next step in the evolution of processors for geophysical descriptions of sea ice is now in design phase; it involves the utilization of data from other sensors and sources and the generation of higher-level products. The augmented data are environmental, e.g., weather agency analyses, satellite-derived surface temperatures and drifting buoy data. These data serve to (1) improve the performance of the basic data product generation, the ice type and motion data sets, by increasing accuracy and shortening processing time, and (2) extend the level of the data products by computation of key geophysical fluxes. Geophysical quantities required from the sea ice processor include the surface heat, momentum, brine and freshwater fluxes, radiation balance, snow cover, melt pond cover and thermodynamic state. The estimation of two of these fluxes, brine and freshwater, is discussed, and the requirements for suitable environmental data are also presented.

Finally, the system design of the ASF-GPS and the follow-on processor, designed initially to utilize SAR data from RADARSAT with weather and other inputs, e.g., AVHRR, and, after upgrade, from the suite of EOS instruments, will be presented. As now envisioned this system will have layered architecture with major branches in data management, user interface and science data analysis and will serve as a prototype design for a wide range of applications.

INTRODUCTION

Imagery from SAR systems has been applied extensively to studies of sea ice in the polar oceans due to its fine resolution and all-weather capability. These studies have focused primarily on deriving meaningful ice types from the backscatter characteristics displayed in the imagery and obtaining fields of ice motion from comparison of pairs of radar imagery. Essentially, SAR imagery can produce accurate maps of ice type and motion, with the reliability of the ice type maps being dependent primarily on radar frequency and surface wetness conditions. The series of upcoming satellites carrying SAR instrumentation that will be flown in this decade (Table 1) will significantly increase the quantities of radar data that will be available over the polar regions. To take advantage of these satellite opportunities, the Alaska SAR Facility was developed to receive, process, and archive the SAR imagery from these sensors. From this, the possibility arose for obtaining high resolution maps of global ice type and motion on a routine basis over long time periods; these maps could then be used to examine the air–ice–ocean interaction and fluxes of heat, salt and freshwater.

	ERS-1,2	JERS-1	RADARSAT	EOS SAR	ESA Polar Platform
SAR					
Frequency	C-band	L-band	C-band	X-, C-, L-band	C-band
Polarization	VV	HH	HH	X/C dual, L-quad	VV
Swath	100 km	75 km	50-500 km	50-400 km	100 km
Resolution	25 m	18 m	10-100 m	15-100 m	25 m
Incidence angle	23°	35°	20-50°	20-60°	23° + -40°
Orientation	right	right	right, some left	right, some left	right
Data storage	none	20 minutes	20 minutes	none, TDRSS	TBD
ORBIT					
Inclination	97.5°	98.5°	98.5°	98.5°	TBD
Altitude	785 km	568 km	790 km	623 km	TBD
Repeat	3, 35 days	41 days	24 days	16 days, some 5	TBD
MISSION					
Launch	ERS-1: May/1991 ERS-2: 1994	Feb./1992	1995	1999	TBD
Lifetime	3 years	2 years	5 years	15 years	TBD
Status	approved	approved	approved	proposed	proposed
Agency	ESA	NASDA	CSA	NASA	ESA
OTHER INSTRUMENTS	Radar Altimeter Wind/Wave Scatterometer mode Along-Track Scanning Radiometer	Visible and Infrared Radiometer	none	none	many, TBD

Table 1. Planned spaceborne SAR missions: mission descriptions.

This interest prompted the development and implementation of operational algorithms that could produce these sea ice products on an automated basis, thereby generating higher order products as well as effectively dealing with the large volumes of data that are anticipated.

The first three upcoming satellites, ERS-1, JERS-1, and RADARSAT, are single frequency, single polarization systems that will provide increasing global coverage access and data rates throughout this decade, beginning with the launch of ERS-1 in 1991 (Table 1). ASF will process the SAR imagery into both full resolution (about 25 m for all systems) and reduced resolution imagery (about 200 m). The scene size is about 100 x 100 km for ERS-1 and JERS-1 but will be between 100 and 500 km^2 for RADARSAT. ASF will also have the capability of processing the imagery into geocoded map reference frames. All processed data will be archived in the Archive and Operations System (AOS). Following these programs, the planned EOS SAR will provide a multiple-frequency polarimetric system with global access.

The Geophysical Processor System (GPS) is an ASF subsystem that is being implemented to produce ice and ocean geophysical products from the SAR imagery [Holt et al., 1990a]. It is a SUN-4 workstation with a high speed array processor and supporting peripherals. The GPS will have the capability to generate maps of ice motion, concentration, and type on a daily and automatic basis (Figure 1). For the ice products, geocoded reduced resolution (200 m) imagery will be utilized. The function of the GPS has been extended to include the routine processing of ocean wave products from the full resolution (25 m) SAR imagery. The completed geophysical products will be placed into the ASF database and be available for distribution. At present the GPS algorithms are designed for the SAR system characteristics of ERS-1 and will be subsequently upgraded to incorporate the other satellites' varying sensor characteristics. Each algorithm will now be discussed separately.

ICE MOTION TRACKING ALGORITHM

The design of the ice motion algorithm at ASF has been discussed in detail by Kwok et al. [1990] and the functional block diagram is shown in Figure 2. The ice motion algorithm derives ice motion vectors from a comparison of two overlapping scenes that are separated in time. As mentioned, the algorithm utilizes SAR image data (100 km by 100 km in size) which have been processed to a reduced resolution of 200 m (100-m pixel size) and then geocoded. The geocoding process provides an accurate earth location (with an uncertainty of 100 m) that is critical for the measurement of absolute ice motion and deformation. The reference map grid to be used for the GPS data is the grid selected for SSM/I, a DMSP passive microwave radiometer system, which is a polar stereographic projection with the secant plane at 70°N/S, designed to minimize distortion of the marginal ice zones.

The algorithm first finds the image pair to be analyzed for ice motion by selecting a reference image that is located within an ice-covered region and has been recently processed. The database is searched to locate a candidate matching image for the reference image using a motion predictor model based on the geostrophic wind and previously derived ice motion information. The candidate image pair

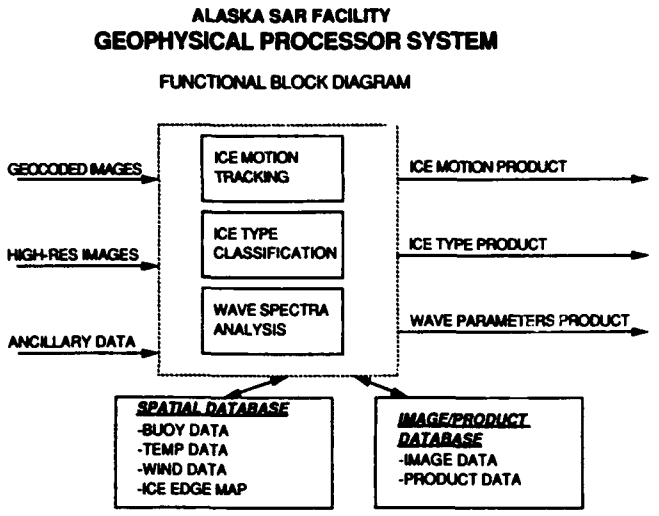


Figure 1. Block diagram of the GPS showing the input data products and ancillary data used by the three algorithms to generate the basic geophysical output products.

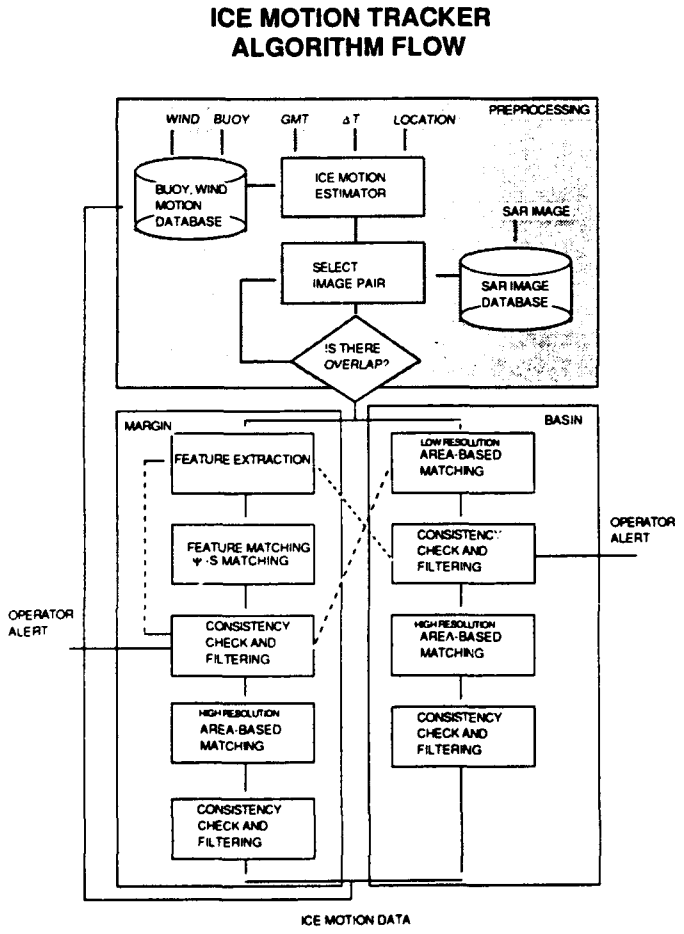


Figure 2. Block diagram showing the flow of the combined feature-based and area-based GPS ice motion tracking algorithm. From Kwok et al [1990].

must have at least 50% overlap and have been obtained within an appropriate time window, which is generally optimum at 3–6 days. Next the algorithm determines whether the image pair is located within the central pack or in the marginal ice zone. Following this, the algorithm performs several levels of feature matching to locate common ice features within the two images. For basin imagery, detailed matching is performed using area cross-correlation techniques which can also consider relatively small floe rotations. The basin output is generally a uniformly distributed motion field. For image pairs at the ice margin, edge detection techniques are used for finding common features which may have significantly translated and rotated. This procedure combines an unsupervised segmentation, to locate the principal textural feature regions of the image pairs, and feature matching, where the features turn out to be the edges of open leads and ice floes. This procedure is followed by area cross correlation which fills in the nonuniformly distributed feature matches to a uniformly spaced grid as much as possible. At each level, the output vectors are run through consistency filters to remove spurious outlying vectors. The vectors are interpolated onto the SSM/I grid with 5-km spacing and output as fields of ice motion vectors which are available as ASCII files and graphic plots on the AOS. The accuracy of the algorithm is between 100–300 m based on detailed manual comparisons. The GPS will be able to generate at least 10 ice motion vector maps per day. The development work for this algorithm has been done almost exclusively with imagery acquired by the Seasat SAR (L-band) in 1978 over the Beaufort Sea and an example is shown in Figure 3.

ICE CLASSIFICATION ALGORITHM

The GPS ice classification algorithm was recently discussed by Holt et al. [1989, 1990b]. The development work on the ice classification algorithm has been done using SAR imagery principally acquired by the JPL AIRSAR system during flights over the Beaufort, Chukchi, and Bering Seas in March, 1988 [Cavalieri et al., 1991]. It has been verified with this data and other similar imagery from different regions that there is a high contrast in radar backscatter at C-band between multi-year and first-year ice types. This high contrast can be effectively used to separate these major ice types by relatively straightforward and efficient approaches.

The ice type algorithm flow chart is shown in Figure 4. The algorithm will begin by the GPS querying the archive for recently acquired imagery over ice-covered regions. This is done in parallel with the ice motion algorithm image search. The daily catalog of images is transferred to the GPS which then goes through a search procedure to identify pairs of imagery suitable for both ice classification and motion analysis. As mentioned previously, the ice classification algorithm utilizes reduced resolution imagery (200 m) with 100 x 100 m sized pixels. The algorithm is seasonally dependent which reflects the changing character of the ice surface conditions. The winter ice conditions are presently better understood than the more complicated transition seasons and therefore the algorithm is expected to be most accurate from about November to May in the Arctic. The summer seasons are more problematic since radar scattering from ice is so dependent on the presence of water in the snow cover and the ice. It is expected that this limitation

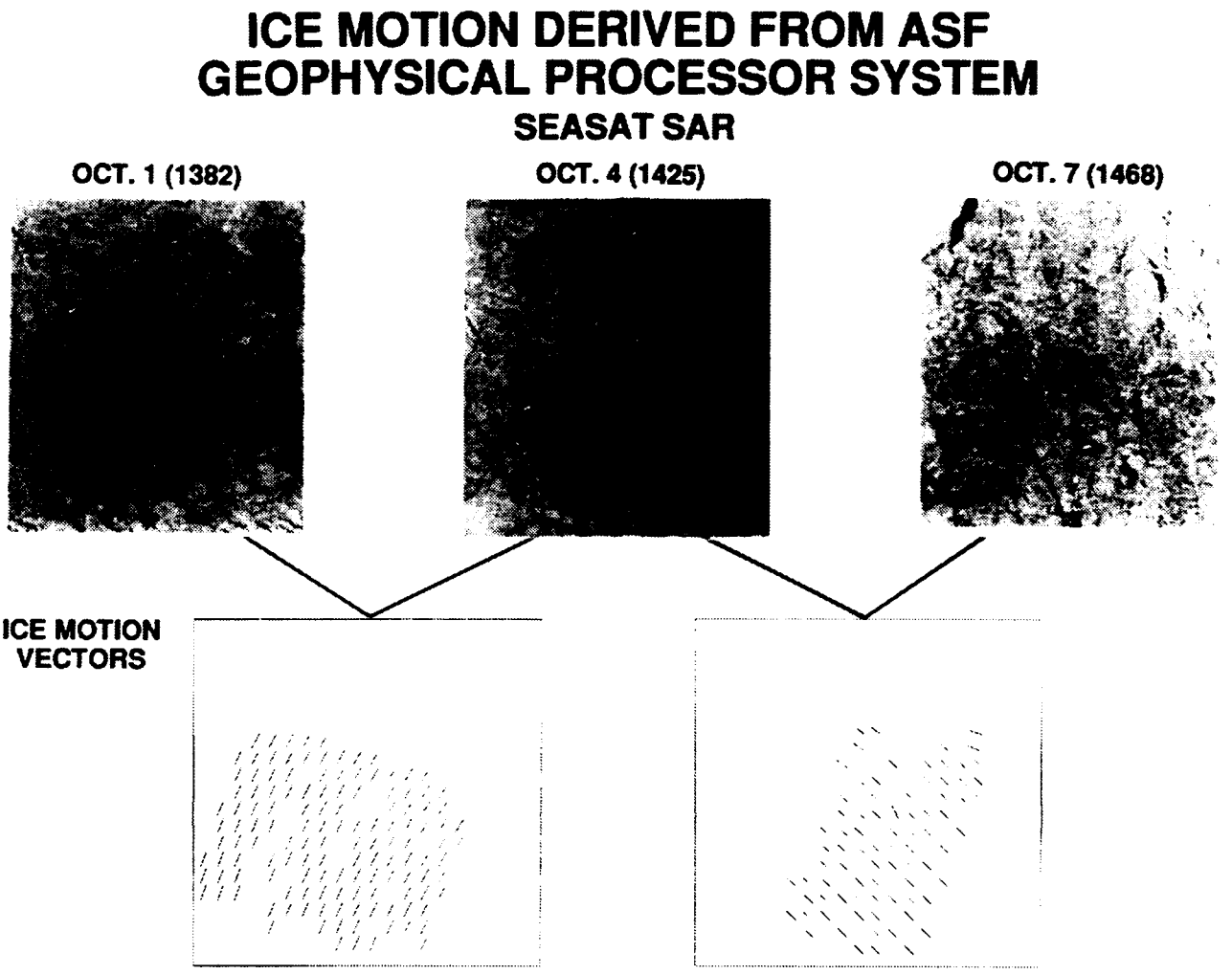


Figure 3. Ice motion vector maps derived by the GPS ice motion algorithm from three sequential images of the same ice field obtained by the Seasat SAR over the Beaufort Sea in 1978. Note the change in the vector direction in the two motion maps.

will be improved by the incorporation of additional radar look-up tables by season and region.

The next step locates the image corners on the SSM/I grid. Following this, the algorithm masks out any land coverage in the image based on a comparison with a digitized land boundary map. This comparison also determines the proximity of the image to the ice edge, which is obtained from weekly ice edge maps produced at the Joint Ice Center, and keys the algorithm to the major ice zones, e.g., if the image lies in the Bering Sea or within the permanent ice pack, for example.

The next key step is the proper selection of the radar look-up table which lists the radar backscatter of several major ice types as a function of incidence angle and season. The selection will be based on regional location, and air temperature and perhaps surface winds from meteorological analysis such as from the National Weather Service. The look-up tables have been compiled by R. Onstott based on surface scatterometer measurements. Each satellite will have separate tables based on frequency and polarization.

The algorithm then utilizes a clustering routine to separate the dominant feature classes into 4–5 major clusters. This is an unsupervised segmentation and requires as input the expected number of classes and the separation in backscatter between these classes. The clusters are then compared to the selected look-up table and are assigned ice classes based on the brightness level and the actual separation. The clustering algorithm is sensitive to the quality or sharpness of the brightest cluster which requires good absolute calibration and radiometric compensation. The accuracy of the classification is sensitive to the separation in backscatter between classes, including multi-year to first-year and thin first-year to grey and young ice. The thin ice classes, which have low radar returns at C-band, are particularly sensitive for the following reason: the ERS-1 SAR data is being designed to have a noise equivalent $\sigma 0$ of -18

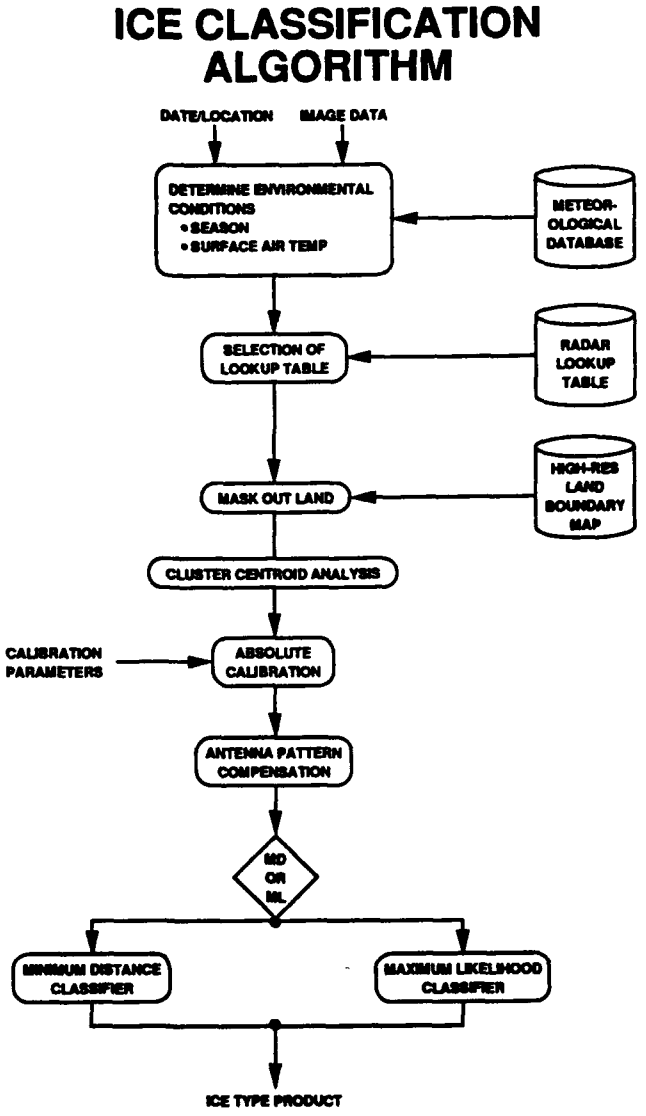


Figure 4. Block diagram showing the flow and program design of the GPS ice classification algorithm.

dB which suggests that ice surfaces with a radar return near this level (such as thin ice) will be approaching the system noise level. Absolute calibration of about ±2.5 dB is required to enable confident separation of ice types. Radiometric compensation is also necessary to remove any non-uniform antenna pattern corrections in order to produce a constant brightness level for multi-year ice across the relatively narrow range of incidence angles in the ERS-1 data (23° ± 3°). However, compensation is not done if there is no multi-year ice in the image and if the variation in the multi-year ice return across the image in range is less than the natural variation. There are many adjustments possible at this step and this will be a key area of examination during the initial months of operation.

The final step in the algorithm is the production of output products. Two products will be available and stored in the archive. The first will be an ice type map of 5-km bins gridded in the SSM/I projection. For each bin, the percentage of each ice type will be listed. This product will be browsable as a contoured graphic file and available for distribution as an ASCII file. The second product will be a map indicating the ice type for each pixel. This will also be browsable in a modified form and available for distribution as an ASCII file. Each file will also include the air temperature and wind speed at the time of image acquisition as derived from the meteorological analyses. The GPS will be capable of generating classification products from 20 images on a daily basis. The accuracy of the classification algorithm is expected to be 5–10% depending on the absolute calibration. Of course, this will be further examined during post-launch validation.

The next two sections discuss briefly an approach for estimating brine and freshwater fluxes in the polar oceans and how the determination of these fluxes would be accomplished through an evolution in the GPS capabilities, involving the use of other sensor data and models to generate the higher-level products. The additional data would serve not only to extend the present capabilities of the GPS but also to improve its current performance by increasing accuracy. The design of the follow-on processor is also discussed.

ALGORITHMS FOR ESTIMATION OF BRINE AND FRESHWATER FLUXES

The sea ice cover effectively insulates the ocean from the atmosphere by altering the surface heat exchange. Heat losses from the ocean to the atmosphere and absorption of solar radiation to the upper ocean are reduced by the presence of the ice cover. These exchanges are then affected by the thickness and movement of the ice. In certain areas, the rejection of salt from growing ice produces dense waters which sink, thus promoting convective overturning of the upper ocean layer and the formation of the ocean's deep water [Aagaard and Carmack, 1989]. The movement toward the equator and subsequent melting of ice adds to the upper ocean fresh, cold water, which acts to stop convection in the upper ocean. The use of SAR in combination with passive microwave instruments such as SSM/I to measure these fluxes appears feasible and approaches to determining brine and freshwater fluxes have been recently outlined [Carsey, 1991].

For determining brine flux, the key ice observations that are needed include mapping of thin ice and tracking its growth and deformation. Thin ice is detectable with a single channel SAR but its backscatter may be confused with calm water and variations in thin ice form, for example. Current research indicates that polarimetric SAR systems may provide more accurate determination of this ice type [Drinkwater et al., 1991]. However, the passive microwave brightness temperatures show a continuous increase as thin ice grows to about 0.5 m in thickness, albeit at a coarser resolution [Grenfell, 1986; Steffen and Maslanik, 1988]. To make use of the brightness temperature record, the ice must be tracked so the brightness changes can be monitored and the ice must be carefully monitored to account for open water production. This is done using SAR motion data. The interpretation of the brightness record in terms of ice growth is complicated by variable snow cover and growth rates, and deformation of the ice cover. Deformation thickens the ice cover in a way that is not related to ice growth and increases the brightness temperature. Deformation is obtainable from the high resolution SAR motion data, where the opening and closing of leads can be monitored. From the combination of

the SAR and brightness temperature records, the determination of heat and brine flux based on new ice thickness distributions is possible.

For estimating freshwater flux, it is necessary to know the thickness of the ice and to determine its rate of decay. Ice thickness can be reliably measured by upward-looking sonar, for example, but cannot be measured by remote sensing instruments. Ice type determination from these instruments serves as a proxy measurement of thickness. In the case of freshwater flux, the thicker ice types are most important and these can be readily separated by both SAR and passive microwave data, especially during the winter. The increase in liquid free water in snow and ice due to warming complicates the signals for both instruments but if used together, the condition of the melting ice cover may be adequately determined throughout the melt season [Onstott et al., 1987]. Ice melt is evaluated through the warm season by examining extended time series of both SAR and passive microwave.

Development of these algorithms will require several stages for refining models for ice thickness, incorporating field campaign data for validation for ice properties and state, and expanding from local single-scene analysis to large, synoptic-scale time series analysis. ERS-1 and JERS-1 SAR imagery will be quite suitable for initial development and test efforts, which should enable a more formalized and complete algorithm to be in place for data from RADARSAT. From the extended time series from RADARSAT and EOS SAR, it will be possibly to assess long-term climatic changes in these fluxes.

To generate these and other flux estimates, several steps must be taken within the GPS environment. The GPS at present is configured to generate sea ice products from ERS-1 and JERS-1. The limited amount of SAR data from these two systems will provide adequate coverage for developing the flux algorithms. The wide swath and onboard storage capabilities of RADARSAT and later EOS SAR will provide the rapid and complete coverage of the polar regions that is needed to produce suitable time series that will enable continuous flux determinations to be made in the key dynamic areas such as the Greenland–Iceland–Norwegian Seas and the Weddell Sea. The GPS will require increased geophysical processing capabilities and more efficient algorithms to handle the more extensive RADARSAT data as well as efficient transfer of the data from the main SAR processor into the GPS.

Key environmental and ancillary data that are needed include weather analyses for air temperature and wind speed and direction, and drifting ice buoy motion. The temperature data are needed especially for monitoring seasonal changes in the ice cover due to the onset of melt and freeze-up. The wind and buoy motion data are valuable for estimating the movement of the ice pack, which is important for locating potential SAR motion image pairs and thereby increasing algorithm speed, and for determining deformation within leads and thin ice condition and state of growth. In addition to being important for the flux estimates, these data will also increase the accuracy of the current motion and classification algorithms. Such data are available through satellite communication systems such as UNIDATA on a routine basis and will form a permanent archive in the GPS.

A critical component of the flux algorithm will be the incorporation of multiple sensor data and weather analyses. These include especially the brightness temperature records from passive microwave sensors such as SSM/I and later EOS instruments. Also, AVHRR data will be important for providing sea/ice surface temperatures as well as ice extent and possibly motion as clouds permit. Within the GPS, these data will be analyzed together with the ice motion and classification products to generate ice growth and brine flux estimates. In the EOS era, data from multiple sensors will be routinely available as data streams through communication network systems.

The follow-on GPS will have a layered architecture that includes data management, user interface, and science data analysis techniques (Figure 5). Many of these functions are generic and can be applied to geophysical processing for other scientific disciplines utilizing SAR imagery with requirements for ancillary and multiple sensor data, so the basic design serves then as a prototype for additional processors.

SUMMARY

By combining geophysical sea ice algorithms currently in place in the ASF GPS with multiple sensor and environmental data and models, it will be possible to compute heat fluxes which are critical to examining air–sea–ice interaction and ocean circulation for effects of climate change. These algorithms will make use of future SAR systems, including RADARSAT and EOS SAR, with wide swath mapping capabilities, which are scheduled to be launched in the second half of this decade. A design for a follow-on GPS system which incorporates these new algorithms will serve as a prototype for other scientific disciplines.

ACKNOWLEDGMENTS

The authors would like to acknowledge the significant contributions to this work by Ross McConnell, Shirley Pang, Eric Rignot and Mark Drinkwater. This work was performed at the Jet Propulsion Laboratory, California Institute of Technology, under contract with the National Aeronautics and Space Administration.

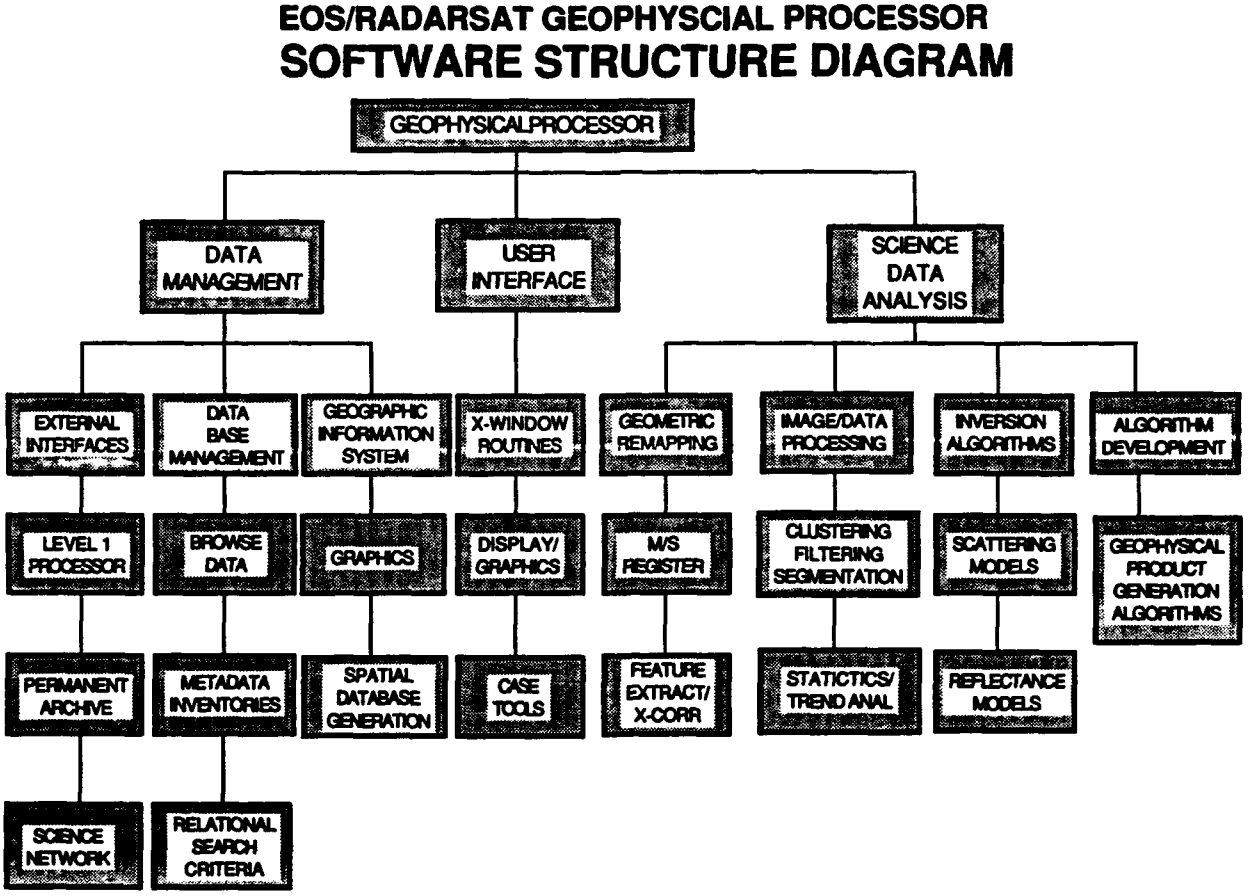


Figure 5. Software structure diagram of a prototype enhanced GPS that is suitable for many scientific disciplines, including polar oceans flux estimates.

REFERENCES

Aagaard, K., and E. Carmack, The role of sea ice and other fresh water in the Arctic circulation, *J. Geophys. Res.*, *94*, 14485–14498, 1989.

Carsey, F. D., An approach to brine and freshwater fluxes interpreted from radar and microwave radiometer data, in *Deep Convection and Deep Water Formation*, edited by J.-C. Gascard, Elsevier, 1991, In press.

Cavalieri, D. J., J. P. Crawford, M. R. Drinkwater, D. T. Eppler, L. D. Farmer, R. R. Jentz, and C. C. Wackerman, Aircraft active and passive microwave validation of sea ice concentration from the DMSP SSM/I, *J. Geophys. Res.*, 1991, submitted.

Drinkwater, M. R., R. Kwok, D. P. Winebrenner, and E. Rignot, Multi-frequency polarimetric SAR observations of sea ice, *J. Geophys. Res.*, 1991, submitted.

Grenfell, T., Surface-based passive microwave observations of sea ice in the Bering and Greenland Seas, *IEEE Trans. Geosci. and Remote Sens.*, *3*, 378–382, 1986.

Holt, B., R. Kwok, and E. Rignot, Ice classification algorithm development and verification for the Alaska SAR Facility using aircraft imagery, *Proceedings of IGARSS'89*, pp. 751–754, Vancouver, 1989.

Holt, B., R. Kwok, F. Carsey, and J. Curlander, An overview of the geophysical sea ice products generated at the Alaska SAR Facility, *Proceedings of the Second International Conference of Ice Technology*, edited by T. K. S Murthy et al., pp. 333–344, Cambridge, Computational Mechanics, 1990a.

Holt, B., R. Kwok, and E. Rignot, Status of the Ice Classification Algorithm in the Alaska SAR Facility Geophysical Processor System, *Proceedings of IGARSS'90*, pp. 2221–2224, University of Maryland, 1990b.

Kwok, R., J. C. Curlander, R. McConnell, and S. Pang, An Ice-Motion Tracking System at the Alaska SAR Facility, *IEEE J. Oceanic Eng.*, 15, 44–54, 1990.

Onstott, R. G., T. C. Grenfell, C. Matzler, C. A. Luther, and E. A. Svendsen, Evolution of microwave sea ice signatures during early summer and midsummer in the marginal ice zone, *J. Geophys. Res.*, *92*, 6825–6835, 1987.

Steffen, K., and J. Maslanik, Comparison of Nimbus 7 Scanning Multichannel Microwave Radiometer radiance and derived sea ice concentrations with Landsat imagery for the North Water area of Baffin Bay, *J. Geophys. Res.*, *93*, 10769–10781, 1988.

A Review of the Antarctic Region Ice Phenomena Based on Satellite Images

L. Hus
Department of Remote Sensing and Marine Cartography, University of Szczecin, Szczecin, Poland

ABSTRACT

Some results of the analysis of sea ice dynamical phenomena observed in Antarctic satellite images are presented. The images were received from the METEOR satellite, an APT system at the Polar Station on King George Island. Many ice features observed and analyzed in the satellite images had been observed and described in real time. Sea ice morphology, and sea ice as an indicator of hydrodynamical phenomena in the ice–ocean–atmosphere system, were studied.

The analysis included both sea–atmosphere interactions, and the influence of ocean conditions (currents, tides, bottom topography) on the creation, distribution and movement of pack ice fields. Results of the investigations show that the Antarctic region is characterized by a high spatial and temporal variability of sea ice extent and arrangement, particularly in the marginal ice zone.

Recent Changes in the Coastal Regions of Antarctica Documented by Landsat Images

J. G. Ferrigno and R. S. Williams, Jr.
U.S. Geological Survey, Reston, Virginia, U.S.A.

B. K. Lucchitta
U.S. Geological Survey, Flagstaff, Arizona, U.S.A.

B. F. Molnia
U.S. Geological Survey, Reston, Virginia, U.S.A.

ABSTRACT

In 1987, a consortium of SCAR (Scientific Committee on Antarctic Research) nations initiated a project to acquire a complete set of Landsat data on the coastal regions of Antarctica to document the present areal extent of ice shelves and outlet glaciers and to monitor any changes that have occurred in this dynamic area. So far, good-quality, cloud-free images have been acquired of approximately 60 percent of the coastal area. The new image data can be compared with (1) historical maps and aerial photographs; (2) the earlier set of Landsat images acquired of Antarctica during the 1970s; and (3) recently acquired data, to determine changes that have occurred during the past few years, the past several decades, or longer, depending on the accuracy and availability of comparative information.

Comparison of the recently acquired images with earlier data has shown substantial changes in the ice volume of several coastal areas. In 1986, more than 11,225 km^2 of the Larsen Ice Shelf and 11,500 km^2 of the Filchner Ice Shelf calved into the Weddell Sea. During the same year, about 1600 km^2 of the glacier ice in the Thwaites Iceberg Tongue and the Thwaites Glacier Tongue broke away. In 1987, a large tabular iceberg, estimated to be more than 4000 km^2, calved from the eastern side of the Ross Ice Shelf. Between 1973 and 1988, 600 km^2 of the Shirase Glacier Tongue calved. Imagery acquired in 1989 shows a continuing reduction of the Wordie Ice Shelf, parts of the Larsen Ice Shelf and several other areas around the continent.

The dynamic Antarctic ice sheet is the major glacier component, about 91 percent, of the Earth's cryosphere. It is reasonable to expect considerable cyclic fluctuation in the coastal regions. However, the recent apparent large-scale retreat or recession in several areas makes it important to continue to monitor and evaluate the changes to determine if they are random, cyclic, or whether they are a signal of global climatic change.

One Glacier's Retreat, a Global Warming does not Make: An Argument for Systematic Monitoring of North American Glaciers

Bruce F. Molnia
U.S. Geological Survey, Reston, Virginia, U.S.A.

ABSTRACT

One predicted response of the Earth to global change is a warming in the northern latitudes, with an increase in the rate of glacier melting and retreat. Since 1986, the terminus of Mendenhall Glacier, a 15-kilometer-long valley glacier near Juneau, Alaska, has been retreating rapidly, at a rate more than ten times greater than its rate during the past few decades. At first glance, some might attribute this rapid retreat to global warming. In reality, the changes at Mendenhall Glacier have little or nothing to do with climatic warming or global change. Rather, ironically, they are the result of an unusual sequence of events, triggered by a small advance of the glacier.

In 1984-85, a minor advance of Mendenhall Glacier dammed Nugget Creek, whose waters then overflowed on to the glacier and created a supra-glacial lake. Located a few hundred meters from the terminus, the lake expanded by ablation and iceberg production. During the summer of 1988, the expanding lake breached the remaining ice of the glacier terminus and merged with Mendenhall Lake. Today, the glacier's terminus has a high rate of iceberg production that contributes to the continuing rapid retreat of the glacier.

In this instance, we were able to closely monitor the sequence of events and the changes at the glacier's terminus, and so determine that the Mendenhall Glacier responded to a sequence of non-climatic events. If we had only a pre-1985 observation and then were to see the Mendenhall Glacier in 1990, our interpretation of the events and changes at the Mendenhall terminus might have been far different, and incorrect. Unfortunately, with most other glaciers, there may be many years between observations.

Glaciers may be sensitive indicators of global change, but we must be very cautious about attributing all future changes in glaciers to global change or climate warming. As the Mendenhall Glacier illustrates, we must refrain from jumping to convenient conclusions. Rather, we need to rely on frequent, systematic observation and monitoring to determine the impacts of human-induced and natural processes on glacier systems.

AD-P007 271

92-17953

Evaluation of Dynamics of Polar Regions Landscapes on The Basis of Remote Sensing Information

L. S. Garagula and V. E. Roujansky
Department of Geocryology, Faculty of Geology, Moscow State University, Moscow, U.S.S.R.

Abstract

The appearance of landscapes in polar regions is caused by the development of cryogenic geomorphic processes in the past and at the present time. This work presents an example of the interpretation of cryogenic processes and phenomena revealed in certain neotectonic, geomorphic, and geocryological conditions in the Tazovsky peninsula in the U.S.S.R.

On the basis of aerial photographs and space images, interpretation of cryogenic processes and phenomena was determined. Three types of dynamic series were defined: asynchronous (evolutional), synchronous, and mixed type. Tracing these series in nature using remotely sensed data has been carried out by identifying the cryogenic phenomena on high resolution photographs and revealing their role in the formation of landscape morphosculpture. Several peculiarities were revealed in using different types of series for geocryological forecasting. Investigations show that forecasting evaluations of landscape condition dynamics are reliable when complex approaches are used.

INTRODUCTION AND OBJECTIVE

Polar landscapes represent a dynamic series of cryogenic processes and phenomena [Veisman, 1978; Grechishev et al., 1984]. These series are due to the paragenesis of geological processes or to the stages of their development. Besides, a cyclic character or process is observed in the development of polar landscapes, which may be explained by rhythmic climate fluctuations, different tectonic movements, and the inner logic of the process development associated with causal relationships. The objective of the research presented herein is to present an example of the interpretation of cryogenic processes and phenomena revealed in certain neotectonic, geomorphic, and geocryological conditions in the Tazovsky peninsula in the U.S.S.R.

According to the manifestation of processes in relief features and geological phenomena, it is possible to determine important features in landscape development both in retrospective and in perspective aspects. So far as remotely sensed data allow one to define geological phenomena in different aspects, as a result of single or several processes, it is obvious that these data may be interpreted from the point of view of both natural and technogenic landscape dynamics.

Such an approach has been realized in the research work of the Department of Geocryology, Moscow State University. For example, on the basis of aerial photographs and space images, interpretation sets of cryogenic processes and phenomena were revealed in certain neotectonic, geomorphic and geocryological conditions in the Tazovsky peninsula. These sets form different paragenetic dynamic series of cryogenic processes and phenomena. Three types of dynamic series of cryogenic processes and phenomena were determined in the Tazovsky peninsula: asynchronous (evolutional), synchronous, and mixed type, as shown in Table 1.

Asynchronous series, which reflect dynamics of landscape and permafrost conditions, correspond to the evolutionary conditions of cryogenic phenomena formation, when one process causes another as a result of a change of natural conditions and a corresponding change of a trend of cryogenic geomorphic processes. By this process, a more ancient phenomenon transforms into a new one.

ASYNCHRONOUS	SYNCHRONOUS	MIXED TYPE
1	2	3
polygonal wedge ice ↓[a]	frost fracturing + [b] formation of ice wedges	frost mounds + frost ridges ↓
thermal erosion topography ↓	thermal erosion topography + slope phenomena + thermokarst topography	polygonal wedge ice + eolian feature (on the surface of mounds and ridges) ↓
solifluction features (on the slopes of thermal erosion gullies)	erosion topography + solifluction features + thermal erosion topography	thermal erosion topography + thermokarst topography (on the surface of mounds, ridges, and in depressions) ↓
Pingo ↓		linear ridge topography
thermokarst lake ↓		frost fracturing + formation of ice wedges
drained depression of thermokarst lake ↓		↓ thermokarst ↓
Pingo		suffosion + thermal erosion
formation of thermokarst lakes ↓		↓ hillocky terrain
thermal abrasion (shores become more smooth and the lakes become overgrown; process of peat formation and accumulation occurs) ↓		
freezing of outlaying parts of the lake basin (formation of polygonal ground and frost mounds within the basin limits)		

[a] An arrow (↓) means that some process (or phenomenon) transforms into a new one; one process causes another one.

[b] A plus (+) means that cryogenic processes are developed simultaneously.

Table 1. Types of dynamic paragenetic series of cryogenic (and other exogenetic) processes and phenomena determined in the Tazovsky Peninsula (some examples).

Synchronous series occur when cryogenic phenomena are developed simultaneously, while mixed series occur when both synchronous and asynchronous development of cryogenic phenomena take place together.

REMOTE SENSING AND FIELD WORK

Tracing these series in nature using remotely sensed data has been carried out by identifying the cryogenic phenomena on high resolution photographs and revealing their role in the formation of landscape morphosculpture. In addition, the character of paragenesis of processes and phenomena has been established on the basis of field observations data and the well-known regularities of cryogenic processes' development [Baulin et al., 1967; Veisman, 1978; Grechishev et al., 1984; Baulin, 1985; Trofimov, 1986]. Identified cryogenic processes and phenomena and their sets were combined in paragenetic dynamic series and subsequently were used to forecast the dynamics of landscape in the Tazovsky peninsula. Several peculiarities were revealed in using different types of series for geocryological forecasting.

Distinguishing and tracing of asynchronous paragenetic series provides a most reliable evaluation of landscape dynamics. It is known, for example, that subsidence of the earth's surface accompanied by the process of bog formation causes thermokarst development. Deepening of the thermokarst lakes causes more intensive thermal abrasion. The shores become more smooth and lakes are overgrown. The process of peat formation occurs, causing freezing of outlying parts of the lake basins and formation of polygonal ground and frost mounds. Thus, the given paragenetic series goes through three successive stages of development and forms three kinds of landscapes, each with a specific topography. If the currently observed landscape belongs to the first or second stages of this paragenetic series development, then it is possible to forecast its next stage, because its realization doesn't require any additional factors or causes. However, the transformation of the external conditions (neotectonics and climate) may cause essential changes in the series development. So, changes in the neotectonic movement's direction can lead to weakening or ceasing of the thermokarst process at the first stage, or intensifying of thermal denudation in the second stage of paragenetic series development.

Climate warming is favorable to the development of processes at the first and second stages and it slows down cryogenic processes at the third stage. Therefore forecasting on the basis of aerial photograph and space image interpretation may be valid, provided the climatic conditions and neotectonic movement of the area of interest are stable for the forecasting period. For example, thermokarst lakes are widespread on the surface of different geomorphic levels within the limits of the Nizhnepursky inherited depression, which is located in the South-East of the Tazovsky peninsula. The photographic images of these lakes testify to the intensive processes of thermal abrasion of their shores, overgrowth, and peat accumulation within degradating lake basins. That is, the natural landscapes observed there are

associated with the second stage of the previously noted paragenetic series of cryogenic processes and phenomena. Consequently, in the case of invariable "outer" conditions (climate and the trend of neotectonic movement), it is possible to forecast the beginning of the third stage of the paragenetic series in a given natural environment.

Another forecasting evaluation of landscape dynamics using satellite data can be given for landscapes with synchronous paragenetic series of cryogenic processes and phenomena. In such a case, an activation or slowing down of a specific cryogenic process depends on the peculiarities of the change of external conditions, which cause their development, rather than on the character of the process manifestation in one or another time interval. It is more appropriate to discuss the intensity of pattern's signature rather than the change of the pattern of topography on the photographs. The extent to which a study area is affected by cryogenic processes testifies to the paleo and present natural conditions, and it is this characteristic that can be used in forecasting.

By this method, the area within the limits of the Severo-Tazovsky meganticline, a positive neotectonic structure which has been uplifted during the Pleistocene-Holocene, landscapes have been identified with synchronous paragenetic series. This series includes erosion and thermal erosion topography, and solifluction features. In case of invariability of both neotectonic movement trends and climate conditions during the forecast period, one can expect the enlargement of the fractional area affected by erosion and thermal erosion, and a corresponding increase of the area occupied by slopes. If a forecast of natural condition development is possible, then one can, in turn, forecast a corresponding change of a given area affected by cryogenic processes.

It is not possible to evaluate landscape dynamics in cases where the surface topography is created by processes which cause both asynchronous and synchronous series of processes and phenomena.

SUMMARY AND CONCLUSIONS

Investigations of cryogenic processes and phenomena in the Tazovsky peninsula using remotely sensed data have shown that forecasting of landscape condition dynamics can be more reliable, when complex approaches are used. This approach includes: (1) regionalization of territory according to neotectonics, geomorphology, geology, the history of permafrost genesis and development, and recent geocryological conditions; (2) determination of their spatial distribution of cryogenic phenomena based on interpretation of aerial photographs and space images; (3) field investigations of permafrost, cryogenic processes and phenomena; and (4) forecast of cryogenic processes and phenomena dynamics on the basis of determination of their paragenetic series and sets as well as using analogous methods and mathematical modeling.

REFERENCES

Baulin, V. V., *Permafrost in Oil and Gas Basins of the U.S.S.R.* (in Russian), 214 pp., Izdatelstvo "Nedra," Moscow, 1985.

Baulin, V. V., E. B. Belopukhova, G. I. Dubikov, and L. V. Shmelev, *Geocryological Conditions of Western Siberian Lowland* (in Russian), 214 pp., Izdatelstvo "Nauka," Moscow, 1967.

Veisman, L. I., Peculiarities of the landscape indicative studies of cryogenic processes (in Russian), in *Cryogenic Processes*, pp. 19-32, Izdatelstvo "Nauka," Moscow, 1978.

Grechishev, S. E., L. V. Chistotinov, and Y. L. Shur, *Fundamentals of the Modelling of Cryogenic Geological Processes* (in Russian), 230 pp., Izdatelstvo "Nauka," Moscow, 1984.

Trofimov, V. T. (Ed.), *Exogeodynamics of the Western Siberian Plate* (in Russian), 288 pp., Izdatelstvo MSU, Moscow, 288 pp., 1986.

AD-P007 272

92-17954

Taiga Forest Stands and SAR: Monitoring for Subarctic Global Change

JoBea Way and Ron Kwok
Jet Propulsion Laboratory, Pasadena, California, U.S.A.

Leslie Viereck and Charles Slaughter
Institute of Northern Forestry, Fairbanks, Alaska, U.S.A.

Craig Dobson and Kyle McDonald
University of Michigan, Ann Arbor, Michigan, U.S.A.

Norman Christensen
Duke University, Durham, North Carolina, U.S.A.

ABSTRACT

In preparation for the first European Earth Remote Sensing (ERS-1) mission, a series of multitemporal, multifrequency, multipolarization aircraft synthetic aperture radar (SAR) data sets were acquired over the Bonanza Creek Experimental Forest near Fairbanks, Alaska in March 1988. Significant change in radar backscatter was observed over the two-week experimental period due to changing environmental conditions. These preliminary results are presented to illustrate the opportunity afforded by the ERS-1 SAR to monitor temporal change in forest ecosystems.

INTRODUCTION

The goal in utilizing remote sensing systems for forest ecosystem analysis is to infer characteristic biophysical parameters from the remotely sensed data. With the proposed launchings of a variety of space-based imaging radar systems throughout the 1990s, there has been an increasing interest in the utility of radar data for forest ecosystem analysis. The first of these spaceborne SARs will be on the European Space Agency's (ESA's) Earth Remote Sensing (ERS-1) satellite to be launched in 1991. During its 3-month commissioning phase, ERS-1 will be in an exact 3-day repeat orbit allowing frequent acquisition of selected forest sites. Beyond the commissioning phase, a longer repeat orbit will allow data collection every few weeks over all seasons.

In utilizing SAR imagery for forest ecosystem analysis, it is important to recognize the sensitivity of radar backscatter to changes in the water status of the vegetation. This status can be can be affected by changes in plant biomass levels associated with seasonal growth and senescence, and changes in the amount and state of plant fluids in response to environmental stimuli, such as variations in solar radiation, availability of water (due to rain or drought), and changes in air temperature. That these changes result in differences in radar backscatter from a forest canopy are clearly indicated by theoretical models as well as measurements made by ground-based scatterometers.

In order to further understand the kinds of biophysical properties that may be detected with spaceborne SAR systems such as ERS-1, a series of multi-season aircraft missions over selected forest sites is in progress [Way et al., 1990]. The first of these occurred in March, 1988 over the Bonanza Creek Experimental Forest (BCEF) [Slaughter and Viereck, 1986; Viereck et al., 1986; Viereck, 1987] near Fairbanks, Alaska. The purpose of these missions was (1) to determine whether changes in plant fluid status associated with thawing and freezing resulted in changes in radar backscatter which could be detected on SAR imagery; and (2) based on measurements of tree geometry and biomass levels, and dielectric measurements of the surface (snow) and

trees, could the changes in radar backscatter be predicted by theoretical models.

Over the two-week period during which aircraft data were acquired, temperatures ranged from unseasonably warm (1 to 8°C) to well below freezing (-8 to -15°C), and the moisture content of the snow and trees changed from a liquid to a frozen state. The resulting difference in image intensity between these two environmental conditions is significant and indicates that changing environmental states are indeed detected by SAR systems.

BACKGROUND

A typical seasonal phenologic cycle for a forest ecosystem may include leaf-on and leaf-off, budding and cone emergence, periods of rapid leaf or needle growth, and sprouting of new branches and suckers. As a result of annual growth cycles, the forest floor changes in its litter composition as well as its undergrowth. Environmentally, a forest may go through droughts and floods, snow and rainy periods, and freeze/thaw events. These environmental variations will not only change the nature of the forest floor, but will change the water relations and sometimes the canopy geometry of the trees themselves due to various stresses. Variations in the upper canopy due to changes in leaf and branch structure will affect the attenuation of longer wavelength radar signatures and the multiple scattering at the shorter wavelengths. Change in the trunk water status (which must also be considered diurnally) [McDonald et al., 1990; McDonald et al., 1991; Way et al., 1991] and the environmental and phenologic conditions at the ground surface will greatly affect the double bounce microwave backscatter return at the longer wavelengths. The ability to monitor these changing seasonal conditions of a forest canopy may provide a key tool for assessing the impact of longer-term climate shifts or other natural or human-induced effects.

In addition, seasonal variations of water with respect to state, quantity, phase mixture, temperature, binding energy and location within the forest canopy, and on and in the soil layer; and foliar biomass within the canopy and on the ground may enhance or suppress various scattering pathways. Even more importantly, the success of any monitoring system in detecting longer-term, directional change in forest properties such as biomass or successional stage will depend on a firm understanding of the intrinsic rates of seasonal

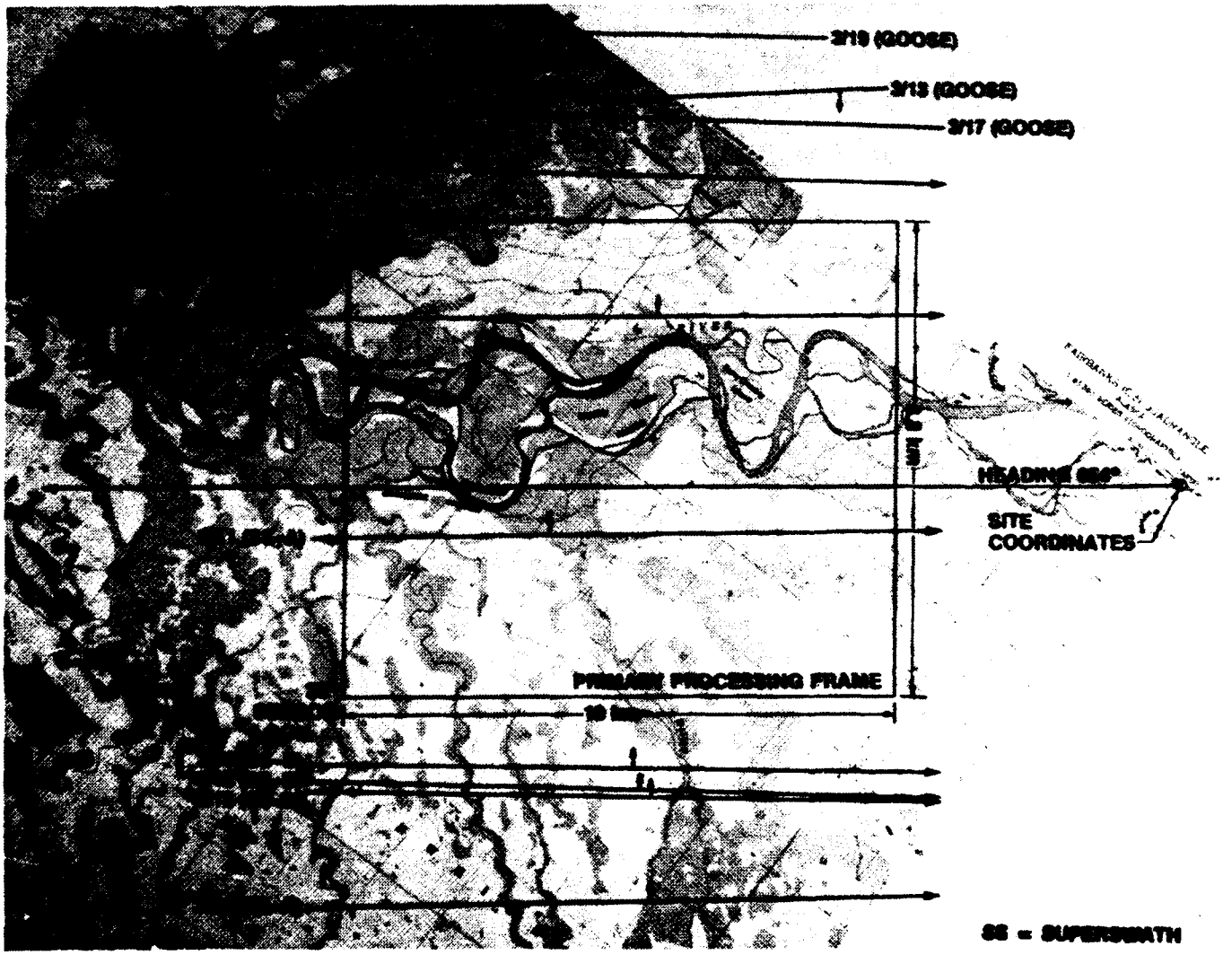


Figure 1. Location of AIRSAR tracks over BCEF for March 1988 flights.

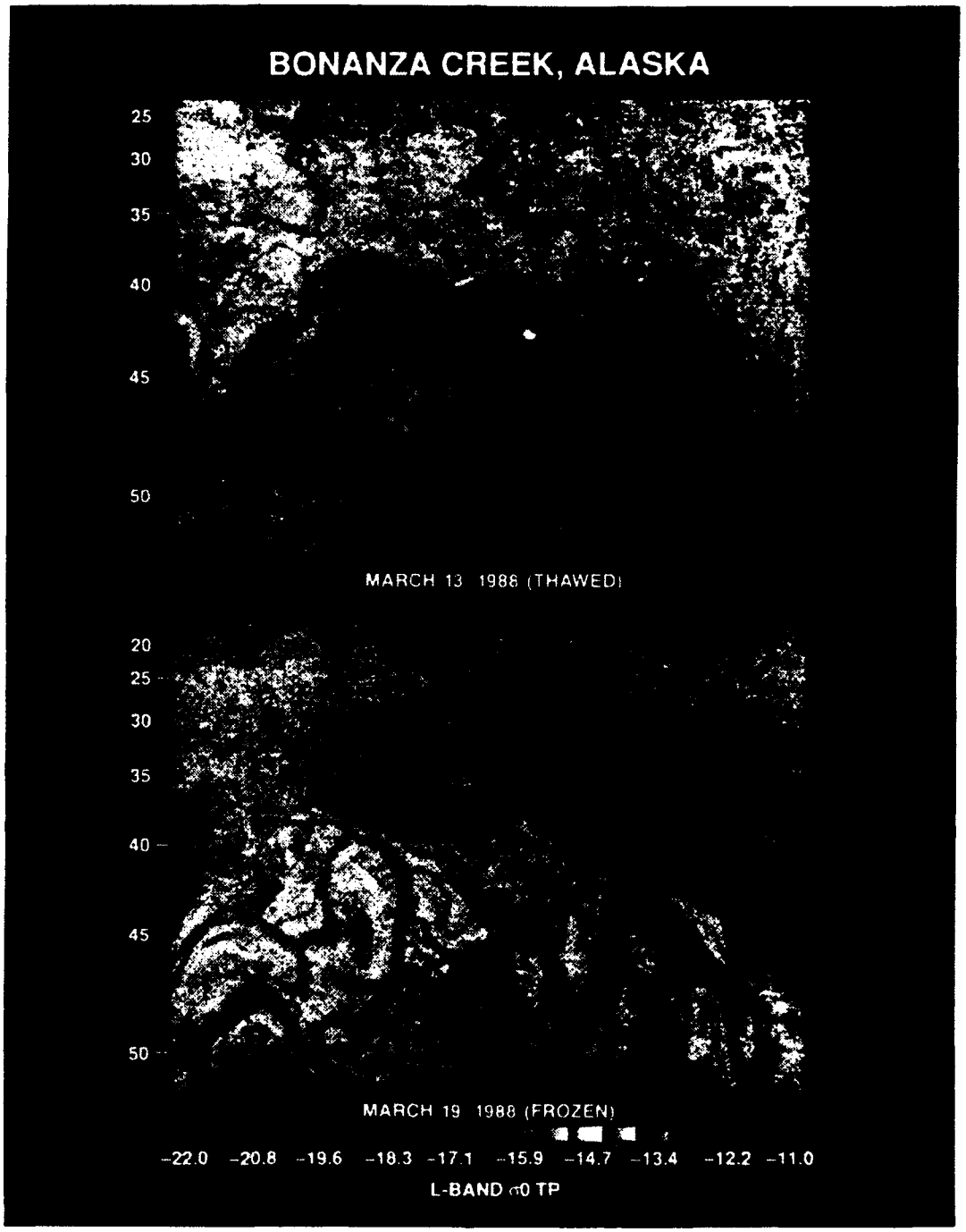


Figure 2. Calibrated total power L-band images of BCEF for March 13 (top) and March 19 (bottom).

change and their effect on the measured signal. Long-term environmental changes resulting from human effects or climatic shifts are not causing static ecosystems to change, but are altering the trajectories of already dynamic systems [e.g., Kasischke and Christensen, 1990].

THE ALASKA EXPERIMENT

The Jet Propulsion Laboratory's (JPL's) P-, L- and C-band (0.450, 1.26 and 5.31 GHz, respectively) quad-polarized SAR (AIRSAR) mounted in NASA's DC-8 aircraft was used to acquire data over the BCEF test site on five separate occasions (Figure 1). Overlapping passes were acquired on March 13, March 17 and March 19, 1988. Data collected on March 11 and March 21 were offset by approximately a half-swath width and will not be used due to incidence angle effects.

The data were calibrated radiometrically to ±1 dB using 6' corner reflectors [Kwok et al., 1991] and total power images were generated for the calibrated L-band data collected on March 13 and 19 (Figure 2). The bright regions along the Tanana River in the 13 March image represent the mature stands of white spruce and balsam poplar found on the

floodplain, while the dark regions in this image represent stands of black spruce or bog.

The L-band backscatter for the cold and the warm days were determined for the twelve stands at three polarizations (HH, VV and HV). The results are plotted as a function of successional age for L-band (actual age for balsam poplar, 100 years plus the age of the white spruce, and 350 years plus the age of the black spruce, resulting in a simulated successional age) and show the difference in backscatter (dB) between the warm day (March 13) and one of the two cold days (March 19) for the black spruce, white spruce and balsam poplar (Figure 3). The difference is significant at all three polarizations but is the greatest at vertical and cross polarizations.

In addition to the magnitude of the backscatter signatures, the polarimetric AIRSAR data may be used to extract phase difference signatures [Kwok et al., 1991] for both the warm and the frozen days (Figure 4). These results also show a significant change in phase rotation as the environmental state of the canopy and ground changes.

GROUND TRUTH

Approximately thirty stands in BCEF have been identified for this study. To date, static canopy characteristics have been collected and processed for five stands [Jaeger, 1988] (Table 1). These static canopy data consist of species age and composition, stand height, diameter at breast height (DBH), and density.

During the aircraft overflights, descriptors of variable scene characteristics (i.e., bole water status and dielectric characteristics, and snow pack characteristics including water equivalent, moisture, depth, density, temperature and dielectric constant) were obtained on Seven Mile Island at the center of the aircraft scene (Table 2). One of the canopy characteristics which changed the most was the bole dielectric constant profile (Figure 5). For white spruce on the thawed day, the real dielectric constant reached a peak of about 35 at about 3 cm depth. At greater depths, the dielectric constant decreases rapidly and reaches a constant value at about 6 cm depth. In comparing the measured dielectric constant profiles with tree cores, the higher dielectric constant region appears to correspond to the xylem tissue with the highest hydraulic activity. The black spruce has a more uniform dielectric profile on the thawed day reaching a peak of about 25 between about 1 and 2 cm

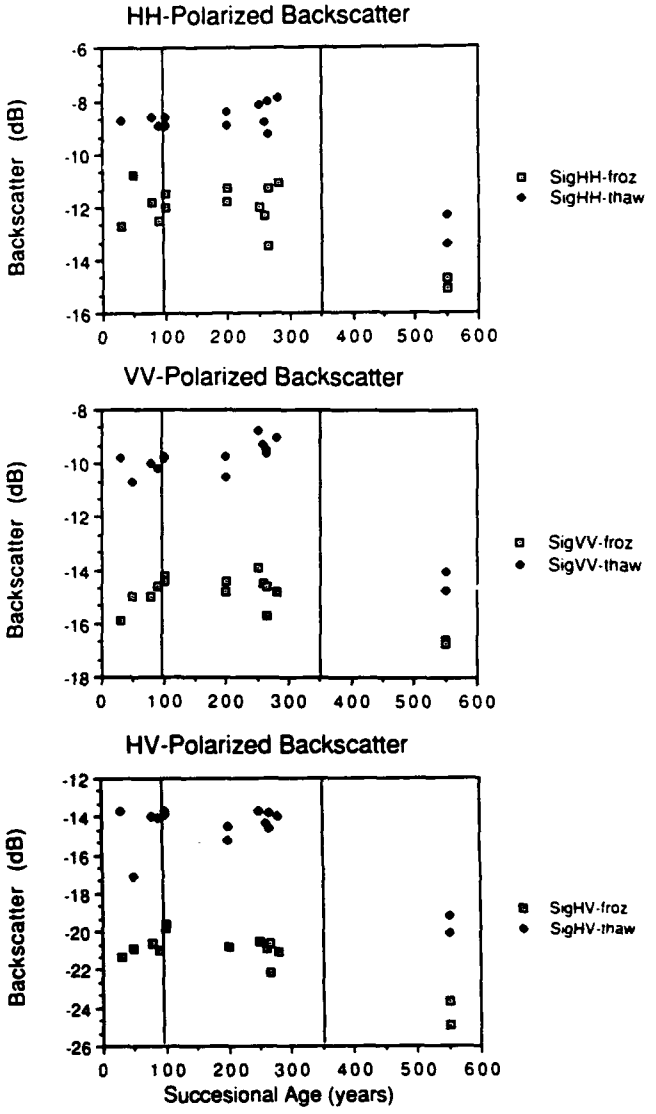


Figure 3. Extracted L-band backscatter signatures for stands in BCEF plotted as a function of age for frozen (March 19) and thawed (March 13) days. HH (top), VV (middle) and HV (bottom) signatures are shown.

Stand	Age (years)	Succ Age (years)	Mean DBH (cm)	Mean Height (m)	Density (#/ha)	Winter* Biomass (m-tons/ha)
BP-2	90	90	18.0	17.6	1615	179 (182)
WS-1	165	265	19.6	22.1	1248	217
WS-2	100	200	14.5	20.1	2073	167
WS-5	180	280	17.9	21.3	1484	181
BS-1	200	500	8.8	7.6	1975	37

* Summer biomass noted in ( ) for balsam poplar

Table 1. Measured Static Canopy Parameters.

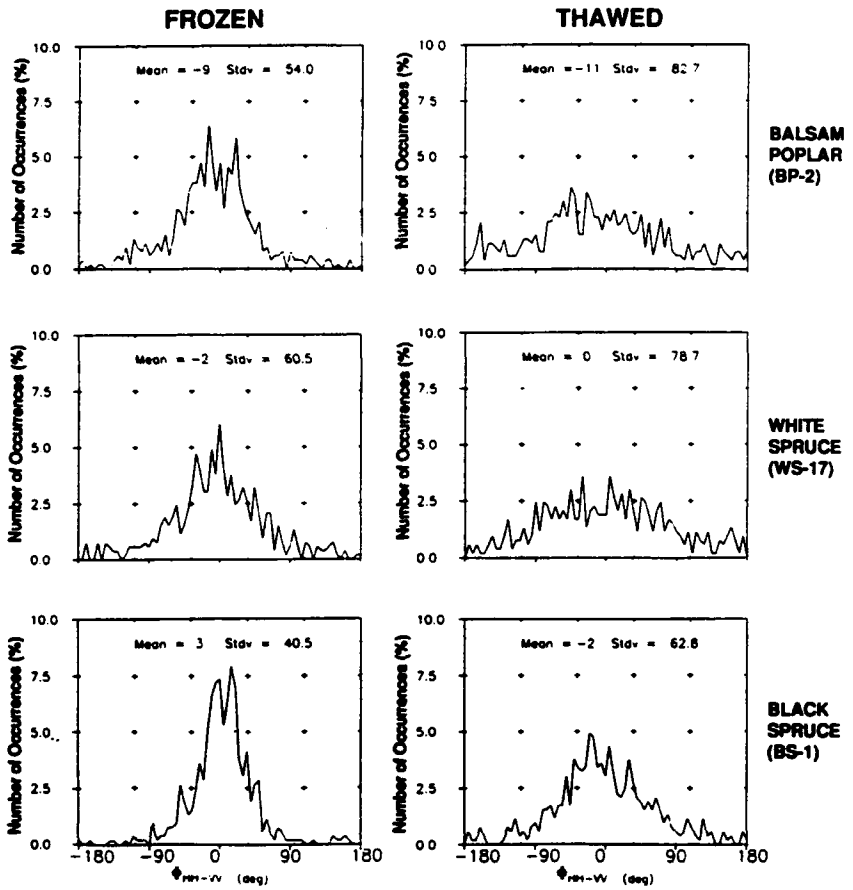


Figure 4. Phase (HH-VV) signatures for frozen and thawed days for balsam poplar, white spruce and black spruce stands.

Date (1988)	Time*	AIRSAR Channels	Incidence Angle**	Air Temp (C)	Soil Temp (C) at 5/50 cm	Snow Temp (C)	Snow Moist. (% vol)	Snow Upper Layer Cond.	Bole Cond.	Bole Max. Real Dielectric Constant
3/11	14:02	P, L, C	9°	7.5	-2/0	0	2–5	wet	thawed	25–30
3/13	15:03	P, L[t]	41°	2.0	-2/0	0	5–7	wet	thawed	25–30
3/17	14:54	L, C[tt]	40°	-13	-3/-1	-13	0	dry	frozen	5
3/19	23:17	L, C[tt]	39°	-14	-3/-1	-12	0	dry	frozen	5
3/21	23:38	L, C[tt]	48°	<-20	-3/-1	-30	0	dry	frozen	5

* Local Alaska time; time of overflight of BCEF
** At center of Seven Mile Island
[t] C-band data contain banding due to aircraft motion during imaging
[tt] H-pol transmitted only on P-band

Table 2. AIRSAR Parameters and Environmental Conditions at Time of Overflights.

depth. On the frozen day, the real dielectric constant profiles for both trees show a dramatic drop to below a dielectric constant of 5 due to freezing of the xylem liquid.

Environmental parameters including air temperature, relative humidity and wind were also monitored hourly using the permanent weather stations located on the BCEF floodplain. In addition, soil temperature at 5, 10, 20 and 50 cm depths at two LTER sites were recorded throughout the duration of the flights. These measurements are discussed in detail by Way et al. [1990] and are summarized in Table 2.

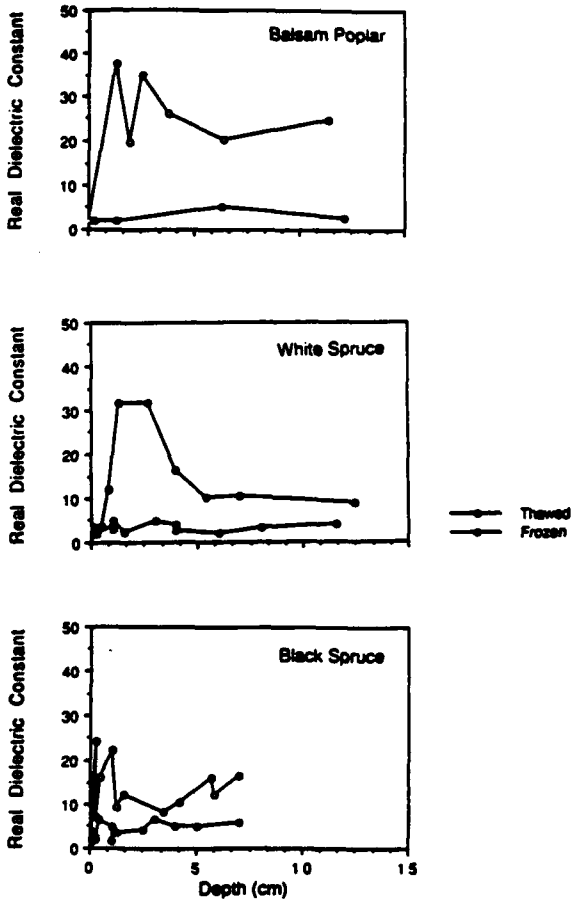


Figure 5. L-band dielectric constant profiles (dielectric constant vs. depth into bole) for white and black spruce on both the frozen and the thawed days.

MIMICS Validation

The measured static and temporally varying ground and canopy characteristics were used to validate the Michigan Microwave Canopy MIMICS Scattering model [Ulaby et al., 1990]. Table 3 summarizes both the modeled and measured L-band backscatter results for five stands at an incidence angle of 40°. Cases where the model and the measured backscatter do match are noted in bold; it is thought that the mismatches are due to the treatment of the surface layer. In the current model, the surface is treated as an infinite snow layer rather than a layer of snow on frozen ground. The results as a function of incidence angle for L-band are shown in Figures 6a–6c.

At L-band, HH polarization dominates except for thawed balsam poplar, probably due to the strong return from the thawed vertical branches. For VV polarization, the return is dominated by scattering from the crown with the exception of frozen balsam poplar and frozen black spruce at L-band which have some trunk–ground contribution at the steeper incidence angles. HH polarization shows dominant trunk–ground scattering for frozen and thawed black spruce and balsam poplar (thawed black spruce shows nearly equivalent trunk–ground and crown scattering when thawed), but shows a dominant direct crown scattering for white spruce for both frozen and thawed conditions.

The above modeling efforts help explain the different polarization phase signatures discussed above (Figure 4) as the canopy freezes. For the thawed canopy, the trunk–ground interaction is largely due to the high dielectric constant of both the bole and the snow upper layer relative to the frozen case. The phase rotation for scattering from a dielectric cylinder is 180° whereas that for specular scattering from the ground is 0°.

DISCUSSION

The results indicate changing environmental conditions strongly affect the microwave backscatter response of forest canopies. In this case, the two parameters that changed most significantly were the snow wetness and associated dielectric constant, and the bole dielectric constant as the bole moisture changed from a liquid to a frozen state. Although not measured, it is presumed that the upper branches also changed in dielectric constant when temperatures changed. Thus, increased multiple scatter within the canopy and

Stand	Thawed SigLVV (dB)	Frozen SigLVV (dB)	Thawed SigLHH (dB)	Frozen SigLHH (dB)	Thawed SigLHV (dB)	Frozen SigLHV (dB)
BP-2	**-10.2 (-11.6)**	-14.6 (-22.0)	**-8.9 (-11.7)**	-12.5 (-14.4)	-14.1 (-17.9)	-21.0 (-32.4)
WS-1	-9.5 (-12.1)	**-14.6 (-15.6)**	**-8.0 (-9.2)**	**-11.3 (-12.2)**	**-13.8 (-14.9)**	-20.6 (-22.8)
WS-2	-9.7 (-12.3)	-14.4 (-16.4)	**-8.4 (-9.1)**	**-11.3 (-12.8)**	**-14.5 (-15.0)**	-20.8 (-23.6)
WS-5	-9.0 (-12.0)	**-14.8 (-15.5)**	**-7.9 (-9.1)**	-11.1 (-12.2)	**-14.0 (-14.9)**	-21.1 (-23.0)
BS-1	**-14.7 (-15.1)**	-16.6 (-23.2)	-13.4 (-10.7)	-15.1 (-16.9)	**-20.1 (-19.5)**	-24.9 (-32.5)

Note: bold indicates match between modeled and measured backscatter values is about 1 dB or better.

Table 3. Measured (and Modeled) Backscatter Signatures.

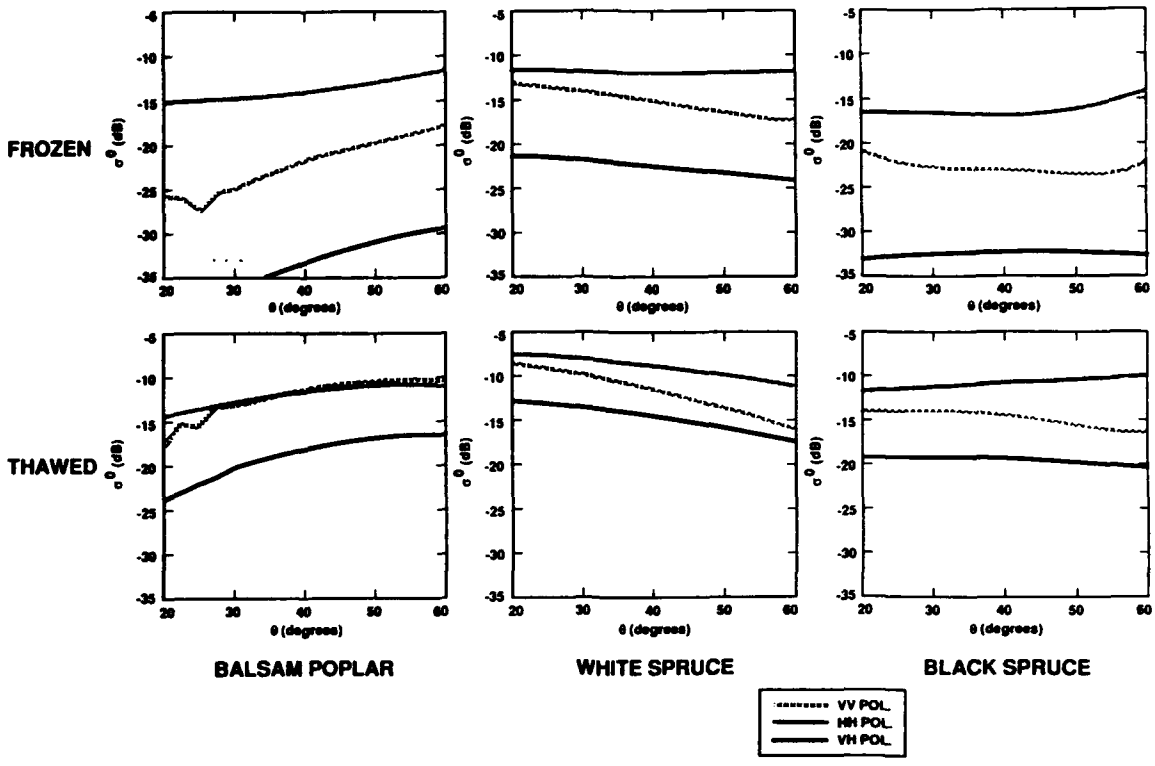


Figure 6a. Modeled L-band backscatter for balsam poplar, white spruce and black spruce for the frozen and the thawed days. HH, VV and HV backscatter vs. incidence angle are shown.

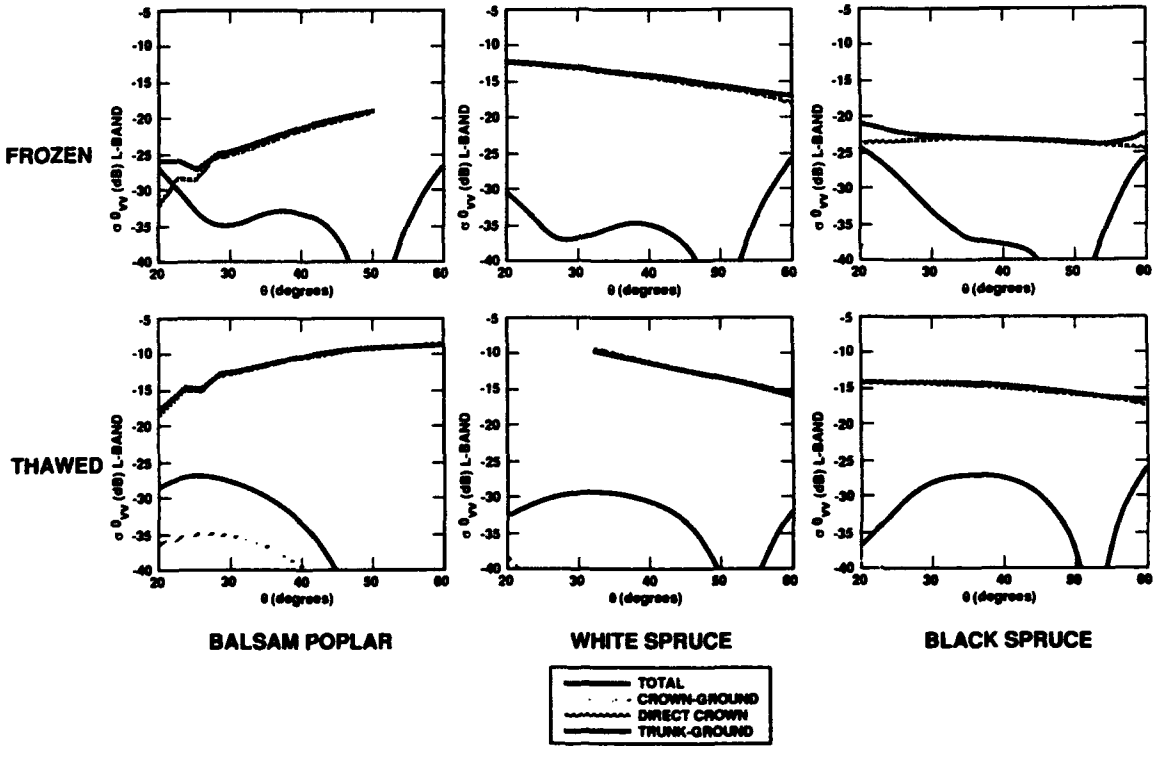


Figure 6b. Modeled L-band VV polarization backscatter vs. incidence angle for balsam poplar, white spruce and black spruce for both the frozen and the thawed days showing the backscatter contribution from the crown–ground, direct crown and trunk ground interactions.

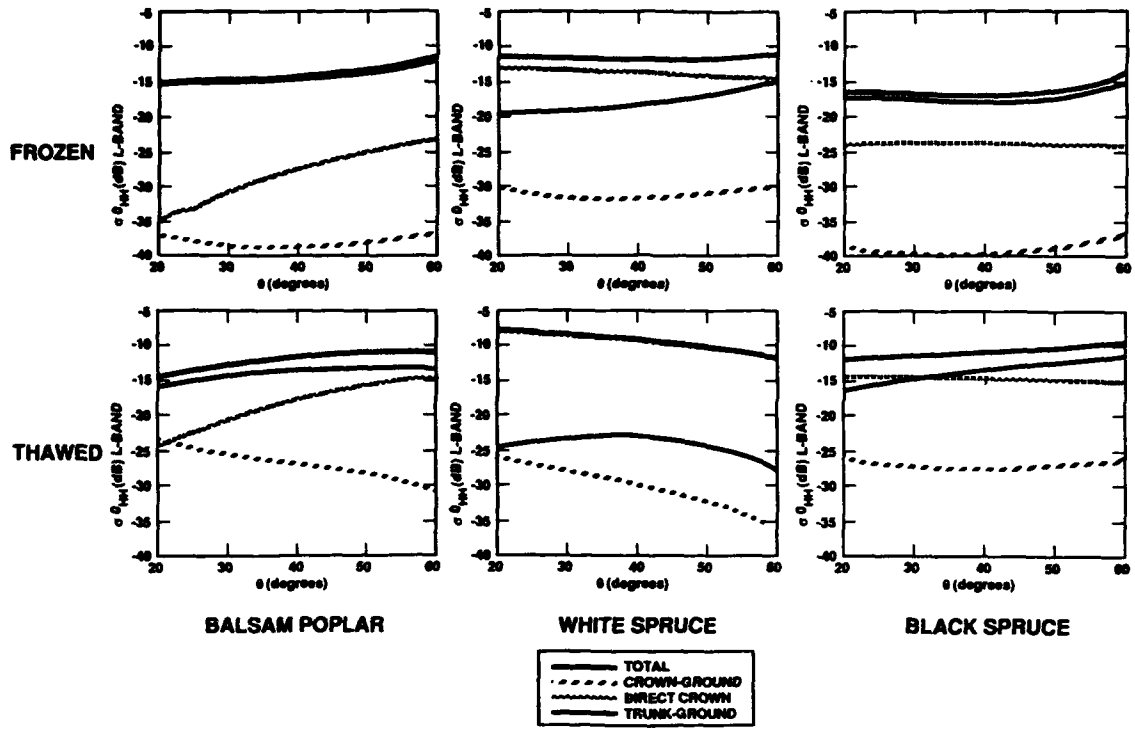


Figure 6c. Modeled L-band HH polarization backscatter vs. incidence angle for balsam poplar, white spruce and black spruce for both the frozen and the thawed days showing the backscatter contribution from the crown–ground, direct crown and trunk ground interactions.

double-bounce scattering between the trunk and the ground could both be responsible for the temporal change in image intensity. The close match of the modeled backscatter and the measured backscatter [Dobson et al., 1991] also indicates that the change in bole dielectric constant is the major contributor to total backscatter change at L-band.

Frozen soil temperatures throughout the duration of the experiment suggest liquid water was not being drawn up through the roots and evapotranspiration was most likely not occurring; however, the thawing of the in-situ liquid within the bole was significant enough to produce a large change in the dielectric constant of the trunk. This, in combination with the thawing upper layer of snow and its associated increase in dielectric constant, resulted in a stronger trunk–ground interaction term thus increasing the VV and cross polarization substantially and the HH polarization significantly. Alternately, the freezing and thawing of the upper branches could have altered the diffuse scattering in the canopy, also resulting in the observed change in backscatter. Polarimetric modeling of the temporal change in backscatter will help unfold the exact scattering mechanisms. Once these mechanisms are understood, options for enhancing or subduing certain pathways with season may provide a key to measuring important canopy properties such as biomass.

SUMMARY

The eventual availability of multi-temporal SAR image data for ERS-1, JERS-1, RADARSAT and EOS SAR will provide an opportunity to monitor changing phenologic and environmental conditions of forest canopies. Results from this experiment indicate it may be possible to use these changing conditions to monitor the environmental condition of the forest. Aircraft data obtained for a boreal forest indicate that freeze/thaw events significantly change the dielectric properties of the trees and the surface snow, resulting in a significant change in microwave backscatter. Preliminary aircraft experiments to address seasonal change in forest stands and its influence on the radar backscatter will provide a basis for defining detailed experiments to monitor temporal change by the ERS-1 mission.

ACKNOWLEDGMENTS

This work was carried out at the Jet Propulsion Laboratory, California Institute of Technology under contract to the National Aeronautics and Space Administration.

REFERENCES

Dobson, M. C., K. C. McDonald, F. T. Ulaby, E. S. Kasischke, and J. B. Way, Modeling the effects of temperature on microwave extinction and backscatter from a boreal forest in winter, *IEEE Trans. on Geosci. and Rem. Sens.*, 1991, In review.

Jaeger, B., *Report on Stand Characteristics Measured in Bonanza Creek Experimental Forest for the SAR-IFIT Project*, Forest Soils Laboratory, University of Alaska, Fairbanks, AK, December, 1988.

Kasischke, E., and N. Christensen, Correcting forest ecosystem and microwave backscatter models, *Int. J. of Rem. Sens.*, *11*, 1277–1298, 1990.

Kwok, R., E. Rignot, J. B. Way, A. Freeman, and J. Holt, Polarization signatures of frozen and thawed forests of varying environmental state, *IEEE Trans. on Geosci. and Rem. Sens.*, 1991, In review.

McDonald, K. C., M. C. Dobson, and F. T. Ulaby, Using MIMICS to model L-band multi-angle and multitemporal backscatter from a walnut orchard, *IEEE Trans. on Geosci. and Rem. Sens.*, *GE-28*, 477–491, 1990.

McDonald, K. C., M. C. Dobson, and F. T. Ulaby, Modeling multi-frequency diurnal backscatter from a walnut orchard, *IEEE Trans. on Geosci. and Rem. Sens.*, 1991, In press.

Slaughter, C. W., and L. A. Viereck, Climate characteristics of the taiga in interior Alaska, in *Forest Ecosystems in the Alaska Taiga. A Synthesis of Structure and Function*, edited by K. Van Cleve, F. S. Chapin III, P. W. Flanagan, L. A. Viereck, and C. T. Dyrness, pp. 9–12, Springer Verlag, New York, 1986.

Ulaby, F. T., K. Sarabandi, K. McDonald, M. Whitt, and M. C. Dobson, Michigan Microwave Canopy Scattering Model, *Int. J. of Rem. Sens.*, *11*, 1223–1254, 1990.

Viereck, L. A., Flood plain succession and vegetation classification in interior Alaska, symposium on land classification based on vegetation: Applications for resource management, *USDA Technical Report INT*, Moscow, Idaho, November 17–19. Ogden, UT, 1987.

Viereck, L. A., K. Van Cleve, and T. C. Dyrness, Forest ecosystem distribution in the taiga environment, in *Forest Ecosystems in the Alaska Taiga. A Synthesis of Structure and Function*, edited by K. Van Cleve, F. S. Chapin III, P. W. Flanagan, L. A. Viereck, and C. T. Dyrness, pp. 22–42, Springer Verlag, New York, 1986.

Way, J. B., J. Paris, E. Kasischke, C. Slaughter, L. Viereck, N. Christensen, M. C. Dobson, F. Ulaby, J. Richards, A. Milne, A. Sieber, F. J. Ahern, D. Simonett, R. Hoffer, M. Imhoff and J. Weber, The effect of changing environmental conditions on microwave signatures of forest ecosystems: Preliminary results of the March '88 Alaskan Aircraft SAR Experiment, *Int. J. of Rem Sens.*, *11*, 1119–1144, 1990.

Way, J. B., E. Rignot, R. Oren, R. Kwok, K. McDonald, M. C. Dobson, G. Bonan, L. Viereck, and J. E. Roth, Monitoring temporal change in Alaskan Forests Using Imaging Radar Data, *IEEE Trans. on Geosci. and Rem. Sens.*, 1991, In review.

AD-P007 273

92-17955

Contamination of U.S. Arctic Ecosystems by Long-Range Transport of Atmospheric Contaminants

Jesse Ford
NCASI, c/o U.S. EPA Environmental Research Laboratory, Corvallis, Oregon, U.S.A.

Dixon H. Landers
U.S. EPA Environmental Research Laboratory, Corvallis, Oregon, U.S.A.

ABSTRACT

Various kinds of atmospheric pollutants are found in Arctic environments, including organic contaminants, radionuclides, and pollutants associated with fossil fuel combustion, smelting, and industrial development. While some of these contaminants originate in the Arctic itself, most are likely a result of long-range transport from lower latitudes. Recent studies suggest that at least some atmospheric contaminants may be susceptible to poleward redistribution, sequestration, and accumulation as a result of their physical and chemical properties. Thus, contamination of the Arctic may be exacerbated by the tendency of selected contaminants produced at lower latitudes to be transported to polar regions and incorporated into high-latitude food chains.

Although awareness of exotic contaminants in high-latitude food chains is not new, international and regional baseline data are needed to document the magnitude, distribution, and ecosystem effects of this potentially serious global (hemispheric) problem. The United States has given little attention to Arctic studies relative to several other circumpolar nations (e.g., Canada, Sweden). The U.S. Environmental Protection Agency (USEPA) is currently designing regional-scale studies to complement existing site-specific studies and reduce this information gap in the U.S. Arctic. A major focus of this activity will be to ensure compatibility with international studies of Arctic contamination as well as with the USEPA's Environmental Monitoring and Assessment Program (EMAP).

BACKGROUND

In recent years, there has been an increasing appreciation of the need to know more about Arctic environments, both because of their environmental sensitivity, highlighted by their role in global warming scenarios, and because of their potential strategic and economic importance. In the international arena, there are currently several forums for discussion of strategies for protection of the Arctic, including the U.S.–U.S.S.R. Agreement on Cooperation in the Field of Environmental Protection, in which 6 of 11 technical areas focus significant research on the Arctic [IARPC, 1990a], and the eight-nation Consultative Meetings on the Protection of the Arctic [IARPC, 1990b].

One aspect of concern is the potential impact of pollutant loadings on Arctic food webs. The presence of various contaminants in Arctic food chains has been known for over 15 years [Salo and Miettinen, 1964; Hanson et al., 1967; Cade et al., 1971; Addison and Smith, 1974; Bowes and Jonkel, 1975]. In contrast to the situation in Canada and the Nordic countries [e.g., Wong, 1985a; Monitor, 1987], however, comparatively little is known about the U.S. Arctic. In part, this may be because the U.S. Arctic occurs

entirely within the state of Alaska, which until recently has often been perceived as being conceptually, as well as spatially, removed from mainstream interests of the "Lower 48."

Traditionally, the magnitude of food web contamination in the North American Arctic has been assumed to be small relative to more southerly environments. This scenario seems reasonable because in North America most of the larger population centers are located far south of the Arctic Circle, and there is only minor industrialization of the North American Arctic. Thus, the position of the Arctic air mass in North America typically does not intersect likely source regions for atmospheric anthropogenic pollutants [Shaw and Khalil, 1989]. This situation is in contrast to Eurasia, where population and industrial centers are generally located 5° to 10° farther north and the polar air masses have lobes that extend farther to the south [Shaw and Khalil, 1989].

Recent work with marine food webs suggests that both the magnitude and the extent of contamination of the North American Arctic may be greater than previously thought [e.g., Muir et al., 1988; Norstrom et al., 1988; Bidleman et al., 1989]. Less information is available for terrestrial ecosystems of North America [e.g., Wong, 1985a], with the possible exception of game birds [Wong, 1985b]. Although there is historical evidence for food chain contamination by both DDT [Cade et al., 1971] and radionuclides [Hanson et al., 1967] there is virtually no recent published information for inland Arctic ecosystems of the United States. The USEPA has therefore initiated a series of research activities that focus on contamination of inland Arctic food chains. This work will focus on terrestrial and inland freshwater ecosystems, with an emphasis on gathering regional scale data on the distribution and potential ecological effects of toxic contaminants.

POTENTIAL SOURCES OF ARCTIC CONTAMINATION

Although industrial development in the North American Arctic is minimal, it is now recognized that the concentrations of pollutants in winter air masses even in towns as small as Fairbanks, AK, can equal or exceed concentrations from temperate latitude cities by two orders of magnitude [Benson, 1986]. This is due primarily to strong and persistent diurnal surface inversions over snow surfaces [Benson, 1986]. In addition, sources remote from the Arctic can also be of considerable importance, both from long-range atmospheric transport, and (for marine systems) inflowing Pacific water from the Bering Sea [Hargrave et al., 1989]. Riverine inputs may also become important in watersheds large enough to integrate substantial indirect inputs via atmospheric deposition [Hargrave et al., 1989].

Extensive research has been conducted on long-range atmospheric transport, mostly with respect to the phenomenon of Arctic haze. Arctic haze is a generic term for spatially well-defined, pollutant-laden aerosols of widespread polar distribution during late winter and early spring [Barrie, 1986; Stonehouse, 1986; Shaw and Khalil, 1989]. Haze development is thought to be fed both by episodic injection of a broad spectrum of anthropogenic contaminants from warmer air masses to the south [Rahn and Lowenthal, 1984; Lowenthal and Rahn, 1985; Barrie, 1986], and by direct emissions to the polar airmass within the industrialized Arctic. The pollutant content of Arctic hazes increases throughout the long, dark polar winter, primarily due to lack of removal processes [e.g., Barrie, 1986]. Concentrations peak around April and then nearly disappear throughout the Arctic basin in summer [Shaw and Khalil, 1989]. Little is known about the processes involved in the transition from polluted winter air to cleaner summer air [Shaw and Khalil, 1989]. One possibility is that late spring atmospheric warming and associated air turbulence may increase rates of direct and indirect deposition, providing a pathway for transfer of contaminants to snow-covered terrestrial and marine landscapes.

It has recently been determined that specific "brown snow" events appear to be related to a second source of long-range atmospheric transport [Welch et al., 1991]. The fine particulates associated with these events are rich in semivolatile organic pollutants and are believed to originate at least in part in Asia [Welch et al., 1991].

CURRENT STATUS OF USEPA RESEARCH ON CONTAMINATION OF ARCTIC ECOSYSTEMS BY LONG-RANGE ATMOSPHERIC TRANSPORT

Research by the EPA on the potential ecosystem consequences of Arctic contamination by long-range atmospheric transport began in early 1990. A small workshop of U.S. and Canadian experts with longstanding research experience in one or more aspects of this problem was convened to help identify and prioritize contaminants of concern and the types of environmental samples that could be used as passive "collectors" of atmospheric deposition. The workshop proceedings have been summarized by Nash [1991], and recommendations from the workshop have guided development of research efforts to date.

The primary goals of our current pilot work are to (1) investigate the technical and logistic constraints affecting the use of various recommended types of environmental samples (lichens, mosses, lake sediments, snow) in the U.S. Arctic, and (2) provide preliminary information on contaminant levels in the U.S. Arctic.

Pilot field work initiated during the 1990 field season examined the use of lichens and mosses as passive collectors of atmospheric deposition. Lichen and moss taxa likely to be widely distributed across a variety of habitats in the U.S. Arctic were identified and sampled at 21 locations across the northern foothills of the Brooks Range (Figure 1). The Arctic foothills were chosen as the primary locus for 1990 study sites, because removal processes from polluted air masses may be accelerated as Arctic haze encounters vertical obstructions, such as mountain ranges, during periods of southward flow [G. Shaw, personal communication, 1990].

Sixteen initial target taxa were selected for study, based on several criteria:

- Broad circumpolar distribution;
- Likely frequent occurrence and high abundance in the study area of interest;
- Ease of identification (ideally, eliminating the need for using chemical tests and dissecting or compound microscopes in the field);
- Representation of a range of growth forms that may influence scavenging efficiency and/or retention; and
- Representation in other similar studies worldwide.

Of the taxa originally identified, 10 were collected for

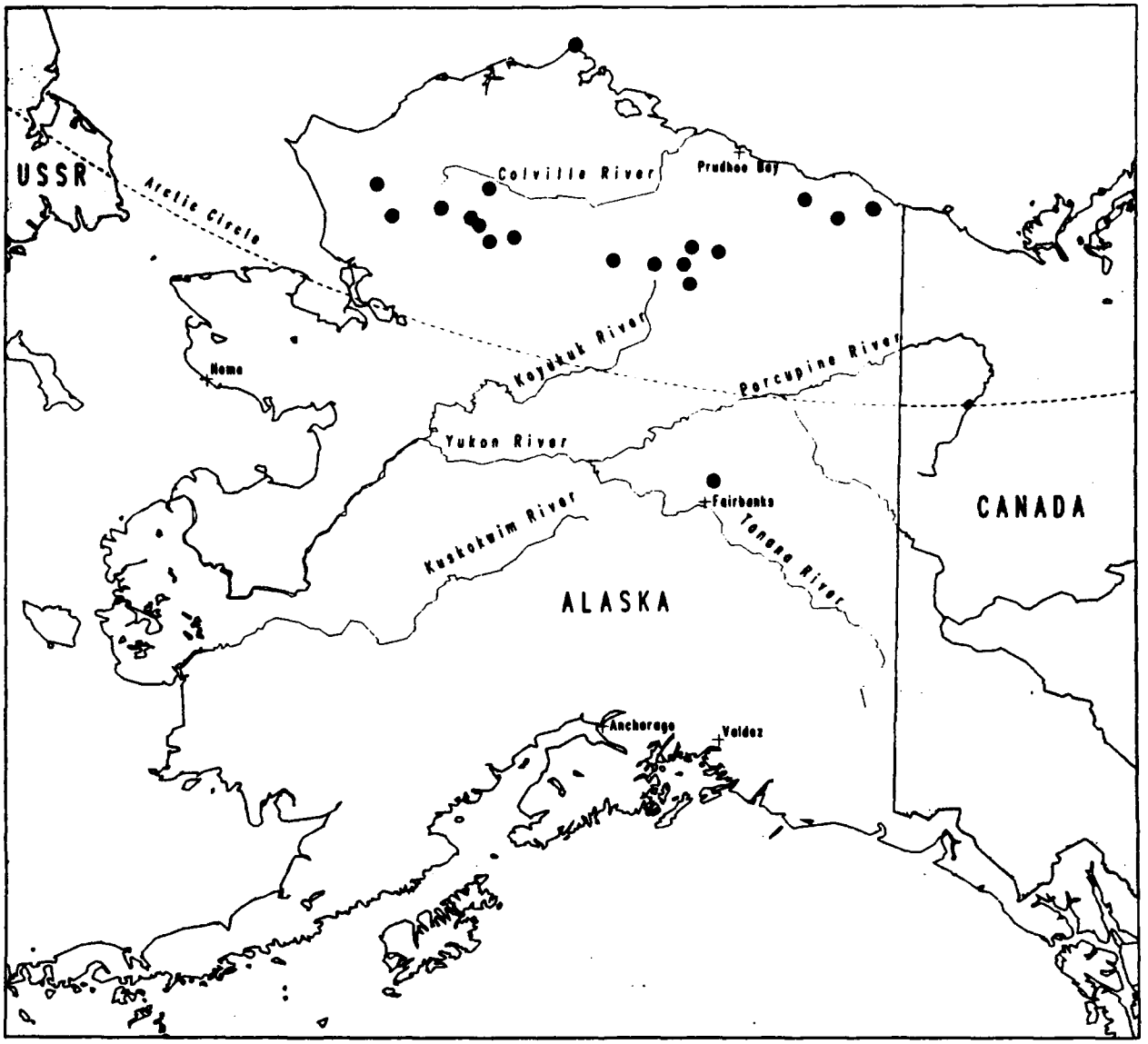


Figure 1. Distribution of sites sampled for lichens and mosses during the 1990 pilot field study. Of 21 field sites, two pairs were closely co-located and thus each appear as a single dot on this map.

analysis at one or more sites, and four (two mosses, *Hylocomium splendens* and *Racomitrium lanuginosum*, and two lichens, *Cetraria cucullata* and *Masonhalea richardsonii*) were studied in detail.

Sampling, storage, and handling techniques appropriate to the extremely remote nature of the collection sites were devised and tested. Samples are currently being analyzed for a suite of heavy metals, trace elements, and organochlorines by the USEPA's Environmental Monitoring and Systems Laboratory in Cincinnati, Ohio. Selected samples are also being analyzed for radionuclides. Findings from this laboratory work may influence the selection of target species taxa for contaminant monitoring. Results from this pilot study will be reported in the open literature upon completion of the analyses.

SUMMARY

Contamination of Arctic ecosystems is an issue of growing international concern. The U.S. Environmental Protection Agency has initiated research to provide preliminary information on the status and extent of contamination of U.S. Arctic ecosystems due to long range atmospheric transport.

ACKNOWLEDGMENTS

The map in Figure 1 was produced using ARCINFO by Suzanne Pierson. We appreciate the review comments of C. Benson, S. Christie, D. Coffey, G. Larson, T. Strickland, and R. Worrest, and technical input from cryptogamic botanists W. Denison (Oregon State University), J. Martin (Tallinn University), T. Moser (NSI), B. Murray (Niversity of Alaska), and S. Pittam (Smithsonian). Preparation of this manuscript has been funded wholly by the U.S. Environmental Protection Agency under contract DW12931230 to the USDA Forest Service. It has been subjected to Agency review and approved for publication.

REFERENCES

Addison, R. F., and T. G. Smith, Organochlorine residue levels in Arctic ringed seals: variation with age and sex, *Oikos*, *25*, 335–337, 1974.

Barrie, L. A., Arctic air pollution: an overview of current knowledge, *Atmos. Environ.*, *20*, 643–663, 1986.

Benson, C. S., Problems of air quality in local arctic and sub-arctic areas and regional problems of Arctic Haze, in *Arctic Air Pollution*, edited by B. Stonehouse, pp. 69–84, Cambridge Univ. Press, New York, 1986.

Bidleman, T. F., G. W. Patton, M. D. Walla, B. T. Hargrave, W. P. Vass, P. Erickson, B. Fowler, V. Scott, and D. J. Gregor, Toxaphene and other organochlorines in Arctic ocean fauna: evidence for atmospheric delivery, *Arctic*, *42*, 307–313, 1989.

Bowes, G. W., and C. J. Jonkel, Presence of polychlorinated biphenyls (PCB) in Arctic and subarctic marine food chains, *J. Fisheries Res. Bd. Canada*, *32*, 2111–2123, 1975.

Cade, T. J., J. L. Lincer, C. M. White, D. G. Roseneau, and L. G. Swartz, DDE residues and eggshell changes in Alaskan falcons and hawks, *Science*, *172*, 955–957, 1971.

Hanson, W. C., D. G. Watson, and R. W. Perkins Concentration and retention of fallout radionuclides in Alaskan Arctic ecosystems, in *Radioecological Concentration Processes*, edited by B. Åberg and F. P. Hungate, pp. 233–245, Pergamon Press, Oxford, 1967.

Hargrave, B. T., W. P. Vass, P. E. Erickson, and B. R. Fowler, Distribution of chlorinated hydrocarbon pesticides and PCBs in the Arctic Ocean, *Canadian Technical Report of Fisheries and Aquatic Sciences, No. 1644*, ix + 224 pp., 1989.

IARPC (Interagency Arctic Research Policy Committee), *Arctic Research of the United States*, Volume 4, Spring 1990, 1990a.

IARPC, *Arctic Research of the United States*, Volume 4, Fall 1990, 1990b.

Lowenthal, D. H., and K. A. Rahn, Regional sources of pollution aerosol at Barrow, Alaska during winter 1979-80 as deduced from elemental tracers, *Atmos. Environ.*, *19*, 2011–2024, 1985.

Monitor, Tungmetaller—förekomst och omsättning i naturen, 182 pp., Naturvårdsverket Informerar, Solna, Sweden, 1987.

Muir, D. C. G., R. J. Norstrom, and M. Simon, Organochlorine contaminants in Arctic marine food chains: accumulation of specific polychlorinated biphenyls and chlordane-related compounds, *Environ. Sci. Technol.*, *22*, 1071–1079, 1988.

Nash, T. H., Strategies for assessing Arctic contamination by exotic air toxics, Document prepared for USEPA Environmental Research Laboratory, Corvallis, OR, 1991, In press.

Norstrom, R. J., M. Simon, D. C. G. Muir, and R. E. Schweinsburg, Organochlorine contaminants in Arctic marine food chains: identification, geographical distribution and temporal trends in polar bears, *Environ. Sci. Technol.*, *22*, 1063–1071, 1988.

Rahn, K. A., and D. H. Lowenthal, Elemental tracers of distant regional pollution aerosols, *Science*, *223*, 132–139, 1984.

Salo, A., and J. K. Miettinen, Strontium-90 and cesium-137 in Arctic vegetation during 1961, *Nature*, *201*, 1177–1179, 1964.

Shaw, G. E., and M. A. K. Khalil, Arctic haze, in *The Handbook of Environmental Chemistry, Vol. 4/Part B*, edited by O. Hutzinger, pp. 69–111, 1989.

Stonehouse, B. (Ed.), *Arctic Air Pollution*, 328 pp., Cambridge University Press, New York, 1986.

Welch, H. E., D. C. G. Muir, B. N. Billeck, W. L. Lockhart, G. J. Brunskill, H. J. Kling, M. P. Olson, and R. M. Lemoine, Brown Snow: A long-range transportation event in the Canadian Arctic, *Environ. Sci. Technol.*, *25*, 280–286, 1991.

Wong, M. P., Chemical residues in fish and wildlife harvested in northern Canada, *Indian and Northern Affairs Canada Environmental Studies, No. 46*, 1985a.

Wong, M. P., Environmental residues in Canadian game birds, *Toxic Chemical Division Report*, 293 pp., Canadian Wildlife Service, 1985b.

Arctic Environmental Data Directory

D. R. Posson and M. O. Jones
U.S. Geological Survey, Reston, Virginia, U.S.A.

ABSTRACT

The Arctic Environmental Data Directory (AEDD) is being developed in cooperation with the U.S. Global Change Research Plan. The AEDD Working Group, with members from U.S. and Canadian agencies and academia, have described more than 300 Arctic data sets in a subset of an online data directory maintained by the U.S. Geological Survey (USGS), ESDD (the Earth Science Data Directory). Through various links known as the Inter-operable Directory, the contents of AEDD are made available to scientists who use the NASA, NOAA, NSF and USGS data directories. Thus, scientists studying global change have access to Arctic data, and scientists studying the Arctic have access to global change data.

The AEDD Working Group has sponsored development of a prototype Compact Disc Read Only Memory (CDROM) containing the indexed contents of the AEDD. Named Arctic Data Interactive (ADI), the disc was developed for use on Apple Macintosh and IBM PC-compatible computers, and uses a graphical and intuitive hypermedia user interface. The disc also contains portions of an Arctic Bibliography prepared in concert with the Polar Library Colloquy, sample full-text articles with illustrations, and selected data sets, including tabular data, text, and imagery. The ADI prototype is prepared as a model for organizing, presenting and distributing large quantities of Arctic and global change data and information to the science community. It is intended to be the first series of CDROMs with a consistent graphic design and user interface to place Arctic data and information on the desktop. The data are packaged with a powerful set of intuitive tools to navigate through and preview data sets from many disciplines and institutions.

AEDD and ADI are sponsored by the Inter-agency Arctic Research Policy Committee (IARPC) and the Inter-agency Working Group on Data Management for Global Change (IWGDMGC), with guidance from the U.S. Arctic Research Commission (ARC). Only a few Canadian and other international data-set references are included in AEDD. However, plans are underway to share the concepts and contents of AEDD and ADI with similar Arctic activities in other countries, with data management projects sponsored by the International Union of Geological Sciences (IUGS), and with the incipient data management activities in Antarctic research.

AD-P007 274

92-17956

Data for Polar Regions Research

Roy L. Jenne
National Center for Atmospheric Research, Boulder, Colorado, U.S.A.

ABSTRACT

Datasets available for polar research on global change topics are summarized. Emphasis is given to data that define the large, including rawinsonde data, surface meteorological observations, cloud drift winds, atmospheric analyses, sea ice, planetary radiation, and ocean forcing. Plans are discussed for making improved atmospheric analyses, using existing data. The use of CD-ROMs and DAT technologies for data distribution is discussed and selected CD-ROMs are listed.

SNOW COVER DATA

Weekly datasets of sea ice and land snow cover are based on satellite data. Many land stations report snowfall, but these data are still often hard to obtain, worldwide. A workshop "Snow Watch 85: Workshop on CO_2/Snow Interactions" produced a report "Snow Watch 85," which has over 20 papers that describe snow cover datasets, and make comparisons. It includes a discussion of weekly sea ice charts available from 1972. Weekly charts of northern hemisphere snow and sea ice boundaries have been prepared since 1966.

MICROWAVE DATA FOR SEA ICE, ETC.

Satellites that recorded passive microwave data from which sea ice and other variables can be estimated were: NIMBUS (ESMR instrument), Dec. 1972–May 1977; NIMBUS-7 (SMMR), Oct. 1978–Aug. 1987; DMSP (SSMI instrument), 9 July 1987–present. The status of the ice products evolves with time. The data are primarily located at NSSDC (Goddard), JPL, and the Snow and Ice Data Center (WDC-A) in Boulder, CO. Sea ice products on CD-ROM are becoming available.

For the north polar area, NCAR has a tape from John Walsh that has tenths of ice coverage on a 1° (60 n.mi.) resolution grid. The period is for each month (1953–1988 inclusive).

DRIFTING ICE ISLANDS

The U.S. took surface and upper-air observations from two Arctic Ocean ice islands, some for a number of years. The data for the IGY period (July 1957–Dec. 1958) are described in the report "Climatological Data for Arctic Stations." The surface data include the normal meteorological variables, and radiation. Similar data are also available for other years. NCAR has notes about data from U.S., U.S.S.R. and other ice islands in the Arctic.

ANALYSES FOR SOUTHERN HEMISPHERE

The availability of daily meteorological analyses for the southern hemisphere is summarized in Figure 1. Most of these are on tape, at NCAR.

COMMENTS ABOUT DATA FOR ANALYSES IN SOUTHERN HEMISPHERE

From about 45°S northward, one can accept the analyses for the whole 1951–1957 period. To describe conditions further south, there were a lot of ship reports for the summer whaling season (Nov.–March) for Nov. 1955 and later. Van Loon says that the summer (Nov.–March) analyses from Nov. 1955–on were of equal quality with IGY analyses. The sector for S. America, Ant. Penn. and Falklands had enough observed data for the whole period. There were very few Antarctic stations before 1956. The IGY analyses started June 1957.

The whalers were in the Atlantic and Indian Ocean areas for summers prior to Nov. 1955, but the Pacific Ocean did not have good ship observations until after that summer.

The S. East Pacific Sector

In early years (about 1952–Nov. 1954), the analysts believed that the subtropical high pressure area should extend farther south than it really does. Thus, they kept trying to force high pressures down into that no-data area.

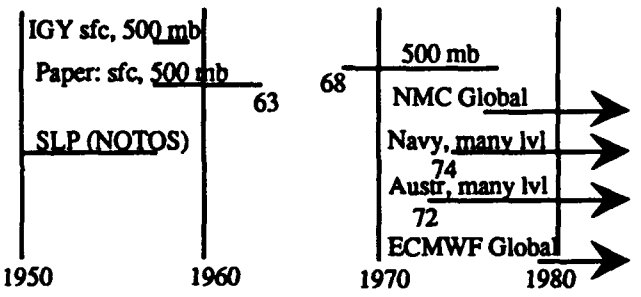


Figure 1. *Meteorological daily analyses for the southern hemisphere. SLP means sea level pressure. Automated analyses at many levels start in 1972. The data are all digital except for the one marked "paper." Archive details and data are at NCAR.*

Bad Easter Island Pressure

The pressure at Easter Island was about 9 mb too low for 18 months; good data started 24 Jan. 1958. This was determined from passing ships, etc. Dumb WMO rules forced the analysts (Van Loon and others) to plot the bad pressure on the maps for IGY, etc. German monthly analyses (published) were affected by the bad pressure.

Van Loon says that the IGY analyses and the summer analyses (Nov. 55 and later) were not affected by the bad pressure. He is fairly sure that all analyses for 1951–1958 used the corrected pressure for Easter Island.

ANALYSES FOR NORTHERN HEMISPHERE

Daily sealevel pressure analyses starting in 1899 are available from NCAR on tape. The Arctic sea level pressure was too high for many years. The analysts had few observations, and believed that an intense polar high pressure cell must exist. NCAR has hemispheric upper air analyses starting about 1946, at 700 and 500 mb. Other levels start in 1950 (300 mb) and 1963 (many levels).

NEW ANALYSES OF PAST ATMOSPHERIC CONDITIONS

From 1987–1990, there has been an increasing interest in making daily reanalyses of the global atmosphere. The data assimilation methods used to analyze the state of the atmosphere have shown major advances during 1985–1990. A forecast is a part of these methods; therefore, the analyses improve when the forecast model is improved. There has been a large advance in the capability of forecast models.

First there was talk about reanalyzing about two years in the 1980s as a pilot project. There has also been a clear interest in doing the whole period 1979–1990. Now there are plans to get ready to do the whole period 1958–1990. There were very few Antarctic observations prior to 1956.

Do we have the data inputs needed to reanalyze the atmosphere? There are many source datasets that can be combined to produce datasets that will be significantly better than the data that any center used for the operational analyses that are now available. Such projects to prepare data are starting for surface land data, rawinsonde data, aircraft data, and satellite cloud wind observations.

For the surface marine data, a project (COADS) was started in 1982 to prepare the best dataset of world observations from 1854–on. This has involved cooperation between NOAA/ERL, NCAR and NCDC/Asheville, [Woodruff et al., 1987]. MEDS, Canada is helping to prepare the drifting buoy data. COADS includes a significant number of additional ship reports obtained by waiting until delayed reports become available. The following table shows the number of reports after duplicates are eliminated for different delay times (during the 1980s):

Ship Reports Available	Delay Time
1200K per year	Real time
1860K per year	after 1 year
2100K per year	after 2 years
2220K per year	after 5 years

There are several existing datasets of global surface land observations, and rawinsonde data. Data are available from both telecom (real-time), from delayed, high quality, archives in national data centers and from previous data collection projects. The plan is to combine data from several sources and have initial datasets ready to start long-period reanalyses by 1993. It will take a 10-year effort to keep improving the availability and quality of data, especially for the earlier years. The results of these data preparation efforts will be valuable for many purposes besides reanalyses.

What data would be available from a reanalysis effort? The normal variables (temperature, pressure, wind, moisture) for the atmosphere would be available. In addition diagnostic terms such as precipitation, clouds, surface radiation, total surface energy budget, etc. would also be available. Also, the boundary layer conditions over the ocean and ice caps will be saved. The new surface winds would be used to drive ocean models for the whole period.

Bengtsson and Shukla [1988] published a paper that helped start the movement toward planning for reanalyses. In early 1989, a small workshop was held to consider the initiative of making reanalyses [Kinter and Shukla, 1989].

Jenne [1988] summarizes the status of datasets (and years of coverage) that can be combined to provide inputs for reanalyses. It also gives a history of reanalyses done for the FGGE period (1979) to help scale the effort. Many additional details are available from NCAR.

OUTPUT OF SNOW, TEMPERATURE, RADIATION, ETC., FROM ANALYSES

Starting in the late 1980s, the assimilation schemes used to analyze the atmosphere are good enough to produce many diagnostic terms from the associated forecast model. The variables include precipitation, snowfall, temperature, winds, clouds, radiation, surface stress, surface heat fluxes, etc. NCAR has a list of the variables that are available.

When reanalyses are made, these terms will be saved from the models, in addition to the normal pressure, temperature, wind, etc.

SATELLITE SOUNDER DATA

Several sets of global satellite sounder data are available. The sounder data have channels (such as window IR) that can be used for other purposes besides deriving atmospheric temperature soundings.

- NIMBUS SIRS, April 1969–April 1971
- NOAA VTPR, Nov. 1972–28 Feb. 1979 (8 IR channels)
- NOAA TOVS, 29 Oct. 1978–Present (channels in visible, IR, microwave, and for the stratosphere)

DATA FROM CLIMATE MODELS (DOUBLE CO_2, ETC.)

NCAR has data from several of the world's climate models. This includes five different model experiments for the present climate (1 x CO_2), and for a doubling of CO_2 (2 x CO_2). There are also two transient runs from GISS, one to the year 2062. EPA sponsored this effort (starting in 1987) to prepare data in common formats to support assessment studies of climate changes on crops, forests, rivers, etc. The primary datasets are 10 to 20 variables (precipitation, temperature, surface radiation, etc.) to support these studies. There are data for monthly means (for 10 years) of 1x and 2 x CO_2 climates. For some runs there are data for each individual model month. For one GFDL run we have daily output for a sample of three years in each of the 1x and 2x runs. The resolution of most climate models is now about 500 km, so they can't show the details of climate changes caused by local topography. Some higher resolution data will become available in May 1991.

USE OF CD-ROM AND DAT TECHNOLOGIES TO DISTRIBUTE DATA

The first CD-ROMs with data for the geosciences were produced in mid-1987. Now a flood of them are being prepared. A CD-ROM holds about 660 MB, compared to 125 on a high-density half-inch tape. Access time to any part of the disk is about 0.5 seconds. A reader costs about $700. The 4-mm digital audio tape drives (DAT) can be purchased for about $2000. These small tapes hold 1300 MB of data.

When a CD-ROM is sent to a user, software to access the data on a PC is also provided. Some simple browse displays are often included.

SELECTED DATA AVAILABLE ON CD-ROMs

The selection of data available on CD-ROMs is increasing rapidly. According to a CD-ROM company in London, there were 390 CD-ROM titles in Jan. 1989, 817 by Jan., 1990 and they expected 1100–1500 in 1991. By the end of 1989, some 340,000 drives had been sold. Following are several CD-ROMs available for the geophysical sciences:

Compact Disk of the National Meteorological Center Gridpoint Dataset. A selection of twice-daily grids for the northern hemisphere is given, resolution about 381 km, on the NMC octagonal grid. Some fields such as sea level pressure (has data from the Navy) and 500 mb are for the period 1946–June 1989. Other data at 850 mb, 700, 250 (winds) and 200 mb (height) start about 1962. This updates an earlier disk. (Produced June 1990, cost $150, contact NCAR or University of WA—address under "World Weather Disk").

International Station Meteorological Climate Summary. Gives detailed climatological summaries for 640 National Weather Service locations, plus domestic and overseas Navy and USAF sites. Limited summaries for another 5000 worldwide sites are given (equivalent to 250,000 pages of printed text). Data can be exported to spreadsheets, etc. Prepared at Asheville, about December 1990 (by NCDC, Naval Oceanography Command and USAF/ETAC. Cost $50). Contact NCDC, Federal Bldg., Asheville NC 28801.

A second disk will be available about Nov. 1991 that includes more data, and data for more stations, all long-period monthly means.

World Weather Disc. Weather and climate information for the world are on one CD-ROM. Some contents are:

- monthly data for about 2000 stations around the world, with some records dating back to the 1700s. This is from the monthly surface data tape from NCAR.
- average weather conditions at thousands of airports worldwide,
- daily weather data at hundreds of U.S. stations,
- data for many U.S. stations on temperature, precipitation, heating/cooling degree days, freeze, drought and soil moisture, wind, sunshine, lightning, thunderstorms, and tornados,
- datasets such as Local Climatological Data (LCD), U.S. Climatic Division Data, U.S. Monthly Normals, COADS ship statistics for oceans, worldwide airfield summaries,
- frequency and movement of tropical cyclones.

Contact C. Mass, Dept. of Atmos. Sciences (AK-40), Univ. of WA, Seattle, WA 98195, (produced in 1989).

Oceanographic Data. Disks with all available global XBTs, MBTs, BTs, etc. will provide temperature and salinity measurements in the ocean for about 1900–1990. The first CD-ROM will be for the Atlantic and Indian Oceans; the second will cover the Pacific (the rest of the world area). Both will be ready about June 1991 (by NODC; disks are low-cost). A prototype disk was prepared in 1989.

Ice and Snow (microwave data). CD-ROMs are being prepared with polar region microwave data from two satellites:

- SMMR, on Nimbus-7, for Oct. 1978–Aug. 1987,
- SSMI, on DMSP, for 9 July 1987–on.

Eight CD-ROMs have been prepared with gridded microwave polar area data for 9 July 1987–June 30, 1989. Data through Dec. 1989 will be ready by April 1991. Only the first 15 months of SMMR are done. The CD-ROMs have several channels of microwave data, on regular polar grids with resolution 25–100 km depending on the channel. Software permits the user to calculate ice variables. Prepared by WDC-A, Ice and Snow (NSIDC, disks are low-cost).

USGS Pristine River Flow Data. The USGS is preparing a set of river discharge data for about 1600 rivers that have not been heavily disturbed by dams. The average record length is 40 years; the longest is 115 years. Most sites provide daily data, about 50 rivers only have monthly discharge in this dataset. The data are in three forms on the CD-ROM; one form is simple ASCII files. The area covered is 50 states, Pacific Islands and Puerto Rico. The CD-ROM will be available in May 1991 from National Water Data Exchange, USGS, 421 National Center, Reston VA 22092. The cost will probably be under $100.

Antarctic Bibliography CD-ROM. The Antarctic Bibliography and other polar bibliographies are available on a CD-ROM from NIST, Suite 6, Wyman Towers, 3100 St. Paul St., Baltimore MD 21218. More information can be obtained from the Polar Information Program, National Science Foundation.

CD-ROMs from EarthInfo. This company has produced several CD-ROMs, mostly daily river discharge, and daily weather data:

- daily values of USGS streamflow, many rivers, for many years (four CDs cover the U.S.),
- peak daily river values (one CD, all U.S.),
- USGS quality of water measurements; (four CDs with surface water, four CDs with ground water),
- daily cooperative station data from NCDC; has daily

precipitation, max./min. temperature, snowfall, and evaporation for some stations. For several thousand U.S. stations, many from 1900–on (four CDs cover the U.S.),
- hourly precipitation (three CDs); most data are for 1948 and later,
- 15-minute precipitation (one CD), and
- surface daily water (streamflow and lake level) data for Canada (one CD).

A single disk costs $495 the first year and updates cost $295 each year. The discount is about 20% when the whole series of three or four disks is subscribed to. The cost is much higher if the intent is to keep a CD without ordering an annual update. Data handling and graphics tools are also sold (EarthInfo, 5541 Central Ave., Boulder, CO 80301).

Solar Variability Data Affecting Earth (sunspots, magnetics, particles). This disk includes sunspot data, magnetic readings from surface stations, and hourly solar wind parameters and interplanetary magnetic field data from satellites for 1963–December 1989. There are hourly, daily, and monthly magnetic data for about 200 world stations. Monthly sunspot data exist from 1749; daily data start in 1848. Most datasets on this CD-ROM end with Dec. 1989 (produced by NGDC June 1990; contact NOAA/E/GC, 325 Broadway, Boulder, CO 80303). This disk updates and replaces NGDC01 produced in 1987.

TOGA CD-ROM. This briefly describes the datasets on a TOGA CD-ROM published by Halpern et al., Oct. 1990. It has surface meteorological data and oceanographic data, plus sea level. All data are for 1985 and 1986.
- Hawaii daily sea level station data (72 stations),
- MEDS drifting buoy observations,
- Surface meteorological analyses from ECMWF (twice daily),
- UKMO ship observations (surface) for TOGA,
- IFREMER ship (subsurface) data,
- CAC sea surface temperature, 1950–1979 averages by months,
- Ocean pseudo stress from FSU (O'Brien) and Orstom (Servain),
- PMEL Moored current meter (2.2 MB) and temperature (0.8 MB) data.

Disks with Planetary Data. CD-ROMs have been prepared by JPL that have information for selected planets. There are now 12 CD-ROMs: Jupiter (3 disks), Saturn (2), Uranus (3), Neptune (4). For each planet, there are browse images and compressed images with good resolution. The disks were prepared 1989–1990. The four disks for Neptune would cost about $38, plus handling, for the general public; a two-disk set is $26. Contact NSSDC, Code 933.4, NASA Goddard, Greenbelt, MD 20771.

Some Additional CD-ROM Titles. A CD-ROM advertisement in *PC* magazine (March 26, 1991) included the following titles. It also had an ad for a CD-ROM drive and six CD-ROMs, all for $649. Selection of titles:
- Countries of the world; has text of over 100 study books;
- history, national anthems (sound), flags, economy, business statistics, etc. ($495);
- U.S. History on CD-ROM ($395);
- Birds of America, pictures and sound ($95);
- Mammals, has pictures and text;
- C library or shareware grab bag ($89);
- CIA world fact book ($99);
- World Atlas (color maps and statistics throughout world);
- News digest, current events; 600,000 entries ($795);

Contact Bureau of Electronic Publishing, Inc., Dept P, 141 New Road, Parsippany, NJ 07054.

NOAA Library CD-ROM Holdings. The NOAA Library (6009 Executive Boulevard, Rockville, MD 20852) maintains a list of its CD-ROM holdings. This list includes some CD-ROMs with reference material not included here, and gives some added comments about the contents of some CDs. Some of the CD-ROMs are:
- Library and Information Network Catalog (LINC): has bibliographic records of 19 NOAA libraries and information centers;
- Microsoft bookshelf: ten sources including a Dictionary, Bartlett's Quotations, World Almanac, business information sources;
- GPO: citations for government publications (books, reports studies, maps, more), updated bimonthly (coverage starts 1976);
- Aquatic sciences and fisheries abstracts.

Water Resource Abstracts. Collection of water-related research reports by government agencies, research institutes, independent contractors, and universities. Over 200,000 records list citations and abstracts to journal articles, monographs, reports, and other publications concerned with development, management and research of water resources. The source of the data is the U.S. Geological Survey, Water Resources Scientific Information Center. Updated quarterly. Produced by National Information Services Corporation. Coverage 1967 to the most recent quarter.

More Information. Much CD-ROM information has been omitted from this list because of space. Please contact NCAR, Data Support Section, P.O. Box 3000, Boulder, CO 80307 for more complete information and updates.

SOURCES OF INFORMATION ABOUT AVAILABLE DATA

Selected sources of information about data that are available are presented. Some indication of the types of information that can be found within each of these major sources is also included.

World Data Center for Glaciology (snow and ice)

The snow and ice data center is located at the University of Colorado (Boulder, CO 80309). It has listings of many datasets, including satellite film data. A few available reports are briefly listed to give a flavor of what is available:

GD7 (1979): Inventory of snow cover and sea ice data
GD15 (1984): Workshop on Antarctic Climate Data
GD17 (1985): Marginal ice zone bibliography
GD19 (1987): Passive microwave users workshop
GD20 (1988): Workshop on the U.S. Antarctic Meteorological Data delivery system

INFOCLIMA

(Catalogue of Climate System Datasets), 1989 edition, WMO/TD-No. 293, Geneva. The WMO (World Meteorological Organization) in Geneva includes divisions for both meteorology and hydrology. This data catalog has 507 pages (2.5 cm thick). It includes individual observations and summaries held at various data centers. It lists data centers world-wide. It has dataset descriptions in the categories:

•Upper air data (54 pages),
•Surface climatological data (140 pages),
•Radiation data at the surface (36 pages),
•Maritime and ocean data (50 pages),
•Cryosphere data (14 pages),
•Atmospheric composition data (18 pages),
•Hydrological data (42 pages),
•Historical and proxy data (28 pages).

920 datasets are listed. Those covering global and regional areas are handled separately from those with only national data. WMO expects to have a floppy disk version of INFOCLIMA (with a few updates) available by July 1991. Because of space, some contents will be shortened. The main version will require Dataease software ($800). WMO will consider preparing an ASCII version also.

U.S. National Online Data Catalog

An effort was organized by NASA, starting about 1987, to provide a central point where the user community could do an online computer search to help locate datasets (for climate and other disciplines). Various government agencies and research laboratories contribute information about their datasets. This central catalog has descriptions of about 1000 datasets, and listings of various data sources. Contact NSSDC, code 633, Goddard, Greenbelt, MD 20771.

National Center for Atmospheric Research (NCAR)

The relatively small data center within NCAR has a large archive of over 375 datasets (over 16 trillion bits). The data are from many sources: NMC, NCDC, various countries, ECMWF, USAF, research laboratories, etc. The catalog "Data Availability at NCAR," 1989, describes the datasets in 24 categories. (These include analyses, rawinsondes, ocean data, stratospheric datasets, paleoclimate, clouds, climate models, data received from U.S.S.R., etc.). The publication includes references to catalogs at other centers.

DOE Carbon Dioxide Information Center

This center at Oak Ridge, TN has a number of datasets relating to the carbon cycle and to climate. These include carbon dioxide measurements, fossil fuel emissions, and the role of oceans (tracers, coral growth, etc.). Many sets of biospheric data are included (carbon in vegetation, FAO land use, changes in soils, carbon in rivers, etc.).

A number of climate and paleoclimate data series are also available (northern hemisphere temperature, 1851–1900; central England temperature, 1659–1983; world-wide cloud cover, etc.). Some of the paleoclimate series include: Climap data 18,000 years ago; tree ring data bank; dryness/wetness indices in China for the past 500 years.

National Climatic Data Center and USAF/ETAC

This NOAA center (NCDC) at Asheville, NC gathers the climate observations for the U.S. It also helps WMO by gathering selected world data such as monthly surface and upper air data, CO_2 flask observations, and atmospheric turbidity for the world. There are many datasets. The most comprehensive summary of data there is in the *Handbook of Applied Meteorology*. Also see the INFOCLIMA listings.

The Air Force Data Center (USAF-ETAC) is co-located with NCDC. It has done a fine job of gathering selected world-wide observations. There are many sets of digitized observations that were not prepared elsewhere, especially international data for periods prior to 1965.

List of Data Types and Sources

A reviewer suggested that a table of data types and sources would be useful. Because of space and available time, this has not been possible to provide. The U.S. online catalog is described; it has a list of data centers. NCAR will prepare a list of data types and main data centers and sources of information.

Other Data Information

A book about the Antarctic [van Rooy, 1957] has much information about data and science. Chapter 2 (Sources of Meteorological Data for the Antarctic) includes the number and distribution of ship observations from 1920–1955. Radiosonde observations as early as 1939 are listed on page 173. Monthly surface data, sunshine observations, and cloudiness are also included.

REFERENCES

Bengtsson, L., and J. Shukla, Integration of space and in-situ observations to study global climate change, *Bull. AMS, 69*, 1130–1143, 1988.

Jenne, R. L., A global reanalysis; data inputs and methods, *Proceedings of the Thirteenth Annual Climate Diagnostics Workshop*, pp 79–84, Climate Analysis Center/NMC, 1988.

Jenne, R. L., *Data Availability at NCAR*, 45 pp., NCAR, P.O. Box 3000, Boulder, CO 80307. 1989.

Kinter, J., and J. Shukla, Reanalysis for TOGA, Panel meeting, Feb. 1989, University of Maryland, College Park, MD 20742. 1989.

Olsen, L. M., *Snow Watch '85: Glaciological Data, GD-18, WDC-A Glaciology*, University of Colorado, Boulder, CO, 80309. 1986.

Olsen, L. M., Data set availability through NASA's Climate Data System (NCDS), 9 pp., NASA/GSFC, Code 634, Greenbelt, MD 20771. 1990.

U.S.-DOE, *U.S.-DOE Carbon Dioxide Research Program, Publications and other Documents (and numerical data)*. CO_2 Information Analysis Center, Oak Ridge National Labs, P.O. Box 2008, Oak Ridge, TN 37831-6335. 1989.

U.S. Government, *Climatological Data for Arctic Stations (July 1957–December 1958) No. 1*, 63 pp., National Weather Service, Washington, DC, 1962.

van Rooy, M. P. (Ed.), *Meteorology of the Antarctic*, Weather Bureau, Pretoria, 1957.

World Meteorological Organization, INFOCLIMA, Catalog of climate system datasets, 508 pp., *WMO/TD-No. 293*, WMO, C. Postale, No 5 Geneva, 1989.

Woodruff, S. D., R. J. Slutz, R. L. Jenne, and P. M. Steurer, A comprehensive ocean–atmosphere dataset, *Bull. AMS, 68*, 1239–1250, 1987.

AD-P007 275

Interactive Information System: Database Elaboration for Biodiversity Research

92-17957

G. I. Belchansky, V. G. Petrosyan, and E. N. Boukvareva
Institute of Animal Evolutionary Morphology and Ecology, Academy of Sciences, Moscow, U.S.S.R.

ABSTRACT

The conceptual framework of an interactive information system (IIS) for biological research, with emphasis on biodiversity is presented. Topics include: (1) the general approach for synthesis of an IIS; (2) the elements of organizational structure of IIS-Biodiversity; and (3) the main problems of biodiversity research. Traditional biohierarchy is considered as the framework for elaborating the database structure and IIS architecture. The discussion is illustrated by some results of concrete elaborations. Under examination were the significance of functional subsystems on the local, state, and regional levels, the problems pertaining to the set-up of conceptional and logical models for a "Mammalian" component, and the elaboration of an integrated database including models for ecological studies with emphasis on biodiversity. Some parts of the present report are considered in general view, because the discussed problem has a multidisciplinary character.

GENERAL PROPOSITIONS

Biological diversity is one of the most generalized multidisciplinary characteristics of biosystems worldwide. Last decade, the attention to interdisciplinary research regarding this problem increased because of the sharp deterioration of global ecological situations, destruction of biodiversity as a result of human activities, and a growing understanding of the importance of biodiversity in biosphere functioning and, thus, in human life.

Rates of biodiversity destruction, as a result of human influence, manifest at different levels of biosystem hierarchy: extinction of species, diminishing areas of natural ecosystems, and the extinction of natural communities as a whole. Loss of stability and availability of the biosphere can be the result of these processes. The mechanisms of biodiversity destruction as well as the influence of diversity on biosphere stability, and its life-supporting functions, are very important aspects of the problem of biodiversity research.

Effective research of biodiversity requires vast amounts of data over a wide set of parameters and indices at different hierarchical levels (Figure 1). The hierarchy, beginning with the morphological structure and physiological parameters of biodiversity at the organismal level, including their genetics and phenotypic diversity, logically ascends to the levels of populations, species, and biocenosis. Interconnections with other biotic and abiotic characteristics are also important, for example, with climatic factors, stability, anthropogenic pressures, and changes of diversity parameters in space and in time, including ontogenetic and phylogenetic aspects.

Environmental biodiversity protection is traditionally considered at species-population level (genetic and phenotypic diversity in populations), and at the biocenotic and biosphere levels (species, community, and ecosystem diversity). It is necessary to solve the following problems for elaboration of effective measures for biodiversity protection: (1) to define critical levels of biodiversity loss, which lead to loss of stability and destruction of biosystems; (2) to define critical values of biosystem parameters (for example, population size or ecosystem area), which are necessary for conservation of required biodiversity level during required period of time; (3) to define the ranges of environmental factors (abiotic, biotic, and anthropogenic), which ensure biodiversity conservation. Solution of these problems can be based on results of fundamental research.

Effective investigations of the complex and multifaceted problem of biodiversity must incorporate contemporary

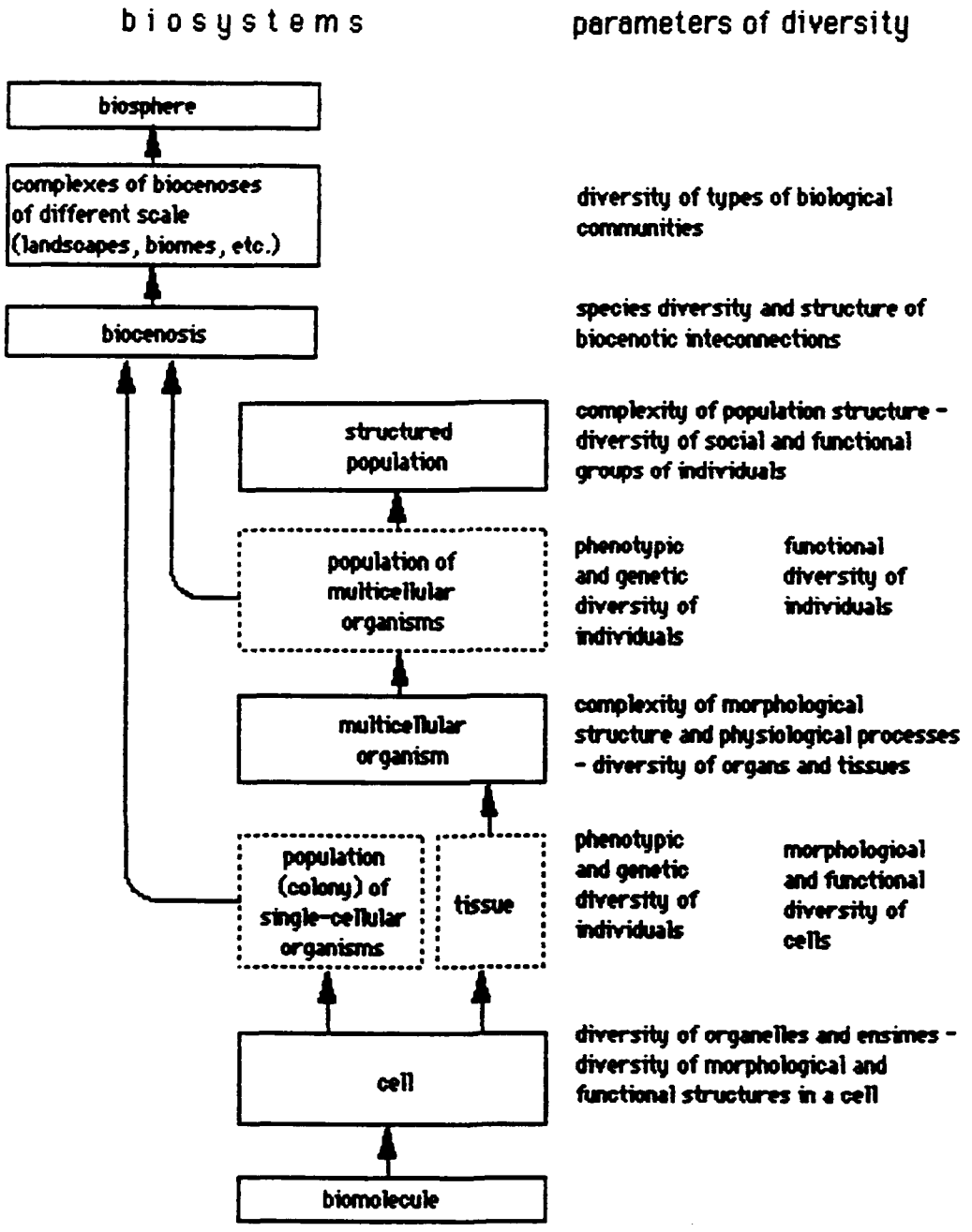


Figure 1. Some parameters of diversity in biosystems at different levels of biohierarchy.

information technologies. The automation and analysis of existing data and information about biosystems at different hierarchical levels, and the creation of an interactive (i.e., with real possibilities to integrate daua) information system is a highly urgent scientific–technical problem.

Our preliminary work in assembling an information system for biodiversity research has shown that standards of measurement, methodologies, and data formats have a fragmentary character. Elaboration and creation of the proposed IIS must have new principal characteristics, and include an elaboration of the general concept, an analysis of the main functional tasks and potential end-users, definition of systems of data collection and their documentation, followed by a step-by-step elaboration and creation of the working IIS subsystems.

Soviet scientists have been monitoring and recording ecological data for many years, largely carried out over the natural ecosystems of the Soviet Union following the Program of the Nature Chronicle initiated in the 1940s. However, to date, there are no automated information systems to support data processing and analyses. This drawback hinders the solution of top-priority tasks, such as the assessment of the

multi-year dynamics of the floral and faunal diversity in the reservations, determination of the optimal ratio between protected and unprotected territories, and so on.

The elaboration of such information systems for polar reservations is of vital importance in view of the necessity to understand the basic tendencies in the changing dynamics of population numbers, the spatial distributions of populations, and the influences of anthropogenic factors. Studies of animals, in particular large and small mammals, are of general biological interest because of the important role they play in biocenosis. Owing to some of their properties, such as their availability, short life span and frequent alteration of generations, the mass species of small mammals can serve as a convenient model to solve many problems of population and evolutionary biology.

In view of the above, scientists in the USSR today are elaborating a hierarchical IIS for reservations that is structured with respect to the traditional methods of monitoring and recording data. At the local level (the level of a reservation) the IIS is oriented at primary data, and will fulfill several basic functions, including: (1) to supply unified data to the IIS of the regional and state levels; and (2) to maintain the informational processes of unique investigations within the territory of the reservation.

The IIS of a region is based on some general principles but, at the same time, it has unique characteristics due to the specific features of the region in question. The IIS of the state level is based on the information received from the regional IIS, with emphasis on parameters that can be extrapolated to larger landscape units derived from remote sensing and regional thematic maps [Petrosyan, 1989]. The IIS of the state level can be employed, for example, to reveal general regularities in the functioning of ecosystems subjected to anthropogenic effects of different scales, to monitor the condition of the environment within the territory of the country, and so on.

THE ELEMENTS OF METHODOLOGY OF DATABASE STRUCTURE

The conclusions above allow discussion of some essential approaches to the synthesis of IIS. One of the most important problems in the elaboration of an information system is the development of the database structure. In general, solution to this problem must be based on a complete description of the functional organization of the database, including stages of info-logical and conceptual relationships (physical databases are created on the basis of logical data relationships and technical data processing capabilities). The detailed study of objectives, including sources of data and information, list of IIS users, forms of information documents, etc., are necessary for analysis of the functional-organization structure of IIS.

Sources of data and information for IIS can include programs of biosystem monitoring: forest service; corresponding sections of the "Annals of Nature" in Nature Reserves; calculations of marketable animals, agriculture and forest pests, and parasitologically important species; biological research programs and special research within the bounds of biodiversity; and information about biosystems that has been accumulated previously (literature, archives, indexes, scientific collections). Information systems that are functional or under development can be incorporated as subsystems of IIS. The IIS can be used by scientific centers for fundamental biodiversity research over different levels of biohierarchy or preparation of monographs and other publications (flora and fauna atlases), by services and organizations of nature protection and management for biodiversity monitoring and elaboration of conservation measures, and by educators in the field of ecological conservation and popular scientific information.

The main feature of the functional organization structure of the proposed IIS is its hierarchical character. Preliminary analysis showed that the IIS must have at least three levels with corresponding databases at local, national (regional), and international levels (Figure 2). Local databases include results from scientific programs at institutes, universities, museums, botanical gardens and other scientific centers, and databases of existing information from long-term monitoring of the biotic and abiotic components of local natural reservations.

One of the first and most important stages of database development is structuring the parameters (definition of main objects) at all levels of the biohierarchy. Data exchange between all levels of IIS must be provided. This work is rather labor-intensive. It must be done by specialists in different fields of biology and must have an integrative character. Effective interaction with the database across different levels of the biohierarchy can be ensured by providing cross-referenced access to parameters at different hierarchical levels in database structure. It is important to define the structure of the biosystem hierarchy during initial stages of the work. This task must be assigned to a special group of experts. Corrections to the initial database structure would be possible during the development of the information system.

Elements of a conceptual structure for diversity parameters at the levels of individuals, populations, communities, and ecosystems are shown in Figure 3. The structure at other hierarchical levels can be defined in an analogous way. In Figure 3, the block "parameters of communities and ecosystems" contains generalized parameters of biosystems, such as the level of spatial heterogeneity, parameters of productivity, etc. Parameters of soils can also be included in this block. Analysis of these parameters, together with parameters of species diversity and of biocenotic interconnections within local territories, allows delineation of biological communities at different scales. Thus, diversity of different types of biological communities over vast territories can be investigated.

Data for individuals within a population (species) provide quantitative measures to investigate diversity within the respective population (species). The fragment of the conceptual model for a local database reflecting the main characteristics of individuals is shown in Figure 4. In Figure 4, the block "parameters of populations" consists of data from field studies of populations. These data provide investigation of population size or density, sex–age structure, spatial structure, coefficients of death rate and birth rate, etc. Analysis of species composition and of sets of population parameters (for example, population sizes and character of biocenotic interconnections) within some territory provides the framework for studying diversity at biocenotic levels.

The fragment of a local database that reflects the main characteristics of mammal populations is shown in Figure 5.

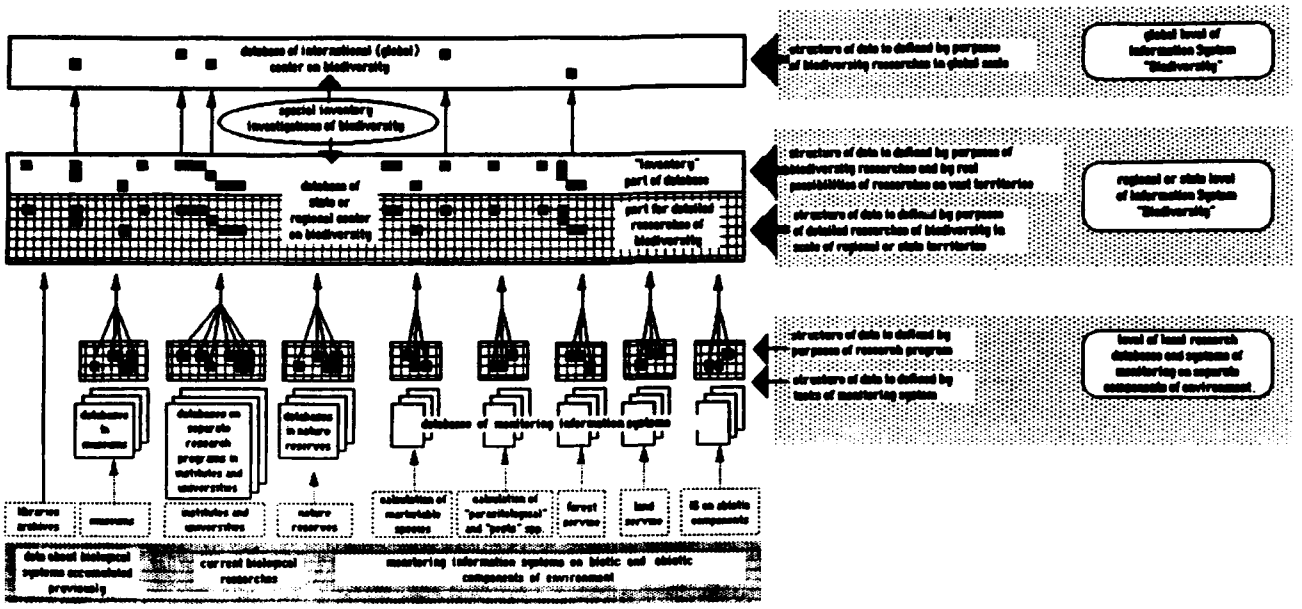


Figure 2. Connections between structures of databases at different levels of Information System "Biodiversity."

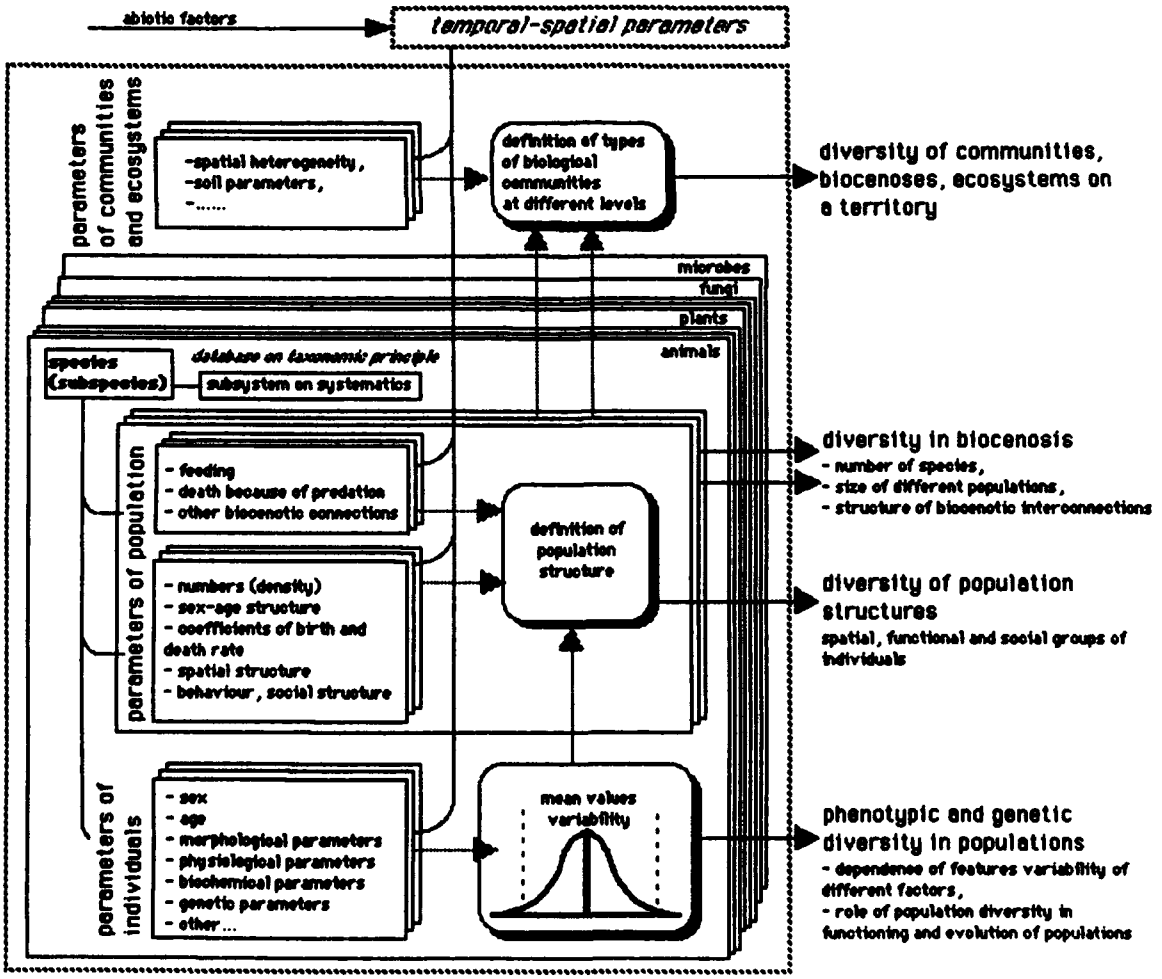


Figure 3. Elements of a conceptual structure for diversity parameters at the levels of individuals, populations, communities, and ecosystems.

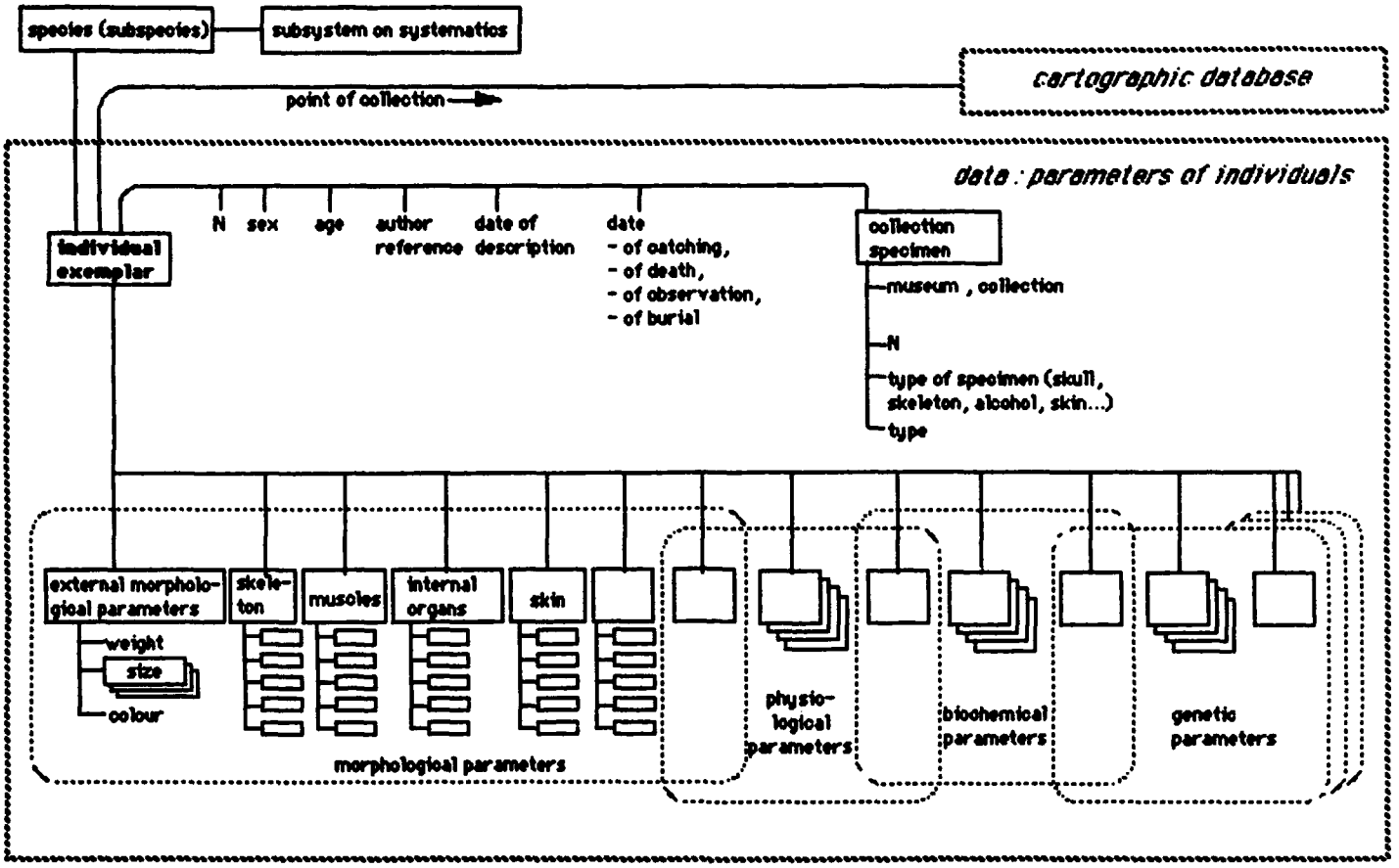


Figure 4. Elements of infological model of local database (preliminary objects).

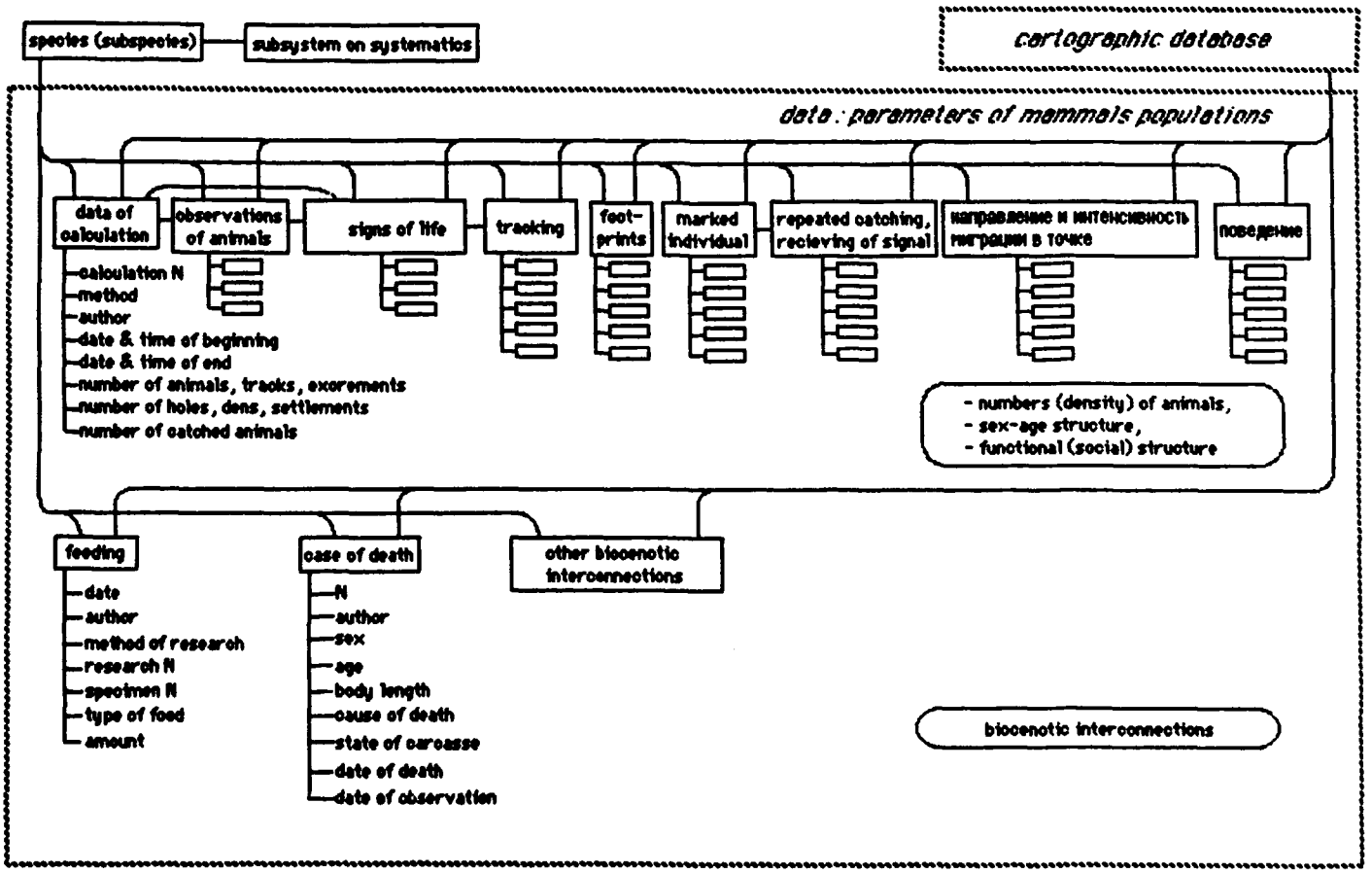


Figure 5. Fragment of infological model of database of a nature reserve (preliminary objects).

The present structure corresponds to the contents of research programs for the Nature Reserves of the USSR. All stages of database development for the IIS subsystem "Fauna" for the Visimsky Nature Reserve have been assembled by the authors of the present report [Belchansky et al., 1990]. The database Fauna of the Visimsky Nature Reserve was structured with respect to the present-day subject concept and collection of data on mammalian fauna for the reservations of the USSR. The conceptual model was based on taxonomy, methods of observation, location, habitat, reproductive status, morphology, physiology, age, etc. The total number of simple and complicated attributes exceeded 176 units. The optimal relational model of parameters was built using special procedures. Here are the following main stages in elaborating the optimal relational model:

(1) Analysis of the existing canonical functional dependencies (CFD) of the attributes in the subject region under consideration and the set-up of the initial system of CFD.

(2) To close the initial system of CFD.

(3) To obtain all possible minimal solutions for closing the CFD.

(4) To build the image of the database model by using the rule of additivity (for CFD).

(5) In case of any disturbance in the semantics of the model, the system of CFD should be additionally determined and all stages repeated, beginning with stage 2.

The databases of the information systems are conditionally divided into two subsystems: a subsystem of parameters of biosystems (above-mentioned subsystems of parameters of individuals, populations and species, which can be constructed on taxonomic principle, subsystems of parameters of communities and ecosystems) and a subsystem of data about spatial structure of biosystems (at species-population and higher levels this subsystem can be presented as a cartographic database). Undoubtedly, the databases of spatial structure and of biosystems parameters must have corresponding interfaces. The databases of spatial structure of biosystems facilitate analyses of the corresponding variables as parameters of diversity in biosystems (for example, parameters of spatial structure of populations, of spatial heterogeneity of biocenosis, etc.).

Integration of parameters at corresponding levels with cartographic databases supports analysis of biodiversity parameters in space and in time, as well as the interconnections between biodiversity and other characteristics of biosystems, and the dependence of these parameters on environmental factors based on the comparison of parameters observed at the same points in both space and time. Interconnections between parameters of different biosystems, for example, between animal and plant populations, can be established in this way.

SOME GENERAL QUESTIONS OF IIS ELABORATION AND CREATION STRATEGY

The general strategy for creating and implementing an IIS must be defined on the basis of its potential users, and on the basis of the realistic possibility of its creation. The information system must support fundamental biological research, biotic monitoring, and elaboration of practical measurements. It is highly important to provide an integral approach to IIS elaboration, including the definition of technical hardware specifications. The integral approach will ensure compatibility of different subsystems. Elaboration, creation and maintenance of IIS software and hardware must be done by a group of specialists in information technologies.

One of the important considerations during the initial stage of IIS development is the distinction between two approaches: (1) elaboration of database structure as a complete reflection of information, which is being collected now and has been accumulated previously; and (2) orientation of data structure for examining concrete hypotheses and dependencies. Strict orientation of data structure to examination of concrete hypotheses and dependencies, which today seems the most interesting approach, reduces possibilities of using the databases for solution of other tasks in the future. Accommodating the complex and multidisciplinary scope of biodiversity requires, in the first turn, systematization of all accumulated knowledge. Elaboration of database structure as the most complete information model of contemporary knowledge about the biodiversity and research directions will allow scientists to expand in required directions for examination of new hypotheses. These approaches can be realized through the creation of a distributed database. Stages of creation, via particular subsystems, can be defined in accordance with today's necessities, while maintaining flexibility for addressing tomorrow's hypotheses.

Detailed information about biodiversity processes and about their role in biosystem functionality, at different hierarchical levels, can be accomplished through research of natural biosystems only in some geographic points, or through results of experiments and modeling. Inventory observations of biodiversity over vast territories can be carried out only for a limited set of parameters (in the first turn, establishing species composition, i.e., faunal and floral research). This group of data can be considered as an "inventory" component of the database. Structure of this data is a necessary fragment of the overall information required for biodiversity research.

In our opinion, the evident necessity to inventory existing biodiversity must not move aside works on detailed research of the fundamental problems of biodiversity. Elaboration and creation of program means and mathematical tools for supporting the above directions must be done simultaneously with inventory, and compatibility of these directions must be ensured.

It is obvious that realization of the present conception requires an interdisciplinary, step-by-step approach [Belchansky et al., 1991]. The distributed hierarchical structure of the database allows the creation of IIS-Biodiversity in a step-by-step, optimum sequence (some subsystems can be created earlier, and others later). The present conception of creation of the information system "Biodiversity" can be considered as a base for corresponding programs, which can be elaborated by special working groups at national and international levels.

ACKNOWLEDGMENTS

The authors gratefully appreciate the professional help offered by David Douglas (Alaska Fish and Wildlife Service Center, U.S. Fish and Wildlife Service) on every step of preparation of this report. Many thanks.

REFERENCES

Belchansky, G. I., E. N. Boukvareva, and V. G. Petrosyan, An interactive information system for a reservation, in *Reservations in the USSR, Their Present and Future*, M., USSR Academy of Sciences (in Russian), 1990.

Belchansky, G. I., E. N. Boukvareva, and V. G. Petrosyan, Nekotorie podkchodi k siutezu interaktivnikch informatsionnikch sistem dlia izychenia biorazuoobrazia. Obschaia biologia, M. An CCCR, 1991.

Petrosyan, V. G., Conceptual elaboration of database for the system of mathematical models of Biosphere Reserves, International Symposium on the State-of-the-Art of Remote Sensing Technologies for Biosphere Studies, Moscow, 18–22 September, 1989.

A Comprehensive Collection of Arctic Meteorological Soundings for use in Climate Studies

Jonathan D. Kahl
Department of Geosciences, University of Wisconsin-Milwaukee, Milwaukee, Wisconsin, U.S.A.

Patrick J. Sheridan and Russell C. Schnell
CIRES, University of Colorado/NOAA, Boulder, Colorado, U.S.A.

ABSTRACT

Recent theoretical and observational evidence has indicated that the Arctic is a region in which climatic warming due to to increasing levels of CO_2 and other greenhouse gases may be first and most easily detected. To date, observational studies of Arctic temperature trends have focused on surface measurements at coastal and inland stations. However, the theoretical studies indicate that climatic warming in the Arctic is not restricted to the surface, but will extend throughout the lower troposphere with increasing intensity toward the North Pole.

We will describe a unique collection of temperature, moisture and wind sounding data north of 65°N. This data base represents the only complete and comprehensive collection of vertical profiles of these parameters both within and surrounding the Arctic basin. The data base includes: (1) the complete historical series (30–40 years) of all coastal and inland radiosonde measurements throughout the North American, Greenland, Scandinavian and Soviet Arctic; (2) aircraft dropsondes from the "Ptarmigan" weather reconnaissance flights in the Alaskan Arctic, 1947–1962; and (3) soundings from U.S. and Soviet drifting ice stations, 1950–1988.

The sounding data base is currently being analyzed to examine temperature trends throughout the Arctic troposphere. The data are also being used to investigate the climatological characteristics of the planetary boundary layer and low-level temperature inversion. Preliminary results of these investigations will be presented.

AD-P007 276

Development of Sea Ice Data Sets from Passive Microwave Satellite Data: Preliminary Lessons

R. L. Weaver, V. J. Troisi, and C. S. Hanson
National Snow and Ice Data Center, CIRES, University of Colorado, Boulder, Colorado, U.S.A.

92-17958

ABSTRACT

On 19 June 1987 the Defense Meteorological Satellite Program launched the Special Sensor Microwave Imager (SSM/I), a passive microwave radiometer that provides near real-time data for operational use. A computer-based data management system installed at the National Snow and Ice Data Center (NSIDC) extracts polar SSM/I data and produces products suitable for immediate scientific use by the research community. This data processing and management system has been jointly developed by the NASA Ocean Data System (NODS) and NSIDC for NASA Polar Oceans Program.

The premise behind this project is that data archiving, quality control, gridding, and distribution are cost-effective when managed at a central data management facility, and that such an effort provides data of interest, and in forms useful, to the polar remote sensing community and to scientists in cognate disciplines such as atmospheric and ocean sciences.

The system design has changed from the initial 1984 online service concept to the 1990 model, distributing data on CD-ROM and relying on the expertise of individual investigators, and the computing resources of their home institutions, for data analysis. The evolution of the data processing and delivery system, the forces that have driven the changes, and a preliminary assessment of user response are presented in this paper.

INTRODUCTION

The polar regions play a key role in the global environment, serving as primary sinks for energy transported from lower latitudes by the atmosphere and the oceans. They may also serve as sinks for anthropogenic aerosols and trace gases. The variable sea ice cover of the polar oceans greatly influences the world ocean circulation and may contribute to climate change. As well, the polar regions have been shown by modern and paleoenvironmental evidence, and by modeling assessments, to be especially sensitive to climate change.

Over the past two decades, remote sensing by satellite sensors employing all portions of the electromagnetic spectrum has played an increasingly important role in monitoring the polar environment. The utility of visible and infrared sensors on satellite systems, such as the NOAA AVHRR, DMSP OLS, Landsat, and SPOT, is limited for monitoring surface conditions due to persistent cloud cover over the polar oceans and low solar illumination during much of the year. The advantage of using microwave radiometers for mapping sea ice is that microwave emissions from the surface can be monitored year-round with minimal interference from atmospheric moisture. Although the global-scale data exhibit considerable noise due to the nature of the sensors, the remote sensing technique provides a good indicator of sea ice variations over interannual time periods.

Data from various microwave sensors have been collected more or less continuously since 1973 (Figure 1), forming the basis for longer-term monitoring of sea ice [c.f. Gloersen and Campbell, 1988]. The sensor now flying on the DMSP F-8 Satellite is the Special Sensor Microwave Imager (SSM/I), the first passive microwave sensor to pro-

SENSOR HISTORY

HISTORY OF PASSIVE MICROWAVE SENSORS

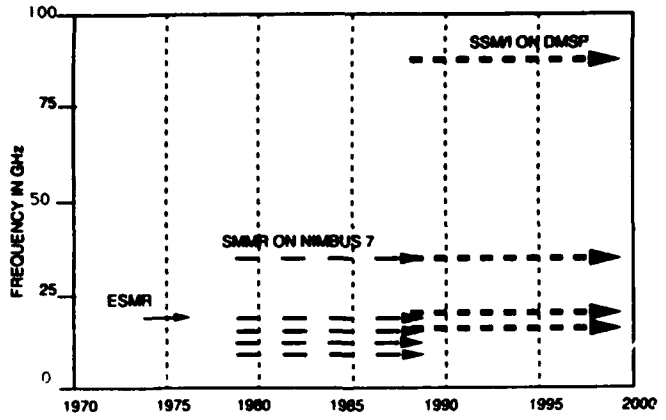


Figure 1. History of passive microwave sensors. Dashed lines of varying thickness indicate time coverage at each frequency in GHz.

1984 MODEL

ALL FUNCTIONS SITUATED ON VAX COMPUTERS AT NSIDC

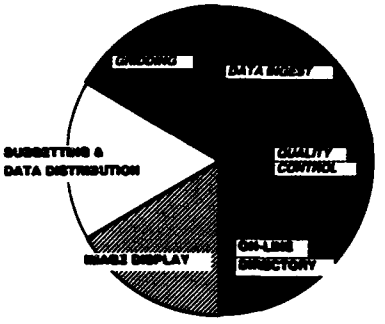


Figure 2. Cryospheric Data Management System, 1984 conceptual model: Central facility.

vide operational data and geophysical products. SSM/I instruments are planned to fly on DMSP platforms for at least the next ten years. The SSM/I provides seven channels of data: dual-polarized radiances at 19.3, 37 and 85.5 GHz and single-polarized radiance at 22.2 GHz. The highest spatial resolution (12.5 km) is provided by the 85 GHz channels.

HISTORY OF THE PROJECT

The NASA-funded effort to archive and distribute SSM/I sea ice products started in 1982. In order to ensure effective use of the SSM/I data for polar cryospheric research, NASA Polar Oceans Program established a Science Working Group (SWG) chaired by Dr. N. Untersteiner. The SWG was tasked to decide which sea ice research problems could most appropriately be addressed using SSM/I data and to define the associated data requirements [NASA-SAWG, 1984].

The general objectives laid out by the SWG included the following:

(1) To provide researchers with gridded brightness temperatures and geophysical data products for the polar oceans;

(2) To make such data conveniently available to a large number of users; and

(3) To facilitate research on (a) sea ice growth, motion and decay, (b) ocean circulation, and (c) climate change.

Rather than design a totally new system for processing SSM/I data, it was decided to adapt the existing Pilot Ocean Data System (now NASA Ocean Data System or NODS). A cooperative project was undertaken by the JPL-NODS and NSIDC staffs to adapt the NODS (PODS) system to the SSM/I data stream, with JPL programming staff to modify the software for SSM/I ingest, product generation and distribution, then "port" it to NSIDC computers, where it would be placed in operation. NODS would be the developer and NSIDC the operator of the SSM/I processing system.

THE 1984 MODEL

When NODS began working on the SSM/I processing system, the only existent model was the centralized data management facility. The following set of assumptions formed the basis for this model:

(1) The system was expected to serve the novice as well as the experienced user;

(2) Minicomputers (VAX class) were the only cost-effective means of data processing for the anticipated volume of data. Scientific workstations were not yet viable; and

(3) Magnetic tape was the internationally accepted medium for transfer of large volumes of data.

Data ingest, quality control, grid production, browse, catalog, data extraction and online display were all part of a closely coupled hardware/software system residing in a single CPU (Figure 2). The model postulated that users would dial up the data system, browse the gridded products, select a subset, and download over the communications circuit. Alternatively, users could request the products be sent by mail on nine-track magnetic tapes.

During 1985–1986, multiple DEC VAX 780s were employed at JPL in a cluster environment, permitting data ingest to be split apart from the various data service functions. This hardware configuration was copied at NSIDC using MicroVAX systems. Also during this time, JPL and others began experimenting with CD-ROM technology as a means of distributing data. These two changes, the availability of small, powerful workstation-type CPUs and the cost-effectiveness of CD-ROM as a distribution medium, led to a more efficient data management operation.

THE 1990 MODEL

The current model (Figure 3) retains portions of the original concept in its central network of CPUs employed for data ingest, quality control, and grid production. Data are distributed on CD-ROMs, moving the subsetting, extraction,

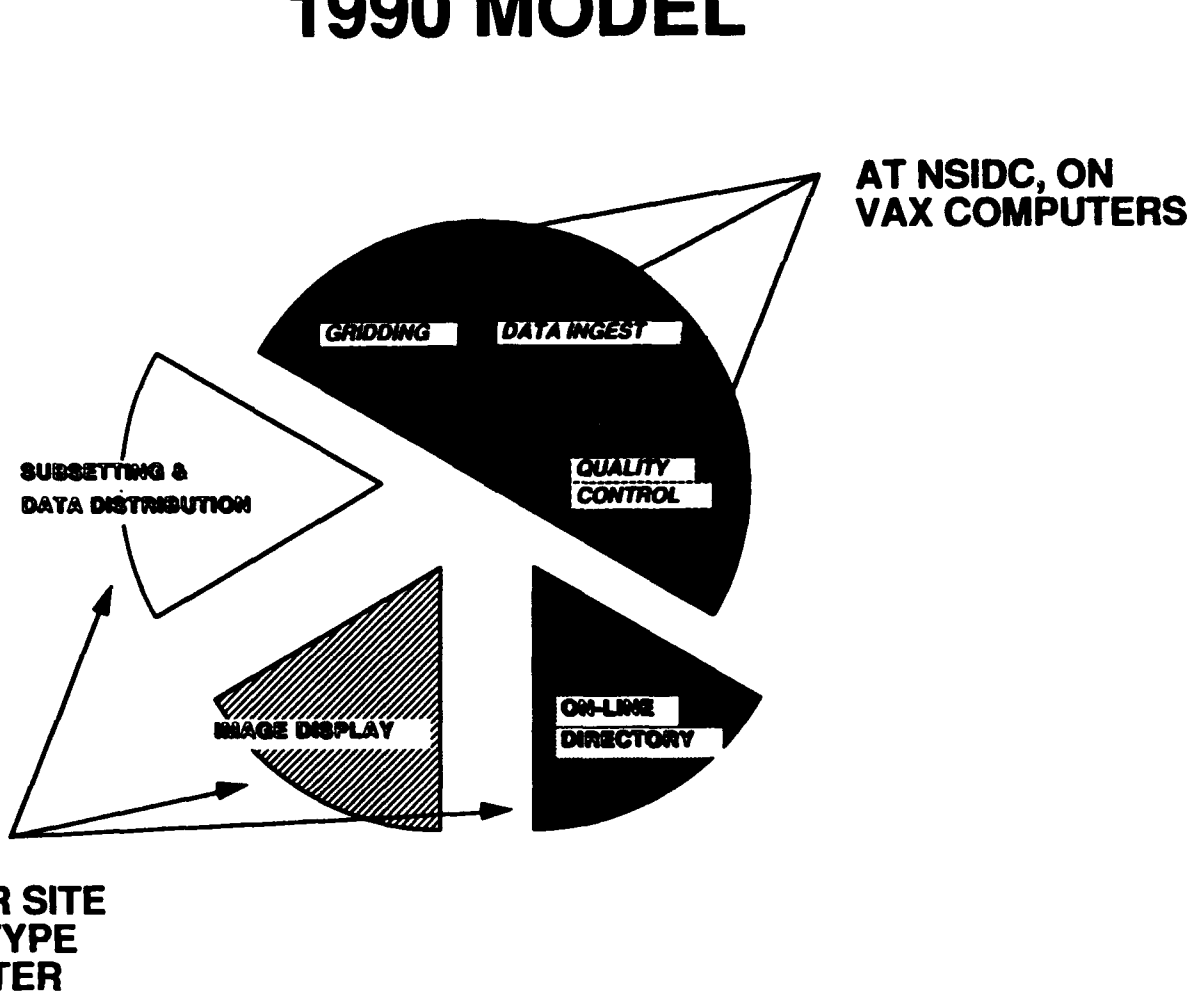


Figure 3. Cryospheric Data Management System, 1990 conceptual model: Distributed system.

and browse (image display) functions to each user's site via software that operates on a PC/AT-class personal computer. The software is provided to users on floppy disks, facilitating distribution of updates and enhancements.

These changes came about in April 1988 at a meeting of the Satellite Ocean Data Systems Science Working Group NODS Advisory Panel. It was decided that the polar oceanographic user community could no longer be considered "novice" computer users, since most had access to PCs and some had acquired scientific workstations. The Panel agreed that AT-class PCs were powerful enough to extract and display the gridded SSM/I products, and in some cases adequate for scientific analysis of the image data. There was also strong support for the concept of distributing the gridded products on CD-ROMs, so that each scientist could have a complete archive on his or her own desk. Thus the concept of a centralized data distribution system for SSM/I data gave way to that of a more limited central facility focusing on data ingest, quality control and grid production with general distribution on CD-ROM. This is the current model at NSIDC.

CURRENT PRODUCTS

The NASA Science Working Group for SSM/I [NASA-SAWG, 1984] recommended four distinct products for the SSM/I archive: global swath-oriented brightness temperatures for all frequencies and polarizations; gridded daily average brightness temperatures for polar regions; gridded total ice concentration, averaged over a 3 day period (i.e., 1 grid/3 days) and multi-year ice fraction for polar regions; and daily ice boundaries. The ice concentrations were to be calculated using the NASA Team Algorithm, which is an implementation of the Nimbus Team Algorithm [Cavalieri et al., 1984; Gloersen and Cavalieri, 1986] with appropriate changes to the brightness temperature tie points.

The Swath-Oriented Brightness Temperature Archive is the basic collection of System Data Records (SDR) from which all data products are generated. These ingest swath antenna temperatures are converted to brightness temperatures through application of an antenna pattern correction algorithm. Time regressions and other irregularities in the lower five channels due to data transmission are removed from the data stream, with the resultant data placed in the NSIDC Rapid Access Archive (RAA). These data are physically stored on 12-inch optical disks.

After launch a significant (up to 75 km) geolocation error was reported by several users. No attempt to correct the geolocation error has been made in the RAA, as only limited access to the RAA is possible. The NSIDC RAA is designed to produce gridded products, not to extract orbital data for

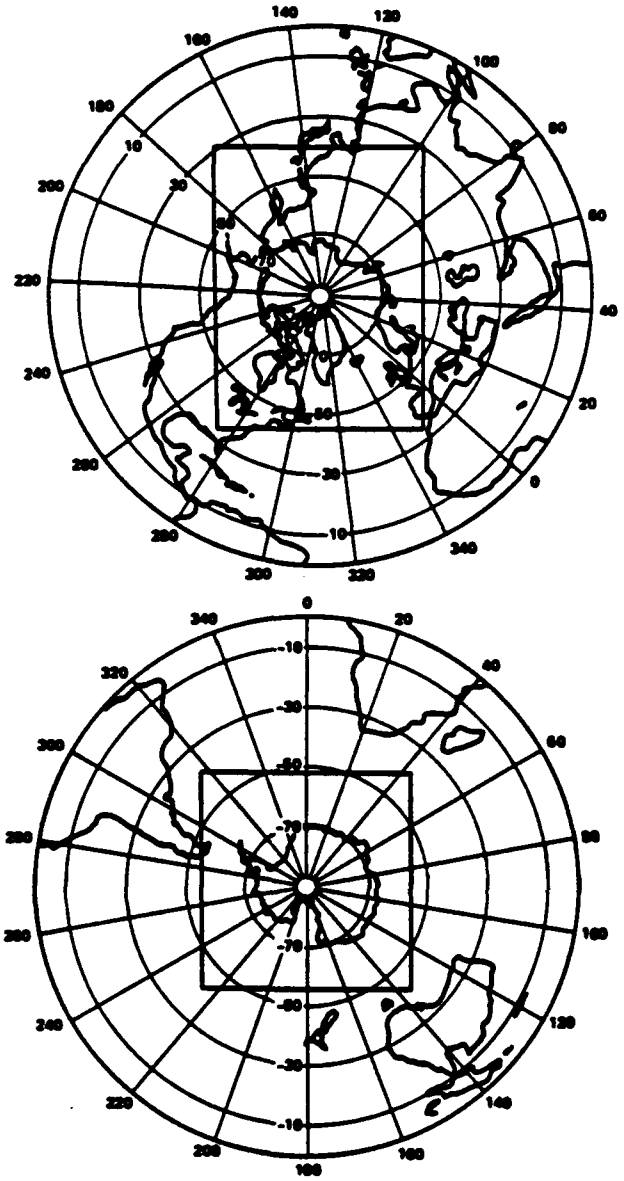


Figure 4. SSM/I North Polar (top) and South Polar geographic grids, polar stereographic projection. Rectangular boxes indicate coverage of the SSM/I gridded sea ice products.

distribution. Most requests for orbital or swath data are directed to NOAA-NESDIS-SDSD (Room 100, Princeton Executive Center, 5624 Allentown Road, Camp Springs, MD, 20233; telephone 301-763-8400), the archive of record for SSM/I orbital data, or to Remote Sensing Systems Inc. (RSS) (Dr. Frank Wentz, Remote Sensing Systems, 1101 College Avenue, Suite 220, Santa Rosa, CA, 95404; telephone 707-545-2904), the current supplier of the SSM/I antenna temperature data.

SSM/I Gridded Products are generated from the RAA onto both north and south polar grids (Figure 4). These are polar stereographic projections, using U.S. Geological Survey formulae [Snyder, 1982] to convert between geodetic and Cartesian coordinates. The ellipsoid is based upon the Hughes ellipsoid, similar to those presented by Snyder. The SSM/I grids have the standard latitude at 70°, with the origin of the grids at each pole.

There are six SSM/I grids, three for the Northern Hemisphere (N3A, N3B and N3C) and three for the Southern Hemisphere (S3A, S3B and S3C). The "A" grids contain the 85 GHz brightness temperatures, the "B" grids contain brightness temperatures from all other channels, and the "C" grids contain calculated sea ice concentrations. Although the resolution varies, each grid represents the same geographic area, with multiple parameters interleaved in each grid cell. Details of the grid structure and content may be found in the SSM/I CD-ROM user's guide [National Snow and Ice Data Center, 1990]. Gridded ice extent was dropped from the product suite because ice extent can be extracted readily by the user from the sea ice concentration grids.

For 1987–1988 data, NSIDC applied a geolocation correction based on the roll, yaw and pitch angles of the DMSP spacecraft. The algorithm that corrects for both along-track and cross-track errors was developed at the University of Massachusetts [NSIDC, 1989]. Beginning with the 1989 data, Remote Sensing Systems, Inc., began computing its own latitudes and longitudes in order to correct these location errors. Even so, a 0.5° yaw error appeared in the data. RSS then supplied NSIDC with an algorithm designed to correct this constant yaw angle offset [Wentz, 1989]. This algorithm has replaced the University of Massachusetts correction algorithm in the production of SSM/I brightness temperature grids at NSIDC.

NSIDC has recently completed a location quality assessment [Sandoval and Troisi, in preparation] with these gridded data without finding concrete evidence of significant geolocation error. Final conclusions have not yet been drawn from this study, but if the results of this or other studies warrant, the data could be reprocessed and a new CD-ROM product made available for distribution.

Gridded brightness temperatures for 9 July 1987 to 24 July 1988 have been released on four CD-ROM disks. To date, no sea ice concentrations have been distributed, although software to calculate sea ice concentration using the NASA Team Algorithm has been provided with all CD-ROM sets sent to users. The NASA SSM/I Sea Ice Algorithm Validation Team Final Report [Cavalieri et al., 1991], containing the final approved tie points for the NASA Team Algorithm, will be released soon. NSIDC will produce and distribute a sea ice concentration product based on this algorithm as soon as the report is released. As of 31 March 1991, the NASA Team Algorithm tie points have been approved and provided to NSIDC. Production of the sea ice concentration time series CD-ROM has begun, with projected completion in third quarter 1991.

At an April 1990 SSM/I Sea Ice Algorithm Workshop at Goddard Space Flight Center several alternate algorithms were presented by members of the community. Intercomparisons of these candidate algorithms are being carried out at this time. If any of these alternative algorithms are shown to perform more accurately than the Team Algorithm, NSIDC may also produce a second sea ice concentration CD-ROM set using the alternate algorithm(s).

ASSESSMENT OF USER RESPONSE

As of 6 June 1990, 229 CD-ROM sets have been distributed (Figure 5). A questionnaire was included with each

CD-ROM DISTRIBUTION

- **229 CD-ROM BRIGHTNESS TEMPERATURE DATA SETS (VOL 1-4) DISTRIBUTED AS OF 6 JUNE 1990**
- **USER TYPES ARE :**

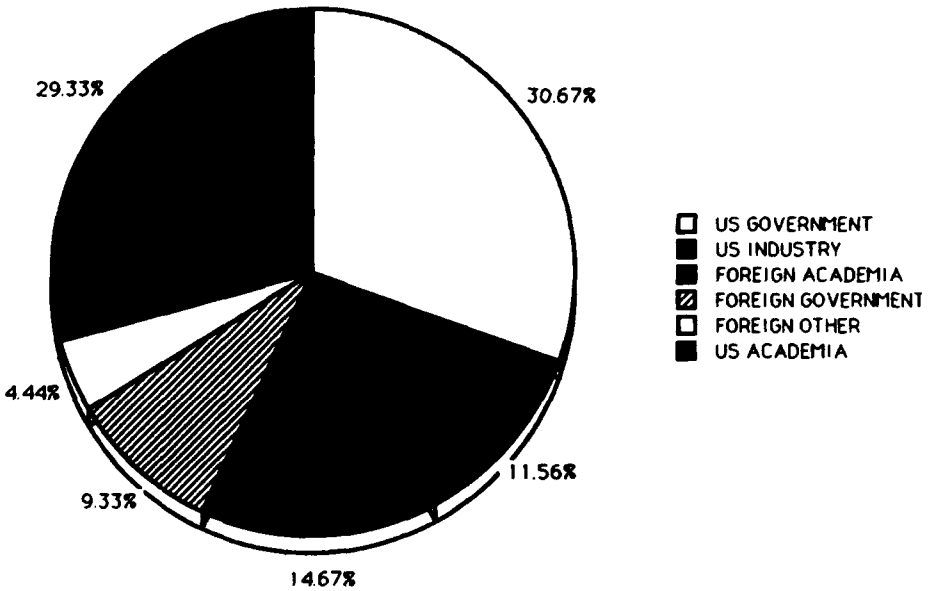


Figure 5. Distribution of SSM/I CD-ROM as of 6 June 1990. U.S. Government and U.S. academic users predominate.

CD-ROM shipment; 29% (67) have been returned to date. Some interesting information is found in the responses:

(1) 93% (62) of users returning the questionnaire would like to receive more SSM/I data on CD-ROM;

(2) 79% (53) of users returning the questionnaire would like to receive the SMMR data (1978–1987), also published on CD-ROM;

(3) Comments added to the questionnaires were uniformly positive with the exception of one non-specific complaint about the software (now being followed up by NSIDC staff) and one very strong demand for Apple Macintosh versions of the extraction and display software.

There is not yet sufficient specific feedback to provide an accurate assessment of user satisfaction. However, the 62 respondents who wish to receive additional SSM/I data on CD-ROM indicate satisfaction with the product at least at the level of willingness to continue using the product. Because the first distributions occurred only five months ago, we believe it may be too early to draw conclusions about either the acceptability of the gridded products or the utility of the distribution format.

CONCLUSIONS

There are several generalizations that can be drawn from the past eight years of effort, regarding data management and the SSM/I data products. It is clear from the relatively rapid technological changes that have taken place that the operative concepts of 1984 do not apply in 1990. We conclude that a responsive data center is one that is able to take advantage of technological advances. NSIDC is fortunate in the case of SSM/I data processing to have had the resources and expertise available, both locally and at JPL, to incorporate changes in technology.

Likewise, the needs and capabilities of the user community to digest digital data have changed markedly as a result of the same technological advances. A data center serving a dynamic user community must adapt to these changing needs, no matter how often they change. It is important to note there is continuing dynamic tension between available resources and meeting these (sometimes strident) demands for modified products.

It is too early to assess completely the adequacy of the gridded passive microwave products or the viability of CD-ROM as a distribution medium. Preliminary indications suggest, however, that both the product and the medium are acceptable and are being used actively for research and algorithm development. NSIDC continues to solicit and monitor user feedback. It is worth noting that verbal comments in support of "getting the data out to the users" by means of the CD-ROMs are numerous and frequent. There

is considerable, but not overwhelming, support for adaptation of the CD-ROM product to SUN, Macintosh, and VAX CPUs. Macintosh access and display software is under development at NSIDC in association with Dr. W. Emery (University of Colorado, Colorado Center for Astrodynamics Research). A "beta" version of this software is now being distributed to users who have indicated an interest, for evaluation and comment.

ACKNOWLEDGMENTS

We wish to acknowledge the continued support of the NASA Polar Oceans Program through Research Grant NAGW-641 to the University of Colorado, which has funded SSM/I data product development. The National Snow and Ice Data Center is operated for NOAA by the University of Colorado, Cooperative Institute for Research in Environmental Sciences.

REFERENCES

Cavalieri, D. J., P. Gloersen, and W. J. Campbell, Determination of sea ice parameters with the NIMBUS-7 SMMR, *J. Geophys. Res.*, *89*, 5355–5369, 1984.

Cavalieri, D. J., J. Crawford, M. Drinkwater, W. Emery, D. T. Eppler, L. D. Farmer, M. Goodberlet, R. Jentz, A. Milman, C. S. Morris, R. Onstott, A. J. Schweiger, R. Schuchman, K. Steffen, C. T. Swift, C. Wacherman, and R. L. Weaver, *NASA DMSP SSM/I Sea Ice Validation Program, Final Report*, 1991, In press.

Gloersen, P., and W. J. Campbell, Variations in the Arctic, Antarctic and global sea ice covers during 1978–1987 as observed with the Nimbus-7 Scanning Multichannel Microwave Radiometer, *J. Geophys. Res.*, *93*, 10666–10674, 1988.

Gloersen, P., and D. J. Cavalieri, Reduction of weather effects in the calculation of sea ice concentration from microwave radiances. *J. Geophys. Res.*, *91*, 3913–3919, 1986.

NASA-SAWG (National Aeronautics and Space Administration, Science Working Group for Special Sensor Microwave Imager), *Passive Microwave Remote Sensing for Sea Ice Research*, 55 pp., NASA, Code EE, Washington, DC, 1984.

NSIDC (National Snow and Ice Data Center), Geolocation correction to be applied to SSM/I gridding procedure, *CDMS Notes*, *3*, 4, 1989.

NSDIC, *DMSP SSM/I Brightness Temperature Grids for the Polar Regions on CD-ROM, User's Guide*, looseleaf, National Snow and Ice Data Center, Boulder, CO, 1990.

Sandoval, N. A., and V. J. Troisi, SSM/I *Brightness Temperature Grids: Quality Control Assessment*, NSIDC (In preparation).

Snyder, J. P., *Map Projections Used by the U.S. Geological Survey*, U.S. Geological Survey Bulletin 1532, 1982.

Wentz, F., *Update for 1989 Compact TA Tapes*, 1989 (also in *DMSP SSM/I Brightness Temperature Grids for the Polar Regions on CD-ROM, User's Guide*, Appendix 1, National Snow and Ice Data Center, Boulder, CO, 1990).

AD-P007 277

Contribution of the Argos System for the Study of the Polar Regions

Jean-Luc H. Bessis
Service Argos, Inc., Landover, Maryland, U.S.A.

92-17959

ABSTRACT

The Argos data collection and location system, aboard the NOAA polar orbiters, has been used by many scientists studying the polar regions. This paper will describe the latest improvements in this, the first worldwide operational location system, and summarize some applications of the Argos System developed by North American users in the polar regions.

Arctic applications include drifting buoy collection of meteorological and/or oceanographic data to support operational programs using the ice as a research platform, e.g., undersea acoustic noise measurements; determination of the effects of long-term loading stresses on sea ice; oil exploration and operations, including pollution and environmental monitoring; tracking movements of wolves, caribou, polar bears and grizzly bears.

Antarctic applications include environmental research for a better understanding of microbial ecosystems; winter data acquisition on ice motion using parachute-dropped buoys; oceanographic drifters to support operational and research programs; automatic weather and geophysical stations; high-altitude balloon experiments to observe supernovas; long-duration balloon experiments to collect data on stratospheric winds; tracking movements of fur and Weddell seals, and penguins.

The applications described above were made possible by specific characteristics and capabilities of the Argos System: systematic polar coverage; two operational satellites since 1979 and probably continuing after the year 2000; near-realtime data availability for platforms within the footprint of the NOAA Fairbanks ground station during every satellite pass; data provided directly to the user's own PC upon request or available in the two redundant data processing centers (Toulouse, France and Landover, Maryland, U.S.A.) 24 hours a day through data transmission networks; location accuracy of 150 m.

Argos-compatible instruments have been designed by numerous governmental and private organizations to operate in the harsh polar environment and to take advantage of the unique platform provided by the ice. The Argos System will continue to provide operational and reliable environmental location and data

THE ARGOS SYSTEM

The Argos Data Collection and Location System (DCLS) has been operational worldwide since 1978, aboard the NOAA polar orbiters, and has been used by many scientists studying the polar regions. It is the result of a cooperative program between the French Space Agency (CNES, Centre National d'Etudes Spatiales) and the National Oceanic and Atmospheric Administration (NOAA).

The Argos Space Segment

The space configuration comprises two NOAA TIROS-N satellites (presently NOAA 10 and 11) in simultaneous low polar orbit (830 km and 870 km) with an inclination angle of 98.7° and a 101-minute period. These satellites are sun-synchronous, therefore orbital revolution intersects the equatorial plane at fixed local solar times every day.

As the satellites orbit, the visibility zone (or footprint), centered on the satellite ground track, sweeps a 5000-km swath around the Earth. Therefore each satellite sees all platforms within this footprint and the Argos DCLS receives all messages transmitted by these platforms.

The User Equipment

All platforms reporting through the Argos system must carry a certified Platform Transmitter Terminal (PTT) for the satellite uplink. Each PTT transmits a short message (360 to 920 ms for respectively 32 to 256 bits). Repetition periods range from 90 seconds for location purposes to 300 seconds for data-collection-only purposes. All PTTs transmit at 401.650 MHz.

The mean number of passes per 24 hours varies from 7 in the equatorial region to 28 in the polar region with an average number of locations from 5 to 17 per day.

The Argos Ground System

The Argos data received by the Argos DCLS is transmitted to ground via three paths: (1) real-time VHF (136.77 MHz), (2) real-time on S-band (1707 MHz), (3) delayed-time using recorded data playback via an S-band (1700 MHz) telemetry downlink each time the satellite passes over one of the three System ground stations located at Wallops Island, Virginia (U.S.A.), Fairbanks, Alaska (U.S.A.), and Lannion (France).

Data are then transmitted to NOAA, National Environmental Satellite Data and Information Service (NESDIS) in Maryland (U.S.A.) then forwarded to the two Argos Global Processing Centers (GPC), one in Toulouse (France), the other in Landover, Maryland.

Each center operates around the clock every day of the week, and is designed for maximum availability and redundancy.

As soon as each telemetry data set is processed the results are disseminated to users or available for direct access by standard data transmission networks.

Data throughput time is less than three hours on average for recorded data.

Latest Improvements (Since 1989)

January 1989. Two new software commands became available at the French and U.S. GPC:

The "DIAG" command provides the user with detailed information about platform location on every satellite pass such as: two solutions in latitude and longitude, number of messages received, signal strength, pass duration, distance from ground track, computed platform frequency, altitude.

The "MOD" command permits the user to modify such system parameters as latitude, longitude, and altitude, and could increase location quality if applied.

After adjustment of erratic link problems between the two GPCs the Lannion recorded and real-time data sets were transmitted then processed at the USGPC on a routine basis.

February 1989. A new software is installed in both FRGPC and USGPC, Service Argos, Inc., processes the platforms for North American users (U.S.A. and Canada) and CLS, Toulouse, all other users. Either center can take over the global processing responsibility and the users have the option to request dual processing if they do not wish to risk interruptions to the realtime distribution or to availability of results.

July 1989. A 56 Kbits digital link is installed between the two GPCs and increases the quality and reliability of the interconnection.

February 1990. All realtime data sets received in the two U.S. ground stations, Fairbanks and Wallops Island, are processed at both centers

May 1990. All recorded data sets are now routed via different physical paths to both centers. Consequently, the entire Argos data flow from the satellite to the users' file in the GPCs has no single point of failure. This step concludes our actions designed to achieve full system reliability.

ARCTIC APPLICATIONS OF THE ARGOS SYSTEM

Ice Study

Long-term sea ice loadings (1990 and beyond). The program conducted by the U.S. Army Corps of Engineers (J. Richter-Menge) is aimed at determining the effects of long-term loading stresses on sea ice at warm temperatures (> -5°), this information being helpful in determining appropriate parameters for use in models that describe creep behavior of ice.

Measurements taken by the platform include air temperature, displacement rate of the ice and temperature of ice using a thermistor string.

Estimation of the ocean heat flux (1984). Estimation performed by the Polar Science Center, University of Washington (N. Untersteiner and A. Thorndike) takes advantage of the ice cover to measure the ocean heat flux. It employs a string of thermistors placed a few centimeters apart around the ice–water interface. The measurement of the differential pressure between the atmosphere and the ice bottom determines the ice mass balance (see Figure 1).

Sea ice dynamics and regional meteorology for the Arctic Polynya Experiment (APEX). The experiment conducted in 1985 by the Pacific Marine Environmental Laboratory (C. Pease) studied sea ice floes in the Bering Sea using drifting buoys (15) and observed the interaction of a wind-created polynya with regional dynamics and thermodynamics.

Oceanographic Research Programs

Electromagnetic noise measurement system (1987–1990). Studies by the U.S. Navy Surface Weapons Center to help the measurement and to process ambient electric and magnetic field noise. The Arctic research buoy position provides the track of the ice flow as well as permits the recovery of the sensors and electronics.

Arctic environmental drifting buoys (1987–1989). Study by the Woods Hole Oceanographic Institution (Dr. S. Honjo) measured particle fluxes under the Arctic sea ice in time and space using an ice-tethered sediment trap array.

The Coordinated Eastern Arctic Experiment (CEAREX). Study also conducted by the WHOI (1988–1990). The float trajectories are the first long-term lagrangian direct current

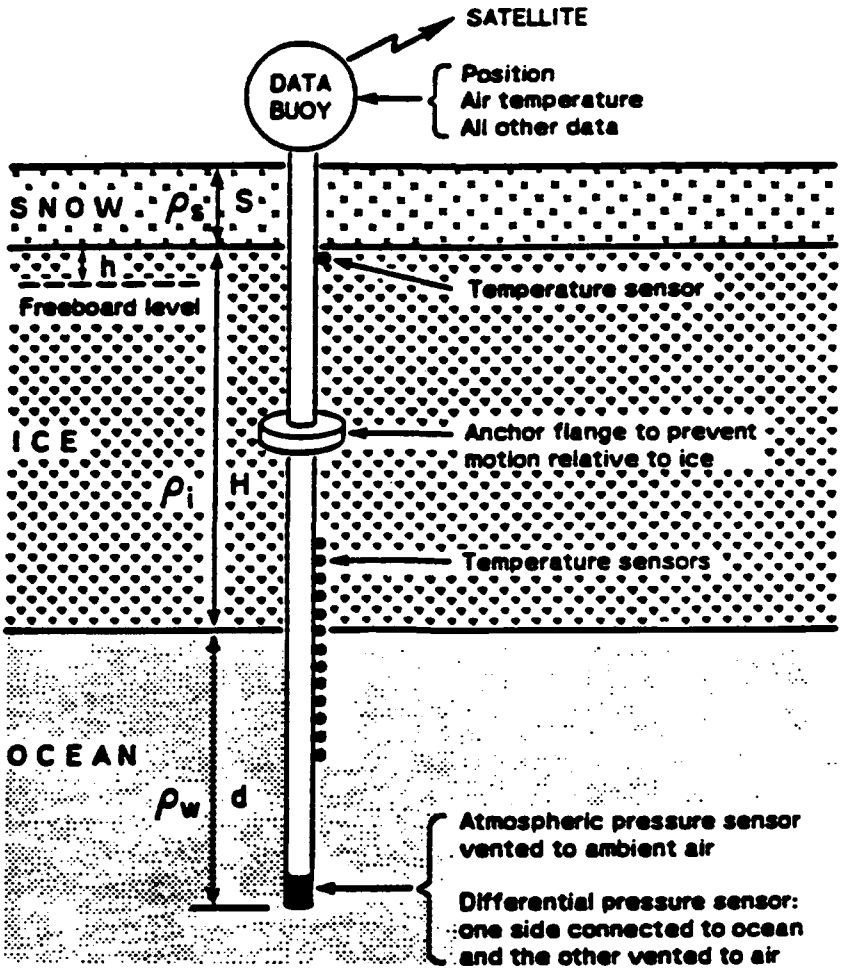


Figure 1. A schematic of the Mass Balance Buoy. Temperature sensors around the ice–water interface allow the ice bottom position and the vertical heat flux in the ice to be measured. A differential pressure transducer measures changes in ice draft (mass). The buoy allows determination of the ocean heat flux as well as changes in ice mass balance. (From Untersteiner and Thorndike [1984].)

measurements in the Arctic Ocean. These trajectories are analyzed to produce a kinematic description of the mean circulation and eddy variability in the Atlantic inflow into the Arctic Ocean.

The Oceanographic acoustics program. Conducted by the Canadian Department of National Defense which studied the ambient undersea noise and acoustic propagation using thermistors and hydrophones.

The Arctic Research for Environmental Acoustics Program (AREA). Study conducted by the Polar Research Laboratory (1980–1990) which analyzes the characteristics of the undersea environment (Arctic Ocean and North Pole) using drifting floating stations measuring ambient acoustic noise spectrum, oceanographic and meteorological data.

Hydrographic Measurements (1982–1990). Very specific SALARGOS buoys developed by the Polar Science Center measure the salinity and the temperature to 300 m using Sea-Bird sensors as well as the air pressure and temperature (see Figure 2).

Collection of Meteorological and/or Oceanographic Data to Support Operational and Research Programs

Coordinated Arctic buoy program (1979–1990). The network of meteorological data measuring atmospheric pressure and temperature installed by the Polar Science Center (R. Colony) studies the kinematics of the ice. Over 15 stations are maintained (Figure 3) to analyze the mean seasonal fields of velocity, vorticity, divergence and shear.

Greenland permanent meteorological observation system of the Danish Meteorological Institute (1980–1990) scattered along the coast of Greenland.

Ice island trajectories (1984–1990). The University of Alaska (Dr. W. Sackinger) is tracking ice island trajectories and measuring barometric pressure, surface temperature, wind speed and direction as well as ice island azimuth.

Operational Arctic program (1985–1990). To support Arctic operations the Naval Oceanographic Office (NAVOCEANO) of the Navy must have realtime environmental intelligence (R. Partridge); in-situ drifting buoys are one of the components of the program and provide a host of data required to analyze and forecast environmental conditions. Measurements include barometric pressure and temperature, together with the acoustic field and subsurface thermal structure of the Arctic Ocean.

Oil and Gas Exploration

The offshore oil and gas industry is mainly using the Argos System for three purposes: operations planning, platform design criteria and preparation for oil spill response and support.

SALARGOS BUOY

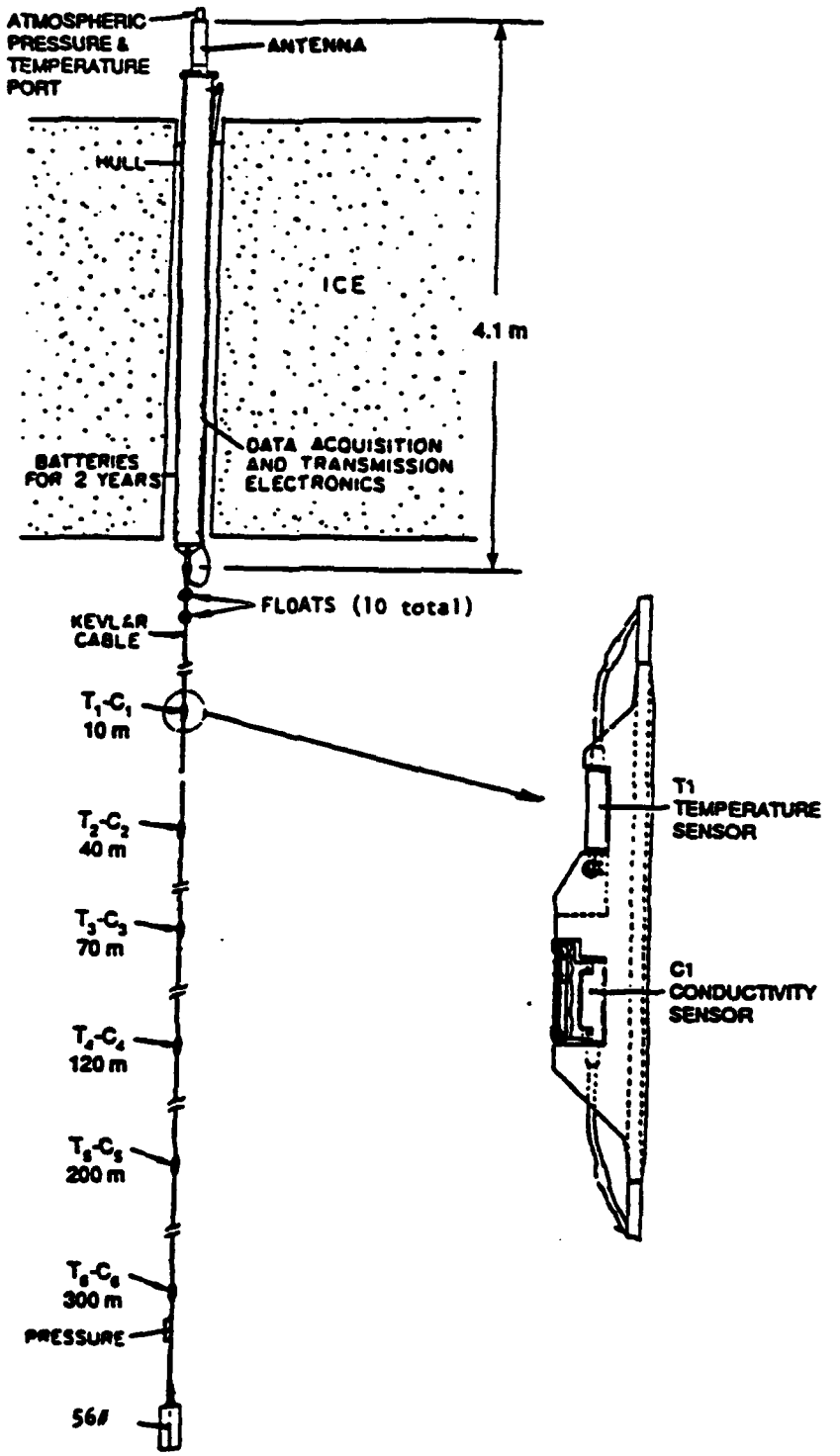


Figure 2. The SALARGOS buoy as it appears in cross section in the ice. The sensor spacings are those that have been chosen for buoys being deployed in 1988. The buoy hull, electronics, and cable are built by the Polar Research Laboratory, and the temperature and conductivity sensors are Sea-Bird units.

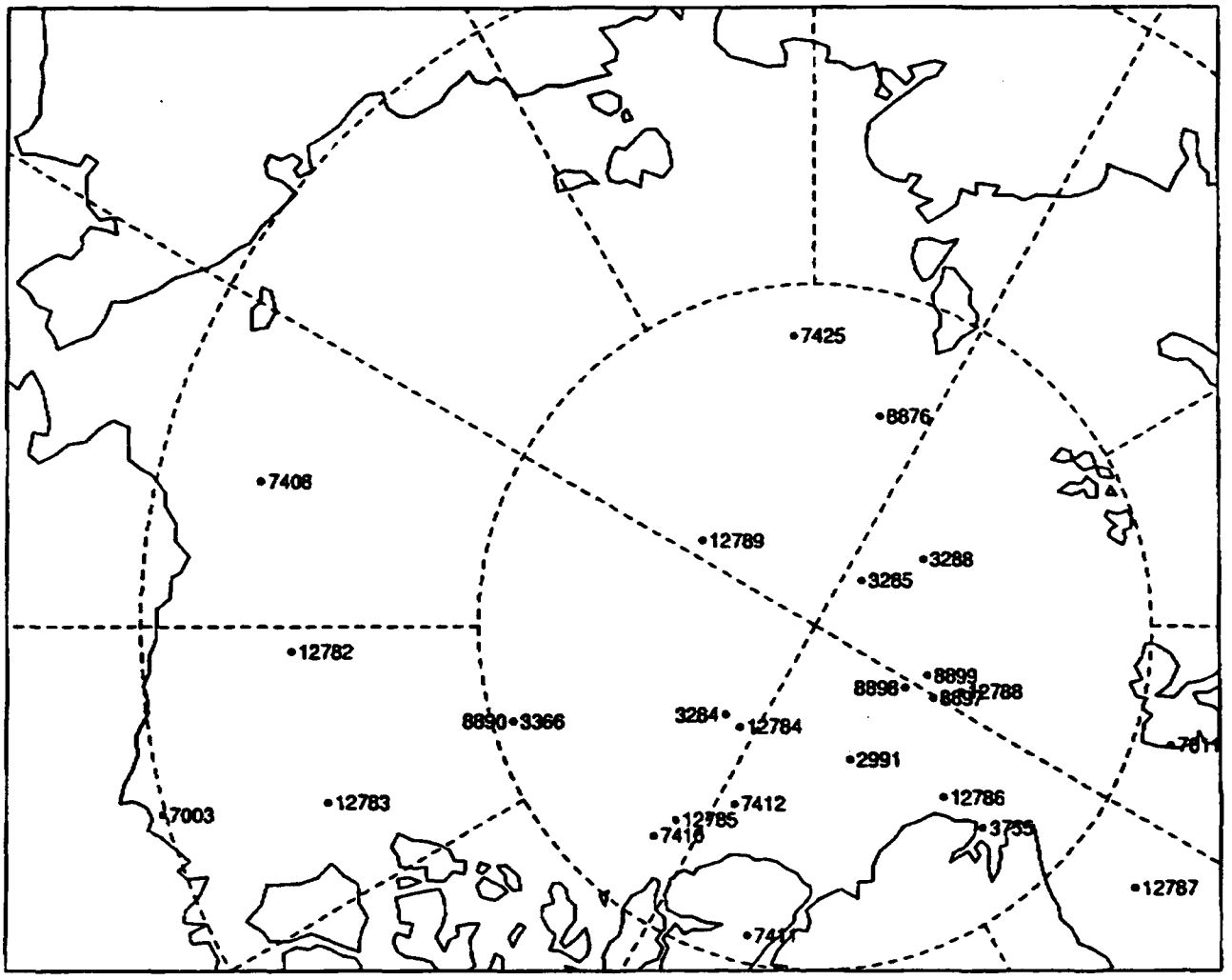


Figure 3. June 4, 1990 arctic buoy positions. (R. Colony)

A typical example of the use of drifting buoys to track oil slicks was the request received April 7, 1989 by the NOAA Data Buoy Center (NDBC) from the National Weather Service Alaska Regional office in Anchorage to deploy some buoys in the Exxon Valdez oil slick (see Figure 4).

Three buoys were deployed April 13–14 and were especially effective in tracking the oil once the slick dissipated and oil congealed into tarry lumps and sank (R. Kozak).

In addition to the effectiveness of the buoy position information, the meteorological data provided by the buoys allowed the NOAA Hazardous Materials Response Team to make major improvements in their oil-spill computer models.

Animal Tracking

In the Arctic, many biologists from the U.S. Fish and Wildlife Service and from the Alaska Department of Fish and Game are monitoring the movement, the behavior and environmental parameters (air temperature) of a number of animal species, including wolves, caribou (several dozen), polar bears, brown bears, musk oxen, moose, bald eagle.

ANTARCTICA APPLICATIONS OF THE ARGOS SYSTEM

Tabular Iceberg Tracking

One of the first Argos users, the Museum d'Histoire Naturelle (Pr. P. Tchernia) started to track icebergs in the early days of satellite location (Post-Eole experiment 73-74).

Several years later Argos platform ID 1064 was tracked for 828 days and its trajectory was very similar (see Figure 5) in mean speed and direction in spite of the differences in size of the icebergs (L = 2500 and 800 m).

Environmental Research for a Better Understanding of a Microbial Ecosystem (1982–1990)

The Florida State University (Friedman and McKay) collects data from two platforms and measures surface wind velocity, solar radiation, air temperature, rock temperature, relative humidity and snow cover.

The aim is to formulate a comprehensive data set of the environment in the Antarctic dry valleys for modeling cryptoendolithic lichen growth.

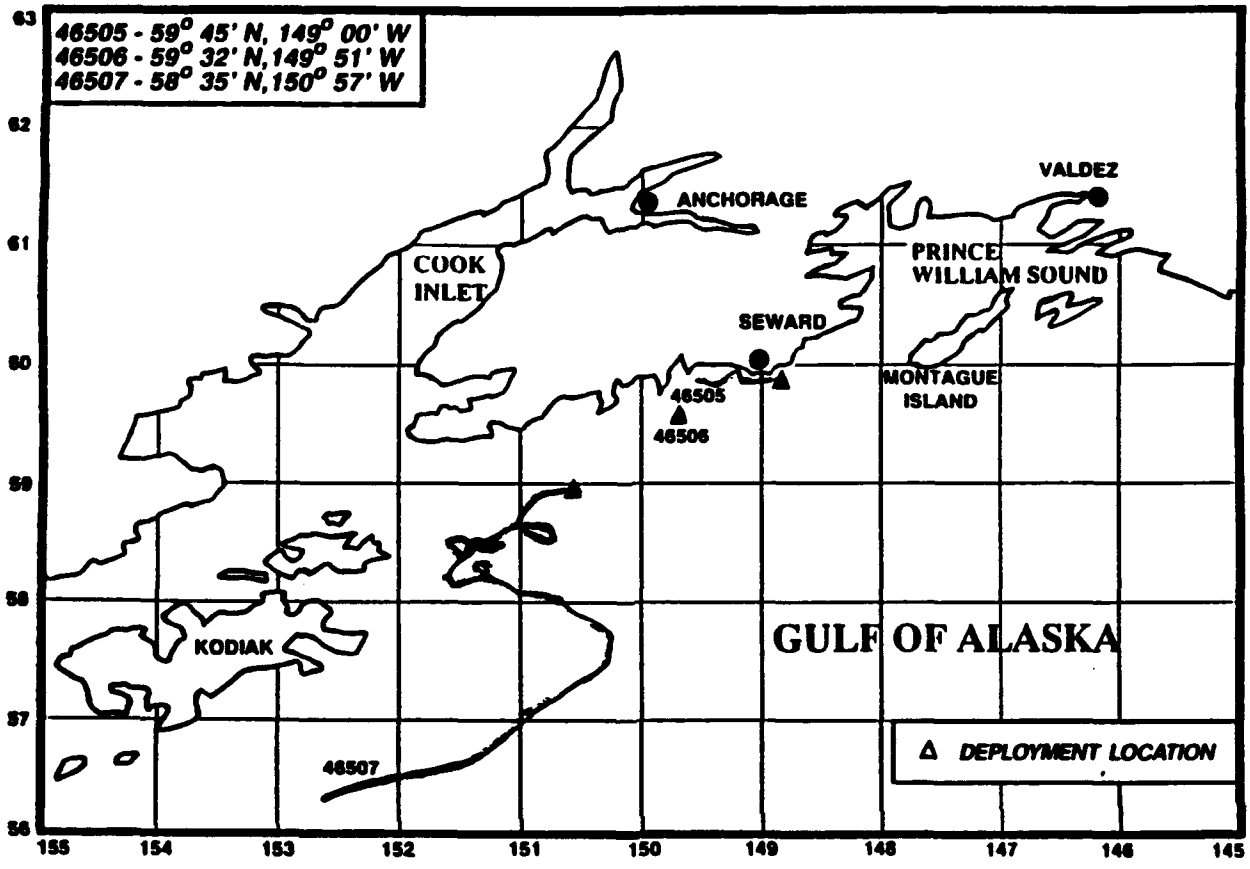


Figure 4. Drifting buoy tracks, Valdez oil spill, April 13 to May 31, 1989.

Wintering Data Acquisition on Ice Motion Using Parachute-Dropped Buoys (1988–1990)

Under the Antarctica buoy program the Polar Science Center, University of Washington (Dr. R. Moritz) is acquiring wintertime data on ice motion, air pressure and temperature in support of research into meteorological and oceanographic processes in the Ross Sea. Analyzed data are archived at the National Snow and Ice Data Center in Boulder, CO and air pressure and position data entered on the GTS (Global Telecommunications System) for use in operational weather analysis.

Antarctic Automatic Weather Stations (1980–1990)

The University of Wisconsin (C. Stearns) now operates 32 Automatic Weather Stations in Antarctica (as well as 3 in Greenland) which are GTS compatible and regularly measure wind speed and direction, temperature (inside and outside), barometric pressure, and station engineering data.

In addition to providing synoptic weather information the AWS allows the study of the katabatic winds.

Automatic Geophysical Laboratory (1989–1990)

Lockheed Palo Alto Research Laboratory (Dr. J. Doolittle) built an unmanned Automatic Geophysical Observatory (AGO) to study solar–terrestrial physics from a network of ground base sites at high geomagnetic latitude as a complement to space-borne measurements.

The need to retrieve frequent snapshots of the operation requires the use of six AGO with eight Argos ID's each in order to accommodate the following sensors: ionospheric opacity to cosmic radio noise, auroral optical intensity, VLF, LF and HF radio emission signal strength, magnetic field intensity and fluctuations.

Antarctic Balloon Programs

High altitude balloons to observe supernovas around McMurdo station (1988). The U.S. Air Force Space Division (Major R. Crombie) conducted this program which flew an advanced gamma ray telescope on a high altitude balloon from McMurdo Station to observe a supernova. Position and altitude of the balloon during the observation period is required because of uncertain winds at the float altitude of 120,000 feet.

Long duration balloon program to collect data on polar stratospheric winds (1989–1990). The National Scientific Balloon Facility (D. Bawcom) has measured during a period of 1 to 4 weeks and at an altitude of 20–40 km polar stratospheric winds, direction, speed and persistence as well as air temperature, earth IR radiation temperature, pressure altitude and balloons housekeeping data.

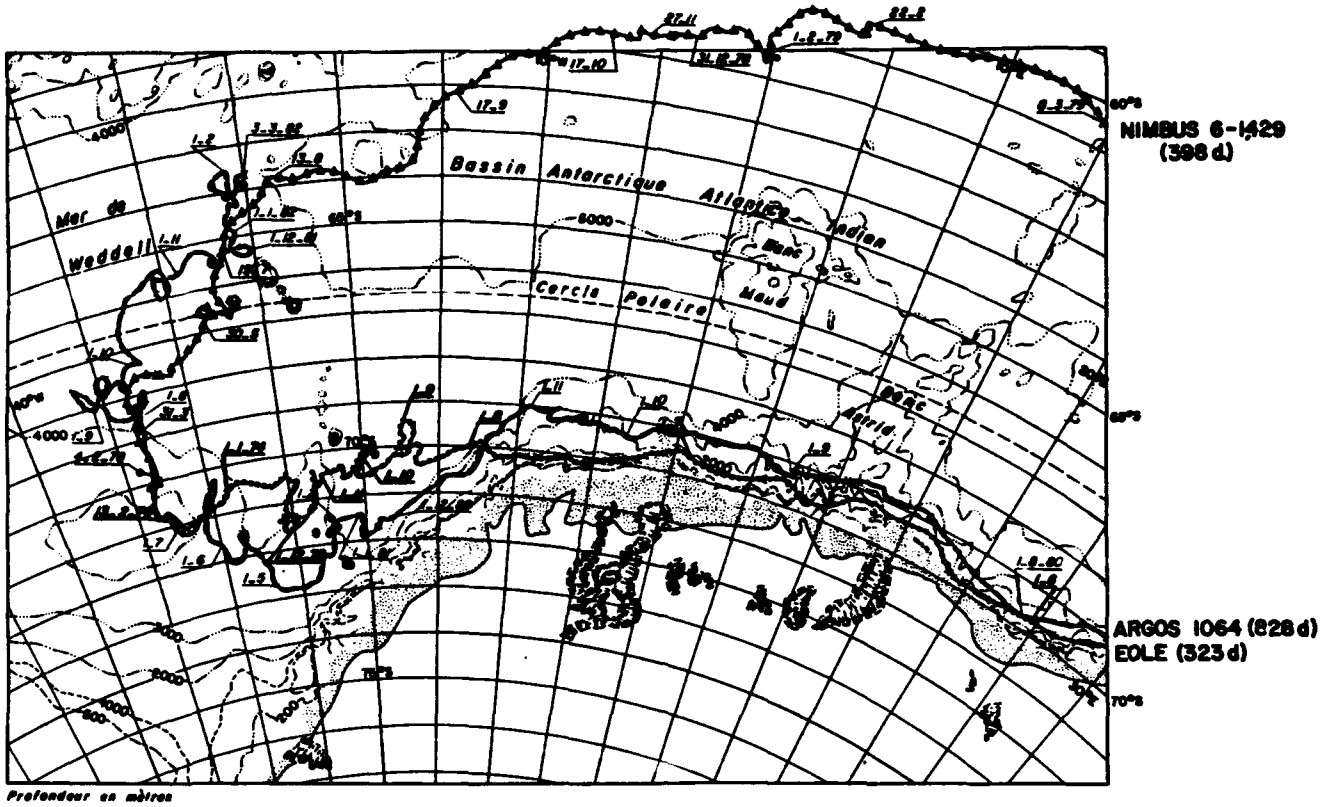


Figure 5. Tabular iceberg tracking. (Pr. P. Tchernia)

Animal Tracking

Antartic Marine Living Resources. National Marine Fisheries Service (Dr. J. Bengston) used an Argos PTT on the deck of the *Alcazar* to track the ship's location during his research program where he instrumented fur seals, chinstrap penguins and macaroni penguins with radio transmitters for a period of several months.

Weddell seals (1990 and beyond). The Institute of Marine Science, Univesity of Alaska (J. Testa) is determining the overwinter movements and diving behavior of Weddell seals in the western Ross Sea. Ten to twenty animals will be tracked and the duration of the period during which the seals are on the surface will be timed.

AD-P007 278

92-17960

Quick-Look Satellite Imagery for Alaska: A Tool for Environmental Monitoring

Tom George, Greta Reynolds, Ken Dean, and John Miller
Alaska SAR Facility, Geophysical Institute, University of Alaska Fairbanks

ABSTRACT

Satellite imagery is a valuable tool for environmental monitoring of natural and man-made events. Analysis of imagery within a few hours is vital if these data are to be used to respond to rapidly changing conditions. Since April of 1982 Landsat imagery from the Quick-Look Project at the Geophysical Institute has been available for real-time applications. The system provides near real-time Landsat MSS imagery for applications including monitoring flood hazards, sea ice motion, forest fires and agricultural development.

As we move into the 1990s additional satellites with new sensors are being launched which will provide more opportunities for near real-time use. To take advantage of the sensors, additional facilities are needed to receive, process and deliver the data in a timely fashion. Candidate sensors and spacecraft include Enhanced Thematic Mapper (ETM) on Landsat-6; Advanced Very High Resolution Radiometer (AVHRR) on the NOAA polar orbiting satellites; SPOT; Japan's Meteorological Observation Satellite (MOS); OPS (Optical Sensor) on the Japanese Earth Resources Satellite-1 (JERS-1) and the Advanced Earth Observing Satellite (ADEOS).

Ongoing projects, such as the Alaska SAR Facility, can provide some components of a multiple satellite receiving system. Such a capability will provide a valuable source of data to study global change in the Arctic. We will describe the capabilities required to use satellite data for environmental monitoring.

INTRODUCTION

During the past two decades, satellite imagery has proven invaluable to earth science studies and environmental monitoring by providing information over a large geographic area during an instant in time. These data support a wide range of uses, such as monitoring sea ice motion and weather dynamics, mapping vegetation and geologic features, documenting changes on the land surface, and circulation of water masses in the ocean. Analysis has largely been on a retrospective basis, months or years after the satellite data were acquired [George and Miller, 1985].

New programs are beginning to focus on study of earth systems, primarily those believed to influence global change. A common need of these projects is to expand our ability to observe and compare observations over large geographic areas. Satellites will play a larger role in these investigations if we can deliver the data promptly.

Very seldom does a satellite image alone solve a problem. Additional information from field observations, airborne sensors or other sources are normally required to quantify field conditions. Studying ephemeral features such as snow cover, sea ice and ocean state requires close coordination between field observation and satellite data collection. To meet these requirements it is often necessary to access, analyze and distribute satellite imagery in near real-time; typically within a few hours of a pass.

Before describing the specific requirements of such a system, we will provide some background and examples of this use of satellite data in Alaska.

THE LANDSAT QUICK-LOOK PROJECT

The System

In April of 1982 the Geophysical Institute at the University of Alaska Fairbanks began operation of the Landsat Quick-Look Project. Subsequently, near real-time Landsat Multi-Spectral Scanner (MSS) data has been provided to university researchers, government agencies and others interested in environmental monitoring activities [Miller, 1984; Burger and Miller, 1986]. Applications include monitoring the 1986 eruption of Mt. Augustine, seasonal flooding of the Yukon River, agricultural changes in interior Alaska, sea ice distribution, ice floe movement, and forest fire surveillance.

Limitations

Although this project provides image products rapidly, inherent limitations of the system can severely reduce the utility of the data. Landsat MSS is an optical sensor and is therefore dependent upon solar illumination. During several months of the year at Alaska's latitudes the northern third of the state has insufficient illumination to acquire data of high quality. Although coarse feature recognition has been achieved with illumination angles as low as 4° below the horizon, large regions lack mid-winter coverage [Miller and Burger, 1986].

The 16-day repeat cycle of Landsat 5 also limits our ability to acquire data on demand. For a monitoring effort to be effective, repetitive coverage is necessary. Users are often interested in changes occurring over one to two days' time. Coverage over Alaska on a given day is limited to two 185-km swaths approximately 900 km apart (Figure 1a).

A positive benefit at high latitudes is that the orbits of Landsat (and other polar-orbiting satellites) converge, providing increased sidelap of adjacent passes. Landsat exhibits 50–70% sidelap on adjacent ground tracks at the 70° latitudes. Within one 16-day cycle a target can be viewed by up to four separate ground tracks (Figure 1b).

Cloud cover is another limitation to optical sensors. In many regions of the Arctic, persistent cloud cover precludes observation of surface features for weeks at a time, greatly limiting our monitoring ability. Experience has shown that useful information may be acquired in spite of partial cloud cover or thin cloud layers. If a target is known or suspected, the satellite observation serves to verify the presence and extent of features which exhibit high contrast, such as water overflowing sea ice, or fresh scars of a wildfire.

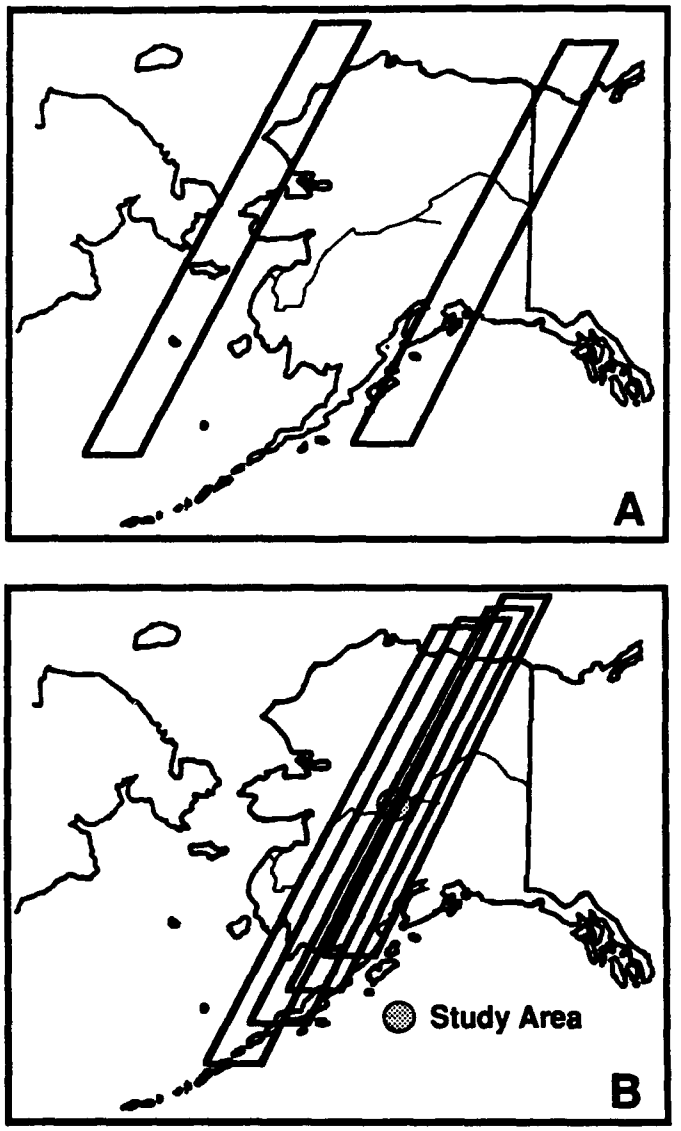


Figure 1. Landsat-5 orbit characteristics. (a) One-day ground coverage over Alaska. (b) Coverage of one Landsat-5 16-day cycle.

USING SATELLITE DATA IN NEAR REAL-TIME

In the past few years, we have gained experience in deriving information from multiple satellite sources in response to different environmental situations. Examining selected case histories provides insight into the potential benefits and limitations of satellite data.

Exxon Valdez Oil Spill

On March 24, 1989 the *Exxon Valdez* ran aground on Bligh Reef in Prince William Sound, causing a world-class oil spill. Within a few days scientists at the Geophysical Institute had contacted NOAA, EOSAT and SPOT to schedule acquisition of satellite imagery of the affected area. The earliest available coverage came from NOAA at the Gilmore Creek Command and Data Acquisition station near Fairbanks. This station routinely acquires Advanced Very High Resolution Radiometer (AVHRR) data and could respond rapidly to our needs. The AVHRR sensor is carried by two operational satellites, NOAA-10 and 11; together they provide between 10 and 12 passes over Alaska each day. The sensor has a pixel size of approximately 1 km, and records radiation in visible, near and thermal infrared wavelengths. It is considered a "survey" instrument, which acquires data along a swath roughly 2000 km wide. These data have been used for many years to monitor synoptic weather patterns in support of operational weather forecasting.

Digital data were analyzed daily to derive sea surface temperature patterns, turbidity, and oil-related signatures at the Alaska Data Visualization and Analysis Laboratory (ADVAL), located at the University of Alaska Fairbanks campus. Digitally enhanced images were transmitted by facsimile each evening to the Alaska Department of Environmental Conservation at Kodiak Island and researchers



Figure 2. SPOT panchromatic image acquired 9 April, 1989. Oil is represented by the light gray areas surrounding Smith Island.

aboard the University of Alaska research vessel *Alpha Helix*. High-quality film products were distributed retrospectively for follow-up analysis. The acquisition, analysis and transmission of the AVHRR data to the field was performed each day to assist in monitoring and research activities. The low resolution AVHRR imagery combined with other observations provided information on the location and extent of large pools of oil until they broke up two weeks or so after the spill occurred [Dean et. al., 1989].

Data acquired from satellites with higher resolution were analyzed as well. SPOT (10- to 30-m resolution) and Landsat TM (30-m resolution) data were available within a month of the spill. Features detected from these satellites included large pools and windrows of oil, as well as evidence of the beach oiling process. These data sets were not available rapidly enough for operational use, although they did provide valuable retrospective information. Figures 2 and 3 show examples of features observed, and the spatial detail that can be expected from this class of sensors. The oil-related features had very subtle signatures and required intensive pre-processing. We believe data from these satellites could provide information for field operations for spill management if they were available in a timely fashion.

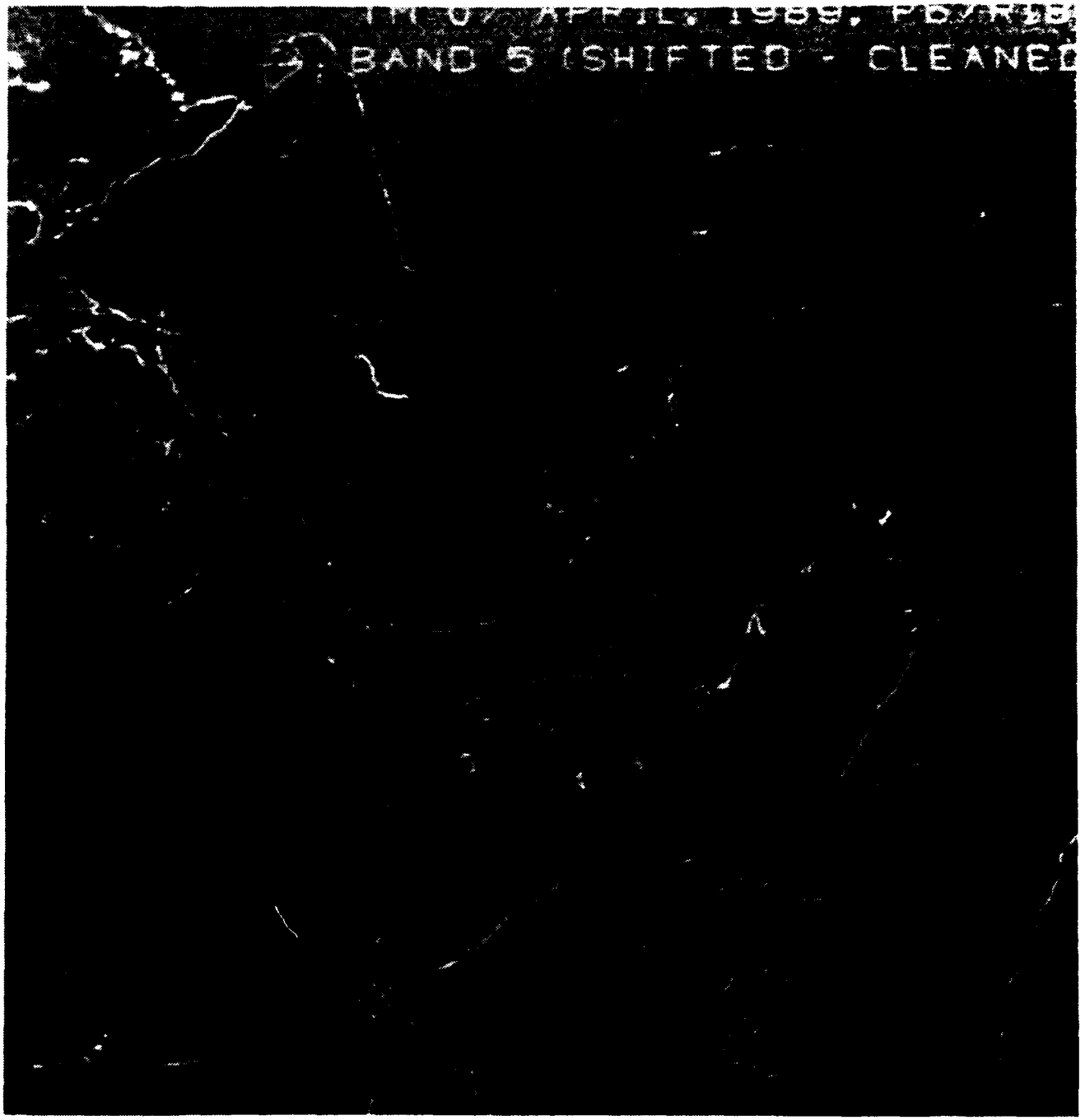


Figure 3. Landsat-5 TM Band 5 image shows oil in the vicinity of Montague and Smith Islands in Prince William Sound. This image required much preprocessing to detect oil signatures, which are seen as thin light tone structures on the image.

Mt. Redoubt Volcano

The eruptions of Mt. Redoubt provide another example of the operational use of satellite imagery. Figure 4 shows the trajectory of the eruption plume and distribution of the ash fall. AVHRR imagery is particularly useful for this application since it is recorded several times a day and can show changes over a period of hours. The signature of the plume is discernible by the spatial pattern seen on the image even through lower cloud layers. Measurements from the thermal bands are connected to temperature, providing an indication of the elevation of the top of the plume. Estimation of plume height is accomplished by comparing the derived temperatures with atmospheric profiles recorded by the National Weather Service, and verified by pilot reports.

Knowledge of plume extent and location could target potentially hazardous areas for airline traffic. This hazard was demonstrated when a Boeing 747 aircraft experienced engine failure and extensive engine damage after flying through the ash cloud northeast of Anchorage. For several days following the 747 event, all jet traffic to and from Alaska was grounded due to the uncertainty of the location of the plume.

Landsat MSS imagery of Mt. Redoubt recorded by the Quick-Look Project (Figure 5) shows the benefits of higher



Figure 4. NOAA AVHRR image showing a volcanic plume from Mt. Redoubt drifting across Cook Inlet and the Kenai Peninsula. This image was acquired 16 December, 1989, approximately 8 hours after an eruption.

resolution data. This image was acquired on January 24, 1990 at 11:48 AM AST, and shows a new river channel that was carved by a flood event due to melting ice and snow on Mt. Redoubt. Flooding posed potential threats to the man-made oil storage facility located on the delta and during several time periods the workers were evacuated.

Earth Science Processes

Beyond monitoring natural or man-caused events, satellite imagery can play an increasing role in interactive studies of science processes, many of which relate to the study of global change. This requires the ability to deliver either an image or derived product to an investigator in a timely fashion. With this data, a science team can direct their resources to collect field observations. Without this information, investigators must fall back on statistically designed search patterns or other means to allocate resources.

In September 1988 the Coast Guard ice breaker *Polar Star* encountered ice that was too severe for normal navigation. In response to a request for assistance, scientists at the Geophysical Institute acquired and analyzed digital AVHRR data of the northern Chukchi Sea to discern sea ice conditions in the region where the ship was operating. Information was relayed daily to the *Polar Star* which enabled

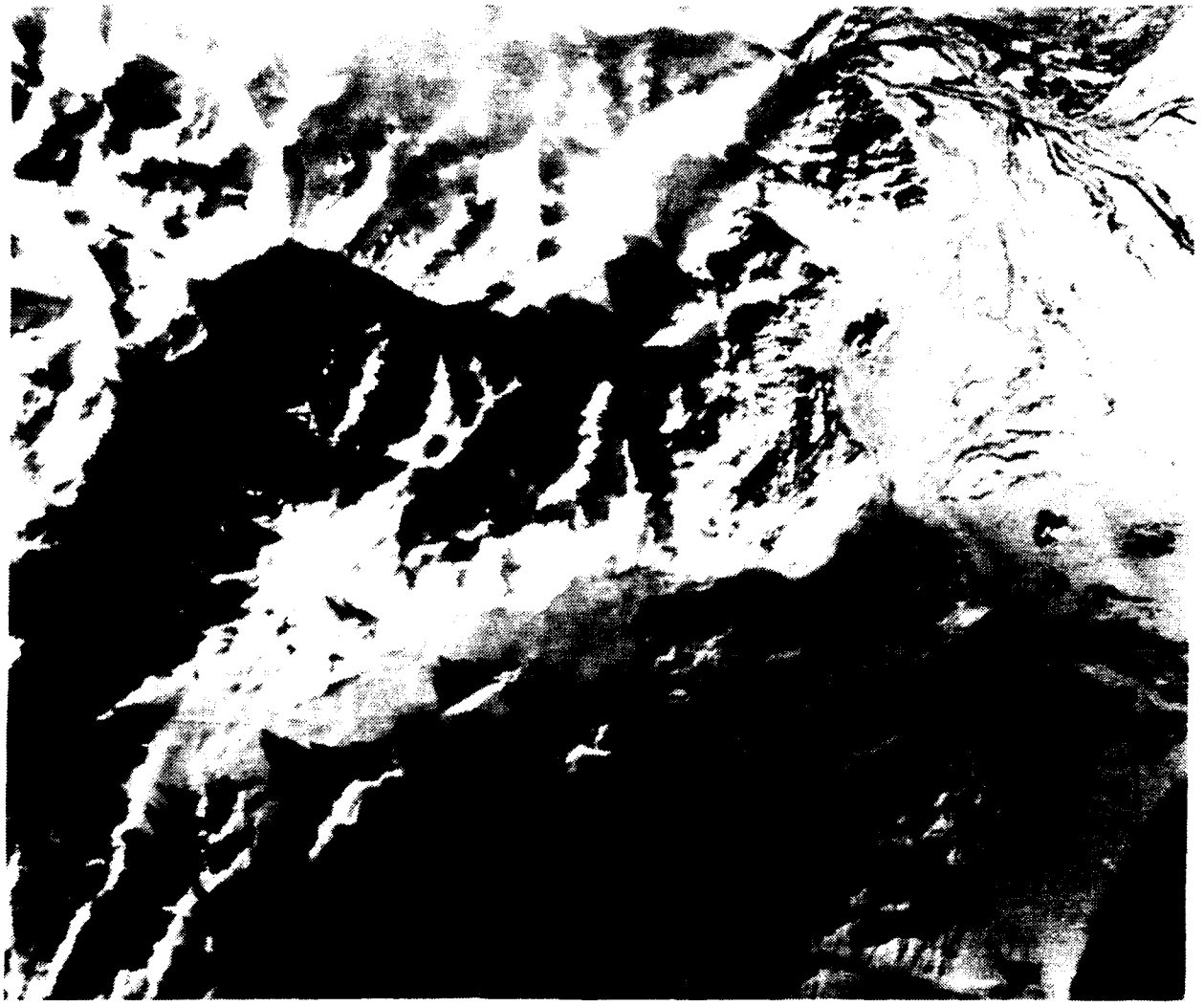


Figure 5. Landsat-5 MSS image acquired by the Quick-Look Project shows a new channel carved by the flooding Drift River. Melting snow and ice from volcanic heat caused flooding that endangered the oil storage facility located on the delta. The new channel, as well as the oil facility, can be seen on the image.

the ship to locate ice conditions suitable for their geological and geophysical studies, thus saving an entire field season for the project. While this effort can be considered largely a logistic application, it illustrates the notion of directing ships, aircraft or other platforms to scientifically important areas to facilitate data collection.

These examples suggest that projects can benefit from satellite-derived information if it can be delivered in a timely fashion. The regional view provided by the satellite can be used to direct collection of field data which is especially important to the process being studied. The large area recorded by the satellite sensor also permits extrapolation of a few point measurements gathered in the field to help describe patterns with great areal extent. Examples of topics that might benefit from this type of data include ocean processes, snow accumulation and melt, characterization of sea ice, and plant phenology studies.

COMPONENTS OF A NEAR REAL-TIME SYSTEM

Based on our experience, and study of the satellite systems available, we believe that a satellite monitoring system should have the following components:

- A means to request satellite data coverage.
- The ability to acquire the data directly from satellites.
- Image manipulation and analysis tools for near real-time processing.
- The means to transmit information to a remote location.

Requesting Coverage

Each satellite is actively controlled by the flight agency which is responsible for its operation. Much attention is paid to adjusting satellite orbits, managing power constraints, and testing and assessing the health of the spacecraft and its systems. Survey-type systems, such as AVHRR, are operated

continuously, and do not require any active communication between the user and satellite controllers.

Other sensors are limited by the amount of data they can acquire, and requests for coverage must be placed prior to acquisition. Landsat TM and SPOT clearly fit in this category. The SAR satellites scheduled to operate in the 1990s will be extremely power limited, requiring users to place requests well in advance to obtain coverage. A communication channel must be established with each flight agency to request data acquisition.

Direct Reception Capability

Based on experience with centralized data distribution systems, we believe that direct data reception from multiple satellites by a ground station is essential for near real-time utilization. The United States has tended to favor centralized systems which involve a separate processing stream for each satellite. The time required to routinely acquire, process and distribute satellite data ranges from weeks to months, far too slow to monitor dynamically changing features. A notable exception to the national trend is the development of small, direct-reception stations for NOAA AVHRR data. These systems support local acquisition, processing and archival of the data independent of the NOAA distribution system. We believe this is an important indicator of future near real-time use of satellite data.

To be responsive to the diverse requirements for earth monitoring, a modular system is essential, which can acquire and process data from a variety of different sensors. Much effort is expended today to register data from different sources. Displaying an AVHRR time series over a Landsat TM base image is one example. With careful design, a modular system can be constructed which makes supporting new sensors faster, easier and less expensive than it is today.

Image Manipulation and Analysis Tools

Once the data are available for analysis, flexible image processing and manipulation tools are required. Basic analysis needs include the ability to enlarge and enhance the image, combine spectral bands, and geometrically warp images to a variety of map projections. Increasingly we see the need to perform calibrations among satellite sensors in order to measure absolute differences in geophysical properties (temperature, concentration, etc.). Display capabilities are required to browse image data and pick the specific scenes needed for detailed analysis.

We often need to combine satellite data with other observations to produce a derived product. The ability to combine satellite raster data with other types of information (shipboard measurements, atmospheric profiles, ground radiometer readings) requires capabilities found in vector Geographic Information Systems. Finally, derived information must be output in forms suitable to disseminate, including hardcopy and digital media.

Transmission to Remote Locations

The final step is to deliver products to remote locations. These might take the form of derived maps, black-and-white line drawings, or digital image data. The equipment required to deliver data and information ranges from a standard office facsimile machine to a microcomputer capable of receiving digital data via network or telephone connection. In some instances derived information is delivered to a research laboratory, or task force office, well supported with telecommunications equipment and computers. Alternatively, the destination might be in a remote setting, such as a field camp at Point Barrow, or a research vessel in the Bering Sea.

HOW DO WE GET THERE?

Having briefly described today's near real-time needs in Alaska, and the requirements of a system to meet those needs, what are the next steps toward implementing this capability? Several necessary components are already in place. The Alaska SAR Facility (ASF), located on the University of Alaska Fairbanks campus, operates a receiving station funded by NASA. This station is presently used to support the state-funded Landsat Quick-Look Program. Additional subsystems will process, archive and distribute satellite imagery from a series of SAR satellites starting in 1991. One capability of this facility will be to process limited quantities of the SAR data within a few hours of a satellite pass. An additional project is underway to transmit SAR image data products via satellite link to the Joint Ice Center in Suitland, Maryland [Montgomery, 1989]. While the ASF is designed primarily to support SAR satellites, the receiving system can be upgraded to acquire data from several other satellites.

The National Weather Service is developing a ground station that will have direct reception of AVHRR data in Anchorage [Hufford, personal communications, 1989–1990]. This system is intended to receive, process and deliver digital data for analysis within a few hours of a satellite pass. It will support operational weather forecasting as well as special projects such as monitoring volcanic eruptions. This system is scheduled to be operational by mid 1991.

While these two programs appear very promising, more work needs to be done with analysis and management of the data, and the distribution systems to deliver derived products to the locations where they are needed.

CONCLUSIONS

We believe that near real-time satellite data is a viable tool for environmental monitoring in the 1990s. Experience indicates that satellite information provides the ability to monitor conditions over large geographic areas through time. Combined with information gathered through more conventional means, we can have a powerful capability to monitor our dynamic northern environment. Problems of policy and funding for data access remain, both for U.S. and the foreign spacecraft whose unique capabilities we need. It will take state and federal agencies working with the academic community and private sector to develop these capabilities. If successful, we stand better equipped to deal with issues concerning global change at high latitudes.

REFERENCES

Burger, G. J., and J. M. Miller, Custom enhanced Landsat imagery in near real-time, *Proceedings of 10th Canadian Symposium on Remote Sensing*, edited by M. D. Thompson and R. J. Brown, pp. 699–703, Edmonton, Alberta, May 1986.

Dean, K., W. Stringer, J. Groves, K. Ahlnäs, and T. Royer, Exxon Valdez oil spill, Alaska, presented at *7th Thematic Conference on Remote Sensing for Exploration Geology*, Calgary, Alberta, October, 1989.

Dean, K., C. P. McRoy, K. Ahlnäs, and A. Springer, The plume of the Yukon River in relation to the oceanography of the Bering Sea, *Remote Sensing of the Environment*, *28*, 75–84, 1989.

George, T. H., and J. M. Miller, The use of satellite imagery for resource mapping in Alaska, *Soil Survey and Land Use Workshop*, Anchorage, Alaska, April 1985.

Kienle, J., K. Dean, W. Rose, and H. Garbeil, The 1989 eruption of Redoubt volcano, Alaska, *EOS*, *71*, 266, 1990.

Miller, J. M., and G. J. Burger, Enhancing Landsat data acquired under very low illumination, *Photogrammetric Engineering and Remote Sensing*, *52*, 801–807, 1986.

Miller, J. M., Applications of real-time Landsat images in Alaska, *Landsat Data Users Notes*, National Oceanic and Atmospheric Administration, March 1984.

Montgomery, D., "SARCOM," *ASF Newsletter*, Alaska SAR Facility, Geophysical Institute, University of Alaska Fairbanks, Vol. 3, No. 4, November 1989.

AD-P007 279

92-17961

Measuring Sea Ice Deformation with Imaging RADAR Satellites

Coert Olmsted
Alaska SAR Facility, Geophysical Institute, University of Alaska Fairbanks, Fairbanks, Alaska, U.S.A.

ABSTRACT

Sea ice pack motion can be detected by comparing pairs of geolocated remote sensing images separated in time by a few days. Pattern recognition algorithms have been applied to develop automatic systems for synthetic aperture radar (SAR) images such as SEASAT and ERS-1. These systems produce a vector field of pack ice displacements. To apply this velocity data to basic problems concerning the distribution of ice types and thicknesses, it is necessary to obtain an accurate measure of the deformation due to opening and closing of leads and to rafting and ridging of floes with each other and with thin new ice.

Preliminary studies indicate that the ice motion is piecewise continuous with shear zones separating more rigid continuum elements made up of many floes. We postulate a turbulent regime for the velocity field which leads to the assumption of simple rotational motion for the continuum elements. Applying image analysis techniques to the displacement vectors enables classification and parameterization of the continuum elements and the characteristic discontinuities which border them. Computations based on this analysis can then quantify the deformation internal to the continuum elements and that due to the relative motion between them.

OBJECTIVE

The area concentrations of sea ice types (open water and various age/thickness groups) of polar pack ice are necessary quantities for estimating surface fluxes and mass/heat balance of the ice–ocean–atmosphere system. The fraction of open water/thin ice that may be expected is of practical value for marine navigation.

Dynamic/statistical models have been designed at local and global scales to incorporate time evolution of concentrations or thickness distributions with remote sensing, drift buoy and meteorological data [Thorndike et al., 1975; Hibler, 1986; Thomas and Rothrock, 1989]. In all such models lead opening/closing and rafting/ridging make important contributions to the change of concentrations. Estimating the rates of these processes requires kinetic information on the relative motion of the mechanical constituents of the ice pack. Thus it is important to quantify opening and closing of ice free leads (open water) and also the rafting and ridging of floes (production of thick ice from thin ice). The former can be obtained by classification of images into ice and open water—at present a difficult problem [Fily and Rothrock, 1990]. The latter must be estimated from measurements of strain. At present only very rough mean estimates are available from buoy tracking [Colony, 1991].

METHOD AND ASSUMPTIONS

SAR images can, however, provide enough information so that pattern recognition techniques can closely track Lagrangian parcels (~10 km) of sea ice and so give a detailed picture of the local velocity field [Kwok et al., 1990]. Samples acquired from about 24 pairs of SEASAT images (100 x 100 km 25 m resolution) and analyzed with the Alaska SAR Facility (ASF) Geophysical Processor System (GPS), which also will work on future SAR satellites such as ERS-1, J-ERS-1, RADARSAT and EOS, confirm that the motion is complex on a range of scales and has jump discontinuities along curves [Curlander et al., 1985; Fily and Rothrock, 1986; Vesecky et al., 1988; Collins and Emery, 1988]. Inspection of these velocity fields shows that the elements between discontinuities are in the size range of tens to

hundreds of kilometers and appear to be relatively rigid. Furthermore their motion is frequently rotational with radii of rotation on the same order of magnitude.

These observations lead us to two hypotheses. The first is that the motion is piecewise continuous and, as a further simplification, piecewise rigid. For the second hypothesis we note that rotational motion also occurs on larger (100- to 1000-km gyres) and smaller (floe size) scales. Thus the velocity field can be characterized as turbulent, i.e., eddy (rotational) motion occurs on cascades of (discrete) scales. For a further simplification, assume that the rotation is simple, i.e., a constant angular velocity around a fixed center. Then the motion is characterized by center coordinates and angular velocity for each piece. When combined with information on the size and position of each piece, this provides moments and eddy sizes. Studying the distributions of these variables for extended data sets would give physical information on the energy cascade and the existence of dissipation.

ANALYSIS

In this study we examine the data derived from SEASAT images from revolutions 1439 (Oct. 5) and 1482 (Oct. 8, 1978). The displacements detected over the 72-hr period are shown in Figure 1. The displacement vectors have their tails on a regular 5-km grid. Where the pattern-matching algorithms of the GPS have poor confidence on the displacement estimate, the grid cells have been left blank. There are a number of possible steps in the analysis.

Isolate discontinuities. There are at least four ways to locate the discontinuities in the velocity field. The first is well studied [4 *op. cit.*]. Applying the displacements to the pixel values of the first image and subtracting from the second produces reconstructed subtracted image intensity. Contrast stretching this picture generally shows thin stripform regions of poor matching of translated ice patterns and therefore poor correlation of surface features and so high ice deformation. This is shown in Figure 2 for the test pair. A second method [4 *op. cit.*] applies the displacements to the intersections of a regular grid to get a deformed grid as shown in Figure 3. Differencing formulas applied to the four corners of each grid cell can give measures of relative strain and so a two-dimensional picture of the deformation.

The pattern-matching algorithm also supplies a confidence estimate for each cell and so a similar picture. A fourth method would be to apply threshholding to the one-dimensional row and column cross sections of the gridded velocity field. Each jump would provide a component of distortion to its cell.

Combining the four effects in a logical and/or statistical manner would provide independent information about the local discontinuities in a number of locations not necessarily on the grid intersections. Curvilinear regression on the resulting clusters would parameterize the discontinuities in an interpolating manner which might reflect something of the physics involved in the formation of the fracture.

Isolate continuum elements. The parameterized discontinuities provide bounding information about the continuum elements. To get internal information we need a method for deciding which displacements belong to the same rotational motion. This is essentially a classification problem. Cluster analysis can be applied if we have a way of characterizing rotational motion as a constant. A first approach involves seeking a common center of rotation. The perpendicular bisectors of each displacement segment of a rigid rotation will meet in a common point—the center. In the presence of errors, however, there will be a possibly large number of close intersections. To avoid the problem of determining and clustering all the intersections we transform the perpendicular bisector data into point data by a method known as *reciprocal polars* [Bracewell, 1990].

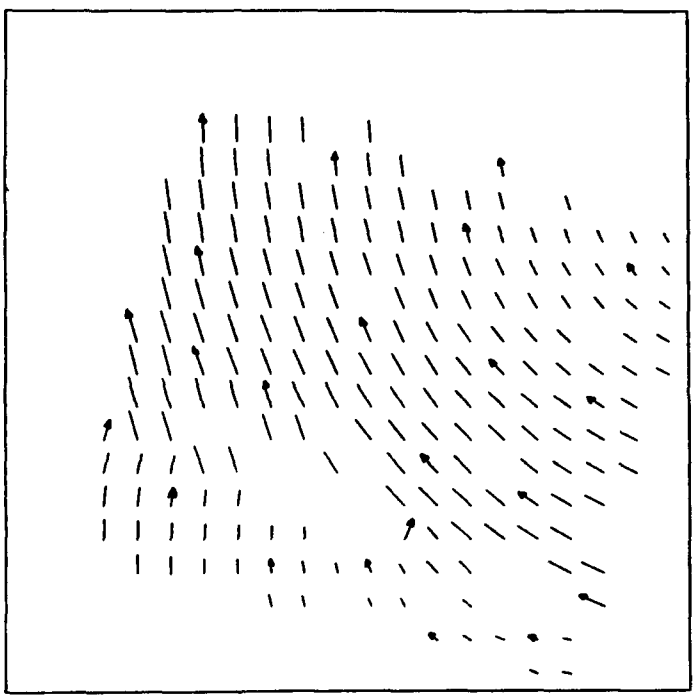


Figure 1. Displacement field for ice motion in the Beaufort Sea between SEASAT revolutions 1439 and 1482. Arrows on some vectors show the direction. The remaining displacements follow similar streamlines. The tails are on a regular 5-km grid.

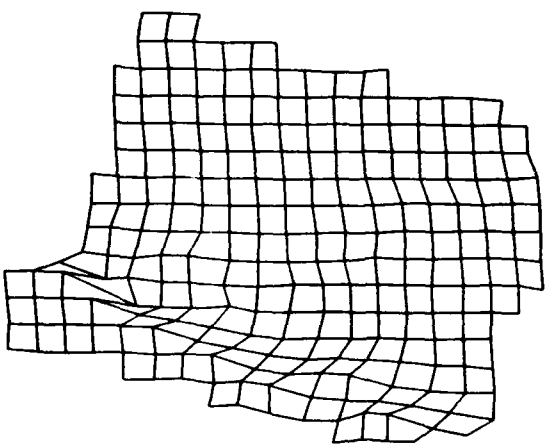


Figure 3. Distorted 5-km grid after application of the displacements. Major deformation features corresponding to Figures 1 and 2 are evident.

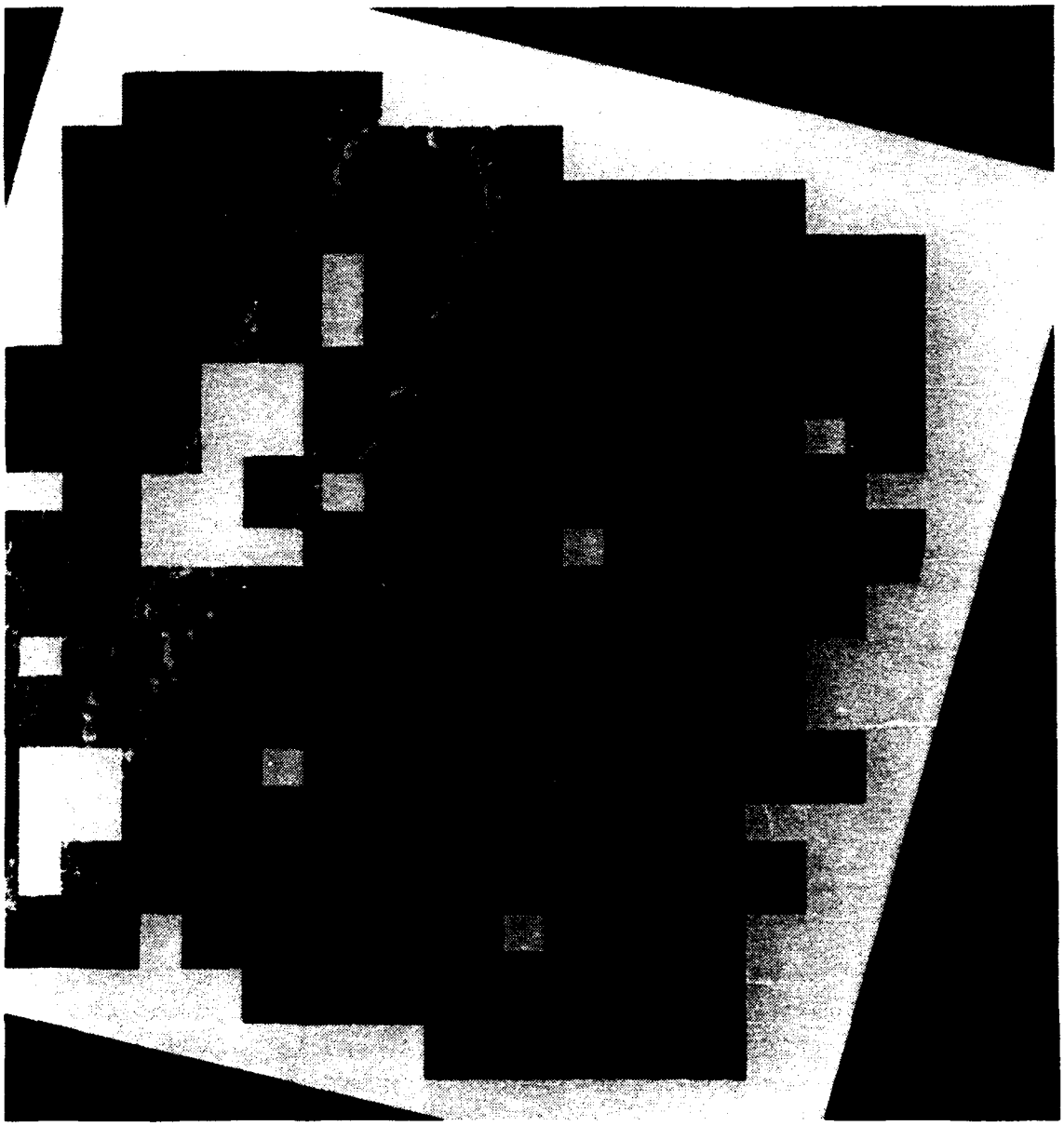


Figure 2. The difference between pixel intensities of Rev 1482 and the displaced intensities of Rev 1439 have been stretched to show contrast. Dark areas correspond to relatively rigid sections of the ice pack. The light filaments are edges where shear and convergence/divergence causes high ice deformation. At blank squares there is no displacement data.

This transformation assigns to each non-vertical line

$$y = ax + b$$

the point (a,b) in the plane. The useful property of this correspondence is that if a number of lines

$$y = a_i x + b_i \qquad i = 1, \ldots, n$$

meet at a common point (x_0, y_0), then their reciprocal polar points lie on a common line

$$b = -x_0 a + y_0$$

in the (a,b) plane.

Thus the perpendicular bisectors of the displacement vectors may be transformed into the reciprocal polar plane where, if they correspond to a common rotation, they will cluster along a line. Standard regression on this data will yield the quantities x_0 and y_0 along with confidence es-

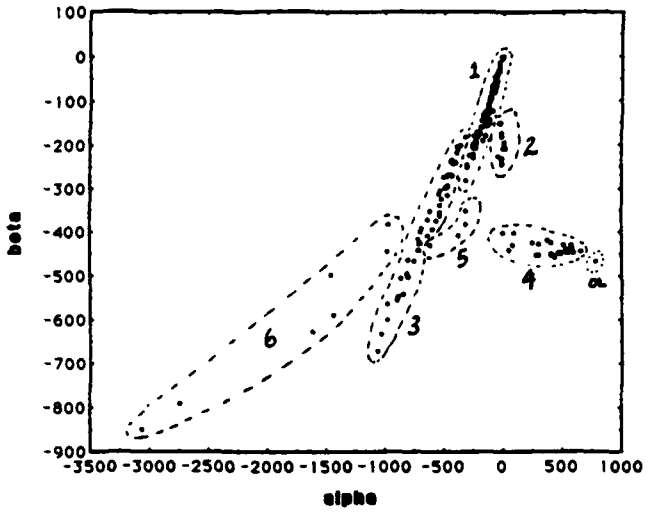


Figure 4. Scatter plot of the reciprocal polar points of all perpendicular bisectors of displacements from Figure 1. These fall into six natural groups as labeled 1 through 6. Where geometrical clustering is ambiguous, additional grouping information can be obtained by considering contiguity in the vector field, and the size of the displacements. Thus the outlier (marked OL) on the far right is compatible with the center of Group 4, but its magnitude is too large. Similarly, the member of Group 5 whose reciprocal polar clusters with Group 3 is too small for that displacement. The units on the axes are pixel numbers scaled for clarity of the plot.

timates on them. In practice we transform *(a,b)* into (α,β) by scaling, rotation and shear to enhance separation between the linear clusters.

When we apply this procedure to the test pair, we obtain the clusters shown in Figure 4. Visual inspection of this scatter plot reveals six clearly identified groups clustered along lines in the plane. Mapping the grouping back onto the velocity field produces the dissection shown in Figure 5. Comparing this picture with Figures 2 and 3 shows clearly how the boundaries of the continuum elements correspond to the high deformation zones. Even the minor break in the displacement field which trends up and to the right from the center of Figure 5 can be easily found in Figure 4. Although it is not at all apparent from visual inspection of the vectors or the deformed grid, it does also appear in the reconstructed subtracted data of Figure 2. Thus information about the structure of the field can be refined by working back and forth between the first two steps of the analysis described above. In an automated procedure, iterative relaxation methods could exploit this reciprocity.

The reciprocal polar method gives only two of the three parameters needed. Thus our clusters may contain extraneous displacements with compatible centers but differing magnitudes, as in the uppermost vector in Group 5. It is possible to make further discrimination by considering the length of the displacement. This can be converted to angular displacement once a center has been found. Comparing the angular displacement to others in the cluster can confirm or eliminate membership in the group. Thus the Group 5 vector under consideration is compatible with the center of both Groups 3 and 5, but its magnitude only fits into Group 5.

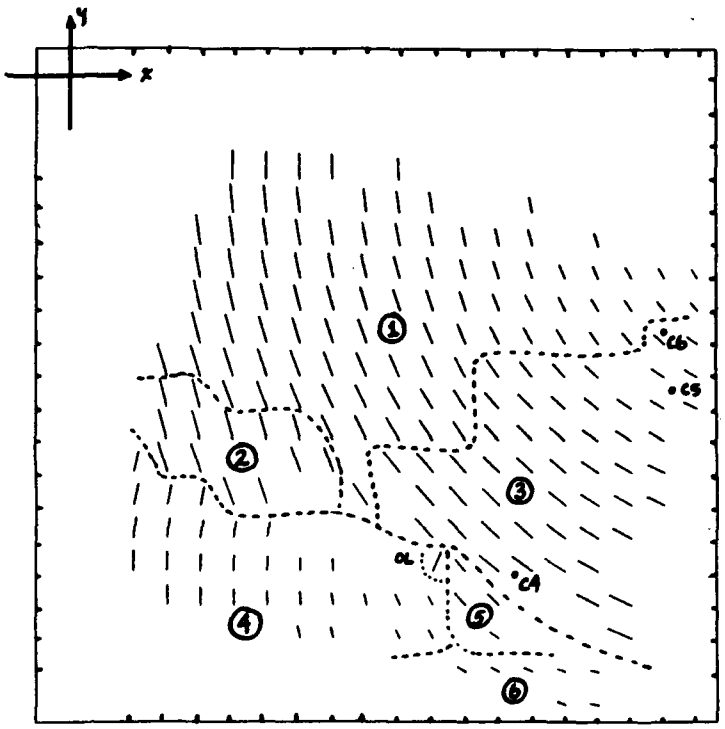


Figure 5. The vectors of Figure 1 grouped by dotted lines into the clusters of Figure 4 and labeled with numerals in circles. Dots at the corresponding centers of rotation are labeled with a C preceding the same numeral. The corresponding angular displacement is given in Table 1. The tic marks are on the regular 5-km grid referenced to the axis origin shown at upper left.

Regression on Mean Rotational Motion

Group	p	q	r^2	x_0	y_0	γ	δ
1	0.5940	-40.17	0.999	123.2	-9.894	3.86	0.06
2	0.7220	-26.77	0.981	179.9	-9.631	3.64	0.09
3	0.5596	-37.98	0.999	113.5	-8.624	4.29	0.15
4	0.2546	-561.7	0.879	67.08	-75.35	5.47	1.17
5	0.4468	-262.0	0.980	90.38	-47.36	4.48	0.72
6	0.4406	-218.4	0.997	89.39	-39.04	2.61	0.06

Table 1. For each group of Figure 5 are listed slope and intercept of the linear regression on the reciprocal polars cluster. The correlation coefficient r^2 indicates goodness of fit. The next two columns give the coordinates of the corresponding center of rotation. The units are kilometers from the origin in the upper left corner of the Figure. In the last two columns are the mean angular rotation in degrees and the standard deviation of the data from that mean.

Parameterize continuum element motion. We have seen above how the centers of rotation may be determined. To complete the parameterization of rotational motion we determine the angular displacement corresponding to each vector and, assuming normally distributed deviation from a constant angular velocity, we can get a best estimate of the rigid motion by using the mean γ of the individual angular displacements. Confidence in this estimate would come from the standard deviation δ. Large deviations would indicate incompatible displacements as in the previous paragraph, leading to revision of the cluster groups. For the test image pair the final results are shown in Table 1 and plotted on Figure 5.

It is worth noting that, except for Group 4, the regressions are all very tight, so that the estimates of the center coordinates will be correspondingly good—on the order of a few percent. Similarly the confidence is good on the angular displacements, with one standard deviation being 3% or smaller on four of the groups. The largest variance in angular displacement also corresponds to the worst regression in Group 4. Group 5 also has large angular variance due to either the small sample size or large deformation of the ice in the area.

CONCLUSIONS

Having parameterized the discontinuities and the motion of the continuum elements, we are now in a position to approach the objective of quantifying the pack ice deformation. The primary result of our analysis is that we can do this in two ways—from consideration of relative motion between adjacent continuum elements, and by differential analysis of the continuous deformation within these elements.

Motion across discontinuities. At each point on a discontinuity curve there will be, provided data is not lacking, a continuum element on either side. From each we can compute a displacement at the point due to the rotation. Differencing the two vectors will give a local divergence vector which can be projected into components normal and perpendicular to the curve. Summing these along the length of the curve will then provide an estimate of, respectively, the divergence/convergence and the shear strain, each integrated over the boundary separating the elements. Where velocity data is missing, a measure of the average deformation can be obtained by selecting the nearest continuum element beyond the gap and performing the above integration around the area of missing data [Thorndike, 1986]. In computing deformation per unit area, the size of the gap would have to be taken into account.

Deformation within continuum elements. For this purpose we can use a more classical approach by approximating partial derivatives of the velocity field and computing standard coordinate measures of deformation as in Volkov et al. [1972]. These authors consider the components u,v of the velocity field,

$$\mathbf{V} = (u(x,y),v(x,y))$$

Let a subscript on a function name denote partial differentiation with respect to the variable appearing in the subscript. Then the following formulae are coordinate invariant:

$$\mathrm{divV} = u_x + v_y$$
$$\mathrm{rotV} = v_x - u_y$$
$$\mathrm{defV} = \sqrt{(v_x + u_y)^2 + (v_y - u_x)^2}$$

The first is the standard divergence, or fluid source/sink. The second is the rotation or curl which, in the case of constant rotational motion, gives one half of the angular velocity. The third is the RMS measure of angular deformation and anisotropy of deformation respectively. DivV and defV can also be transformed to polar form by the Pythagorean and arctangent formulas which have useful physical interpretations [Fily and Rothrock, 1990; Colony, 1991]. To compute all these we need to approximate the partial derivatives.

Consider four points in the plane $\{(x_i,y_i):i=1,\ldots 4\}$ which are the vertices of a roughly regular quadrilateral, i.e., the sides and angles are comparable in magnitude. Let the diagonally opposite vertices be labeled 1, 3 and 2, 4. Let D_{ij} be the difference operator between points i and j, and $f(x,y)$ be a function of two variables. Using some straightforward approximations and mean value theorems for derivatives produces the following linear system in the partial derivatives evaluated at a point within the quadrilateral,

$$\Delta_{42}x\, f_x + \Delta_{42}y\, f_y = \Delta_{42}f$$
$$\Delta_{31}x\, f_x + \Delta_{31}y\, f_y = \Delta_{31}f$$

Solving this for the derivatives gives

$$f_x = (\Delta_{42}f\, \Delta_{31}y - \Delta_{31}f\, \Delta_{42}y)/D$$
$$f_y = (\Delta_{31}f\, \Delta_{42}x - \Delta_{42}f\, \Delta_{31}x)/D$$

where

$$D = \Delta_{42}x\, \Delta_{31}y - \Delta_{31}x\, \Delta_{42}y$$

Using these formulae with f replaced by u and v gives the values needed to compute the deformation measures in the vicinity of the four data points. These numerical formulae for their derivatives are also given by Tabata et al. [1979] who agree with Volkov et al. [1972] as to substance but not derivation.

ACKNOWLEDGMENTS

I am indebted to Frank Carsey and Willy Weeks, lead scientists at the Alaska SAR Facility, for many helpful discussions on this subject. Ron Kwok of the Jet Propulsion Laboratory (JPL) provided essential technical information as well as stimulating ideas on the algorithmics. The images and data were supplied courtesy of Shirley Pang, also of JPL. This work was performed under contract to the National Aeronautics and Space Administration.

REFERENCES

Bracewell, R. N., Reciprocal polars in the plane, Personal communication, 1990.

Collins, M. J., and W. J. Emery, A computational method for estimating sea ice motion in sequential Seasat synthetic aperture radar imagery by matched filtering, *J. Geophys. Res.*, *93*, 9241–9251, 1988.

Colony, R., Seasonal mean ice motion in the Arctic Basin, *This Volume*, 1991.

Curlander, J. C., B. Holt, and K. J. Hussey, Determination of sea ice motion using digital SAR imagery, *IEEE J. Ocean. Eng.*, *10*, 358–367, 1985.

Fily, M., and D. A. Rothrock, Extracting sea ice data from satellite SAR imagery, *IEEE Trans. Geosci. Remote Sensing*, *24*, 849–854, 1986.

Fily, M., and D. A. Rothrock, Opening and closing of sea ice leads: Digital measurements from synthetic aperture radar, *J. Geophys. Res.*, *95*, 789–796, 1990.

Hibler, W. D. III, Ice dynamics, in *The Geophysics of Sea Ice*, edited by N. Untersteiner, Plenum Press, New York, 1986.

Kwok, R., J. C. Curlander, R. McConnell, and S. S. Pang, An ice–motion tracking system at the Alaska SAR Facility, *IEEE J. Ocean. Eng.*, *15*, 44–54, 1990.

Tabata, T., T. Kawamura, and M. Aota, Divergence and rotation of an icefield off Okhotsk sea coast of Hokkaido, in *Sea Ice Processes and Models*, edited by R. S. Pritchard, University of Washington Press, Seattle, 1980.

Thomas, D. R., and D. A. Rothrock, Blending sequential scanning multichannel microwave radiometer and buoy data into a sea ice model, *J. Geophys. Res.*, *94*, 10907–10920, 1989.

Thorndike, A. S., Kinematics of sea ice, in *The Geophysics of Sea Ice*, edited by N. Untersteiner, Plenum Press, New York, 1986.

Thorndike, A. S., D. A. Rothrock, G. A. Maykut, and R. Colony, The thickness distribution of sea ice, *J. Geophys. Res.*, *80*, 4501–4513, 1975.

Vesecky, J. F., R. Samadani, M. P. Smith, J. M. Daida, and R. N. Bracewell, Observation of sea-ice dynamics using synthetic aperture radar images: Automated analysis, *IEEE Trans. Geosci. Remote Sensing*, *26*, 38–48, 1988.

Volkov, N. A., Z. M. Gudkovich, and V. D. Uglev, Results of the study of nonuniform ice drift in the Arctic Basin (translated from Russian), *AIDJEX Bulletin*, *16*, 82–96, 1972.

Section B:

Climate Variability and Climate Forcing

Chaired by

W. Budd
University of Melbourne
Australia

Ya. Kondratyev
Institute of Lake Research
U.S.S.R.

How Climate Changes

J. O. Fletcher
NOAA Environmental Research Laboratories, Boulder, Colorado, U.S.A.

ABSTRACT

Climate variability on time scales of years through centuries seems to be dominated by two kinds of recurring fluctuations, each exhibiting characteristic evolution in time. One is the El Niño/Southern oscillation phenomenon, a tropical ocean/atmosphere autofluctuation that is phase locked to the annual cycle and recurs at 3 or 4 year intervals. The other fluctuation exhibits a recurrence period of about 1 1/3 century and appears to be forced from high latitudes in winter, more strongly from the Arctic than from the Antarctic. This paper is an overview of the morphology and teleconnections associated with this longer period fluctuation.

The dynamic forcing is exhibited most strongly as deepening (or shallowing) of the sub-polar surface pressure trough in both the Atlantic and Pacific sectors and some changes in the central pressure of the subtropical highs. This can be visualized as strengthening (or weakening) of the mean winter fields of pressure and wind, reflected by southward displacement and strengthening of the major wind and SST fields over the Atlantic and Pacific. These dynamical relationships are reflected in teleconnections extending from the Arctic far into the southern hemisphere. The range of variability of surface wind strength is 20%–30%, (a factor of 2 in wind stress on the ocean) with wind strongest in the 1860s, sudden weakening in the northern hemisphere in the 1870s, continued weakening to a minimum in 1930s, strengthening since then, especially since the 1960s.

High Latitude Climate Forcing by 18.6-Year Lunar Tidal Fluctuations

T. C. Royer
Institute of Marine Science, University of Alaska Fairbanks, Fairbanks, Alaska, U.S.A.

ABSTRACT

Upper layer ocean temperatures in the northern North Pacific increased by more than 2°C in 10 years beginning in 1972. Proxy time series indicate that this is not a monotonic signal but rather a very low frequency fluctuation. The sea surface temperatures, which began in 1946, and the air temperature at Sitka since 1910, show fluctuations of 15–25 years. A least squares fit of the 18.6-year lunar declination signal to the 5-year block-averaged air temperature at Sitka can account for 44% of its variance. A modification of the mean ocean circulation by the change in lunar tides is suggested as the cause for this fluctuation.

Similar sea surface temperature fluctuations have been observed for the northern North Atlantic Ocean from 1876 to 1965 but they appear to be out of phase with the North Pacific. The Atlantic fluctuations also have a small amplitude; 0.24°C versus 0.52°C for the North Pacific. Low frequency cycles are also evident in the air temperatures from the Hudson Bay region since 1700. The opposite phasing of the water and air temperatures of the North Atlantic and North Pacific is consistent with the tidal modulation of the mean ocean circulation. The most recent minimum for the Sitka air temperature should have occurred in September 1989.

AD-P007 280

92-17962

Cloud Radiation Interaction and the Earth's Climate: Relevance to the Climate of the Arctic

Graeme L. Stephens
Department of Atmospheric Science, Colorado State University, Ft. Collins, Colorado, U.S.A.

ABSTRACT

The influence on the energy balance of the earth's climate system is reviewed and is based on recent satellite observations of the Earth's Radiation Budget (ERB) and other satellite-derived cloud information. The special difficulties that polar cloudiness poses in analysis of ERB data are discussed. The role of arctic cloudiness on the snow-ice albedo feedback is examined and the possible influence of this feedback to global cloudiness and thus to the radiation balance on the earth are explored.

INTRODUCTION

Clouds exert a dominant influence on the amount of solar energy absorbed by the Earth and on the amount of infrared radiation emitted to space. It is known that clouds present a paradox: they act to cool the planet by reflecting solar radiation to space, and warm the planet by reducing the amount of radiation emitted to space. These two radiative processes tend to produce reciprocal effects on a net influence of clouds on the radiative budget of the Earth (ERB) such that the net effect of clouds on the ERB is less than their effect on the individual components of this budget [e.g., Stephens, 1981; Ramanathan et al., 1987]. This observation is occasionally mistakenly interpreted to mean that the sensitivity of the Earth's climate to cloud, and thus cloud feedback, is small. However, the extent to which these reciprocal processes compete and how they vary with time, location, and with cloud type and structure is neither well known nor well understood. Furthermore the specific effects of polar clouds on this radiative balance are not well known, partly because of the difficulty in observing these clouds from space. One of the aims of this study is to provide a simplified perspective of the effect of clouds on the Earth's radiation budget on the global scale and to contrast these effects against those of polar clouds.

While it is known that clouds generally exercise a strong control over the energetics of the climate system, the way they in turn depend upon the climate system is much less certain and constitutes the poorly understood aspect of the cloud climate feedback problem [e.g., Arking, 1991]. In fact, several feedbacks have been hypothesized in the literature over the past several years but generally with little observational support. This paper illustrates how the observations provide little support to many of these proposed feedbacks. It is difficult to extend these arguments about cloud feedback to polar regions largely because of the lack of data on cloudiness over the poles. In view of this observational shortcoming, a simple theoretical account of clouds on the polar radiation budget is described and the hypothetical relevance of cloudiness to the snow/ice–temperature feedback is briefly addressed.

DATA SOURCES

Full details of the data used in this study are provided in the study of Stephens and Greenwald [1991a,b]. The present study uses ERB data taken from two sources: the narrow field-of-view, broadband scanning radiometer data of Nimbus-7 for the 1979 calendar year, and the broadband scanning data ERBE for the 1985 calendar year. The principal use of the ERBE data is for comparison to the Nimbus-7 data in order to examine similarities and identify any discrepancies between the two. Cloudiness data used in the study are those derived from Nimbus-7 THIRS/TOMS observations of Stowe et al. [1988] for 1979. The sea surface temperature (SST) data are those provided by the National Meteorological Center that cover this same observational period. The passive microwave observations obtained from the Scanning Multichannel Microwave Radiometer (SSMR), which was also flown on the Nimbus-7 satellite,

provide the basis for the water vapor and liquid water information used [Prabhakara et al., 1982, 1983].

OBSERVED EFFECTS OF CLOUDS ON THE ERB

A convenient mode of analysis of ERB data is the method described by Charlock and Ramanathan [1985] and referred to as cloud radiative forcing. This method relies on the estimation of clear sky fluxes and the following flux difference quantities

$$C_{LW} = F_{clr} - F_{obs}$$

$$C_{SW} = \frac{Q_o}{4}(\alpha_{clr} - \alpha_{obs}) \qquad (1)$$

$$C_{net} = C_{LW} + C_{SW}$$

where F_{clr} and α_{clr} are respectively the estimated clear sky longwave flux and the clear sky albedo and F_{obs} and α_{obs} are the respective values observed. Q_o is the solar insolation. The three flux quantities defined by (1) are interpreted as a direct measure of the impact of clouds on the longwave (LW), shortwave (SW) and net (net) fluxes respectively.

Global Distributions

The global distribution of the flux difference quantities defined by (1) have been discussed in previous studies [Ramanathan et al., 1989; Harrison et al., 1990; Stephens and Greenwald, 1991a,b]. These studies have emphasized the following important features of these distributions:

- generally negative values of C_{SW} everywhere but especially in relation to the ITCZ, SPCZ and midlatitude storm tracks;
- generally positive values of C_{LW} with largest effects associated with the ITCZ and especially the deep convection over Indonesia; and
- the near cancellation of C_{LW} and C_{SW} over these convective regions, the predominant negative values of the storm tracks, and the somewhat smaller negative values associated with the regions of stratocumulus clouds.

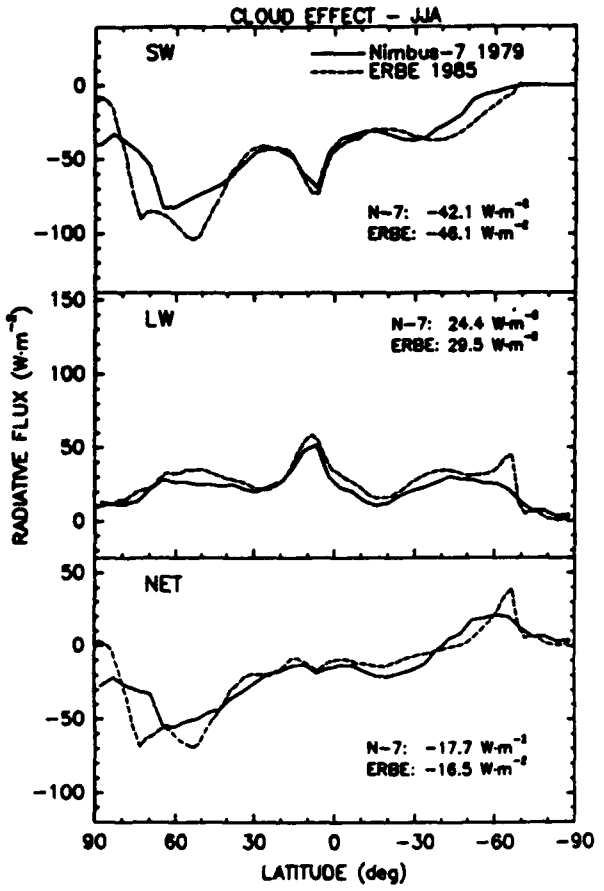


Figure 1a. Zonally averaged values of the three cloud flux quantities C_{LW} (*LW*), C_{SW} (*SW*), C_{NET} (*NET*) in $W\ m^{-2}$ as a function of latitude determined from Nimbus-7 and ERBE data for the JJA season. Also listed are globally averaged fluxes.

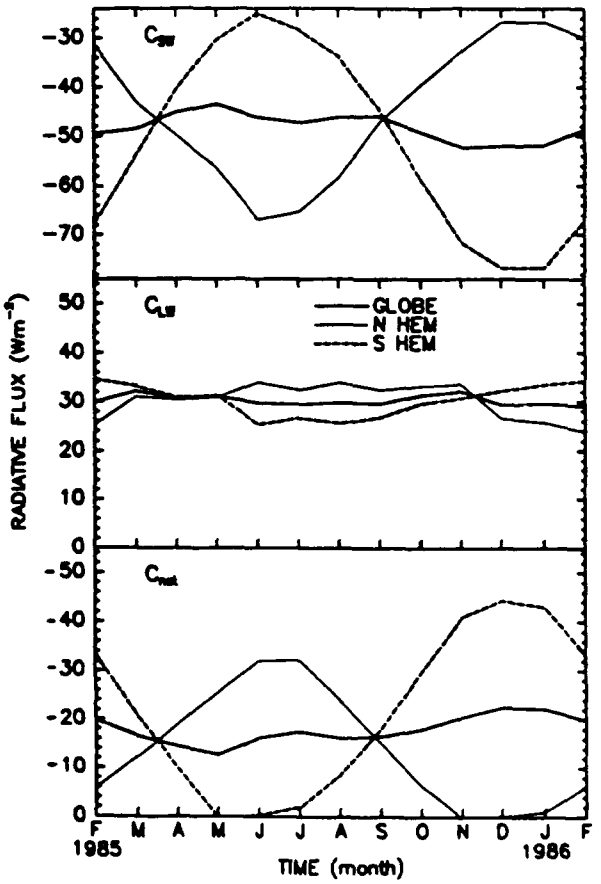


Figure 1b. The annual cycle of the hemispherically and globally averaged fluxes derived from ERBE data.

Season	C_{SW}	C_{LW}	C_{net}
JJA	-42.1 (-46.1)	24.4 (29.5)	-17.7 (-16.5)
SON	-44.0 (-49.1)	24.5 (30.9)	-19.5 (-18.2)
DJF	-44.5 (-50.5)	22.2 (29.2)	-22.2 (-21.3)
MAM	-44.7 (-45.5)	25.2 (31.2)	-19.5 (-14.3)
Annual	-43.8 (-47.8)	24.1 (30.2)	-19.7 (-17.6)

Table 1. Globally averaged quantities of C_{LW}, C_{SW} and C_{net} ($W\ m^{-2}$) derived from Nimbus-7 and ERBE (in parentheses) data.

Zonal and Global Averages

The significance of the midlatitude storm track clouds on the zonal and hemispherically averaged flux quantities is shown in Figure 1a and b for JJA. Evident in the zonal average profiles of C_{SW} and C_{net} is the effect of the pronounced minimum in C_{SW} (i.e., a maximum in reflected solar radiation) in the illuminated northern midlatitudes around 60°N. The bright midlatitude clouds in each summer hemisphere also dominate the annual cycle of C_{SW} and C_{net} as shown in Figure 1b. The amplitude of C_{net} is almost completely dictated by the amplitudes of C_{SW} which, in turn, is largely influenced by the reflection of solar radiation by midlatitude cloudiness and the seasonal change in the solar insolation reaching these clouds. The reflection of solar radiation by these clouds also dominates the globally averaged values of C_{net} as listed in Table 1. Analysis of ERB data shows that, on the global scale, the albedo effect of clouds dominates over compensating greenhouse effect with $C_{net} \sim -20\ W\ m^{-2}$.

THE GREENHOUSE EFFECT OF CLOUDS

Stephens and Greenwald [1991a,b] define the greenhouse effect G over oceanic regions as

$$G = \frac{\sigma T_s^4}{I} \qquad (2)$$

where T_s is the sea surface temperature (SST) and I the radiation emitted to space. Figure 2 shows values of G derived for cloudy skies as a function of the SST. The clear sky relationship is shown by the open symbols and arises from the impact of the water vapor on the greenhouse effect and the relationship between water vapor and SST [Stephens, 1990; Stephens and Greenwald, 1991a,b]. The difference between clear and cloudy sky G thus gives quantitative measure of the greenhouse effect of clouds. In Figure 3, G is shown to increases systematically with liquid water path (LWP). This result directly contrasts with several studies of cloud feedback scenarios that assume the greenhouse effect of the atmosphere to remain unchanged when the LWP is increased [e.g., Sommerville and Remer, 1984]. Clearly feedback scenarios based on this assumption are not supported by the observations.

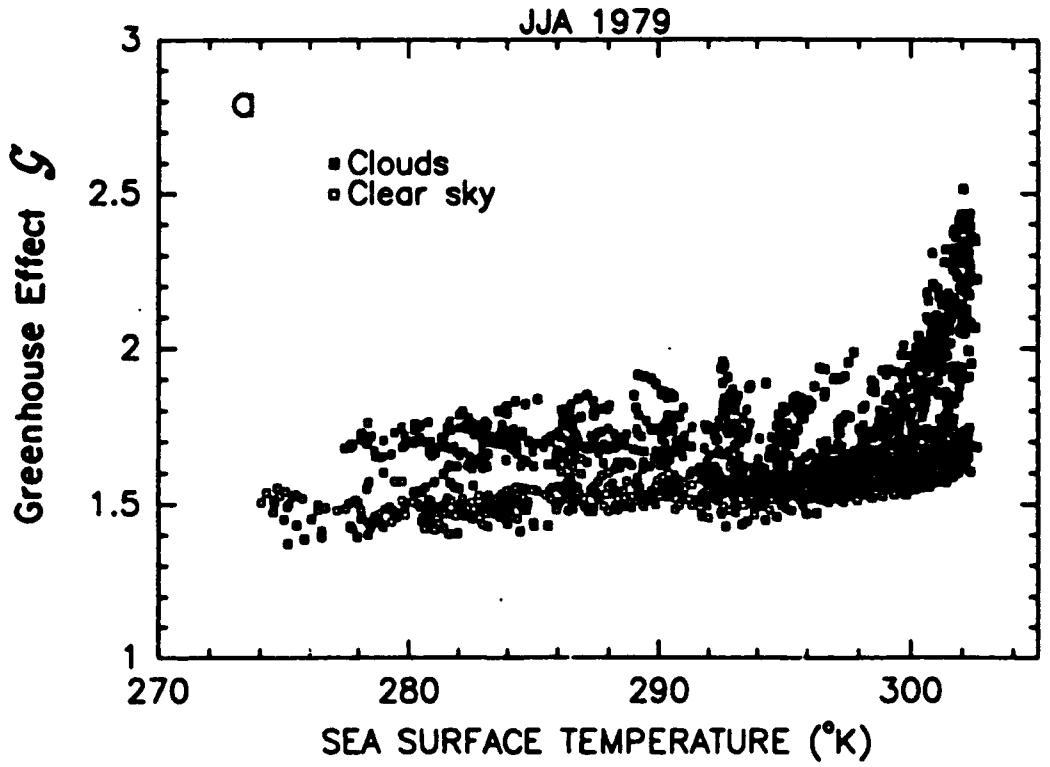


Figure 2. The greenhouse effect parameter G for cloudy skies (filled squares) and clear skies (open squares) as a function of SST for JJA, 1979.

THE ALBEDO EFFECT OF CLOUDS

We noted above the general dominance of the albedo effect of clouds over their greenhouse effect in the midlatitudes of the summer hemisphere. Using an analysis procedure developed by Stephens and Greenwald [1991a,b], the albedo of clouds was derived from estimates of α_{clr} and measurements of α_{obs}. The cloud albedos derived from this procedure were categorized in terms of the solar zenith angle at the time of observations. These data are presented as frequency plots in Figure 4a for clouds further classified as midlatitude or tropical clouds. Midlatitude clouds are those clouds found poleward of ±22.5° latitude and tropical clouds refer to those clouds that are found in the equatorial belt defined by these latitudes. These frequency distributions indicate the increased brightness of midlatitude clouds in comparison to tropical clouds for the same solar geometry. This difference is further exaggerated when the albedo corresponding to the solar zenith angle range 15–30° is correlated with LWP as shown in Figure 4b. We observe that the albedo–LWP relationship of tropical clouds appears to be systematically different from that of midlatitude clouds. For the same range of solar zenith angles and for the same liquid water path, midlatitude clouds are apparently substantially brighter than tropical clouds. It should however be emphasized that the relationships on this diagram do not represent a true albedo–optical mass relationship because of the insensitivity of the SMMR observations to ice crystals, which obviously also contribute to the cloud albedo. However, it is unlikely that the differences shown are due entirely to the neglect of ice mass as it would require the presence of substantially more ice in midlatitude clouds relative to tropical clouds to bring the two observed relationships into broad agreement.

These results indicate that the albedo effect of clouds varies with LWP in a manner that we can perhaps associate with the morphology of clouds (e.g., tropical clouds are more convective in nature than midlatitude clouds). At present we have no way of defining this effect in terms of parameters predicted by climate models. Given the significance of the effect, it is clearly important to establish how climate change may act to alter the morphology of clouds. As a specific example, do midlatitude clouds become more tropical in character under the scenario of global warming?

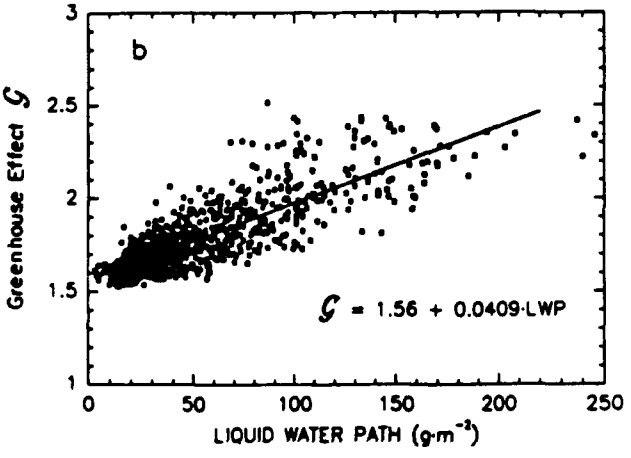


Figure 3. The relationship between $\mathcal{G}$ versus SMMR-derived liquid water path (gm^{-2}) for JJA 1979.

APPLICATION TO THE RADIATIVE BUDGET OF POLAR REGIONS

Global effects of clouds on the ERB have been studied extensively over the past decade or so using the high quality measurements made available from programs like ERBE and the Nimbus series [e.g., Stephens et al., 1981; Ramanathan et al., 1987; among others]. We learn from these studies that the albedo effect of clouds dominates on the whole by the order of 20 $W\ m^{-2}$ (refer to Table 1). We also learn that the albedo effect of clouds shows distinct differences depending on whether these clouds are found in the tropics or midlatitudes and furthermore that the greenhouse effect of clouds systematically increases with both SST and LWP. By comparison, the effect of polar clouds on the ERB has received much less attention owing to the difficulties associated with the discrimination of cloud from bright cold polar surfaces.

At present it is thought that the influence of polar clouds on the net radiation budget is such that $C_{net} \geq 0$. However, this anticipated small effect on the ERB does not mean that polar clouds are unimportant to cloud feedback nor does it mean that changes in polar cloudiness cannot exert a more global influence on the energetics of the climate system. Unfortunately we have no way of examining this possibility with our present method of observations. We are thus forced to invoke simple theoretical arguments in an attempt to formulate some understanding about the actions of these clouds on the climate of polar regions. As an example, consider the simple scenario conveyed in Figure 5. Suppose a change in cloud occurs which produces a change in the surface radiation budget. In considering the change in this budget, suppose only the albedo and emittance of clouds alters and designate these changes by $\Delta\alpha$ and $\Delta\varepsilon$ respectively. Thus we are able to write the change in the surface balance in the form of the following inequality

$$\Delta\sigma\ T_s^4 \begin{matrix} \text{heating} \\ > \\ < \\ \text{cooling} \end{matrix} 0 \qquad (3)$$

and that

$$\mathcal{T}_L \sigma T_s^4 \Delta\varepsilon \begin{matrix} > \\ < \end{matrix} \frac{Q_o}{4} \mathcal{T}_I (1-\alpha_s) \Delta\alpha \qquad (4)$$

In this expression $\mathcal{T}_L$ and $\mathcal{T}_S$ are respectively the transmission of longwave and shortwave radiation below the cloud layer, α_s is the surface albedo and T_1 is the temperature of the cloud. The inequality of (4) states that a surface warming predominates when the change in emission by the cloud (i.e., $\sigma\ \mathcal{T}_I^4 \Delta\varepsilon$) exceeds the loss by the enhanced reflection by the cloud ($Q_o \Delta\alpha/4$). We learn from this simple statement that the tendency for clouds to cool/warm the surface depends on the change of $\Delta\varepsilon$ relative to $\Delta\alpha$ as well as the magnitude of Q_o and α_s. The latter point is particularly relevant to polar regions whose climate is characterized by small values of Q_o and large values of α_s. Under these conditions even modest increases in the longwave emission by

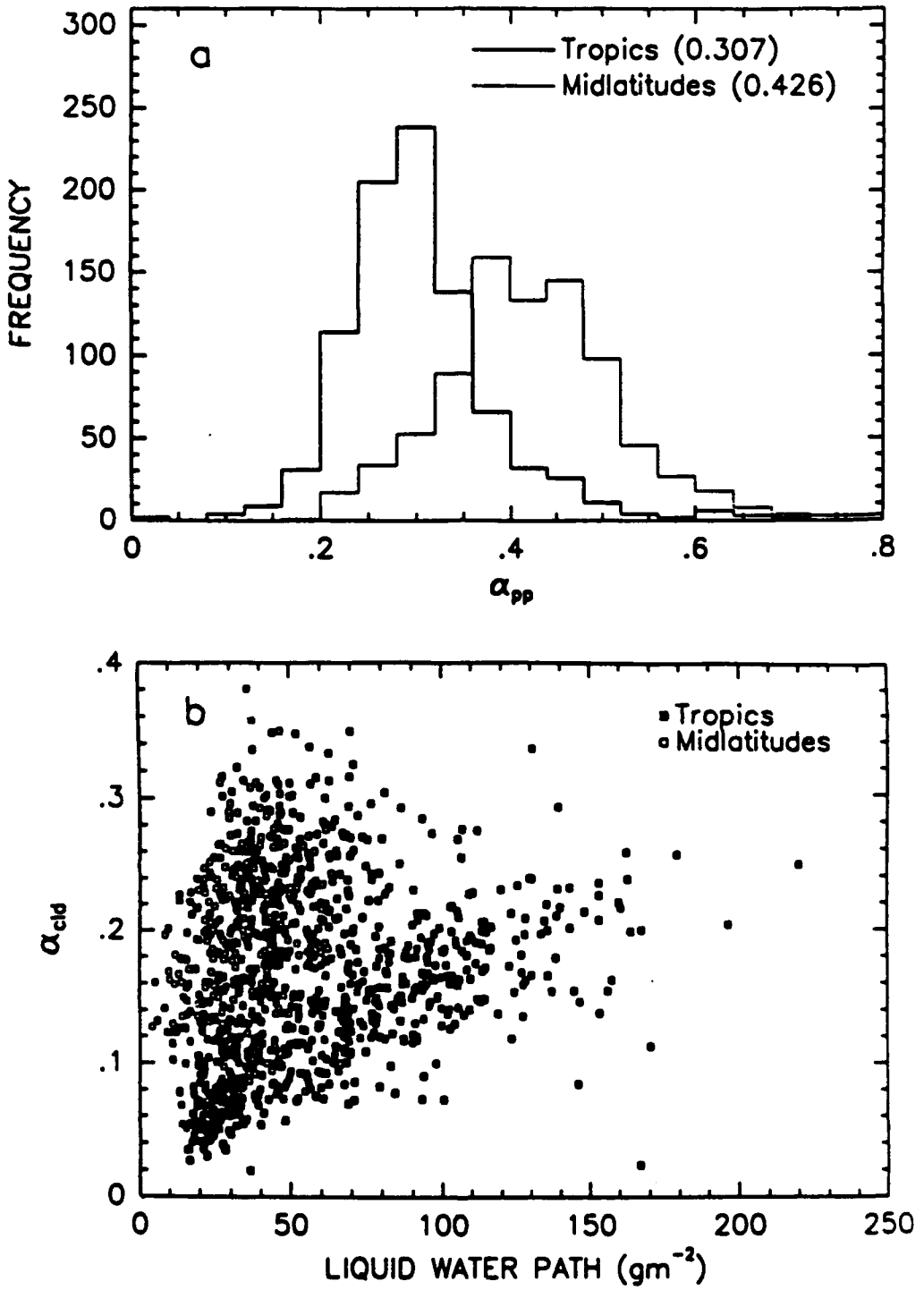


Figure 4a. Frequency distribution of cloud albedo in the midlatitudes and the tropics for the range of solar zenith angles between 15° and 30°. For a definition of tropics and midlatitudes, consult the text. **4b.** The relationship between cloud albedo and cloud liquid water path.

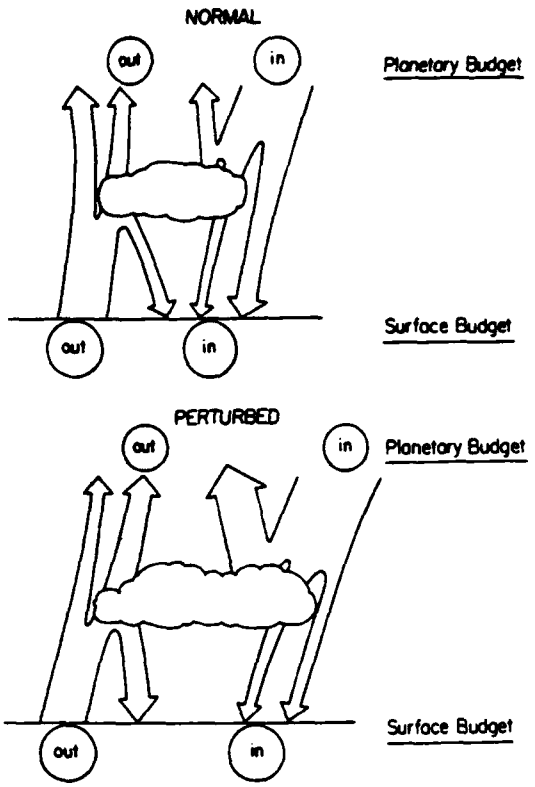


Figure 5. Schematic depiction of the radiation balance of the Earth-atmosphere system under hypothetically normal and perturbed conditions.

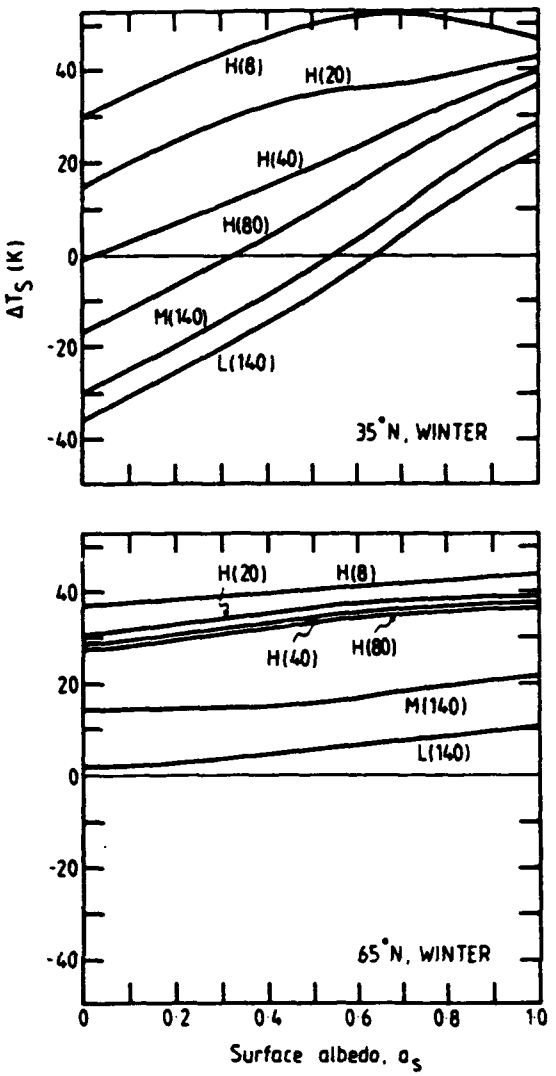


Figure 6. The difference in the thermal equilibrium temperature derived for overcast and clear sky conditions by a one-dimensional climate model shown as a function of surface albedo. The symbols *L*, *M*, and *H* refer to low, middle, and high clouds and the numbers in parentheses refer to the LWP specified in the calculations [from Stephens and Webster, 1981].

clouds can offset the ensuing decrease by reflection. This observation is supported by predictions of the thermal equilibrium of high latitude regions by climate models [e.g., Stephens and Webster, 1981]. Figure 6 shows examples of these predictions, expressed in terms of the surface temperature difference between overcast and clear skies as a function of surface albedo. For the case of 35°N, the presence of clouds warms the high albedo surfaces relative to clear skies whereas all clouds warm regardless of α_s and the assumed LWP for the more polar conditions represented by 65°N. The general positive slope of these ΔT_s - α_s relations implies that under conditions of fixed cloud, a decrease in α_s as predicted under the global warming scenario by present climate model may lead to a surface cooling rather than surface warming. Whether the precise details predicted by this kind of model can be believed is not the question. Rather these results suggest that the relative role of clouds on the surface energy balance of polar regions is mutually dependent on the surface albedo and vice versa. Thus it is somewhat futile to discuss surface albedo–surface temperature feedbacks without due recognition of the cloud conditions.

CONCLUSIONS

The paper provides a brief glimpse at selected results obtained from analysis of ERB data in relation to how clouds affect the ERB. From these results we can show how the albedo effect of cloud dominates on the global scale producing a net effect on the ERB of about 20 $W\ m^{-2}$. By further analysis of the ERB in relation to cloud liquid water information, the albedo effect of clouds is shown to be distinctly different depending on whether these clouds are found in the tropics or midlatitudes and furthermore that the greenhouse effect of clouds systematically increases with both SST and LWP. By comparison, the effects of polar clouds on the ERB have received much less attention owing to the difficulties associated with the discrimination of cloud from the bright cold polar surfaces.

A discussion of the impact of clouds on the surface radiation budget of polar regions is given. It is argued that for climates defined by low solar insolation and high surface albedo, the greenhouse effect of clouds is likely to be more dominant than the albedo effect. Any increase in polar cloudiness will produce the tendency to warm the surface. Simple radiation budget arguments are invoked to show the surface radiation balance is mutually dependent on cloudi-

ness and vice versa. The precise nature of any feedback associated with a surface warming must consider not only changes in surface properties but any associated change in cloudiness.

ACKNOWLEDGMENTS

Portions of the research described in this proposal were funded under National Science Foundation grant ATM 8907414 and NASA grant NAG 5-1122, SUPL-01.

REFERENCES

Arking, A., The radiative effects of clouds and their impact on climate, *Bull. Amer. Meteorol. Soc.*, *72*, 795–813, 1991.

Charlock, T. P., and V. Ramanathan, The albedo field and cloud radiative forcing produced by a general circulation model with internally generated cloud optics, *J. Atmos. Sci.*, *42*, 1408–1429, 1985.

Harrison, E. F., P. Minnis, B. R. Barkstrom, V. Ramanathan, R. D. Cess, and G. G. Gibson, Seasonal variation of cloud radiative forcing derived from the Earth Radiation Budget Experiment, *J. Geophys. Res.*, *95*, 18687, 1990.

Prabhakara, C., H. D. Chang, and A. T. C. Chang, Remote sensing of precipitable water over the oceans from Nimbus-7 microwave measurements, *J. Appl. Meteorol.*, *21*, 59–68, 1982.

Prabhakara, C., I. Wang, A. T. C. Chang, and P. Gloersen, A statistical examination of Nimbus-7 SMMR data and remote sensing of sea surface temperature, liquid water content in the atmosphere and surface wind speed, *J. Clim. Appl. Meteorol.*, *22*, 2033–2037, 1983.

Ramanathan, V., R. D. Cess, E. F. Harrison, P. Minnis, B. R. Barkstrom, E. Ahmad, and D. Hartman, Radiative cloud forcing and climate: Results from the Earth Radiation Budget Experiment, *Science*, *243*, 57–63, 1989.

Sommerville, R. C., and L. A. Remer, Cloud optical thickness feedbacks in the CO_2 climate problem, *J. Geophys. Res.*, *89*, 9668–9672, 1984.

Stephens, G. L., On the relationship between water vapor over the oceans and sea surface temperature, *J. Climate*, *6*, 634–645, 1990.

Stephens, G. L., and P. J. Webster, Clouds and climate: Sensitivity of simple systems, *J. Atmos. Sci.*, *38*, 235–247, 1981.

Stephens, G. L., and T. J. Greenwald, Observations of the Earth's Radiation Budget in relation to atmospheric hydrology. Part I, *J. Geophys. Res.*, *96*, 15311-15324, 1991a.

Stephens, G. L., and T. J. Greenwald, Observations of the Earth's Radiation Budget in relation to atmospheric hydrology. Part II, *J. Geophys. Res.*, *96*, 15325-15340, 1991b.

Stephens, G. L., G. G. Campbell, and T. H. Vonder Haar, Earth radiation budgets, *J. Geophys. Res.*, *86*, 9739–9760, 1981.

Stowe, L. L., Nimbus-7 global climatology, Part I: Algorithms and validation, *J. Climate*, *1*, 445–470, 1988.

Polar Forcing of Natural Variability of the Atmospheric Climate

G. V. Alekseyev
The Arctic and Antarctic Research Institute, Leningrad, U.S.S.R.

ABSTRACT

A comparative analysis of the latitudinal distribution of the climatic variability of different characteristics of the upper atmospheric state and heat balance constituents from data of climatic archives reveals the features of the variability forcing in the direction of the North Pole. The polar forcing of the variability of thermodynamic atmospheric parameters (temperature, pressure, geopotential) is shown to be formed by the fluctuations of meridional air exchange. Intercorrelated analytical expressions are obtained for root-mean-square deviations of average zonal values of the parameters, indicating the effect of polar forcing in the observed variability. The effect of polar forcing of air temperature variability is simulated and its dependence on albedo changes and the "Greenhouse" effect is considered by means of the energy-balance zonal atmospheric model.

92-17963

AD-P007 281

Interannual Changes in Northern Hemispheric Tropospheric Temperatures, 1960-1989

Gary A. Herbert
Climate Monitoring and Diagnostics Laboratory, Environmental Research Laboratories, Boulder, Colorado, U.S.A.

ABSTRACT

Tropospheric temperatures were calculated from geopotential thicknesses based on analyzed data for two layers, 850–700 and 700–500 hPa, for the past three decades. Comparison of the interannual changes in thickness temperatures with radiosonde thickness temperature and surface temperatures show substantial agreement, especially at the time of major changes such as cooling periods after the eruption of the Agung and El Chichón volcanoes. The temperature increase between two 13-year periods, 1964–1976 and 1977–1989, was greatest in the winter season at both levels. The increase in temperature of the 850–700 hPa layer exceeded that of 700–500 hPa layer for comparable times of the year and grids. The polar region showed the largest temperature change. A plot of the 850–700 hPa layer, winter temperature changes for the octagonal grid, shows the largest positive change over Alaska, northern Canada, and western China. The dominant cooling occurred over the north Pacific and western Europe. The warm–cold couplet in the north Pacific suggests a change in the strength of the Aleutian low.

TROPOSPHERIC TEMPERATURES FROM GEOPOTENTIAL THICKNESS

For the past decade, model predictions of climate change resulting from the increase in concentration of "greenhouse" gases have consistently suggested significant warming of the surface and the lower troposphere at high latitudes. Although Hansen and Lebedeff [1987] found greater warming in the northern hemispheric polar region than at middle latitudes, radiosonde observations of temperatures in the midtropospheric layer [Angell, 1988] have not shown a significant trend in the last three decades.

This study explores the interannual variability of temperatures calculated for two layers in the lower troposphere from gridded archives of 850, 700, and 500 hPa analyses. Such considerations as missing data and changes in the analysis techniques [Trenberth and Olson, 1988], along with significant differences that have been found in the analyses of different centers [Parker, 1980], are important to the interpretation of the resulting time series. Thus, surface and radiosonde temperatures are compared with geopotential thickness temperatures from the gridded archives to assess any systematic changes. Yet this comparison is limited, because the gridded data provide, in effect, a spatially smoothed version of the radiosonde data; thus the two data sets are not independent.

The National Center for Atmospheric Research (NCAR) maintains an archive of the National Meteorological Center (NMC) final analyses of geopotential heights in gridded form [Jenne, 1975]. Selected meteorological variables, for which long records existed, were transcribed to compact disk read-only memory (CD-ROM) by Mass et al. [1987]; this is called the NMC Grid Point Data Set. For this study, monthly mean geopotential heights were obtained from the CD-ROM [National Meteorological Center Grid Point Data Set Version II, 1990] in gridded form (NMC octagonal grid) at 850 hPa (1961–1988), 700 hPa (1958–1988), and 500 hPa (1958–1988). To extend the time series to the present, I calculated monthly mean geopotential heights for 1989 for the octagonal grid from the currently available, daily, 65 x 65 grids obtained from NCAR. The octagonal grid (Figure 1), a Cartesian grid overlaid on the polar stereographic projection centered at the North Pole, is a subgrid of the 65 x 65 grid with the same spacing between grid points.

Thickness temperatures were calculated for the 850–700 and 700–500 hPa layers, assuming hydrostatic equilibrium

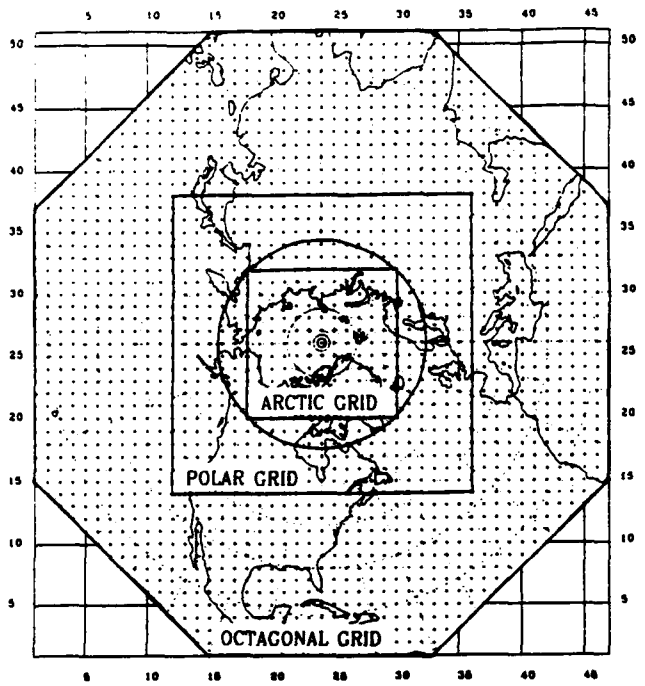


Figure 1. NMC octagonal grid (47 x 51) [Jenne, 1975].

and neglecting moisture effects. In the absence of the 1000 hPa surface it was not possible to calculate geopotential temperature below 850 hPa. The basic data set therefore consists of monthly mean temperatures for the 1977 grid points in the octagonal grid, for 1963–1989 in the 850–700 hPa layer and for 1958–1989 in the 700–500 hPa layer. To evaluate the influence of the polar and temperate climatic regions in terms of grid-averaged mean temperatures, two subgrids of the octagonal grid, the polar (60°–90°N) and temperate (30°–60°N) grids were formulated (Figure 1).

The monthly mean geopotential heights at 850 hPa for 1961–62 are limited to January, April, July, and October, the central month in each season. Therefore, to have a 30-year record for both layers and to maintain consistency with other investigators, seasonal average temperatures were estimated for 1961–62 from the midseason months and combined with the seasonal averages calculated in the conventional fashion for the remainder of the period. Annual average temperatures presented in subsequent figures are the average of the four seasons, December–February (DJF), March–May (MAM), June–August (JJA), and September–November (SON). In each case the seasonal differences are calculated from the seasonal mean for the period 1963–1989.

The main source of error in geopotential heights in gridded form is the changes that can occur because of changes in the analysis methods. Parker [1980] found equivalent temperature differences of 0–0.5°C between the United Kingdom and German Federal Republic analyses, in the 1000–500 hPa layer, for 1964–1978. Although Parker concludes that the differences between the various analyses make it impossible to determine hemispherically averaged trends, a general similarity in year-to-year changes is found with the geopotential temperatures from radiosonde observations from Angell and Korshover [1977].

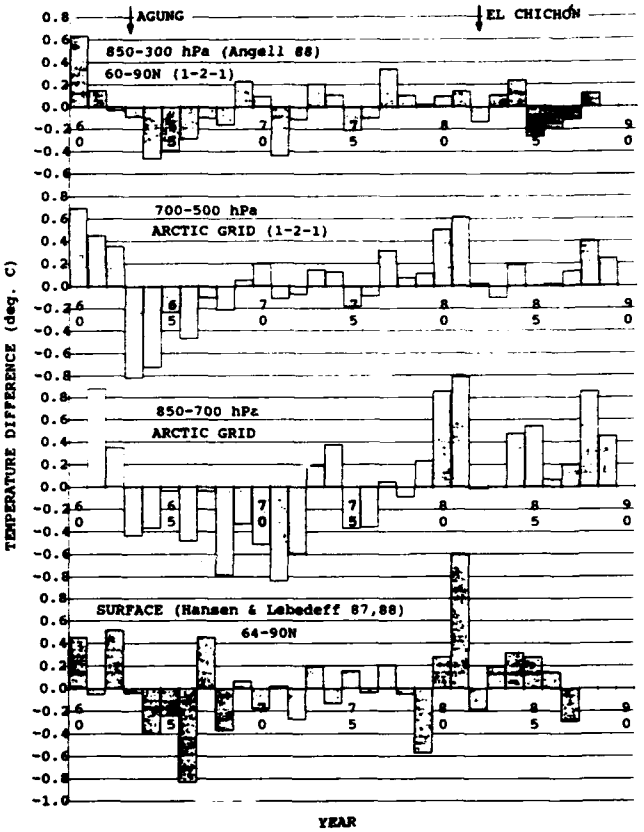


Figure 2. Annual average polar region temperature differences from the 1963–1989 mean.

COMPARISON OF LAYER, RADIOSONDE, AND SURFACE TEMPERATURES

How do layer-averaged geopotential thickness temperatures for the polar region compare with surface temperatures and geopotential temperatures from radiosonde observations? Figure 2 depicts the average annual temperature differences from the 1963–1989 mean for the 850–700 and 700–500 hPa layers. Temperatures for the 850–300 hPa layer were calculated from radiosonde data by Angell [1988, 1991]. Figure 1 shows the location of the radiosonde stations. For both the 850–300 and 700–500 hPa layers, annual mean temperatures were calculated from the four seasonal means after a binomial smoothing (1-2-1) was applied, twice. The 700–500 hPa temperatures and the 850–300 hPa temperatures are not altogether independent, in that the geopotential heights used in the analysis are based on the radiosonde observations as well. And although the thickness of the 700–500 hPa layer is only about 34% that of the 850–300 hPa layer, it is positioned near the middle of the thicker layer.

Both 850–300 and 700–500 hPa time series begin with the largest positive differences in the past 30 years (Figure 2). By 1963–64 the lowest temperatures in the period occur. Relatively cool periods occur in the middle of each decade for the remainder of the period, and slightly above-normal temperature differences occur in 1977–1981. Angell [1988], Mass and Portman [1989] attribute the temperature decreases of 1962–63 and 1981–82 to stratospheric aerosol

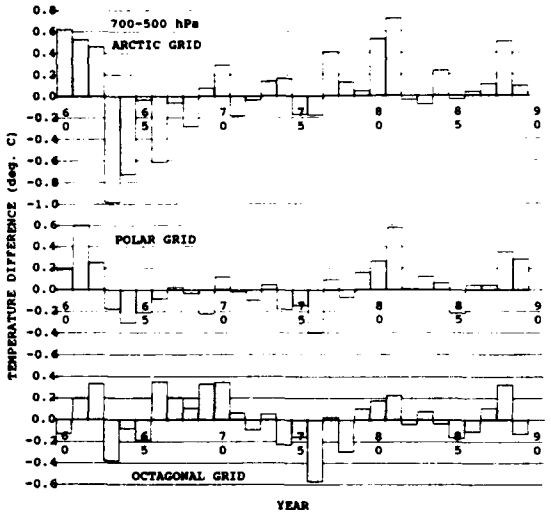


Figure 3. Annual average temperature differences, seasonal year departures from the 1973–1989 mean, for the 700–500 hPa layer.

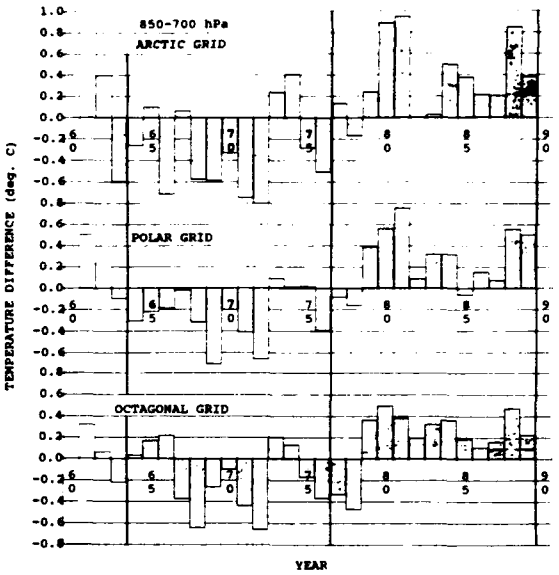


Figure 4. Annual average temperature differences, seasonal year departures from the 1963–1989 mean, for the 850–700 hPa layer. Vertical lines denote two 13-year periods used in Table 1.

loading from the eruptions of Agung and El Chichón volcanoes. The cold anomaly in 1964–1966 and the warm anomaly in 1980–81 are considerably larger for the 700–500 hPa layer than for the 850–300 hPa layer. The correlation coefficient for the two time series is r = 0.68 (0.5–0.8, 95% limits). For the 850–700 hPa layer in the polar region the character of the time series is different, in that the temperatures in 1968–1972 are much colder and for the period 1979–1989 are above average. The correlation coefficient for the two time series is r = 0.46 (0.1–0.7, 95% limits).

The surface temperature differences for 64°–90°N [Hansen and Lebedeff, 1987, 1988] are shown in Figure 2. In this instance the annual average was calculated from the four seasonal means without the 1-2-1 filtering. Above-normal temperatures occur in the early 1960s and again in 1979–1981. Because surface temperature data were not available after 1987, no comparison can be made with data from the other sets that show a warm period in 1987–88. Surface temperature differences agree with the other sets for the below-normal periods in 1965–66, but not for the cool periods of 1968–1972 at 850–700 hPa. The correlation coefficient for the surface anomalies with those at 850–700 hPa (r = 0.58, 0.2–0.8, 95% limits) is slightly greater than the correlation with the radiosonde data.

REGIONAL VARIATIONS IN INTERANNUAL TEMPERATURE DIFFERENCE

Figure 3 presents the time series of temperature differences for the 700–500 hPa layer from the three grids in Figure 1 for the period 1958–1989. Interannual variability in all grids in Figure 3 shows the basic pattern of warm periods in the early 1960s, 1969–70, 1980–81, and 1987–88, separated by below-normal temperatures in the middle of each decade. The amplitude of the differences clearly decreases for the temperate region and as the subtropical latitudes are included in the octagonal grid. In the case of the warm period in 1966–1970 and the cool period in mid-1970 for the octagonal grid, the pattern is significantly different for the polar region. From 1978 on, the three grids are similar to each other.

Figure 4 shows the 850–700 hPa temperature difference for the three grids for 1961–1989. In this case there are warm periods in early 1960, early 1980, and late 1980, as was the case at the upper level. In the mid-decade periods the temperatures are below normal, as is the upper level. When compared with the 700–500 hPa layer, the main difference is that during 1968–1972, temperatures are significantly below normal, whereas at 700–500 hPa, temperatures are normal. The 1971–72 period is cooler than the post-Agung 1963–64 period at this level. Rather than a gradual increase in temperature, as is the case at 700–500 hPa, at this level the 29-year period separates naturally into two regimes, a cool period (1963–1972) and a warm period (1979–1989) with a transition period lasting 6 years.

INTERDECADAL TEMPERATURE CHANGES

Table 1 shows the temperature differences between two 13-year periods, 1964–1976 and 1977–1989 (see also Figure 4) for the three grids and for all four seasons. The winter difference (DJF) is the largest for each grid. Generally, the differences observed for spring (MAM), summer (JJA), and autumn (SON) are approximately one-half that of winter, and are probably not significantly different from one another. At both levels and for all seasons there is a decrease in the difference in temperate latitudes compared to the polar region. Differences in the 700–500 hPa layer temperatures are 0.5°C or less for all grids. Warming occurs at all times except for MAM, JJA, and SON, for the octagonal grid.

The temperature differences for the 850–700 hPa layer are about a factor of 2 greater than those for the 700–500 hPa layer, for comparable regions and seasons. The maximum temperature difference is 1.2°C in the polar winter. With the exception of the octagonal grid differences for the annual average, MAM, JJA, and SON temperatures, and the polar region SON temperatures, at 700–500 hPa, all tem-

	Annual	DJF	MAM	JJA	SON
			700–500 hPA		
Polar region	0.32	0.54	0.31	0.26	0.27
Temperate region	0.08	0.10	0.05	0.07	0.12
Octagonal grid	0.01	0.18	-0.06	-0.08	-0.02
			850–700 hPa		
Polar region	0.65	1.10	0.56	0.43	0.53
Temperate region	0.23	0.32	0.28	0.13	0.20
Octagonal grid	0.33	0.42	0.24	0.24	0.27

Table 1. Temperature differences (°C) between two 13-year periods, (1977–1989)–(1964–1976).

peratures are significantly different from zero at the 95% level using a student-t test.

Figure 5 shows the geographical distribution of the difference in the mean temperature for two successive 13-year periods, 1964–1976 and 1977–1989, for the 850–700 hPa layer in winter. Above-normal temperatures for the latter period extend from over northern Canada and Alaska, across the Pacific side of the Arctic Basin, across central Asia to western China. Regions of temperature difference in excess of 3°C are observed over northern Canada and Alaska, and over western China. The Asian warm region lies along the northern edge of the Himalaya Mountains, where both the 850 and 700 hPa levels are below the surface; thus one may question the validity of the analysis in this region. A second region of warming is over Iran. Regions of cooling are located in the north central Pacific and the north Atlantic and western Europe. The central and southeastern United States shows a slight decrease in temperature during this period as well. The couplet of cooling over the north Pacific and warming over northern Canada and Alaska would suggest a change in the strength or position of the Aleutian Low during this period, see Trenberth [1990].

CONCLUSION

Time series of the interannual variations in layer temperature for both levels show major warm anomalies before 1962, 1980–81, and 1988–1989 in both the polar and temperate regions. For these same grids the cool anomalies are confined to 1963–1966 in the polar region, and 1974–1977 in the temperate region at 700–500 hPa. At 850–700 hPa the cool anomaly from 1963–1972 is more pronounced at high latitudes than in middle latitudes. When all of the 1977 grid points in the octagonal grid are considered, the amplitude of the interannual variations is significantly less than for the polar region and comparable to the temperate region, for some periods. There is also less evidence of cooling in 1963 (Agung) or 1982 (El Chichón) for the temperate latitudes than for the more northern subgrid.

When I consider the temperature change as a function of level, season, and region for the periods 1964–1976 and 1977–1989, the polar region shows the largest changes at

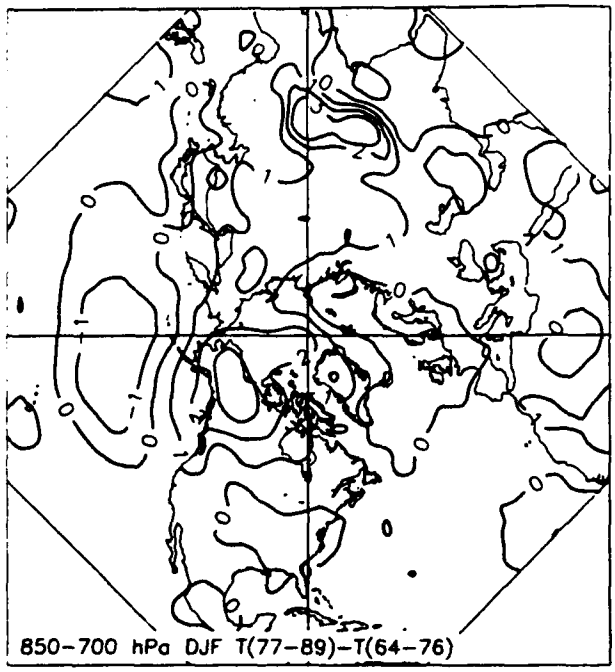


Figure 5. Mean temperature differences between two 13-year periods, (1977–1989)–(1964–1976), for the 850–700 hPa layer for DJF. Contours are drawn every 1°C.

both levels. This is in contrast to the Angell [1991] radiosonde results for similar periods (1970–1978 and 1980–1988), when no significant warming was found in high latitudes (Figure 2). In a sense the layer-averaged gridded geopotential temperatures are a spatial rendering of all the radiosonde data. As such they provide better coverage than the eight soundings used by Angell to represent the Arctic. In this case it is likely that the radiosonde stations did not adequately cover the region of maximum warming.

The coupled warming over Alaska and northern Canada, and cooling over the north central Pacific and over the north Atlantic and western Europe indicates changes in the strength and position of the subpolar lows. This pattern is consistent with changes found by Fletcher [1991] in the study of surface temperatures and by Trenberth [1990] in the study of changes in the central pressure of the Aleutian Low. Although these results are consistent with the model predictions for climate change in the Arctic as a result of CO_2 doubling, that is, increasing temperature changes with increasing latitude and decreasing altitude [Stouffer et al., 1989], the maximum changes occur in isolated regions at a latitude strongly influenced by sub-polar circulations.

ACKNOWLEDGMENT

This work was stimulated by the release of the NMC Grid Point Data Set on CD-ROM. We thank the staff of the Compact Disc Group, Department of Atmospheric Science, University of Washington, for this very useful archive of meteorological data. Monthly average geopotential heights for the period 1985–1989 were calculated from daily analyses by Mike Ellis of CMDL, NOAA.

REFERENCES

Angell, J. K., Variations and trends in tropospheric and stratospheric global temperatures, 1958–87, *J. Climate*, *1*, 1296–1313, 1988.

Angell, J. K., Changes in tropospheric and stratospheric global temperature, 1958–88, in Greenhouse-Gas–Induced Climatic Change: A Critical Appraisal of Simulations and Observations, edited by M. E. Schlesinger, pp. 231-247, Elsevier, Amsterdam, 1991..

Angell, J. K., and J. Korshover, Estimate of the global change in temperature, surface to 100 mb, between 1958 and 1975, *Mon. Wea. Rev.*, *105*, 375–385, 1977.

Fletcher, J. O., How climate changes (Abstract), *This Volume*, 1991.

Hansen, J., and S. Lebedeff, Global trends of measured surface air temperature, *J. Geophys. Res.*, *92*, 13345–13372, 1987.

Hansen, J., and S. Lebedeff, Global surface air temperatures: Update through 1987, *Geophys. Res. Lett.*, *15*, 323–326, 1988.

Jenne, R., Data sets for meteorological research, *NCAR-TN/JA-111*, 194 pp., National Center for Atmospheric Research, Boulder, Colorado, 1975.

Mass, C. F., and D. A. Portman, Major volcanic eruptions and climate evaluation, *J. Climate*, *2*, 566–593, 1989.

Mass, C. F., H. J. Edmond, H. J. Friedman, N. R. Cheney, and E. R. Recker, The use of compact disks for the storage of large meteorological and oceanographic data sets, *Bull. Amer. Meteor. Soc.*, *68*, 1556–1558, 1987.

Parker, D. E., Climate change or analysts' artifice? - A study of grid-point upper-air data, *Meteor. Mag.*, *109*, 129–152, 1980.

Stouffer, R. J., S. Manabe, and K. Bryan, Interhemispheric asymmetry in climate response to a gradual increase of atmospheric CO_2, *Nature*, *341*, 660–662, 1989.

Trenberth, K. E., Recent observed interdecadal climate change in the Northern Hemisphere, *Bull. Amer. Meteor. Soc.*, *71*, 988-993, 1990.

Trenberth, K. E., and J. G. Olson, Evaluation of NMC global analyses: 1979–1987, NCAR Tech. Note, *NCAR/TN-299+STR*, 82 pp., NCAR, Boulder, Colorado, 1988.

AD-P007 282

Interannual Variability of the January Meridional Heat Transport by Planetary Waves in the Northern Latitudes

Kaz Higuchi
Climate Diagnostic Research Group, Atmospheric Environment Service, Downsview, Ontario, Canada

Charles A. Lin
Dept. of Meteorology, and Centre for Climate and Global Change Research, McGill University, Montreal, Quebec, Canada

Amir Shabbar and J. L. Knox
Climate Diagnostic Research Group, Atmospheric Environment Service, Downsview, Ontario, Canada

92-17964

ABSTRACT

Evidence of large temporal and spatial variability in the eddy fluxes of sensible heat in the lower troposphere (100–50 kPa thickness layer) in January, from 1946 to 1988, is presented.

The spatial distribution of the standing eddy heat flux is dominated by three main features, or "centers of action": (1) a region north of Korea (extreme eastern Siberia), (2) northeastern Atlantic Ocean, and (3) the Gulf of Alaska. Even though the center just north of Korea is the most active heat transport area, most of the interannual variability of the January standing eddy heat flux is associated with the heat transport centers over the northeastern Atlantic and the Gulf of Alaska, correlated with the positions of the Icelandic Low and the Aleutian Low, respectively. This year-to-year variability in these two geographical locations is due to interannual variability in the planetary waves [van Loon and Williams, 1980], and a significant role of the air–sea interaction in this respect cannot be ruled out.

INTRODUCTION

The flux of sensible heat constitutes an important component of the total flux of energy across a latitude circle, with the standing and transient eddy heat fluxes playing a much more important role at midlatitudes than the mean meridional circulation [Oort and Rasmusson, 1970]. Previous investigations [e.g., van Loon, 1979; van Loon and Williams, 1980; Oort, 1983] have shown that the magnitude of the zonally averaged standing eddy component peaks around 50°N. The latitudinal distribution of the standing eddy follows a Gaussian distribution, while the distribution of the transient eddy is relatively flat and broad with no identifiable strong peak.

The climatology of the geographical distribution of the eddy heat fluxes has been investigated before by, for example, Blackmon et al. [1977] and Haines and Winston [1963], and references listed therein. Blackmon et al. [1977], using a record covering a nine-winter period from 1965-66 to 1968-69, and 1970-71 to 1974-75, noted that the spatial distribution of the standing eddy heat flux during the winter season at the 850 mb level is dominated by three main features: (1) the transport of cold air southward over a region north of Korea; (2) the transport of warm air northward over the northeastern Atlantic Ocean; and (3) the transport of warm air northward over the Gulf of Alaska. The transient eddy heat transports show a much broader distribution, correlating well with patterns of kinetic energy and major storm tracks.

The main purpose of this study is to present evidence of large temporal and spatial variability in the eddy fluxes of sensible heat in the lower troposphere (100–50 Kpa thickness layer) in January, from 1946 to 1988. Since sensible heat is concentrated in the lower tropospheric levels [Oort and Rasmusson, 1970], eddy sensible heat fluxes calculated

in this study are representative of the whole atmospheric column integrated fluxes across a latitudinal circle. Furthermore, since the variability of the eddy heat fluxes is accounted mostly by the interannual variability of the standing eddy heat fluxes, only the sensible heat transport by the standing eddy is discussed in this paper.

DATA AND PROCEDURE

The primary data for this investigation consisted of daily (1200 GMT) 50 kPa and 100k kPa height analyses of the Northern Hemisphere (20°N to 75°N) on a 432-gridpoint network of 5° latitude by 10° longitude for the period from 1946 to 1988. For latitudes 70°N and 75°N, gridpoint values were given every 20° longitude; these values were then linearly interpolated, using neighboring values to the east and to the west, to obtain values every 10° longitude. The data from 1946 to 1981 were obtained from the National Center for Atmospheric Research (NCAR) on an octagonal 1977-point grid and were converted to the Canadian Meteorological Centre 455 grid (15°N to 90°N), of which the data set used in this study is a subset. The balance of the dataset to 1988 was obtained from the Canadian Meteorological Centre (CMC). For a more complete description of the data, see Knox et al. [1988] and Shabbar et al. [1990].

Using the above data, the standing $\overline{V}^{*}\overline{T}^{*}$ and the transient $\overline{V'T'}$ eddy heat flux terms were obtained, where V is the mean meridional wind in the 100–50 kPa layer calculated as a linear average of the meridional 100 kPa and the 50 kPa wind fields. The 100 kPa wind values were obtained from subtracting the 100–50 kPa thermal wind from the 50 kPa geostrophic wind. The mean temperature T was calculated from the thickness field. The overbar denotes monthly average.

DISCUSSION

The 43-year averaged (1946–1988) geographical distribution of the January standing eddy heat transports is shown in Figure 1a. The pattern and the values are in very good agreement with the standing eddy heat transports calculated from the National Meteorological Center (NMC) 850 mb data for the period 1980–1988 (Figure 1b), as well as with values obtained by Blackmon et al. [1977], who used a record covering a nine-winter period from 1965-66 to

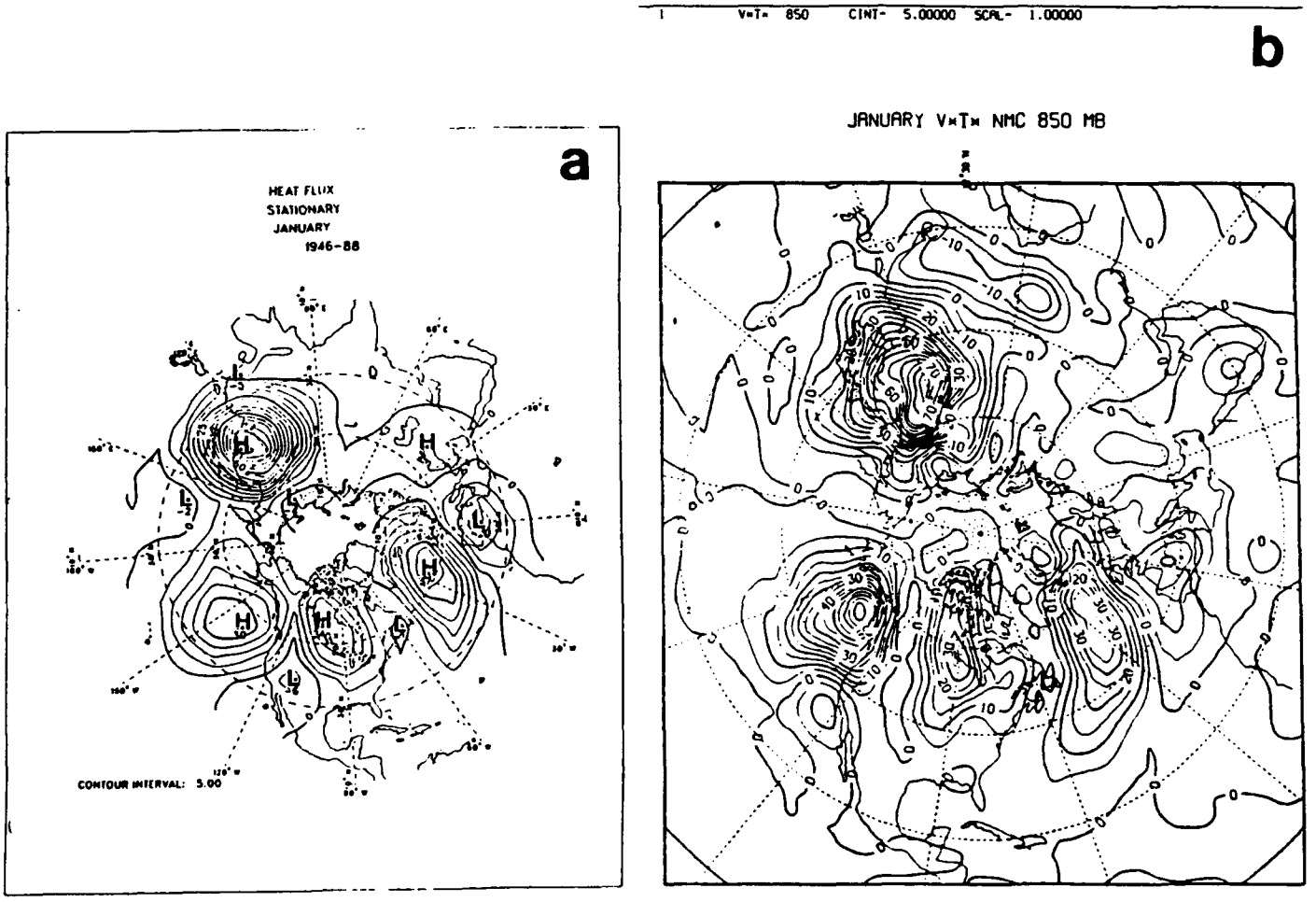
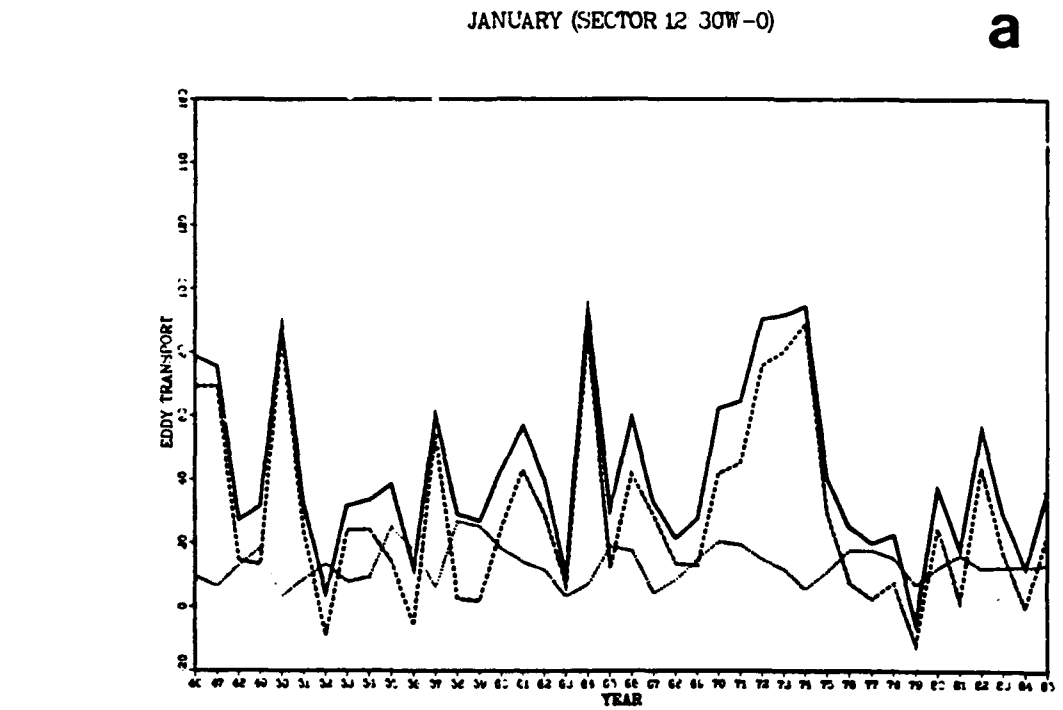


Figure 1. (a) A 43-year average (1946–1988) of the geographical distribution of the January standing eddy heat flux. (b) The January standing eddy heat transport calculated from the NMC 850 mb data for the period 1980–1988. Note the five centers of heat transport mentioned in the text. Given the entirely different sources and length of the two data sets, agreement in magnitude and pattern between the two maps is quite remarkable. Units are in m/s deg. C.



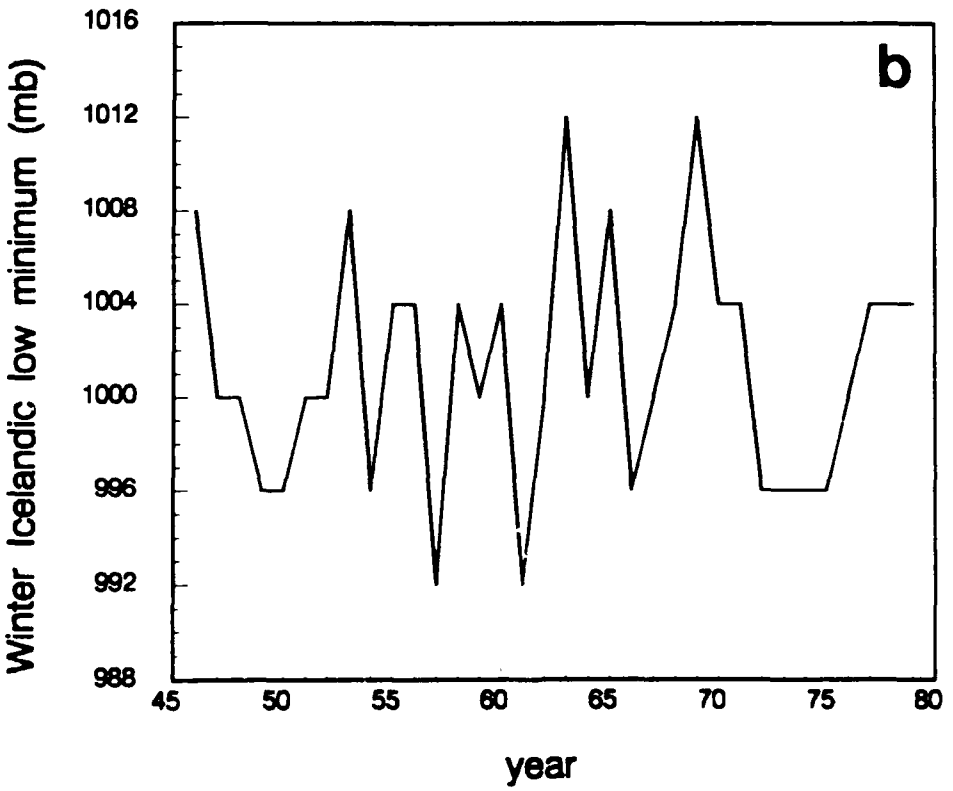


Figure 2. (a) Time series of spatially averaged transient eddy heat flux (dot), standing eddy heat flux (dash), and total eddy (standing plus transient) heat flux (solid) across 55°N latitude over a 30° longitude zone from 30°W to 0° (Sector 12). (b) Time series of winter low pressure minimum of the Icelandic Low. The two time series are negatively correlated. See text for explanation.

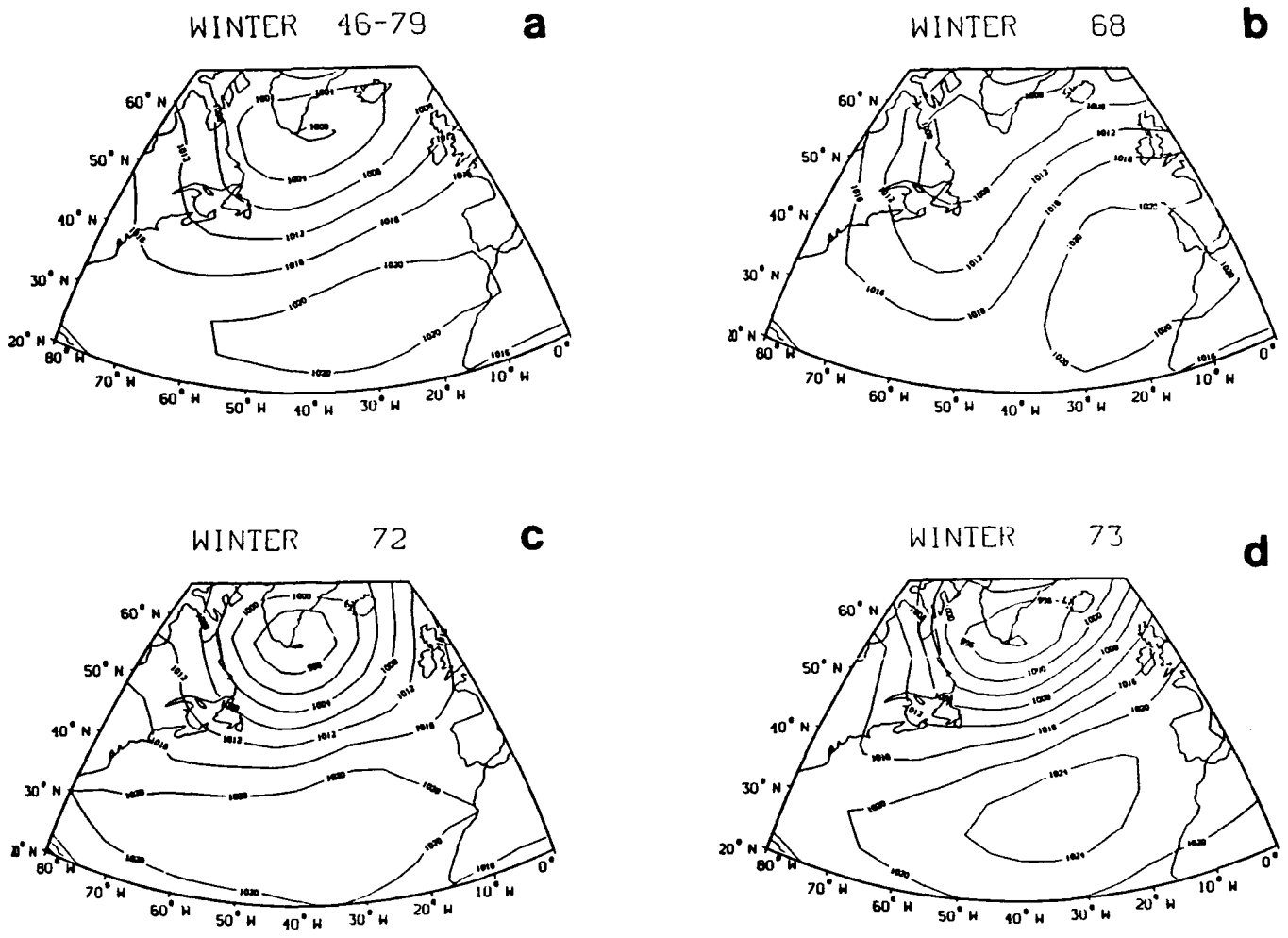


Figure 3. Winter mean sea level pressure pattern of the Icelandic Low for (a) a climatological period 1946 to 1979, (b) the winter of 1968, (c) the winter of 1972, and (d) the winter of 1973.

1968-69, and 1970-71 to 1974-75. We see that the spatial distribution of the standing eddy heat flux is dominated by three "centers of action": (1) the transport of cold air southward over a region north of Korea, (2) the transport of warm air northward over the northeastern Atlantic Ocean, and (3) the transport of warm air northward over the Gulf of Alaska. This agrees well with Blackmon et al. [1977] and Haines and Winston [1963]. A fourth feature, not mentioned by Blackmon et al. [1977], is the transport of cold air southward over central Canada. Another interesting feature is the negative transport of heat over the western Mediterranean (warm air southward). The sign of the eddy heat transport is dependent upon the correlational relationship between the meridional wind and the temperature fields. This relationship in turn is a function of the long stationary planetary wave pattern around the midlatitudes. Even though the center just north of Korea is the most important in terms of local heat transport by the standing eddy component, we have found that much of the interannual variability is associated with the heat transport centers over the northeastern Atlantic and the Gulf of Alaska. In this study, we have focused on the year-to-year variability of the January standing eddy heat flux over the northeastern Atlantic Ocean. The interannual variability in the heat transport over this region could be induced by the interaction of the atmosphere with the oceans [Mysak et al., 1990].

Figure 2a shows the time series (1946–1985) of spatially averaged transient eddy heat flux, standing eddy heat flux, and total eddy (transient and standing) heat flux across 55°N latitude over a 30° longitude width from 30°W to 0° meridian (Sector 12). An important feature to note is the large interannual variability in the transport of sensible heat in Sector 12, with several major peaks occurring over the 40-year period: 1946, 1950, 1964, and 1970–1974. The most noteworthy among these large deviation peaks is the positive anomaly during the first half of the 1970s, which is coincident with the great salinity anomaly signal at that time [Dickson et al., 1988]. From 1975 to 1985, the magnitude and the interannual variability of the standing eddy heat transport in the northeastern Atlantic are both smaller than for the period prior to 1975.

The standing eddy heat transport in the atmosphere is achieved by stationary eddies. This leads to the idea that the standing eddy heat transport in the northeastern Atlantic is due to the Icelandic Low, and the variability in the eddy heat flux is then due to the variability in the intensity of the Icelandic Low. This idea is borne out by a strong positive correlation (significant at the 99% level) between the in-

tensity of the standing eddy heat flux in Figure 2a and the intensity of the winter minimum pressure of the Icelandic Low (Figure 2b). This is consistent with the results of van Loon [1979] and Carleton [1988].

It has been found by previous investigators [see Carleton, 1988 and references therein] that the interannual variability in the intensity of the standing eddy sensible heat flux is associated with the interannual variability in the North Atlantic Oscillation (NAO). The NAO is basically a north–south dipole structure with one center near Greenland and the other over the Atlantic just west of the Azores. In the positive phase of the NAO structure, the Icelandic Low is very weak, and, in extreme cases, displaced westward by a blocking high [Moses et al., 1987; Carleton, 1988]. The pressure anomaly field shows positive values north of the mid to polar latitudes in the North Atlantic, while showing negative values over the region of the subtropical high. The standing eddy component of the sensible heat flux is correspondingly reduced.

When the NAO is in the negative phase, however, the standing eddy heat flux is increased, in association with intensified Icelandic Low. The pressure anomaly field shows negative values over the Greenland area, and positive values over the region of the subtropical high in the central Atlantic west of the Azores.

The relationship between the interannual variabilities of the Icelandic Low and the standing eddy heat transport in the northeastern sector of the North Atlantic Ocean is illustrated more clearly in Figure 3. The latter, taken from Allingham et al. [1987], shows the winter climatology (1946–1979) distribution of the mean sea level pressure of the Icelandic Low, as well as for the individual winters of 1968, 1972, and 1973. When the pressure of the Icelandic Low is abnormally low, as in the winters of 1972 and 1973 (Figure 3c, d), the pressure gradient is increased around the Low, causing an enhanced westerly flow south of Iceland and Greenland [Carleton, 1988]. However, over our study area between Iceland and the British Isles, the atmospheric flow also displays a very significant meridional component, advecting warm air northward.

When the pressure of the Icelandic Low is above normal, as in the winter of 1968 (Figure 3b), the pressure gradient is significantly weaker, causing decrease in the atmospheric flow. In the specific case of 1968, the Icelandic Low occupies its climatological position, but its central pressure is high and the associated pressure gradient is relatively weak. A weak meridional flow is set up in the mid-North Atlantic, south of Greenland. This flow becomes basically zonal southeast of Iceland, reducing the northward transport of warm air there.

In extreme cases, such as January of 1963 [see Moses et al, 1987], a blocking high in the northeastern Atlantic is formed and disrupts the normal climatological flow of air over the region. Instead of having a northwesterly flow (Figure 3a), a meridional flow is set up to the west of the block. In 1963, a weakened Icelandic Low center was displaced westward to southern Baffin Island. A weak southerly meridional flow was formed between the Low and the blocking high just southeast of Iceland. Meridional flow to the east of Iceland was considerably weakened, causing a considerable reduction in the northward transport of warm air over that region.

A similar relationship probably exists between the center of the standing eddy heat transport over the Gulf of Alaska and the Aleutian Low. This is presently under investigation.

CONCLUSION

The flux of sensible heat constitutes an important component of the total flux of energy across a latitudinal circle. In this study we have presented evidence of large temporal and spatial variability in the standing eddy fluxes of sensible heat in the lower troposphere (100–50 kPa layer) in January, from 1946 to 1988.

The climatological pattern of the geographical distribution of the standing eddy heat flux is dominated by several "centers of action," the most significant of which is the center located just north of Korea. However, the interannual variability of the January standing eddy heat transport is associated with the heat transport centers located over the northeastern Atlantic Ocean and the Gulf of Alaska. The magnitude of the interannual variability is comparable to the respective mean values. The northeastern Atlantic center is connected with the activities of the Icelandic Low. A similar relationship probably holds between the Gulf of Alaska center and the Aleutian Low.

The eddy heat transport across 55°N, averaged over the 30°W–0° longitude sector (Sector 12) in the North Atlantic, shows a steady increase in the northward transport of heat during the early 1950s to the mid 1970s, then a decrease up to 1985. There are several years with maximum heat transport, the most prominent of which is the sustained peak during the first half of the 1970s. This peak corresponds to several years of intense Icelandic Low. This is also coincident with the great salinity anomaly signal at that time.

ACKNOWLEDGMENTS

We thank Dr. Steve Lambert of the Canadian Climate Centre for providing Figure 1b. We are also grateful to Professor Lawrence Mysak of McGill University for stimulating and helpful discussions. Comments and suggestions by Professor Andrew Carleton of the Indiana University and by an anonymous reviewer were very much appreciated. CAL acknowledges research grants from the Atmospheric Environment Service and the Canadian Natural Sciences and Engineering Research Council.

REFERENCES

Allingham, A. M., K. Hamilton, and L. A. Mysak, Climatic Atlas of the North Atlantic: Seasonal Sea Level Pressures and Sea Surface Temperature Anomalies, 1919–1979, *CRG Report #87-4*, 248 pp., Dept. of Meteorology, McGill University, Montreal, Que., 1987.

Blackmon, M. L., J. M. Wallace, N.-C. Lau, and S. L. Mullen, An observational study of the Northern Hemisphere winter circulation, *J. Atmos. Sci.*, *34*, 1040–1053, 1977.

Carleton, A. M., Meridional transport of eddy sensible heat in winters marked by extremes of the North Atlantic oscillation, 1948/49–1979/80, *J. Climate*, *1*, 121–223, 1988.

Dickson, R. R., J. Meincke, S. A. Malmberg, and A. J. Lee, The "Great Salinity Anomaly" in the northern North Atlantic 1968–1982, *Prog. Oceanog.*, *20*, 103–151, 1988.

Haines, D. A., and J. S. Winston, Monthly mean values and spatial distribution of meridional transport of sensible heat, *Mon. Wea. Rev.*, *91*, 319–328, 1963.

Knox, J., K. Higuchi, A. Shabbar, and N. Sargent, Secular variation of Northern Hemisphere 50 kPa geopotential height, *J. Climate*, *1*, 500–511, 1988.

Moses, T., G. N. Kiladis, H. F. Diaz, and R. G. Barry, Characteristics and frequency of reversals in mean sea level pressure in the North Atlantic sector and their relationship to long-term temperature trends, *J. Climatol.*, *7*, 13–30, 1987.

Mysak, L. A., D. K. Manak, and R. F. Marsden, Sea-ice anomalies observed in the Greenland and Labrador Seas during 1901–1984 and their relation to an interdecadal Arctic climate cycle, *Clim. Dyn.*, *5*, 111–133, 1990.

Oort, A. H., Global atmospheric circulation statistics, 1958–1973, *NOAA Prof. Paper 14*, 180 pp., 1983.

Oort, A. H., and E. M. Rasmusson, On the annual variation of the monthly mean meridional circulation, *Mon. Wea. Rev.*, *98*, 423–442, 1970.

Shabbar, A., K. Higuchi, and J. Knox, Regional analysis of Northern Hemisphere 50 kPa geopotential heights from 1946 to 1985, *J. Climate*, *3*, 543–557, 1990.

van Loon, H., The association between latitudinal temperature gradient and eddy transport. Part I: Transport of sensible heat in winter, *Mon. Wea. Rev.*, *107*, 525–534, 1979.

van Loon, H., and J. Williams, The association between latitudinal temperature gradient and eddy transport. Part II: Relationships between sensible heat transport by stationary waves and wind, pressure and temperature in winter, *Mon. Wea. Rev.*, *108*, 604–614, 1980.

AD-P007 283

Low-Frequency Variability of Polar Atmosphere due to Blocking Formations: A Numerical Experiment of Blocking

H. L. Tanaka
Geophysical Institute, University of Alaska Fairbanks, Fairbanks, Alaska, U.S.A.
(Now at: Institute of Geoscience, University of Tsukuba, Tsukuba, Japan)

92-17965

ABSTRACT

Arctic climate in winter depends on occurrence of large-scale atmospheric blocking and amplification of planetary waves. Understanding the development of blocking formations is an important research subject in polar regions as well as in middle latitudes for time scales of a month to a season.

In this study, we carried out nonlinear numerical simulations of amplification of low-frequency planetary waves and the concurrent development of blocking. The simulations were conducted using a barotropic spectral model derived from three-dimensional spectral primitive equations with a basis of vertical structure functions and Hough harmonics. The model is truncated to include only barotropic Rossby components of the atmosphere with simple physics including biharmonic diffusion, topographic forcing, baroclinic instability, and zonal surface stress. We find that these four physical processes are sufficient to produce a realistic and persistent dipole blocking with a sharp transition from zonal to meridional flows on a sphere.

The simulations confirmed an amplification of the meridional dipole mode due to the up-scale energy cascade from synoptic disturbances under an environment of persistent wavenumber 2. The energy supply from synoptic disturbances contributes to the sharp transition from zonal to meridional flows.

INTRODUCTION

The Arctic is one of the more sensitive regions of the globe in terms of anticipated climate change as well as natural climate variability. Abnormal global-scale anomalies tend to propagate toward high latitudes by the nature of the meridional dispersion of quasi-stationary planetary waves [Hoskins and Karoly, 1981]. Concentration of the wave energy in high latitudes seems to cause the large variability observed in the polar atmosphere.

A separation of a natural climate variability from a human-induced climate change due to anthropogenic greenhouse gases is an urgent problem in global change research. However, our present understanding of natural low-frequency variability with time scales of a month to a season is still insufficient. Atmospheric blocking, which has typical time scales of a week to a month, has long been one of the unsolved central problems in medium-range forecasting. We have neither physical understanding of nor prediction skills for blocking systems. Since the arctic climate depends strongly on the occurrence of large-scale blockings [e.g., Tanaka and Milkovich, 1990], understanding of the atmospheric natural variability associated with the blocking may be one of the the first steps for global change research.

There is as yet no universally accepted theory to explain the blocking, despite a number of proposed theories. Every theory describes a unique energy flow to excite the blocking system. However, there are various blocking cases in which baroclinic or barotropic instability plays an important role, and cases in which the up-scale energy cascade from synoptic disturbances dominates energy supplies. The implication is that the energy source for blocking systems varies from case to case, but reveals the same characteristic structures and behaviors.

In light of this result, Tanaka and Kung [1989] discussed a possibility that blockings can be understood as atmospheric eigenmodes excited by energy sources which vary from case to case. The common persistent features are intuitively understood as the system is a low-frequency eigenmode. The characteristic structure may be understood as the eigenvector has a dipole configuration. The eigenmode may be excited by various energy or vorticity supplies because it is a free mode. The positive and negative anomalies should have similar structures [see Dole, 1986]. The possible mechanisms are focused on barotropic and baroclinic instabilities [Frederiksen, 1982], since the system should be explained by homogeneous equations without a specific forcing term.

We conducted a study of low-frequency, unstable planetary waves in the zonally varying basic state, along the line of studies by Frederiksen [1982] and Frederiksen and Bell [1987], using spectral primitive equations on a sphere. We found two different types of slow-moving Charney modes in planetary waves, showing different meridional structures. One of the Charney modes, M_1, becomes stationary, indicating nearly barotropic structure at a preferred geographical location. It resembles so-called Ω blockings in the atmosphere. The other Charney mode, M_2, shows a meridional dipole structure in the zonally varying basic state. The structures and behaviors of the dipole Charney mode markedly resemble dipole blockings in the atmosphere (see Figure 1). We proposed that dipole Charney modes of wavenumber 1, which is modulated by the steady wavenumber 2, is responsible for large-scale, dipole-blocking formations. The model suggested that the amplification was supported by the up-scale energy cascade from synoptic disturbances.

Yet, it is necessary to confirm the hypothesis using a fully nonlinear time-dependent model, because our previous results are based on a linear model under a restriction of small amplitudes.

The purpose of this study is to simulate the blocking formations as realistically as possible, using a fully nonlinear primitive equation model which is as simple as possible. The hypothesis that blocking results from up-scale energy cascade from synoptic disturbances under a persistent wavenumber 2 is examined.

We constructed a three-dimensional spectral primitive equation model with a basis of three-dimensional normal mode functions for the motionless atmosphere [see Tanaka and Kung, 1989]. The model was then truncated to include only the barotropic component of the atmosphere. The contributions from the baroclinic components were parameterized as baroclinic-barotropic interactions. The model physics include biharmonic diffusion, topographic forcing, baroclinic instability, and zonal surface stress. The up-scale energy cascade from synoptic disturbances to planetary waves is achieved by nonlinear wave–wave interactions. It will be shown that these combinations of physical processes are sufficient to produce a realistic and persistent dipole blocking with a sharp transition from zonal to meridional flow.

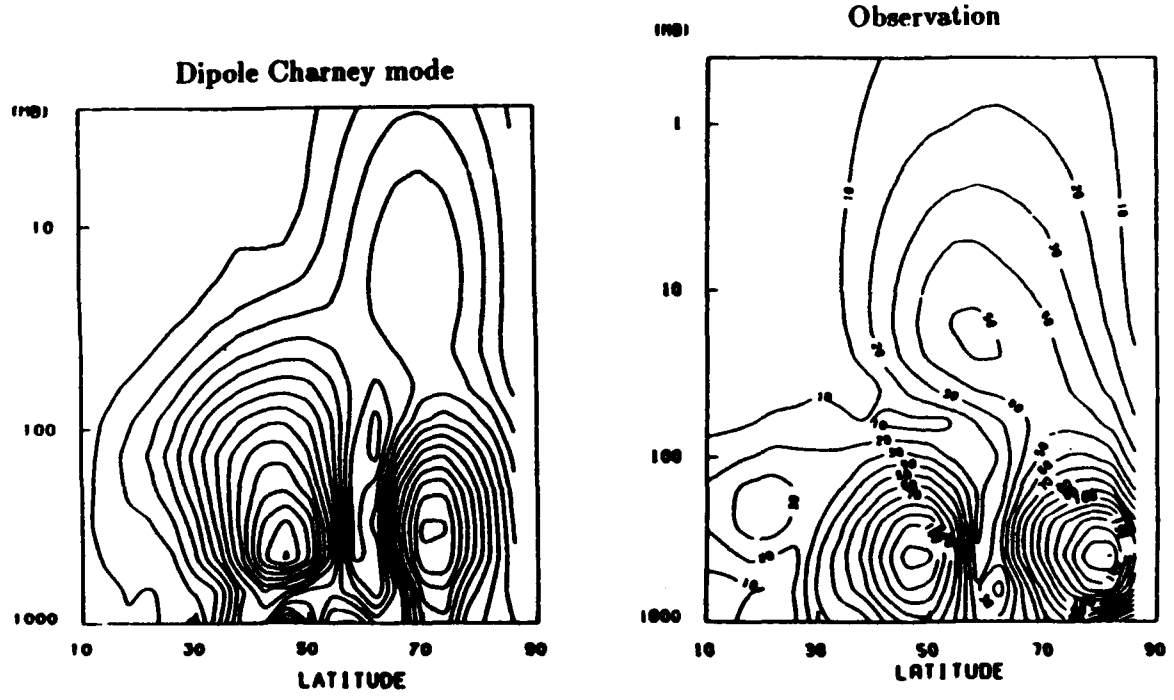


Figure 1. Meridional-height section of the dipole Charney mode M_2 of n=1 in the baroclinic atmosphere [see Tanaka and Kung, 1989], compared with the observed dipole structure of n=1 during the Pacific blocking in January, 1979 [see Tanaka et al., 1989]. Amplitudes of the geopotential height are multiplied by $\sigma^{1/2}$ to remove a density stratification effect.

A DESCRIPTION OF THE SPECTRAL PRIMITIVE EQUATION MODEL

A system of primitive equations in a spherical coordinate system with longitude λ, latitude θ, normalized pressure $\sigma = p/p_b$, and normalized time $\tau = 2\Omega t$ may be reduced to three prognostic equations of horizontal motions and thermodynamics. The three dependent variables are horizontal wind speeds, $V = (u,v)$, and perturbation geopotential ϕ from the reference state of the global mean. Using a three-dimensional spectral representation, these equations may be written as:

$$\frac{dw_i}{d\tau} + i\sigma_i w_i = -i \sum_{j=1}^{M} \sum_{k=1}^{M} r_{ijk} w_j w_k + f_i, \; i = 1,2,\ldots, M, \quad (1)$$

where w_i and f_i are the Fourier expansion coefficients of dependent variables and diabatic processes, σ_i are Laplace's tidal frequencies, r_{ijk} are interaction coefficients, and M is the total number of the series expansion for the 3-D atmospheric variables. Any choice of expansion basis functions will result in the representation of (1) after a proper diagonalization of the linear terms. The resulting expansion basis functions will consist of vertical normal modes and Hough harmonics. Refer to Tanaka and Sun [1990] for details. The vertical normal modes comprise barotropic and baroclinic components.

We confirmed that observed features of blockings can be represented sufficiently by their barotropic components. Based on this observed fact, we collected only the barotropic components of the expansion coefficients. The rest of the interaction terms and diabatic terms are combined in a single term designated as s_i, which describes the formal source–sink term of the barotropic model:

$$\frac{dw_i}{d\tau} + i\sigma_i w_i = -i \sum_{j=1}^{N} \sum_{k=1}^{N} r_{ijk} w_j w_k + s_i, \; i = 1,2,\ldots, N, \quad (2)$$

where

$$s_i = (DF)_i + (TF)_i + (BI)_i + (ZS)_i$$

Here, N is the total number of the series expansion for the barotropic model, and $(DF)_i$, $(TF)_i$, $(BI)_i$, $(ZS)_i$ are respectively the formal source–sink terms derived from diffusion, topographic forcing, baroclinic instability, and zonal surface stress to be described later. Given the formal source–sink term s_i, the nonlinear equation (2) becomes a closed system of the prognostic equation.

It is important to notice that the barotropic component of the diabatic heating term becomes zero under a minor assumption, since the heating may be assumed to be zero under the ground. Every heat-related energy source in the atmosphere goes to the baroclinic components, and the energy is then transformed into the barotropic component through the baroclinic-barotropic interaction. This is one of the major attractions of constructing the barotropic primitive equation model from the 3-D spectral model. The complicated heating fields produced by numerous physical processes are concentrated to the single concept of the baroclinic-barotropic interaction.

Diffusion

In this study, we approximate biharmonic type diffusion based on the 3-D scale index σ_i combined with the Rossby wave dispersion (for wavenumber $n \neq 0$) as:

$$(DF)_i = -K\left(\frac{n}{\sigma_i}\right)^2 w_i \quad (3)$$

where K is a diffusion coefficient and $K(2\Omega a^4) = 2.0 \times 10^{16}$ $m^4 s^{-1}$.

Topographic Forcing

A kinematical uplift of an air column by the surface topography H has been parameterized by a forced upward motion w_0 which is induced by the barotropic flow V_0. We use the topography of

$$H(\lambda,\theta) = -A sin^2(\pi\mu^2) cos(2\lambda) \quad (4)$$

where A = 400 m and $\mu = sin\theta$. The spectral representation of w_0 gives $(TF)_i$.

Baroclinic Instability

When the norm of $w_i(\tau)$ for eddies is small compared with that of the zonal component, we can predict the direction to which $w_i(\tau)$ grows; this direction is the unstable subspace ξ_i due to the atmospheric baroclinic instability. When $w_i(\tau)$ grows along the unstable subspace, both the baroclinic and barotropic components of $w_i(\tau)$ will grow exponentially, maintaining consistent structure. It is in this process that the zonal baroclinic energy is transformed to the eddy barotropic energy. It is suggested by Tanaka and Sun [1990] that this process operates even for finite amplitude planetary waves. Following this concept, we attempted to parameterize the atmospheric baroclinic instability for our barotropic model by

$$(BI)_i = \frac{da(\tau)}{d\tau}\xi_i = -i\nu a(\tau)\xi_i \quad (5)$$

where $a(\tau) = \sum_i w_i(\tau)\xi_i^*$, and ν is the complex eigenvalue of the stability problem associated with ξ_i. The growth rates and phase speeds used in this study are listed in Table 1.

n	1	2	3	4	5	6
Mode	M_2	M_2	M_2	M_2	M_C	M_C
day^{-1}	0.06	0.11	0.15	0.18	0.25	0.35
° day^{-1}	8.9	9.1	9.0	8.6	8.1	8.4

Table 1. Mode name, growth rates (day^{-1}), and phase speeds (°day^{-1}) of the baroclinically unstable modes for wavenumbers n=1-6. M_2 is the dipole Charney mode and M_C the shallow Charney mode.

Zonal Surface Stress

As the baroclinic waves grow, the nonlinear zonal-wave interaction begins to accelerate the zonal motion. A northward shift of the subtropical jet occurs due to the northward eddy momentum transport induced by the baroclinic waves. For the barotropic flow, the important physics that must be considered to balance the northward shift of the jet are the surface stress and mountain torque. We adopt the following parameterization of the zonal surface stress:

$$(ZS)_i = -\alpha(w_i - \bar{w}_i) \quad \text{for} \quad n = 0 \tag{6}$$

where $\bar{w}_i$ is the monthly mean for January 1979, and $\alpha(2\Omega) = 2.32 \times 10^{-6}\ s^{-1}$ which corresponds to the relaxation time of 5 days.

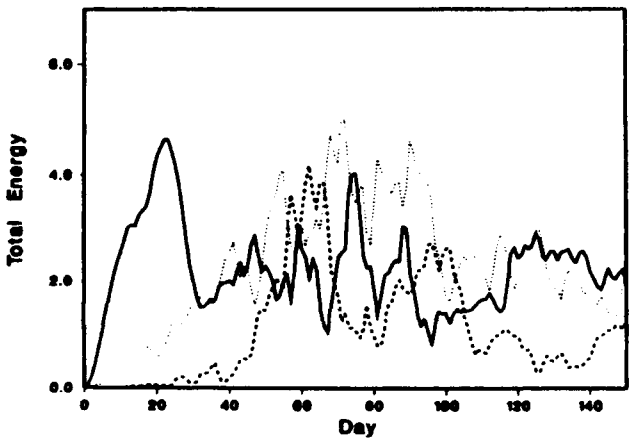


Figure 2. Time series of total energy of zonal wavenumber n=1 (dashed line), n=2 (solid line), and the sum of n=3-6 (dotted line). Units are $10^5\ J\ m^{-2}$.

n	E_n	NL_n	DF_n	TF_n	BI_n	ZS_n
0	1136	258	-11	-44	0	-203
1	131	25	-28	0	11	0
2	204	-185	-54	207	32	0
3	76	4	-35	3	31	0
4	72	-9	-39	9	39	0
5	56	-15	-38	-2	58	0
6	50	-83	-48	-2	138	0

Table 2. Averaged energy variables for wavenumbers n=0-6 during days 30-200. The symbols designate total energy E_n, nonlinear interaction NL_n, diffusion DF_n, topographic forcing TF_n, baroclinic instability BI_n, and zonal surface stress ZS_n. The units are $10^3\ J\ m^{-2}$ for energy and $10^{-3}\ Wm^{-2}$ for energy transformations.

RESULTS OF THE SIMULATION

The results of the numerical integration are shown first in Figure 2 for time series of eddy energies in contributions from n=1, n=2, and the sum of n=3–6. It is clear that the initial growth of eddy energy is caused by topographic forcing of n=2. The energy of n=1 increases after day 40, indicating energy peaks around day 60. During the peak period of n=1, a pronounced blocking occurred in the model atmosphere.

Figure 3a–b illustrates barotropic geopotential fields during the model days 54–61. The barotropic geopotential field roughly corresponds to the 500 mb height field. The coastal line is drawn for reference in the model results. During days 54–69, a blocking high appeared near 0°E along 60°N. The wavenumber 2 amplifies with its troughs along 90°E and 90°W. A dipole structure of wavenumber 1 with its high pressure center at 60°N and low pressure center at 40°N is superimposed on the wavenumber 2. A sharp transition from zonal to meridional flow is clear up-stream of the blocking system. The duration of the blocking is more than two weeks and the results reasonably resemble observed blocking characteristics. Our nonlinear barotropic model seems to capture the essential mechanism of blocking systems. We can conclude, at least, that the blocking can be simulated using a barotropic model with four physical processes, i.e., diffusion, topographic forcing, baroclinic instability, and zonal surface stress.

The results of the energy and energy transformations are summarized in Table 2 for time averages of days 30–200. The eddy energy is largest at n=2, and second largest at n=1. The higher wavenumbers contain less energy. There are two major energy sources; one is the topographic energy source at n=2, and the other is the baroclinic energy source at n=6. The energy is then redistributed by the nonlinear interactions toward n=0. As in observation, n=1 receives energy through the nonlinear interactions. There is a main energy sink at n=0 from the zonal surface stress. Diffusion is evenly distributed over the waves. The important role of the nonlinear triad interactions is evidently to transfer energy from the source at n=2 and 6 to the sink at n=0. The transfer is characterized as the up-scale cascade from small-scale motions to large-scale motions. We confirmed that the up-scale energy cascade into n=1 increased rapidly during the onset of the blocking in the model atmosphere.

SUMMARY

We have shown that a simple barotropic model with four physical processes of diffusion, topographic forcing, baroclinic instability, and zonal surface stress can simulate a realistic and persistent blocking. The basic structure of large-scale blocking is explained by a superposition of a meridional dipole structure of wavenumber 1 and a monopole structure of wavenumber 2. The problem in large-scale blocking is then reduced to explain why these planetary waves are amplified. A model run without topography failed to simulate the large-scale blocking since the planetary waves were not amplified. The existence of quasi-stationary planetary waves is essential for the blocking. As found by our energy budget, the important amplification of low-frequency wavenumber 1 is caused by the nonlinear wave-wave interactions. We confirmed that the largest portion of the energy supply came from synoptic disturbances. The energy supply from the topographic forcing appears to be of

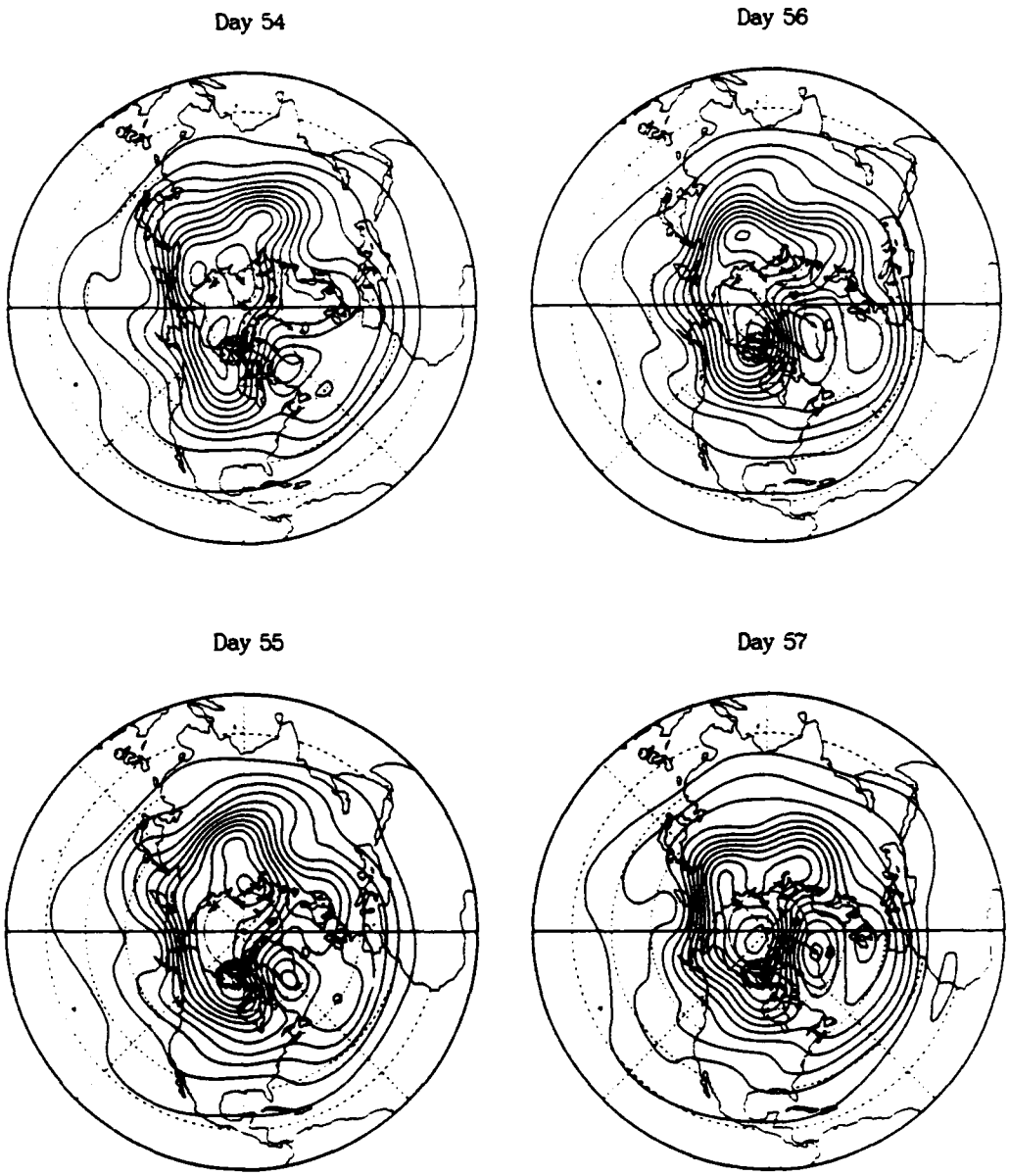


Figure 3a. Geopotential fields during 54-57 days when a blocking occurred in the model atmosphere. The contour interval is 100 m.

secondary importance. Synoptic disturbances contribute to the amplification of wavenumber 1 and to the sharp transition from zonal to meridional flows when the quasi-stationary planetary waves already exist. Therefore, excitations of quasi-stationary planetary waves and synoptic disturbances are both important for blocking formations.

ACKNOWLEDGMENT

This research was supported by the National Science Foundation under grant ATM-8923064.

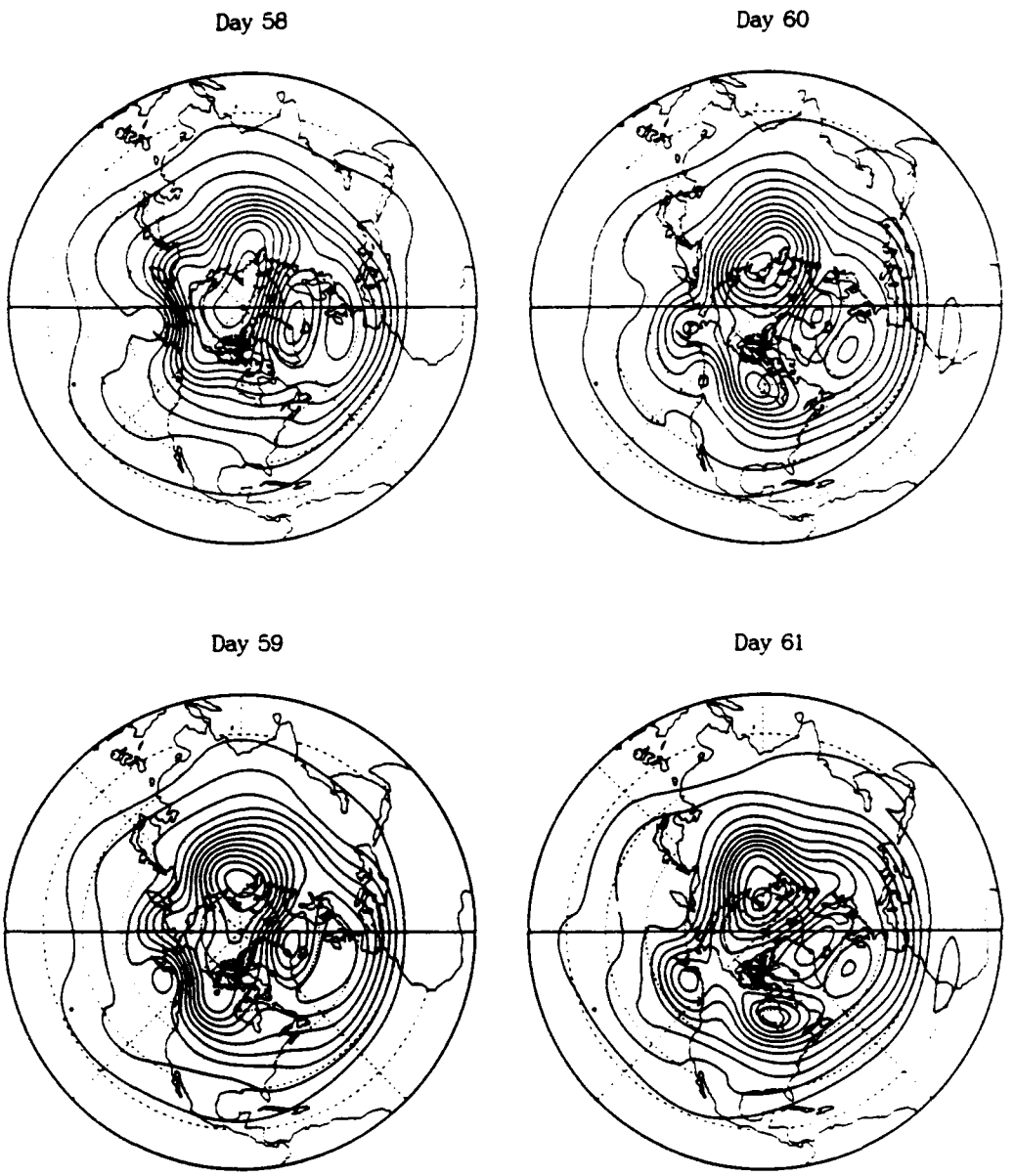


Figure 3b. Geopotential fields during 58-61 days when a blocking occurred in the model atmosphere. The contour interval is 100 m.

REFERENCES

Dole, R. M., The life cycle of persistent anomalies and blocking over the north Pacific, *Advances in Geophys.*, *29*, 31–69, 1986.

Frederiksen, J. S., A unified three-dimensional instability theory of the onset of blocking and cyclogenesis, *J. Atmos. Sci.*, *39*, 969–982, 1982.

Frederiksen, J. S., and R. C. Bell, Teleconnection patterns and the role of baroclinic, barotropic and topographic instability, *J. Atmos. Sci.*, *44*, 2200–2218, 1987.

Hoskins, B. J., and Karoly, D. J., The steady linear response of a spherical atmosphere to thermal and orographic forcing, *J. Atmos. Sci.*, *38*, 1179–1196, 1981.

Tanaka, H. L., and E. C. Kung, A study of low-frequency unstable planetary waves in realistic zonal and zonally varying basic states, *Tellus*, *41A*, 179–199, 1989.

Tanaka, H. L., and M. F. Milkovich, A heat budget analysis of the polar troposphere in and around Alaska during the abnormal winter of 1988/89, Mon. Wea. Rev., 118, 1628–1639, 1990.

Tanaka, H. L., and S. Sun, A study of baroclinic energy source for large-scale atmospheric normal modes, *J. Atmos. Sci.*, *47*, 2674–2695, 1990.

Tanaka, H. L., E. C. Kung, and W. E. Baker, Normal mode energetics and error analysis of GLA GCM simulations with different horizontal resolutions during a winter month, *Beitrage zur Physik der Atmosphare*, *62*, 99–111, 1989.

AD-P007 284

Trends in Global and Polar Cloudiness from Satellite Data

Igor I. Mokhov
Institute of Atmospheric Physics, Academy of Sciences of the USSR, Moscow, USSR

92-17966

ABSTRACT

Trends of cloudiness change are estimated on the basis of Soviet satellite data 1971–1985). Besides the general tendency of global cloudiness increasing (separately for the Northern and Southern hemispheres) with increasing global surface temperature, there are regions with the opposite tendency. Differences in the cloudiness–temperature relationship in interannual evolution for different seasons are noted. Analysis of the trends of intramonth (from day to day) cloudiness dispersion in relation to the evolution of the temperature regime is also made.

Particularly in Northern hemisphere (NH) high latitudes the total cloudiness n increases with the increase of NH surface temperature T_p ($dn/dT_p>0$) for summer and fall seasons in interannual evolution. Negative values of dn/dT_p were estimated in polar latitudes mainly for winter and spring.

The intramonth cloudiness dispersion σn^2 decreases in the interannual evolution with hemispheric warming for most of the annual cycle and for most of the NH. In polar latitudes the opposite tendency dominates and only for winter and spring were negative values of $d\sigma n^2/dT_p$ estimated.

Among the average tendencies of cloudiness changes the peculiarities of certain years were noted. For example, the cloudiness on satellite data over the NH and particularly over the North Atlantic region for the winter of 1982/83 during the El Niño period was less than for other winters between 1980–1985.

One of the important but as yet unsolved problems in climate theory is the effect of cloud cover on radiation and thermal conditions in the earth's climatic system (ECS), and conversely the dependence of cloud cover on thermal and circulation conditions. Estimation of the climatic significance of clouds is complicated by the fact that their influence on solar and thermal radiation is different for different types of clouds as well as for different regions of the ECS.

At present there is uncertainty even as to the sign of the relationship between the change in cloud cover and the temperature change in climatic models of various levels from simple energy-balance ones to the most detailed models of the general circulation (GCM). A considerable uncertainty in the sensitivity of the climatic GCM, including change in atmospheric CO_2 content, is connected with cloudiness. The uncertainty in the data on cloudiness also complicates the task. Particularly, there are significant differences between different satellite and ground-based data.

The large-scale relationship between the amount of cloud cover n and the surface temperature T in the ECS was studied from different sets of ground-based and satellite data in the annual cycle and interannual variability. Using ground-based data from Berlyand and Strokina [1980], Mokhov [1982] found the tendency of an increase of cloudiness with an increase of surface temperature of the Northern (NH) and Southern (SH) hemispheres on the whole in the annual cycle. On the basis of linear regressions Mokhov [1982] obtained estimates of $dn(NH)/dT(NH)=0.004$ K^{-1} (standard deviation 0.001 K^{-1}) for the NH and of $dn(SH)/dT(SH)=0.009$ K^{-1} (standard deviation 0.003 K^{-1}) for the SH. The largest positive values of dn/dT in the NH were estimated for polar latitudes (with negative values in middle and subtropical latitudes).

On the basis of cloudiness data (1971–1980) from Meteor-type satellites [Matveev and Titov, 1985], Mokhov [198.] obtained the practically identical estimate of $dn(NH)/$

dT(NH)=0.004 K^{-1} for the NH (standard deviation 0.001 K^{-1}) in the annual cycle. However, for the SH the differences between satellite and ground-based data are significant, particularly in the polar latitudes. According to Mokhov [1985] the general tendency of increased cloudiness with increased surface temperature is exhibited also in the interannual variability for the NH, SH and ECS on the whole (with a larger estimate for dn/dT in comparison with estimates for the annual cycle).

The tendency of cloudiness increase with warming was also marked for climatic changes (in Europe and the United States during several tens of years), as determined from ground-based data by Henderson-Sellers [1986a,b].

The relationship of cloudiness and surface air temperature was determined for the NH in the annual cycle and interannual variability on the basis of satellite (Meteor-type) cloudiness data for the 15-year period 1971–1985 [Arsky et al., 1990]. An estimate for dn/dT similar to that in Mokhov [1985] was found in the annual cycle for the NH on the whole (0.0046 K^{-1}, coefficient of correlation r=0.93). Separately over land and ocean there were found 0.0021 K^{-1} (r=0.56) and 0.0083 K^{-1} (r=0.97). In contrast to the general tendency of increased cloudiness with warming, regions with opposite tendencies were also exhibited.

Analysis of zonal estimates for dn/dT_p in the annual cycle showed positive correlation between total cloud amount and temperature near the surface for latitudes of the Hadley and polar cells and negative correlation for the latitudes of the Ferrell cell and also on the equator (Figure 1). A positive correlation was noted for high latitudes and the continental regions. Negative correlation was found, particularly, over extratropical oceans and the polar regions.

Analysis of zonal estimates for dn/dT_p in the interannual data from Matveev and Titov [1985], Aristova and Gruza [1987], and Gruza and Ran'kova [1980] shows the peculiarities of polar latitudes. According to Figure 2, cloudiness increased with warming over most of the NH during most of year. This is most remarkably exhibited over continents for tropical latitudes in summer, over ocean for polar latitudes in fall and also for tropical and subtropical latitudes on the whole in summer. The negative values of dn/dT_p in the interannual variability $(dn/dT_p)_{iv}$ shown in Figure 2 are estimated mainly for high latitudes in spring–winter. The maximum absolute value estimates of $(dn/dT_p)_{iv}$ were marked for polar latitudes in April–May. Over land, negative values of $(dn/dT_p)_{iv}$ are also found for middle latitudes in winter, and in fall for tropical and subtropical latitudes. Over ocean, negative estimates of $(dn/dT_p)_{iv}$ were obtained for polar latitudes (end of summer–beginning of fall) and for middle latitudes (summer).

Analysis of the latitude–longitude distributions showed that in winter negative values of the correlation coefficient $r(n:T_p)$ for interannual variability are characteristic over continents (excluding Africa). Over most of the oceans r is positive and $dn/dT_p>0$. For polar latitudes, on the whole, the coefficient of correlation is negative, but for tropical latitudes it is positive (r>0). The regions with |r|>0.6 are over North America and the subtropical Atlantic.

The regions with negative r over Eurasia and North America and also over the western part of the Pacific Ocean are smaller in spring than in winter. In spring on the whole, as in winter, the value of r is negative for polar latitudes, but for tropical latitudes it is positive. The regions with r<-0.6 were the polar latitudes, and those with r>0.6 were over the eastern part of North America and tropical parts of the Pacific and Atlantic Oceans.

In summer the regions with r>0 dominate (by area). The regions with r<0 were in the Arctic (over Greenland and to the north of Alaska and the Chukchi Peninsula), over the eastern part of North America and over the Pacific Ocean. The regions with r>0.6 were in subtropical and tropical latitudes over the Atlantic, over Africa, and subtropical and tropical latitudes over the Pacific Ocean near continents.

In fall on the whole as for summer the regions with r>0 dominate. The regions with r>0.6 were over the eastern part of North America from subtropical to subpolar latitudes, over the central Atlantic, and over a region in the north part of South America.

It should be noted that for all seasons in the interannual variability the values $r(n:T_p)$ are mainly positive for tropical latitudes.

Along with the analysis of correlations of cloudiness changes with temperature changes, tendencies of intramonth cloudiness variances were also analyzed [Arsky et al., 1990]. Such tendencies were studied both for interannual variability (for 15-year data set from Meteor-type satellites) and for the annual cycle. Zonal and hemispheric mean tendencies were estimated for σ_n^2 averaged on area (not for variance of cloudiness averaged on area).

For the NH on the whole a decrease of $(\sigma_n^2)_p$ under a decrease of T_p in the annual cycle was obtained. It should be noted that the correlation of intramonth cloudiness variances with temperature is positive over oceans and negative over continents.

For almost all latitudes the characteristics of the σ_n^2 and T_p relationship in the annual cycle are of different sign over oceans and continents. The strongest (positive) correlation and largest coefficients of the relationship $\sigma_n^2(T_p)$ over ocean were obtained in subtropical and middle latitudes. The largest absolute value coefficients of the relationship and coefficients of correlation (negative) over land were obtained for 20–30°and 50–60°latitudes and also near 5°N. The local minimum for the coefficient of the relationship of σn^2 with T_p $(d\sigma_n^2/dT_p)_{ac}$ and for the absolute value of r was noted for the 40° latitudes. The effect of the ocean dominates in these latitudes under zonal averaging.

The difference in characteristics of the relationship σ_n^2 (T_p) in the annual cycle over ocean and land is exhibited from the analysis of the latitude–longitude distributions. Over oceans there are mainly positive values of coefficients of regression and correlation. Over land these values are mainly negative. This is particularly characteristic for the belt from tropical to polar latitudes.

The largest regions with a relatively strong relationship between σ_n^2 and T_p in the annual cycle were found over North America, the Atlantic (particularly in the western part) and for the western part of the Pacific Ocean. The largest regions with a large coefficient of the σ_n^2:T_p regression were obtained over the northern part of North America, over the northern part of Africa and over the Near East (negative) and also over the western part of the Pacific Ocean (positive).

For changes of the intramonth variance of cloudiness in the interannual variability, the tendency of the decrease

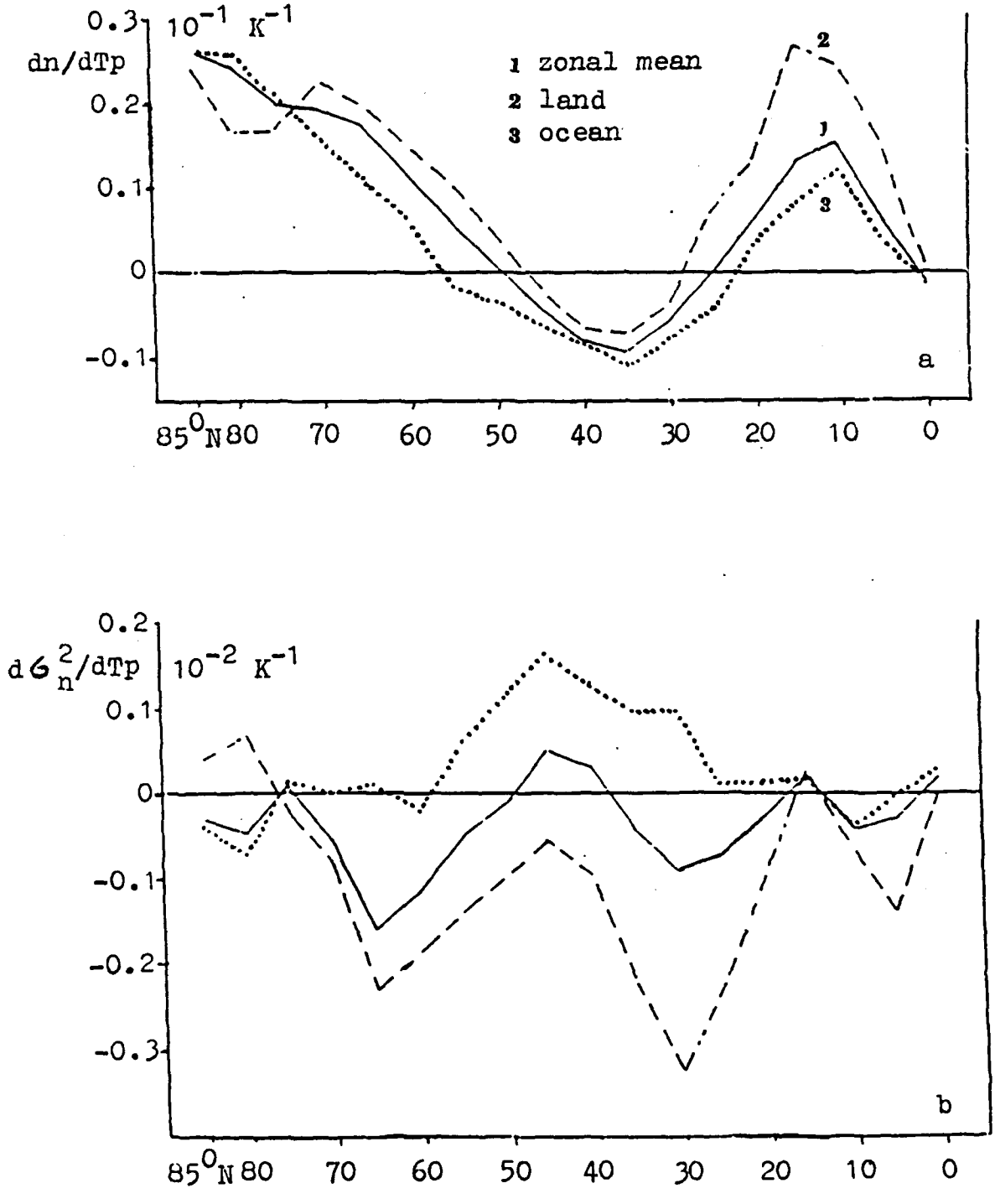


Figure 1. Dependence of d_n/dT_p (a) and $d\sigma_n^2/dT_p$ (b) on latitude in the annual cycle.

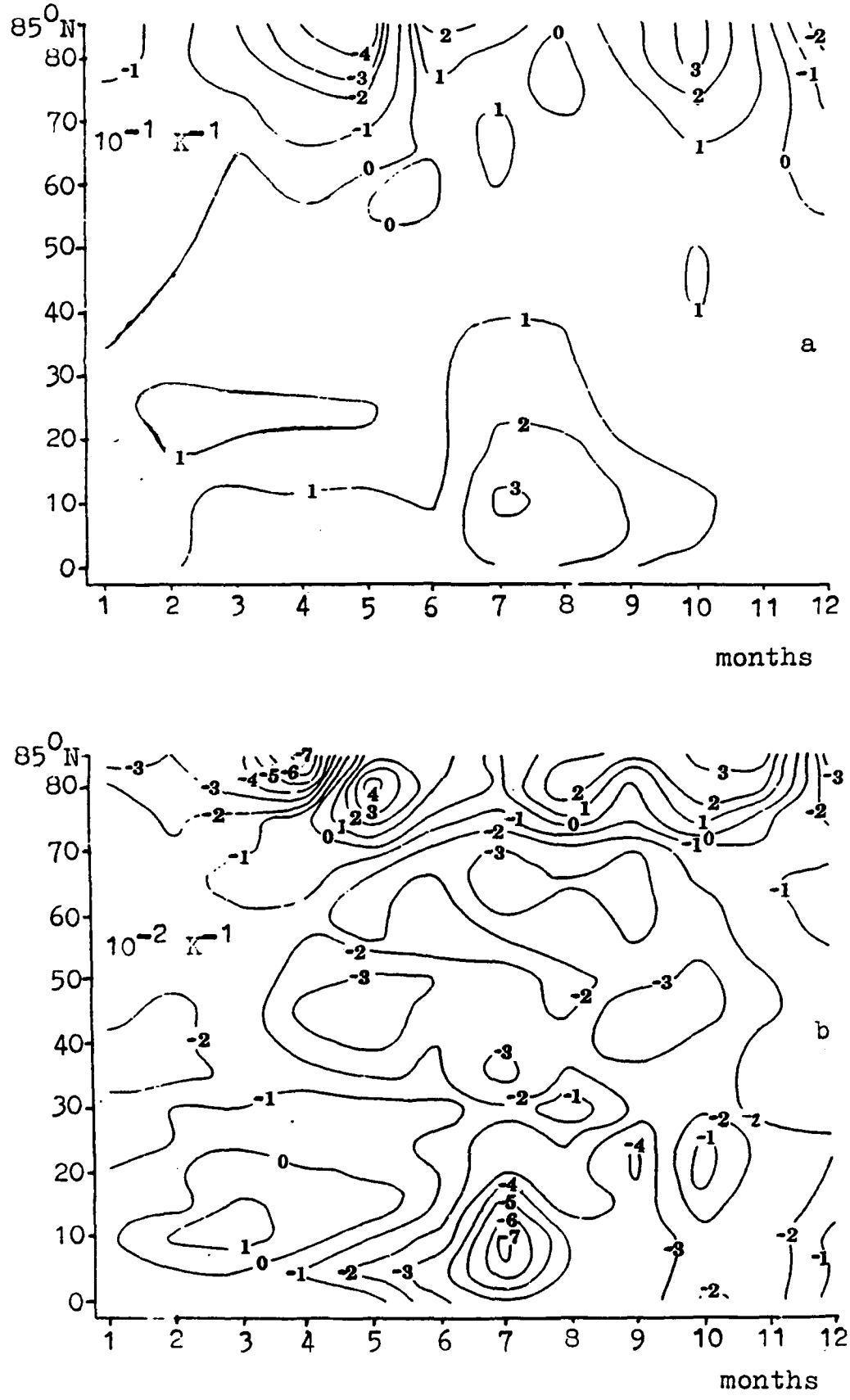


Figure 2. Dependence of d_n/dT_p (a) and $d\sigma_n^2/dT_p$ (b) on latitude for different months in the interannual variability.

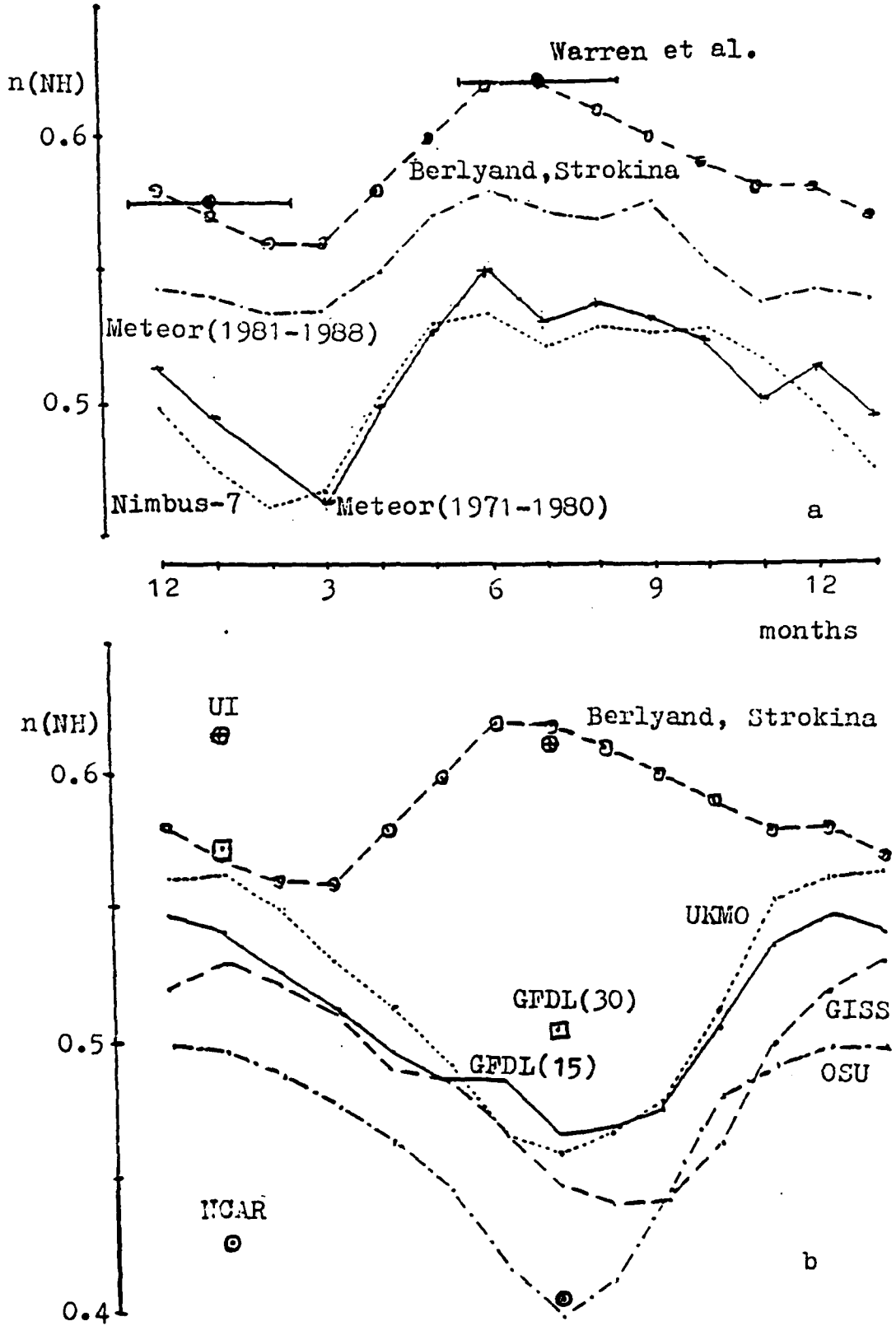


Figure 3. Total cloud amount in the Northern Hemisphere in the annual cycle: (a) on different observational data and (b) for different GCM (GCM GFDP with different horizontal resolutions—GFDL (15) with 15 harmonics and GFDL (30) with 30 harmonics).

	July 1983		January 1984		D	
	NH (7)	SH (7)	NH (1)	SH (1)	NH (7-1)	SH (1-7)
ISCOP						
I: N=1	0.58	0.60	0.54	0.64	0.04	0.04
N=20	0.58	0.60	0.53	0.62	0.05	0.02
II: N=1	0.54	0.58	0.52	0.62	0.02	0.03
N=20	0.54	0.58	0.51	0.60	0.03	0.02
Meteor	0.60	0.69	0.53	0.69	0.07	0.01
Nimbus-7	0.50	0.50	0.46	0.55	0.04	0.05

Table 1. Total cloudiness for Northern (NH) and Southern (SH) Hemispheres in July 1983 and January 1984 and the differences (D) between July (7) and January (1) for NH and between January (1) and July (7) for SH on satellite data with different variants for ISCCP data (I - for solar and infrared radiation, II - for infrared radiation; N - number of days per month with a minimum of 8 observations per day.

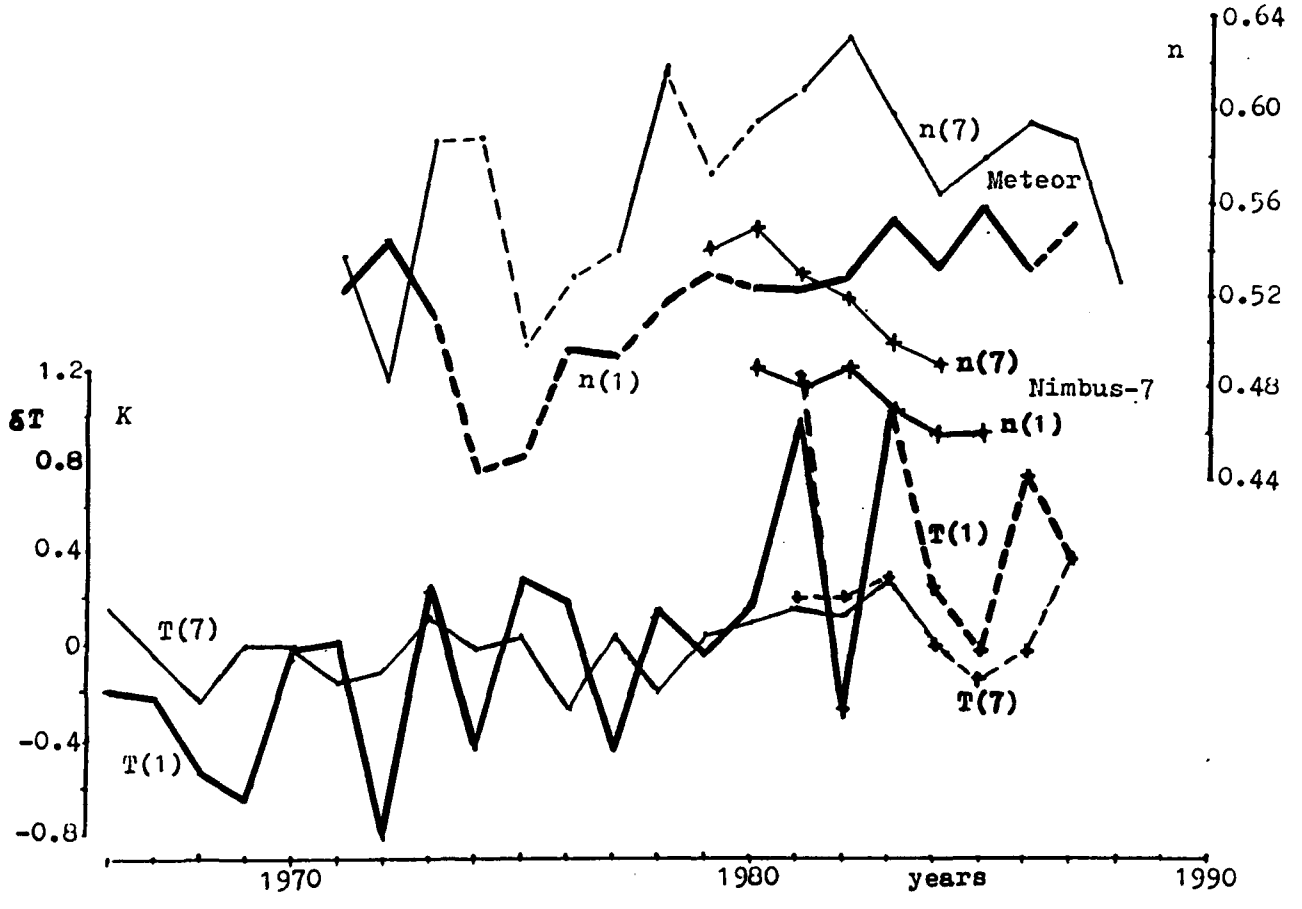


Figure 4. Interannual (July and January) variability of total cloudiness and temperature near the surface for the Northern hemisphere on different data.

(excluding March over land) with the increase of T_p ($(d\sigma_n^2/dT_p)p<0$) is characteristic for the NH on the whole. The maximum absolute value quantities of $(\sigma_n^2/dT_p)_p$ are characteristic for July and September, while the minimum quantities are characteristic for March. On the whole opposite tendencies are exhibited of the temperature sensitivity for cloudiness and for cloudiness variance.

On the basis of the analyzed satellite data, the intramonth cloudiness variance in interannual variability decreases with hemispheric warming for most of the NH during most of the year. The exception is in polar latitudes (where $(d\sigma_n^2/dT_p)_{iv}$ <0 only in spring and winter) and for tropical latitudes in winter and spring.

Generally, negative values of $(d\sigma_n^2/dT_p)_{iv}$ were exhibited for the latitudinal belt 30°–70°N for all months. In tropical latitudes the maximum of $(d\sigma_n^2/dT_p)_{iv}$ in the winter–spring months (better expressed over continents) is changed by the minimum for the summer–fall period. The opposite is exhibited for polar regions, with a minimum in winter–spring and a maximum in the other half of the year.

In winter the regions with r<0 (and with $d\sigma_n^2/dT_p<0$ in the interannual variability) dominate (by area), though large regions with r>0 ($d\sigma_n^2/dT_p>0$) are exhibited in the northern and eastern parts of the Atlantic, over tropical Africa, over Asia, and north of Alaska in the Arctic. The largest positive values of r were marked in the subtropical Atlantic near Africa.

The regions with r>0 are more extensive in spring, especially over the north part of Asia, and also in the tropical and subtropical latitudes. Nevertheless, the regions with r<0 dominate, as in winter. The largest negative values of r are found in the polar regions.

The regions with r<0 dominate on the whole also for summer. The most extensive regions with large values |r| (r<0) were marked over the Pacific Ocean (from equator to middle latitudes) and also over the equatorial Atlantic (in the eastern part of the Atlantic up to the subtropics). The extensive regions with a positive r were over the western Atlantic and over the eastern part of America, over the northern part of the Pacific Ocean, over the Arctic and over regions of Africa.

In fall, the trend of a positive correlation of σ_n^2 with T_p was exhibited in polar latitudes. In the middle latitudes the regions with r<0 dominate on the whole. In the subtropical and tropical latitudes there are regions with both positive and negative values of r.

To obtain more reliable climate change estimates, it is necessary to simulate the present climate more accurately, particularly the annual cycle and interannual variability. Therefore, it is useful to carry out detailed mutual diagnostics of satellite and ground-based observational data and model results. In Figures 3 and 4 and in Table 1 are some results of comparison of the cloudiness data from Meteor-type satellites (SSCO) with ISCCP [Schiffer and Rossow, 1983, 1985] with Nimbus-7 [Stowe et al., 1989] satellite data, and with ground-based observations [Berlyand and Strokina, 1980; Warren et al., 1986, 1988]. In Figure 4 for the interannual variability of cloudiness (for July and January) is also represented the appropriate data [Jones, 1988] for temperature near the surface in the NH. Though there are large differences and uncertainties for different observational (satellite and ground-based) data, it should be noted that for all these data sets the total cloudiness is larger for the warmer season (in summer) than for the colder season (in winter) for the NH on the whole.

The comparison was made not only for observational data, but also for cloudiness simulations in different GCMs: GFDL [Wetherald and Manabe, 1988], GISS [Hansen et al., 1983], UKMO [Wilson and Mitchell, 1987], OSU [Schlesinger and Zhao, 1989] and UI [Oh, 1989]. Noticeable differences between the model and observational results were thereby revealed. Particularly, it is characteristic for all observational data that the cloudiness in the NH on the whole in summer is greater than in winter. However, the contrary tendency was found for GCMs. This is an important difference. It should be noted that in GCMs the tendency of a decrease of cloudiness is exhibited under an increase of the CO_2 content in the atmosphere (cloudiness is less for warmer climate). For estimates of the potential changes, it is necessary (although not necessarily sufficient) to reproduce the present climate changes. The similar results for different models in contradiction with observational data indicate the necessity to verify the general parameterizations of cloudiness. (It should be stressed that there is also a large uncertainty in observational data.)

REFERENCES

Aristova, L. N., and G. V. Gruza, Data on the structure and variability of climate. Total cloudiness on satellite observations. Northern and Southern Hemispheres. ASRIHMI-MDC, Obninsk, 1987.

Arsky, A. A., I. I. Mokhov, and V. K. Petukhov, Modelling of trends of the Earth's climate variability characteristics, *Izv. Akad. Nauk SSSR, FAO, 25*, 3–13, 1989a.

Arsky, A. A., I. I. Mokhov, and V. K. Petukhov, Study of variability characteristics evolution of the Earth's climatic system in the energy-balance model, *Proc. Intl. Conf. "Climatic change in the historical and the instrumental periods,"* Brno, 1989b.

Arsky, A. A., N. Yu. Arsky, and I. I. Mokhov, Intercomparison of cloudiness and atmospheric temperature fields for the Northern Hemisphere in the annual cycle and interannual variability, Preprint N1, 46 pp., Institute of Atmospheric Physics, Moscow, 1990.

Berlyand, T. G., and L. A. Strokina, The global distribution of the total cloud cover, Gidrometeoizdat, Leningrad, 1980.

Gruza, G. V., and E. Ya. Ran'kova, Structure and variability of observed climate. Air temperature of Northern Hemisphere. Gidrometeoizdat, Leningrad, 70 pp., 1980.

Hansen, J., G. Russell, D. Rind, P. Stone, A. Lacis, S. Lebedeff, R. Ruedy, and L. Travis, Efficient three-dimensional global models for climate studies: models I and II, *Mon. Wea. Rev., 111*, 609–662, 1983.

Henderson-Sellers, A., Cloud changes in a warmer Europe, *Climatic Change, 8*, 25–52, 1986a.

Henderson-Sellers, A., Increasing cloud in a warming world, *Climatic Change, 9*, 267–309, 1986b.

Jones, P. D., Hemispheric surface air temperature variations: recent trends and an update to 1987, *J. Climate, 1*, 1988.

Matveev, Yu. L., and V. I. Titov, Data on the climate structure and variability. Global cloudiness field. ASRIHMI-MDC, Obninsk, 99 pp., 1985.

Mokhov, I. I., The correlation of cloud cover with temperature in large-scale spatial averaging, *Meteorologiya i Gidrologiya, 10*, 35–45, 1982.

Mokhov, I. I., Global relationship between cloudiness and temperature as revealed by data on their interannual variability, *Izvestiya, Atmospheric and Oceanic Physics, 21*, 700–704, 1985.

Oh, J.-H., Physically-based general circulation model parameterization of clouds and their radiative interaction, Ph.D. dissertation, 315 pp., Department of Atmospheric Sciences, Oregon State University, Corvallis, OR, 1989.

Schiffer, R. A., and W. B. Rossow, The International Satellite Cloud Climatology Project (ISCCP): The first project of the World Climate Research Programme, *Bull. Amer. Meteor. Soc., 64*, 779–784, 1983.

Schiffer, R. A., and W. B. Rossow, ISCCP global radiance data set: A new resource for climate research, *Bull. Amer. Meteor. Soc., 66*, 1498–1505, 1985.

Schlesinger, M. E., and Z.-C. Zhao, Seasonal climatic changes induced by doubled CO_2 as simulated by the OSU atmospheric GCM/mixed-layer ocean model, *J. Climate, 2*, 459–495, 1989.

Stowe, L. L., H. Y. M. Yeh, T. F. Eck, C. G. Wellemeyer, and H. L. Kyle, Nimbus-7 global cloud climatology. Part II: First year results, *J. Climate, 2*, 671–709, 1989.

Warren, S. G., C. J. Hahn, J. London, R. M. Chervin, and R. L. Jenne, Global distribution of total cloud cover and cloud type amounts over land, *NCAR Technical Note TN-273+STR*, Boulder, CO, 1986.

Warren, S. G., C. J. Hahn, J. London, R. M. Chervin, and R. L. Jenne, Global distribution of total cloud cover and cloud type amounts over the ocean, *NCAR Technical Note TN-273+STR*, Boulder, CO, 1988.

Washington, W. M., and G. A. Meehl, Seasonal cycle experiment on the climate sensitivity due to a doubling of CO_2 with an atmospheric general circulation model coupled to a simple mixed-layer ocean model, *J. Geophys. Res., 89*, 9475–9503, 1984.

Wetherald, R. T., and S. Manabe, Cloud feedback processes in a general circulation model, *J. Atmos. Sci., 45*, 1397–1415, 1988.

Wilson, C. A., and J. F. B. Mitchell, A doubled CO_2 climate sensitivity experiment with a global climate model including a simple ocean, *J. Geophys. Res., 92*, 13315–13343, 1987.

AD-P007 285

Cloud Radiative Effects and Associated Changes in Tropospheric Temperatures and Winds at the South Pole During Austral Winter

Robert S. Stone
Cooperative Institute for Research in the Environmental Sciences, University of Colorado, Boulder, Colorado, U.S.A.

Jonathan D. Kahl
Dept. of Geosciences, University of Wisconsin-Milwaukee, Milwaukee, Wisconsin, U.S.A.

ABSTRACT

Both the increasing concentrations of greenhouse gases and potential changes in cloud distributions are likely to affect the surface energy budget of the polar regions. Changes in the polar atmosphere are linked to dynamical processes that control the transport of mass, heat, and moisture from lower latitudes and in turn, feed back into the global circulation. An assimilation of radiation and meteorological data collected at the South Pole during the 1986 austral winter is analyzed to gain a better understanding of the relationships between cloud radiative effects, transport processes and the vertical distribution of temperature and wind. An algorithm is developed to characterize the quasi-permanent surface-based temperature inversion and the "warm" radiatively active layer above it. Mean winter temperature and wind profiles for clear and overcast conditions are combined with surface radiation measurements to study the mechanisms that cause periodic weakening of the inversion. Results support previous studies that ascribe this weakening to (1) warm air advection, (2) downward vertical mixing of sensible and latent heat, and (3) longwave cloud radiative heating. The integrity of the inversion depends on the combined effects of all three mechanisms. Parameters representing the intensity of the inversion and the bulk wind shear through the lower troposphere are suggested as appropriate indices for the detection of climate change in the region of the Antarctic Plateau.

INTRODUCTION

Theoretical models of the atmosphere's general circulation indicate that high latitude regions are particularly susceptible to "greenhouse" warming because of increasing concentrations of radiatively active trace gases [e.g., Schlesinger and Mitchell, 1985]. It is curious that despite significant upward trends in the concentration of many greenhouse gases detected at the South Pole [Elkins and Rosson, 1989], most of the Antarctic Plateau has been cooling at a rate exceeding 0.25°C per decade [Jones, 1988]. If only radiative effects due to trace gases are considered, model simulations predict that the climate in this region should be warming. To the authors' knowledge, no definitive explanation for the observed cooling trend has been given. Clearly, factors other than greenhouse warming must influence the South Pole climate. In this paper we clarify the interaction of some of these processes that affect that region and suggest appropriate indices for the detection of climate change there.

One key factor that dramatically impacts the climate of the Antarctic Plateau is cloudiness associated with the poleward transport of sensible and latent heat. Ramanathan et al. [1989] presented satellite-based remote-sensing results from the Earth Radiation Budget Experiment, showing that whereas clouds generally have a net cooling effect on the

surface of the earth, they contribute to anomalous surface warming in high-latitude snow-covered regions.

The crucial role that clouds play in forcing the earth–atmosphere radiation balance in polar regions is still poorly understood. Clouds both absorb and emit longwave (LW) radiation while increasing the planetary shortwave (SW) albedo. The net cloud radiative forcing results from the competition between warming due to LW cloud emissions and cooling due to SW cloud albedo effects, and depends on highly variable physical, microphysical, and radiative properties of the cloud field not readily measured remotely using satellites. Consequently, it is very difficult to quantify cloud radiative effects over snow-covered surfaces using satellite radiance data alone.

Ground-based radiation measurements, however, confirm that anomalous surface warming does occur in polar regions when clouds are observed. The effects of high-latitude cloudiness on the surface radiation balance have been reported by Cogley and Henderson-Sellers [1984] for one station in the Arctic. Stone et al. [1989] studied short-term variations in the surface radiation balance and temperatures associated with cloudiness at the South Pole. Both studies indicate that clouds tend to heat the surface in snow-covered polar regions and that the heating effects are monotonic with increasing cloud cover and/or cloud optical depth. Since radiative forcing due to clouds potentially far exceeds that due to gaseous greenhouse warming [Ramanathan et al., 1989], even small changes in frequency, type, or spatial distribution of clouds could result in significant climate change on a regional scale. In turn, such changes may perturb the larger-scale circulation. For example, an increasing trend in sky cover during January, February, and March for 1976–1988 has recently been detected at the South Pole. This increase is negatively correlated with a trend in the global SW irradiance reaching the surface [Dutton et al., 1991]. Though the causes and effects of these trends have not been determined, feedbacks between cloud radiative and dynamical processes, or perhaps large-scale changes in circulation, may explain these observations.

As noted by Fletcher [1970] and others, changes in regional climate are associated with changes in the larger-scale circulation. To gain a better understanding of climatological trends, Fletcher recommended evaluating circulation changes that result in specific variations in boundary conditions, i.e., conditions near the surface. The motivation for the present study is thus twofold: (1) to qualitatively understand the mechanisms that force the lower tropospheric radiation, temperature and wind fields at the South Pole, and (2) to identify locally measurable, climatologically important indices that may be used to detect changes in boundary conditions thought to be linked to changes in the larger-scale circulation patterns.

METEOROLOGICAL DATA BASE

The South Pole Observatory (SPO), established in 1972 as one of the National Oceanic and Atmospheric Administration's Geophysical Monitoring for Climatic Change (NOAA/GMCC) baseline atmospheric monitoring stations, provides an ideal laboratory to study short-term variability and long-term climate trends representative of a large region of the Antarctic Plateau.

Surface and upper-air data for SPO were assimilated for this study. The surface data consist of upward and downward broadband fluxes of LW radiation, as well as the standard meteorological observations including sky cover. Time series of daily mean values of surface temperature (T_s), downward LW irradiance (LWD), and sky cover (SC) are presented to show the seasonal and short-term variability associated with cloudiness at the South Pole. Details of the surface radiation measurements were presented by Dutton et al. [1989]. In addition, analyses of selected hourly mean values of LWD, net irradiance (NET), and wind speed and direction are compared with rawinsonde data to characterize better the physical state of the lower troposphere under clear and overcast conditions.

We stratified the data according to sky cover observations. Only "clear-sky" (SC < 1/10) and "overcast" (SC > 9/10) conditions are analyzed here to contrast clearly the state of a cloudy atmosphere relative to clear conditions. This simple approach is designed to minimize any ambiguity related to sky cover observations [Schneider et al., 1989]. Results for the austral winter months of 1986 are presented in this paper.

RESULTS AND DISCUSSION

Time Series

We first introduce the problem of short-term surface temperature variability as it relates to wintertime cloud effects. Figure 1 shows time series plots for April–August 1986 of daily mean values of T_s (Figure 1a) and LWD and SC (Figure 1b). The smooth curves are quadratic fits to the clear-sky data for T_s and LWD.

As is discussed in more detail in subsequent sections, clear-sky conditions at the pole are generally characterized by a weak, steady katabatic flow of cold air from higher terrain, and a strong, persistent surface-based temperature inversion. Transient weather disturbances, on the other hand, are characterized by increased cloud cover, surface warming, a shift in wind direction, increased wind speed, and a weakening of the inversion. Figure 1 shows that surface warming is well correlated with enhancements of downward LW irradiance which, in turn, correlate with increased sky cover. The linear correlation coefficient between T_s and LWD is 0.91 for this particular time series. Positive correlation between T_s and LWD is expected, since LWD is dominated by thermal emissions from the lower levels of the troposphere whether or not clouds are present. Increases in LWD, or other factors associated with clouds, are apparently responsible for most of the variability in the time series: the overall range of observed temperature is 39°C, whereas the range for clear-sky conditions is only 18°C.

Clouds over the Antarctic Plateau tend to form in the warm layer capping the surface-based inversion [Schwerdtfeger, 1984]. Because thermal emissions from these "warm" clouds tend to be greater than emissions from the cooler, drier subcloud layer, we attribute the enhancement of LWD under overcast skies mostly to cloud radiative forcing. These observations are consistent with earlier studies that related surface warming to LW heating from clouds formed during upper-level intrusions of moisture [e.g., Schwerdtfeger, 1968]. Such intrusions are frequently laden with cloud condensation nuclei reaching the pole from the

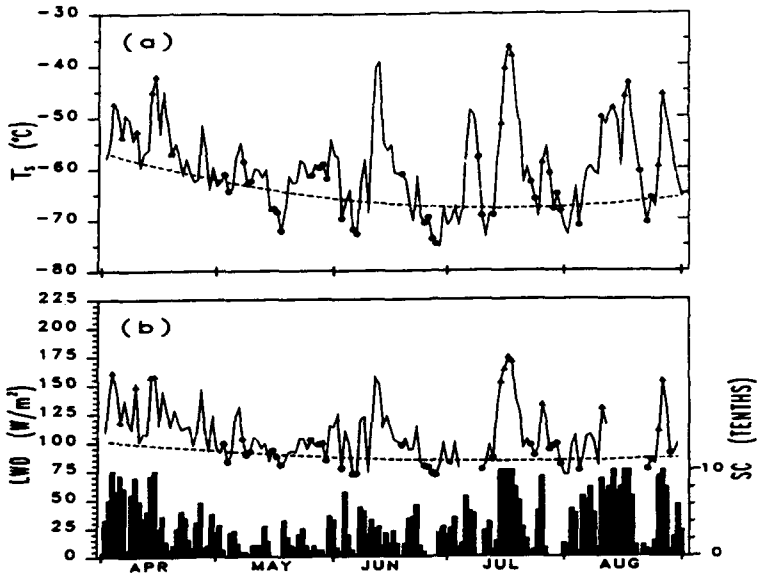


Figure 1. Time series of (a) surface temperature T_s and (b) downward longwave irradiance LWD (line referenced to left scale) and sky cover SC (bars, right scale) for April-August 1986 at the South Pole. The smooth curves are quadratic fits to the clear-sky days denoted by circles. Overcast days are denoted by filled triangles.

Weddell Sea, producing a variety of cloud types [Ohtake, 1978].

Carroll [1983] suggested two possible mechanisms for surface warming at the South Pole: (1) downward mixing of warm upper-level air, and (2) northerly warm-air advection (with north taken to be the Greenwich meridian). Bodhaine et al. [1986] observed episodic and sometimes dramatic enhancements of sea-salt aerosols at the South Pole associated with rapid transport of moist air from coastal regions. Their analysis also suggests that upper-level air is mixed downward through the inversion layer as it weakens. Hogan et al. [1982] illustrated that heat, water vapor, and aerosols are transported poleward at preferred levels in the troposphere when the position of the polar high-pressure ridge shifts from a northeasterly to a more northerly orientation.

It is clear that the surface temperature field at the South Pole responds to complicated, interrelated radiative and dynamical forcings that are somehow linked to large-scale circulation patterns. We seek to understand these interrelated mechanisms better in the context of a changing climate and to quantify indices of regional climate change that may relate to the general circulation.

Net Cloud Radiative Effects

It is of interest to contrast the net wintertime radiation (NET = LWD - the upward component of the LW radiation balance) under clear and overcast conditions to understand better how clouds influence the total surface energy budget at the South Pole. Figure 2 is a scatter plot of 2300 UT and 0000 UT hourly mean values of net surface irradiance stratified according to 0/10 SC and 10/10 SC for the 1986 winter season. The 2300 UT and 0000 UT time periods were selected to bracket the rawinsonde launch times. The dashed and solid lines in Figure 2 denote the mean values for 35 clear and 20 overcast days, respectively. Despite the wide

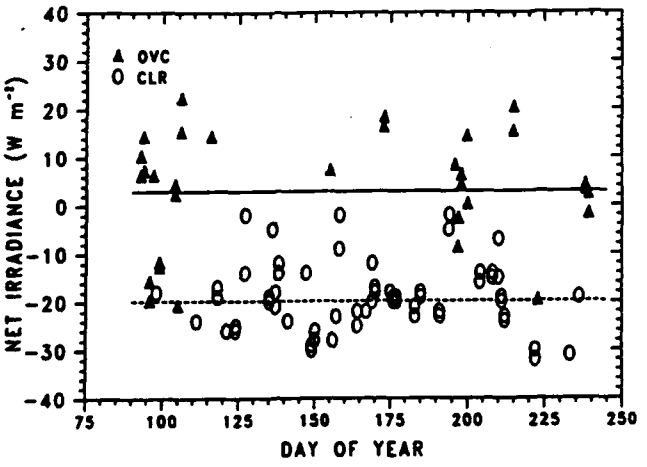


Figure 2. Selected 2300 UT and 0000 UT hourly mean values of net surface irradiance for April–August 1986. Circles denote clear conditions and filled triangles denote overcast conditions. The dashed and solid lines are the mean values for the subsets of 35 clear and 20 overcast days, respectively.

range for either subset of data, a clear separation exists in the means. A large negative value of net irradiance characterizes clear days, and a slightly positive value is observed for overcast conditions. Nearly half the overcast days show net gains exceeding 10 W m^{-2} which represents a significant convergence of radiant energy at the surface available to warm the snow pack and near-surface air. Optically thick warm clouds combined with vigorous turbulent downward mixing of sensible heat very likely exist when large positive net radiation is measured. The cluster of overcast days with negative NET (centered at day 100) is attributed to the occurrence of mostly thin sky cover during that period.

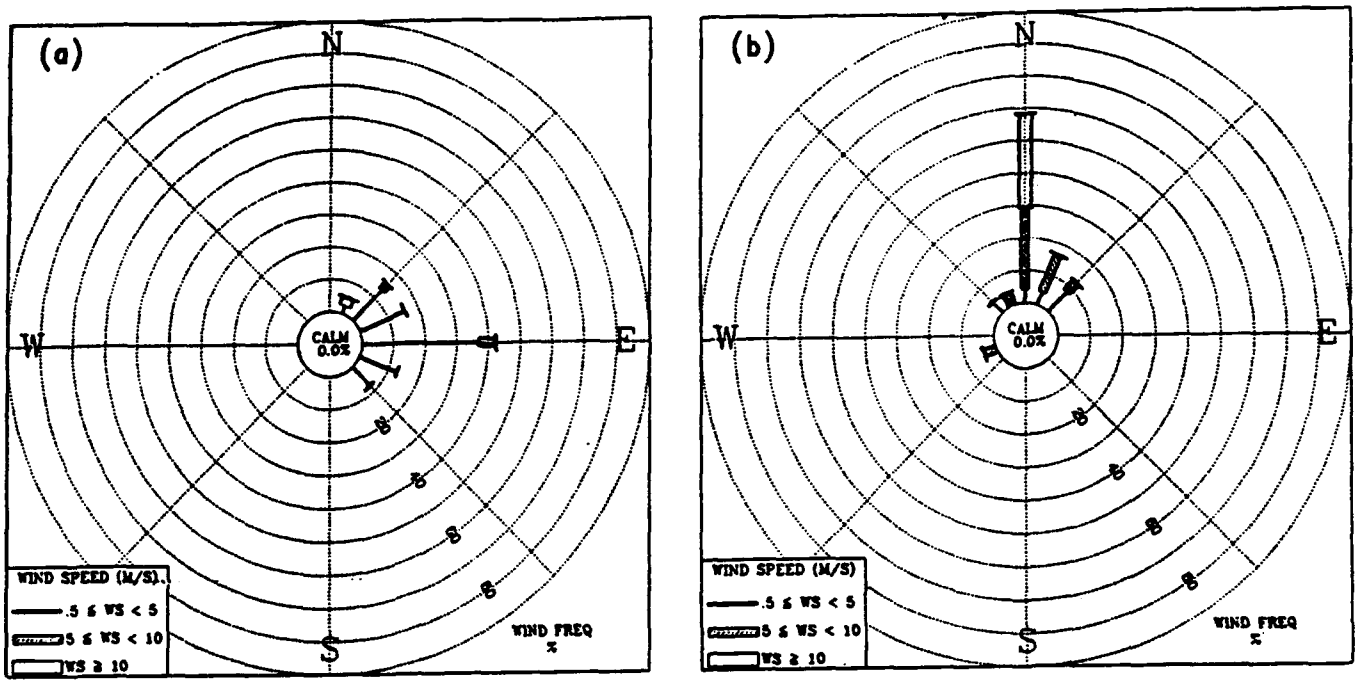


Figure 3. Surface wind roses for (a) 35 clear days and (b) 20 overcast days. The subsets of days coincide with the data presented in Figure 2 for the austral winter of 1986.

Surface and Upper Level Temperatures and Winds

Transport processes are important in the formation and spatial distribution of clouds. Figures 3a and 3b are surface wind roses for the 35 clear and 20 overcast days, respectively. The contrast is striking. Clear days are characterized by surface flow that is weak and from the easterly quadrant 90% of the time, whereas overcast days are mostly characterized by much stronger northerly winds.

Coincident 0000 UT rawinsonde profiles of temperature and wind were used in an effort to extend the analysis in the vertical. Algorithms modified from those developed by Kahl [1990] for arctic inversion studies were used to characterize the temperature and the wind profiles for clear and overcast conditions. Individual soundings were interpolated into prescribed height intervals to enable averaging of the desired subsets of days. A shallow surface-based layer of positive temperature gradient overlain by a rather deep quasi-isothermal layer of much warmer air characterizes the lower troposphere during the austral winter months. The boundary between these layers, in most cases, is readily defined by a sharp inflection in temperature gradient between two adjacent layers, which we define as the upper boundary of the inversion. We define the upper boundary of the warm layer as the level at which the temperature decreases to the point where it is equal to the temperature at the inflection point. Though determining the height of these levels depends on the vertical resolution of the rawinsonde profiles, for the period analyzed in this study, the lowest levels were consistently and reasonably well-resolved. The radiative effect of the warm layer depends not only on its temperature and thickness, but more important, on its effective thermal emissivity, i.e., thin, cloud-filled layers emit LW radiation more efficiently then do thick, cool, cloud-free layers of equivalent mean temperature.

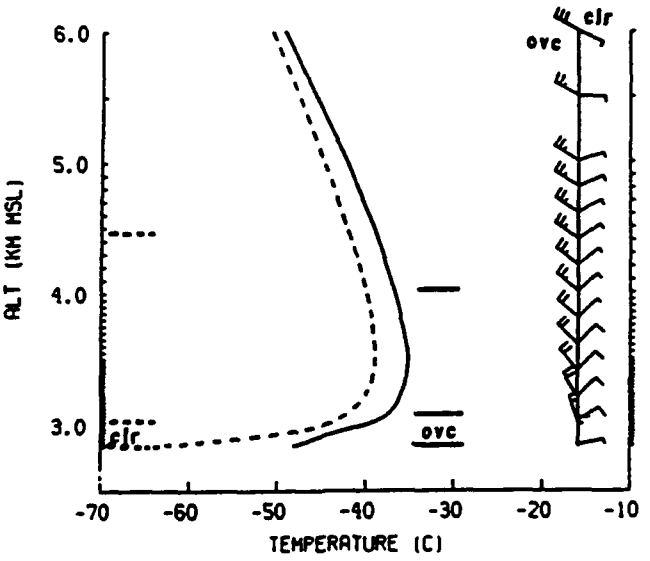


Figure 4. Composite mean temperature profiles (to 6 km altitude) at 0000 UT for 35 clear days (dashed) and 20 overcast days (solid) during the austral winter of 1986 at the South Pole. Inversion depths and the upper boundaries of the warm layer are denoted by solid and dashed horizontal lines, respectively. The mean wind profile for overcast conditions is on the near right and for clear conditions is on the far right. One full barb is equal to 5 knots.

Figure 4 is a composite of the resultant mean temperature and wind profiles for the lowest 3165 m of the SPO atmosphere for clear and overcast winter days. The relative depths of the inversions are indicated by solid horizontal lines immediately to the right of the temperature profiles and the upper boundary of the warm layers are shown as

dashed horizontal lines directly above. The wind barbs for selected levels appear on the near (overcast) and far (clear) right. The contrast in wind between clear and overcast conditions is readily apparent. The mean clear-sky wind profile shows weak northeasterly flow through the entire depth of the lower troposphere. The overcast-sky profile, however, is characterized by much stronger winds increasing and veering with height. The overcast-sky profile is thus indicative of the advection of warm, moist air from the north and northwest.

Though the depth of the inversion layer is slightly greater (in the mean) under overcast conditions, as indicated in Figure 4, its intensity is actually much weaker. Belmont [1957] introduced an index for quantifying the inversion intensity I. The temperature gradient ($\Delta T/\Delta Z$) is weighted by the difference in temperature across the inversion (ΔT). In doing so, both the slope of the lapse rate and its duration are considered. We denote the quantity I as

$$I = (\Delta T)^2/\Delta Z \qquad (1)$$

where ΔZ is the depth of the inversion. Because the inversion intensity is sensitive to the net convergence of radiation in the boundary layer as well as to the vertical and horizontal fluxes of sensible and latent heat, we suggest that it may be an appropriate indicator of changing boundary conditions related to regional-scale climate change.

The wind shear through the boundary layer $\langle s \rangle$ is another potentially useful index of climate change. Following Kahl and Samson (1988), this quantity is defined as

$$\langle s \rangle = \frac{[(\sum_{i=1}^{n-1} \Delta u_i)^2 + (\sum_{i=1}^{n-1} \Delta v_i)^2]^{1/2}}{h} \qquad (2)$$

where Δu and Δv represent the change in the u and v components of the wind between successive rawinsonde measurement levels, h is the depth of the layer, and n is the number of levels. The bulk formulation of $\langle s \rangle$ includes the effects of both speed and directional shear throughout an entire layer, not just at the upper and lower boundaries.

Turbulent mixing within the boundary layer transports sensible and latent heat into the lower levels of the atmosphere and reduces its stability. The degree of mixing is directly related to the wind shear through the boundary layer. Thus, we suggest that $\langle s \rangle$ may be used to characterize the combined effects of horizontal and vertical advection within the lower troposphere in the polar regions. If boundary conditions change because of dynamical effects, this quantity is also expected to change. Thus, a trend in $\langle s \rangle$ may also indicate a change in the regional tropospheric circulation pattern.

Table 1 gives a quantitative summary of I [Equation 1], $\langle s \rangle$ [Equation 2], and other variables that characterize the mean wintertime rawinsonde profiles at the South Pole under clear and overcast conditions. Clear conditions are characterized by intense, relatively shallow temperature inversions with low values of bulk shear. Overcast conditions, on the other hand, exhibit deeper, weaker inversions with large shear. The weakening of the inversions during cloudy periods is due to (1) warm air advection, evidenced by

Variable	Clear	Overcast
Inversion intensity I, deg^2 m^{-1}	2.4	0.5
Bulk wind shear for surface to 5-km height $\langle s \rangle$, m s^{-1} km^{-1}	3.0	5.8
Temp. difference across inversion ΔT, °C	21.4	11.3
Depth of inversion ΔZ, m	195.0	240.0
Mean temperature, °C		
-at the surface	-64.1	-48.3
-for the warm layer	-40.0	-37.8
Mean vector winds, m s^{-1}		
-at the surface	2.9 NNE	6.7 N
-for the warm layer	4.5 NE	10.9 NW

Table 1. Mean Values of Variables Characterizing Vertical Profiles of Temperature and Winds at the South Pole for Clear and Overcast Conditions, April-August 1986.

strong, veering north-northwest winds, (2) downward mixing of sensible and latent heat, indicated by a large relative value of wind shear $\langle s \rangle$, and (3) LW cloud radiative heating, discussed earlier.

Lower tropospheric temperatures respond to the combined effects of all of the above-mentioned processes, but it is not possible to ascertain the relative contribution of each individual process in the present study. Earlier studies, however, have estimated that the sensible and radiative fluxes are approximately equal in value and the latent heat flux is an order of magnitude less [e.g., Carroll, 1982]. An evaluation of the long-term rawinsonde record for the South Pole may reveal trends in the magnitudes of the inversion intensity and/or bulk wind shear, which are driven by these processes. Such an investigation would, in turn, yield valuable information about the net effects of dynamical and radiative forcing of the surface temperature in that region. If detected, such trends should then be related to changes in global circulation patterns to establish possible teleconnections between the lower and high latitudes.

SUMMARY AND CONCLUDING REMARKS

Analysis of the 1986 austral winter South Pole radiation data indicates that positive LW radiative forcing occurs when overcast conditions at the South Pole prevail. Under such conditions there is usually a convergence of net radiation near the surface, which weakens the surface-based temperature inversion. The bulk wind shear through the lower troposphere increases significantly, indicating the occurrence of more vigorous turbulent processes than exist un-

der clear skies. These mixing processes result in the vertical transport of sensible and latent heat to the surface, which further weakens the surface inversion. Horizontal warm-air advection (typically from the northern quadrant) also tends to warm the entire lower troposphere when overcast conditions prevail.

The inversion intensity I and bulk shear $\langle s \rangle$ are suggested as appropriate indices to characterize the lower troposphere under varying regional circulation patterns. As such, they may be useful indicators of climate change. Trend analyses of these suggested indices based on the historical rawinsonde record are recommended as possible means for explaining the observed cooling trend over the Antarctic Plateau as well as for detecting any periodic anomalies or long-term trends in other boundary layer properties. If detectable, such anomalies may be due to changes in the general circulation linked by teleconnections to anomalous patterns in the lower latitudes.

ACKNOWLEDGMENTS

We thank the NOAA/GMCC field personnel who maintain the South Pole Observatory and those involved in editing and processing the data used in this study. R. Stone wishes to thank Vernon Derr for his continued support. Support for J. Kahl was provided by NSF (DPP-8822472), NOAA Climate and Global Change Program, and EPRI (RP2333-07).

REFERENCES

Belmont, A. D., Lower tropospheric inversions at Ice Island T-3, *J. Atmos. Terr. Phys.*, Special Supplement (*Proceedings of the Polar Atmosphere Symposium-Part I*), 215–284, 1957.

Bodhaine, B. A., J. J. DeLuisi, and J. H. Harris, Aerosol measurements at the South Pole, *Tellus, 38B*, 223–235, 1986.

Carroll, J. J., Long-term means and short-term variability of the surface energy balance components at the South Pole, *J. Geophys. Res., 87*, 4277–4286, 1982.

Carroll, J. J., Studies of atmospheric energy transfer at the South Pole, *Ant. J. U.S., 18*, 248–249, 1983.

Cogley, J. G., and A. Henderson-Sellers, Effects of cloudiness on the high-latitude surface radiation budget, *Mon. Wea. Rev., 112*, 1017–1032, 1984.

Dutton, E. G., R. S. Stone, and J. J. DeLuisi, South Pole radiation balance measurements April 1986 to February 1988, *NOAA Data Report ERL ARL-17*, 49 pp., NOAA/ERL Air Resources Laboratory, Boulder, CO, 1989.

Dutton, E. G., R. S. Stone, D. W. Nelson, and B. G. Mendonca, Recent interannual variations in solar radiation, cloudiness, and surface temperature at the South Pole, *J. Clim.*, 1991, In press.

Elkins, J. W., and R. M. Rosson (Eds.), *Geophysical Monitoring for Climatic Change, No. 17: Summary Report 1988*, NOAA/ERL Air Resources Laboratory, Boulder, CO, 1989.

Fletcher, J. O., Polar ice and the global climate machine, *Bull. Atom. Sci.*, Dec., 40–47, 1970.

Hogan, A., S. Barnard, J. Samson, and W. Winters, The transport of heat, water vapor and particulate material to the South Polar Plateau, *J. Geophys. Res., 87*, 4287–4292, 1982.

Jones, P. D., Hemispheric surface air temperature variations: Recent trends and an update to 1987, *J. Clim., 1*, 654–660, 1988.

Kahl, J. D., Characteristics of the low-level temperature inversion along the Alaskan Arctic coast, *Int. J. Climatol., 10*, 537–548, 1990.

Kahl, J. D., and P. J. Samson, Shear effects on wind interpolation accuracy, *J. Appl. Meteorol., 27*, 1299–1301, 1988.

Ohtake, T., Atmospheric ice crystals at the South Pole in summer, *Ant. J. U.S., 13*, 174–175, 1978.

Ramanathan, V., R. D. Cess, E. F. Harrison, P. Minnis, B. R. Barkstrom, E. Ahmad, and D. Hartmann, Cloud-radiative forcing and climate: Results from the Earth Radiation Budget Experiment, *Science, 243*, 57–63, 1989.

Schlesinger, M. E., and J. F. B. Mitchell, Model projections of equilibrium climatic response to an increased carbon dioxide concentration, in Projecting the climatic effects of increasing carbon dioxide, *DOE/ER-0237*, edited by M. C. MacCracken and F. M. Luther, pp. 81–147, U.S. Dept. of Energy, Carbon Dioxide Research Div., 1985.

Schneider, G., P. Paluzzi, and J. P. Oliver, Systematic error in the synoptic sky cover record of the South Pole, *J. Clim., 2*, 295–302, 1989.

Schwerdtfeger, W., New data on the winter radiation balance at the South Pole, *Ant. J. U.S., 3*, 193–194, 1968.

Schwerdtfeger, W., *Weather and Climate of the Antarctic*, Elsevier Science, Amsterdam, 1984.

Stone, R. S., E. G. Dutton, and J. J. DeLuisi, Surface radiation and temperature variations associated with cloudiness at the South Pole, *Ant. J. U.S., 24*, 230–232, 1989.

Precipitation Trends Over Polar Ice Sheets from Atmospheric Moisture Fluxes

D. H. Bromwich
Byrd Polar Research Center, The Ohio State University, Columbus, Ohio, U.S.A.

ABSTRACT

Recent work has suggested that precipitation changes over Greenland and Antarctica may play an important role in variations of global-mean sea level. However, such changes are not easily monitored by direct observations. Gauge determinations of snowfall are strongly contaminated by wind transport of previously deposited snow. In addition, snowfall amounts at high polar elevations are often too small for confident measurement. Glaciological accumulation values are a potentially important source of precipitation data, but the requirements for broad areal coverage, the lack of annual time resolution in many regions and the uncertain impact of wind reworking are problematic.

Convergence of moisture transported by the atmosphere across the margins of ice sheets yields areally averaged ($>1 \times 10^6$ km^2) values of precipitation minus sublimation/evaporation for seasonal and longer time scales. Coastal moisture fluxes can be derived from synoptic arrays of rawinsonde stations around the margins, provided the systematic errors associated with humidity measurements are small. Thus, few departures from routine practice are needed, no field programs in ice sheet interiors are required, and large quantities of previously collected data can be used to construct past variations.

Conditions for Antarctica and Greenland are markedly different. It is shown that climatological atmospheric data sets substantially underestimate the moisture flux into Antarctica. Moisture transport convergence estimates for East Antarctica in 1972 and the whole continent for 1979 (FGGE year) strongly suggest that this approach can yield reliable precipitation estimates, and identify the probable causes of the above deficiencies. The capability exists to monitor precipitation trends over most of East Antarctica, but the data gap along the West Antarctic coast must be eliminated before continental precipitation rates can be inferred. For Greenland the situation is much better. Upper air stations ring the ice sheet at an average spacing of 660 km and have records covering the last 25 years. However, little effort has been expended to evaluate this valuable data set.

On the kelationship Between Antarctic Katabatic Winds and Large-Scale Tropospheric Circulations

T. R. Parish
Department of Atmospheric Science, University of Wyoming, Laramie, Wyoming, U.S.A.

ABSTRACT

Gravity-driven katabatic winds occur with regularity over the Antarctic ice fields in the lowest few hundred meters of the atmosphere. The strongest katabatic winds are generally associated with the steep coastal periphery. Along various near-coastal sections of Antarctica, cold air drainage currents from the interior of the continent converge and provide an enhanced source of cold air available to feed katabatic winds. Such "confluence zones" are responsible for anomalously intense katabatic wind regimes near Adélie Land and Terra Nova Bay.

The persistent drainage of cold air off the elevated Antarctic ice dome requires upper level convergence of warmer air from lower latitudes and subsidence throughout much of the troposphere. This meridional mass exchange generates cyclonic vorticity over the continent which, coupled with the horizontal temperature gradient in the lower atmosphere, results in the development of the large-scale circumpolar vortex in the troposphere above Antarctica and the high southern latitudes.

Numerical simulations of the establishment of the circumpolar vortex have been conducted using a three-dimensional primitive equation model. Results clearly show that the katabatic wind regime is critical in the development of the tropospheric circulations. Model simulations suggest that the evolution and the positioning of the large-scale tropospheric circulations require accurate representation of the Antarctic katabatic windfield.

AD-P007 286

Plateau Weather:
A Synoptic Study of IAGO and ANARE AWS Observations in East Antarctica

Uwe Radok
CIRES, University of Colorado, Boulder, Colorado, U.S.A.

Gerd Wendler
Geophysical Institute, University of Alaska Fairbanks, Fairbanks, Alaska, U.S.A.

92-17968

ABSTRACT

Automatic weather stations (AWS) have been operated for a number of years by U.S. and French scientists cooperating in Project Interactions Atmosphere, Glace, Ocean (IAGO) and by the Australian National Antarctic Research Expeditions (ANARE). Six of these stations are sufficiently close to one another on the East Antarctic Plateau for a synoptic interpretation of their observations. The data for 1987 have been reduced to a common format in order to identify episodes of regionally coherent changes. One of these episodes is described and used to outline steps that will be needed for clarifying the relative importance of the local energy balance and the large-scale circulation for the onset, duration, and cessation of katabatic winds on the plateau.

INTRODUCTION

The early explorers found plateau weather to be trying; Shackleton spoke of "this cutting south wind with drift" (diary entry for 1 January 1909). More detailed views developed from the extended occupation of inland stations during the IGY. While their distances ruled out convincing synoptic interpretations of their observations, these added up to a first climatology of the ice sheet region. Its outstanding features are the "coreless" winters and the high directional constancy of the surface flow over the sloping parts of the ice sheet. On the Antarctic plateau, where the controlling gradients (produced by the surface slope and the large-scale pressure field) are more evenly balanced, a wider range of wind directions is observed [e.g., Dalrymple et al., 1966]. The changes in pressure gradients and cloudiness associated with the Antarctic weather systems imply changing rates of heat transfers from the atmosphere to the ice sheet surface [Carroll and Fitzjarrald, 1979; Neff, 1981]. In this way the plateau weather is linked to the Antarctic and southern hemisphere circulations which in their turn respond to regional forcing by the state of the southern sea ice [Budd and Simmonds, *this volume*], a global characteristic. Thus a study of meteorological events on the Antarctic plateau (where the modelers predict enhanced greenhouse effects) can contribute to a better understanding of the role of the polar regions in global change.

The means for a detailed study of plateau weather have been provided for the first time by a network of automatic weather stations (AWS) reporting at close time intervals via satellites. They were established by U.S. and French scientists cooperating in Project IAGO (Interaction Atmosphere, Glace, Ocean) [Wendler et al., 1986], and by the Australian National Antarctic Research Expeditions (ANARE) [Allison and Morrissy, 1983]. Figure 1 shows the locations of the AWS used for this study; the geographical coordinates and altitudes are listed in Table 1. Magnetic tapes with the complete data for 1987 were used to establish a common format and to display the data in different combinations on several time scales. These displays showed up associated changes in the four climatic elements recorded by the AWS (surface pressure, temperature, wind speed, and wind direction) at individual locations and the relative timing of changes at the different AWS. The transitional month of March 1987, expected to contain both circulation-controlled and energy-balance-controlled episodes, was chosen to illustrate this exploratory work.

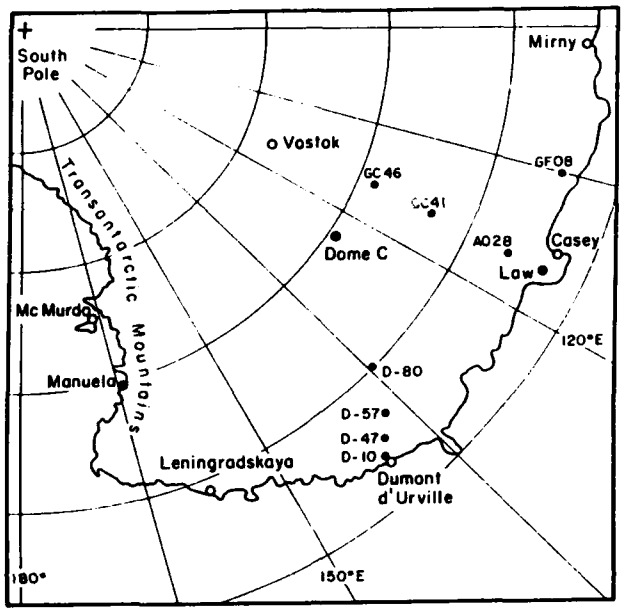


Figure 1. The AWS network on the East Antarctic plateau.

	Lat.	Long.	Alt. (m)
Australian Stations			
LAW	66°44'S	112°45'E	1370
A028	68°24'S	112°10'E	1630
GF08	68°30'S	102°11'E	2118
GC41	71°36'S	111°15'E	2740
GC46	74°08'S	109°50'E	3070
U.S. Stations			
D10	66°42'S	139°48'E	240
D47	67°23'S	138°43'E	1560
D57	68°11'S	137°31'E	2105
D80	70°01'S	134°43'E	2500
DOME C	74°30'S	123°00'E	3280

Table 1. Details of automatic weather stations (AWS) on the East Antarctic Plateau.

AWS	Pressure Rise (time and date, GMT)		Temperature Rise (time and date, GMT)	
D10	13	3/16/87	no signal	
D47	15		20.5	3/15/87
D57	17		20.5	
D80	20		21	
DOME C	no clear signal			
LAW	8	3/17/87	no signal	
A028	9		22	3/15/87
GC41	12		23	
GF08	20		12	3/16/87

Table 2. Onset times of pressure and temperature rises at plateau AWS, 15-17 March 1987.

LOCAL CHANGES IN WEATHER ELEMENTS

A visual examination of the different AWS records for March 1987 (cf. Figure 2) revealed a large measure of regional coherence, with similar events but slightly different timing. The main episodes can therefore be described with a single record. Figure 3 shows temperature,wind speed, and pressure curves for AWS 41. The month started with a gradual cooling, followed by marked rises in temperature and pressure around the middle of the month. There is a suggestion of katabatic flow developing around 6 March, not long after the onset of cooling, and of a more pronounced wind pulse during the sharp cooling from 17 to 20 March; in both cases the accelerated flow did not strengthen with further cooling but instead appeared to respond to pressure changes.

The significance of such local associations between different elements will become clearer as a number of similar episodes are analyzed. As a first step a statistical analysis was undertaken, with all AWS data for March and April 1987, to determine any tendency for peaks, troughs, rises, and falls, in pressure and wind speed to be associated. There was some suggestion that pressure troughs (ridges) were associated with wind speed peaks (troughs), but this tendency proved not to be statistically significant on a chi square test.

As another statistical characteristic, correlation coefficients between the surface pressures and temperatures of March 1987 were calculated for each AWS. This eliminated the effects of altitude, the dominant factor for both pressure and surface temperature. With the exception of that for Dome C (+0.11), all the correlations were negative and decreased in absolute magnitude from about -0.4 near the coast to -0.1 on the plateau. The negative signs presumably reflect the greater cloudiness associated with pressure troughs, and the inland decrease in magnitudes the diminishing influence of the Southern Ocean weather systems.

INTER-STATION COMPARISONS

In order to compare the detailed course and timing of events at different AWS the data were displayed on a much larger time scale than that used for Figure 3. This made it possible to narrow down the beginnings of a marked inland warming and a substantial rise in all surface pressures which took place between March 15–18. From the onset times in Table 2 it can be seen that the pressure rise started at the coast (AWS D10) and spread inland along the IAGO line, reaching AWS D80 7 hours later; no distinct signal was reported from Dome C. The pressure rises further west were delayed by 17 to 19 hours and again started at the coast (AWS Law); a further delay of 8 hours occurred before the pressure started rising even further west at AWS GF08.

Much smaller intervals ensued between the onsets of strong warming at the higher AWS; on Dome C the temperature rise was interrupted after 10 hours, indicating perhaps a different event, but the subsequent cooling started almost simultaneously at all these stations. The AWS nearer the coast experienced no distinct changes in temperature. By contrast, wind speeds increased temporarily at the sites nearer the coast only, shortly after the onset of the inland warming. Wind directions remained unchanged except on Dome C where a steady backing from 225° on March 15 through 0° to 270° on March 19 was recorded, again pointing to a separate event.

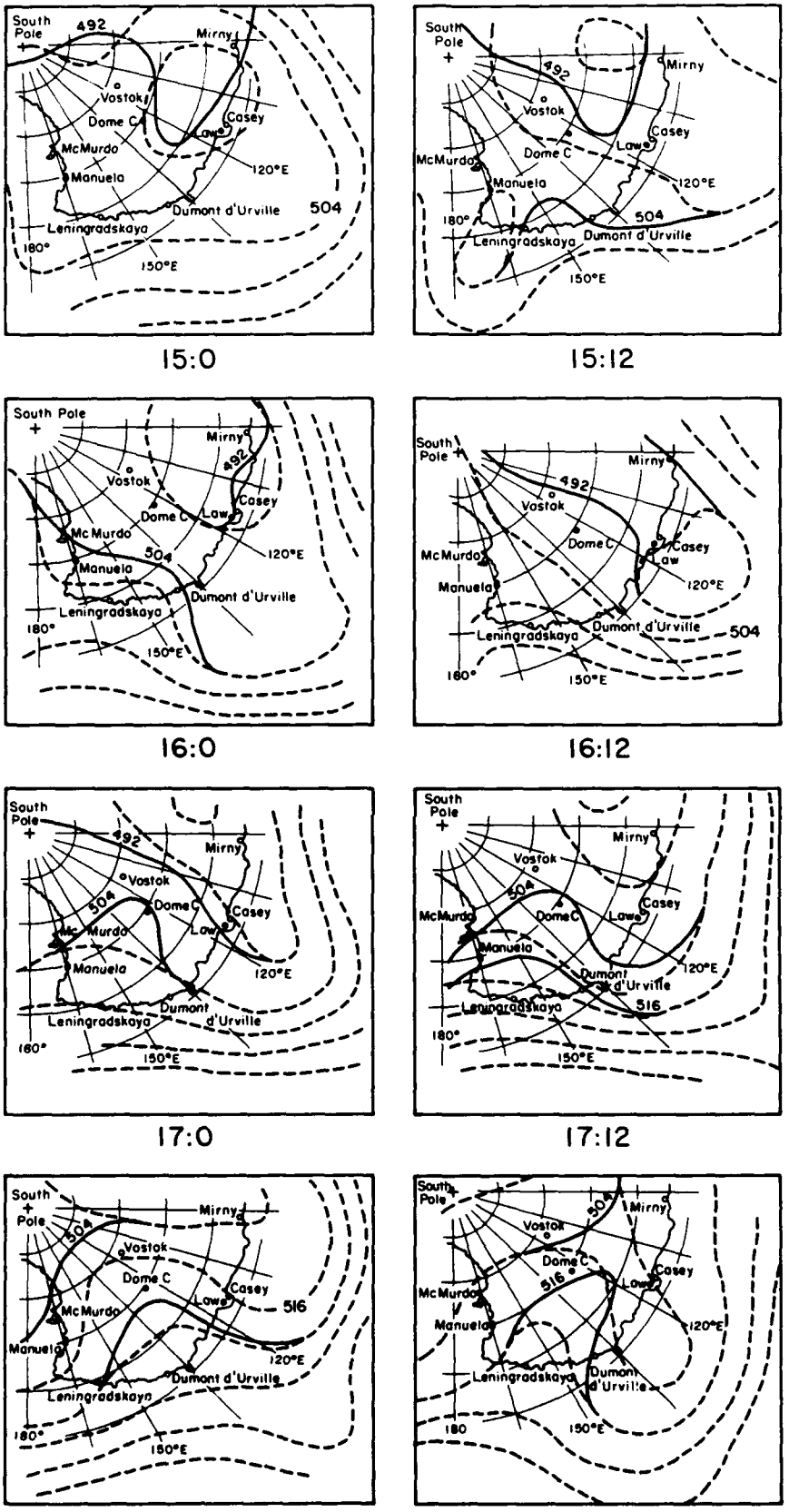


Figure 2. AWS records for March 1987.

DISCUSSION

The concept of westward-moving pressure pulses like that described in the preceding section has a long Antarctic history. They were first proposed by Simpson [1919] and thoroughly investigated by Loewe [1935, 1945, 1967] who demonstrated that the pressures observed at Cape Evans (Ross Island) during June 1912 were closely repeated 13.5 hours later at Cape Denison, 120 km east of Dumont d'Urville. No such agreement was obtained here by comparing the March 1987 pressures recorded on Inexpressible Island (AWS Manuela) and 15 hours later at Dumont d'Urville (AWS D10). The correlation between these two series, with D10 pressure trailing Manuela by various intervals, remained around 0.3; however, it increased to 0.67 for Manuela lagging 2.5 days behind D10.

A more extensive set of AWS data will be used for a further test of Simpson and Loewe's hypothesis. An alternative synoptic explanation of such pressure pulses [Ramage, 1944] calls for closely spaced weather charts, but the common practice of extending the sea level charts over the ice sheet is unacceptable in this context. Instead the height contours of a constant pressure surface not intersecting the ice sheet (e.g., 500 hPa) need to be constructed. Ball [1960] has shown how pressure gradients and surface slopes combine to determine the direction of the total force acting on the surface air. Ball's equation was

$$\frac{\nabla p}{\rho} = \frac{\nabla P}{\rho} + g\frac{\theta'}{\theta}\nabla E \qquad (1)$$

where ∇p and ∇P are the pressure gradients in the surface layer and in the free atmosphere, respectively, ρ is the air density, g is the gravity acceleration, $\theta' = \theta_1 - \theta$ is the difference between the potential temperatures θ_1 above the inversion and θ in the layer, and E is the surface elevation. For use on the plateau the pressure gradients in (1) can be replaced by constant pressure surface slopes to render (1) independent of altitude:

$$g\nabla z' = g\nabla_p z_{500} + g\frac{\theta'}{\theta}\nabla E \qquad (1')$$

The right hand side of (1') defines the slope of a composite constant surface pressure height field z'. On the plateau in winter the ratio θ'/θ is of order 0.1, and the construction of the z' field can then be effected, in analogy to Ball's procedure, by graphically adding the 500 hPa height contours in dekameters to the surface elevation contours spaced 100 m apart. Division of (1') by the Coriolis parameter f gives the direction and magnitude of the force acting on the surface air in the form of a composite geostrophic wind,

$$V_{g_s} = V_{g_{500}} + V_{g_E} \qquad (2)$$

The actual surface wind depends not only on the assumed friction and boundary layer thickness [Ball, 1960] but also on other factors such as the mass and evaporation of blowing snow [Gosink, 1989].

Routine 500 hPa charts over the East Antarctic ice sheet lack details, due to the sparse network of radiosonde stations. It would be useful if the AWS data could fill some of the observational gaps. Phillpot [to be published] has analyzed radiosonde results for several stations on the ice sheet and established statistically significant linear relationships between the surface temperatures of stations not too far below the 500 hPa level and the temperature adjustments Δz_i to the thickness of the layers between the station level

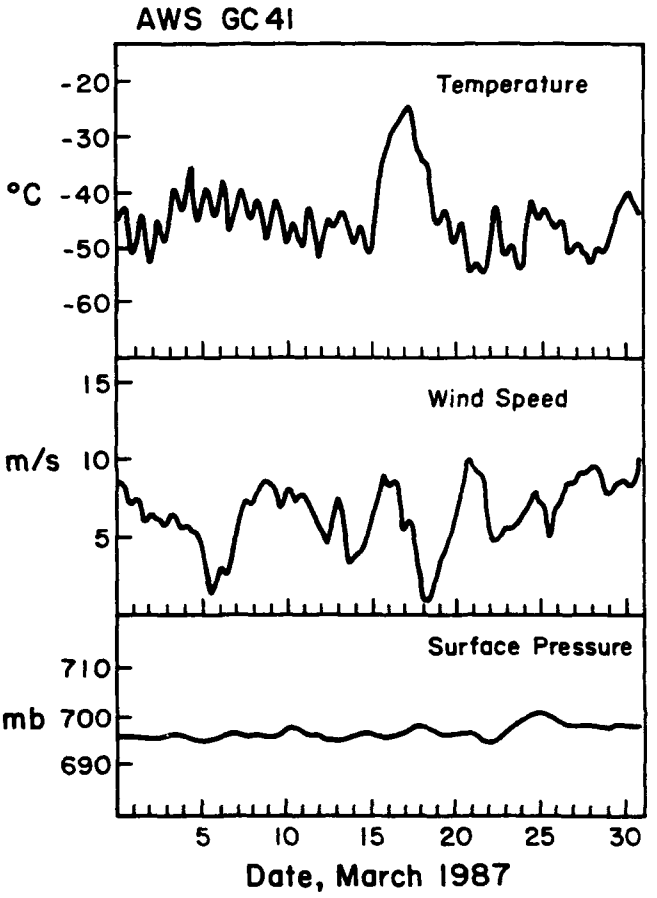


Figure 3. Temperature, wind speed, and pressure changes at AWS 41, March 1987.

AWS	Elevation (dekameters)	$\Delta Z_{t_S} = c \times t_S - m$ (pot. dekameters)
D57	211	$\Delta Z_{t_S} = 0.43t_S - 22.50$
D80	251	$\Delta Z_{t_S} = 0.36t_S - 20.50$
DOME C	328	$\Delta Z_{t_S} = 0.25t_S - 16.50$
08	213	$\Delta Z_{t_S} = 0.42t_S - 22.50$
41	275	$\Delta Z_{t_S} = 0.33t_S - 19.30$
SOUTH P.	284	$\Delta Z_{t_S} = 0.27t_S - 21.60$

Table 3. Regression equations for the thickness correction required for the departure of the mean layer temperature from 0°C [Phillpott, to be published].

and the height of the 500 hPa surface. Phillpot's regression equations for the AWS on the East Antarctic plateau were then found by interpolation and are reproduced in Table 3 for the stations here used.

The physical basis for these relationships is that the thickness adjustment follows from the hydrostatic equation,

$$\Delta z_{500\text{-}p_s} = \frac{273}{g/R} \ln \frac{p_s}{500} + \frac{\bar{t}}{g/R} \ln \frac{p_s}{500} \qquad (3)$$

where p_s is the surface pressure and $\bar{t}$ is the mean temperature of the layer between the surface and the 500 hPa level. That mean temperature can be defined in terms of the surface temperature, t_s, and an average lapse rate γ over the layer as $\bar{t} = \frac{1}{2}(t_s + (t_s - \gamma\Delta z))$. Then (3) takes the form

$$\Delta z = (273 + t_s) \frac{\ln \frac{p_s}{500}}{\frac{g}{R} + \frac{\gamma}{2} \ln \frac{p_s}{500}} \qquad (4)$$

The factor $g/R = 0.034$ °/m is the "autoconvective" lapse rate of a constant-density atmosphere and an order of magnitude larger than the average layer lapse rate γ which can be positive or negative and increases in absolute magnitude with decreasing surface elevation (increasing surface pressure). The denominator in (4) therefore is the sum of two roughly equal terms one of which can be positive or negative. That accounts for the substantial differences between the regression coefficients in Table 3.

A more stable relationship that could apply even for lower surface elevations follows from (3) for the mean temperature of the layer between the AWS level and the 500 hPa surface, viz.

$$(273 + \bar{t}) = \frac{\frac{g}{R}}{\ln \frac{p_s}{500}} \Delta z = (273 + t_s) \left[1 + \frac{\gamma}{2\frac{g}{R}} \ln \frac{p_s}{500} \right]^{-1} \qquad (5)$$

Here the factor $\ln \frac{p_s}{500}$ has been eliminated except in the denominator where it is multiplied by a small quantity of order 0.05 or less. This suggests that a single regression line of the layer mean temperature on surface temperature could be valid for a considerable height range. A preliminary form of such a regression line, computed with Phillpot's thickness estimates for 4 AWS sites, is shown in Figure 4. Its location for the highest surface temperatures was fixed by means of directly observed 500 hPa heights at Casey coupled with the surface pressures and temperatures observed at AWS Law, and with those at Dumont d'Urville and AWS D10. The mean temperature estimates for South Pole were added subsequently to test the validity of the regression line at low surface temperatures. The large scatter of the Law Dome values reflects the fact that layer mean temperature errors are magnified in the calculated layer thickness by a factor $\Delta z_0/273$, where Δz_0 is the layer thickness for a mean temperature of 0°C. This underlines Phillpot's point that the surface temperature regressions cannot be used for low-level AWS.

The relationship in Figure 4 remains to be more firmly defined directly with observed 500 hPa heights and surface observations. It was used here to estimate 500 hPa heights from all the AWS surface pressures and temperatures for the period 14 through 19 March 1987. The 500 hPa analyses issued by the Australian Bureau of Meteorology for this period are shown as broken lines in Figure 5, while adjustments suggested by the AWS estimates are indicated by solid lines. Although preliminary, pending firmer estimates of the AWS 500 hPa heights, Figure 5 suggests that the pressure pulse during this period arose when a ridge east of the AWS area strengthened and expanded in a southwesterly direction.

The warming pulse that occurred a little earlier could have arisen from intensified northerly flow in the tightening gradient west of the ridge. A possible alternative or contributing factor would have been increased cloudiness. Stone and Kahl [*this volume*] have reported changes in downward infrared radiation at the South Pole due to variations in cloudiness which accounted for appreciable surface temperature changes. For the case here considered, imagery of the Defense Meteorological Satellite Program (DMSP) available in WDC-A Glaciology (Snow and Ice) showed no substantial change in cloud cover was responsible for the warming of March 1987.

Finally, the wind speed changes during the period considered resulted from a combination of circulation and energy balance changes. An intensified analysis of AWS observations from the Antarctic plateau will aim to clarify the detailed interaction of these major factors controlling plateau weather.

ACKNOWLEDGMENTS

We are indebted to Drs. Charles Stearns (University of Wisconsin-Madison) and Ian Allison (Australian Antarctic Division) for the AWS data here used; to Mrs. Yuqi Zhoa (University of Alaska Fairbanks) for varied displays; to Linda Keller (Wisconsin) for numerical printouts of detailed IAGO data; to Rob Bauer (WDC-A, Boulder) for the extraction of DMSP images; and to Tim Brown (University of Colorado) for various statistical calculations. All this help is gratefully acknowledged. In addition, suggestions by Ian Allison and an anonymous reviewer have helped to improve this paper.

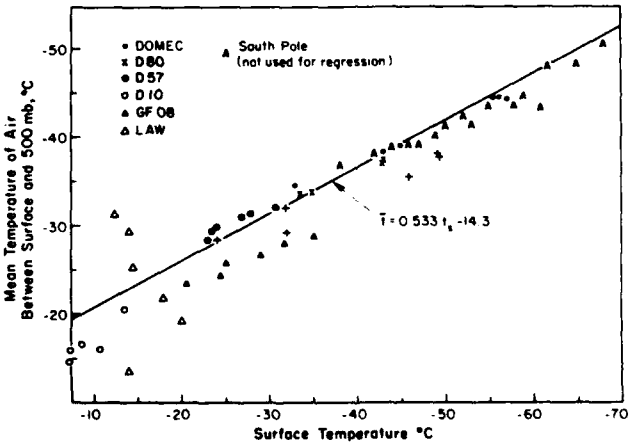


Figure 4. Regression of surface-500 hPa layer mean temperature on surface temperature. For details see text.

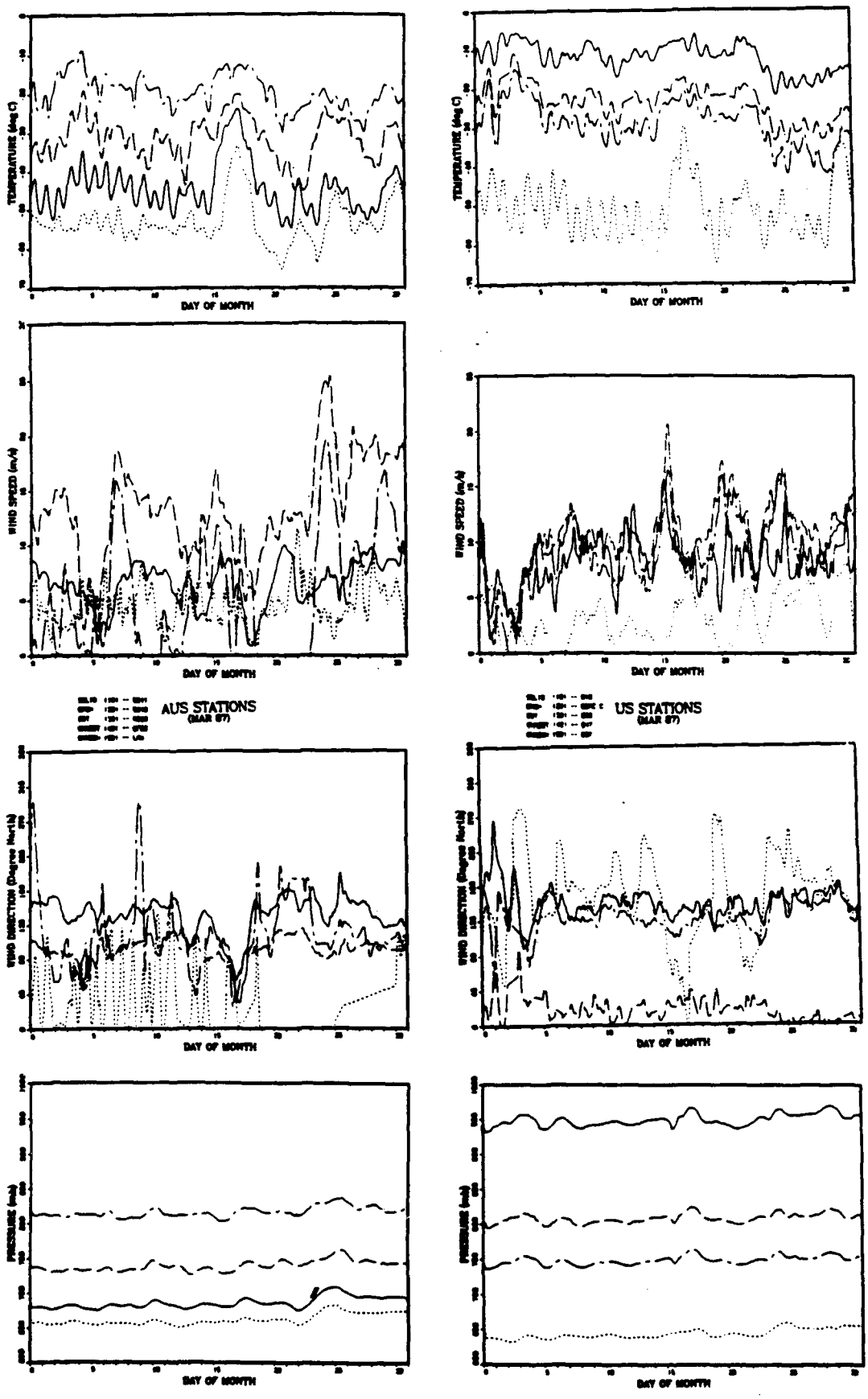


Figure 5. 500 hPa countours (pot. dekameters) of the Australian Bureau of Meteorology analyses (broken lines), and adjustments (full lines) suggested by the AWS observations.

REFERENCES

Allison, I., and J. V. Morrissy, Automatic weather stations in the Antarctic, *Austr. Meteor. Magazine*, *31*, 71–76, 1983.

Ball, F. K., Winds on the ice slopes of Antarctica, in *Antarctic Meteorology*, edited by Director of Meteorology, pp. 9–16, Pergamon, 1960.

Budd, W. F., and I. Simmonds, The impact of global warming on the Antarctic mass balance and global sea level, *This volume*, 1991.

Carroll, J. J., and D. E. Fitzjarrald, Atmosphere–surface interactions in the unsteady stable planetary boundary layer, presented at Symposium on Antarctic Meteorology, International Commission for Polar Meteorology, Canberra, December, 1979.

Dalrymple, P. C., H. H. Lettau, and S. W. Wollaston, South Pole micrometeorology program: Data analysis, in Studies in Antarctic Meteorology, edited by M. J.Rubin, *Antarctic Research Series 9*, 13–57, American Geophysical Union, 1966.

Gosink, J. P., The extension of density current model of katabatic winds to include the effects of blowing snow and sublimation, *Boundary-Layer Meteorology*, *49*, 367–394, 1989.

Loewe, F., Pressure waves in Adelie Land, *Quart. J. R. Meteor. Soc.*, *61*, 441–445, 1935.

Loewe, F., A further note on Antarctic pressure waves, *Quart. J. R. Meteor. Soc.*, *71*, 344–350, 1945.

Loewe, F., On Antarctic pressure variations, *Quart. J. R. Meteor. Soc.*, *93*, 373–381, 1967.

Neff, W. D., An observational and numerical study of the atmospheric boundary layer overlying the East Antarctic ice sheet, *NOAA Tech. Mem. ERL WPL-67*, 1981.

Phillpot, H. R., The derivation of 500 hPa contour heights from automatic weather station surface observations in the Antarctic continental interior. Department of Meteorology, University of Melbourne, to be published.

Ramage, C. S., The atmospheric circulation of the Ross Sea area, *New Zealand Met. Office Prof. Note #2*, 1944.

Simpson, G. C., British Antarctic (Terra Nova) Expedition, 1910–1913, *Meteorology*, *1*, 208, 1919.

Stone, R. S., and J. D. Kahl, Cloud radiative effects and associated changes in tropospheric temperatures and winds at the South Pole during austral winter, *This volume*, 1991.

Wendler, G., Y. Kodama, and J. P. Gosink, Automatic weather stations in East Antarctica, *Antarctic J. U.S.*, *19*, 212–213, 1986.

On the Effect of Global Warming on the Snowmelt in an Arctic Permafrost Area

K. Kodama, D. Kobayashi, N. Ishikawa and G. Wakahama
Institute of Low Temperature Science, Hokkaido University, Sapporo, Japan

ABSTRACT

Seasonal snow cover is an important factor for the global heat balance and determines the overall albedo of the earth. Snow has a high albedo of 0.8–0.9, while bare ground has an albedo of about 0.2–0.3. The shift of the date of melting of the seasonal snow cover by global warming would drastically change the global heat balance. In other words, the date of disappearance of the snow is one of the major potential feedbacks in global climatic change. In this paper, the details of the energy balance over the snow in the arctic tundra is studied and, assuming a simple global warming, the expected change in the heat balance is discussed.

The energy balance observations were made at Imnavait Creek on the North Slope of Alaska. This watershed lies over the continuous permafrost. The net radiation is obtained by a net radiometer. The sensible heat flux, latent heat flux and heat flux in snow are calculated from meteorological and glaciological data.

The result of energy balance calculations showed that the most important component for snowmelt is net radiation. Since the global radiation over cloud and fog and the melting snow surface temperature are almost constant, the net radiation is mainly dependent on cloudiness, albedo of snow and atmospheric radiation. An increase of cloudiness due to global warming would suppress snowmelt, while a decrease in snow albedo and an increase in atmospheric radiation due to global warming would enhance snowmelt.

AD-P007 287

Impacts of Projected Global Warming: A Research Proposal for the Mackenzie Basin

S. J. Cohen and J. B. Maxwell
Canadian Climate Centre, Atmospheric Environment Service, Downsview, Ontario, Canada

ABSTRACT

As part of the Government of Canada's "Green Plan," an assessment of the impacts of global warming scenarios in the Mackenzie Basin is being initiated by the Canadian Climate Centre (CCC). These scenarios include outputs from General Circulation Models, such as the new one produced by CCC, as well as arbitrary and other climate scenarios where possible. Hydrology, permafrost and other first-order physical impacts will be investigated. These will be linked to second-order biological studies describing impacts on vegetation, fire potential, terrestrial and freshwater wildlife. Third-order socioeconomic studies will consider activities of the native and non-native communities in the region, including energy, transportation, tourism and subsistence. An additional set of "integration" tasks will also be undertaken.

Some of these and other issues will not easily lend themselves to quantitative investigation. Our ability to address these challenges will depend on the quality of researchers that would be willing to participate in this exercise. A multidisciplinary team is being established, utilizing the expertise and cooperation of many government and non-government entities with long-term interests in the Mackenzie. Information from ongoing programs will be combined with commissioned research. Most of the study tasks should begin during 1991, with the main study report due in 1996.

INTRODUCTION

Atmospheric concentrations of CO_2 have increased by more than 25% since the Industrial Revolution began in the 19th century. Concentrations of other greenhouse gases (e.g., CH_4) have also increased. Experiments with atmospheric General Circulation Models (GCM) indicate that if these concentrations were to increase to the radiative equivalent of a doubling of CO_2 (i.e., $2xCO_2$), the so-called greenhouse effect would strengthen and global climate would experience unprecedented warming [WMO, 1986, 1988; Jaeger, 1988]. In high latitude regions, projected winter warming is expected to be more than double the global average temperature change [Jaeger, 1988].

One of those high latitude regions is the Mackenzie Basin, a large watershed in Canada which drains into the Arctic Ocean (Figure 1). A wide range of terrain features are found here, including discontinuous and continuous permafrost, forest and tundra zones, the Mackenzie Delta and other important wildlife habitats, and major sources of freshwater. Some important natural boundaries cross the basin (e.g., permafrost, treeline). Most of the Northwest Territories' native and non-native population live and work here, and global warming would certainly affect their activities, and possibly their lifestyles. In addition, since the Mackenzie Delta's coastline is already submerging [Egginton and Andrews, 1989], attention will have to be given to potential impacts of sea level rise.

From the above, one can appreciate that global warming could lead to significant impacts on the natural environment of the Mackenzie Basin [e.g., French, 1986; Marsh and Hey, 1989; Maxwell and Barrie, 1989; Mysak, 1989], but what about the socioeconomic impacts? These do not lend them-

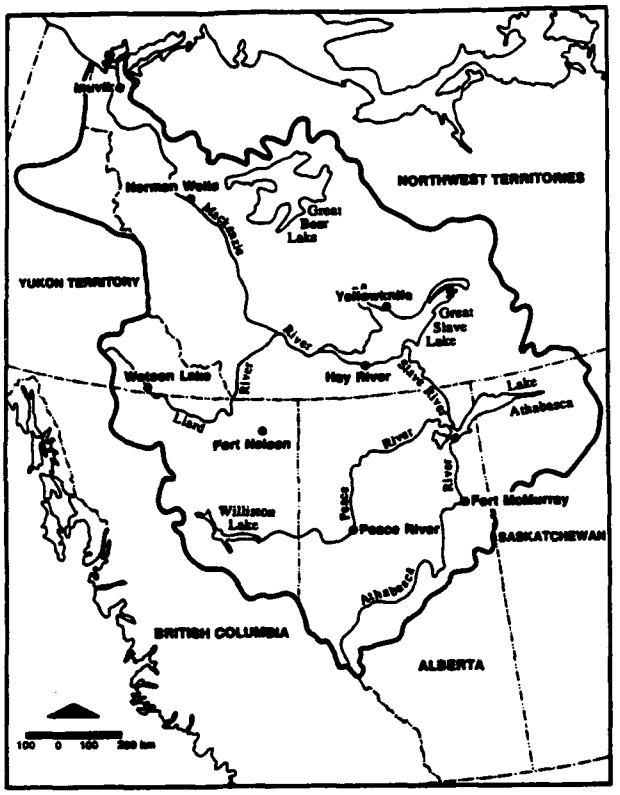


Figure 1. Mackenzie Basin, Canada.

selves to easy description, since many other factors are involved. Societal changes have been taking place throughout the world in recent decades. The Canadian Arctic has experienced substantial changes brought on by the resource and strategic interests of other regions of Canada and elsewhere. These include temporary booms associated with the fur trade, gold rush, World War II, and now, fossil fuel exploration and extraction [Pretes, 1988], and the long-term presence of non-native government in social and economic programs, which have generated mixed reactions from the various interests involved [e.g., Young and McDermott, 1988; Irwin, 1989; Malone, 1989; TFN, 1989].

The purpose of this paper is to describe a proposed multiyear multidisciplinary study program, focusing on describing the impacts of present climatic variability and scenarios of global warming on the physical and human environments of the Mackenzie Basin. Given its physical features, geographical setting and human history, the Basin could serve as a model for the study of regional impacts of global warming on high latitude and remote regions.

BACKGROUND

Applications of Global Warming Scenarios

GCMs can simulate global scale patterns of climate, but many uncertainties exist regarding clouds and ocean feedbacks [Mitchell, 1989], changes in variability of climatic parameters [Mearns, 1989] and projections of regional scale climate [e.g., Grotch, 1988]. For studies on the impacts of global warming "scenarios," we assume some confidence in the ability of GCMs to be sensitive to changes in forcing factors (e.g., atmospheric trace gas concentrations) and to project global scale changes of temperature and other "basic" parameters, but there is a preference to use station observations as the baseline until GCMs show greater reliability. Thus, the global warming "scenario" is a composite of the GCM-projected anomaly "added" to a "normal" obtained from station observations [Cohen, 1990].

Uncertainties associated with GCM results must be reflected in uncertainty in impact study results, particularly in their ability to project regional scale changes. One example is the wide variation between GCMs of projected changes in sea ice [e.g., Washington and Meehl, 1984, 1989; Wilson and Mitchell, 1987]. It is preferable that more than one GCM be used for impacts studies, since their regional scale climatic projections can differ from each other, and so can estimates of their resulting impacts [e.g., Cohen et al., 1989; Météoglobe, 1989].

Compared to the 1951–1980 "normal" climate, most GCM-based scenarios indicate higher temperature and precipitation for all seasons in the study area, though the magnitude of these changes varies. For example, winter temperature increases indicated by several GCMs' outputs range from 5–10°C. New GCM outputs are being produced and their scenarios may be different from those used in previous studies.

Regional Impacts Linkages

A wide range of possible Arctic impacts have been described by Maxwell and Barrie [1989]. This information has been used to produce a simplified framework for an integrated assessment of climate change impacts in the Canadian Arctic. Figure 2 shows some of the major linkages between climate and the region's physical and human environments. Key elements that are sensitive to climatic variation are sea ice, hydrological parameters, snow cover and soil temperature. Changes in these elements, combined with changes in basic climatic parameters (e.g., air temperature) would lead to impacts on temporal and spatial patterns of vegetation and wildlife, with subsequent impacts on the economic sectors that depend on them. Changes in permafrost distribution would have important implications for

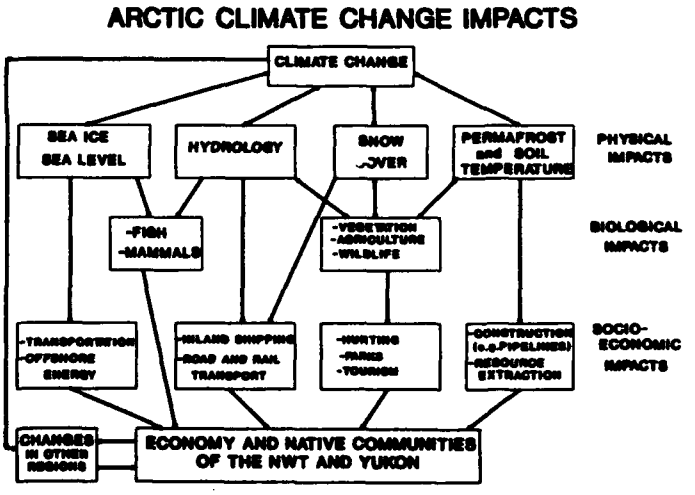


Figure 2. Generalized framework for Arctic impacts research.

construction and hydrological processes. In addition, we must not forget that the region's ecology and economy are strongly influenced by events that occur elsewhere. Examples include waterfowl migration, the price of oil and other exploitable resources, and technological change in other cold regions, all of which may be affected in some way by global warming.

The bottom of the figure also includes native communities within the same box as the economy, which is generally dominated by non-natives. However, the reality of future impacts will certainly be a more complex series of interactions within and between both communities as they adjust to changes in the physical and biological environment. The investigation of the specific nature of these impacts, and their subsequent effects on how the communities relate to each other, will be major research challenges.

If this exercise is to achieve its "mission" of bringing the global warming issue down to the regional scale [Cohen, 1990], then it must meet the challenge of monitoring and modeling (sometimes qualitatively) physical, biological and human processes in a large region with few observing sites and sparse data records. The human infrastructure is rapidly changing in response to global technological and economic trends, political events, and decisions made outside the region. What difference would global warming make?

In the near term, one possible approach would be for impact studies to include scenarios of climate and other changes (e.g., population), so that the sensitivity of the region could be investigated. As our knowledge improves and the ranges of global warming scenarios begin to narrow, future research efforts will benefit from the experiences gained during this early phase.

OUTLINE FOR PROPOSED IMPACTS STUDY

Purpose

The main purpose of this study is to describe the impacts of past variability and scenarios of future global warming on the Mackenzie Basin. This should be done quantitatively where possible, and should be broad enough to include all major elements of the physical and human environments of the region that are climate sensitive.

Certain questions will not easily lend themselves to quantitative investigation, nor are quantitative methods necessarily the most appropriate in all instances. This should not deter us from our goal of providing a sound and useful analysis of regional impacts.

Choice of Global Warming Scenarios

At the outset, it is important to provide clear guidance on the development and application of global warming scenarios, as well as providing a list of scenarios that all individual studies shall address. This will enable the individual study results to be merged into a more integrated regional study, since all components will have considered the same assumed climatic conditions.

It is expected that 3–5 climatic change scenarios will be used in this project. At least two will originate from GCM simulations of a new "equilibrium" climate for an atmosphere with double the pre-industrial concentrations of CO_2 (i.e., $2xCO_2$), one of which will be the Canadian Climate Centre (CCC) GCM [Boer et al., forthcoming]. Others being considered include (a) a historically based scenario from the instrumental record, (b) a paleoclimate-based scenario, based on the Climatic Optimum, circa 4000–5000 years B.P. (if data are available), and (c) arbitrary cases of 2°C and 4°C warming, with -20%, 0%, +20% precipitation change.

The assumed baseline will be the 1951–1980 average. Whether or not the baseline and scenario outputs should be interpolated onto a regular grid is an important technical matter which should be resolved during the early planning phase of this study.

Sea level rise is assumed to be 1.0 m for the $2xCO_2$ scenarios.

Objectives and Products

Objective 1 - Physical Impacts. First-order physical impacts of global warming scenarios will be determined on the following:

- freshwater resources, including streamflow, ice and snow;
- land resources, including permafrost and capability for agriculture; and
- sea ice in the Beaufort Sea.

The freshwater task will include the application of scenarios of projected warming to existing subbasin models (e.g., Peace River) and/or basin models. Surface and remotely sensed data will be used to provide information on sensitivities of lake ice and other parameters to past climatic variability. Observations during recent warm years may represent useful "analogues" of physical impacts of future warm conditions. Linkage with the Global Energy and Water Cycle Experiment or GEWEX [WCRP, 1988] is being investigated.

Objective 2 - Biological Impacts. The purpose is to describe second-order biological impacts of global warming scenarios. A number of activities are planned within two main areas:

- terrestrial ecosystems, including forests (growth, species changes, fire) and wildlife; and
- freshwater ecosystems.

In much of the above, explicit assumptions will have to be made regarding changes in regions outside the Mackenzie Basin, since these changes could also be important (e.g., wildlife migration). It may be appropriate to specify scenarios of exogenous changes that may be relevant to the tasks above. Feedback effects of third-order changes (see below) may also be important.

Objective 3 - Socioeconomic Impacts. Third-order socioeconomic impacts of global warming scenarios would be described. Physical and biological impacts data would be obtained from the results of Objectives 1 and 2. Research would focus on seven areas:

- energy and mineral production;
- transportation and infrastructure;
- settlements, including subsistence activities (e.g., hunting);
- agriculture potential;
- parks/tourism;
- forest industry; and
- defense.

The energy and transportation tasks could build on the efforts of the recently completed study by a team from McMaster University [Lonergan et al., forthcoming].

Objective 4 - Regional Impacts. The purpose is to integrate the results of the individual studies from Objectives 1–3 and produce a picture of the region as a whole. Several activities will be pursued, including a regional economic analysis and an assessment of potential land use conflicts arising from projected changes in land capability.

PROPOSED STUDY ORGANIZATION AND SCHEDULE

Participants

A number of federal and provincial/territorial agencies have agreed to participate. In October, 1990, an Interagency Working Committee (WC) was formed to assist in planning, coordination, review and publication of results. As of April, 1991, WC members include:

- Canadian government agencies (Environment, Energy Mines & Resources, Indian and Northern Affairs, Forestry, Agriculture, Tourism, Fisheries and Oceans);
- provincial/territorial agencies from Alberta (Environment), British Columbia (BChydro), Northwest Territories (Renewable Resources, Energy Mines & Petroleum Resources), and Yukon Territory (Renewable Resources);
- native organizations (Dene, Metis, Inuvialuit, Indian Association of Alberta); and
- private industry (ESSO Resources Ltd.).

Schedule

This project will extend over a five-year period, though many of the tasks would be of shorter duration. The need for this somewhat lengthy schedule is that certain tasks in Objectives 3 and 4 could not proceed beyond an initial phase without results from other tasks. Most of the tasks will start in 1991. Interim reports are planned for fall, 1992 and winter 1993/94, describing current baseline conditions, assumed scenarios, preliminary results from the physical and biological tasks and an early progress report on the socioeconomic tasks. The main report is targeted for spring, 1996. Reports on individual tasks would be issued as they are completed.

CLOSING REMARKS

Regional impacts studies is a long-term multidisciplinary and interdisciplinary research issue, but the field is still in its infancy. In Canada, nearly 60 regional case studies have been completed since 1984. Most of them were short-term efforts, in which climate change scenario data were applied to a region using existing impacts models from various disciplines (e.g., hydrology, agriculture, etc.). Despite the time constraints, a number of regional sensitivities were identified, thereby laying the groundwork for more extensive investigations. What is needed now is a small number of long-term regional studies that include integration of sectoral impacts.

Another important challenge is in monitoring and archiving. It is no secret that the arctic data base for many environmental parameters, including climate, is less than ideal. Recent interest in climate change detection and advances in technology (e.g., automatic stations) has led to the establishment of some new monitoring sites in the Arctic. These include the Canadian Climate Centre's four new permafrost stations, which have been providing climate and soil temperature data on an hourly basis [Etkin et al., 1988], and a large number of new snow courses installed in the Great Slave Lake and Mackenzie River subbasins [B. Latham, personal communication, Dept. of Indian and Northern Affairs, Yellowknife]. In addition, paleoclimate activities are generating more information about past climates, allowing us to place present trends in the context of longer-term variations, and in conjunction with native oral histories, providing important information on sensitivities to past climates.

If our planet's climate warms in the 21st century, as the GCMs indicate, what will happen to the Mackenzie Basin? This unique region will undoubtedly experience a number of changes, but at this time, only a rough qualitative picture can be provided. We need to place ourselves in a position that will allow us in a few years' time to provide a more complete answer to this question. This study will contribute towards accomplishing this goal.

ACKNOWLEDGMENTS

T. Agnew assisted in producing Figure 2. My thanks to F. Roots and an anonymous reviewer for their comments. This paper now includes updates on the Study's plan, reflecting progress made since June, 1990. The opinions expressed herein are the author's, and are not necessarily those of Environment Canada.

REFERENCES

Boer, G. J., N. A. McFarlane, J.-P. Blanchet, and M. Lazare, *Greenhouse gas induced climatic change simulated with the CCC second generation GCM*, Atmospheric Environment Service, forthcoming.

Cohen, S. J., Bringing the global warming issue closer to home: The challenge of regional impact studies, *Bull. Am. Meteorol. Soc.*, *71*, 520–526, 1990.

Cohen, S. J., L. E. Welsh, and P. Y. T. Louie, Possible impacts of climatic warming scenarios on water resources in the Saskatchewan River Subbasin, *Canadian Climate Centre Report No. 89-9*, National Hydrologic Research Institute, Saskatoon, Saskatchewan, 1989.

Egginton, P. A., and J. T. Andrews, Sea levels are changing: Current and future relative sea levels in Canada, *GEOS*, *2*, 15–22, 1989.

Etkin, D. A., A. Headley, and K. Stoker, Permafrost–climate activities within the Canadian Climate Centre, *Canadian Climate Centre Report No. 88-7*, 92 pp., Atmospheric Environment Service, Downsview, Ontario, 1988.

French, H. M., Arctic climate change impacts: a summary and proposals for action, *Canadian Climate Program Workshop*, March 3–5, 1986, Geneva Park, Ontario. Canadian Climate Centre, Atmospheric Environment Service, Downsview, Ontario, 1986.

Grotch, S. L., Regional intercomparisons of General Circulation Model predictions and historical climate data, *Report #DOE/NBB-0084*, U.S. Department of Energy, 1988.

Hill, F. I., Commentary on "Prospects for the north Canadian native economy," *Polar Record*, *23*, 142, 91–94, 1986.

Irwin, C., Lords of the Arctic: wards of the state—a summary report, *Northern Perspectives*, *17*, 2–12, and "postscript," 19–20, 1989.

Jaeger, J., Developing policies for responding to climatic change, *World Climate Impact Studies Programme, WCIP-1 (WMO/TD-No. 225)*, World Meteorological Organization and United Nations Environment Programme, 1988.

Lonergan, S., R. Difrancesco, and M. Woo, *Climatic change and transportation in northern Canada: An integrated impact assessment*, forthcoming.

Malone, M., The view from Yellowknife (response to Irwin), *Northern Perspectives*, *17*, 13–14, 1989.

Marsh, P., and M. Hey, The flooding hydrology of Mackenzie Delta lakes near Inuvik, N.W.T., Canada, *Arctic*, *42*, 41–49, 1989.

Maxwell, J. B., and L. A. Barrie, Atmospheric and climatic change in the Arctic and Antarctic, *Ambio*, *18*, 42–49, 1989.

Mearns, L. O., Climate variability, in *The Potential Effects of a Global Climate Change on the United States*, edited by J. Smith and D. Tirpak, Report to Congress, Environmental Protection Agency, Washington, DC, 1989.

Météoglobe Canada Inc., *Consequences des scenarios de changement climatique sur les infrastructures liées à la production d'hydroélectricité au Québec*, report prepared for Atmospheric Environment Service, Quebec Region, Montreal, 1989.

Mitchell, J. F. B., The "Greenhouse" effect and climate change, *Rev. Geophys.*, *27*, 115–139, 1989.

Mysak, L., Environment, presented at Symposium on the Arctic and Global Change, October 25–27, 1989, Ottawa. Climate Institute, Washington, DC, 1989.

Pretes, M., Underdevelopment in two norths: The Brazilian Amazon and the Canadian Arctic, *Arctic*, *41*, 109–116, 1988.

Tungavik Federation of Nunavut (TFN), An Inuit response (to Irwin), *Northern Perspectives*, *17*, 15–18, 1989.

Washington, W. M., and G. A. Meehl, Seasonal cycle experiment on the climate sensitivity due to a doubling of CO_2 with an atmospheric general circulation model coupled to a simple mixed-layer ocean model, *J. Geophys. Res.*, *89*, 9475–9503, 1984.

Washington, W. M., and G. A. Meehl, Climate sensitivity due to increased CO_2: experiments with a coupled atmosphere and ocean general circulation model, *Climate Dynamics*, *4*, 1–38, 1989.

Wilson, C. A., and J. F. B. Mitchell, A doubled CO_2 climate sensitivity experiment with a global climate model including a simple ocean, *J. Geophys. Res.*, *92*, 315–343, 1987.

World Climate Research Programme (WCRP), Concept of the global energy and water cycle experiment, Report of the JSC Study Group on GEWEX, *WCRP-5*, *WMO/TD-No. 215*, March 1988, World Meteorological Organization, Geneva, 1988.

World Meteorological Organization (WMO), International Conference on the Assessment of the Role of Carbon Dioxide and of Other Greenhouse Gases in Climate Variations and Associated Impacts, Report on the Villach, Austria Conference, 9–15 October, 1985, *WMO-No. 661*. World Meteorological Organization, Geneva, 1986.

World Meteorological Organization (WMO), *The Changing Atmosphere: Implications for Global Security*, Conference Proceedings, 27–30 June, 1988, Toronto. WMO No. 710, World Meteorological Organization, Geneva, 1988.

Young, R. A., and P. McDermott, Employment training programs and acculturation of native peoples in Canada's Northwest Territories, *Arctic*, *41*, 195–202, 1988.

Allowance for the Relaxation Effects in Global Processes of Heat Transfer

N. Yu. Doronin and G. A. Zablotsky
Arctic and Antarctic Research Institute, Leningrad, U.S.S.R.

ABSTRACT

The analysis of assumptions made to derive the differential form of the thermal energy conservation laws indicates that one of the "strongest" allowances for non-equilibrium thermodynamics is not fulfilled for geophysical scales. This is the hypothesis of local equilibrium, which assumes that evolution of a thermodynamic system is approximated by a set of equilibrium states at non-related time intervals. The orders of magnitudes of the relaxation time and of the duration of geophysical processes of heat transfer are comparable. This shows the transitional (unsettled) character of the latter and, hence, confirms that the local equilibrium principle is not applicable. Allowing for the finite velocity of a macro-disturbance propagation in the mathematical formulation of the conservation law yields high order derivatives by time from the specific internal energy. Conventional consideration of this problem results in the assumption of infinitely great velocity of thermal disturbance propagation in a medium. A generalized equation of heat conductivity is then derived; it coincides with an equation obtained earlier by P. Vernotte and A. V. Lykov, although it was derived in a different way and for processes at a different scale. However, the initial assumption of the finite velocity of the thermal disturbance propagation in a medium is common. The formation of the heat flux front, moving with a finite velocity, at initial stages of relaxation is the principal difference in the solution of the generalized heat transport equation from the classical one. The resultant generalized equation is an attempt at an approximate linear description of essentially non-linear processes of heat transfer in the ocean.

AD-P007 288

Problems With the Use of Climatological Data to Detect Climatic Change at High Latitudes

S. A. Bowling
Alaska Climate Research Center, Geophysical Institute, University of Alaska Fairbanks, Fairbanks, Alaska, U.S.A.

92-17970

ABSTRACT

Although warming due to increased amounts of CO_2 and other greenhouse gases in the atmosphere is predicted to be greatest in high latitudes, results of the GISS model have already indicated that the ratio of warming to interannual variability will be relatively small, which will make any change hard to detect [Hansen et al., 1988]. In addition, the climatological data set at high latitudes is scanty and subject to most of the same problems as those in the temperate zone. In fact, the extreme ground inversions, low sun angles, and seasonal polar night or continuous daylight conditions may lead to systematic errors with magnitudes much greater than would be predicted from midlatitude experience.

The Alaskan record demonstrates possible magnitudes of some of these systematic errors. Both winter and summer heat island effects are large. Site changes (including documentation problems) may have unexpectedly large effects, and virtually the entire state was affected by a change in time zones made in 1983.

INTRODUCTION

Instrumental records from high latitudes suffer from the same problems as those elsewhere: changes in observation methods, observation sites, instrumentation and site surroundings can all affect the validity of apparent long-term trends. Some of these problems are more difficult to correct for at high latitudes. Thus low station density makes it unusually difficult to correct for station location changes, and extreme variation in sunset and sunrise times is expected to complicate correction for observation time. In Alaska, this correction must be applied to almost every station, as time zone changes in October 1983 produced observation time changes of 1 to 2 hours at every station in Alaska except Yakutat. In other cases, problems may actually be of greater magnitude at high latitudes. For instance, extreme ground inversions lead to large temperature changes over short distances (magnifying the potential effects of station changes) and unexpectedly large urban heat island effects.

This paper deals with three examples of local variations or apparent "climate changes" probably due to urban effects, plus one possible real variation in Alaskan climate.

AN APPARENT LONG-TERM SUMMER WARMING

While looking for differences in the character of summer and winter temperature records across the state, we noticed that virtually all of the large negative summer minimum temperature anomalies at Fairbanks occurred during the early years of the record, while the large positive anomalies were recent. When trend lines were fitted to individual monthly mean minimum and maximum temperatures, the May, June, July, and August minimum temperatures at Fairbanks showed significant upward trends with time (Figure 1). No trends were noted in other seasons, in summer maxima, or at other stations. As the Fairbanks record is far from uniform, we repeated the analysis using only data from the current Fairbanks International Airport location, and found similar trends, though with slightly weaker correlations (Figure 2). As there is no sign of such effects in areas with smaller populations, it appears that the trend is most likely due to a combination of station changes and a summer climatological heat island (due to the increasing amount of building materials in the vicinity of the airport) of previously unsuspected intensity.

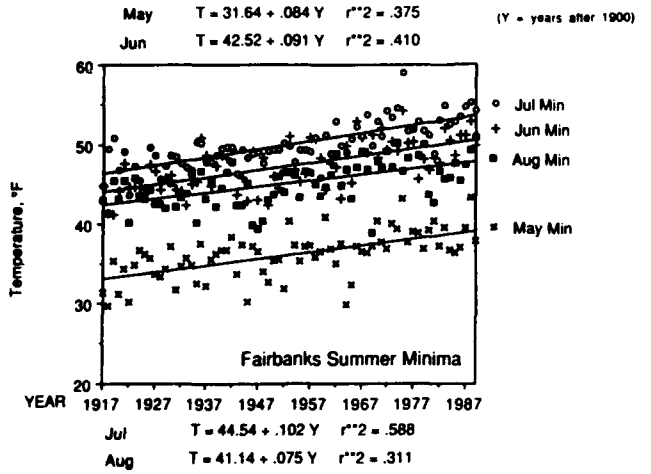


Figure 1. Summer-month mean daily minimum temperatures at Fairbanks. This is an extremely heterogeneous record, with major station moves in 1929, 1942, 1943, and 1951, but no similar trends appear in other months or at other stations checked. The four correlation coefficients shown are significant at the 99.9% confidence level.

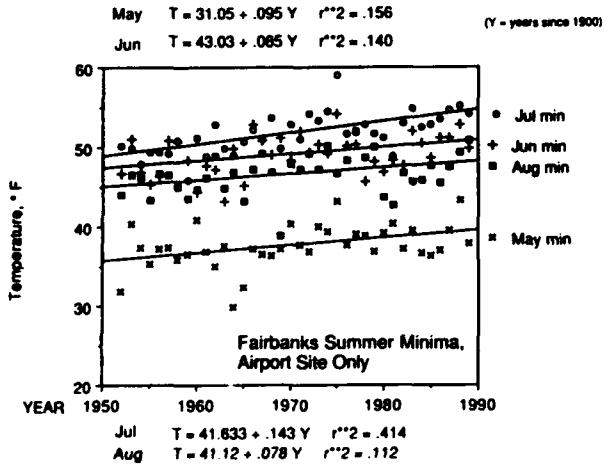


Figure 2. Same as Figure 1, but only for the recent, homogeneous period of record. For 38 years of record (36 degrees of freedom) an r^2 of roughly 0.1 would be significant at the 95% level, and one of 0.18 at the 99% level.

The Fairbanks area is subject to strong urban heat island effects (measured to be as much as 13°C) when skies are clear in winter [Bowling and Benson, 1978]. Summer heat islands have hardly been looked at, but they now appear likely to have more effect on recorded climate than do the large winter ones, which are masked by large year-to-year variability in winter and seem to be more confined to the city core.

Why doesn't Anchorage show a similar effect? The most probable culprit is the Good Friday Earthquake of 1964. The earthquake leveled the Control Tower, which required that the instruments be relocated. The max/min thermometers were at Point Campbell, farther from pavement and nearer the waters of Cook Inlet, by 1971, but there is apparently no record of their location during the intervening period.

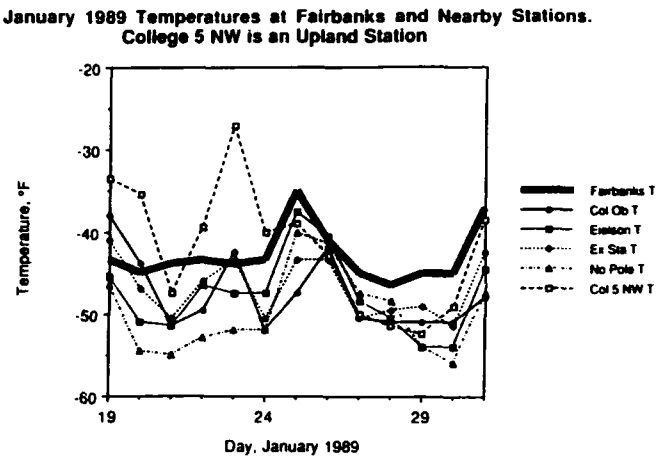


Figure 3. Daily mean temperatures at Fairbanks and nearby stations during a severe cold spell. Heavy line is Fairbanks International Airport, elevation 133 m. Other stations are: Col Ob = College Magnetic Observatory, on the West Ridge of the University of Alaska at elevation 189 m; Eielson = Eielson Air Force Base, about 40 km SE and upvalley of the Airport at elevation 167 m; Ex Sta is the University Experiment Station, near the base of the West Ridge at elevation 145 m; No Pole is North Pole, between Fairbanks and Eielson at elevation 145 m; and Col 5 NW is in the uplands 5 miles NW of the two campus sites, elevation 290 m.

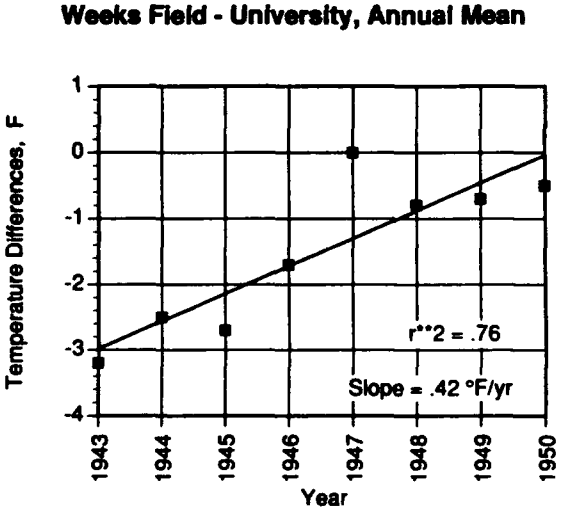


Figure 4. Annual mean differences between Fairbanks Weeks Field temperatures and University Experiment Station temperatures, showing increasing heat island as the city of Fairbanks grew around Weeks Field.

LOCAL VARIABILITY DURING JANUARY 1989

January of 1989 was a record-setter in much of Alaska. Not, however, officially in Fairbanks, where the official temperatures are recorded downwind of the city. Unofficial temperatures on the upwind side of Fairbanks were much lower, as were many at surrounding climatological stations (Figure 3). All of the stations shown are within a radius of 40 km, with Eielson being the only one that far from the Fairbanks site. The difference between the experimental station and the airport can probably be attributed to the heat island effect combined with a time of observation error; the

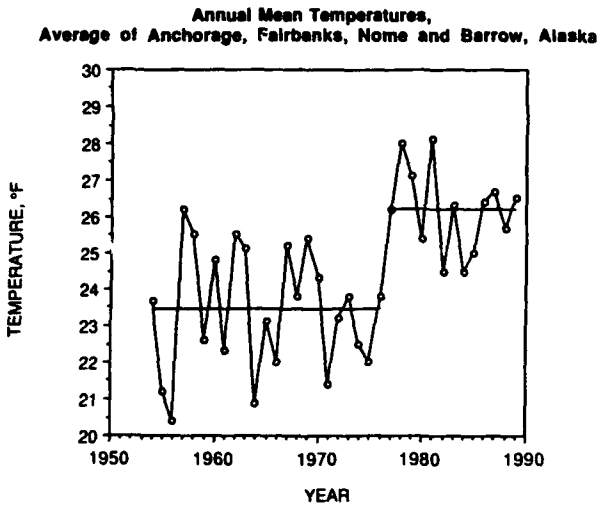


Figure 5. Annual mean temperatures, average of Anchorage, Barrow, Fairbanks, and Nome, since all four airports stabilized positions in the mid-1950s. (Changes in instrument location at Anchorage may have led to apparent warmer winters and cooler summers, but Anchorage does not in any way dominate the trend shown, which is strongest at Fairbanks and Nome.)

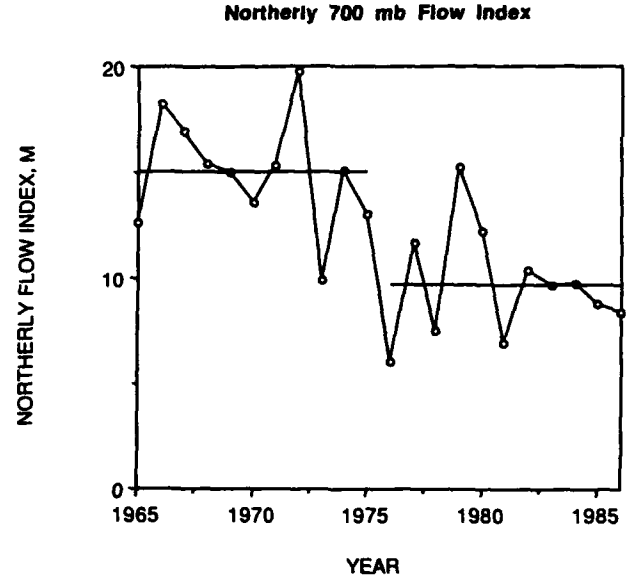


Figure 6. Northerly wind index over Alaska, annual values from 1965 through 1986 calculated as described in text. A least-squares regression (not shown) gives a slope of -0.4 m yr^{-1} and a correlation coefficient of 0.68, significant at the 99% level. Note that this index cannot by its nature be negative, so this trend represents a decrease in northerly flow intensity of more than a third over 20 years.

spread among the other lowland stations indicates local variability. The difference between College 5 NW and the other stations during the first half of the cold spell indicates a strong inversion, especially on the 23rd.

THE MISPLACED MOVE AND THE ENCROACHING CITY

Recorded station moves are not necessarily consistent among different sources, nor are the dates always accurate. Take the case of the downhill move at the University Experiment Station. The station list in *Climatological Data, Alaska* shows an elevation change from 500 feet to 475 feet in the summer of 1947. Was it real, or the result of resurveying the area? With known current winter inversion strengths in the University area, such a move could have produced a decrease of a few degrees in recorded winter temperatures. Comparison of the University record for December and January with the Fairbanks record from Weeks Field (near where the Borough Library is now located) did indeed show either a decrease in University temperature or an increase in the Weeks Field temperature, but suggested a change in the summer of 1946 rather than 1947. The actual station history for the University Experiment Station confirms that the move was real, but it took place in *1933*, 15 years before it was finally brought up to date in *Climatological Data*.

Month	Points	Slope, °F yr^{-1}	Correlation Coefficient	Significance
January	8	0.76	0.70	>0.90
February	8	0.08	0.17	<0.80
March	8	0.89	0.59	>0.80
April	8	0.05	0.05	<0.80
May	9	0.21	0.51	>0.80
June	9	0.29	0.74	>0.95
July	9	0.27	0.73	>0.95
August	8	0.34	0.84	>0.99
September	8	0.42	0.95	>0.999
October	8	0.27	0.85	>0.99
November	8	0.65	0.67	>0.90
December	8	0.68	0.71	>0.95

Table 1. Trends of temperature differences (Weeks Field–University), 1943–1951.

The trend of increasing temperature at Weeks Field relative to University affects all summer, fall, and early winter months (Table 1). It is most logically explained as due to an increasing heat island effect as Fairbanks grew around Weeks Field. Although the time period is very short for high significance (May 1, 1943 through mid-August 1951) the trends are extremely consistent from month to month outside of the spring period, with an increase of almost half a degree per year (Figure 4). Some of the large deviations from the trend line can even be explained: December 1946 and January 1947, both of which show large positive deviations from the trend line, are known to include a record-setting cold spell which, from previous studies, is known to be an ideal setting for a large heat island effect. But unanswered questions remain. Why does the heat island appear to weaken during late winter and spring? Why do so many months have large deviations from the trend line in 1947?

THE 1976 TEMPERATURE STEP: A REAL CHANGE?

The 1976-77 winter in Alaska was astonishingly warm. At Fairbanks, pussy willows bloomed in November (author's observation) and daily average temperatures never reached -30°F. Subsequent winters followed the same trend

to a lesser degree, with degree days below -40°F showing a reduction quite noticeable to long-term residents. An average of four Alaskan stations with good, continuous records, Anchorage, Barrow, Fairbanks, and Nome, show what appears to be a change in mean annual temperatures at around this time (Figure 5). All of these stations are in areas that could be affected by urban effects, but a similar step, which there appears to interrupt an overall downward trend, appears at McGrath, with a population of under 1000 people. Is it real? And will it last?

In an attempt to find a somewhat independent measure of climate shift, be it temporary or permanent, we used 700-mb grid point heights at 60°N 150°W, 65°N 160°W, 65°N 140°W, and 70°N 150°W to estimate changes in geostrophic flow. The usual net north–south and east–west flows would have been ambiguous as to whether an increase in net southerly flow, for instance, was caused by an increase in the frequency or intensity of southerly flow or a decrease in northerly flow. To get around this, we summed the positive differences between 160°W and 140°W as northerly flow and the negative differences as southerly flow at 65°N over Alaska, dividing by the actual number of soundings used to compensate for missing data. The differences between 60°N and 70°N at 150°W were similarly treated, with positive differences contributing to westerly flow and negative differences to easterly flow.

The somewhat unexpected result was that all four indices decreased in absolute value over the period from 1965 through 1986, suggesting a general reduction in the intensity of circulation over Alaska. The only significant decrease, however, was that in northerly flow, which showed a fairly consistent high level early in the time series, rather violent oscillations for several years around the apparent temperature change, and a second steady period, at around two-thirds the previous level, in the first half of the 1980s (Figure 6). It thus seems likely that the observed warming in the mid 1970s in Alaska is real and associated with a circulation shift. Whether it is part of an unusually long-period oscillation or has something to do with carbon dioxide is still a mystery.

CONCLUSIONS

Use of high-latitude instrumental data to deduce long-term trends is risky at best, and should be attempted only with reference to the fullest available station histories and some knowledge of the local topography, settlement history, and microclimates. Changes documented by more than one type of data (e.g., soundings as well as surface temperatures) can be considered better supported than simple temperature measurements, but such data are rarely available for really long time series.

REFERENCES

Bowling, S. A., Climatology of high-latitude air pollution as illustrated by Fairbanks and Anchorage, Alaska, *J. Clim. Appl. Meteorol.*, *25*, 22–34, 1986.

Bowling, S. A., and C. S. Benson, Study of the subarctic heat island at Fairbanks, Alaska, *EPA Report EPA-600/4-78-027*, 149 pp., 1978.

Hansen, J., I. Fung, A. Lacis, D. Rind, S. Lebedeff, R. Ruedy, and G. Russell, Global climate changes as forecast by Goddard Institute for Space Studies three-dimensional model, *J. Geophys. Res.*, *93*, 9341–9364, 1988.

AD-P007 289

A Winter Season Synoptic Climatology of Alaska: 1956–1986

Mary F. Milkovich
Institute of Marine Science, University of Alaska Fairbanks, Fairbanks, Alaska, U.S.A.

92-17971

ABSTRACT

An objective, descriptive study of Alaska's winter climate is undertaken to identify regional monthly mean surface temperature and precipitation variability during the thirty-year period from 1956-57 to 1985-86. Ten basic anomaly 700-mb height patterns are described in terms of frequency of occurrence and possible associations with the surface climate variability observed in the nine NOAA land-based climate divisions of Alaska and the Gulf of Alaska (tenth division). Results indicate a cool, dry period from 1964–1976. Anomaly height patterns occurring during this period were predominantly characterized by northerly/northwesterly flow from the High Arctic or northeasterly flow from the Canadian Interior. The period from 1956–1962 was generally warm, and the most frequently occurring anomaly height patterns were characterized by southerly flow. The period following 1977 is the most variable of the thirty-year record. This period also includes some of the warmest temperatures seen in the records. "Cold" anomaly height patterns are interspersed among the slightly more frequent "warm" anomaly height patterns from 1977–1986. Overall seasonal-scale linear (best-fit approximations) trends appear to indicate a warmer, drier shift in the Interior climate and a warmer, wetter shift in the southern coastal climate.

INTRODUCTION

The Alaska climate system is an important, but little understood part of the Arctic and, in turn, global climate system. As more emphasis (International Geosphere–Biosphere Program, First Global Atmospheric Research Program) is now being placed on global change and the global climate system, it is becoming increasingly apparent how little is known about the Arctic region's climatology. However, current investigations of climatic variability have indicated that the Arctic and sub-Arctic are the regions with the greatest potential for change [Spelman and Manabe, 1984; Lachenbruch and Marshall, 1986; Bowling, 1988]. In an effort to respond to this challenge for a more complete understanding of the region's climate behavior, a renewed emphasis is being placed on Alaska and Arctic climate research [IGBP; Barry, 1985; Milkovich, 1989; Royer, 1991; Walsh and Chapman, 1991]. One of the first major steps in this renewed Arctic effort is to objectively define Alaska's basic winter climate elements—the surface climatology and the major upper-air circulation features associated with the winter climate [Milkovich, 1989].

The climate of Alaska's winter is characterized by a large variability in weather parameters. The dynamic meteorology of the region is the result of multi-directional feedback loops between atmospheric, land, and ocean components. Current research is primarily focused on the winter season because it is the most dynamically variable season in Alaska and the Arctic, and because climate models indicate that the greatest global change may take place during the Arctic winter season. Previous research has shown that two of the most prominent atmospheric features directly affecting Alaska's winter climate variability are the somewhat persistent Aleutian Low (Gulf of Alaska) and the Siberian High (interior and northern sections of the state). The Gulf of Alaska and the entire North Pacific sector are well-noted regions of intense cyclogenesis and storm decay [Namias, 1975; Anderson et al., 1988].

The components of Alaska's surface climatology and the overlying atmospheric circulation play equally important roles in determining the region's overall climate. The wide range of topography found in Alaska and the actual geographic area covered by the state contribute to a great diversity of localized winter phenomena. Alaska is also surrounded by three major bodies of water—the North Pacific (Gulf of Alaska), the Bering Sea, and the Arctic Ocean. The latter two are ice-covered to varying extents throughout the winter season.

In this paper, Alaska's winter climate is investigated in terms of a synoptic climatology. As defined by Barry and Perry [1973], a synoptic climatology is "concerned with obtaining insight into local or regional climates by examining the relationships of weather elements, individually, or collectively to atmospheric circulation processes." Weather elements considered here are monthly mean temperature and precipitation. Atmospheric circulation processes are limited here to the monthly mean 700-mb anomaly height patterns.

DATA

The data used in the circulation pattern classification presented here are adapted from the 700-mb Northern Hemisphere analysis charts (NMC) which have been interpolated by NCAR to a 5 x 5 longitude–latitude spacing of geopotential heights [Jenne, 1975]. Both 0000 GMT and 1200 GMT data are included in the analysis presented here. The initial NCAR data set was reduced to emphasize the region bounded by 40°N–80°N and 0°E–360°E in order to focus on the Arctic/sub-Arctic region. The six winter months (October 1 to March 31) for the winters of 1956-57 to 1985-86 were used. The winter months were defined based on the "breaks" in the temperature records in all regions, and through discussion [personal communication with T. Fathauer, NWS Fairbanks; S. A. Bowling, G. Weller, and others, Geophysical Institute, University of Alaska Fairbanks]. Twice-daily data were averaged into monthly mean grids. If more than 80% of a month's data were missing, the entire month of data was declared to be missing. After screening the data, 169 out of 180 months remained. Long-term (30-year) means for each of the six winter months were calculated and then the mean values were subtracted from the appropriate individual months to obtain anomaly patterns. These anomaly patterns were then used in the pattern classification processing.

The surface climate of Alaska was represented by monthly mean surface temperature and precipitation. The same six-month winter period was employed. Because of the wide variety of winter weather occurring in Alaska, multiple climate divisions were used rather than statewide averages. The divisions (Figure 1) consist of: Southeastern, South Coast, Southwestern Islands, Copper River, Cook Inlet, Bristol Bay, West Central, Interior Basin, Arctic Drainage, and Gulf of Alaska. The first nine are the NOAA climate divisions for the state and are based on similarities in geographic, temperature, and watershed characteristics. The Gulf of Alaska was represented by sea surface temperature, but no precipitation data.

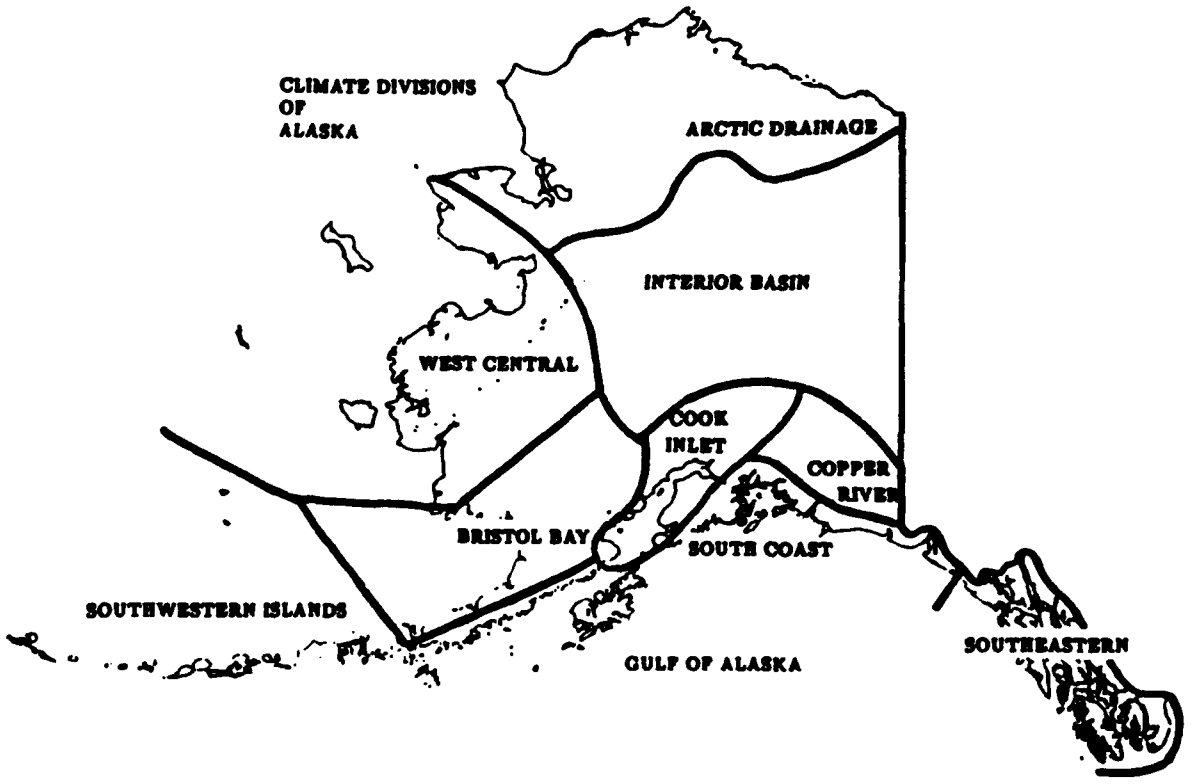


Figure 1. The ten climate divisions of Alaska, after NOAA [1956–1986].

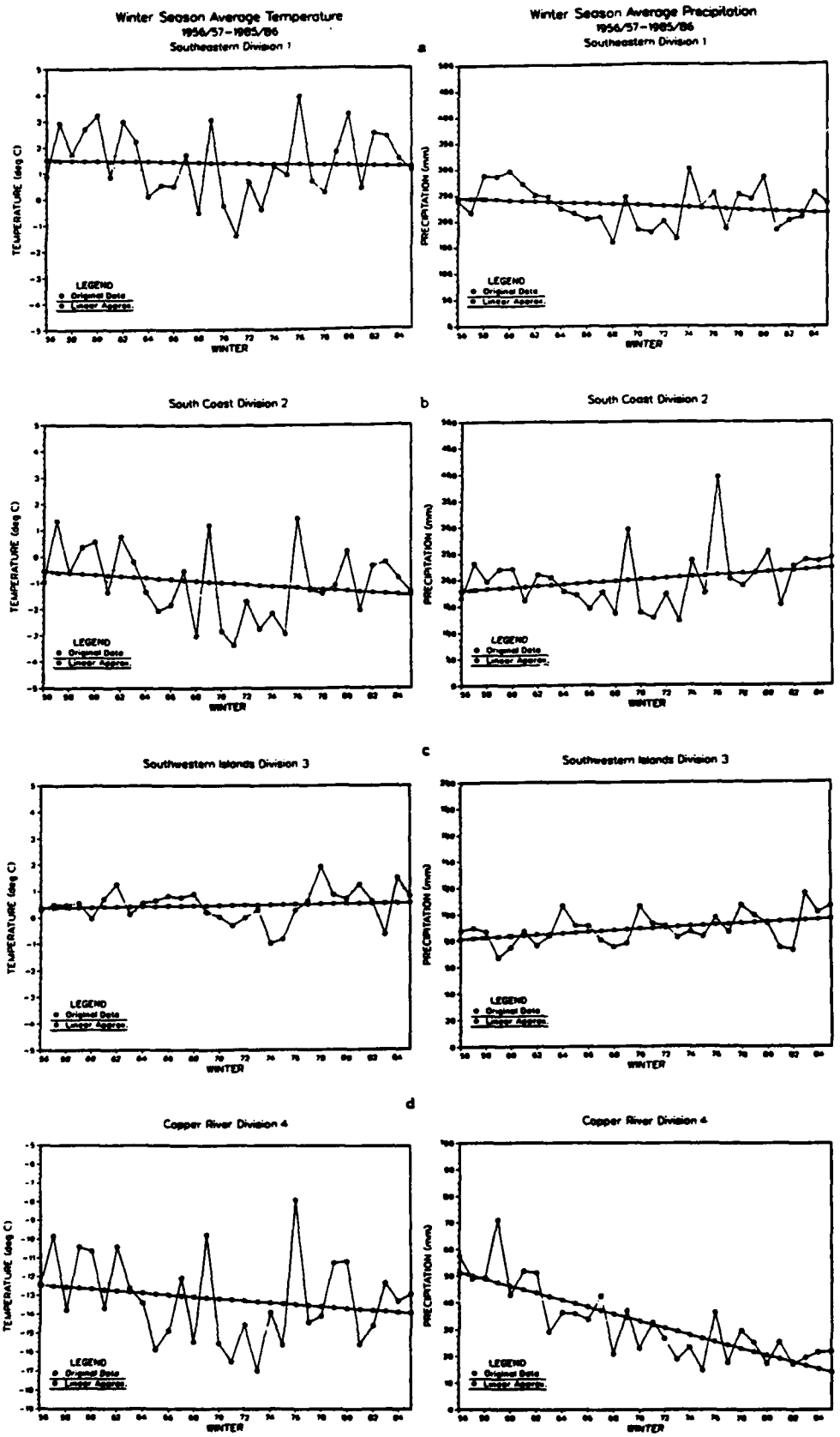


Figure 2 (a-d). Winter season average temperature and precipitation—Winter 1956–1986. Winter season data are an average of the winter months' (October, November, December, January, February, March) monthly mean data. Temperature units are deg C, precipitation units are mm. NOTE: The temperature and precipitation scales are NOT necessarily uniform from division to division; these scale variations were found necessary to show the within-division variability.

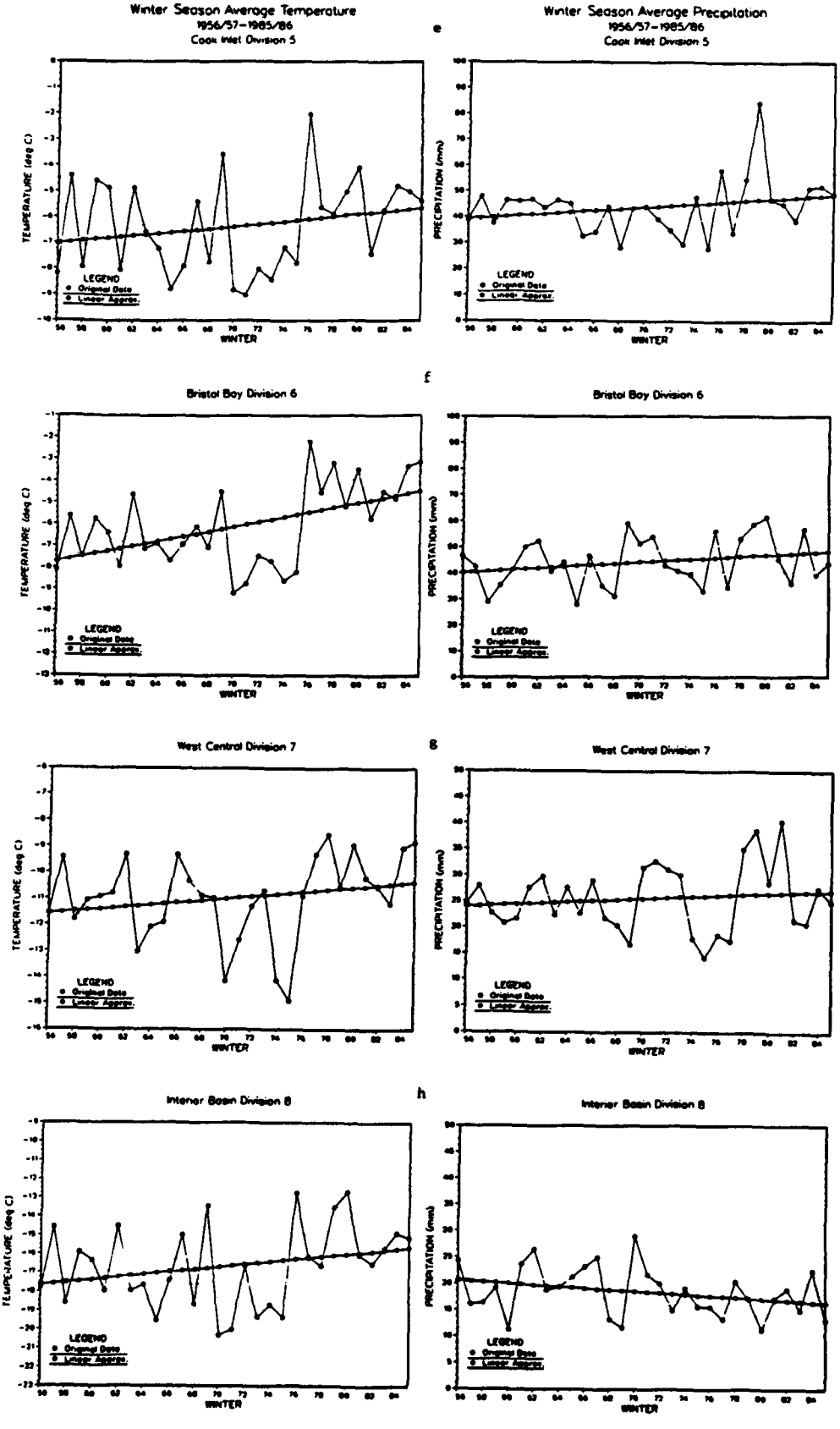


Figure 2. (e-h). Same as for Figure 2 (a-d).

Monthly mean temperature and precipitation values for each division were calculated from daily average values at long-term stations within each division [NOAA, 1956–1986].

Pattern	Original	Final
1	29	28
2	29	24
3	15	16
4	17	15
5	6	10
6	9	9
7	7	8
8	8	8
9	5	7
10	6	6

Table 1. Anomaly pattern classification results. Original refers to the map distribution during the initial Basic Anomaly Pattern selection process; Final refers to the map distribution after all maps were sorted into their respective "best" Basic Anomaly Pattern category; *minimum thresholds* used in the classification process: r_{AB}=0.6 and 5 maps per category.

METHODOLOGY

An adaptation of the Lund [1963]/Kirchhofer [1973] pattern classification scheme was applied to the 700-mb anomaly data in order to obtain a catalog of basic patterns occurring over the thirty winter seasons from 1956-57 to 1985-86. The method classifies individual maps into categories based on similarities between maps as determined by a correlation coefficient threshold in a least squares–based calculation. The method is an objective or "computer-assisted" technique [Yarnal, 1984]; although, as with any known classification scheme, there is some subjectivity involved as one must choose optimum thresholds to be satisfied [Yarnal and White, 1987]. In this case, thresholds included the r value, the minimum association size for basic pattern designation, and extent of geographic area covered. After several test runs, the optimal thresholds chosen were r=0.60, five-map minimum to be a category, and a geographic area bounded by 40°N–80°N and 140°E–115°W.

Surface temperature is presented as time series both for individual months and for season averages. A linear best-fit trend approximation has also been calculated. An identical procedure was performed for precipitation. A total of 14 division-based time series (one precipitation series and one temperature series for each division for each winter month; one winter season precipitation series and one winter season temperature series for each division) were examined for the nine land-based divisions, and seven time series (no pre-

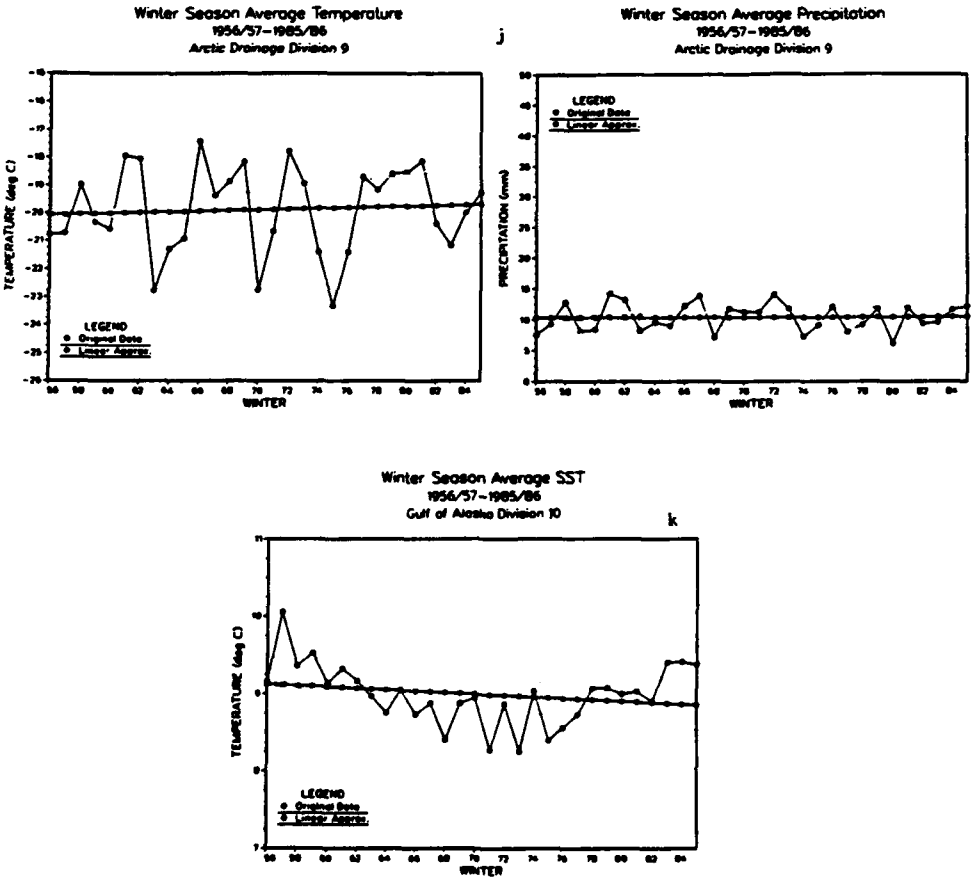


Figure 2. (j-k). Same as for Figure 2 (a-d).

Pattern	Temperature	Precipitation
Southeastern (Division 1)		
1	cool	dry
2	warm	wet
3	warm	wet
4	cool	dry
5	warm	dry
6	warm	wet
7	cool	dry
8	cool	dry
9	warm	wet
10	w/c	wet
South Coast (Division 2)		
1	cool	dry
2	warm	wet
3	warm	wet
4	cool	dry
5	warm	wet
6	w/c	wet
7	cool	dry
8	warm	dry
9	cool	dry
10	cool	wet
Southwestern Islands (Division 3)		
1	warm	dry
2	warm	w/d
3	warm	dry
4	c/w	dry
5	w/c	dry
6	cool	wet
7	c/d	d/w
8	warm	wet
9	w/c	dry
10	w/c	dry
Copper River (Division 4)		
1	cool	dry
2	warm	dry
3	warm	wet
4	cool	dry
5	w/c	dry
6	warm	wet
7	cool	dry
8	warm	wet
9	w/c	d/w
10	warm	wet
Cook Inlet (Division 5)		
1	cool	d/w
2	warm	d/w
3	warm	wet
4	cool	dry
5	warm	w/d
6	warm	w/d
7	cool	dry
8	warm	dry
9	cool	dry
10	cool	wet
Bristol Bay (Division 6)		
1	cool	d/w
2	warm	d/w
3	warm	dry
4	cool	dry
5	warm	wet
6	cool	dry
7	cool	wet
8	warm	dry
9	cool	d/w
10	cool	dry

Pattern	Temperature	Precipitation
West Central (Division 7)		
1	cool	wet
2	warm	dry
3	warm	dry
4	c/w	d/w
5	warm	d/w
6	cool	dry
7	c/w	d/w
8	warm	wet
9	warm	d/w
10	cool	dry
Interior Basin (Division 8)		
1	cool	wet
2	warm	dry
3	warm	dry
4	cool	d/w
5	warm	d/w
6	cool	w/d
7	cool	w/d
8	warm	wet
9	warm	dry
10	cool	wet
Arctic Drainage (Division 9)		
1	c/w	wet
2	warm	d/w
3	cool	w/d
4	c/w	d/w
5	warm	d/w
6	cool	w/d
7	cool	d/w
8	warm	wet
9	warm	d/w
10	cool	w/d
Gulf of Alaska (Division 10)		
1	cool	na
2	cool	na
3	warm	na
4	cool	na
5	warm	na
6	cool	na
7	c/w	na
8	warm	na
9	cool	na
10	cool	na
Statewide (all Divisions)		
1	cool	dry
2	warm	w/d
3	warm	dry
4	cool	dry
5	warm	w/d
6	cool	wet
7	cool	w/d
8	warm	dry
9	w/c	dry
10	cool	wet

Table 2. Regional correlation results: monthly mean climate and Basic Anomaly Pattern associations. Climate variables include montly mean temperature and precipitation characteristics. w/d = mixed precipitation, w/c = mixed temperature. (See text for further explanation.)

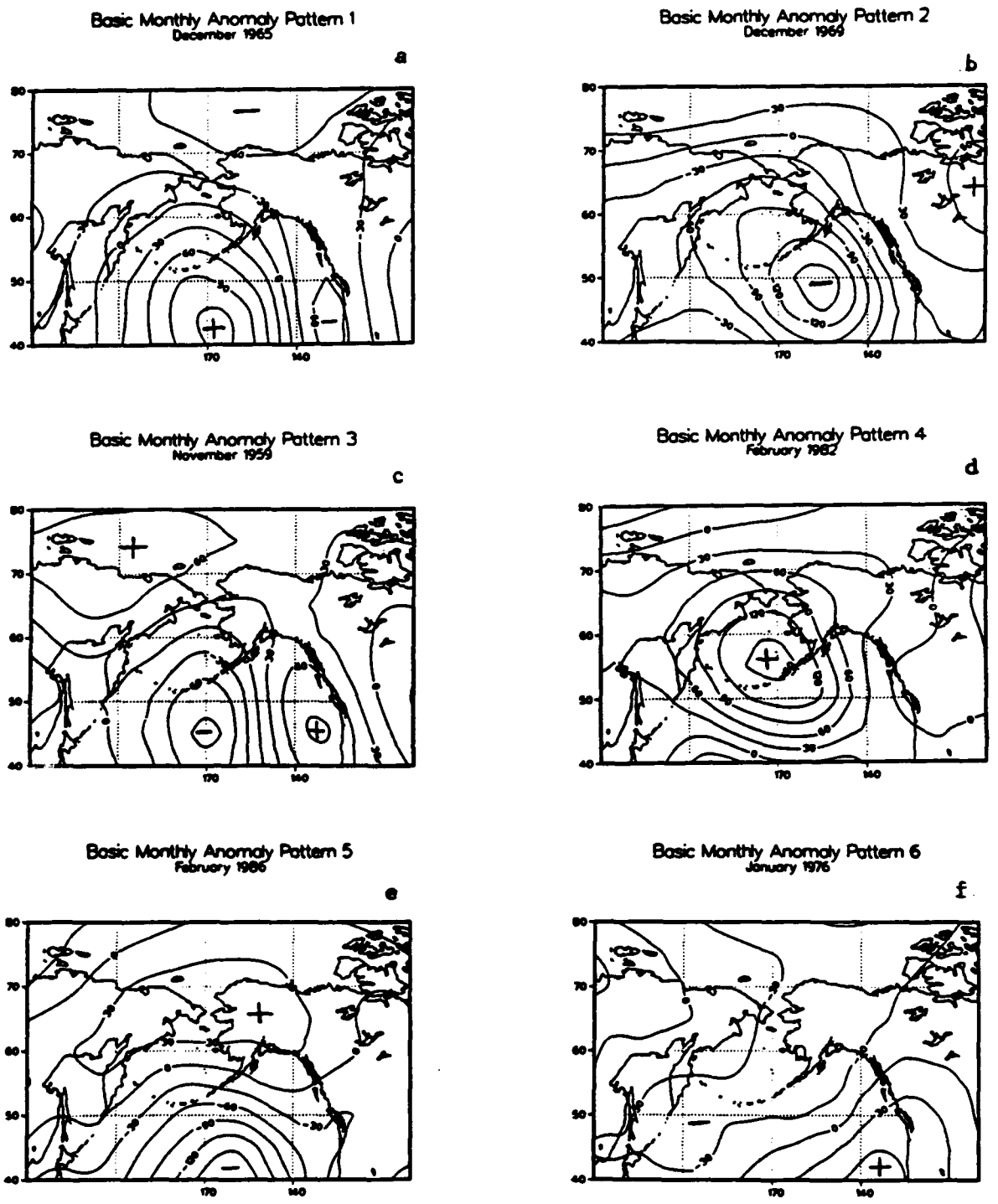


Figure 3 (a-f). Basic Anomaly Patterns: the date on the patterns refers to the actual date of the basic pattern map—the Basic Anomaly Patterns are not an average of several different maps; units are meters, and contours are 30-m departures from the thirty-year mean 700-mb geopotential heights for the corresponding month.

cipitation) were examined for the Gulf of Alaska. The winter season time series for each division are presented in Figure 2a–k. The time series were examined visually to note cycles, persistent warm or cool/wet or dry periods, and periods of extreme variability [Milkovich, 1989]. The different divisions were then subjectively compared to each other to distinguish similarities and differences over the thirty years within each division.

In order to complete the synoptic climatology process, it was necessary to examine the correspondence between the circulation patterns and the surface weather. In this study, circulation patterns were defined to be warm/cool/mixed

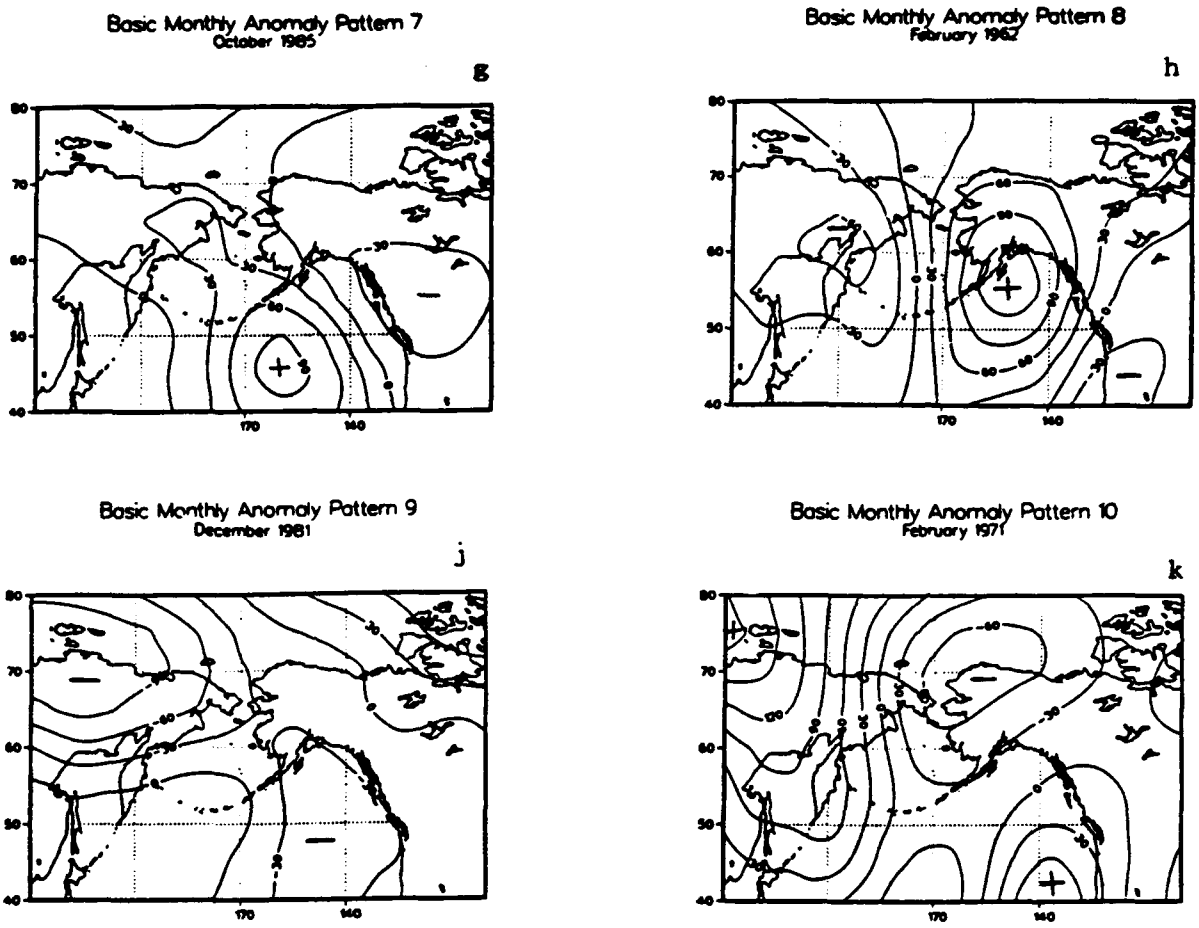


Figure 3 (g-k). Same as Figure 3 (a-f).

and wet/dry/mixed patterns based on the predominant climate observed at the times the pattern occurred over the thirty-year period. A pattern was considered to be a warm pattern for a specific division if the majority of its occurrences took place when the temperature in that division was above the associated thirty-year mean for that division. Similarly, cool patterns were those occurring primarily when the temperature was below the associated thirty-year mean. Mixed patterns were those in which there was no predominant temperature mode. Precipitation characteristics were handled similarly. The associations were noted within each of the ten divisions, and then on a statewide basis. The statewide associations were determined similarly. The only difference was that the thirty-year mean values applied were statewide averages determined by averaging the ten divisional values.

DISCUSSION

Anomaly Patterns

The classification procedure described above resulted in ten basic pattern (BP) categories. Seventy-eight percent of the 169 complete anomaly maps were classified into these ten categories. Table 1 shows the individual number of maps in each basic pattern category at the two stages of map sorting. Basic pattern descriptions follow.

The most dominant feature of Basic Pattern 1 (BP1, Figure 3a) is a broad positive anomaly centered at 170°W, 45°N. Alaska is under a region of below-normal heights. The largest central departure of the anomaly pattern is +120 m. The basic pattern is from December 1965. The pattern is well distributed throughout the winter season. It occurred consistently until 1976. There are 28 similar maps.

BP2 (Figure 3b) is noted for its area of negative height departures centered at 50°N, 155°W. Central departure value is -150 m. Southeast flow results over mainland Alaska. The basic pattern is from December 1969 and there are 24 maps similar to it. Fifty percent of these similar maps occurred prior to 1971. The maps are concentrated from 1972–1982.

BP3 (Figure 3c) is based on November 1959 and there are 16 similar maps. The pattern was nonexistent from 1960 to 1975. It is primarily a December/January pattern. Alaska is situated under an area of above-normal heights. Interior Alaska experiences northerly flow, while the remainder of the state receives S/SE flow.

BP4 (Figure 3d) has 15 maps similar to it. The basic pattern is from February 1982. It occurs most frequently after 1969. Alaska's Interior receives northerly flow from the Arctic and the Bering Sea coast is in a belt of westerlies.

BP5 (Figure 3e) places Alaska under weak west or east flow. There are 10 maps similar to the basic pattern and the

basic pattern is dated February 1986. The pattern is most frequent after 1979 and is predominantly a February pattern.

BP6 (Figure 3f) is from January 1976 and there are 6 maps similar to it. It is most prevalent in the 1960s and early 1970s. It is a mid-winter pattern and is not seen after 1976.

BP7 (Figure 3g) is similar to the West Pacific Oscillation Pattern as denoted by Barnston and Livezey [1987]. There are 8 maps similar to the basic pattern and the basic pattern comes from October 1985. The pattern is most concentrated from 1967–1971.

BP8 (Figure 3h) also has 8 similar maps. The basic pattern is from February 1962. The pattern seems to occur in late winter and interestingly, only in seasons distinguished by ENSO events [Namias, 1976; Douglas et al, 1982; Cane, 1983; Niebauer, 1988]. The most prominent feature is a broad positive anomaly.

BP9 (Figure 3j) splits the flow pattern over Alaska. There are 7 maps similar to it and the basic pattern is from December 1982. The maps are scattered throughout the thirty years.

BP10 (Figure 3k) places Alaska under below normal heights everywhere. The basic pattern is from February 1971 and there are 6 maps similar to it. The pattern occurs from 1969–1971.

To summarize, the most common map featured a large positive anomaly centered over the ocean just south of the Aleutian Chain. The second most common map resembled the Aleutian Low pattern positioned over the western Gulf of Alaska

Surface Climate

Alaska's surface climate data were broken into ten geographic divisions (Figure 1) [NOAA, 1956–1986] and represented by monthly mean temperature and precipitation (Figure 2a–k). Results are presented by division as time series of seasonal averages of monthly data. The heaviest precipitation was seen in the divisions along the north and east boundaries of the Gulf of Alaska (Figure 2a,b,e). This was also the region of greatest variability in precipitation amounts. The driest period of the record was seen from the mid-1960s to the mid-1970s.

Temperature variability is greatest in the West Central and Interior Basin divisions. In all divisions, the temperatures in the 1950s were warmer than their respective divisional thirty-year mean values. The period from 1964 to 1977 was cold and dry. This departure was most pronounced in the Interior Basin and the coastal divisions. The coldest seasons occurred from 1968–1977. Gulf of Alaska sea surface temperatures and land-based temperatures were both lower than their respective divisional thirty-year mean values. In fact, throughout the records, the sea surface temperature seems to behave similarly to the land-based temperatures or vice versa. The period following 1977 is the most variable of the thirty-year record both from winter to winter and from division to division. It is generally warmer than the thirty-year mean values in all divisions.

Based on a linear trend at the 90% confidence level, only the Bristol Bay Division shows significant warming. Copper River Division shows the only significant precipitation trend—a decrease. In a broad sense, however, there appears to be a warming tendency in the Interior and coastal regions, a drier tendency in the Interior, and a wetter tendency along the Gulf of Alaska coastline. There is no indication of any change in the Arctic Drainage division.

Other trends may exist elsewhere in the state, but due in part to the cyclic nature of the data (especially temperature), they are not evident based on linear fits to the data. One such hidden trend might be the Gulf of Alaska sea surface temperatures which seem to exhibit a very low frequency oscillation of about 20 years [Royer, 1991].

Synoptic Climatology

As the final part of the study, Basic Patterns are now described in terms of the climate predominant during their occurrences. Table 2 shows the warm, cool, or mixed temperature, and wet, dry, or mixed precipitation characteristics of each of the Basic Patterns on a divisional basis and finally on a statewide basis.

Winter season monthly mean temperatures seem to be strongly tied to advective processes of heat transport and thus, atmospheric circulation. The coolest periods during the 1960s and 1970s appear in both SST and land temperature records. Douglas et al. [1982] found that the most prevalent 700-mb circulation present during that period had strengthened northerly flow. This corresponds well with the results presented here. During the cold period from 1964–1976, BP3 and BP8 (warm patterns) did not occur. Pattern 1 (cold, dry) was very common. During the period from 1977 on, BP1 did not occur, but BP2 (warm), BP3, and BP8 were common. This seems to indicate a strong connection between 700-mb circulation fluctuation and the variability in SST and land-based temperatures. This concept is also supported by Namias et al. [1988].

Unfortunately, the relation between precipitation and monthly mean circulation patterns is not as well defined. This may be due to the fact that precipitation is a shorter-period event and more sensitive to individual storms rather than monthly mean scale patterns.

SUMMARY

Alaska's winter climatology has been described in terms of the associated 700-mb geopotential height anomaly patterns and regional surface level temperature/precipitation records. In doing so, monthly scale circulation anomaly patterns have been classified into ten distinct basic categories. A total of 78% of the monthly anomaly maps from 1956-57 to 1985-86 can be classified ($r>0.60$) into these categories. Among the major features seen in these patterns are a positive or negative anomaly over the western Gulf of Alaska, a positive anomaly over Siberia, a negative anomaly over southeastern Alaska, and a zero height departure zone over the Interior Division.

Regional climate has been described in terms of its temperature and precipitation over the same thirty-year winter period (1956–1986). Ten climate divisions were used. The most variable precipitation occurred closest to the Gulf of Alaska. The most variable temperatures occurred in the Interior Basin and Arctic Drainage divisions. There appears to be a connection between the Gulf of Alaska sea surface temperatures and the precipitation variability in the coastal divisions and a connection with the temperatures throughout the state. On a seasonal scale, it was shown that the coldest extended period occurred from 1964–1975, the warmest extended period was prior to that. The most variable winters

and, in a few cases, the warmest winters followed after 1975. A linear least squares fit to the time series of winter season average temperatures and precipitation indicates the possibility of a significant (90% CI) warming in the Bristol Bay Division and a slight warming (though not significant at 90% CI) in the Interior Basin division.

Seasonal precipitation averages were quite variable throughout the state, and from season to season. The linear trend approximation indicates a tendency towards wetter in the Southwestern Islands division and a significant drying in the Copper River division.

When the atmospheric circulation anomalies were combined with the surface climate, associations were quite evident. The basic patterns could, in fact, be defined according to the most prevalent climatic characteristics of a region, as specific patterns tended to exist during specific types of weather. Warm and/or wet patterns were not present during the cold, dry winters, but they were present in the periods prior and after. Patterns with local northwesterly/northerly and, in some cases, westerly flow occurred concurrently with cool SST and cool air temperatures. Overall, however, precipitation was not well described by the monthly anomaly patterns.

This research was meant to serve as a foundation for future Alaska climate research. Although it has provided new information about Alaska's winter climate, there is still much more work yet to be accomplished in terms of understanding Alaskan climate and its role in the Arctic climate system.

REFERENCES

Anderson, J. R., J. R. Gyakum, and M. Nadeau, Pacific Ocean cyclone regimes and global circulation patterns, *Proc. Palmen Mem. Symposium*, preprint, 1988.

Barnston, A. G., and R. E. Livezey, Classification, seasonality, and persistence of low-frequency atmospheric circulation patterns, *Mon. Wea. Rev.*, *115*, 1083–1126, 1987.

Barry, R. G., The cryosphere and climatic change, in Detection of CO_2 induced climate change, *DOE/ER-2035*, pp. 109–148, U.S. Dept. of Energy, 1985.

Barry, R. G., and A. H. Perry, Synoptic Climatology—methods and applications, 555 pp., Methuen and Company, Ltd., 1973.

Bowling, S. (Ed.), Things are heating up in Alaska, *Geophys. Inst. Quarterly*, *6*, 1–4, 1989.

Bryan, K., and M. J. Spelman, The ocean's response to a CO_2-induced global warming, *J. Geophys. Res.*, *90*, 11679–11688, 1985.

Cane, M. S., Oceanographic events during El Nino, *Science*, 222, 1189–1195, 1983.

Douglas, A. V., D. R. Cayan, and J. Namias, Large-scale changes in North Pacific and North American weather patterns in recent decades, *Mon. Wea. Rev.*, *110*, 1851–1862, 1982.

Jenne, R. L., Data sets for meteorological research, *NCAR Tech. Note NCAR TN/IA-111*, 194 pp., 1975.

Kirchhofer, W., Classification of European 500mb patterns, *Swiss Meteorologische Institut Arbeits 3*, 16 pp., 1973.

Lachenbruch, A. H., and B. V. Marshall, Changing climate: geothermal evidence from permafrost in the Alaskan Arctic, *Science*, *234*, 680–695, 1986.

Lund, I. A., Map pattern classification by statistical methods, *J. Appl. Met.*, *2*, 56–65, 1963.

Milkovich, M. F., A synoptic climatology of Alaska: winter 700mb height anomaly patterns and surface climate variability 1956–1986, M.S. Thesis, 240 pp., Geophysical Institute, University of Alaska Fairbanks, Fairbanks, Alaska, 1989.

Namias, J., Some statistical and synoptic characteristics associated with El Nino, *J. Phys. Oceanog.*, *6*, 130–138, 1976.

Namias, J., *Short Period Climatic Variations, Collected Works 1934-1974*, 905 pp., U.C. San Diego, 1975

Namias, J., X. J. Yuan, and D. R. Cayan, Persistence of North Pacific sea surface temperature and atmospheric flow patterns, *J. Climate*, *1*, 682–703, 1988.

NOAA, Local climatological data—annual summary with comparative data–Alaska, USDOC NCC, 200 pp., 1956–1986.

Royer, T. C., Upper ocean temperature variability in the Northeast Pacific Ocean: an indicator of global warming?, *J. Geophys. Res.*, *94*, 18175–18183, 1991.

Walsh, J. E., and W. L. Chapman, Short-time climatic variability of the Arctic, *J. Climate*, *3*, 237–250, 1991.

Yarnal, B., A procedure for the classification of synoptic weather maps from gridded atmospheric pressure surface data, *Computers and Geosciences*, *10*, 397–410, 1984.

Yarnal, B., and D. A. White, Subjectivity in a computer-assisted synoptic climatology I: classification results, *J. Climo.*, *7*, 119–128, 1987.

AD-P007 290

A Two-Year Record of the Climate on the Greenland Crest from an Automatic Weather Station

George A. Weidner and Charles R. Stearns
Department of Meteorology, University of Wisconsin-Madison, Madison, Wisconsin, U.S.A.

92-17972

ABSTRACT

An automatic weather station (AWS) was installed on the Greenland Summit (72.30°N, 38.00°W, 3210 m) in May 1987. The AWS unit operated for two years until May 1989 when it was moved to Fresh Air Site (72.82°N, 38.82°W, 3185 m), an air sampling site, where it is still operating. The AWS data were transmitted to the ARGOS data collection system on the NOAA polar-orbiting satellites. The AWS unit measures wind speed and direction, air temperature, and the relative humidity at a nominal height of 3 m, air pressure at the height of the electronics enclosure, and the vertical air temperature difference between 3.0 and 0.5 m. The latent and sensible heat from the snow surface to the air were estimated using the wind speed, vertical air temperature difference, and the relative humidity.

The data are compared with those from two earlier stations, Eismitte (70.90°N, 40.70°W, 3000 m) from September 1930 through August 1931 (Wegener's expedition) and Station Centrale (70.92°N, 40.64°W, 2993 m) from September 1949 through August 1951 (Victor's expedition). The winds observed at Cathy Site were quite similar to those observed at the two previous stations. Also, the large fluctuations in temperature observed during the winter months at the two historic stations were observed at Cathy Site. The transition from positive to negative values for the sensible and latent heat flux occurred in October.

INTRODUCTION

An automatic weather station (AWS) unit was placed at 72.30°N, 38.00°W on the Greenland Ice Sheet at an elevation of 3210 meters on 4 May 1987 at Cathy Site (see Figure 1). The AWS unit was the type used in the Antarctic and is described by Stearns and Weidner [1990]. The AWS unit measures air temperature, relative humidity, and wind speed and direction at a nominal height of 3 m above the surface, air pressure at the height of the electronics enclosure, and the air temperature difference between 3.0 and 0.5 m. The AWS unit was in place at Cathy Site for two years, being removed at the end of May 1989

The data are collected at 10-minute intervals and transmitted to the NOAA series polar-orbiting satellites. Of a possible 144 values at 10-minute intervals in 24 hours, 120 values are usually received, depending on a particular satellite orbit and the location of the AWS unit. The data are then formatted into three-hourly summaries similar to the Local Climatic Data sheets provided by the National Climate Center from observing stations in the United States. The following analyses are based on this data set.

COMPARISON WITH EISMITTE AND STATION CENTRALE

Historical data are available [Putnins, 1970] from the expeditions of Wegener (1930–1931) at Eismitte (70.90°N, 40.70°W, 3000 m) and Victor (1949–1951) at Station Centrale (70.92°N, 40.64°W, 2993 m). The locations are shown in Figure 1.

Air temperature data are compared in Figure 2. The data from the earlier expeditions are plotted so as to conform to the May through May time period at Cathy Site; thus monthly values are not necessarily consecutive. The large variability of the air temperature during the winter months

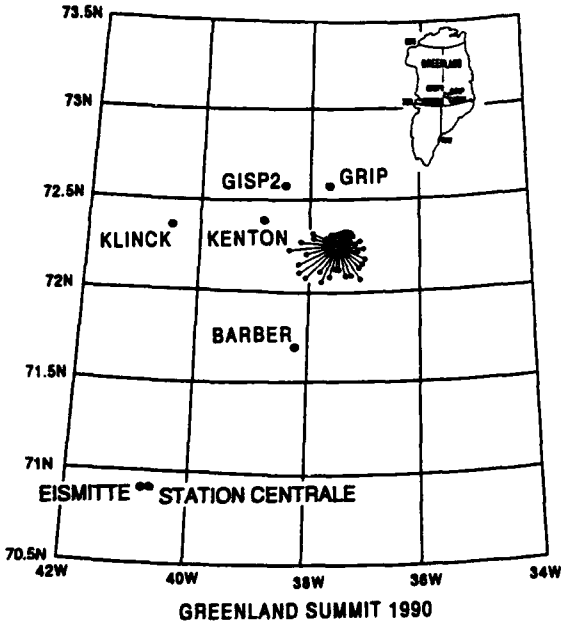


Figure 1. Map of Greenland Crest showing location of Cathy Site, Eismitte, and Station Centrale. The wind rose at Cathy site gives the percentage of wind observations in 10° wide sectors. The scale below the wind rose is the percent of observations related to the length of the lines used in the wind rose. AWS units were installed at GRIP, GISP2, and Kenton in June 1989.

observed at Eismitte and Station Centrale was also observed at Cathy site, as evidenced by the wide range in monthly mean values. However, May 1989 at Cathy site was colder by some 7°C than the other values. In November 1987 the maximum air temperature at Cathy site was -6.9°C (the same as May 1987) and the minimum was -55.2°C, a difference of 48°C. The standard deviation for the three-hourly values was over 10°C, compared with values of 3–4°C for AWS units in the interior of Antarctica. As others have observed it is the advection of warm air onto the Greenland Ice Sheet that regulates the climate of the interior during the winter months.

Figure 3 shows the monthly mean values of pressure at Cathy site for the 25 months of data available. There is again more variability during the winter months as one would expect given the more frequent and intense storm systems.

A wind rose showing percent of wind observations from each 10° wind direction sector is given in Figure 1. Winds were more frequently from the southwest quadrant at Cathy site than at Station Centrale, where two-thirds of observed wind directions were from 80 to 170° [Putnins, 1970]. Figure 4 gives the mean wind speed versus direction at Cathy site. Winds were strongest (5.1 m s^{-1}) on average from the 160°–170° and the 240°–250° sectors. The mean wind speed for the year was approximately 4 m s^{-1}. The aerovane would "freeze" up for extended periods during the winter months, introducing some bias in the monthly mean wind speed. Maximum wind speeds were frequently over 15 m s^{-1} with the absolute maximum wind speed observed equal to 20 m s^{-1}. Being near or at the Greenland crest the katabatic or downslope winds are not present at Cathy site.

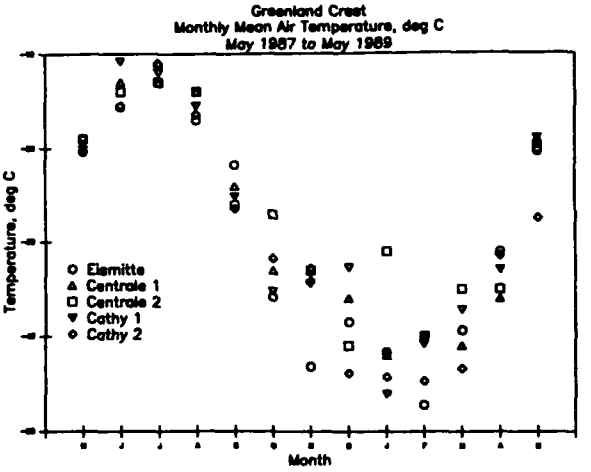


Figure 2. Plot of monthly mean temperatures for Cathy Site, Eismitte, and Station Centrale. Cathy 1 refers to the first year of data.

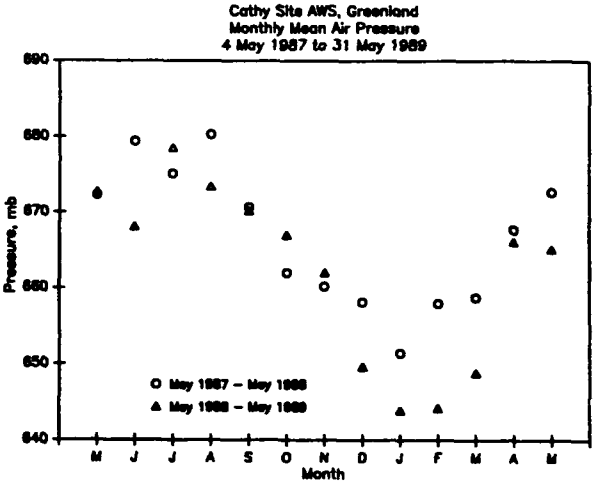


Figure 3. Plot of monthly mean pressures for Cathy Site.

SENSIBLE AND LATENT HEAT FLUX ESTIMATES

The bulk aerodynamic method based on the surface layer theory of Lettau [1979] for strong inversion cases is used to estimate the sensible heat flux using the vertical temperature difference, the wind speed, and an assumed surface roughness [Stearns, 1985]. The surface temperature, obtained from the sensible heat flux estimate and profile theory, determines the surface vapor pressure assuming saturation with respect to ice at the surface. Then an estimate of the latent heat flux can be made from the wind speed and the specific humidity difference between 3 m and the surface using the bulk aerodynamic method.

The bulk aerodynamic method of estimating the sensible and latent heat flux in the surface layer requires that the surface roughness and displacement height of the surface be known. The snow surface height increases with time relative to the AWS installation and the surface roughness may change with wind speed. A change of surface roughness from 0.3 mm to 1 mm increases the sensible heat flux by 20%. An increase in the displacement height of 0.25 m will increase the sensible heat flux by 25% for negative heat

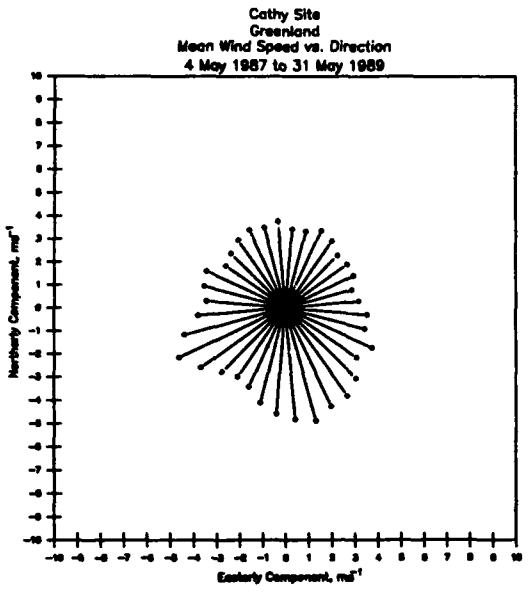


Figure 4. Mean wind speed as a function of 10°-wide wind direction sector for Cathy Site. The units of wind speed in the vertical and horizontal are m s^{-1} with positive values for an easterly and northerly wind direction.

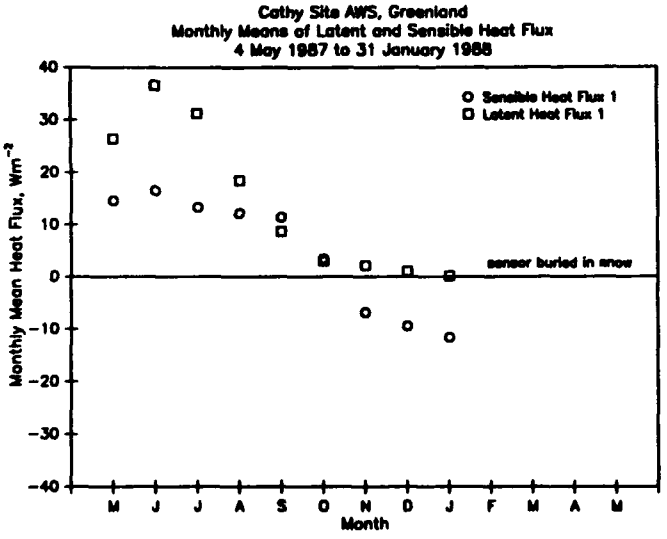


Figure 5. Plot of estimated monthly mean values of sensible and latent heat fluxes for May 1987 through January 1988.

fluxes and 50% for positive heat fluxes assuming a constant surface roughness. Because of the uncertainty in the value of the surface roughness and the displacement height the results are estimates and could be in error by as much as 50%.

Each data sample produces a heat flux value by an iterative method. The heat fluxes are then averaged for a mean value. Individual values of latent heat fluxes are also computed and then averaged. The estimated values for the first nine months of data are given in Figure 4. In February 1988 the bottom sensor became buried in snow. Positive values indicate heat fluxes away from the surface to the air. In order to reduce radiation errors as much as possible, fluxes were not computed when the wind speed was less than 1.0 m s^{-1}.

The values for sensible and latent heat fluxes agree with similarly obtained values from Antarctica using similar equipment and method [Stearns and Wendler, 1988]. However, the values of latent heat flux are greater than expected and correspond to the sublimation of ice amounting to the removal of about ten centimeters of ice from May through November 1987. Comparisons are being made between evidence from snow pits and the AWS data. The humidity sensor range of observations decreases with decreasing temperature until -40°C, at which temperature the output is essentially constant at 50%. The maximum value of relative humidity is less than ice saturation at temperatures below freezing. Thus it is not likely that reasonable values of latent heat flux can be obtained during the winter months.

The displacement height of the surface was also not taken into account. An acoustic depth gauge was not functioning correctly but in the future it is hoped that these devices can provide reliable surface height data. In addition, a future AWS unit measuring snow temperature profiles can provide another estimate of the snow surface temperature.

SUMMARY

The use of automatic weather stations in remote regions provides an excellent opportunity to provide long-term records of the local climate. The single AWS unit deployed on the Greenland Ice Sheet from May 1987 through May 1989 proved successful in operating in a climate as extreme as that found in the interior of Antarctica. With future modifications and expanded sensor inputs, an AWS could be a valuable tool in monitoring climate trends in remote regions.

ACKNOWLEDGMENTS

The AWS program in Greenland is supported by the National Science Foundation Division of Polar Programs grant 8821804. Field support is provided by the Polar Ice Coring Office, Fairbanks, Alaska, and transportation is provided by the 109th Air National Guard Group in Scotia, New York.

REFERENCES

Putnins, P., *World Survey of Climatology Vol. 14, Climates of the Polar Regions*, edited by S. Orvig, pp. 3–128, Elsevier, New York, 1970.

Lettau, H., Wind and temperature profile prediction for diabatic surface layers including strong inversion cases, *Boundary Layer Meteorology, 17*, 443–464, 1979.

Stearns, C. R., and G. A. Weidner, The polar automatic weather stations project of the University of Wisconsin, *this volume*, 1991.

Stearns, C. R., and G. Wendler, Research results from Antarctic automatic weather stations, *Rev. Geophys., 26*, 45–61, 1988.

AD-P007 291

92-17973

Snow Temperature Profiles and Heat Fluxes Measured on the Greenland Crest by an Automatic Weather Station

C. R. Stearns and G. A. Weidner
Department of Meteorology, University of Wisconsin-Madison, Madison, Wisconsin, U.S.A.

ABSTRACT

In June 1989 three automatic weather station (AWS) units were installed on the Greenland crest at the GISP2 (78.58°N, 38.46°W, 3205 m) and GRIP (78.57°N, 37.62°W, 3230 m) ice coring sites and at Kenton (72.28°N, 38.80°W, 3185 m), the air sampling site. The purpose of the AWS units is to measure the local meteorological variables, including snow temperatures at various depths, in support of ice coring studies. The AWS units measure wind speed and direction, air temperature, and relative humidity at a nominal height of 3.6 meters, air pressure at the electronics enclosure, and air temperature difference between 3.6 m and 0.5 m. The AWS units at GISP2 and GRIP also measure solar radiation, and seven snow temperatures from the surface to a depth of approximately 4 m in the snow. The data are updated at 10-minute intervals and transmitted to the ARGOS data collection system on board the NOAA series of polar-orbiting satellites. The air temperature and snow temperatures are presented as a function of time for the period from June 8, 1989 to August 31, 1990 and as tautochrones at 30-day intervals. The heat flux into the snow is determined from the daily mean snow temperature between the day after and the day before using the volumetric heat capacity of the snow assuming a snow density of 300 kg m^{-3}. The daily mean heat flux into the snow between the highest and the lowest levels of snow temperature is presented as a function of time.

INTRODUCTION

An automatic weather station (AWS) was installed at Cathy site (72.3°N, 38.0°W, 3210 m) on the Greenland Crest in May 1987. The AWS unit operated until June 1989 when it was removed and installed at Kenton (72.28°N, 38.80°W, 3185 m), the air sampling site. During the same month AWS units were installed at GISP2 (78.58°N, 38.46°W, 3205 m), the U.S. ice coring site, and at GRIP (78.57°N, 37.62°W, 3230 m), the European ice coring site. Figure 1 and Stearns and Weidner [1990] show the locations of the AWS sites on Greenland. The purpose of the AWS units is to monitor the meteorology on the Greenland Crest in support of the ice coring studies. The AWS units measure wind speed and direction, air temperature, and relative humidity at a nominal height of 3.6 m, air pressure at the electronics enclosure, the vertical air temperature difference between 3.6 and 0.5 m. The AWS units at GISP2 and GRIP also measure solar radiation, and seven snow temperatures from the surface to a depth of approximately 4 m in the snow. The data are transmitted to the ARGOS data collection system on board the NOAA series of polar-orbiting satellites. More details on the AWS unit are given in Stearns and Weidner [1990].

SNOW TEMPERATURE MEASUREMENT

The AWS units at GISP2 and GRIP are equipped with an Intersil ICL-7605 differential amplifier with a gain of 480 and an RCA-CD4097B eight-channel differential multiplexer. The snow temperature difference sensors are two-junction copper-constantan thermocouples inserted into 1/4-inch aluminum tubing 30 cm long, potted with room temperature vulcanizing rubber, and wrapped with aluminized

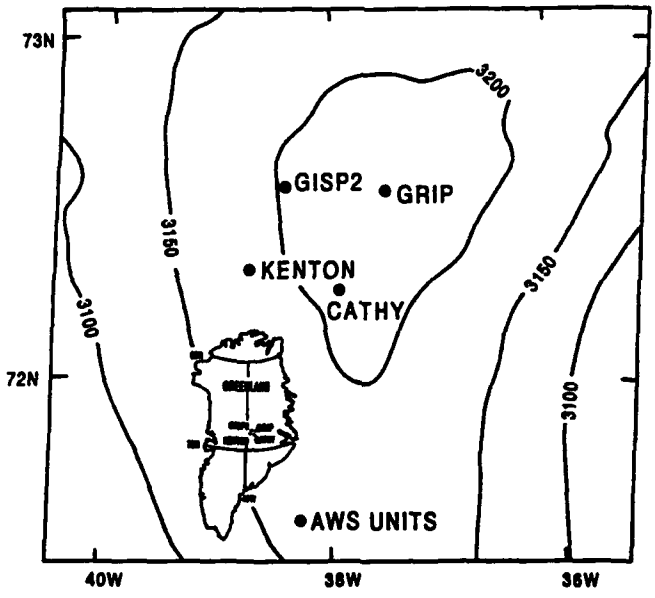


Figure 1. Map of Greenland showing the locations of the automatic weather station units as of June 1989. Cathy site operated from May 1987 to June 1989 then was moved to Kenton site at the GISP2 air sampling site. GISP2 and GRIP were installed in June 1989. The contour line units are meters above mean sea level. The insert map shows the locations of GISP2, GRIP, and Kenton sites on Greenland.

mylar to minimize the absorption of solar radiation. The snow sensor depths at the time of installation are 0.20, -0.05, -0.30, -0.55, -1.05, -2.05, and -4.0? m. The sensors from -0.05 m to -2.05 m were inserted horizontally into the corner of a 2-m-deep pit about 4 m from the AWS tower relative to the snow surface at the time of installation. Negative depths are below the initial snow surface and positive depths are above the snow surface at the time of installation. The 0.20-m and unused 0.45-m sensors were supported above the snow with a styrofoam frame. The 0.20-m sensor was quickly covered with drifting snow probably due to the surface being disturbed during the installation of the AWS unit. The -4.0?-m sensor was installed by drilling a 6-inch-diameter hole in the bottom of the 2-m pit to a depth of more than 4 m from the surface. The exact depth of the -4.0?-m temperature sensor is not known but appears to be about -3.6 m. The thermocouple voltages are measured between adjacent depths and the snow temperature is measured at the -1.05-m level with a 1000-ohm resistance thermometer. Solar radiation, measured with a Kipp and Zonen solarimeter, and the air temperature between 0.5 and 3.6 m complete the eight multiplexer channels. The present values and the values 20 minutes earlier are transmitted to the ARGOS system at 10-minute intervals.

Data are used from June 8, 1989 to August 31, 1990 from the AWS unit at GISP2. The GRIP AWS data are not presented because the unit was received intermittently. The thermocouple voltages were converted to temperature differences based on the thermocouple voltage output as a function of temperature for two copper constantan junctions. Considering the vertical axis as positive upwards, a positive thermocouple output resulted when the higher sensor was warmer. Starting at the -1.05-m level, where the temperature was measured, the temperature differences were added to obtain the temperature at the next level up and subtracted for the next level down. Between 2 and 30 data sets at each level in the snow and air for each day are averaged to obtain the mean temperature for the day.

SNOW TEMPERATURE RESULTS

The snow surface level on the crest of Greenland changes during the course of the year and can amount to as much as 0.75 m/year increase in the height relative to the temperature profile. The actual snow accumulation around the AWS unit from June 8, 1989 to July 25, 1990 was about 0.5 m. The actual times of changes in the snow level are not known.

Figure 2 shows the snow temperature tautochrones or lines of constant time as a function of depth on the ninth day of each month from June 1989 to August 1990. Weller and Schwerdtfeger [1977] present snow temperature tautochrones measured at Plateau Station, Antarctica (78.25°S, 40.50°E, 3624 m) in 1967. At GISP2 the mean snow temperature at a depth of 4.0? m is -32.6°C and at Plateau Station is -60.5°C. Dalrymple et al. [1963] present snow temperature tautochrones measured at the South Pole (90.00°S, 2835 m) from March 1 to December 31, 1957. The annual mean temperature at South Pole was -50°C and the annual range of temperature at the snow surface was 42°C. The annual range of temperature at 0.20 m at GISP2, based on Figure 2, is 43°C and at Plateau Station the annual range of temperature is about 35°C. The annual range of temperature is similar for the three sites but the mean values at -4.0 m differ significantly. The AWS sites at D-80 (70.02°S, 134.72°E, 2500 m), Dome C (74.50°S, 123.00°E, 3280 m), and Clean Air (90.00°S, 2835 m) had mean air temperatures of -41.6°C, -51.5°C, and -51.0°C respectively in 1989 [Keller et al., 1990] which should be comparable to the mean snow temperature at a depth of -4 m. The higher mean 4.0?-m snow temperature at GISP2 is due to something other than just differences in latitude in comparison to Antarctica. D-80 is 10°C colder although 2° latitude farther from the pole and 730 m less in elevation above sea level than GISP2. The difference in mean annual temperatures are likely due to the frequent advection of warm air onto Greenland. Examples of that are apparent in Figure 2 for December 9, 1989. Figure 3 shows the daily mean air temperature at 3.6 m and the daily mean snow temperature at -0.55 m versus the number of the day starting with June 8, 1989. The December 9, 1991 day number is 185 and several periods of higher air and -0.55-m snow temperatures are apparent. The GISP2 air temperature seldom dropped as low as the annual mean temperature at Plateau Station. The rapid increase in the GISP2 air temperature that occurred about May 2, 1991 or day 328 is a characteristic spring for the three years of AWS data on the Greenland Crest. Figures 3, 4, 5, and 6 show the daily mean snow temperature records for 0.20 m and -1.05 m, -0.05 m and -2.05 m, and -0.30 m and -4.0? m, respectively. The snow temperatures at the two levels nearest the surface were frequently higher than the air temperature during the months of June, July and August.

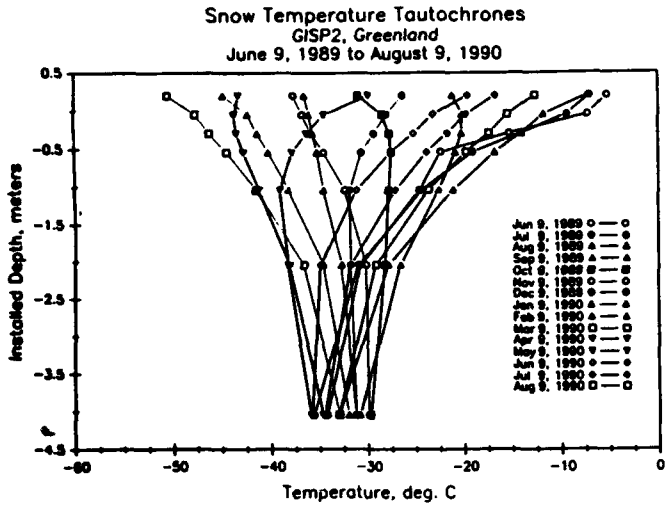


Figure 2. Daily mean snow temperature tautochrones or lines of constant time from June 1989 to August 1990 at the GISP2 site. The dashed line is used for tautochrones that use the same symbol the second time. The depth of the -4.0?-m temperature sensor is uncertain and may actually be -3.6 m.

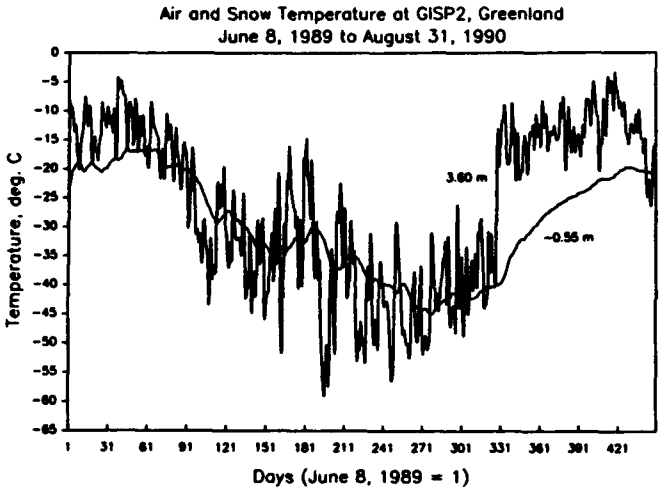


Figure 3. Daily mean temperature versus days starting with June 8, 1989 as 1 for the air temperature at 3.6-m and the -0.55-m snow temperature.

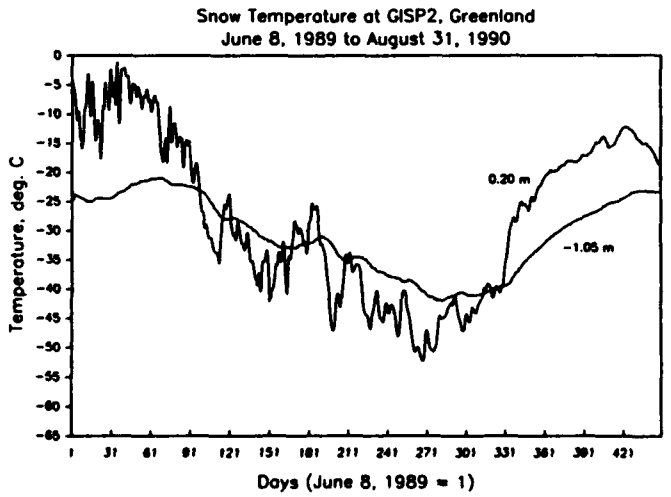


Figure 4. Daily mean temperature versus days starting with June 8, 1989 as 1 for the snow temperature at 0.20 m and the -1.05 m.

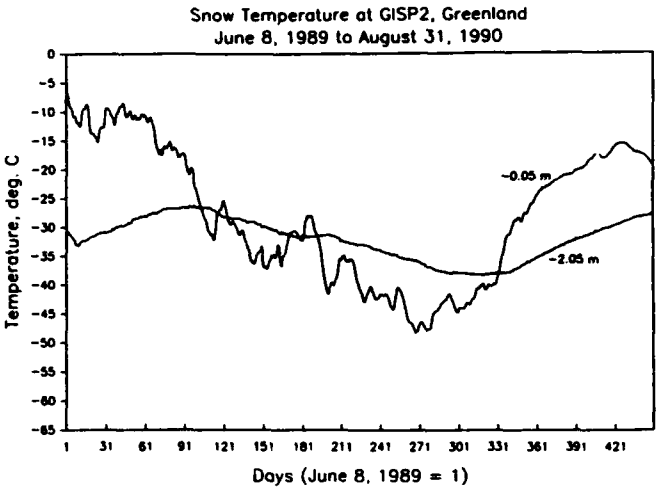


Figure 5. Daily mean temperature versus days starting with June 8, 1989 as 1 for the snow temperature at -0.05 m and the -2.05 m.

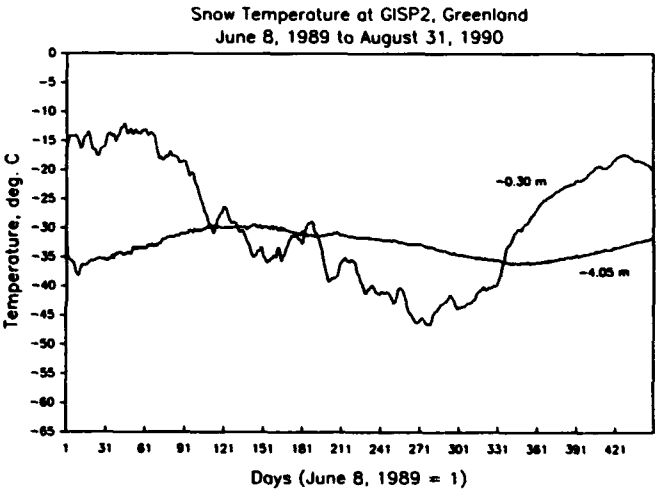


Figure 6. Daily mean temperature versus days starting with June 8, 1989 as 1 for the snow temperature at -0.30 m and the -4.0? m.

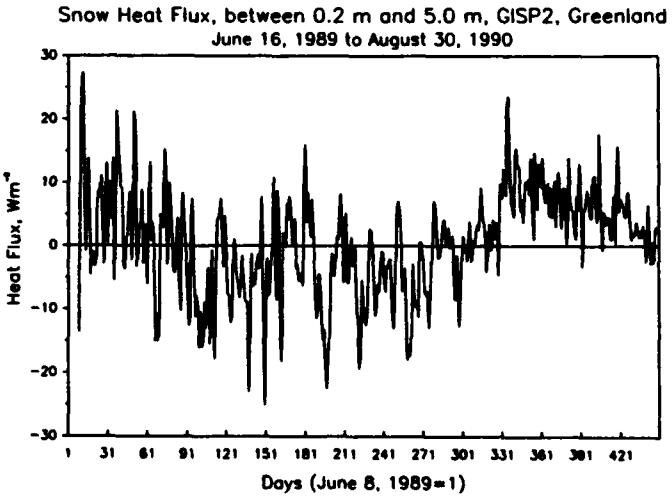


Figure 7. The snow heat flux between the 0.20-m and the -5.0-m levels centered on the indicated day number. The snow heat flux is based on the estimated volumetric heat capacity of the snow and the daily mean snow temperature difference between the day after and the day before the indicated day.

SNOW HEAT FLUX

A depth interval corresponding to one-half the depth interval between the sensors above and below the level of temperature measurement is assigned to each snow temperature level. The -4.0?-m level is assigned a depth interval of 1 m lower for estimating the heat flux at that level. The uncertainty about the depth of the -4.0?-m level is neglected. The volumetric heat capacity of the snow is estimated to be 1.26 x 106 J m^{-3} $°C^{-1}$ assuming the snow density is 300 kg m^{-3}. The difference in the heat storage between the next day and the previous day divided by the time interval in seconds gives the heat flux in W m^{-2} between the 0.20-m level and the -5.0-m level for the present day. The results are shown in Figure 7 as a function of the day number. The data for the first ten days are not presented because the snow used to fill the snow pit was cooling. The snow heat flux is generally positive during the months of May, June, July, and August.

DISCUSSION

The AWS unit at GISP2 is performing satisfactorily and should provide two years of data for analysis using the method described by Dalrymple et al. [1963]. The annual mean temperature at GISP2 is significantly higher than the annual mean temperature at South Pole and Plateau stations due to the frequent advection of warm air onto the Greenland Crest. The annual snow accumulation on Greenland is greater than the Antarctic stations. The large accumulation of snow is expected to increase the difficulty of the data analysis especially near the snow surface.

The AWS unit does appear to be making reliable measurements of the temperatures in the snow. Another temperature profile system is planned for 1991 that increases the number of channels to 16, extends the depth to 16 m, and includes flux plates at the four upper levels of temperature measurement.

ACKNOWLEDGMENTS

Support was supplied by the National Science Foundation Division of Polar Programs grant 8821894, The Polar Ice Coring Office, and the 109th Air National Guard.

REFERENCES

Dalrymple, P. C., H. H. Lettau, and S. H. Wollaston, South Pole micrometeorology program: Data analysis, in *Studies in Antarctic Meteorology*, Antarctic Res. Ser., Vol 9, edited by J. M. Rubin, pp. 13–57, AGU, Washington, DC, 1966.

Keller, L., G. A. Weidner, and C. R. Stearns, *Antarctic automatic weather station data for the calendar year 1989*, 354 pp., University of Wisconsin, Madison, Wisconsin, 1990.

Stearns, C. R., and G. A. Weidner, The polar automatic weather station project of the University of Wisconsin, *this volume*, 1991.

Weller, G., and P. Schwerdtfeger, Thermal properties and heat transfer processes of low-temperature snow, in *Meteorological Studies at Plateau Station, Antarctica*, Vol. 25, edited by J. A. Businger, pp. 27–34, AGU, Washington, DC, 1977.

92-17974

AD-P007 292

Studies of -40°C Isothermal Layers at High Latitudes

R. E. Stewart
Cloud Physics Research Division, Atmospheric Environment Service, Toronto, Canada

C. A. Lin
Department of Meteorology and Centre for Climate and Global Change Research, McGill University, Montreal, Canada

ABSTRACT

Atmospheric soundings reveal that isothermal layers at temperatures near -40°C sometimes occur at high latitudes. In the absence of sufficient ice nuclei, supercooled water frozen by homogeneous freezing would act to produce such layers. The formation of such layers by homogeneous freezing should furthermore result in significant dynamic responses in the atmosphere.

INTRODUCTION

The existence of 0°C isothermal layers in the atmosphere is well documented [e.g., Stewart, 1984; Stewart and Patenaude, 1988; Stewart and Macpherson, 1989]. The basic process responsible for such layers, the melting of snow, was first noted by Findeisen [1940].

The homogeneous freezing of water at -40°C is another strongly temperature-dependent microphysical process [see for example Schaefer, 1949]. This process is also expected to produce isothermal layers in the atmosphere with temperatures of about -40°C. Within rising air, some of the associated supercooled water will begin to freeze at this temperature. The freezing would raise the air temperature just above -40°C and so homogeneous freezing would cease. With continual ascent, the air would again cool to -40°C, more water would freeze and the cycle would continue until all of the water had frozen. Stewart and Lin [1991] showed that layers having temperatures near -40°C sometimes occur within extra-tropical cyclones.

In this paper, we will show that high latitude soundings sometimes contain layers having temperatures near -40°C, we will examine the possibility that homogeneous freezing contributed to their formation, and we will discuss some of the implications of such temperature perturbations on the atmosphere.

OBSERVATIONS OF NEAR -40°C ISOTHERMAL LAYERS

Rawinsonde information from a site in the Arctic and in the Antarctic were examined in order to determine whether isothermal layers near -40°C occurred at high latitudes. The site in the Arctic was Alert, North West Territories. Alert is located at 82°30'N, 62°20'W. The site in Antarctica was Molodeznaja, located at 67°40'S, 45°51'E.

Many layers exceeding 5 kPa in depth and occurring at temperatures near -40°C were found in the 27 years of data (1961–1987) from the Arctic. About 1% of the soundings illustrated such a layer. One such layer is illustrated in Figure 1. Such layers either occurred near the surface or aloft.

Ten years of rawinsonde observations over Antarctica (1978–1987) revealed that -40°C layers also occurred in this region but they were very rare (<0.1%). One such sounding is illustrated in Figure 2. The lapse rate below the -40°C layer was close to being neutrally stratified. Temperatures aloft consistently dropped to -65°C or lower.

When the Antarctic soundings were checked to determine whether a change in lapse rate occurred within a degree of -40°C, the results showed that many such cases occurred. Over 15% of the soundings illustrated this characteristic. As in the Arctic, the change in lapse rate occurred either near the surface or aloft.

FORMATION OF NEAR -40°C LAYERS

The amount of freezing or melting required to produce an isothermal layer near -40°C and 0°C, respectively, can be estimated. The basic governing equation relates the heat liberated upon freezing or extracted upon melting to the ensuing atmosphere temperature change accompanying such phase changes [Lin and Stewart, 1991].

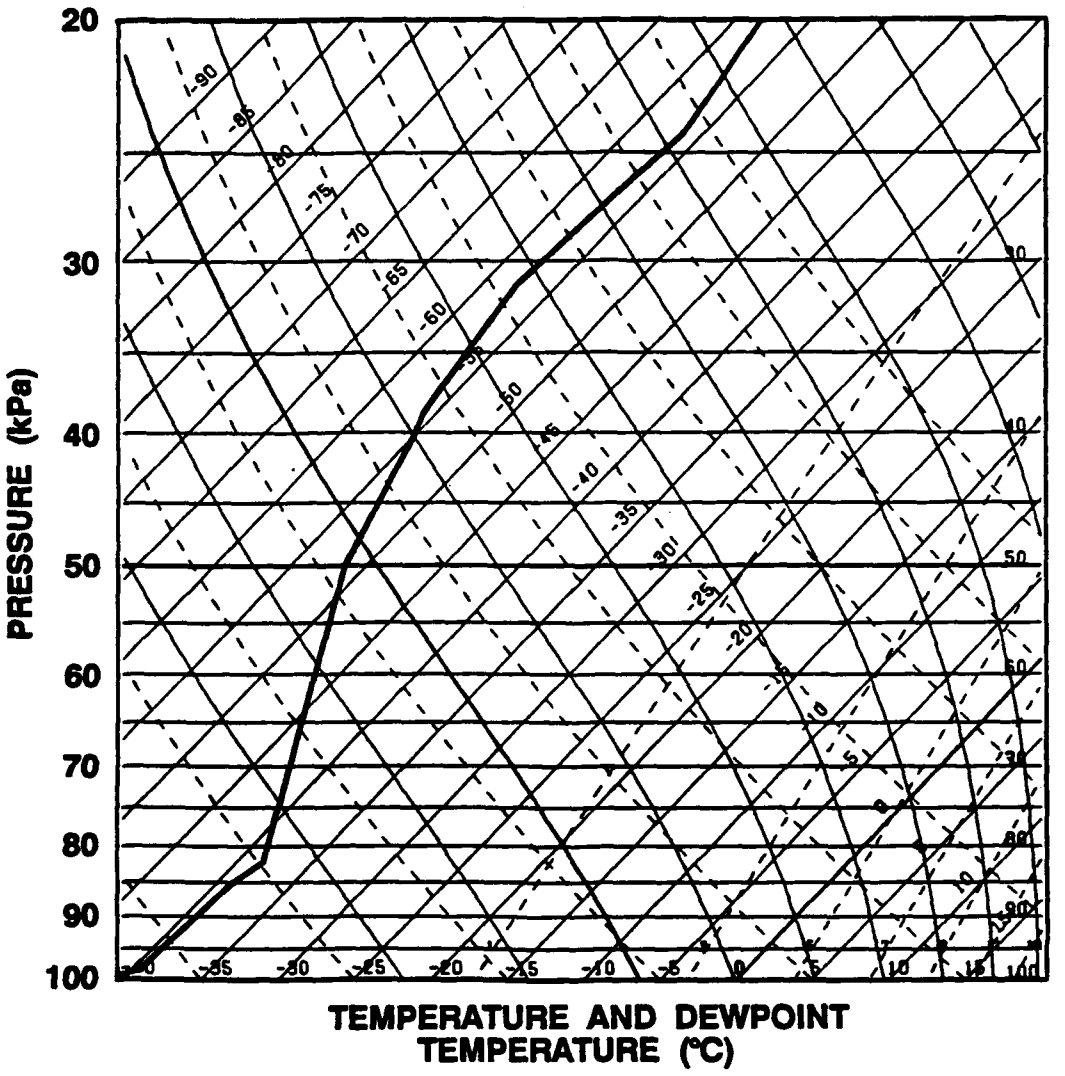


Figure 1. A skew T-log p diagram from Alert at 1200 UTC on February 7, 1979. Only temperatures are available.

Figure 3 shows the influence of homogeneous freezing and melting on an initial sounding having a lapse rate of 5°C km^{-1}. It is evident that small amounts of freezing and melting can affect a significant depth of the atmosphere. Convective overturning should also be associated with the formation of these layers. Absolute instability should be produced at the top of the -40°C layer by heating and at the base of the 0°C layer by cooling.

The amounts of water required to produce significant temperature perturbations in the atmosphere are potentially available. For example, Stewart and Lin [1991] determined the amount of liquid water which is available for freezing at -40°C within ascending air. They further showed that detectable near -40°C layers could be produced in the absence of heterogeneous ice nucleation even if surface temperatures were -30°C. Horizontal advection could also carry more liquid water into a region than expected from the simple ascent of air.

CONSEQUENCES OF NEAR -40°C LAYERS

The formation of near -40°C layers will affect the dynamics of the atmosphere. The effect should be similar to but opposite to that associated with the production of near 0°C layers by melting.

Lin and Stewart [1986] showed that the cooling of the atmosphere by melting would produce descent below the region of melting and ascent in adjacent areas. In a baroclinic environment, Szeto et al. [1988] further showed that ascent should preferentially occur over the region having temperatures everywhere below 0°C. The overall circulation would be "thermally indirect" in the sense that descent would occur over the "warm" air subjected to melting and ascent would occur over the "cold" air not subjected to melting.

Stewart and Lin [1991] showed that homogeneous freezing would lead to ascent within the region subjected to the warming and to descent in the adjacent areas. In a baroclinic

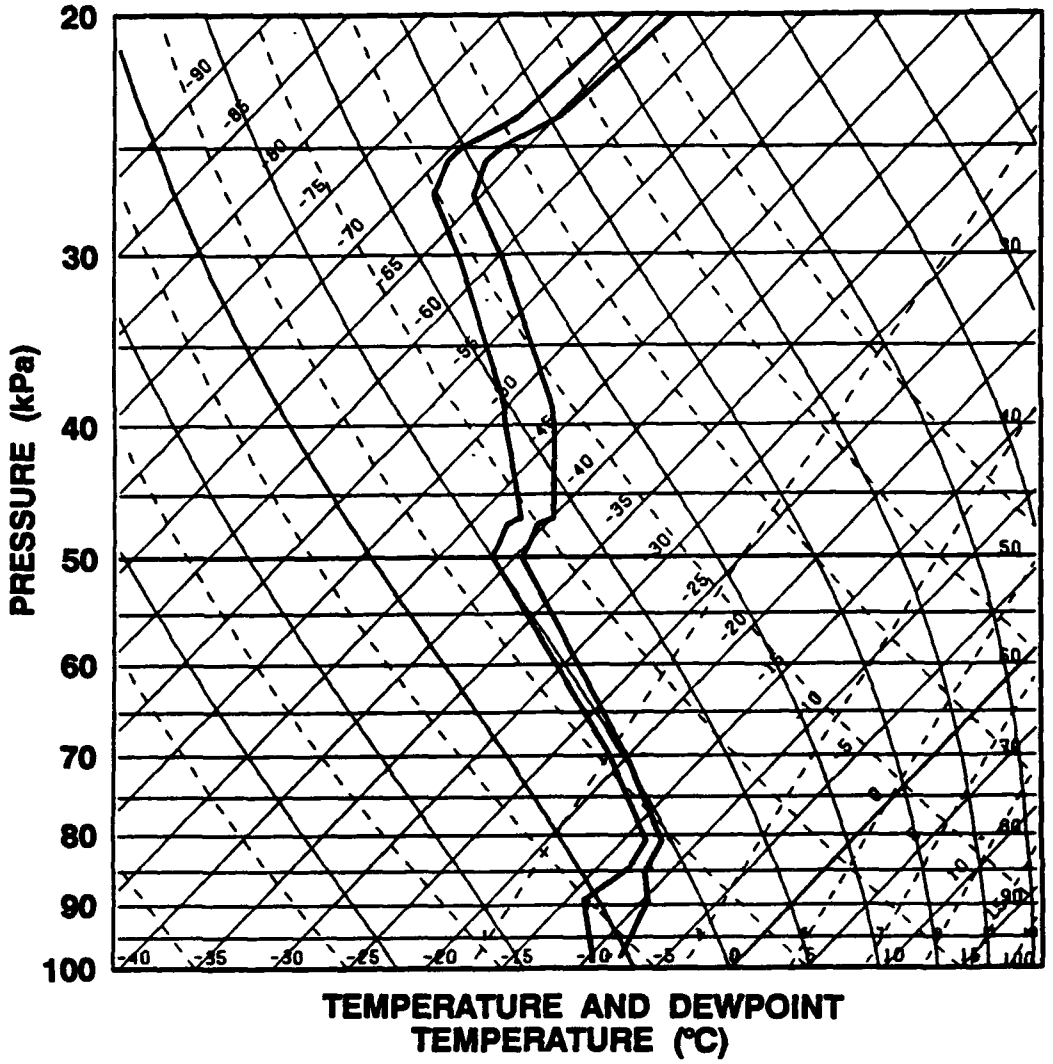


Figure 2. A skew T-log p diagram from Molodeznaja, Antarctica at 1200 UTC on May 16, 1982. Both temperature and dew point temperature are plotted but the measurement of dew point temperature is sometimes subject to considerable uncertainty.

environment, a circulation should develop in a manner similar to that discussed by Szeto et al. [1988]. In the case of homogeneous freezing, however, the circulation should be "direct" with ascent occurring within the region at and warmer than -40°C and descent occurring in the region everywhere below -40°C (Figure 4). At high latitudes, this would normally mean that descent should be driven to occur on the poleward side of the circulation.

CONCLUDING REMARKS

We have shown that isothermal layers or perturbations to the environmental lapse rate sometimes occur at temperatures near -40°C. Such layers or perturbations are found in the Arctic, Antarctic, and mid-latitudes. Homogeneous freezing of water, which, like melting, is a strongly temperature-dependent microphysical process, is one means of producing such layers. The production of such regions should also lead to dynamic consequences in the atmosphere with homogeneous freezing leading to "thermally direct" circulations.

The formation of layers or perturbations at particular temperatures requires the presence of precipitation-sized ice particles near 0°C and small water droplets near -40°C. The latter situation may occur relatively infrequently but the presence of polluted air would undoubtedly decrease its likelihood even more. Any ice nuclei linked with the polluted air [Pearson and Smith, 1975] would freeze more of the water at warmer temperatures and there would be less liquid available for homogeneous freezing.

The likelihood of homogeneous freezing at high latitudes should consequently have evolved with time. Before the industrial revolution, the Arctic air, especially in winter, should have been quite pristine. With the land being covered by snow and ice for thousands of kilometers, there would be few local sources of ice nuclei. More of the moisture advected into the region, sublimated from the surface, or

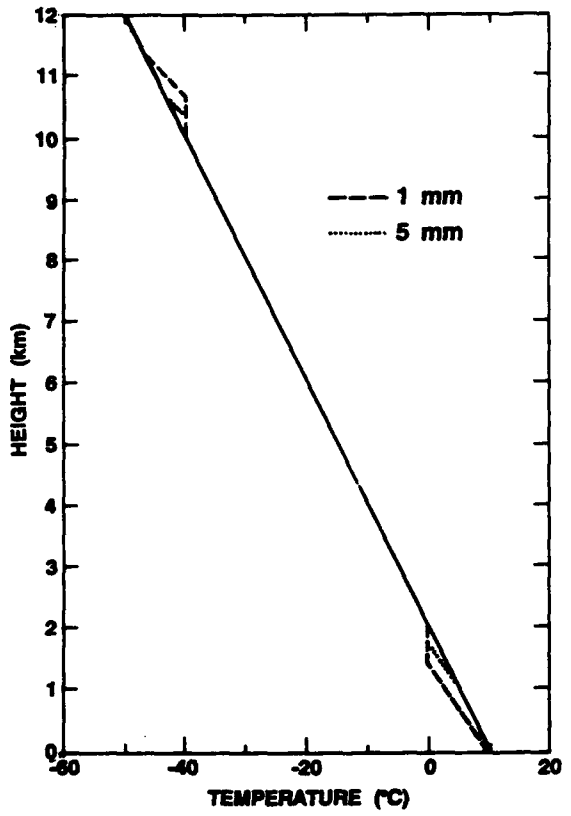


Figure 3. The temperature changes to an initial 5°C km^{-1} lapse rate associated with homogeneous freezing at -40°C and melting at 0°C. The depth of the liquid precipitation undergoing a phase transition is indicated.

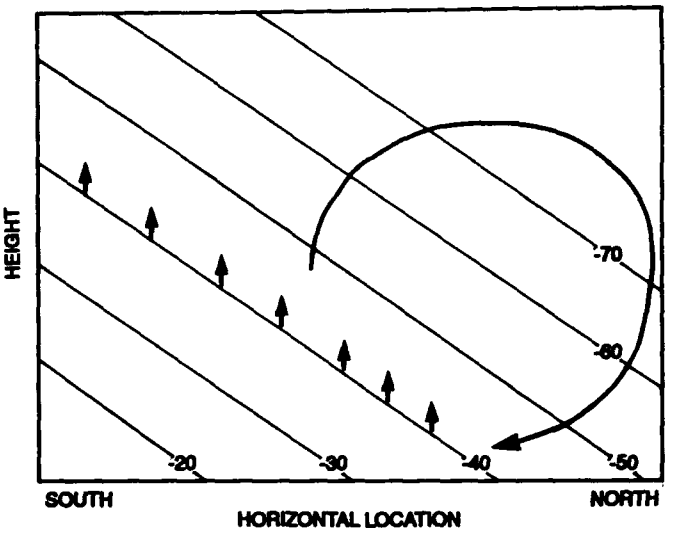


Figure 4. Schematic diagram illustrating the potential circulation resulting from homogeneous freezing in the northern hemisphere. Isotherms (°C) are shown.

evaporated from open ocean may have remained vapor or liquid unless subjected to homogeneous freezing. In the present polluted environment, more plentiful ice nuclei would be expected to freeze more of the liquid at warmer temperatures. From this perspective, there should be a distinct pollutant-produced signature on the nature of the high latitude environment. The production of temperature perturbations near -40°C should be reduced and the dynamic response of the atmosphere to such perturbations should be correspondingly decreased.

Although it is suggested that homogeneous freezing could contribute to the formation of near -40°C layers, other processes may be responsible for some of the observations as well. Perhaps subsidence and/or thermal advection can also produce the observed effects. To determine the actual formation processes, it is crucial that detailed in-situ observations be made. These observations would need to include the measurement of liquid water as well as the determination of the basic state parameters.

In summary, microphysical processes operating only near specific temperatures can alter the thermodynamic and dynamic nature of the atmosphere. Whether the polar regions are pristine or polluted may affect the likelihood and consequences of such processes.

REFERENCES

Findeisen, W., The formation of the 0°C isothermal layer and fractocumulus under nimbostratus, *Met. Zeit.*, *57*, 49-54, 1940.

Lin, C. A., and R. E. Stewart, Mesoscale circulations initiated by melting snow, *J. Geophys. Res.*, *91*, 13229-13302, 1986.

Lin, C. A., and R. E. Stewart, Diabatically forced mesoscale circulations in the atmosphere, *Adv. Geophys.*, 1991, In press.

Pearson, R. W., and D. W. Smith, Fairbanks: a study of environmental quality, *Arctic*, *28*, 99-109, 1975.

Schaefer, V. J., The formation of ice crystals in the laboratory and the atmosphere, *Chem. Rev.*, *44*, 291-320, 1949.

Stewart, R. E., Deep 0°C isothermal layers within precipitation bands over southern Ontario, *J. Geophys. Res.*, *89*, 2567-2572, 1984.

Stewart, R. E., and C. A. Lin, Strongly temperature dependent microphysical processes and the atmosphere, *J. Geophys. Res.*, 1991, Submitted.

Stewart, R. E., and S. R. Macpherson, Winter storm structure and melting-induced circulations, *Atmos.-Ocean*, *27*, 5-23, 1989.

Stewart, R. E., and L. M. Patenaude, Rain-snow boundaries and freezing precipitation in Canadian East Coast winter storms, *Atmos.-Ocean*, *26*, 377-398, 1988.

Stewart, R. E., R. W. Shaw, and G. A. Isaac, Canadian Atlantic Storms Program: the meteorological field project, *Bull. Amer. Meteor. Soc.*, *68*, 338-345, 1987.

Szeto, K. K., R. E. Stewart, and C. A. Lin, Mesoscale circulations forced by melting snow. Part 2: application to meteorological features, *J. Atmos. Sci.*, *45*, 1642-1650, 1988.

AD-P007 293

92-17975

Variations in Cloudiness, Temperature and Satellite-Derived Outgoing Longwave Radiation for Alaska

Gerd Wendler
Geophysical Institute, University of Alaska Fairbanks

ABSTRACT

Monthly values of outgoing longwave radiation (OLR) from 1974 to 1990 were obtained from NOAA satellites. Seasonal variations in the OLR were related to cloudiness and surface temperature data for Alaska. It was found that higher amounts of cloudiness increase the OLR in winter for most of Alaska, but decrease it in summer.

For one particular location, Barter Island, trends in cloudiness, temperature, and OLR will be discussed and the seasonal sensitivity of OLR to changes in cloud amount will be examined. For Barter Island, a decrease of less than 7% in the amount of cloudiness was found to decrease the OLR by 5 W m^{-2} during the spring months, a season in which cloudiness and OLR are positively correlated. During the summer, however, OLR and cloudiness are anti-correlated owing to the relatively cold radiative temperatures at cloud-top height compared to the surface temperature in the absence of strong surface temperature inversions, which persist for most of the rest of the year. Hence relatively small changes in the amount of cloudiness may have a large effect on the radiation balance in the Arctic, even more so than changes expected due to increasing concentration of CO_2 and other radiatively active gases. As parameterization of sky cover in GCMs is not well advanced, studies like this should help in a better quantitative understanding of sky cover and OLR.

INTRODUCTION

General circulation models (GCMs) predict large temperature increases due to the increase in CO_2 and other trace gases in the atmosphere [e.g., NRC, 1982; Ramanathan, 1988; Mitchell, 1989]. The magnitude of these increases has recently been disputed [Budyko and Sedunov, 1988; Ellsaesser, 1990], because GCMs predict much larger temperature increases for the last century than what has actually been observed [Lindzen, 1990]. Large uncertainties exist due to difficulties in modeling feedback mechanisms, especially the effect of cloudiness on the radiation balance.Since 1974 NOAA has collected satellite-derived OLR data from the NOAA satellite series and reduced it to a monthly format on a 2.5° latitude–longitude grid [Winston et. al., 1979; Janowiak et al., 1985]. The data are not totally consistent over time, since they were derived from different satellites equipped with different sensors. Neither the spectral window nor the time of the equator crossing have been constant over time. Furthermore, there is a ten-month period in 1978 for which no data were obtained. However, corrections to account for these differences have been carried out and the data present a unique and valuable data source [e.g., Janowiak et al., 1985].

Until now, OLR data have been successfully used in tropical regions, especially in relating OLR to rainfall amount over ocean surfaces [Winston et. al., 1977; Murakami, 1980; Prasad et. al., 1985; Arkin et. al., 1989; Haque and Lal, 1991]. In this study, I attempt to use these data for arctic and subarctic regions, where models predict that the maximum warming should occur due to increased CO_2 content.

RESULTS

Adjacent grid points showed similar values of outgoing longwave radiation as long as the terrain characteristics

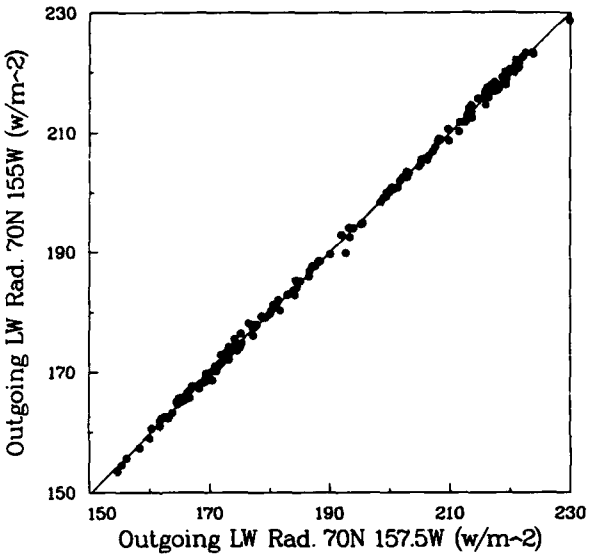


Figure 1. Outgoing longwave radiation (OLR) as derived from satellite measurements for two adjacent grid points (70°N, 155°W and 157.5°W). The area is in northern Alaska, with uniform surface characteristics (tundra).

were fairly homogeneous. Large uniform areas are found in northern Alaska (North Slope) where tundra underlain by permafrost exists. In Figure 1 monthly data points for two adjacent grid points (70°N, 155°W and 157.5°W) are plotted against each other. A very good correlation exists (correlation coefficient larger than 0.99) in this case. Such tests for many different pairs of data points indicated that spatial consistency in the data exists.

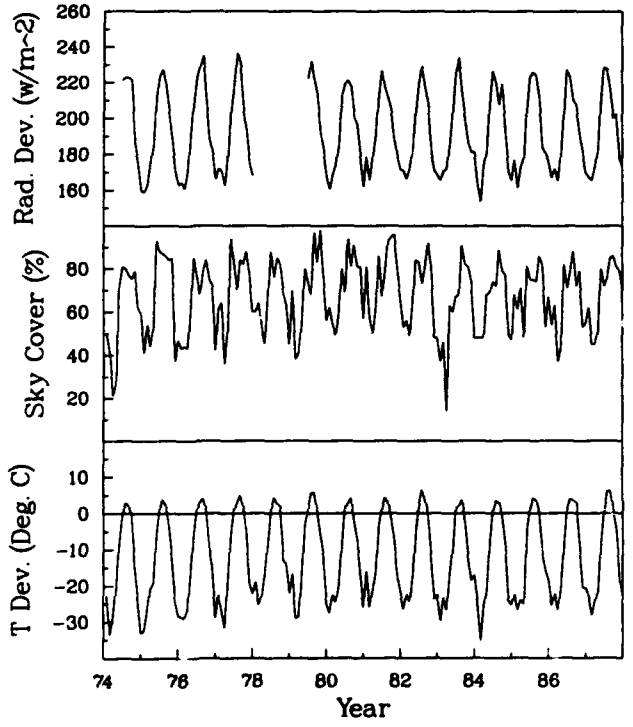


Figure 2. Time series of (a) outgoing longwave radiation (70°N, 142.5°W), (b) amount of sky cover, and (c) temperature for Barter Island (70°8'N, 143°38'W). Radiation and temperature have well-developed annual cycles, with maxima in summer and minima in winter. For cloud cover a less well-established annual cycle can be observed with maxima in late summer.

The following analysis pertains to Barter Island, located at 70°8'N, 143°38'W, which is in contrast to Barrow, where a large amount of development has occurred during the last two decades, a pristine site. Barrow and Barter Island are the only long-term first class weather stations in arctic Alaska (NOAA 1974–1989). It should be pointed out that the cloud data in winter are probably not very reliable because observations during times of continuous darkness are difficult.

A time series of the sky cover and temperature for Barter Island and the OLR data for 70°N, 142.5°W is shown in Figure 2. Large annual variations exist in all three traces, OLR and temperature having their maxima in summer and minima in winter, while cloudiness has its maximum in late summer, and its minimum in spring. Because the annual variations are so large, significant trends are difficult to detect. Tendencies in the data are easier to detect by studying the deviations from the means shown in Figure 3. In this figure deviations have been smoothed using a 12-point running average. The deviation in the smoothed outgoing longwave radiation varies between about +3.5 to -2.5 W m^{-2}. Beginning in 1974, we see an increase peaking around 1978–1980; thereafter the values decrease significantly, leveling off between 1982–1986, and have rapidly increased again since 1987. The time series are much too short for testing for periodicities. Generally speaking, however, there is no clear overall trend, but instead an indication of a cyclic behavior, seen in the temperature record elsewhere in Alaska [Milkovich, 1989].

Cloudiness showed a variation of ±8% for the smoothed time series. No clear relationship between OLR and cloudiness can be seen. The smoothed temperature trace correlates better with the OLR. Temperature showed a strong increase of 5°C from 1974 to 1978, then dropped in the mid-eighties

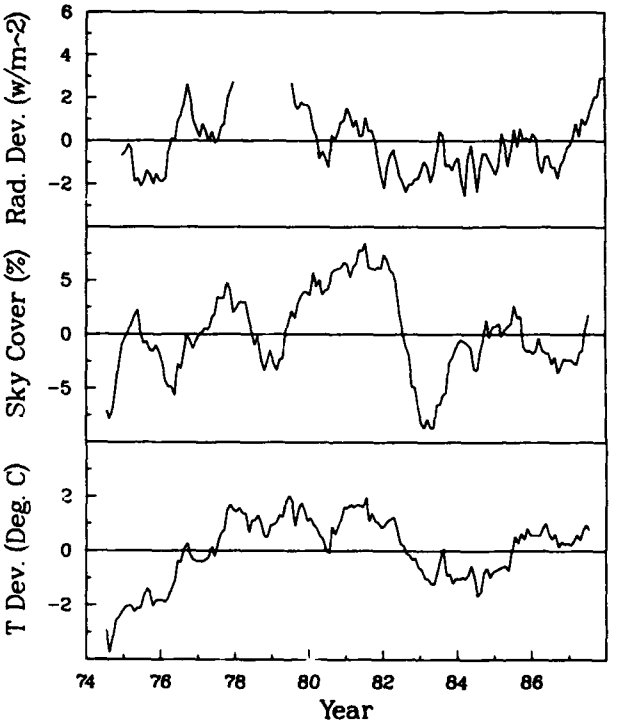


Figure 3. Deviation from the mean (mean annual cycle was deducted) of (a) outgoing longwave radiation, (b) cloudiness, and (c) temperature for Barter Island. These curves were smoothed with a 12-point running average.

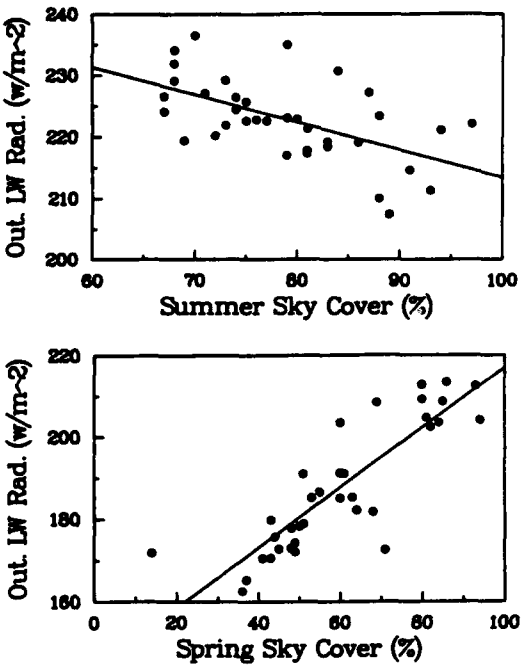


Figure 4. Outgoing longwave radiation, plotted against the amount of cloud cover for Barter Island. It can be seen that for (a) summer (June, July and August) the radiation values increase with decreasing cloudiness, and for (b) spring (March, April and May) the radiation increases with increasing cloudiness.

by 3°C and has recently increased again, but to slightly lower values than around 1980 following similar tendencies as for the OLR record.

In Figure 4, the OLR is plotted against sky cover. If one does this for all the data points, lots of scatter and no clear relationship are observed. However, if one produces seasonal scatter plots clear relationships are revealed. During summer [June, July, August (Figure 4a)] for instance the radiation flux decreases with increased cloudiness. This is understandable since the atmosphere gets colder with height, and during times of increased cloudiness, the clouds radiating at relatively cold temperatures contribute a large part to the measured OLR. There is a fair amount of scatter probably due to competition between and greenhouse effects of different cloud types and surface properties. A correlation factor of -0.59 was found. If one fits a straight line through the data using the least squares method, this line would give a decrease of 5 W m^{-2} for an increase of cloudiness of 8%. For each of the other seasons the opposite relationship holds; that is, increased sky cover tends to increase the OLR. This is explained by the semi-permanent strong surface inversions [Billelo, 1966; Wendler and Nicpon 1975] that exist in the Arctic. Since clouds are warmer than the surface under inversion conditions they radiate at higher effective temperatures and thus the OLR increases. Also during the dark season competing albedo effects of clouds are non-existent, hence there is no negative shortwave cloud effect. This feature is illustrated in Figure 4b for spring at Barter Island, where we observed a positive correlation coefficient of 0.86. Now a decrease of 5 W m^{-2} would be caused by a decrease in cloudiness of 7%.

Temperature and OLR were generally correlated; with increasing temperatures increasing values of OLR were

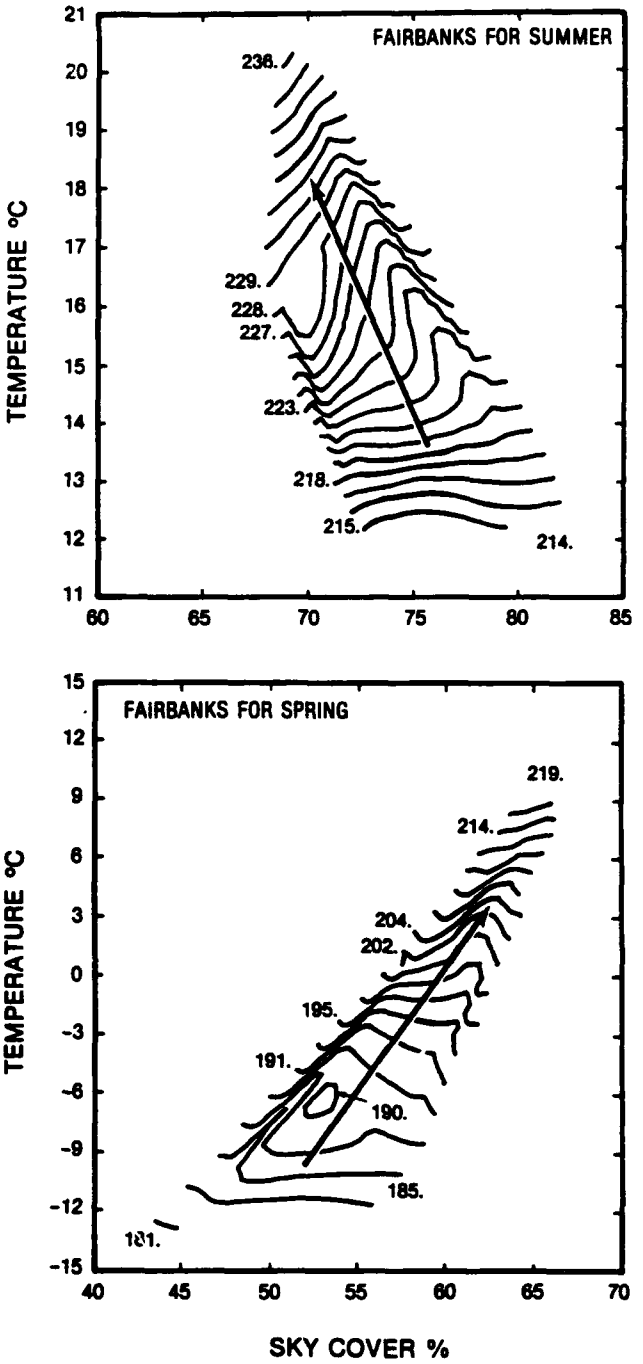


Figure 5. Outgoing longwave radiation (65°N, 147.5°W) as a function of cloudiness and temperature for Fairbanks (64°49'N, 147°52'W). The data was smoothed before the contours were calculated. For summer the radiation values increase with increasing temperature and decreasing cloudiness, while for spring the radiation flux increases with increasing temperature and increasing cloudiness.

observed. In Table 1 the correlation factors for all seasons and for the stations located in arctic, continental, and maritime southern Alaska are presented. In general the correlations between OLR and temperature are greater than between OLR and cloudiness, and for arctic Alaska these correlations are the highest. One explanation is that northern Alaska has the least topographic variability of the sites investigated. Furthermore, northern Alaska has the longer

dark season with more frequent and longer lasting inversions.

In addition, Table 1 gives the slope of the line of best fit, from which the sensitivity of the OLR to cloudiness and temperature can be estimated. Also, a multiple correlation coefficient between OLR and both cloudiness and temperature is provided. These values are naturally higher for two parameter cross-correlations. However, it should be pointed out that cloudiness and surface temperature are not independent of each other, and that such dependency has an annual course. In winter increased sky cover brings above-normal temperatures to northern and interior Alaska, a well-known fact to people living in the area, as clouds destroy or at least weaken the surface inversion and allow the warmer air aloft to reach the surface. In summer after the snow has melted, the positive effects of the sky cover for the infrared radiation are overcompensated by the effects of the short-wave radiation, and temperature and sky cover are normally negatively correlated [Ambach, 1974]. This does not hold true for the maritime climate of Kodiak. Here, the relatively warm water in winter prevents the formation of a surface inversion, and clouds are always colder than the surface; hence a negative correlation factor between sky cover and temperature is found for all four seasons.

There is one odd value in Table 1, which is the negative correlation between temperature and OLR in winter for Kodiak. I do not have an obvious explanation for this value.

In Figure 5, the OLR grid point centered at 65°N, 147.5°W is presented as a function of cloudiness and temperature for Fairbanks (64°49'N, 147°52'W). The data were smoothed by averaging the temperature and cloudiness over small increments. From this smoothed data the contours were objectively determined. In summer (Figure 5a), the radiation values were found to increase with increasing temperature and decreasing cloudiness, while for the rest of the year OLR increased with increasing temperature and increasing cloudiness, as represented by the springtime analyses shown in Figure 5b. This result shows clearly that clouds in GCMs cannot be treated independently by season and geographic location.

In Figure 6 the mean annual radiation map for Alaska is presented. Generally, a north–south increase in the OLR can be observed, a result to be expected. There is a secondary minimum between interior Alaska and the Gulf of Alaska, an effect of the Alaska Range. There is generally an increase when going west, due to the influence of the Bering Sea, which makes the area more maritime (warmer in winter). Altogether, the map appears to be reasonable.

CONCLUSION

Sky cover and outgoing longwave radiation as derived from satellite measurements are definitely related. But the quantitative relationship depends on local geographic and topographic features in Alaska as well as on the time of year, as day length, solar elevations, surface albedo, inversion strength and cloud parameters influence such a relationship. Hence carefully observed variations in cloudiness will be very important for the determination of climate change in arctic and subarctic regions. Also, improved parameterizations of sky cover in GCMs should be attempted.

	Sky cover vs. OLR corr. coeff.	slope	Temp. vs. OLR corr. coeff.	slope	Mult. Corr. coeff.
Barter Is. - ARCTIC					
Spring	0.86	0.73	0.97	1.82	0.97
Summer	-0.59	-0.47	0.07	0.27	0.62
Fall	0.54	0.56	0.93	1.54	0.94
Winter	0.39	0.24	0.81	1.12	0.82
Fairbanks - CONTINENTAL					
Spring	0.29	0.37	0.94	1.64	0.95
Summer	-0.74	-0.79	0.64	2.50	0.81
Fall	0.14	0.1	0.91	1.28	0.96
Winter	0.01	0.01	0.50	0.63	0.58
Kodiak - MARITIME					
Spring	-0.13	-0.09	0.52	1.06	0.71
Summer	-0.67	-0.58	0.58	2.21	0.76
Fall	-0.29	-0.29	0.58	1.21	0.73
Winter	-0.82	-0.42	-0.24	-0.61	0.86

Table 1. Correlation coefficient between the outgoing longwave radiation as derived from satellite, and (a) cloud cover, and (b) temperature, and (c) cloud cover and temperature for three stations in different climatic zones of Alaska. Also, the slope of the line of best fit is given.

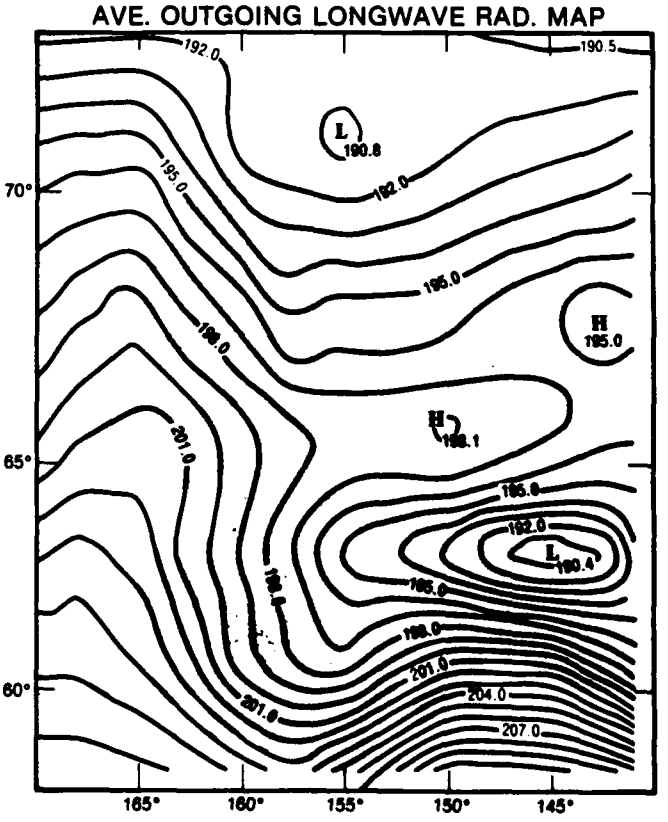


Figure 6. Mean annual map of outgoing longwave radiation for the State of Alaska. There is generally a north-south increase in the radiation flux, other than a small minimum over the Alaska Range. There is generally an increase in the radiation flux when going west, due to the influence of the Bering Sea.

ACKNOWLEDGMENT

Mr. John Janowiak supplied the data tape of the satellite-derived radiation data and provided valuable advice. Dean Prichard, with great dedication did all the computer work, and Dr. Gunter Weller read the manuscript and made comments, which improved the paper. Two people reviewed the manuscript, one of whom went to a great extent to improve the clarity of the paper. To all of them my sincere thanks. Financial support was obtained from the Alaska Climate Research Center.

REFERENCES

Ambach, W., The influence of cloudiness on the net radiation balance of a snow surface with high albedo, *J. Glaciol.*, *13*, 73–84, 1974.

Arkin, P. A., A. V. R. Krishna Rao, and R. R. Kelkar, Large-scale precipitation and OLR from INSAT-1B during the 1986 south-west monsoon season, *J. Climatol.*, *2*, 619, 1989.

Bilello, M. A., Survey of Arctic and sub-Arctic temperature inversions, *CRREL Technical Rep. 161*, 36, 1966.

Budyko, M. I., and Yu. S. Sedunov, Anthropogenic climatic changes, paper presented at Climate and Development Conference, Congress Centrum, Hamberg (FRG), 7–10 Nov., 1988.

Ellsaesser, H. W., A different view of the climatic effect of CO_2 - Updated, *Atmósfera*, *3*, 3, 1990.

Gruber, A., Determination of the earth–atmosphere radiation budget from NOAA satellite data, *NOAA Technical Rep. NESS76*, p. 28, NOAA, U.S. Dept. of Commerce, Washington, DC, 1977.

Haque, M. A., and M. Lal, Diagnosis of satellite-derived outgoing longwave radiation in relation to rainfall in India, *Meteorology and Atmospheric Physics*, *45*, 1–13, 1991.

Janowiak, J. E., A. F. Krueger, P. A. Arkin, and A. Gruber, Atlas of Outgoing Longwave Radiation Derived from NOAA Satellite, *NOAA Atlas No. 6*, NOAA, U.S. Dept. of Commerce, Silver Spring, MD, 1985.

Lindzen, R. S., Some coolness concerning global warming, *Bulletin of the A.M.S.*, *71*, No. 3, 288–299, 1990.

Mitchell, J. F. B., The "Greenhouse" Effect and climatic change, *Rev. Geophys.*, *27*, 115, 1989.

Murakami, T., Empirical Orthogonal Function Analysis of satellite-observed OLR during summer, *Mon. Wea. Rev.*, *108*, 205, 1980a.

Murakami, T., Temporal variations of satellite-observed OLR over the winter monsoon region, Part I: Long Period (15–30 day) oscillations, *Mon. Wea. Rev.*, *108*, 407, 1980b.

Murakami, T., Temporal variations of satellite-observed OLR over the winter monsoon region, Part II: Short Period (4–6 day) oscillations, *Mon. Wea. Rev.*, *108*, 427, 1980c.

NRC (National Research Council), Changing Climate, (Board of Atmospheric Sciences and Climate), National Academy of Sciences, Washington, DC, 1983.

NOAA, Local Climatological data for Alaskan 1st class weather stations, 1974–1989.

Prasad, K. D., and R. K. Verma, Large-scale features of satellite-derived OLR in relation to monsoon circulation over the Indian region, *J. Climatol.*, *5*, 297, 1985.

Ramanathan, V., The greenhouse theory of climatic change: A test by an inadvertent global experiment, *Science*, *240*, 293, 1988.

Winston, J. S., and A. F. Krueger, Diagnosis of the satellite-observed radiating heating in relation to the summer monsoon, *Pure Appl. Geophys.*, *115*, 1131, 1977.

Winston, J. S., A. Gruber, T. I. Gray, Jr., M. S. Varnadore, D. L. Earnest, and L. P. Mannello, Earth–atmosphere radiation budget analysis derived from NOAA satellite data, June 1974–February 1978, Vols. 1 and 2, NOAA, U.S. Dept. of Commerce, 1979.

Wendler G., and P. Nicpon, Low-Level Temperature Inversions in Fairbanks, Central Alaska, *Mon. Wea. Rev.*, *103*, 34, 1975.

Study of the Influence of Gravity Flows on the Antarctic Circulation Using Simulations with the French General Circulation Model

P. Pettré and M. Déqué
Centre National de Recherches Météorologiques, Toulouse, France

ABSTRACT

Atmospheric General Circulation Models (GCMs) have been widely applied to climate problems in polar regions. The GCM's simulation of the Antarctic contains aspects that are strikingly deficient, such as the pressure distribution over the peripheral Antarctic Oceans, the distribution of surface air temperature over central Antarctica and the position or intensity of the antarctic circumpolar lows.

Katabatic winds blow strongly for several hours or days, over very large distances along the slopes of Antarctica. These large-scale flows transport cold air from polar to sub-polar regions, probably inducing circulations and interactions between the atmosphere and other parts of the climate system. We believe that a bad simulation of katabatic flows largely explains the deficiencies of the GCM. We hope to achieve an improvement by a better parameterization of the boundary layer, taking into account the most important driving mechanisms of the slope flows in this region.

A one-dimensional analytical model of katabatic wind derived from the bulk two-layer model of Ball has been developed. This model is validated using the data set (70 soundings) collected during the IAGO experiment at D47 (67°24'S, 138°43'E, altitude 1564 m), 110 km inland from the coast of Adélie Land. The parametric model is then introduced into the French GCM. The most significant effect of the parameterization is a 50-m increase of the geopotential height over the South Pole. The surface temperature at the South Pole increases (2°C), reducing the pole to mid-latitude thermal gradient. The westerly circulation at 50°S is slowed down (4 m s^{-1} at 850 hPa), and the surface pressure at the South Pole increases (4 hPa). These results, consistent with an increase of katabatic winds, would, however, be improved by a better coupling between the parameterization and the GCM boundary layer.

Climatic Impacts of the Boundary Layer Circulation over Antarctica

D. H. Bromwich
Byrd Polar Research Center, The Ohio State University, Columbus, Ohio, U.S.A.

ABSTRACT

Prolonged periods of strong radiational cooling over the sloping ice fields of Antarctica produce cold, negatively buoyant air in the lowest layers of the atmosphere. This cooling generates a continental-scale, near-surface wind-field which is highly irregular. Cold air in the interior is channeled into narrow zones that enable the downstream coastal katabatic winds to become anomalously strong and persistent. This probably means that the boundary layer transport of air across the Antarctic coastline is concentrated in a small number of narrow regions, and that previous quantitative evaluations of the importance of this boundary layer circulation are likely to be substantially in error.

From continuity considerations, the time-averaged outflow of cold surface air must be compensated by inflow aloft and sinking over the continent. This time-averaged meridional mass circulation plays a dominant role in the heat budget of the Antarctic atmosphere by adiabatic compression in the statically stable atmosphere. The tropospheric convergence and sinking motion also generate cyclonic vorticity which is comparable in magnitude to that arising from the temperature contrast between the ice sheet and the surrounding ocean. That is, the circumpolar vortex is centered over the East Antarctic ice sheet in part because of the tropospheric mass convergence.

The concentration of cold surface air transport from the ice sheet into narrow coastal zones has important consequences for sea ice formation and cyclonic development. Katabatic jets can force coastal polynyas where very active sea ice formation and associated brine rejection produce saline shelf water. This water mass is a component of Antarctic Bottom Water. Such water mass formation provides a way to couple climatic variations over the ice sheet to the deep ocean on relatively short time scales. Coastal baroclinic zones associated with intense katabatic winds appear to be active sites for generation of mesoscale cyclones. The downstream impacts of such cyclogenesis have not yet been identified, but case studies hint that they may be substantial.

AD-P007 294

The Surface Condition on the Antarctic Ice Sheet

Katsumoto Seko and Teruo Furukawa
Water Research Institute, Nagoya University, Nagoya, Japan

Okitsugu Watanabe
National Institute of Polar Research, Tokyo, Japan

92-17976

ABSTRACT

NOAA AVHRR data reveal clear images of meso-scale (spatial scale on the order of tens of kilometers) undulating topography, surface properties and katabatic wind field on the Antarctic ice sheet.

Katabatic wind is visualized as fluctuations of brightness temperature which align parallel to the wind direction. The temperature fluctuation is probably caused by the fluctuation of wind velocity.

Two typical patterns of undulations on the ice sheet were detected. One of them appears on the slope region where katabatic wind prevails. The band-shaped undulations develop normal to the prevailing wind with a spacing of a few tens of kilometers and an amplitude of a few tens of meters. A few percent of albedo change associated with the variation of accumulation co-exists with the undulation. The eolian process can be considered a dominant force in making this pattern.

Another undulating pattern can be seen further inland on the plateau. This undulation has a different orientation with an approximate spacing of 50 km and an amplitude of a few tens of meters.

INTRODUCTION

Low temperature and strong winds are major climate features of the Antarctic ice sheet, where snow remains as eolian particles on the surface. Snow drift transport changes topography, and the topography alters the katabatic wind field again. It is a feedback system between the cryosphere and atmosphere. The redistribution of snow makes the accurate estimation of accumulation difficult.

Understanding the pattern of topographic undulations on the ice sheet also involves information of subglacial topography. The investigation of surface conditions of the ice sheet can provide much information about the ice field.

Intensive field studies on the ice sheet can provide invaluable data, but the coverage is restricted along a line. Recent development of remote sensing provides a powerful tool for the investigation of the polar ice sheets. Several studies have investigated surface features on the ice sheet using Landsat images [Orheim and Lucchitta, 1987, 1988]. However, the areal coverage of Landsat images is too small to survey the whole region of the ice sheet within a reasonable cost and effort.

The purpose of this study is to detect the surface topography and surface properties on the Antarctic ice sheet from NOAA AVHRR data and to compare them with ground survey data.

DATA

NOAA AVHRR data received at Syowa station, Antarctica were used in this study. Figure 1a,b shows the two analyzed areas: area-A covers half of the East Antarctic ice sheet and area-D covers the region where the JARE over-snow traverse has been carried out. The compiled data have a pixel resolution of 4.4 km and 2.2 km, respectively. Brightness temperature (Tb) on channel 4 (10.5–11.5 μm) and albedo on channel 2 (0.725–1.1 μm) were mainly used for this study. The accuracy of the topographic location of the satellite image is deemed to be within a few pixels by geographical position matching with outstanding rocks and blue ice fields.

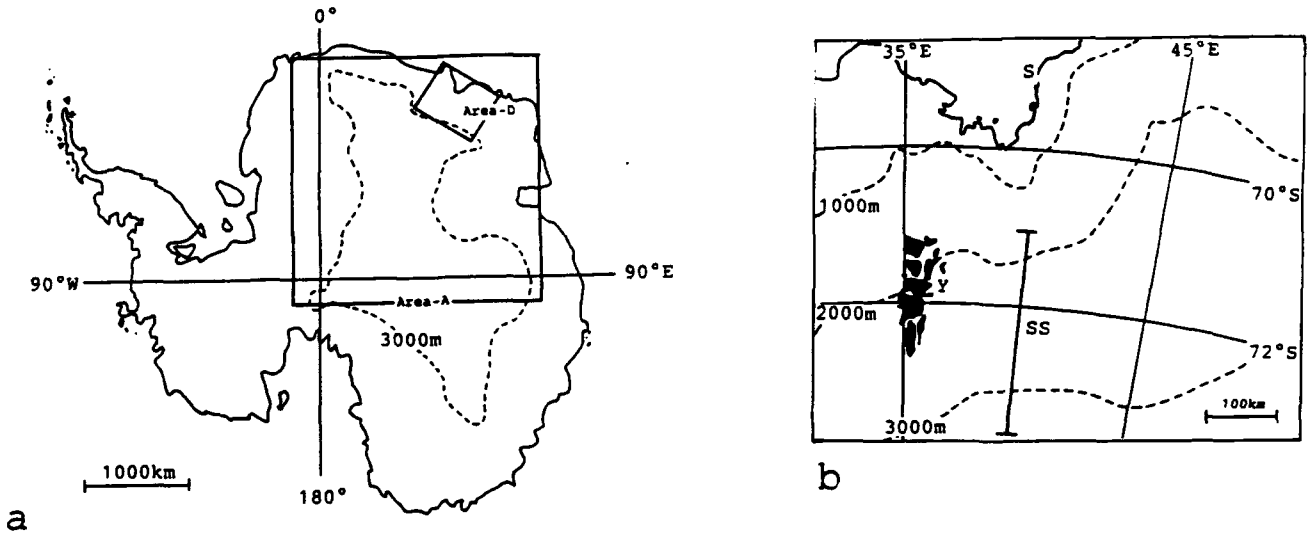


Figure 1.(a) Analyzed areas of NOAA AVHRR data (area-A and area-D). Contours of 3000 m in altitude are shown as dashed lines. (b) Detailed map of area-D. Topographic names are as follows: S: Syowa station; Y: Yamato mountains; SS: SS-route (used in Figure 5a,b).

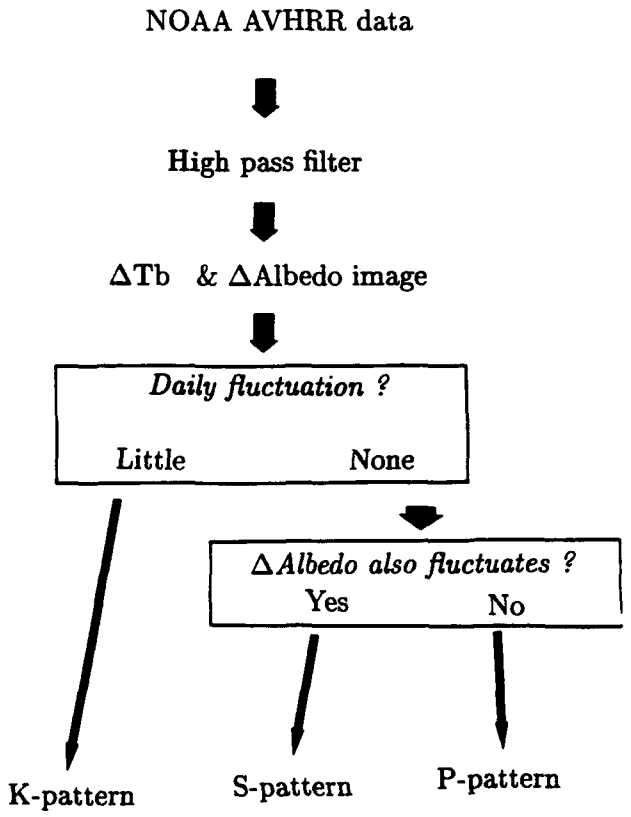


Figure 2. Flow chart of the image processing used in this study.

Figure 2 shows the procedures of image processing. Clouds over the ice sheet can be distinguished by their transient character, and only images from clear days were selected. A spatial high-pass filter is applied to the original images for enhancing structures less than 100 km in horizontal scale. We refer to the filtered images on channel 4 as ΔTb images hereafter.

TYPICAL STRUCTURES

We found three patterns in the filtered images as follows.

a) K(Katabatic)-pattern. Figure 3a shows a winter ΔTb image in area-D. Several streaks can be seen which represent the Tb fluctuation of 1 K. The alignment of streaks coincides with the direction of katabatic wind compiled from ground survey data [Watanabe, 1978]. Each streak is maintained over a few hundred kilometers, while its position fluctuates according to synoptic weather conditions [Seko, 1991].

b) S(Slope)-pattern. Figure 3b is a typical summer ΔTb image in area-D. The S-pattern appears as stripes of ΔTb fluctuation on the katabatic wind slope from 3000 to 1000 m a.s.l. The spacing between stripes is a few tens of kilometers, and it becomes broader with increasing altitude. It is interesting that the orientation of stripes is normal to the direction of katabatic wind but not ice sheet flow. The albedo on channel 2 reveals a fluctuation of ±3% which is negatively correlated with the fluctuation of ΔTb. It is noteworthy that the S-pattern can be seen also in the winter ΔTb image obscurely under the K-pattern (Figure 3a).

c) P(Plateau)-pattern. Figure 4 shows winter ΔTb image in area-A, in which the P-pattern can be seen on the interior plateau (above 3000 m a.s.l.) of the ice sheet (large box in the figure). The P-pattern can be distinguished from the K-pattern (two small boxes in the figure) by its temporal invariance. The P-pattern is band-shaped with an approximate spacing of 50 km and aligns parallel to altitude contours. The amplitude of the ΔTb fluctuation is about ±5 K, but no corresponding albedo fluctuation in summer images is found.

The characteristics of these patterns are summarized in Table 1.

MECHANISM OF VISUALIZATION

Interpretation of these patterns is necessary to understand what is occurring on the ice sheet. We will describe the mechanism of the visualization of each pattern.

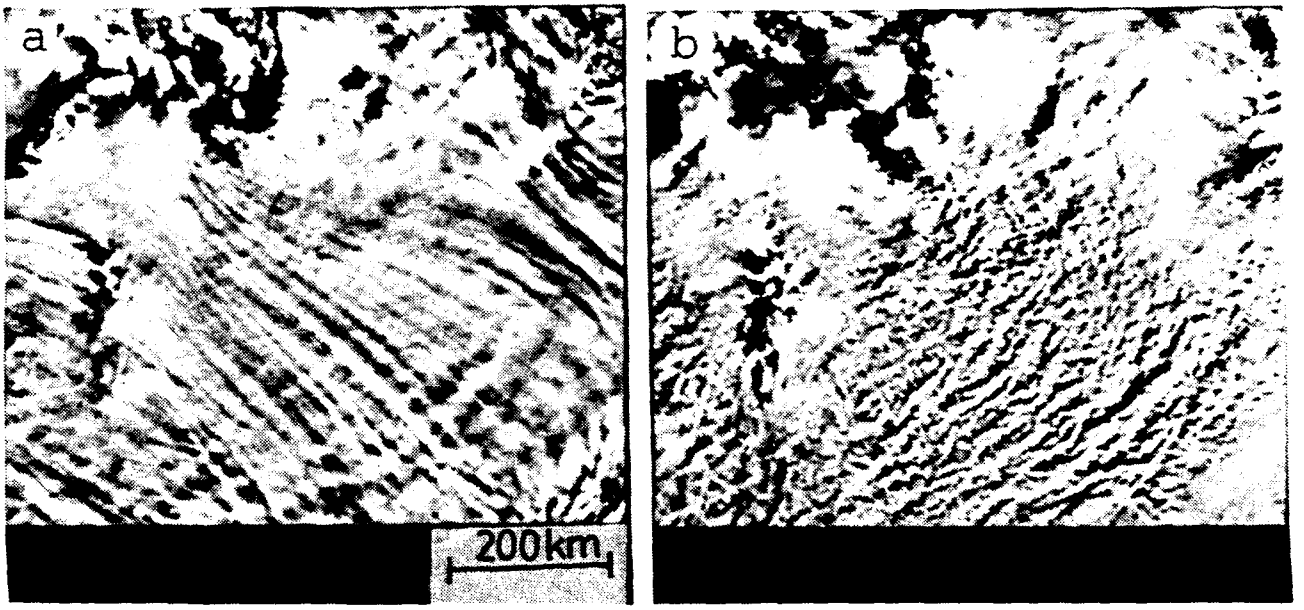


Figure 3. ΔTb image in area-D in (a) winter and (b) summer.



Figure 4. Winter ΔTb image in area-A. P-pattern appears in a large box.

Type	Katabatic (K)	Slope (S)	Plateau (P)	Cloud
Daily Fluctuation	Little	None	None	Large
Appeared region	Slope	Slope	Plateau	-
Appeared season	Winter	Summer (Both)	Winter	-
Scale (km)	10 x 100	20 x 100	50 x 100	-
Orientation	parallel to u	normal to u	normal to∇h	-
ΔTb (K)	±1	±1	±5	-
ΔAlbedo (%)	None	±3	None	-

Table 1. Characters of each pattern.

a) K-pattern. Under the inversion within the boundary layer, the ground temperature will increase where wind velocity is strong enough to break up the inversion. A temperature rise of 1 K can be expected with 0.5 m s^{-1} of wind increase [Seko, 1991]. Bromwich [1988] described the visualized katabatic wind in the coastal region and explained it by a similar mechanism.

b) S-pattern. The net accumulation rate obtained from field observation [Nishio et al., 1988] is shown in Figure 5a. A very good correlation exists between albedo and accumulation. Ratio of channel 2 to channel 1 which can detect surface properties (i.e., snowy or icy) rather than topography reveals similar variation as channel 2. Fujii et al. [1987] also found a similar relationship along another traverse route. Sintering of snow particles in low accumulation makes albedo on channel 2 low [Warren, 1982], and it can be said that Tb on channel 4 is negatively correlated with the albedo fluctuation through the surface heat balance, and the S-pattern can be seen on both channels in summer.

It is also revealed from field data [Nishio et al., 1986, 1988] that lower accumulation occurs in steeper regions (Figure 5b). This relationship can explain the appearance of the S-pattern in winter ΔTb image (Figure 3a), because the wind speed fluctuates according to the undulating slope, and surface temperatures can fluctuate due to mechanisms similar to those affecting the K-pattern.

c) P-pattern. The P-pattern appears in winter, or nighttime in other seasons when a strong inversion exists. Under the strong inversion, lower topographic areas (basins) act as pools of cold air. A comparison with the altitude measurement during an inland traverse [Ageta et al., 1987] confirms this idea. The estimated amplitude of undulating topography is a few tens of meters. A large amplitude of Tb can be explained by a strong inversion [Schwerdtfeger, 1984].

DISCUSSION

a) Undulation. The S- and P-patterns develop in different regions complementally. It is a general picture that there are meso-scale topographic undulations over nearly the entire ice sheet. There are two plausible mechanisms to explain the development of undulations on the ice sheet. One of them is the eolian process, which acts in the development of sand dunes; and the other is the interference from subglacial topography [Budd, 1970; Budd and Carter, 1971].

The orientation and appearance of the S-pattern resembles the configuration of a transverse dune in the desert [McKee, 1979]. The orientation of this pattern and the phase-lag relationship between accumulation and slope gradient (Figure 5b) suggest that the eolian process is a dominant factor in its formation. Wind speed can be affected by the undulation of a few tens of kilometers and causes convergence of drifting snow. Black and Budd [1964] and Whillans [1975] mentioned the eolian process to maintain and move undulation. According to their kinematic relationship, it is deduced that the S-pattern migrates with a speed of 100 m yr^{-1}. The estimated hiatus period by the moving surface condition is several tens of years. This phenomenon may be important in determining the variation of accumulation from ice core studies.

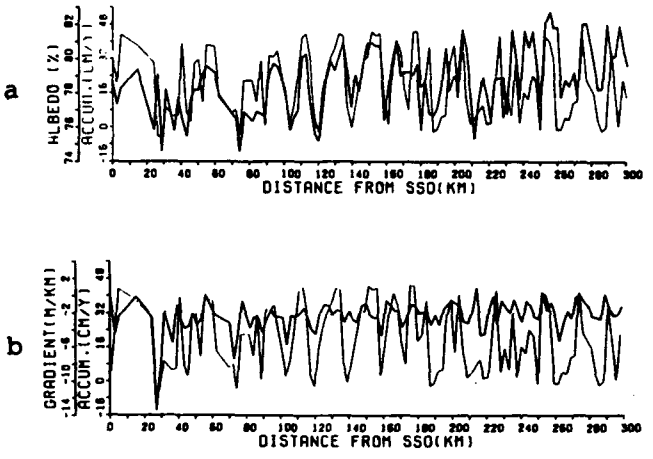


Figure 5.(a) The relationship between accumulation (thin line) and albedo (thick line) on channel 2 along a traverse route (SS-Route in Figure 1b). (b) The relationship between accumulation (thin line) and surface slope gradient (thick line).

Similar patterns can be found in the drainage of the Lambert glacier and on the western flank of the inland plateau in places other than area-D, but we do not have enough data to discuss the mechanisms which form either these patterns or the P-pattern in these areas. It is necessary for further understanding of accumulation and ice flow to investigate the origins of undulations; whether eolian processes or interference from subglacial topography.

b) Katabatic wind. Tracing the K-pattern provides useful information of wind direction on the ice sheet, and AVHRR data is a good tool to investigate katabatic wind from a climatological point of view.

The mechanism which causes wind speed to fluctuate is unknown. It may be the self-acceleration of wind by loading of snow particles [Kodama et al., 1985], or some kind of instability within the boundary layer.

ACKNOWLEDGMENTS

The authors would like to express their thanks to Dr. F. Nishio of NIPR for providing field data. The authors are grateful to Prof. S. Kawaguchi and Dr. T. Yamanouchi of NIPR for conducting satellite research under ACR (Antarctic Climate Research) project. The authors are indebted to 29th JARE wintering members for assistance during observation.

REFERENCES

Ageta, Y., T. Kikuchi, K. Kamiyama, and F. Okuhira, JARE Data Reports No. 125 (*Glaciology 14*), 1987.

Black, H. P., and W. F. Budd, Accumulation in the region of Wilkes land, Antarctica, *J. Glaciol.*, *5*, 3–15, 1964.

Bromwich, D., Satellite analyses of Antarctic katabatic wind behavior, *Bull. Am. Met. Soc.*, *70*, 738–749, 1989.

Budd, W. F., Ice flow over bedrock perturbations, *J. Glaciol.*, *9*, 29–48, 1970.

Budd, W. F., and D. B. Carter, An analysis of the relation between the surface and bedrock profiles of ice caps, *J. Glaciol.*, *10*, 197–209, 1971.

Fujii, Y., T. Yamanouchi, K. Suzuki, and S. Tanaka, Comparison of the surface conditions of the inland ice sheet, Dronning Maud Land, Antarctica, derived from NOAA AVHRR data with ground observations, *Ann. Glaciol.*, *9*, 1–4, 1987.

Kodama, Y., G. Wendler, and J. Gosink, The effect of blowing snow on katabatic winds in Antarctica, *Ann. Glaciol.*, *6*, 59–62, 1985.

McKee, E. D., *A Study of Global Sand Seas*, U.S. Geological Survey Professional Paper 1052, 429 pp., 1979.

Nishio, F., H. Ohmae, and M. Ishikawa, JARE Data Reports No. 110 (*Glaciology 12*), 1986.

Nishio, F., H. Ohmae, and K. Osada, JARE Data Reports No. 137 (*Glaciology 16*), 1988.

Orheim, O., and B. K. Lucchitta, Snow and ice studies by thematic mapper and multispectral scanner Landsat images, *Ann. Glaciol.*, *9*, 109–118, 1987.

Orheim, O., and B. K. Lucchitta, Numerical analyses of Landsat thematic mapper images of Antarctica: surface temperatures and physical properties, *Ann. Glaciol.*, *11*, 109–120, 1988.

Schwerdtfeger, W., *Weather and Climate of the Antarctic*, 261 pp., Elsevier, Amsterdam, 1984.

Seko, K., A preliminary study of katabatic wind by using NOAA AVHRR data, *Proc. NIPR Symp. on Polar Meteorol. and Glaciol.*, *5*, 1991, Submitted.

Warren, S. G., Optical properties of snow, *Rev. Geophys. & Space Phys.*, *20*, 67–89, 1982.

Watanabe, O., Distribution of surface features of snow cover in Mizuho Plateau, *Mem. Nat. Inst. Polar Res.*, *7*, 44–62, 1978.

Whillans, I. M., Effect of inversion winds on topographic detail and mass balance in inland ice sheets, *J. Glaciol.*, *14*, 85–90, 1975.

Study on Characteristics and Evolution of the High Asia Cryosphere and Its Effects on Natural Environments of the Earth

Xie Zichu and Cheng Guodong
Lanzhou Institute of Glaciology and Geocryology, Academia Sinica, Peoples Republic of China

ABSTRACT

The central high land of Asia, with the Qinghai-Xizang (Tibet) Plateau as its main body, is the third polar region, the highest pole of the Earth besides the Arctic and Antarctic. Because of its sub-tropical latitude, high altitude and large area, it greatly influences the climate, environments and ecological evolution of Asia and the Earth.

The High Asia Cryosphere formed due to strong uplift of the Qinghai-Xizang Plateau and caused great changes of topography, hydrology, atmospheric circulation and ecosystems. Because of the various combinations of latitude, longitude, altitude, and moisture and heat conditions, the High Asia Cryosphere has very complicated and unique characteristics and structure.

The High Asia Cryosphere is sensitive to global warming. While climatic change will directly affect the natural and human use of the environment, changes to the High Asia Cryosphere as a result of climate change will produce a set of second-order effects. For example, changes in glacier and snow cover can lead to significant alterations of runoff and dynamics of rivers originating in High Asia. The degradation of permafrost on the plateau will potentially accelerate the process of desertification of the plateau, and produce serious consequences to the environment and ecosystems of East Asia.

After many years of research by Chinese and foreign scientists it is necessary to view the High Asia Cryosphere and its effects on environments as a whole and do a synthesis study at a higher level. This will include: theoretical syntheses of scattered regional investigations; reconstruction of evolution history of the High Asia Cryosphere using ice core records, permafrost borehole temperature records and relics of Quaternary glaciation; systematic monitoring of glaciers, snow cover, permafrost and periglacial phenomena; studies of atmosphere, hydrosphere, lithosphere, biosphere and cryosphere interactions; and predicting the effects of the High Asia Cryosphere on global change.

Section C:

Ocean–Sea Ice–Atmosphere Interactions and Processes

Chaired by

A. Gordon
Columbia University
U.S.A.

N. Untersteiner
University of Washington
U.S.A.

Arctic Sea Ice Balance and Climate

N. Untersteiner
Department of Atmospheric Sciences, University of Washington, Seattle, Washington, U.S.A.

ABSTRACT

Proxy data and local historical records show that sea ice extent has undergone large secular variations over past millennia and centuries, for reasons that are only qualitatively understood.

Since the onset of systematic observations in situ (data buoys) and satellites (mainly passive microwave radiometers), the record shows a remarkable constancy of the annual cycle of the arctic sea ice cover. This cycle is described by a continuity equation that is used to discuss the mechanisms relating ice extent and thickness to climate, and to illustrate how ice formation, transport, and melting combine to produce the seasonal cycle of sea ice cover. The heat balances and stresses at the surface and bottom of the sea ice are external forcing functions with small-scale and large-scale feedbacks. Examples are the stable stratification of the ocean boundary layer caused by bottom melting and surface drainage which suppress the vertical ocean heat flux, and the arctic summer stratus which forms over ice-covered ocean regions and limits surface melting.

Recent efforts to model the seasonal cycle of sea ice in the Arctic are discussed in light of the observational record. A promising new development is the incorporation of satellite data (such as the concentrations of first-year and multi-year ice) as explicit variables carried in dynamic–thermodynamic ice models.

Of special interest in the context of climate is the fresh water budget of the Arctic Basin. Its largest components, the runoff generated by mid-latitude precipitation over the Eurasian continent, and the ice export driven by the wind field over the Arctic Basin, have no immediately apparent connection. Taking into account all other components of the fresh water balance, Aagaard and Carmack [1989] estimate that the contemporary influx and outflux of fresh water at the perimeter of the Arctic Basin are equal. The unraveling of the mechanisms responsible for this equality, and the consequence of a possible imbalance remain challenging questions.

Sea Ice and the Arctic Ocean: Issues in Climate and Hydrology

K. Aagaard
NOAA/PMEL, Seattle, Washington, U.S.A.

E. C. Carmack
IOS, Sidney, British Columbia, Canada

ABSTRACT

The Arctic Ocean is strongly salt stratified, with about 100,000 km^3 of fresh water being stored in the upper 200 m of the ocean. Under present climatic conditions, this stratification is self perpetuating and severely limits the direct interaction between the atmosphere and the ocean. Instead, the Arctic Ocean is primarily forced to communicate with the atmosphere at its peripheries. The role of sea ice in this system is of special significance. Freezing is a distillation process in which the separation of salt and fresh water constitutes a source of buoyancy for the upper ocean and of density for the interior ocean. Both the resultant thermohaline circulation and the wind-driven mode redistribute the products of the distillation process, with profound consequences for the ocean, including regions external to the Arctic. Within the Arctic Ocean, the vast adjacent shelf seas produce a large surplus of ice each winter and are the primary sites for water mass transformation within the Arctic Ocean. The brines ejected during freezing drive a circulation which gives the Arctic Ocean much of its characteristic structure, and they also provide forcing for that ocean's deep interaction with the convective gyres in the Greenland and Iceland seas, thereby contributing to the large-scale circulation of the world ocean. The fresh water distillate from the freezing process is also exported to the Atlantic sector of the world ocean. There it appears to exercise significant control over the convection which ventilates the deep ocean. The present fresh water outflow through Fram Strait in fact appears to be about twice as large as the runoff from the Laurentide Ice Sheet during the last deglaciation, the disposition of which has been argued to be responsible for the climatic reversal of the Younger Dryas, about 10,000 years ago.

AD-P007 295

92-17977

The Southern Ocean: Its Involvement in Global Change

Arnold L. Gordon
Lamont-Doherty Geological Observatory of Columbia University, Palisades, New York, U.S.A.

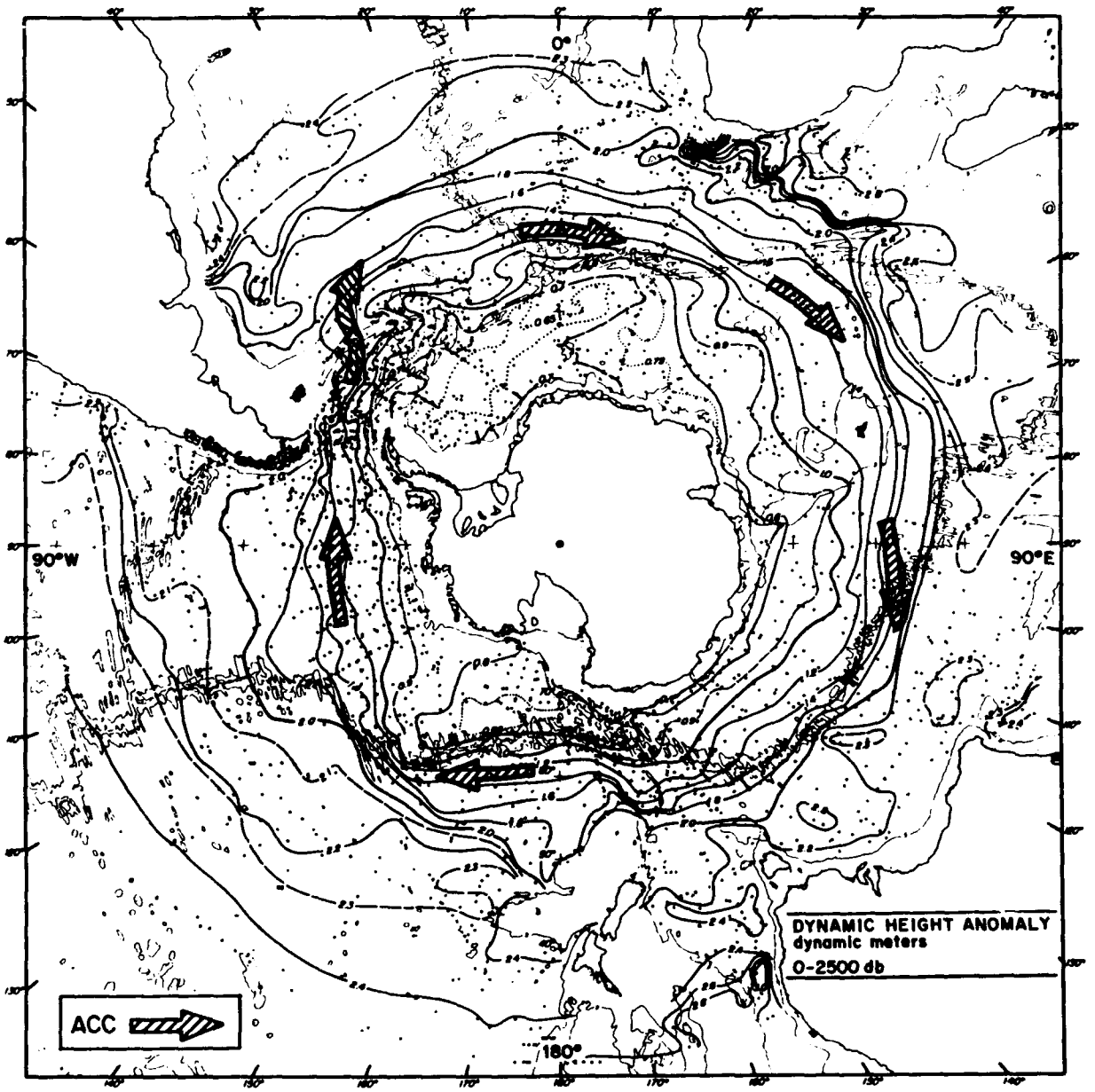
ABSTRACT

The Southern Ocean is the site of considerable water mass formation which cools and ventilates the modern world ocean. At the polar front zone, formation of cool, low salinity water sinks and spreads northward at intermediate depths limiting the downward penetration of the thermocline. Within the seasonal sea ice zone and along the margins of Antarctica, convection injects very cold oxygenated water into the deep and bottom ocean. These conditions developed as Antarctica shifted into its present configuration and grew a persistent glacial ice sheet, about 14 million years ago. The potential of the Southern Ocean to ventilate the deep and bottom ocean layers is related to occurrence of polynyas that form within the winter sea ice cover. Global climate changes would be expected to alter the polynya size and frequency. Under greenhouse-induced warming offshore polynyas may become less common as the static stability of the Southern Ocean mixed layer increases. This would diminish the Southern Ocean's cooling influence on the deep layers of the world ocean, resulting in a warmer deep ocean. The fate of coastal polynyas is less clear. It is likely that they would continue at close to their present form providing a setting conducive to Antarctic Bottom Water formation. Within the polar front zone, global warming is expected to create lower salinity though slightly cooler surface water. A reduction in the salt input to the Antarctic Intermediate Water would inject it into a shallower horizon at the thermocline base, further limiting the thickness of the thermocline. Less heat storage in the thermocline would tend to counteract the proposed deep ocean warming. The thermocline change would occur at a faster rate than would deep ocean warming (based on present-day resident times), its effect would precede the polynya influence. Inspection of the magnitude and exact time scales of these proposed changes requires a global coupled ocean–atmosphere model that properly simulates the ocean's thermohaline circulation.

INTRODUCTION

The Southern Ocean is intricately involved with water mass modification and thermohaline fluxes at the global scale. An array of processes within the Southern Ocean cool, freshen and add oxygen to the intermediate, deep and bottom layers of the world ocean. They also establish the physical setting for the unique Southern Ocean ecological system and may influence the stability of the glacial ice sheet of Antarctica. The global cooling influence of the Southern Ocean stems primarily from the low static stability of the water column found south of the Antarctic Circumpolar Current (ACC). Within this zone upwelling of deep water drawn from the world ocean is modified by air–sea exchanges and promptly returned to the deep ocean. Within the 50° to 60°S belt of the ACC cool, low salinity water is forced northward within the Ekman boundary layer, where it is subducted below the less buoyant thermocline water.

The slow downward diffusive fluxes of heat and salinity across the ocean's thermoclines, plus formation of the relatively warm and salty North Atlantic Deep Water tend to warm and increase the salinity of the deep ocean [Gordon, 1975]. Additionally, the descent of organic particles from



Figures 1. Dynamic topography of the sea surface relative to the 2500 decibar pressure surface [from Gordon and Molinelli, 1982, Plate 232]. A dynamic meter is approximately equal to a geometric meter. The lowering of sea level toward the south balances the geostrophic eastward-flowing Antarctic Circumpolar Current (ACC), which transfers 118 to 146 x 10^6 m^3 sec^{-1} through the Drake Passage [Whitworth, 1983]. The ACC prohibits warm surface water advection into the Southern Ocean, contributing to the thermal isolation of Antarctica. The axis of the ACC (hatched arrows) responds to the position of the submarine ridges and fracture zones.

the sea surface layer consumes the oxygen concentrations within the deep ocean. Therefore, should the ventilating powers of the Southern Ocean diminish, the deep ocean would be expected to become warmer, saltier and lower in oxygen as the chilling effects of the oxygenated AABW diminished.

Would the expected greenhouse-induced global warming tend to invigorate Southern Ocean ventilation processes or to attenuate them? Whether the formation rate of North Atlantic Deep Water would change under a global warming trend is also a hotly debated issue. In the discussion below I assume that there is no change in North Atlantic Deep Water. Attenuation of Southern Ocean ventilation would provide a negative feedback as more heat (and perhaps CO_2) would be stored in the deep ocean, rather than in the atmosphere; this would forestall global warming. An invigorated response would in turn cool the deep ocean, prohibiting excess heat storage, and thus act as a positive feedback. To investigate this issue and provide some thought as to what might happen during the impending global warming, we must first understand the Southern Ocean role in the present day ocean. This task is not yet accomplished to sufficient detail, but an approximate picture has emerged from 60-odd years of Southern Ocean exploration [recent reviews: Carmack, 1986; Gordon, 1988; Jacobs, 1989; Patterson and Whitworth, 1990].

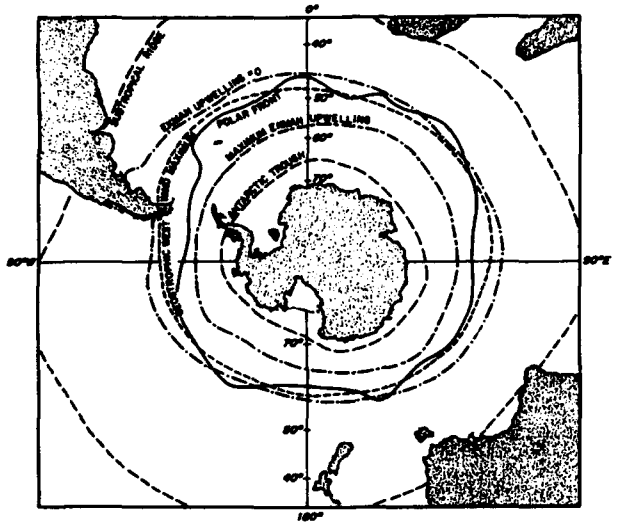


Figure 2. Position of various oceanic and atmospheric regimes within the Southern Ocean. The Antarctic Circumpolar Current is closely associated with the polar front, which separates cold antarctic surface water from subantarctic surface water. South of the wind's maximum westerlies there is general upwelling of deep water forced by oceanic Ekman Layer divergences. Zero Ekman upwelling occurs just north of the maximum westerlies due to the spherical Earth. The belt of atmospheric low pressure, separating westerlies from easterlies, is the Antarctic Trough.

SOUTHERN OCEAN RELATION TO THE GLOBAL OCEAN

The lack of a continuous western boundary pathway spanning the deep circum-antarctic 50° to 60°S belt disallows advection of warm upper layer waters into the Southern Ocean. Establishment of the deep ocean band with the resident Antarctic Circumpolar Current (ACC) and strong water mass zonation, tends to thermally isolate Antarctica (Figure 1). Sea ice and some continental glaciation probably began 38 million years ago as the circumpolar band was forming, with a persistent glacial ice sheet developing 11–14 million years ago [Kennett, 1977]. With the cooling of the Southern polar regions came cooling of the deep ocean. Deep ocean temperatures at the end of the Eocene 38 million years ago were well above 10°C, falling below 5°C by mid-Miocene, 13 million years ago, to the present-day values of near 0°C [Shackleton and Kennett, 1975a,b].

The ACC path and associated polar front position are aligned with the position of the maximum westerly winds (Figure 2) [Nowlin and Klinck, 1986], but guided to a significant degree by bottom topography [Gordon et al., 1978]. As the ocean surface temperature pattern responds to the circulation pattern, we have the surprising result that the bottom topography may influence the position of the maximum westerlies. A relationship between wind patterns and mountains may be not be surprising, but a relationship between wind and the shape of the sea floor is an unexpected link. Perhaps the ACC and coupled wind field are not as free to shift with changes in climate as might be expected?

While the warm upper layer of the ocean is prohibited from advecting across the circumpolar belt into polar regions, geostrophic balance of the ACC allows deep and bottom water to have isopycnal access to the cold polar atmosphere. Density characteristic of the sea floor north of the ACC is found near the sea surface to the south of the ACC. It may be said that the ACC baroclinic mode is as strong as it can get with today's large scale ocean stratification. Exposure of upwelled deep water to the antarctic atmosphere produces cold water which can then mix along isopycnal surfaces into the deep and bottom stratum of the world ocean. It is suspected that the deep water cooling observed within the Weddell Sea during the 1970s in response to a large polynya [Gordon, 1982] eventually cooled the deep ocean to the north by isopycnal spreading.

Additionally, the Southern Ocean directly influences two strata within the global ocean: there is the chilling effect of Antarctic Bottom Water (AABW) and there is the cooling, freshening effect of Antarctic Intermediate Water (AAIW).

Antarctic Intermediate Water (AAIW)

Within the polar front zone (Figure 2), a water mass boundary closely associated with the ACC, polar surface water, fed from regional Ekman-induced upwelling south of the ACC with dilution by excess precipitation, sinks and spreads northward forming a salinity minimum layer. This layer, AAIW, demarcates the lower boundary of the southern hemisphere thermoclines. The low salinity of AAIW allows cool (4°C in the Atlantic; 4–5°C in the Indian and 5°C in the Pacific [Gordon and Molinelli, 1982, Plate 201]) water to be delivered to a low density stratum controlling the depth of the Southern Hemisphere's thermoclines, by limiting downward migration of tropical heating. In the Atlantic AAIW spreads north of the equator, with remnants flowing into the northern North Atlantic [Tsuchiya, 1989]. AAIW helps balance the global water budget by transferring polar excess precipitation into the evaporative subtropic regions. It also injects high oxygen water into the lower thermocline, confining the subtropical oxygen minimum layer to the mid-thermocline.

What might be considered as a less dense variety of AAIW forms in the subpolar region and invades the mid to lower thermocline; this is called Subantarctic Mode Water (SAMW) [McCartney, 1977]. It is drawn from the deep winter mixed layer formed just north of the polar front zone. Like AAIW it cools, freshens and oxygenates the thermoclines of the Southern Hemisphere.

Antarctic Bottom Water (AABW)

The water colder than 2°C in the world ocean is derived for the most part from AABW. AABW intrudes into each ocean basin along specific routes, but eventually its cooling effects spread throughout the world ocean. About 57% of the ocean is colder than 2°C; a percentage of the ocean that may be considered to be directly influenced by AABW [Gordon, 1988b]. However, indirectly AABW density dictates the density for other deep water sources if they are to compete with AABW for a piece of the deep ocean volume. Because AABW is reworked deep water drawn from the world ocean, as long as the Southern Ocean does not experience greatly increased fresh water input, its chilling effects on upwelled deep water ensure that it can produce denser water, at least at the large scale.

Vigorous modification of ocean water occurs over the continental shelf of Antarctica. Very cold shelf water is the prime contributor to the deep-reaching convective plumes over the continental slope leading to the formation of AABW [Foster and Carmack, 1976; Foldvik et al., 1985].

Included within the AABW category one may consider cooling of the deep water strata by isopycnal spreading of Southern Ocean deep water, as mentioned above, in addition to the more classically defined AABW formed along the continental margins. In a sense, the Southern Ocean deep water spreading above the continental margin–produced AABW forms the bottom water far to the north.

Formation of traditionally defined AABW formed along the continental margins, and the open ocean deep water cooling by convection within the deep ocean, may be strongly related to the occurrence of polynyas. As they represent "holes" in the insulating blanket of sea ice, with ocean–atmospheric heat flux 10 to 100 times that of the ice-covered ocean, polynyas cool the ocean [Gordon, 1988a]. It is important to be able to predict the future trends in polynya size and frequency, if we are to predict the Southern Ocean role in global change.

ANTARCTIC INTERMEDIATE WATER AND GLOBAL CHANGE

Changes in circumpolar belt surface water temperature and salinity would be expected to alter the thermohaline characteristics of AAIW. The density layer that "holds" the salinity minimum core layer under the thermocline would also change. For example, a salinity change of AAIW by 0.1 psu changes the density anomaly, sigma-0, by 0.1, altering the salinity minimum depth by 50 meters (with today's thermocline density stratification). A temperature change of 1.0°C would have a similar result. Therefore, solely from the alterations in AAIW density, the salinity minimum depth and associated thermocline thickness along with thermocline storage of heat and fresh water would be altered.

What will happen to surface water characteristics in the polar front zone during the impending global warming? Models vary on this point, mainly due to different parameterizations of sea ice. Manabe et al. [1990] found that within the 50–60°S band, sea surface temperatures decrease by 1°C in a 60-year period following an abrupt doubling of atmospheric CO_2 as upward flux of deep water heat is greatly reduced by increased mixed layer stability, a consequence of greater precipitation. Surface salinity in the 50–60°S belt decreases by 0.4 psu, decreasing surface water density sufficiently to overcome density increase of the slight cooling. The wind stress on the sea surface is somewhat increased in the 50–60°S band. This suggests that AAIW formation rate, forced by cross frontal Ekman transport, would continue or be enhanced. Therefore, in the greenhouse-warmed world we might expect continued formation of AAIW, but at a slightly lower density (lower in salinity though slightly cooler). This would inject AAIW into a shallower level within the thermoclines to the north. Surface water does not account for all of the AAIW volume, but it is instructive to point out that AAIW which is 0.4 psu lower in salinity and 1°C cooler would decrease the density of the salinity minimum layer sufficiently to have AAIW injected into the 10°C stratum, a condition which is similar to today's North Pacific Intermediate Water. The conclusion is that greenhouse-warmed climate may indirectly limit downward penetration of the thermocline and associated ocean heat storage.

What of the role of SAMW? As surface water becomes less dense, the winter mixed layer just north of the Polar front zone would not extend as deep. Less SAMW would form, though what did form would spread into a shallower (less dense) layer within the thermocline. Study of the changing roles of AAIW and SAMW under a climate-altered state is the job of a model that properly stimulates the thermohaline circulation.

ANTARCTIC BOTTOM WATER AND POLYNYAS

The sea ice cover acts to decouple the ocean from the atmosphere, limiting ocean cooling by the polar atmosphere. However, the sea ice blanket is broken by polynya "holes" which are centers of extreme ocean–atmosphere interaction [Smith et al., 1990]. Coastal polynyas are "sea ice factories" that produce dense water leading to formation of AABW [Zwally et al., 1985].

The deep ocean north of the margins is also directly affected by polynyas. The water column within the central Weddell Gyre was cooled to near 3000 m during the Weddell Polynya event of the mid-1970s (Figure 3). Salinity and density profiles indicate the cooling was accomplished by deep-reaching convection. While the Weddell Polynya was observed only in the mid-1970s, small, short-lived polynya events in the same region are common [Comiso and Gordon, 1987]. Their influence may not be as dramatic as the giant polynya of the 1970s, but their overall toll on the ocean's climatic thermohaline condition may be substantial.

Observations from the *Polarstern* in winter 1986 along the Greenwich Meridian shed some light on the winter period vertical thermohaline fluxes and their relationship to the ice cover. The mixed layer beneath the winter sea ice cover is significantly depressed in oxygen saturation [Gordon and Huber, 1990]. Incorporation of WDW into the winter mixed layer is responsible for this undersaturation (Figure 4). WDW also introduces heat and salinity into the surface layer which strongly influences the mixed layer stability, sea–air exchanges and sea ice formation processes. The total WDW transfer into the mixed layer along the Greenwich Meridian from the ice edge to the margins of Antarctica averages 45 m yr^{-1}, implying a residence time for the surface water of 2.5 years. The associated winter heat flux is 41 W m^{-2}, which limits ice thickness to about 55 cm, agreeing quite well with observations [Wadhams et al., 1988]. The air temperatures measured during the 1986 *Polarstern* cruise are just sufficient to remove the WDW heat input in the presence of observed ice thickness and concentration. This suggests that the sea ice cover and WDW heat input into the mixed layer are in approximate balance by mid-winter.

The static stability between the cold, low salinity mixed layer floating above the warmer, saltier deep water is quite weak; small factors influencing the salinity budget can upset it, causing vigorous convection and deep ocean ventilation. It is likely that a network of negative feedbacks maintains the thin veneer of sea ice in a more-or-less stable configuration [Gordon and Huber, 1990; Martinson, 1990]. This balance depends for the most part on the fresh water budget, including the sea ice formation and melting rates, and may be upset by additional salt input into the surface layer by topographic-induced upwelling; by large sea ice divergence, or perhaps by a colder or longer winter season. The Weddell Polynya of the mid-1970s demonstrates that a deep-reaching convective mode can develop when the weak regional sta-

bility is upset [Gordon and Comiso, 1988; Gordon, 1988a]. The removal of the insulating sea ice cover during a polynya event greatly enhances ocean–atmospheric fluxes as the sea surface is exposed to the polar atmosphere.

The extreme seasonality and rapid spring melting of the present-day Southern Ocean sea ice cover implied a significant role for ocean heat flux [Gordon, 1981]: the buildup of heat within the mixed layer induces melting even before the atmospheric radiation balance and temperatures warm sufficiently to melt ice directly. Ocean heat flux also limits sea ice thickness during the winter. As vertical oceanic heat and salinity flux is responsible for the spring melt and limited winter sea ice thickness, we may consider that the vigor of Southern Ocean ventilation potential is directly linked to sea ice seasonality. Year-round constant sea ice cover is indicative of a strongly stratified ocean with small vertical heat flux, whereas a strongly seasonal ice cover is dependent on substantial vertical oceanic fluxes. Variations in vertical heat flux are expected to yield interannual changes in ice cover extent and seasonality.

While it seems unlikely that the present mode of stratification can be overcome with the present ocean–sea ice–atmosphere coupling, offshore polynyas do occur. Gordon and Huber [1990] suggest that excess salt required to destabilize the stratification is derived from an external source: enhanced upwelling over topographic features, e.g., Maud Rise (64°S and 2°E).

As a consequence of circulation interaction with topography, the Maud Rise water column stands out as an anomaly relative to the surrounding region, with a significantly more saline and dense mixed layer [Gordon and Huber, 1990]. Below the mixed layer the water column over the crest of the Rise is identical to that over the flanks if the latter water column is upwelled by 400 meters. This uplifting is believed to be a response of the upstream flow encountering the Rise. Increased upstream flow would be expected to increase Maud Rise upwelling and the dependent salinity (density) of the mixed layer [e.g., Huppert and Bryan, 1978]. Slight increases in the mixed layer density over Maud Rise could trigger a convective mode and generation of a polynya. Additionally, around Maud Rise and to its west are patches of warm WDW [Gordon and Huber, 1990]. These patches seem to be the consequence of a wake phenomena. Accompanying them is a shallowed pycnocline. The combination of the shallow pycnocline and warm WDW encourages vertical fluxes and might trigger "chimney" convective cells and polynyas [Ou and Gordon, 1986].

It is hypothesized by Gordon and Huber [1990] that the combination of circulation to topographic coupling and spin-up of the Weddell Gyre's barotropic circulation induced by an increase of the regional wind stress curl would enhance the probability of polynya development in the vicinity of Maud Rise.

POLYNYAS AND GLOBAL WARMING

During a global warming phase would offshore polynyas become more common, cooling the deep ocean, or might they become less common, allowing warming of the deep ocean and slowing the rate of global warming?

Again we turn to the Manabe et al. [1990] model, which finds that south of 60°S the sea surface temperature remains unchanged (floating sea ice essentially anchors the surface temperature to near the freezing point) during the first 60 years after doubling of atmospheric CO_2, while the surface salinity decreases by up to 0.4 psu 50 years after doubling of atmospheric CO_2. The salinity decrease comes about from decreased convection with the deep water forced by an approximately 10% increase in precipitation minus evaporation from their model run with the present CO_2. The model sea ice thickness generally increases, in sharp contrast to the greatly thinned sea ice cover of the Arctic. The model results imply that decreased surface salinity and increased mixed layer stability suppress deep convection, making offshore polynyas less common. The model also shows warming of the deep water of the Southern Ocean as "... the CO_2 induced reduction of convective cooling causes the very slow but significant warming of the subsurface ocean layer of the model ..." [Manabe et al., 1990, pp. 739–740].

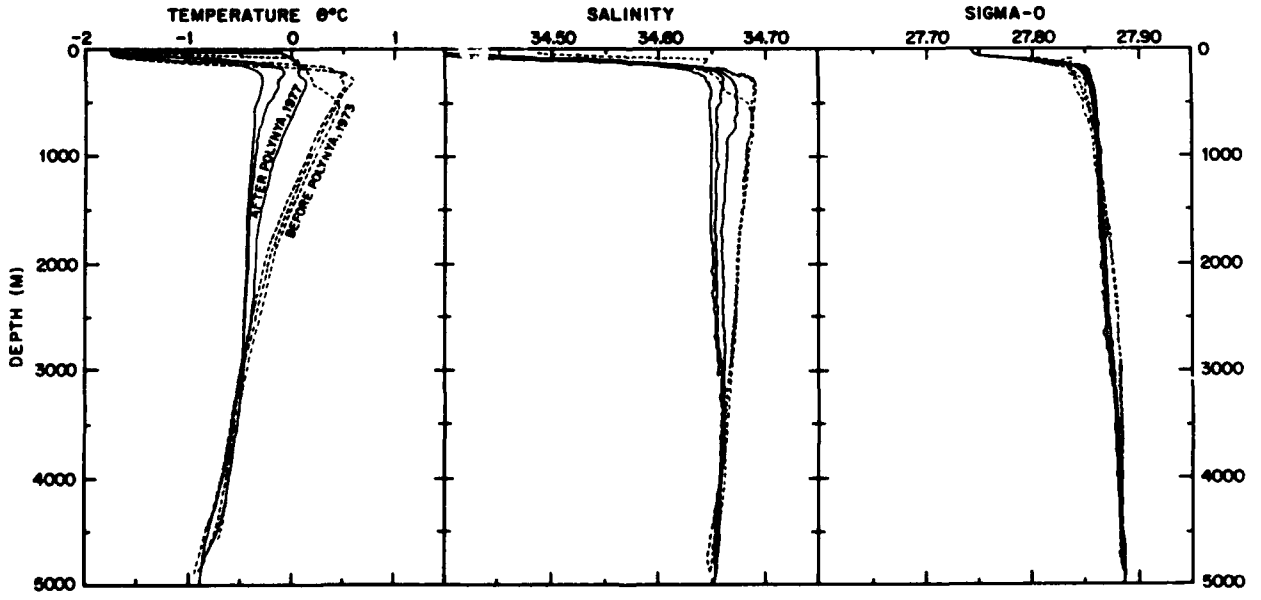


Figure 3. Potential temperature, salinity and density profiles before and after the Weddell Polynya occurrence of 1974-1976 [from Gordon, 1982].

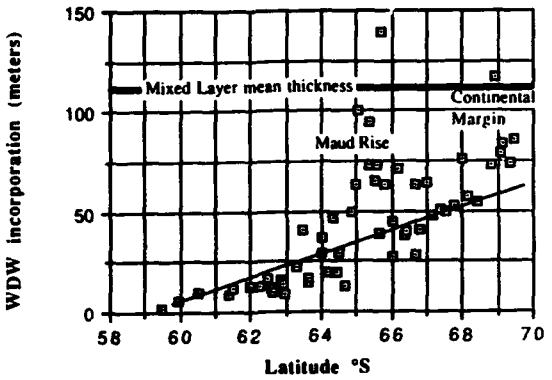


Figure 4. Weddell Deep Water (WDW; in meters) incorporation into the winter mixed layer below the sea ice cover. Values are based on oxygen undersaturation with the assumptions that oxygen is a conservative property below the winter sea ice [Gordon and Huber, 1990]. WDW entrainment increases towards the south. Maud Rise and the continental margins have higher WDW than suggested by the linear trend. This is an effect of uplifting of the water column by interaction of circulation and topography. The mean thickness of the mixed layer is 110-115 meters, which is replaced in about 2 years by WDW.

The model shows that the wind stress on the sea surface remains unchanged over 60–70°S. Therefore, the proposed relationship between wind-driven circulation and the topography-induced upwelling, mentioned above, may not be altered in the greenhouse-warmed state.

How might coastal polynyas react to global warming? This is a more difficult question since inspection of coastal wind conditions, which are driven by local factors, with global circulation models may not be justified. A speculation follows. During the early years of global warming most scientists believe that the Antarctic ice sheet will stay close to its present size and might even grow due to greater amounts of precipitation, as appears to be the case for the present-day ice sheet [Bentley and Giovinetto, 1991]. However there are large uncertainties in the various components of the ice sheet budget, including the rather significant ocean-induced melting at the base of the ice shelves [Jacobs, 1991]. This would allow continuation of drainage of cold Antarctic air directly into the coastal regions, continuing presence of coastal polynyas and associated AABW formation. If Manabe et al. [1990] are correct in that air temperatures over the sea ice zone would become colder, coastal winds driven by the contrast between air temperatures over Antarctica and air temperatures over the ocean would weaken, and polynyas would become smaller with less AABW formation. However, the colder air would compensate the smaller polynya width, producing similar amounts of sea ice [Ou, 1988]. Prediction of the response of coastal polynyas to global warming is elusive (even at the speculative level), but it is important to understand how they may change and what effect that would have on formation of AABW.

CONCLUSIONS

Greenhouse-induced global warming would be expected to influence both the formation rates and traits of AABW, AAIW and the general cooling of the global ocean's deep water. Within the polar front zone, global warming is expected to create lower salinity surface water. A reduction in the salt input to the AAIW would inject it into a shallower horizon at the thermocline base, reducing the thickness and volume of the thermocline from today's value.

Further south, within the seasonal sea ice zone, global warming may change the frequency of Southern Ocean polynyas. This would alter the ventilation potential of the Southern Ocean. If polynya frequency decreases and the sea ice cover is more complete there would be less ventilation of deep global ocean by cold antarctic water masses, resulting in warmer deep ocean (assuming the warming of the deep ocean by downward diffusion across the thermocline and formation of North Atlantic Deep Water continues). Greater heat storage in deep ocean forestalls global warming, a negative feedback to overall global warming.

Will coastal and offshore polynyas become more or less common as global warming takes hold? To answer this question we need an understanding of the forces that initiate, maintain and terminate present-day polynyas. We need to understand these processes well enough to have them properly represented in global-scale coupled general circulation models. We are not yet at this point and cannot make quantitative forecasting of polynya frequency and the effects of Southern Ocean processes on global warming. However, as always we are free to speculate, to provide an educated albeit qualitative guess. Expected: Coastal polynyas would continue in much their present form; continued formation of AABW along the continental margins of Antarctica is expected. Offshore polynyas would become less common as the mixed layer becomes more stable. This would lead to diminished open ocean convection and ventilation. Which effect is more important in regard to global ocean ventilation? That answer awaits improved, more quantitative understanding of Southern Ocean processes.

The speculations offered in this paper suggest that open ocean convection would be reduced, leading to a warmer deep ocean. However, decreased salinity of AAIW would force it to invade a shallower density horizon, limiting the thermocline's thickness and volume to less than that found in today's ocean. This counters the warming effect of the deep water. Coastal polynyas and associated AABW may not change, at least not until the Antarctic ice sheet shrinks in response to global warming, a very long-term prospect. As the thermocline change would occur at a faster rate than the deep ocean warming (based on present-day resident times, decadal to century time scales for the thermocline, with century to millennia time scales for the deep ocean), its effect would precede the polynya influence. Thus the initial influence of the Southern Ocean to global warming would be to limit heat storage within the thermocline. A longer-term influence would be to increase heat storage within the deep ocean. The latter may be more influential in the long run, due to the greater volume and heat storage ability of the deep ocean. Inspection of the magnitude and exact time scales of these proposed changes requires a global coupled ocean–atmosphere model that properly simulates the ocean's thermohaline circulation.

ACKNOWLEDGMENTS

The author's global ocean research is supported by NSF Division of Polar Programs (DPP 85-02386), Office of Naval Research (N00014-90-J-1233) and NASA (NAG W-1752). Lamont-Doherty Geological Observatory contribution number 4762.

REFERENCES

Bentley, C. B., and M. B. Giovinetto, Mass Balance of Antarctica and Sea Level Change, *This volume*, 1991.

Carmack, E. C., Circulation and mixing in ice-covered waters, in *The Geophysics of Sea Ice*, edited by N. Untersteiner, pp. 641–712, Plenum Press, 1986.

Comiso, J. C., and A. L. Gordon, Recurring polynyas over the Cosmonaut Sea and the Maud Rise, *J. Geophys. Res.*, *92*, 2819–2833, 1987.

Foldvik, A., T. Gammelsrød, and T. Tørresen, Circulation and water masses on the southern Weddell Sea shelf, in Oceanology of the Antarctic Continental Shelf, *Ant. Res. Ser.*, *43*, pp. 5–20, Am. Geophys. Union, Washington, DC, 1985.

Foster, T. D., and E. C. Carmack, Frontal zone mixing and Antarctic Bottom Water formation in the southern Weddell Sea, *Deep-Sea Res.*, *23*, 301–317, 1976.

Gordon, A. L., General ocean circulation, in Numerical Models of Ocean Circulation, Symposium, Durham, NH, 17–20 Oct, 1972, *NAS Publ. 39-53*, 1975.

Gordon, A. L., Seasonality of southern ocean sea ice, *J. Geophys. Res.*, *85*, 4193–4197, 1981.

Gordon, A. L., Weddell deep water variability, *J. Mar. Res.*, *40*(suppl), 199–217, 1982.

Gordon, A. L., Southern oceans and global climate, *Oceanus*, *31*, 39–46, 1988a.

Gordon, Spatial and temporal variability within the Southern Ocean, in *Antarctic Ocean and Resources Variability*, edited by D. Sahrhage, pp. 41–56, Springer, 1988b.

Gordon, A. L., and J. C. Comiso, Polynyas in the Southern Ocean, *Sci. Am.*, *256*, 90–97, 1988.

Gordon, A. L., and B. A. Huber, Southern Ocean winter mixed layer, *J. Geophys. Res.*, *95*, 11655–11672, 1990.

Gordon, A. L., and E. J. Molinelli, *Southern Ocean Atlas*, Columbia University Press, New York, 1982.

Gordon, A. L., E. Molinelli, and T. Baker, Large scale relative dynamic topography of the Southern Ocean, *J. Geophys. Res.*, *83*, 3023–3032, 1978.

Hays, J. D., Quaternary sediments of the Antarctic Ocean, *Progr. Oceanogr.*, *4*, 117–131, 1967.

Huber, B. A., P. Mele and A. Gordon, Report of the Winter Weddell Sea Project, ANT V/2, Hydrographic data, *L-DGO-89-1*, Lamont-Doherty Geological Observatory, Palisades, NY, 1989.

Huppert, H. E., and K. Bryan, Topographically generated eddies, *Deep-Sea Res.*, *23*, 655–679, 1976.

Jacobs, S. S., Marine controls on modern sedimentation on the Antarctic continental shelf, *Marine Geol.*, *85*, 121–153, 1989.

Jacobs, S. S., Sea level response to ice sheet evolution: an ocean perspective, in *West Antarctic Ice Sheet Initiative Science an Implementation Plan*, NASA Conference Publication, 1991, in press.

Kennett, J. P., Cenozoic evolution of Antarctic glaciation, the circum-antarctic ocean, and their impact on global paleoceanography, *J. Geophys. Res.*, *82*, 3843–3860, 1977.

Manabe, S., K. Bryan, and M. Spelman, Transient response of a global ocean–atmosphere model to a doubling of atmospheric carbon dioxide, *J. Phys. Oceanogr.*, *20*, 722–749, 1990.

Martinson, D. G, Evolution of the southern ocean winter mixed layer and sea ice: open ocean deepwater formation and ventilation, *J. Geophys. Res.*, *95*, 11641–11654, 1990.

Martinson, D. G., P. D. Killworth, and A. L. Gordon, A convective model for the Weddell Polynya, *J. Phys. Oceanogr.*, *11*, 466–488, 1981.

McCartney M. S., Subantarctic Mode Water, in A Voyage of Discovery, edited by M. Angel, *Supplement to Deep-Sea Research*, *24*, 103–119, 1977.

Nowlin, W. D., Jr., and J. M. Klinck, The physics of the Antarctic Circumpolar Current, *Rev. Geophys. Space Physics*, *24*, 469–491, 1986.

Ou, H. W., A time dependant model of a coastal polynya, *J. Phys. Oceanogr.*, *18*, 584–590, 1988.

Ou, H. W., and A. L. Gordon, Spin-down of baroclinic eddies under sea ice, *J. Geophys. Res.*, *91*, 7623–7630, 1986.

Patterson, S. L., and T. Whitworth, Physical oceanography, in *Antarctic Sector of the Pacific*, edited by G. P. Glasby, pp. 55–93, Elsevier, 1990.

Shackleton, N. J., and J. P. Kennett, Cenozoic oxygen and carbon isotope changes at DSDP site 284: Implications for glacial history of the northern hemisphere and Antarctica, in *Initial Reports of the Deep Sea Drilling Project, vol 29*, p. 801, U.S. Government Printing Office, Washington, DC, 1975a.

Shackleton, N. J., and J. P. Kennett, Paleotemperature history of the Cenozoic and the initiation of Antarctic glaciation: Oxygen and carbon isotope analysis in DSDP sites 277, 279 and 281, in *Initial Reports of the Deep Sea Drilling Project, vol 29*, p. 743, U.S. Government Printing Office, Washington, DC, 1975b.

Smith, S., R. Muench, and C. Pease, Polynyas and leads: an overview of physical processes and environment, *J. Geophys. Res.*, *95*, 9461–9480, 1990.

Tsuchiya, M., Circulation of the Antarctic Intermediate Water in the North Atlantic Ocean, *J. Mar. Res.*, *47*, 747–755, 1989.

Wadhams, P., M. Lange, and S. Ackley, The ice thickness distribution across the Atlantic sector of the Antarctic Ocean in midwinter, *J. Geophys. Res.*, *92*, 14535–14552, 1987.

Whitworth, T., Monitoring the transport of the Antarctic Circumpolar Current at Drake Passage, *J. Phys. Oceanogr.*, *13*, 2045–2057, 1983.

Zwally, H. J., J. C. Comiso, and A. L. Gordon, Antarctic offshore leads and polynyas and oceanographic effects, in Oceanography of Antarctic Continental Margin, edited by S. S. Jacobs, *Antarctic Research Series of the AGU*, *43*, 203–226, 1985.

AD-P007 296

Model Studies of the Effects of Global Warming and Antarctic Sea Ice Changes on Antarctic and Global Climates

Ian Simmonds and W. F. Budd
Department of Meteorology, University of Melbourne, Parkville, Victoria, Australia

92-17978

ABSTRACT

We discuss the results obtained in three experiments by changing the global ocean temperatures and the concentration and distribution of Antarctic sea ice in a General Circulation Model of July climate, with a view to determining the local and global impacts of Antarctic sea ice variations alone, as distinct with those coupled with global scale temperature changes which may be associated with global warming. In all cases there were significant changes in the upward flux of sensible heat over the sea ice zone associated with the reductions of sea ice.

The response of weaker westerlies between 40 and 65°S was common to all three experiments. Our analyses suggest that a significant proportion of this is a response to the change in sea ice concentration alone. (Not surprisingly, further north of this region most of the changes induced in the wind structure in the global forcing experiment can be seen as due unambiguously to the differential changes in ocean temperatures.). This weakening of the westerlies means there is less mechanical forcing of the ocean in this region. From this we suggest that when consideration is given to the possible impact of feedbacks not considered in these experiments, sea ice changes alone, and particularly those in the Southern Hemisphere, have the potential to induce changes on a hemispheric scale.

INTRODUCTION

The sensitivity of global climate to changes in various forcings is now assuming much more than academic interest as we come to realize that the climate may be very susceptible to some changes and that the time rate of change may be quite rapid. Over the past century the surface air temperature and sea surface temperature (SST) over much of the earth's surface, particularly in the south polar region [e.g., Jones, 1990; Jacka and Budd, 1991], appear to have a positive trend. In addition to any changes to the forcing on the global scale, any alteration to the boundary conditions in polar regions is of considerable importance [e.g., Budd, 1982]. One of the reasons for this is that the presence of ice and snow in these regions adds to the number of feedback processes which go into determining climate. Hence the response of climate to changes on global and polar scales may be rather different.

In this paper we use a General Circulation Model (GCM) to examine the response of local climates to some specific changes in the boundary conditions in the high latitudes and also examine the extent (realized or potential) of changes on a global scale to these changes. We also consider the problem from the reverse direction; that is to say, what is the effect on polar, and particularly Antarctic, climate of changes made in remote locations or even on a global scale. The purpose is to clarify the importance of specific forcings on atmospheric climate in certain regions.

EXPERIMENTAL DESIGN

The GCM used in these experiments is a 21-wave version of that described in Simmonds [1985] and its features of relevance to sea ice are presented in Simmonds [1981] and Simmonds and Budd [1990]; the model's performance is compared with climate statistics in Simmonds et al. [1988] and Simmonds and Dix [1989]. The specification of polar sea ice includes a fractional area of open water, f_w, at each grid point in the model. The model was run in "perpetual" July mode, with a prescribed global distribution of SST.

(The use of the "perpetual" month model is not seen as a significant reduction on the useful interpretation of these idealized experiments. It has been shown [e.g., by Zwiers and Boer, 1987] that the difference between perpetual and annual cycle model tropospheric climatologies is relatively small in mid to high southern latitudes in July.)

The "control" simulation was run with $f_w = 0.0$ (i.e., continuous sea ice) in both hemispheres. The first experiment was performed with f_w set to 0.5 in both hemispheres (i.e., 50% open water in the sea ice in both polar regions). (This is the same experiment reported in Simmonds and Budd [1990]; in that publication it was erroneously stated that f_w in the Northern Hemisphere (NH) ice had been set to 5%.) We denote this experiment as *H* referring to "Half" sea ice concentration. The second experiment upon which we report here was one in which we removed all sea ice, referred to as *R* (for "Removal").

In the third of the anomaly experiments (which we denote by *W*, for "Warm") we have increased the ocean temperatures globally. The sea surface temperature anomaly imposed in *W* is a function of latitude only and is shown in Figure 1. It was derived from the average of the four models surveyed by Grotch [1988] of the response of predicted June/July/August surface air temperature associated with a doubling of CO_2. This anomaly has been added to all the SST at a given latitude and hence the longitudinal gradients of SST are not changed. In addition to this change, at each longitude on the computational grid the two grid points containing sea ice closest to the equator in both hemispheres the sea ice was removed and replaced by open water at a temperature of -1.8°C. (Notice that two ice grid points may not exist at all longitudes.) The leads fraction was set to 0.2 in the sea ice which remained. (A similar experiment has been reported by Mitchell and Lupton [1984], but they did not consider the influence of sea ice leads. We mention that we are performing additional experiments in this series with a view to exposing the effect of changing individual parameters one at a time). The control simulation was carried out for 600 days while each of the sensitivity runs were integrated for 300 days.

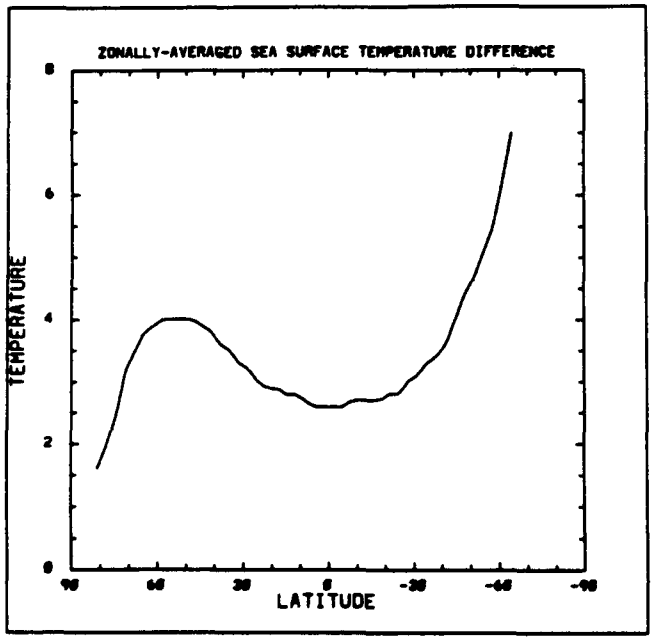


Figure 1. Latitudinal profile of the ocean temperature anomaly used in experiment *W*.

RESULTS

In the 50% leads case the sensible heat exhibits positive anomalies over all of the Antarctic sea ice region (Figure 2a). The area-weighted mean change is 75.6 W m^{-2}, with an extreme change of 236 W m^{-2} in the Ross Sea. In the control run (no leads) the sensible heat flux over most of the Antarctic sea ice is downward and hence these differences come from terms with opposite signs. We have not explicitly shown the distribution of sea ice in the model but it is in fact that region bordered by the zero sensible heat flux change in Figure 2a. In a narrow latitudinal belt to the north of the sea ice edge the sensible heat flux anomaly becomes negative. This structure has been commented upon before [e.g., Simmonds, 1981; Simmonds and Budd, 1990], and is attributed to the fact that as air flows off the continent it picks up more sensible heat over the sea ice with leads than it would over continuous sea ice. Hence such air reaches the ice-free regions warmer than in the control and is responsible for a downward anomalous sensible heat flux. The complete removal of the July sea ice (experiment *R*, Figure 2b) results in a rather similar pattern of change but, not surprisingly, the magnitudes are greater. It will be noticed, however, that this parameter shows a degree of nonlinearity with respect to f_w. The change averaged over the sea ice domain in this case is 102.9 W m^{-2}, much less than twice the value for the $f_w = 0.5$ experiment. This suggests the relatively large impact of even small open water fraction.

In experiment *W* the pattern of change is rather similar to those shown above but with some interesting differences. Near the edge of the sea ice the changes are similar to those in *R*, as might be expected. The removal of the two most equatorward ice points at each longitude in the model virtually removes all sea ice from around the east Antarctic coast so in this vicinity the forcing is the same as in *R*, but the magnitude of the sensible heat flux changes between 90 and 130°E is somewhat smaller. Further south, over the sea ice itself, the changes are small, even though there is 20% open water there. This is probably consistent with the explanation offered above. One imagines that synoptic systems in *W* would be responsible for advecting warm air to these extreme south parts of the ice pack, thus making it warmer than it would be in the control run. The increased surface temperature caused by 20% open water is nearly balanced by the increased air temperature caused by advection from the north. The sensible heat flux changes are positive over most of the far southern ice, so the effect of the leads is just sufficient to offset that of the warmer surface air temperatures. Overall, the change in the sensible heat flux averaged over the (old) sea ice region is 58.2 W m^{-2}, considerably smaller than both *H* and *R*.

In *W* there is a region of negative heat flux change just to the north of the ice edge in the control simulation. The magnitude of the changes here are smaller than those in *R* but are comparable with those in *H*. Because the SST in this vicinity had been increased by about 6°C one might have expected the region of positive heat flux anomaly to extend

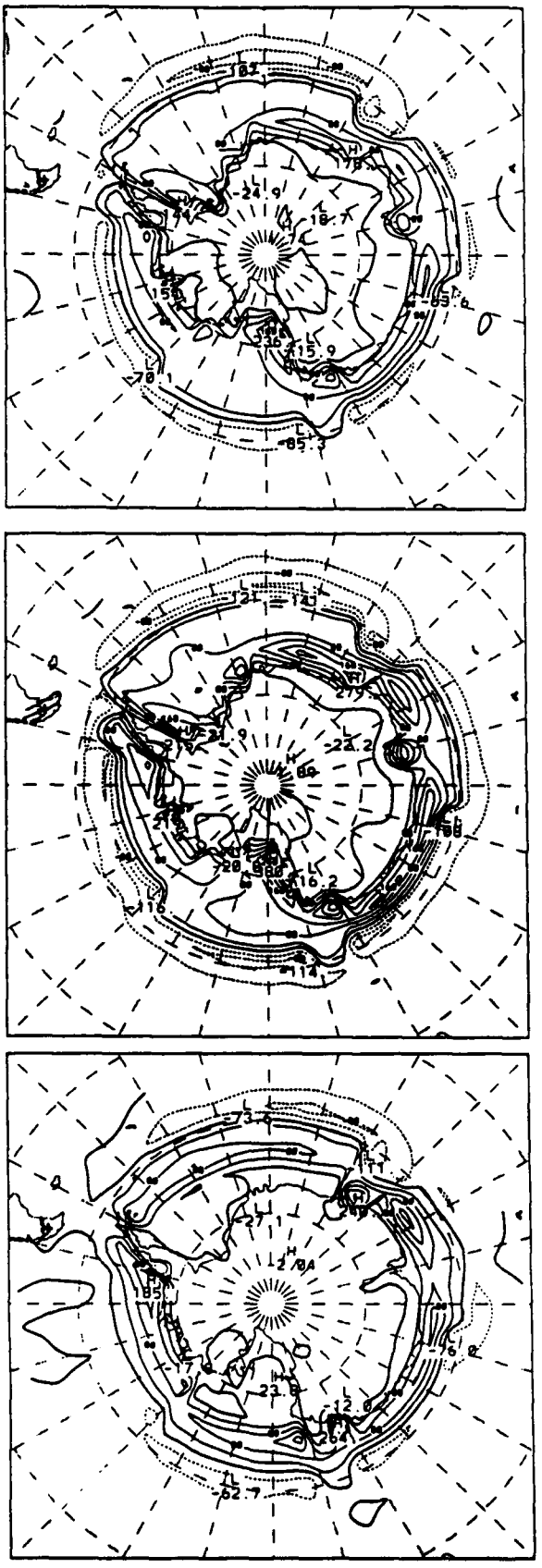


Figure 2. Difference between the (upward) surface sensible heat flux of the *H* (a) (top) *R* (b) (middle), and *W* (c) (bottom) and the control simulations. The contour interval is 40 W m^{-2}, the zero contour is accentuated and negative contours are dashed.

beyond the old sea ice edge. The fact that it does not, and that it shows similar structure to the other experiments, means that the air which flows north over the region of ice removal reaches this area with a temperature excess over that in the control sufficient to offset the effect of the increase in SST. (The air which flows *from* the north in synoptic systems will have equilibrated to a surface temperature which has been increased by a similar amount, so most of the effect discussed above is probably due to northward-flowing episodes.)

The changes in the zonal mean eastward wind component in the three experiments are presented in Figure 3. (In the Figure, stippling denotes regions where changes are significantly different from zero at the 95% confidence level (using a univariate test [Simmonds, 1981])). The reaction in *H* is virtually confined to the southern extratropics (Figure 3a). It is dominated in this region by a belt of negative (i.e., easterly) anomalies extending through the entire atmosphere between about 30 and 65°S with positive (i.e., westerly) anomalies further to the south. There is a small region of significant strengthening in the upper troposphere at 30°S. Figure 3b exhibits a rather similar pattern of change for the *R* experiment, while the magnitudes in the troposphere have increased. The negative anomalies in the mid to high latitudes of the NH have gained in intensity. Most of the significant tropospheric response in *W* (part (c)) occurs in the Southern (winter) Hemisphere. The reduction in the strength of the westerlies between 45 and 65°S are in excess of 3 m s^{-1} at the tropopause. To the north of this is a region of significantly strengthened westerlies in the upper troposphere and westerly anomalies are also simulated further to the south through much of the lower levels. Significant westerly anomalies cover much of the stratosphere outside the southern extratropics. Most of these features are similar to those simulated by Mitchell and Lupton [1984].

DISCUSSION

The experiments we have performed allow us to assess the impact on global and Antarctic climate of changes made both globally and in the polar regions only. The change in sensible heat flux over the region of the (original) Antarctic sea ice was smallest in *W*. This at first sight appeared puzzling when one considered that a large amount of Antarctic sea ice was "removed" in this experiment. (In the control experiment there was 15.7 x 10^6 km^2 of ice in this region, 7.9 x 10^6 km^2 in *H* and only 3.7 x 10^6 km^2 in *W*.) The reason for this apparently unexpected result was explained earlier and stresses the dangers of expecting quasi-linear responses in these sorts of studies.

All simulations show significant easterly anomalies (i.e., reduced westerly winds) between 40 and 65°S and westerly anomalies to the south of this. In addition, all show a slight intensification in the westerlies near 30°S in the troposphere (most pronounced in *W*). These effects tend to represent a general reduction in the strength of the circulations south of the high pressure belt with reduced sea ice and warming. The zonal wind response south of about 35°S in *H* and *R* is a sizable fraction of that simulated in *W*, indicating the important impact perturbations to the sea ice distribution and concentration alone. However, it appears that the influence of these polar changes does not extend equatorward of this latitude.

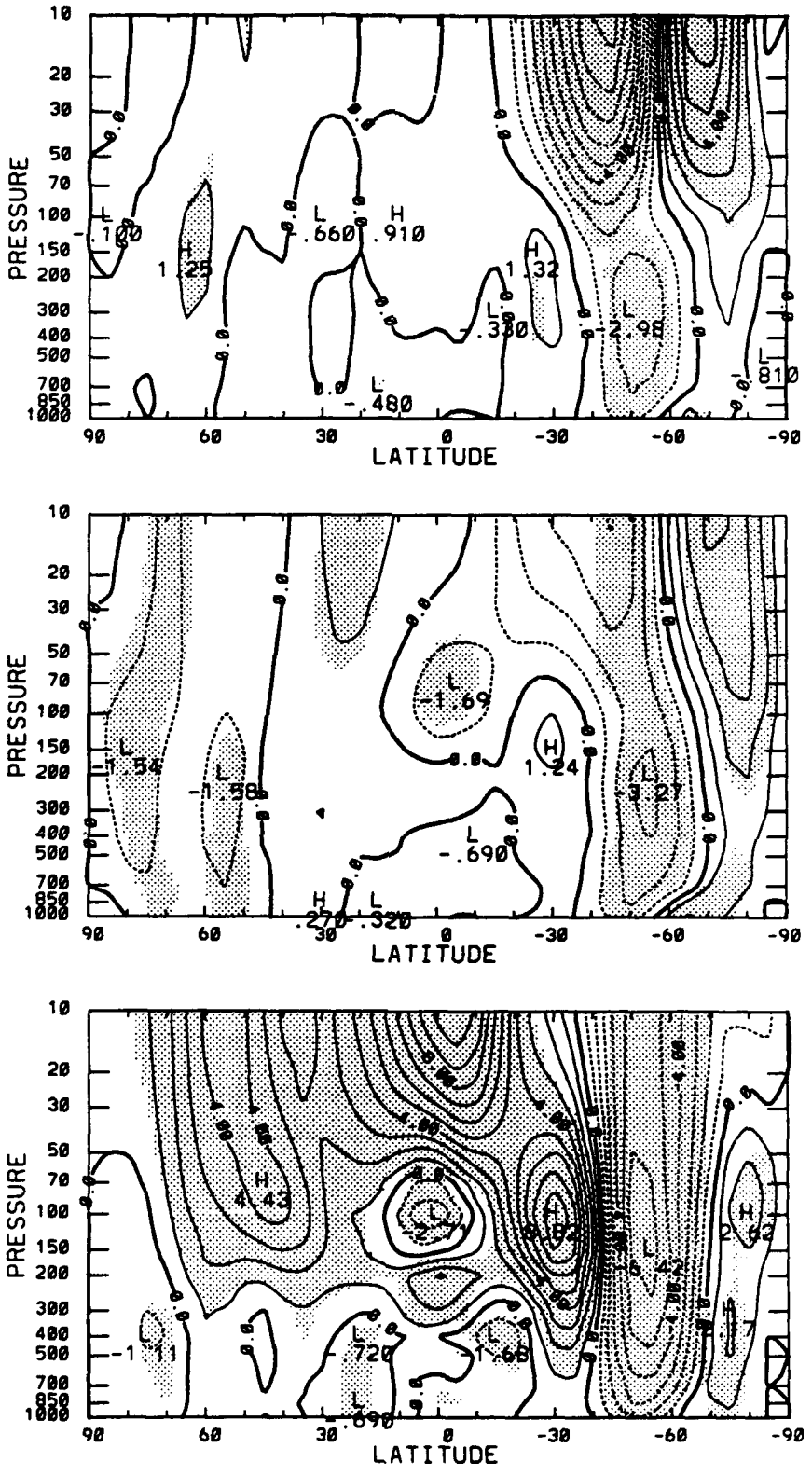


Figure 3. Difference between the zonally averaged eastward component of the wind of the *H* (a) (top) *R* (b) (middle), and *W* (c) (bottom) and the control simulations. The contour interval is 1 m s^{-1}, the zero contour is accentuated and negative contours are dashed. Regions of differences significant at the 95% confidence level are stippled.

The induced changes have an influence on the momentum balance through changes to the surface drag coefficient C_D and the surface fluxes of energy and momentum. These latter are of importance in inducing changes to the ocean circulation which in turn give rise to a redistribution of heat and SST [Budd, 1986]. In particular, the weakening of the midlatitude westerlies in the Southern Hemisphere simulated in all the experiments might be expected to change the strength of the large anticyclonic ocean gyres which are important in the maintenance of the east–west temperature gradient in the various ocean basins. Regional scale climate is quite sensitive to this gradient [e.g., Simmonds et al., 1989] and changes to it can induce large effects remotely. In our case we simply prescribe the SST and hence the ocean is not able to respond in the manner outlined above. However, we have seen that a significant part of our change induced in the southern midlatitudes comes about as a response to the sea ice modifications alone. Hence high latitude changes may be able to influence regions further removed than those considered here through the medium of oceanic response. There is much evidence to suggest that anomalies at mid to high southern latitudes do have impacts of this nature. For example, van Loon and Shea [1985] have found that the (southern) winters before Southern Oscillation Warm Events are marked by weaker surface westerlies in the central and eastern Pacific between 30 and 60°S (and westerly anomalies to the north of this belt). It may be that changes in the atmospheric flow induce changes in the oceanic circulation whose effects are felt some time later and at remote locations. The fact that significant positive correlations have been found between Antarctic sea ice extent and the Southern Oscillation Index when ice area *leads* the Index [Chiu, 1983] suggests that Antarctic sea ice is a forcing mechanism of some importance in this sequence. This is consistent with the picture presented above. The validity of these ideas can only really be tested in a reliable coupled atmosphere–ocean model.

We can examine, however, the changes in the exchange coefficients (which depend on wind speed, stability and surface type in the manner detailed in Simmonds [1985]) and surface stresses induced in these simulations. The zonal average of C_D in the three experiments and the control is displayed in Figure 4. The drag coefficient simulated in the control run is about 1.0×10^{-3} in midlatitudes and decreases slowly towards the sea ice edge. Due to the increased roughness of sea ice compared to that of open water the drag coefficient rises to over 2.0×10^{-3} over the sea ice and drops back to about 1.0×10^{-3} over the Antarctic continent, due to the extreme low level stability. Mitchell and Senior [1989] have also found that a change in surface roughness contributed substantially to the response to reduced (continuous) sea ice extents.

As leads are opened up in the pack ice there are two competing influences in changing C_D. First, as warm water is exposed beneath a cold atmosphere the stability dependence in the drag coefficient will tend to increase C_D. On the other hand, in the model the roughness length of the exposed water is considerably less than that of the sea ice so this will tend to diminish the drag coefficient. It is clear from Figure 4 that the second influence dominates. Andreas and Murphy [1986], among others, have studied the behavior of bulk transfer coefficients over sea ice with leads. This behavior

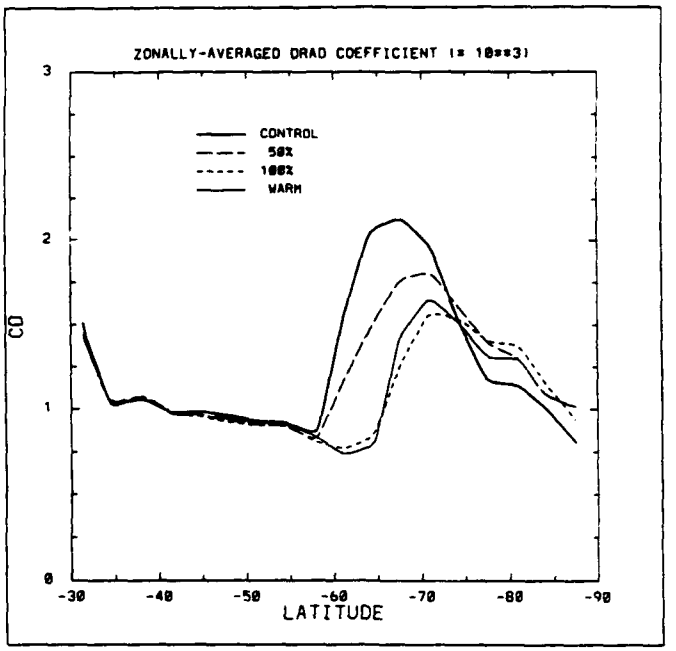


Figure 4. Zonally averaged drag coefficient (x 10^3) in the *H* (50%), *R* (100%), *W* (WARM) and control (CONTROL) simulations.

of the drag coefficient with sea ice concentration is consistent with the observations and atmospheric boundary layer model results of Burns [1990]. She found that the drag coefficient decreased almost linearly with f_w, and under "rough" sea ice conditions (floe sizes between 5 and 50 m) the drag coefficient decreased by about a factor of two in association with a change of f_w from 0.0 (solid ice) to 1.0 (open water). The data presented in Figure 4 show our modeled C_D to exhibit a very similar behavior. The zonal averages presented here must be treated with a little caution because at certain latitudes the zonal average contains other than sea ice points. To allow a better appreciation of changes over the sea ice region (as defined in the control simulation) we have calculated the mean drag coefficient over this region in the various experiments. The mean of C_D is 2.19×10^{-3} in the control. This is reduced by 1.30, 0.60 and 1.36×10^{-3} in *W*, *H* and *R*, respectively. The reductions effected in the last two are rather similar to the values of Burns [1990].

The changes in the drag coefficient and the near-surface winds have implications for the momentum flux across the earth–atmosphere boundary which are of relevance to the forcing of the ocean circulation. The meridional distribution of the eastward component on the surface stress in the control run and the three experiments are displayed in Figure 5. North of the sea ice edge (about 60°S) there is a reduction in the stress in the *H* experiment compared to the control and an even greater reduction in *R*. Differences are seen as far north as 40°S. For the most part there is an even greater reduction in *W*. From Figure 4 it is seen that there is very little change in C_D over this latitude domain (even in *W* in which the surface temperatures had been changed dramatically), so any changes in the stress come about as a result of changes in the wind speed. This is consistent with the surface wind changes displayed in Figure 3. Over most of the

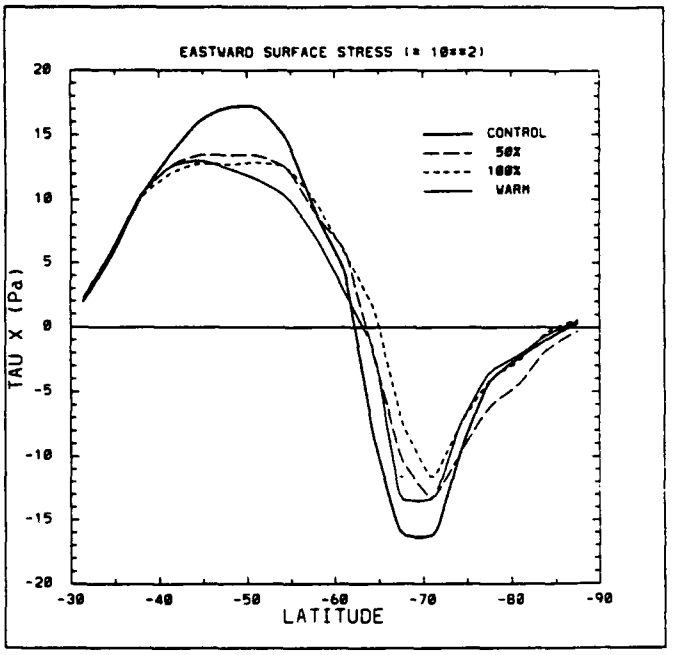


Figure 5. Zonally averaged eastward surface wind stress (x 10^2 Pa) in the *H* (50%), *R* (100%), *W* (WARM) and control (CONTROL) simulations.

sea ice zone there is a reduction of the westward stress in *H* and *R*, which is more marked in the latter. In this case the change comes about as a result of two complementary influences; the progressive reduction of the drag coefficient from the control, through to *H* and *R* (Figure 4) and the presence of westerly surface wind anomalies in this region, being stronger in *R*. Interestingly, the eastward stress in *W* is more similar to the control over this region than either *H* or *R* is to the control. This is in spite of the fact the C_D associated with this simulation is further removed from the control than that for *H*. Over the sea ice region the eastward surface stress on the atmosphere in the control simulation is -0.65 Pa and positive anomalies of 0.38, 0.48 and 0.78 Pa are simulated in *W*, *H* and *R*, respectively.

CONCLUDING REMARKS

We have compared the global and high southern latitude atmospheric response of a GCM to the specification of fraction of open water in the Antarctic winter pack ice. Experiments have been performed with this fraction set at 50% and at 100% (i.e., complete ice removal) and we have compared these simulations with one in which the ocean temperatures on a global basis were specified to be those which might be expected under global warming conditions and an associated reduction of sea ice by about 7° of latitude. Our results allow us to estimate the local and global impact of local and global changes in the surface conditions which may be associated with global warming.

In all cases the surface flux of sensible heat across the area of Antarctic sea ice zone increased significantly. The smallest increase was simulated in the *W* experiment, even though the Antarctic sea ice specified in this case was less than that in *H*. We have discussed the reasons for this apparently contradictory response. At high southern latitudes the changes in the zonal average of the eastward wind component showed similar tropospheric structure in all three experiments, with weaker westerlies between 40 and 65°S and anomalous westerlies further south. The amplitude of these responses are smallest in *H*, and greatest in *W*. The results demonstrate the important role in these changes played by perturbations of sea ice concentration on its own. (Further north of this region most of the changes induced in the wind structure in *W* can been seen as due unambiguously to the differential changes in ocean temperatures.) Even though the surface temperature in this vicinity has been changed in *W* the zonal average of the computed surface drag coefficient in the experiment, and indeed the other two, is very similar to that in the control. The weakening of the westerlies mentioned above suggests less mechanical forcing of the ocean in this region which, in turn, may have implications on changes on a larger scale. The results of these experiments point to some of the roles which may be played by Antarctic sea ice variations alone in a global warming and in association with some feedbacks not considered here.

REFERENCES

Andreas, E. L., and B. Murphy, Bulk transfer coefficients for heat and momentum over leads and polynyas, *J. Phys. Oceanogr.*, *16*, 1875–1883, 1986.

Budd, W. F., The role of Antarctica in southern hemisphere weather and climate, *Aust. Met. Mag.*, *30*, 265–272, 1982.

Budd, W. F., The Southern Hemisphere circulation of atmosphere ocean and sea ice, *Proceedings of the Second International Conference on Southern Hemisphere Meteorology*, pp. 101–106, Wellington, New Zealand, December, 1986, Amer. Met. Soc., 1986.

Burns, B. A., SAR image statistics related to atmospheric drag over sea ice, *IEEE Transactions on Geoscience and Remote Sensing*, *28*, 158–165, 1990.

Chiu, L. S., Antarctic sea ice variations 1973–1980, in *Variations in the Global Water Budget*, edited by A. Street-Perrott, M. Beran, and R. Ratcliffe, D. Reidel, 1983.

Grotch, S. L., Regional intercomparisons of general circulation model predictions and historical climate data, *DOE/NBB-0084*, 291 pp., 1988.

Jacka, T. H., and W. F. Budd, Detection of temperature and sea ice extent changes in the Antarctic and Southern Ocean, *this volume*, 1991.

Jones, P. D., Antarctic temperatures over the present century—A study of the early expedition record, *J. Climate*, *3*, 1193–1203, 1990.

Mitchell, J. F. B., and G. Lupton, A 4 x CO_2 integration with prescribed changes in sea surface temperatures, *Progress in Biometeorology*, *3*, 353–374, 1984.

Mitchell, J. F. B., and C. A. Senior, The Antarctic winter: simulations with climatological and reduced sea-ice extents, *Quart. J. Roy. Meteor. Soc.*, *115*, 225–246, 1989.

Simmonds, I., The effect of sea ice on a general circulation model of the Southern Hemisphere, *Sea Level, Ice, and Climate Change: Proceedings of the IUGG Canberra Symposium, December 1979*, *IAHS Publ. No.131*, pp. 193–206, 1981.

Simmonds, I. Analysis of the 'spinup' of a general circulation model, *J. Geophys. Res.*, *90*, 5637–5660, 1985.

Simmonds, I., and W. F. Budd, A simple parameterization of ice leads in a GCM and the sensitivity of climate to a change in Antarctic ice concentration, *Ann. Glaciol.*, *14*, 266–269, 1990.

Simmonds, I., and M. Dix, The use of mean atmospheric parameters in the calculation of modelled mean surface heat fluxes over the world's oceans, *J. Phys. Oceanogr.*, *19*, 205–215, 1989.

Simmonds, I., G. Trigg, and R. Law, The Climatology of the Melbourne University General Circulation Model, *Pub. No. 31*, Department of Meteorology, University of Melbourne, 67 pp. [NTIS PB 88 227491.], 1988.

Simmonds, I., M. Dix, P. Rayner, and G. Trigg, Local and remote response to zonally uniform sea-surface temperature in a July general circulation model, *Intl. J. Climatology*, *9*, 111–131, 1989.

van Loon, H,. and D. J. Shea, The Southern Oscillation: The precursors south of 15°S to the extremes of the Oscillation, *Mon. Wea. Rev.*, *113*, 2063–2074, 1985.

Zwiers, F. W., and G. J. Boer, A comparison of climates simulated by a general circulation model when run in the annual cycle and perpetual modes, *Mon. Wea. Rev.*, *115*, 2626–2644, 1987.

AD-P007 297

92-17979

Antarctic Sea Ice and Temperature Variations

John E. Walsh
Dept. of Atmospheric Sciences, University of Illinois, Urbana, Illinois, U.S.A.

H. Jay Zwally
Oceans and Ice Branch, NASA Goddard Space Flight Center, Greenbelt, Maryland, U.S.A.

John W. Weatherly
Dept. of Atmospheric Sciences, University of Illinois, Urbana, Illinois, U.S.A.

ABSTRACT

Monthly antarctic station temperatures are used in conjunction with grids of sea ice coverage in order to evaluate temporal trends and the strength of associations between the two variables at lags of up to several seasons. The trends of temperature are predominantly positive in winter and summer, but predominantly negative in spring. The spatially aggregated trend of temperature is small but positive, while the corresponding trend of ice coverage is small but negative. Cross-correlations between concurrent anomalies of the two variables are negative over most of the continent and are strongest over the Antarctic Peninsula, especially in winter. In regions other than the Antarctic Peninsula, lag correlations between seasonal anomalies are generally stronger with ice lagging the summer temperatures and with ice leading the winter temperatures.

INTRODUCTION

Temperature fluctuations in the polar regions are of particular interest in the context of global change because of the possible amplification of these fluctuations by various feedback mechanisms. Among the factors that may be involved in such feedbacks are changes in polar clouds and atmospheric water vapor, the vertical stratification of temperature, and sea ice coverage. The latter is associated with large surface albedo fluctuations that underlie the so-called "temperature–ice–albedo feedback," which contributes to the polar amplification of the climatic warming projected by global climate models under various scenarios of increasing greenhouse gas concentrations. The land-based observational record shows that the northern hemisphere warming of the 1900–1940 period was approximately three times larger in the Arctic than in middle latitudes [e.g., Hansen and Lebedeff, 1987, Figures 6–7].

Despite its potential climatic importance, however, there has been surprisingly little quantitative assessment of this feedback on the basis of either observational data or model output. The feedback will clearly depend on the magnitudes of the effects of sea ice and air temperature on each other. One of the aims of this study is an evaluation of lead–lag relationships involving sea ice and air temperature, with an eye toward feedbacks that may enhance climatic change. A second aim is an evaluation of the recent trends of surface air temperature in the Antarctic. This evaluation is motivated by the possibility that a spatially coherent pattern of high-latitude temperature trends could be an early indicator of climatic change in view of climate models' relatively strong polar sensitivities to prescribed changes of greenhouse gas concentrations. However, the recent (1965–present) hemispheric "warming" has not been amplified in the Arctic [Hansen and Lebedeff, 1987], and the spatial pattern of recent arctic and subarctic temperature changes is quite complex [Jones, 1988, Figure 2]. Several northern subregions (e.g., Europe, Baffin Bay–Davis Strait) even display a net cooling trend since 1967. There have been no systematic evaluations of the spatial and seasonal variations of the trends of recent antarctic air temperatures, especially

in the context of corresponding sea ice variations. A companion paper in this volume [Zwally et al., 1991] describes the trends of satellite-derived sea ice coverage during 1973–1987 over the antarctic waters and various subregions.

DATA SOURCES

The computations utilize data from two sources. The air temperatures are the monthly antarctic station temperatures compiled by Jones and Limbert [1988]. This dataset contains temperatures for 29 stations (Figure 1 and Table 1) with varying periods of record. As shown in Table 1, most of the records began in the 1950s (generally in conjunction with the IGY) and extend through the present. This study does not utilize data subsequent to December 1987, which is the ending date of the record of available sea ice data. The Jones and Limbert [1988] compilation drew primarily on data from the *World Weather Records*, *Monthly Climatic Data for the World*, and supplemental sources such as the records of weather services of individual nations.

	Name	Period of Record	Latitude (S°)	Longitude (°)
1	Rothera Point	1946-1988	67°34'	68°08'W
2	Faraday	1944-1988	65°15'	64°15'W
3	B. A. Arturo Prat	1966-1988	62°30'	59°41'W
4	Bellinghausen	1944-1988	62°12'	58°56'W
5	Pdte. Eduardo Frei	1969-1988	62°15'	58°56'W
6	B. A. Bernardo O'Higgins	1963-1988	63°19'	57°54'W
7	Esperenza	1945-1988	63°24'	56°59'W
8	Vicecomodoro Marambio	1970-1988	64°14'	56°49'W
9	Signy Is.	1947-1988	60°45'	46°30'W
10	Islas Orcadas	1903-1988	60°44'	44°44'W
11	General Belgrano	1955-1979	77°58'	38°48'W
12	Halley Bay	1956-1988	75°30'	26°39'W
13	S. A. N. A. E.	1957-1988	70°19'	2°21'W
14	Novolazarevskaja	1961-1988	70°46'	11°50'E
15	Syowa	1957-1988	69°00'	39°35'E
16	Molodeznaja	1963-1988	67°40'	45°51'E
17	Mawson	1954-1988	67°36'	62°53'E
18	Davis	1957-1988	68°35'	77°59'E
19	Mirny	1956-1988	66°33'	93°01'E
20	Vostok	1958-1988	78°27'	106°52'E
21	Casey	1957-1988	66°15'	110°32'E
22	Dumont D'Urville	1956-1988	66°40'	140°01'E
23	Leningradskaja	1971-1988	69°30'	159°23'E
24	Scott Base	1957-1987	77°51'	166°45'E
25	McMurdo	1956-1988	77°51'	159°23'E
26	Russkaja	1980-1988	74°42'	136°51'W
27	Byrd Station	1957-1975	80°01'	119°23'W
28	Siple	1978-1986	75°55'	83°55'W
29	Amundsen-Scott	1957-1988	90°00'	–

Table 1. Antarctic stations: Periods of record and locations.

The sea ice computations are based on the digitized weekly ice charts of the Navy/NOAA Joint Ice Center [e.g., Gross, 1986]. These charts have been produced operationally since January, 1973 and have been subsequently digitized at ~25-km resolution. The primary input for the antarctic ice charts is satellite imagery, especially the passive microwave images obtained from the Nimbus-5 and Nimbus-7 satellites. Our transformation of these grids into monthly grids at somewhat coarser resolution is described in the following section.

COMPUTATIONS

The digitized weekly ice charts for the Antarctic were processed into a slightly coarser grid for determining the temporal variations of ice cover. The ice concentrations for the end of each month were obtained by interpolating in time between the last week of the month and the first week of the next month. The concentrations were then interpolated bilinearly to a polar stereographic grid with a cell size of 110 km x 110 km. Thus, one grid of sea ice concentrations in the Southern Ocean was created for each month of the record. From these, the actual ice area was computed for fixed 20° longitudinal sectors by summing the products of the ice concentrations and the corresponding ocean areas of all grid cells in each 20° sector. The areal ice extent was computed by summing the areas of all grid cells with concentrations greater than 15%.

For the purposes of the analyses of trends and cross-correlations, the actual ice areas in 20° longitudinal sectors were averaged over three-month seasons (Jan.–Mar., Apr.–June, July–Sept., Oct.–Dec.). The surface station air temperatures were also grouped into seasonal averages. Seasons with all three months of temperatures missing were included in neither the trend nor correlation computations.

The trends in air temperature and sea ice area and extent were obtained using the seasonal "anomalies" or departures from the 15-year mean of 1973–1987. For each season the data were fit to a straight line by the method of least squares. The slope of that line is said to be the trend over that period. Statistical significance of the trends was tested

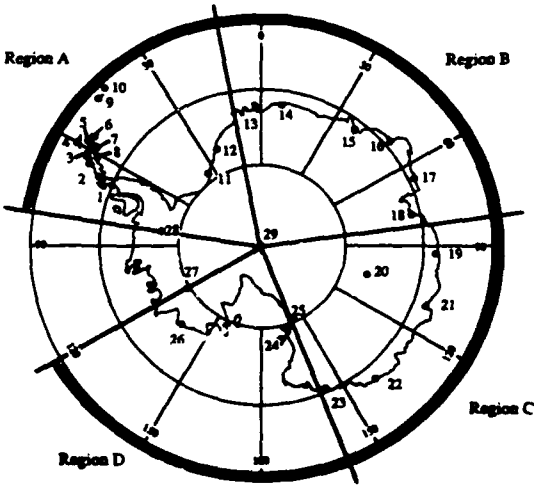


Figure 1. Locations of the 29 stations listed in Table 1. A–D are regions over which results are consolidated (see text). (Adapted from Jones and Limbert [1988].)

by comparing the slope of the linear regression line to the standard deviation of slopes expected from a normal distribution of values about the line.

The relationship between the air temperature and ice area anomalies was investigated by computing the correlation coefficient between the seasonally averaged temperatures at an observing station and the actual ice area of the 20° longitudinal sector in which the station is located. The correlation of the two variables was computed for cases with no seasonal lag, and with lags of one and two seasons. Correlations are shown in the following section for the various leads and lags of the ice anomaly relative to the temperature anomaly of a given season. Finally, the correlations were also regionally averaged according to the divisions in Figure 1. Region A includes the largest number of stations, near to and on the Antarctic Peninsula. Regions B and C include most of East Antarctica. Region D, which contains very few stations, includes the western Antarctic and the Ross Sea.

RESULTS

Figure 2 shows the time series of end-of-the-month sea ice coverage and sea ice extent for the entire antarctic region. The time series is dominated by the seasonal cycle, as the ice-covered area varies from approximately 3 x 10^6 km^2 in late summer to 18–20 x 10^6 km^2 in late winter. However, substantial interannual variability is also present, especially in the late-winter maxima. The greatest ice extent and areal coverage were reached in the early years of the record (1973–1975), after which the smallest late-winter maximum occurred (1977). These interannual variations are very similar to those computed directly from the satellite passive microwave data [Zwally et al., 1991]. There is also fairly close agreement in Figure 2 between the interannual fluctuations of ice extent and areal coverage, implying that either measure of sea ice variability is a reasonable proxy for the other.

The envelopes of the annual maxima and minima in Figure 2 vary rather smoothly from year to year, indicating that the interannual fluctuations are autocorrelated at lags of a year. Relative minima in the late-winter (maximum) ice coverage occurred in 1977 and 1987, while relative minima in the late-winter (minimum) ice coverage occurred in 1974, 1980 and 1985. The overall linear trends of the time series of both ice extent and areal coverage are slightly negative, primarily because of their large maxima in the first three winters. However, the trends are not statistically significant. Zwally et al. [1991] report similar conclusions from a trend analysis of the passive microwave data for the Antarctic.

The linear trends of surface air temperature for winter (July–September) and spring (October–December) are shown in Figure 3. (The plotted trends are for the period 1973–1987, inclusive; stations for which no value is plotted were missing more than one-third of the months of data.) The trends for each season show some spatial coherence in the sense that adjacent stations generally (but not always) have trends of the same sign. The stations with trends of the largest magnitude are also generally in the same region, e.g., the Antarctic Peninsula in winter, the Davis Sea in spring. While the winter map is dominated by positive (warming) trends, the spring map contains mostly negative (cooling) trends. The four-season summary in Table 2 shows that summer and winter are characterized by a general warming, and that spring is characterized by a general cooling. In

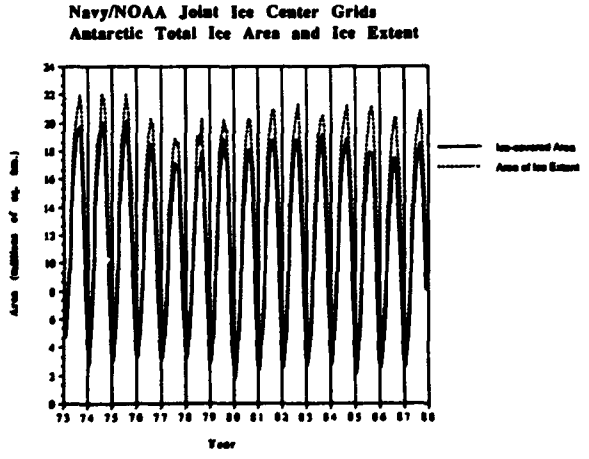


Figure 2. Time series of ice-covered area (solid line) and areal ice extent (dashed line) for the entire antarctic region, 1973–1987. Labels on abscissa denote start of calendar year.

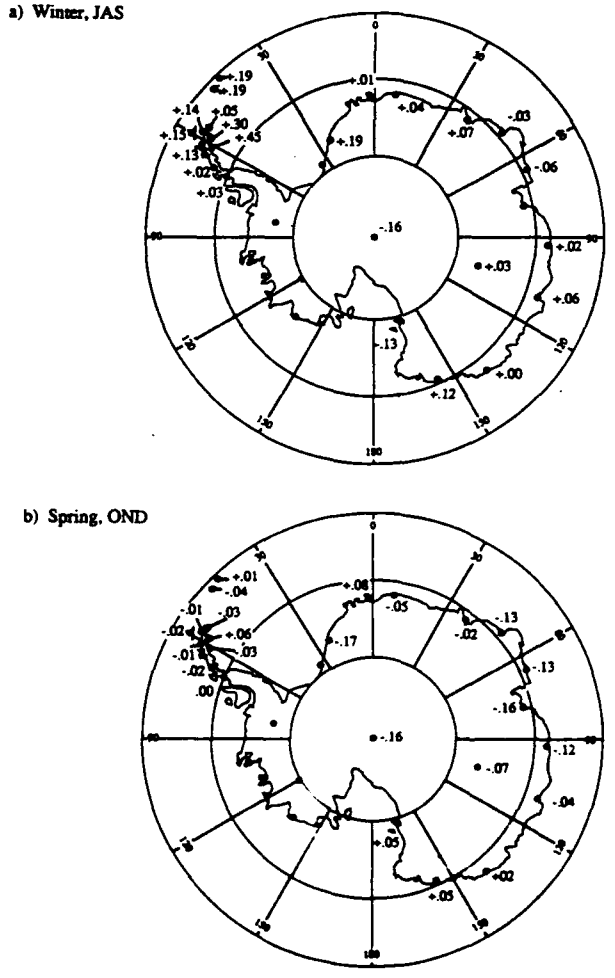


Figure 3. Temperature trends (°C yr^{-1}) at individual stations for (a) winter (July–September) and (b) spring (October–December).

Season	Stations w/ warming	Stations w/ cooling
Winter—JAS	17	8
Spring—OND	8	17
Summer—JFM	21	4
Autumn—AMJ	12	13

Table 2. Numbers of Antarctic stations with warming and cooling trends over the period 1973-1987 by season.

autumn, warming and cooling are indicated at approximately equal numbers of stations. The results thus illustrate the dangers of extrapolating trends from one season to another. Overall, the seasonally and areally averaged trend for the Antarctic is slightly positive but not significantly different from zero. This weakly positive annual trend is consistent with the very weak negative trend in overall antarctic sea ice coverage. We emphasize that neither trend is statistically significant (at the 95% level) for the Antarctic as a whole.

It should be noted that the regional trends of temperature and sea ice are generally larger than the areally and seasonally averaged trends. In the Weddell Sea, for example, ice extent during winter shows a statistical decrease from the late 1970s into the 1980s; the corresponding trends of winter temperature are positive. Specific "clusters" of years also show consistent anomalies of sea ice and temperature in the Weddell Sea, e.g., the positive ice and negative temperature anomalies in the winters of 1979–1981, and the opposite anomalies of each variable in 1982-83.

The consistency between anomalies of air temperature and sea ice coverage was examined more systematically in terms of cross-correlations between the respective anomalies. While they are quantitative measures of associations, these cross-correlations are not necessarily indicators of causality because both variables may be influenced by other "external" factors. However, cross-correlations of the two variables at various lags can be used to construct so-called "cross-correlation functions," in which asymmetries may indicate that the association is stronger with one variable leading than with the same variable lagging the other. Cross correlations of northern hemisphere sea ice and temperature [e.g., Lemke et al., 1980] are indeed characterized by a distinct asymmetry such that the larger correlations occur when temperature leads ("forces") the ice. In the sense that these asymmetries can suggest which links of a feedback loop are stronger, the cross-correlations can be regarded as the "building blocks" of a quantitative diagnosis of feedback loops.

Figure 4 shows the zero-lag cross-correlations computed from the concurrent seasonally averaged air temperature and sea ice coverage during the 1973–1987 period. (The plotted cross-correlations are averages of the values for all stations in each of the four regions—A, B, C, D—shown in Figure 1. The cross-correlation for each station is based on ice coverage in the 20° longitudinal sector containing the station.) Except for the data-sparse Region D, the cross-correlations are consistently negative, indicating the general coincidence of positive sea ice anomalies and negative temperature anomalies (and the converse). The cross-correlations are largest in Region A (Antarctic Peninsula) in the autumn and winter seasons, when the average values of -0.7 to -0.9 indicate that over half the variance in one variable can be described by the other. The cross-correlations in the other regions are smaller, especially in spring (OND). The small correlations in spring suggest that springtime temperatures are least likely to affect concurrent sea ice anomalies, probably because the springtime ice distribution is determined largely by the atmospheric and oceanic forcing of the previous two seasons.

Figure 5 shows the cross-correlations for lags of up to ±2 seasons relative to summer and winter temperatures. The summer results for Regions A–C display the asymmetry that characterizes the northern hemisphere results [e.g., Lemke et al., 1980]; the cross-correlations are larger when ice lags

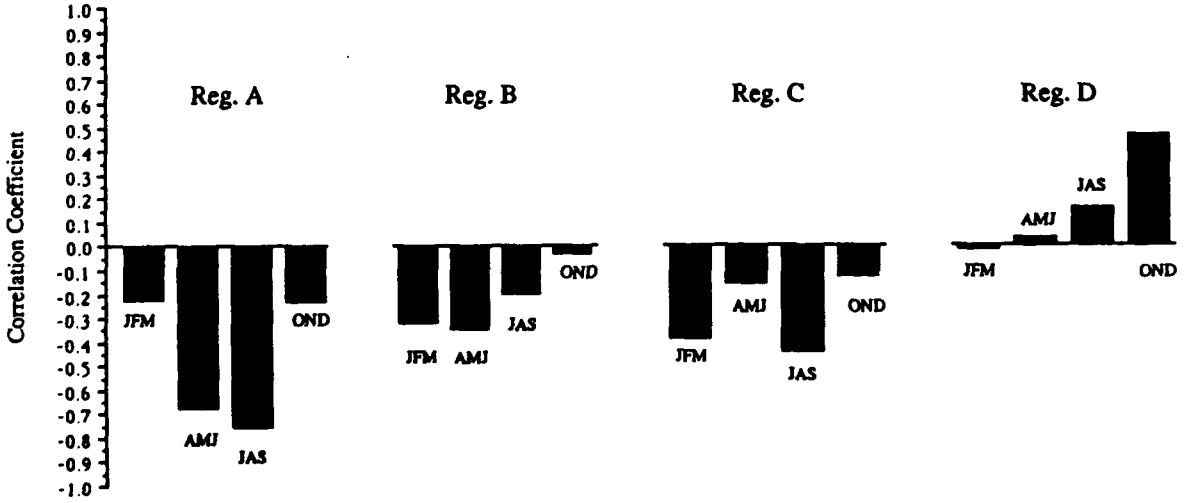


Figure 4. Zero-lag correlations between seasonally averaged surface air temperature and sea ice area in 20° longitudinal sector of corresponding station. Correlations are averaged over all stations in Regions A–D (see Figure 1). Regional average correlations are plotted for each three-month season (JFM = summer, AMJ = autumn, etc.).

temperature, suggesting that an ice anomaly tends to be a "response" to the thermal forcing in the immediate vicinity. The small values for Region D result from a combination of the sparse network of temperature data and the general absence of summer sea ice in Region D.

Perhaps the most noteworthy feature of Figure 5 is the asymmetry of the opposite sense in the *winter* temperature results, which indicate that the cross-correlations are larger (in Regions B, C, D) when the ice anomaly leads rather than lags the winter temperature anomaly. These results suggest that, in Regions B–D, winter temperatures are influenced by the ice conditions of the antecedent summer and autumn. Statistically, this influence is stronger than the influence of winter temperature on the ice of the *subsequent* spring and summer. Taken together, the top and bottom portions of Figure 5 indicate that summer and autumn temperature anomalies influence winter ice anomalies in the East Antarctic (Regions B and C) and that the ice anomalies, in turn, influence the air temperatures of the following two seasons. This feedback of ice to temperature is stronger than that found in corresponding arctic data analyses, although such a feedback has been detected *locally* in autumn data for Barrow, Alaska [Rogers, 1978].

CONCLUSION

The results described here show that anomalies of antarctic sea ice and temperature are consistent in the sense that the anomalies are negatively correlated, e.g., above-normal air temperatures are associated with below-normal ice coverage. This consistency was detectable in the weak temporal trends and in the cross-correlations of seasonal anomalies. The fact that the cross-correlations are largest over the Antarctic Peninsula is noteworthy because it implies that the results obtained here may underestimate the true strength of the associations in Regions B–D, where the air temperatures are for stations considerably poleward of the ice margin during much of the year. The peninsular stations, on the other hand, are actually in the marginal ice zone during a large portion of the year.

Several findings obtained here are potentially relevant to global change. First, spatially averaged trends of annual mean antarctic station temperatures are quite small, but these broad averages obscure regional and seasonal trends that can be large. For example, the temperature trends are generally positive in winter and summer but negative in spring. Second, there are quantitative indications of a temperature feedback involving sea ice. High latitude temperature feedbacks have been the subject of considerable speculation [e.g., Kellogg, 1975], but little use has been made of actual data for the quantitative diagnosis of such feedbacks. It is hoped that the results presented here will stimulate further analysis of both model output and observational data in order to clarify the role of sea ice feedbacks in the climate system.

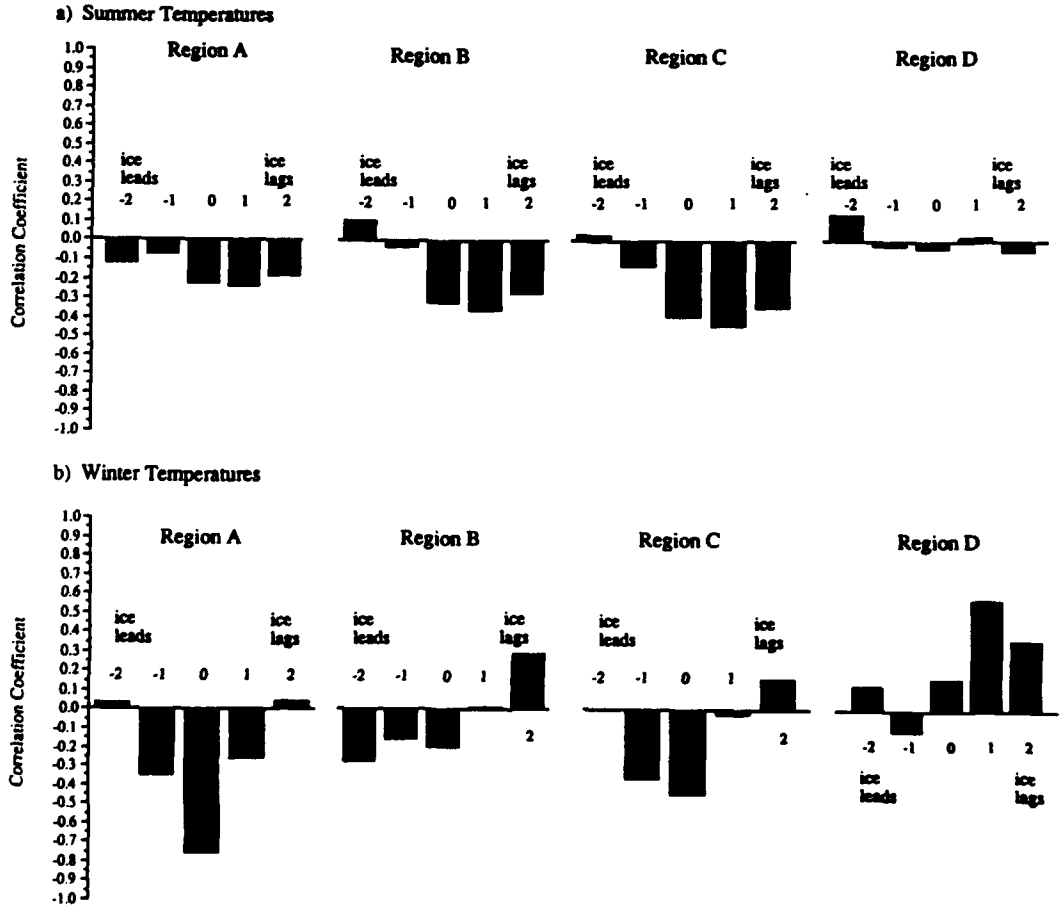


Figure 5. Regional averages of correlations between seasonally averaged surface air temperature and sea ice area in 20° longitudinal sectors of corresponding stations. Correlations are plotted as a function of lag of sea ice relative to (a) summer (JFM) temperature and (b) winter (JAS) temperature.

REFERENCES

Gross, C. E., Joint Ice Center global sea ice digital data, in *Snow Watch '85*, edited by G. Kukla, R. G. Barry, A. Hecht, and D. Wiesnet, pp. 125–126, *Glaciological Data GD-18*, World Data Center for Glaciology, Boulder, CO, 1986.

Hansen, J., and S. Lebedeff, Global trends of measured surface air temperature, *J. Geophys. Res.*, *92*, 13345–13372, 1987.

Jones, P. D., Hemispheric surface air temperature variations: Recent trends and an update to 1987, *J. Climate*, *1*, 654–660, 1988.

Jones, P. D., and D. W. S. Limbert, Antarctic surface temperature and pressure data, *NDP032*, Carbon Dioxide Information Analysis Center, Oak Ridge National Laboratory, Oak Ridge, TN, 1988.

Kellogg, W. W., Climatic feedback mechanisms involving the polar regions, in *Climate of the Arctic*, edited by G. Weller and S. A. Bowling, pp. 111–116, Geophysical Institute, Univ. of Alaska Fairbanks, 1975.

Lemke, P., E. W. Trinkl, and K. Hasselmann, Stochastic dynamic analysis of polar sea ice variability, *J. Phys. Oceanogr.*, *10*, 2100–2120, 1980.

Rogers, J. C., Meteorological factors affecting interannual variability of summertime ice extent in the Beaufort Sea, *Mon. Wea. Rev.*, *106*, 890–897, 1978.

Zwally, H. J., J. C. Comiso, and J. E. Walsh, Variability of antarctic sea ice, *this volume*, 1991.

Zwally, H. J., C. L. Parkinson, and J. C. Comiso, Variability of Antarctic sea ice and CO_2 change, *Science*, *220*, 1005–1012, 1983.

AD-P007 298

92-17980

The Role of the Southern Ocean/Sea Ice Interaction in Global Climate Change

Douglas G. Martinson
Lamont-Doherty Geological Observatory, Palisades, New York, U.S.A.

ABSTRACT

The seasonal sea ice field of the Southern Ocean strongly modulates climate through its insulating effect and high albedo. Consequently, it plays a significant role in global climate and must be adequately parameterized for inclusion in large-scale circulation models attempting to predict the nature of global change. Recent field studies and modeling work show that the ice field is highly sensitive to the static stability and vertical fluxes in the Southern Ocean water column. Given the marginal stability and strong fluxes of the present-day water column, relatively small changes in the ocean/atmosphere may lead to significant changes in the stability or fluxes and thus the nature of the sea ice cover. These interactions link the local- and regional-scale processes to the global-scale processes, forming a Southern Ocean/climate feedback loop. The local-scale processes operate at sub-grid scales in most climate models; therefore the results of a local process-oriented model are reviewed to examine the nature of the local–regional interactions which are critical to this system. The model scalings, which describe the system parameter dependence, indicate the direction and magnitude of change of the key external parameters which will drive the system toward a more stable or more unstable state. They also allow a computationally efficient means of monitoring the key elements of the ocean/sea ice system in large-scale models. The main external parameters include: (1) depth of the pycnocline; (2) ratio of heat to salt through the pycnocline; (3) strength of the pycnocline; and (4) magnitude of atmospheric cooling. The divergence of the ice field also plays an important role. Consideration of the influence of the local–regional interactions in light of anticipated changes in these variables given an assumed global warming suggest that the Southern Ocean may become less stable (initially) leading to a reduced sea ice cover and enhanced deep water ventilation.

INTRODUCTION

The sea ice zone of the Southern Ocean is characterized by a large, predominantly seasonal, sea ice cover whose areal extent in winter is ~50% larger than the area of permanent ice cover on the Antarctic continent [Zwally et al., 1983]. The sea ice has been shown to play a significant role in global climate [e.g., Hansen et al., 1984; Schlesinger and Mitchell, 1985]. Unfortunately, most studies examining this role have not considered the sensitivity of the sea ice field to the upper ocean stability. Because this stability plays a critical role in the sea ice distribution, it suggests an intimate coupling between the ocean, sea ice, and atmosphere which constitutes the Southern Ocean/climate feedback loop. The feedbacks, together with the marginal stability of the Southern Ocean water column, elevate the role of the local and regional air/sea/ice (ASI) interactions to a globally significant component of the ocean/climate system.

The purpose of this paper is three-fold: (1) to conceptually describe the Southern Ocean/climate feedback loop; (2) to describe the nature of the local air/sea/ice interactions which are critical to this loop (and therefore which must be included in global-scale models); and (3) to speculate

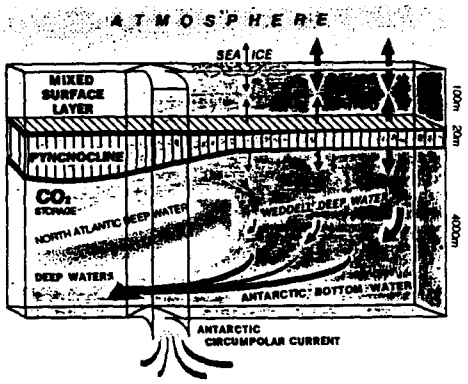


Figure 1. Schematic showing dominant interactions between the various components of the air/sea/ice system in the high latitude Southern Hemisphere. ACC represents the Antarctic Circumpolar Current. NADW represents both the southward-flowing North Atlantic and Circumpolar Deep Waters which supply deep water to the Southern Ocean; AABW is Antarctic Bottom Water which flows out of the Southern Ocean region. The pycnocline represents the steep density gradient separating the colder fresher surface waters from the significantly warmer and saltier deep waters immediately below.

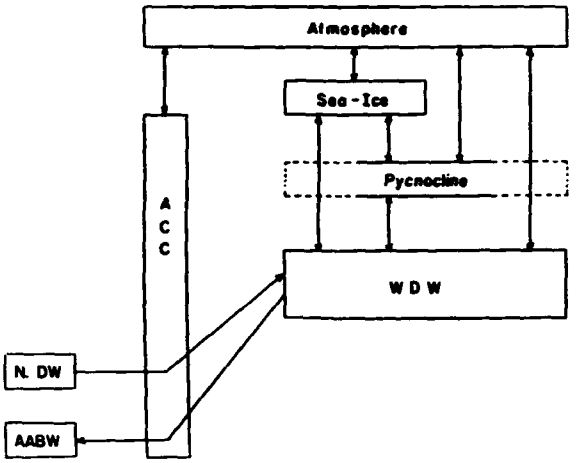


Figure 2. Overview of the main interactions occurring in Figure 1 showing the nature of the air/sea/ice coupling. A change in any one component will influence all other components in the system.

regarding the Southern Ocean response to a global warming, based upon the information presented in (1) and (2).

SOUTHERN OCEAN/CLIMATE FEEDBACK LOOP

The Southern Ocean/climate feedback loop operates over a variety of length and time scales and serves to link the local and regional ASI processes to global climate. The link between the regional and global scales occurs through both the oceans and atmosphere. A simplified schematic representation of this complex link is shown in Figure 1. Oceanographically, regional- and local-scale processes drive significant deep and bottom water formation which serves to ventilate the world's deep water. That is, this is one of only two regions in the world (the North Atlantic being the other) in which there is direct exchange of heat, salt and atmospherically active gases between the deep water reservoir and atmosphere. Atmospherically, the region modulates climate through the strong insulating effect and high albedo of the seasonal sea ice cover. The sea ice field, however, is intimately coupled to the ocean/atmosphere system since its temporal and spatial distribution is controlled by the ocean density structure and the atmospheric forcing. This atmospheric forcing is modified by the very presence of ice, and the ocean density structure is modified by the growth/decay and drift of the ice as well as by the atmospheric forcing directly (which drives the freshwater balance and dynamical configuration).

This strong feedback loop thus couples the local-, regional- and global-scale processes. The coupling, summarized in Figure 2, assures that a change in any one component of the ASI system will influence all other components in the system. In the Southern Ocean, the weak stability across the pycnocline, which is as weak as the stability of the deep ocean elsewhere in the world [Gordon, 1981], represents the weak link in the system. It thus plays a pivotal role since a relatively small change in any component of the system will influence the vertical stability which can force a large system response. For example, an excess growth of ~15 cm of ice during a winter would be sufficient in some regions to destabilize the water column resulting in deep convection [Martinson, 1990]. The associated convective heat flux will eliminate the ice cover and the salt flux will precondition the water column for convection in the following year [Martinson et al., 1981; Motoi et al., 1987]. The large Weddell Polynya [Zwally and Gloersen, 1977] present from 1974-1976 is presumably an example of a local destabilization [Gordon, 1978; Killworth, 1979; Martinson et al., 1981]. It presumably had a significant influence on both the ventilation and air/sea exchange (Gordon, 1982; Gordon and Huber, 1984].

Destabilization may be sensitive to, among other things, eddies or topographic influences [e.g., Martinson et al., 1981; Gordon and Huber, 1984]—local-scale processes which are in turn sensitive to the regional-scale wind stress forcing the polar gyres. Because of this dependence on the local processes, the global influence of the sea ice cover and deep water ventilation is also dependent upon the local interactions. These dictate whether or not a relatively small change in any one component of the system is sufficient to induce destabilization. Consequently, the feedback loop is clearly sensitive to processes operating over all scales. It is thus important to understand the nature of the local interactions so that they can be adequately parameterized for inclusion in the larger-scale models since they represent processes operating at typical sub-grid–scale levels.

LOCAL AIR/SEA/ICE INTERACTIONS

In the austral winter of 1986, a detailed investigation within the Antarctic sea ice cover along the eastern margin of the Weddell Sea was conducted during the first leg of the Winter Weddell Sea Project (WWSP-86) [Schnack-Schiel, 1987] onboard R.V. *Polarstern*. This leg concentrated on physical measurements along a cruise track which covered the region between 5°W and 10°E from the ice margin, near 59°S, to the Antarctic continent. During this period, detailed measurements of the ocean, sea ice and atmosphere were made, providing the first extensive data set describing winter conditions within the Antarctic seasonal sea ice field. These data allowed us to better develop our understanding of the local ASI interactions.

Based on the WWSP-86 observations, a local, one-dimensional model has been developed [Martinson, 1990;

described conceptually below] which clearly reveals the system parameter dependence. The external parameters of the local model (pycnocline depth; ratio of heat to salt across the pycnocline; pycnocline strength and air–sea heat exchange) are controlled by the regional-scale processes (e.g., the vigor of the cyclonic circulation controls, to some respect, the pycnocline depth). Therefore, this model provides a first-order link between the local and regional scales. The model scalings provide a simple explicit expression of this linkage, that is, how the local response will change given a change in a regionally controlled variable. As such, these scalings represent a computationally efficient means for parameterizing the local processes.

Figure 3 presents a schematic representation of the important local winter ASI interactions and processes which dominate the system through the winter period. The winter mixed layer is typically too deep, O(100 m), for turbulent mixing (wind stirring) to drive entrainment effective in deepening the mixed layer further [Martinson, 1990; and work in progress]. However, such mixing serves to maintain a well-mixed surface layer by mixing downward any positive buoyancy introduced at the surface, such as a meltwater, and mixing upward those properties that are fluxed across its base. This latter mixing also serves to maintain a sharp interface between the mixed layer and pycnocline. The heat and salt fluxes (F_D) across the base of the mixed layer (parameterized in terms of a turbulent diffusive flux) is large because of the strong thermal and salt gradients through the pycnocline. The deep water is significantly warmer (2.5–3°C) and saltier than the surface mixed layer

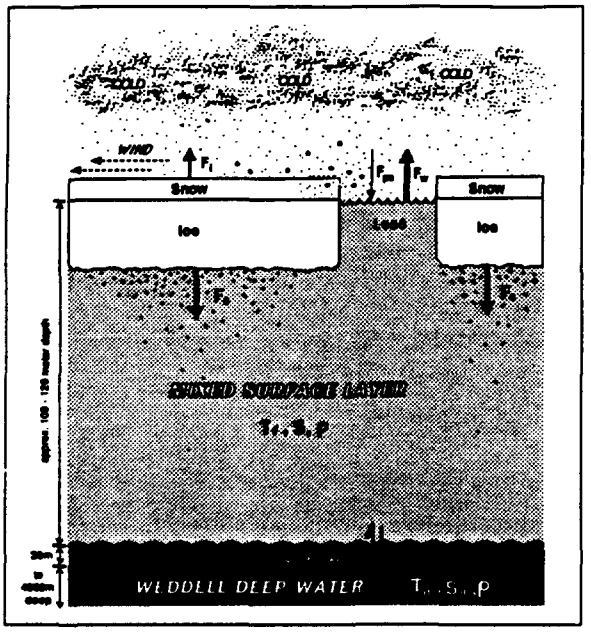


Figure 3. Schematic of dominant processes controlling the winter evolution of the ocean/sea ice system. Heat is lost from the ocean to the atmosphere. Through the leads (F_w) this loss is uninhibited while through the ice and snow (F_i) it is by conduction. Mechanical mixing, driven by the wind (τ), maintains a well-mixed surface layer. The surface layer expands by free convection, induced by dense surface water, made dense by salt injection (F_S) during ice growth. Heat and salt is fluxed (F_D) from the deep water across the thin pycnocline which offsets much of the heat lost to the atmosphere and significantly reduces the amount of ice growth.

water [Huber et al., 1989] and the pycnocline separating these two water masses is only 20–40 m thick, so there is a fairly strong exchange of properties by turbulent diffusion. Typically, the diffusive heat flux (F_{DT}) contributes ~25–30 W m^{-2} to the mixed layer. This heat gain tends to offset much of the atmospheric heat loss which is uninhibited through leads (F_w) and by conduction through the ice and snow (F_i). Since the flux through leads is typically 10–20 times larger than that through the ice/snow in the Antarctic, an area of 5% leads [consistent with observations; Wadhams et al., 1989] vents approximately as much heat to the atmosphere as a 95%-ice-covered area. In this respect, the area and distribution of leads is extremely important.

The average atmospheric heat loss ($F_{atm} \approx$ 30–35 W m^{-2}), while tempered by the oceanic heat gain, initially dominates the balance resulting in a net heat loss (~5–10 W m^{-2}). This drives ice growth which introduces a salt flux (F_S) due to haline rejection associated with the ice growth process. This salt flux (slightly offset by a freshwater flux, F_{pe}, in the form of snow entering through leads) destabilizes the mixed layer by making the surface water slightly denser than the water immediately below it in the uppermost layers of the pycnocline. This static instability is relieved by vertical mixing (free convection) to a depth at which point the water column is again stable. The convection deepens the mixed layer by eroding into the pycnocline and, in so doing, releases the heat contained within the entrained water into the mixed layer. This introduces an additional heat flux. Consequently, this entrainment heat flux reduces the net heat loss of the system and serves as a negative feedback. So, the stronger the net heat loss, the more ice growth and the more entrainment and entrainment heat flux. This supplements (by 10–40%) the heat entering the mixed layer by turbulent diffusion and offsets more of the heat being lost to the atmosphere so less ice grows. For observed or expected parameter ranges, over 5 months of winter, less than 20 cm grows (~40 cm of ice grows rapidly during fall as the seasonal pycnocline is eroded), and the pycnocline is eroded by ~5–20 m [see Martinson, 1990 for details].

The processes outlined above reveal how stability is maintained and how the Southern Ocean is able to support a sea ice cover at all. That is, in a marginally stable system such as this, one would expect that as the ice grows the density buildup in the surface layer would overcome the weak pycnocline, causing the system to overturn (eliminating the ice cover and ventilating the deep water). However, this doesn't presently happen in the Southern Ocean despite a pycnocline so weak that upon first consideration overturn seems inevitable. The key lies with the strong ocean heat flux into the mixed layer. This minimizes the net heat loss and therefore reduces the net ice growth so there is a minimal amount of salt buildup to destabilize the system. Furthermore, as ice does grow, it drives the additional negative feedback which contributes additional heat, reducing further ice growth as discussed above.

Without these oceanic heat fluxes, the wintertime atmospheric cooling of the Southern Ocean region is sufficient to grow ~3 m of ice (similar to what grows in the arctic regions where the oceanic heat is minimal). Instead, observations show ~60-75 cm of ice growth by the end of winter [Wadhams et al., 1987; Ackley et al., 1982] in some areas where calculations suggest that only 90–100 cm of ice

growth would be enough to induce overturning [Martinson, 1990]. That is, as little as 15 cm of additional ice growth may be sufficient to completely destabilize the system and eliminate the ice cover in some regions—a radical change in the regional character which can also be induced by upsetting the present heat balance by as little as 3 W m^{-2} [Martinson, 1990]. This reveals how delicate the balance is between the atmosphere, ocean and sea ice in the Southern Ocean and the importance of accounting for even the local interactions in global-scale modeling.

The above interactions have been described by a system of equations which are solved analytically. The solutions simulate the observations [see Martinson, 1990] and provide explicit indications of how the various processes interact. Furthermore, they allow us to isolate the importance and roles of each of the individual processes involved so that we can predict how specific changes in the external parameters will influence the response. In particular, the solutions to the equations describing this system can be used to estimate how changes in any one part of the system will influence the likelihood of destabilization.

This is effectively shown in Figure 4 where the amount of entrainment is shown as a function of the different system components. For example, Figure 4a shows that in the present day, the pycnocline depth is typically 100 m and after 5 months of winter, ~7 m of the pycnocline has been eroded away and incorporated into the mixed layer. If the pycnocline is only 20 m thick initially, then an additional 13 m of entrainment will overturn the system. If the system changes so that the pycnocline is shallowed to only 50 m depth, then after 5 months of winter, ~15 m of the pycnocline is eroded. While this may not be enough to overturn the system, it is a clear indication that if the pycnocline is made shallower, the system is more likely to overturn. Whether this explicit change alone will induce overturn of course depends upon the exact pycnocline thickness and what effect other changes have on the system. In general, as seen from Figure 4, the shallowing of the pycnocline, the decrease in the ratio of heat to salt within the pycnocline, the direct weakening of the pycnocline strength and the cooling of the atmosphere all tend to destabilize the system and drive it toward overturning. Changes in the opposite direction tend to stabilize the system.

RESPONSE TO GLOBAL WARMING; SPECULATION

Based on the model results, it is now possible to infer changes in the Southern Ocean ASI system, relative to today, given anticipated changes in the climate or ocean induced by a global warming. These inferences are simple speculations since each change is considered in isolation, ignoring other changes and feedbacks taking place. Also, we cannot be sure that the "anticipated" warming effects are correct. For more reliable estimates, the above model for the Southern Ocean interactions must be incorporated into the large-scale climate models so that all processes and changes are considered together.

Probably the most certain consequence of the greenhouse effect is the expected warming. By itself, this leads to a weaker heat loss to the atmosphere (F_{atm}) which tends to stabilize (less ice growth) as shown in Figure 4d. In addition to this direct effect, if the warming is stronger in the high latitude regions than in the subtropical regions, then this may tend to weaken the earth's equator-to-pole thermal gradient. (While most model results support this assumption for an equilibrium response to a global warming, recent coupled model results of Manabe et al. [1990] suggest that this may not be true for the transient response.) If such a weakening occurs over the Southern Ocean (dynamical complexities may lead to a decrease in some regions and increase in others), this would lead to a weaker atmospheric circulation. Currently, the atmospheric circulation drives a vigorous Antarctic Circumpolar Current and cyclonic polar gyre which raises the deep waters, and pycnocline, to shallower depths (it can also influence the strength of the pycnocline and ratio of heat to salt through the pycnocline indirectly as well). A decrease in the vigor of the atmospheric circulation would tend to relax the ocean circulation resulting in a deeper pycnocline. A deeper pycnocline is associated with a stabilizing influence (Figure 4a).

Also, the present polar ocean circulation is climatically divergent, so leads in the ice are opening on average. Decreasing the vigor of the atmospheric circulation would reduce the ice divergence and thus the lead area. Recall that the heat loss through leads is ~10–20 times more effective than through the ice and snow cover. Therefore, decreased lead area would result in a further reduction of F_{atm}. From the ocean's viewpoint, this is equivalent to increased atmospheric warming and additional stability. A reduction in ice divergence will also tend to reduce the freshwater flux associated with ice melt in the more northern extent of the gyres (nearshore ice not drifting as far from its formation area) while increasing the freshwater flux in the southern extent (more ice melting in its formation region). This will tend to increase the surface salinity in the open ocean regions (strongly destabilizing) and decrease it in the coastal regions (strongly stabilizing). Also, the decreased divergence coincides with reduced upwelling which effectively decreases the oceanic heat flux to the mixed layer (here parameterized as a turbulent diffusive flux). This also imparts a strong destabilizing influence (less ocean heat to offset the atmospheric heat loss, so more destabilizing ice growth).

The net effect of the above anticipated changes depends upon the relative magnitude of the individual components, which cannot be easily estimated in the absence of a large-scale model. Furthermore, no attempt has been made to estimate changes in deep water characteristics, or in the freshwater budget not related to ice drift, which play a significant role in the stability (see Figure 4b,c). As presented, those changes that tend to destabilize influence portions of the system that are particularly sensitive, and if not fully compensated a global warming could drive a reduction in the Southern Ocean sea ice cover and increased open ocean ventilation. Alternatively, a relatively small increase in the thermal gradient across the pycnocline, possibly reflecting subtle changes in the circulation dynamics, could easily result in stabilizing the system (more ice cover and less convection). In either case, it is clear that the consideration of system changes over local, regional and global scales is very important if we are to properly predict the response of the Southern Ocean and make reliable climate predications.

ACKNOWLEDGMENTS

This work was supported by National Science Foundation research grant DPP 8501976. Lamont Doherty Geological Observatory contribution number 4775.

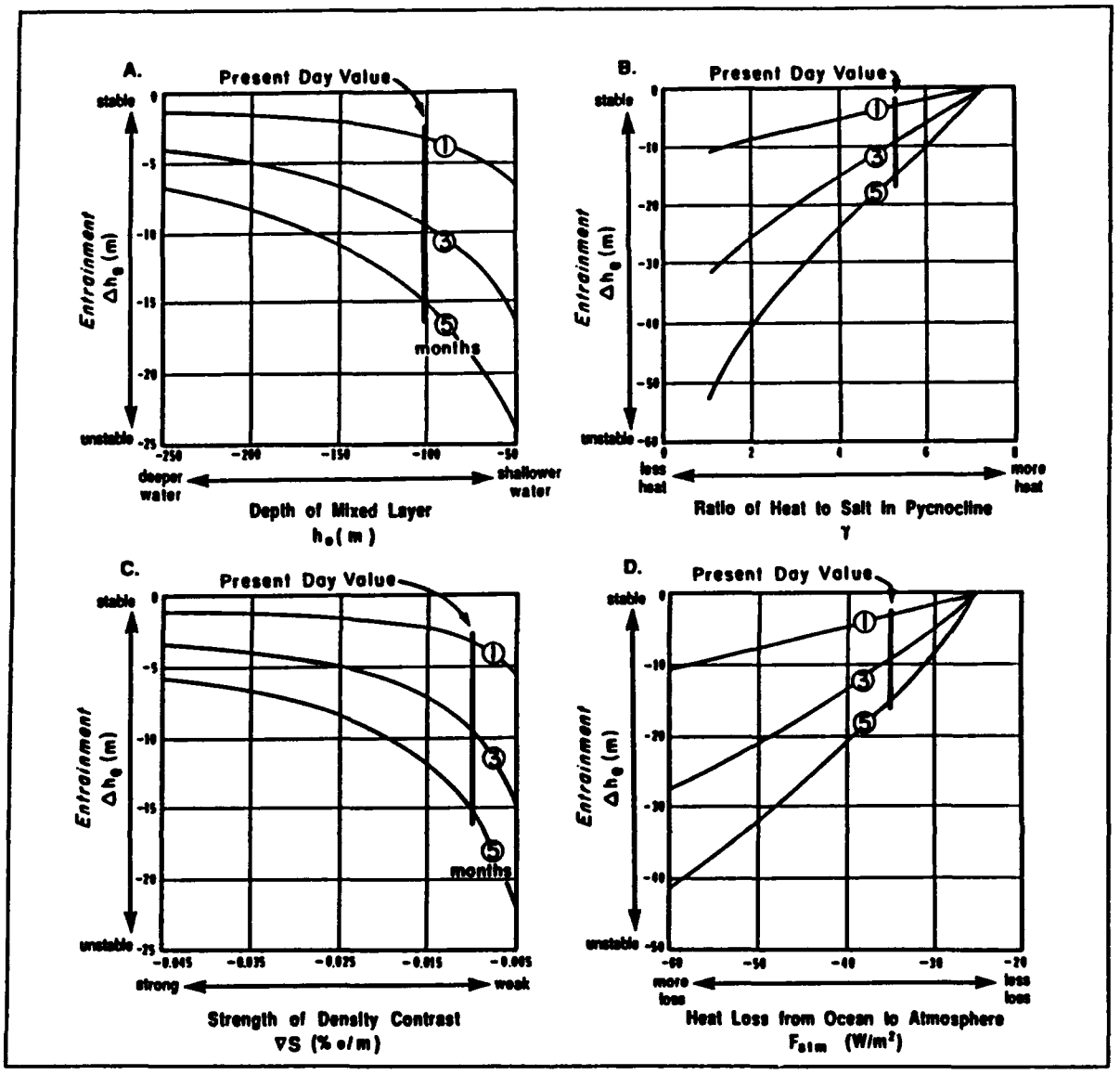


Figure 4. Sensitivity of the system to destabilization as a function of changes in any particular component of the system. Decreasing stability coincides with increasing entrainment (Δh_e; erosion of the pycnocline). The bold lines use parameter values representative of waters near the eastern edge of the Weddell Sea and the light lines waters further to the east. The numbers 1-5 on the lines indicate the amount of entrainment after 1 month, 3 months, etc. The vertical bars mark the location of the current values of the system variables for the two regions. Panels show amount of entrainment as a function of (a) h_0 - the initial winter mixed layer thickness which corresponds to the upper level of the permanent pycnocline; (b) γ - essentially the ratio of heat to salt in the pycnocline; (c) ∇S - the pycnocline strength; and (d) F_{atm} - the atmospheric heat loss.

REFERENCES

Ackley, S. F., D. B. Clarke, and S. J. Smith, Weddell Polynya Expedition preliminary data report: Physical, chemical and biological properties of ice cores. Technical note, U.S. Army Cold Water Regions Res. and Eng. Lab., Hanover, NH, 1982.

Gordon, A. L., Deep Antarctic convection of Maud Rise, *J. Phys. Oceanogr.*, *8*, 600-612, 1978.

Gordon, A. L., Seasonality of Southern Ocean sea ice, *J. Geophys. Res.*, *85*, 4193-4197, 1981.

Gordon, A. L., Weddell Deep water variability, *J. Marine Res.*, *40*, 199-217, 1982.

Gordon, A. L., and B. A. Huber, Thermohaline stratification below the Southern Ocean sea ice, *J. Geophys. Res.*, *89*, 641-648, 1984.

Gordon, A. L., and B. Huber, Southern Ocean winter mixed layer, *J. Geophys. Res.*, *95*, 11655-11672, 1990.

Hansen, J., A. Lacis, D. Rind, G. Russell, P. Stone, I. Fung, R. Ruedy, and J. Lerner, Climate sensitivity: analysis of feedback mechanisms, in *Climate Processes and Climate Sensitivity*, Geophysical Monograph 29, Maurice Ewing Volume 5, pp. 130-163, American Geophysical Union, 1984.

Huber, B. A., P. Mele, and A. L. Gordon, Report of the Winter Weddell Sea Project, ANT V/II, Hydrographic data, *L-DGO-89-1*, Lamont-Doherty Geol. Observ., Palisades, NY, 1989.

Killworth, P. D., On "chimney" formations in the ocean, *J. Phys. Oceanogr.*, *9*, 531-554, 1979.

Manabe, S., K. Bryan, and M. J. Spelman, Transient response of a global ocean-atmospheric model to a doubling of atmospheric carbon dioxide, *J. Phys. Oceanogr.*, *20*, 722-749, 1990.

Martinson, D. G., Evolution of the Southern Ocean winter mixed layer and sea ice; open ocean deep water formation and ventilation, *J. Geophys. Res.*, *95*, 11641-11654, 1990.

Martinson, D. G., P. D. Killworth, and A. L. Gordon, A convective model for the Weddell Polynya, *J. Phys. Oceanogr.*, *11*, 466-488, 1981.

Motoi, T., N. Ono, and M. Wakatsuchi, A mechanism for the formation of the Weddell Polynya in 1974, *J. Phys. Oceanogr.*, *17*, 2241-2247, 1987.

Schlesinger, M., and J. Mitchell, Model projections of the equilibrium climatic response to increased carbon dioxide, in The Potential Climatic Effects of Increasing Carbon Dioxide, *DOE/ER-0237*, pp. 81-148, U.S. Dept. of Energy, 1985.

Schnack-Schiel, H., The winter expedition of RV POLARSTERN to the Antarctic (Ant V/1-3), *Berichte zur Polarforschung*, *39*, 1-259, 1987.

Wadhams, P., M. A. Lange, and S. F. Ackley, The ice thickness distribution across the Atlantic sector of the Antarctic Ocean in midwinter, *J. Geophys. Res.*, *92*, 14535-14552, 1987.

Zwally, H. J., and P. Gloersen, Passive microwave images of the polar regions and research application, *Polar Rec.*, *18*, 431-450, 1977.

Zwally, H. J., J. C. Comiso, C. L. Parkinson, W. J. Campbell, F. D. Carsey, and P. Gloersen, *Antarctic Sea Ice, 1973-1976: Satellite Passive-Microwave Observations*, 206 pp., NASA Scientific and Technical Information Branch, Washington, DC, 1983.

AD-P007 299

92-17981

Antarctic Sea Ice: Its Development and Basic Properties

M. A. Lange
Alfred-Wegener-Institute for Polar- and Marine Research, Bremerhaven, Germany

ABSTRACT

We report investigations on sea ice properties carried out during a number of expeditions into the Weddell Sea, Antarctica. The results provide important baseline data, against which possible changes in the Antarctic sea ice cover as induced by climatic changes can be compared. This paper concentrates on results dealing with the textural properties and the ice thickness distributions of Antarctic sea ice. In addition, we look at the contribution of meteoric ice (snow ice) to the sea ice cover by means of $\delta^{18}O$ measurements. While changes in extent and thickness are to be expected as a result of possible climatic warming, we propose that the amount of snow ice will serve as an additional indicator of such changes.

INTRODUCTION

The role of the polar sea ice covers as important components of the global climate system is beyond debate. Sea ice can be considered as one of the most effective indicators of climatic changes. This is primarily due to the well-known ice albedo–temperature feedback process, which might amplify any temperature signal in the atmosphere at high latitudes [e.g., Manabe and Stouffer, 1980; more recent model results indicated less pronounced enhancement of temperature change at high latitudes, e.g., Bryan et al., 1982]. Climatic changes will also be seen in the sea ice thickness distribution, the areal coverage and the ice concentration values, as warming of the ocean and increased mixed layer heat fluxes will lead to decreased ice growth rates. It should be noted, however, that feedback processes between atmospheric warming and the global sea ice regime are still not entirely understood nor adequately modeled.

In addition to its role as an indicator of climatic changes, sea ice acts as a link between Antarctica and the global climate system. The presence or absence of a sea ice cover, as well as its areal extent, strongly influences the global radiation budget through the contrast in the albedo between sea ice versus open water. The formation of bottom water at high latitudes is also coupled to the sea ice growth rates through a number of feedback processes [Hoffert, 1990]. Finally, the global carbon dioxide balance is significantly influenced by the biological activity at high latitudes and the uptake of CO_2 by near-surface phytoplankton. However, the uptake in turn is controlled by the extent of the sea ice cover and the amount of open water.

Sea ice finally plays an important role for the marine ecosystem at high latitudes. As has been shown, sea ice is a habitat for a wide variety of organisms, ranging from seals and birds to bacteria, many of which are directly dependent on its presence [Spindler et al., 1990]. The significance of the sea ice biocoenoses as a food source for higher tropic levels, in particular krill [e.g., Marshall, 1988], has only recently been realized, while its importance with regard to the initiation of phytoplankton blooms is still enigmatic.

Thus climate changes and their influence on the sea ice regime will translate into changes of parameters that are linked to basic sea ice properties. The assessment of changes in these parameters will consequently provide clues on possible changes in the climate system. However, the detection of altered sea ice properties requires a comprehensive knowledge of the current state of the polar sea ice covers and a basic understanding of major processes that lead to their alteration. Aside from satellite-based remote sensing observations, field observations remain an essential source of information in this respect.

As part of a long-term research program, we have undertaken a total of seven expeditions into the Weddell Sea on the ice-breaking RV *Polarstern*, during different seasons. The Weddell Sea is one of the few places in Antarctica where perennial sea ice can be found. It is also characterized by a major oceanographic current system of the southern

ocean, the Weddell Gyre. As such, it provides basic information on Antarctic sea ice properties throughout the year. In addition one gains data that can not be obtained elsewhere in the Antarctic.

In the following we will briefly discuss our observations and analytical techniques and present major results of our investigations. We will summarize these results, draw major conclusions and finally discuss new promising ways to detect climatic changes through sea ice investigations.

EXPEDITIONS; FIELD WORK; ANALYTICAL TECHNIQUES

As part of our field work in Antarctica, we have conducted extensive investigations and analysis on sea ice of the Weddell Sea. Over the last seven years, we have carried out three summer expeditions, two winter expeditions and two late winter/early spring expeditions on the German ice-breaking research vessel *Polarstern*. In this paper, we will concentrate on results obtained during winter and late winter/early spring expeditions. The cruise tracks of these expeditions are given in Figure 1. Also shown are the study areas of the *Polar Sea* expedition [Gow et al., 1987] and of the expedition on the *M. Somov* [Clarke and Ackley, 1984], another late winter/early spring expedition which was carried out by other groups.

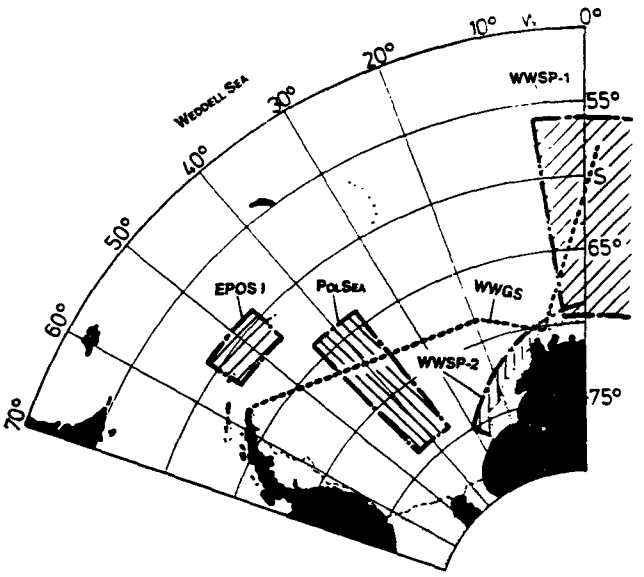


Figure 1. Cruise track and working areas of several expeditions into the Weddell Sea.

Major elements of our field work during daily ice stations include: ice core drilling, in situ measurements of ice properties, detailed surface characterizations (both physical and chemical) in conjunction with in situ remote sensing observations and snow and ice thickness measurements in at least 100 and up to 200 mechanically drilled holes along one or two profiles. During the traverse of the vessel through ice-covered waters, hourly observations of general ice conditions were performed. They were supplemented by helicopter reconnaissance flights and still and video photography. Laboratory investigations consist of: detailed textural analysis on ice cores, on both thick and thin sections; physical, chemical and biological measurements on individual core sections with consistent texture [c.f. Clarke and Ackley, 1984; Lange, 1988]; and measurements of ^{18}O-concentration on the same sections [Lange et al., 1990]. Part of this work was done in a mobile cold laboratory on board *Polarstern*. Here, thick sections were cut along the entire length of the cores and analyzed for texture. This results in a continuous core stratigraphy, which serves as the basis for subsequent samplings and analysis [for details see Lange, 1988]. In our textural analysis, we distinguish five different classes [Lange et al., 1989; Eicken and Lange, 1989; Table 1]. Whenever assignment of a texture class was questionable, thick sections were supplemented by vertical and horizontal thin sections. Based on the occurrence of columnar versus granular ice (the radiative frequency of both classes normalized to one for each core) we defined five genetic ice classes, which reflect the particular developmental history of each ice floe [for detail see Lange et al., 1989; Eicken and Lange, 1989; Table 2]. Thus, assessing the genetic ice classes both in time and space will provide us with a fairly good explanation of sea ice processes and developments in the Weddell Sea area throughout the year.

Sea ice thicknesses were obtained through direct measurements in mechanically drilled holes along straight profiles at least 100 meters long [for details, see Wadhams et

Textural Class	Grain Size (m)	Grain Shape	Brine Inclusions
Granular			
Polygonal granular	$<10^{-2}$	isometric; planar boundaries meeting at 120°	spherical droplets at grain junctions
Orbicular granular	$<10^{-2}$	isometric; convex, rounded grain boundaries	irregular pockets and droplets between grains
Columnar	10^{-2} - $>10^{-1}$	elongate	parallel layers within grains
Intermediate columnar/granular	10^{-2} - 10^{-1}	slightly elongated; grains indented and interlocked	oblong; strings of isolated pockets
Mixed columnar/granular	$<10^{-2}$ - $>10^{-1}$	domains of granular and columnar texture occurring next to each other	
Platelet	$<10^{-2}$ - 10^{-1}	inclusion-free, platy crystals in matrix of granular, mixed or intermediate columnar/granular	pockets and layers within and between grains

Table 1. Textural classification of sea ice samples.

Genetic Ice Class	Textural Type	Occurrence in Core (%)
Predominantly congelation	columnar	>80
Mainly congelation	columnar	>60
Predominantly frazil	granular	>80
Mainly frazil	granular	>60
Mixed frazil/ congelation	granular/ columnar	30-50

Table 2. Genetic ice classes: definitions based on ice texture.

al., 1987; Lange and Eicken, 1991a]. We also measured snow and freeboard heights at each point of the profile.

A representative set of cores was subsequently sampled for $\delta^{18}O$ in our laboratory in Bremerhaven [see Lange et al., 1990]. Here, as in other analyses, we strictly followed the textural distribution of the ice within each core and sampled each textural unit separately. Equilibrium fractionation will lead to $\delta^{18}O$ values of +2 to +3‰ in freezing sea water [see Lange et al., 1990]. However, meteoric contributions to the sea ice cover, by means of snow ice formation, will be clearly detectable by their negative $\delta^{18}O$ signature. Thus, we are able to assess snow ice and meteoric contributions even though they might not show up texturally. This enables us to assess the total contribution of meteoric ice to the sea ice cover under consideration.

RESULTS

Table 3 gives the fractions of frazil versus congelation ice (normalized to one) for each of the expeditions as shown in Figure 1. In our analysis, we distinguish between textural ice classes, referring to the crystallographic or textural character of an ice core section and genetic ice classes, which indicate major formational or developmental characteristics of a core section [for further details, see Lange et al., 1989; Eicken and Lange, 1989]. As can be seen, frazil ice clearly dominates the distribution of genetic ice classes in the Weddell Sea. Given the "classical" model of sea ice growth, this is an unusual and surprising result. In the Arctic, frazil ice comprises only about 5 to 10% and up to 25% of the overall genetic ice classes [Weeks and Ackley, 1986; Maykut, 1986].

The geographical distribution of genetic ice classes as seen, e.g., during the first leg of the Winter Weddell Sea Project (WWSP), gives an indication of spatial processes that control the sea ice development in the Weddell Sea [see Lange et al., 1989]. This result, in conjunction with detailed ice observations [Casarini and Massom, 1987], leads to a model of new ice formation that has been described as the "pancake cycle" [Lange et al., 1989] (Figure 2). A major result of ice formation through the "pancake cycle" is the very large proportion of frazil ice within the newly formed sea ice cover. However, as can be seen in Table 4, the proportion of frazil ice is also large within the second-year ice fraction that we have sampled during EPOS I. Thus unlike

Expedition	Observed Growth frazil (%)	congelation (%)	Authors
PolSea	57.4	42.6	Gow et al., 1987
WWSP-1	57.1	42.9	Lange et al., 1989
WWSP-2	51.7	48.3	Eicken and Lange, 1989
EPOS-I	63.8	36.2	Lange, 1989
WWGS	41.9	58.1	unpublished
Mean	54.4	45.6	
Std. deviation	7.3	7.3	

Table 3. Observed sea ice textures during a number of expeditions into the Weddell Sea. PolSea = *Polar Sea* expedition; WWSP = *Winter Weddell Sea Project* (Legs 1 and 2); EPOS-I = first leg of the *European Polarstern Study*; WWGS = *Winter Weddell Gyre Study*

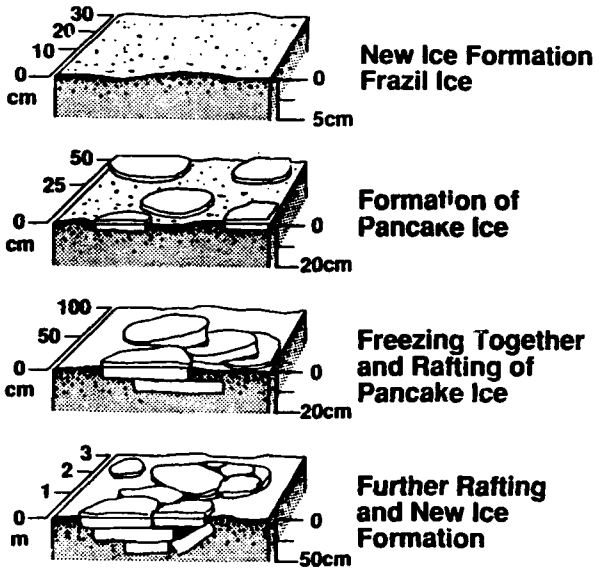


Figure 2. Schematic representation of the pancake cycle.

the Arctic, even ice growth during the second year must be strongly influenced by processes that further the growth of frazil rather than of congelation ice. Figure 3 gives schematically a number of processes that contribute substantially to formation of frazil ice in first- and/or second-year ice. These processes are closely linked to deformation of the ice cover and subsequent processes [see Lange and Eicken, 1991b].

Sea ice thicknesses as obtained during the first leg of the Winter Weddell Sea Project comply to a very narrow size spectrum [see Wadhams et al., 1987]. This is a result of (a) the formation of new ice through the "pancake cycle" which essentially stops once thicknesses of about 0.4 to 0.7 meters have been reached, and (b) of very small if not negative growth rates of sea ice subsequent to the initial formation as due to large oceanic heat fluxes in the winter mixed layer in the Weddell Sea [Gordon and Huber, 1990].

Thickness data obtained during EPOS I sh[illegible] more

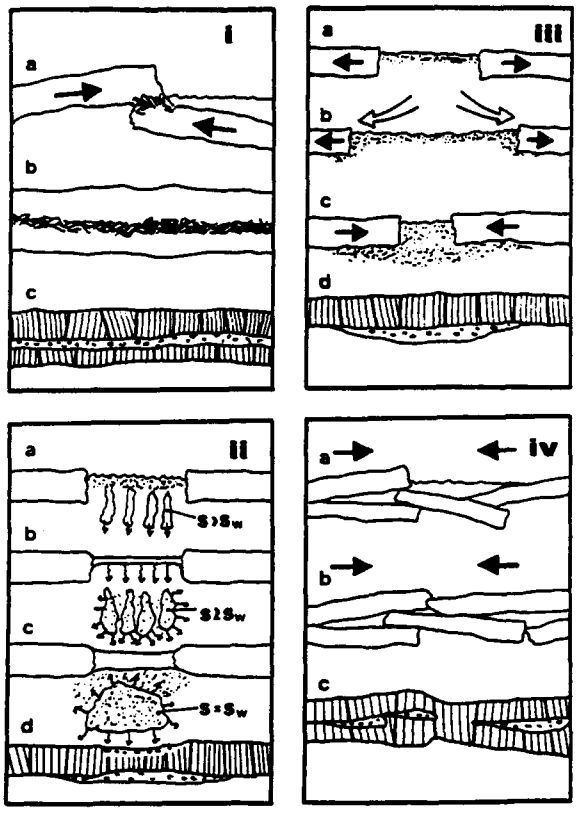


Figure 3. Schematic representation of deformation-related processes that lead to the observed large fraction of frazil ice in first- or second-year ice. The four panels depict: (i) frazil formation due to brash ice formed through rafting and ridging of floes; (ii) rapid frazil growth at the sea surface in newly derived leads; (iii) frazil formation due to double diffusion as a result of rapid ice growth in leads (s and sw refer to mean salinities in the ice cover and the underlying ocean, respectively); (iv) growth of frazil in gaps and voids of rafted floes. For a key to the textural classes depicted in the lowermost part of each panel, see Figure 5 (for further details see text and Lange and Eicken [1991a]).

complex distribution. Figure 4 gives the distribution of sea ice and snow thicknesses for the entire EPOS data set in the form of probability density functions (PDF). As can be seen, the thickness data have been distributed into four classes (I–IV). These classes can be distinguished by certain characteristics in their PDFs. They reflect different modes of sea ice development in the course of its transport within the Weddell Gyre. As such, we interpret classes I and IV as representing strongly deformed first- and second-year ice whereas classes II and III mainly represent less deformed and/or undeformed first- and second-year ice, respectively [Lange and Eicken, 1991a].

Figure 5 gives the textural distribution of four representative cores, which have been obtained on floes of classes I through IV, respectively. As can be seen, particularly cores of class I and IV show a large proportion of frazil ice as well as sections that are strongly indicative of deformational processes. This is also reflected in bottom topographies of class I and IV floes [for details see Lange and Eicken, 1991a]. The importance of ice deformation for the development of sea ice in the Weddell Sea region is also reflected by data as shown in Figure 6. The lack of any conclusive trend between the fraction of congelation ice versus core length as expected based on the "Arctic experience" is a clear sign of disturbances in orderly ice growth by ice deformation processes. While thick Arctic sea ice floes consist primarily of columnar ice, congelation fractions of Antarctic sea ice of cores longer than two meters amount to less than 40%.

Expedition	L_M (m)	C_M (%)	t_M (m)	R_M	N
WWSP-1	0.66	30.6	0.17	1.7	39
WWSP-2_c	0.59	14.2	0.26	1.3	10
WWSP-2_{sc}	0.83	53.4	0.59	1.4	22
EPOS-I (1st year)	0.71	31.2	0.23	2.0	10
EPOS-I (2nd year)	2.00	35.9	0.42	1.8	21

Table 4. Stratigraphic data of ice cores from different expeditions. (L_M = mean core length; C_M = mean fraction of columnar ice; t_M = mean length of stratigraphic units; R_M = mean ratio of the number of stratigraphic units in the top versus the bottom halves of cores; N = total number of analyzed cores). See Table 1 for explanation of Expeditions.

Figure 7 gives the $\delta^{18}O$ values of an ice core as obtained during the first leg of the Winter Weddell Sea Project [for details see Lange et al., 1990]. As can be seen, two sections of the ice core having negative $\delta^{18}O$ values thus indicate the contribution of meteoric ice (snow ice) to the overall ice thickness. Essentially the same can be seen in a much longer core (Figure 8) which also shows negative $\delta^{18}O$ values in the upper third of the ice core. In addition, there is an excursion to a slightly negative value at a larger depth, indicating a top of a floe that has been rafted under the existing ice sheet. Based on the $\delta^{18}O$ values as well as on assumptions of densities and ^{18}O values of sea water and precipitation, we can compute the total contribution of meteoric ice in a given floe [for details see Lange et al., 1990]. This has been done for a number of representative samples as obtained during the first leg of the Winter Weddell Sea Project (Figure 9). As can be seen, the amount of meteoric ice can reach substantial fractions. The mean value lies at about 3% of the overall ice thickness and appears quite small. However, based on our textural work we conclude that there is little or no congelation growth underneath an existing ice sheet. Thus the contribution of meteoric ice becomes significant. We believe that the small increase in sea ice thicknesses as seen during our northward journey as compared to the southward track during WWSP, is indeed due to the addition of snow ice to the overall ice cover [for details see Wadhams et al., 1987].

DISCUSSION AND CONCLUSIONS

What can we learn from the results of our expeditions into the Weddell Sea about the general course of development of sea ice in this region? Sea ice formation starts in the open waters around the coast of the Weddell Sea and the edge of the perennial sea ice zone and rapidly proceeds northward. We identify the pancake cycle as the major process of the advancing ice edge, as discussed above [see

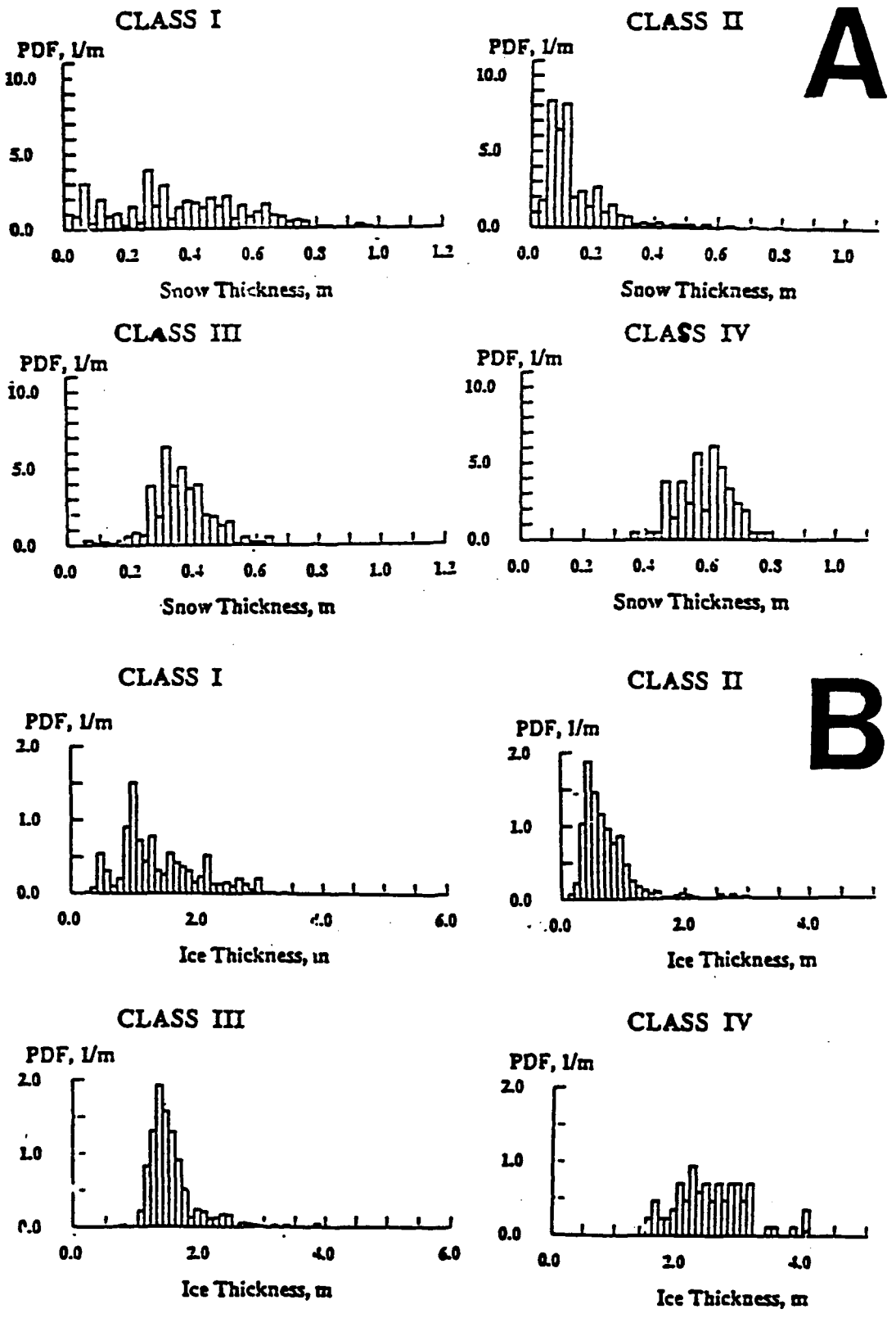


Figure 4. Snow and ice thickness PDFs for each of the floe classes I to IV, as seen during the EPOS cruise.

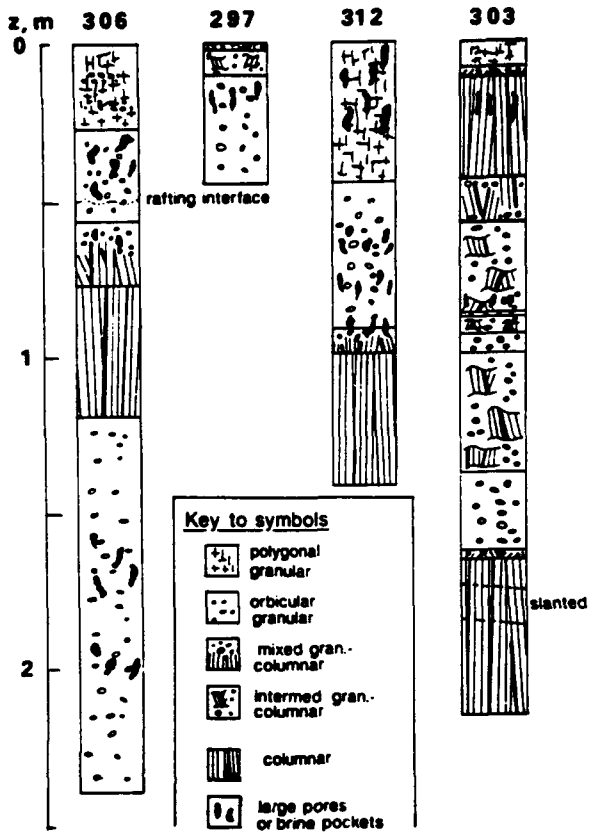


Figure 5. Stratigraphies of ice cores versus depth, z, obtained during the EPOS-I expedition in the northwestern Weddell Sea. The core numbers are given at the top of each profile. The cores represent floe classes I to IV from left to right, respectively.

Lange et al., 1989]. This process leads to (a) an ice cover that consists primarily of frazil ice due to the granular nature of individual pancakes, and (b) ice thicknesses of around 0.4 to 0.7 meters. The latter observation can be explained by two effects: (a) damping of the short-wave part of the wave spectrum as one proceeds into the developing pack-ice field, and (b) decreasing energy content of the remaining oceanic wave field due to increased distances from the open water. Both effects lead to a cessation of the rafting processes associated with the pancake cycle as one moves away from the ice edge. Our observations show that this occurs when ice thicknesses have reached 0.4 to 0.7 m.

These conclusions are strongly supported by our ice core texture record as well as by our ice thickness studies. They can be used to explain the large fraction of granular ice as seen in first-year ice in the Antarctic. The major processes of first-year ice growth also explain the narrow thickness spectrum of undeformed first-year ice as seen during the Winter Weddell Sea Project [Wadhams et al., 1987] and during EPOS I [Lange and Eicken, 1991a].

As a consequence of the pancake cycle, ice growth takes place primarily at the open water rate, in the uppermost layer of the ocean. This allows an effective heat exchange between ocean, the growing sea ice, and the cold atmosphere. In contrast to the "conventional" sea ice model, our observations demonstrate that the restriction on growth rate that is caused by the insulation effect of a coherent sheet of young ice does not apply in the Antarctic situation. Thus this mechanism of ice growth also provides a ready explanation for the rapidity of ice advance during fall and winter.

Once the ice cover has reached its maximum extent, both in thickness as well as in areal coverage, the ice growth essentially stagnates. This can be seen primarily in our tex-

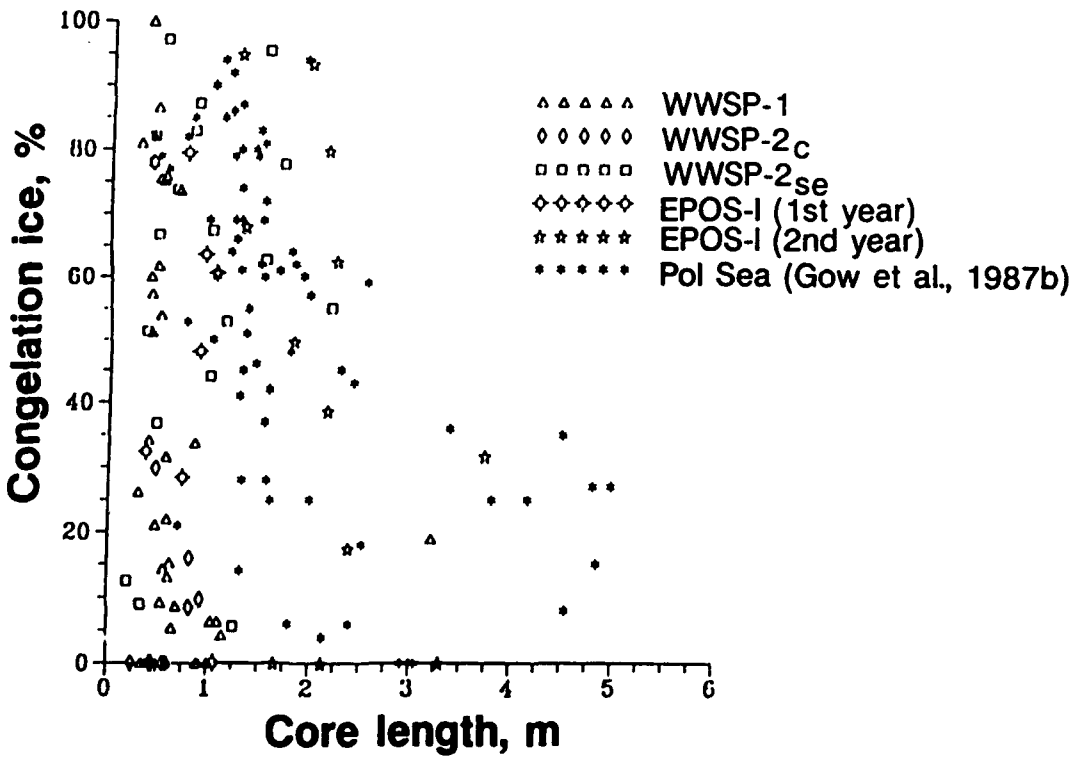


Figure 6. Fraction of congelation ice versus core length in ice cores obtained during a number of expeditions (for an explanation of acronyms see Table 3 and text).

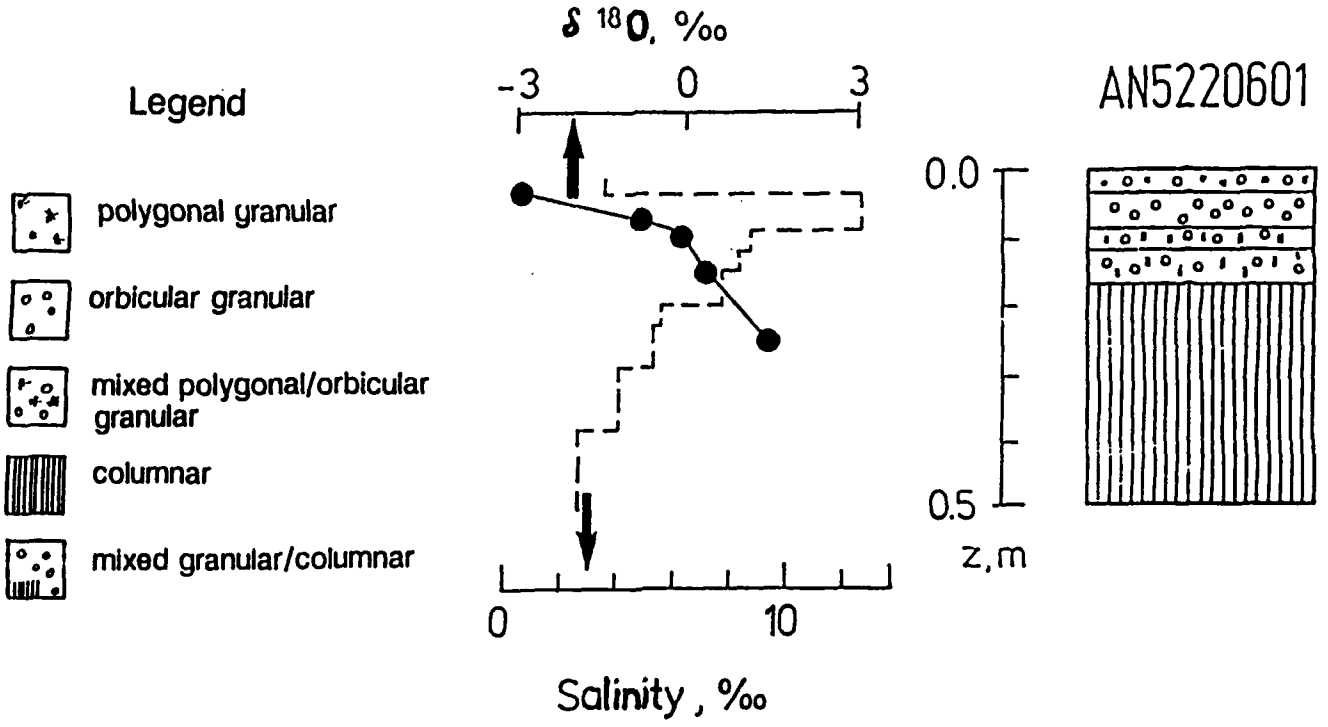


Figure 7. Profiles of $\delta^{18}O$ (filled circles) and salinity (dashed line) as a function of depth in a sea ice core of mainly congelation (a) and predominantly frazil ice (b), along with ice texture.

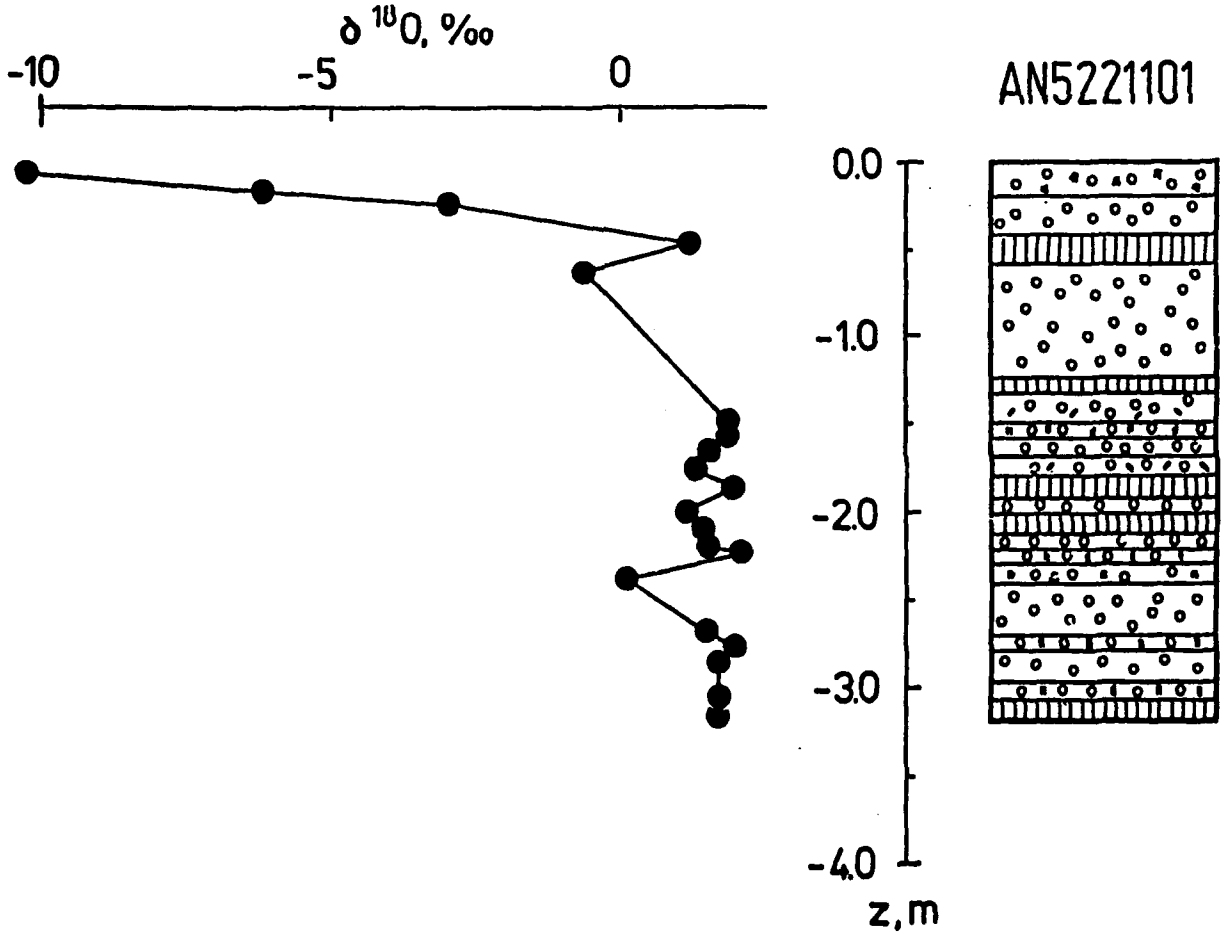


Figure 8. Profile of $\delta^{18}O$ and ice texture as a function of depth in sea ice core AN 5221101.

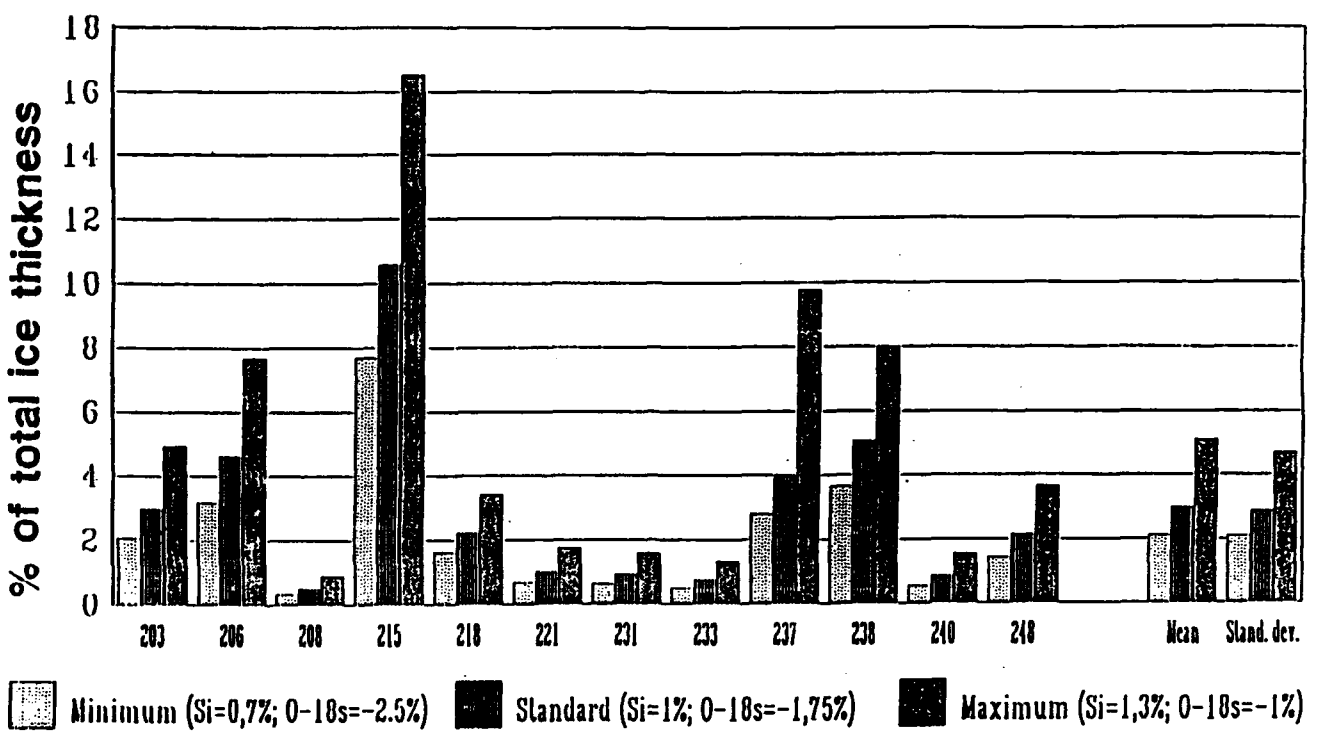


Figure 9. Meteoric ice fractions in a sea ice core in % of total ice thickness based on model calculations for different combinations of the free parameters: ice core section salinity (Si) and $\delta^{18}O$ value for snow component (^{18}Os) in a given core section (please note that values are given in percent and not in ppt).

tural record, and less clearly in the ice thickness record. However, ice deformations in the interior pack lead to frequent openings of the pack and lead formation. Based on a network of drifting buoys, Kottmeier and Hartig [1990] have demonstrated that for an area of about 10,000 km^2, daily areal changes in the ice cover of up to 10% take place. Thus extensive ridging and rafting on the one hand and lead formation on the other result from these convergent or divergent ice movements. Our observations show that in the interior pack, leads are the major places of a rapid and extensive energy exchange between ocean and atmosphere and result in the extensive formation of new sea ice. Due to their limited size, the open water patches usually do not allow the buildup of a significant wave field, even in the presence of substantial surface winds. This results in new ice that is formed according to the "classical model" of sea ice growth. This ice is texturally characterized by the transition from granular over mixed granular/columnar into columnar ice and a dominance of columnar over granular ice. It is primarily this ice that accounts for the fraction of congelation ice that has been seen in our core record (Table 1).

The absence of continental boundaries around Antarctica is primarily responsible for the mobility of the Antarctic sea ice cover. Sea ice movement is basically driven by surface winds. These surface winds also drive the major oceanic circulation in the Weddell Sea, the Weddell Gyre [see, e.g., Kottmeier and Hartig, 1990]. Ridging and rafting, as caused by wind-driven ice deformation, contributes also to the overall thickening of the sea ice cover. It is this process that accounts for the apparent additional growth, rather than congelation growth, at the bottom of already existing ice floes. This conclusion is supported by our thickness data, as obtained during EPOS I [Lange and Eicken, 1991a] as well as during the Winter Weddell Gyre Study 1989 [unpublished]. In addition, it is this deformation activity that also leads to the large fraction of granular ice in second- and/or multi-year ice through a number of different processes as discussed above (Figure 3). Thus, we conclude that ice deformation is the dominant process of sea ice development in the Weddell Sea and in Antarctica in general. We also conclude that changes in general climate, i.e., the prospect of increasing storminess at all latitudes, will increase the intensity of deformational activities in the sea ice belt around the Antarctic continent.

As was shown by Gordon and Huber [1990] the mean mixed layer heat fluxes in the central Weddell Sea are extremely high (up to 40 W m^{-2}). This is the main reason for the near-absence of any substantial congelation growth underneath the existing sea ice cover aside from new ice formation in leads. In the absence of congelation growth another process becomes significant, the incorporation of meteoric ice due to snow ice formation at the surface of sea ice floes. Our results demonstrate that these contributions become significant, even though our statistical base is at present very scarce. This subject requires additional investigations that are underway.

POSSIBLE DETECTION OF CLIMATIC CHANGES IN THE SEA ICE REGIME OF ANTARCTICA

Possible climatic changes, i.e., global warming induced by increased emission of greenhouse gases, will have a number of consequences for the sea ice regime of the polar regions. One of the consequences has briefly been discussed in the preceding section. The possibility of increased intensities of surface winds would lead to increased ice deformations in the sea ice regime of Antarctica and the Arctic. This might be detected through detailed and repeated ice thickness surveys at pre-determined localities, either through conventional drilling activities or through more modern approaches such as upward-looking sonars at a number of strategic sites in the Weddell Sea. An overall increase in bottom roughness, as seen through such investigations, would be a clear indicator of such increase in deformational processes. Similarly, increased surface roughnesses may be detectable by radar backscattering signals, as obtained through satellite remote sensing.

Another approach is directed toward the amount of meteoric ice as incorporated into sea ice floes. Overall warming will lead to decreasing ice growth rates and consequently to decreased ice thicknesses. However, a warmer atmosphere will contain more moisture, which will lead to increased snow accumulation rates at high latitudes. This snow will also be deposited on the sea ice cover and will, in the presence of a relatively thin sea ice sheet, lead to substantial growth of snow ice. Thus the overall increase in the snow ice fraction relative to previous investigations as seen through ^{18}O measurements will become a possible indicator of such processes.

In addition, as has been shown by Lytle et al. [1990], radar backscattering signals are highly sensitive to flooding of the sea ice cover, i.e., the intrusion of sea water at the snow ice interface. This, however, is a necessary prerequisite for snow ice formation and a precursor of such processes. Thus remote sensing signals could be analyzed with the aim of detecting widespread flooding and thus the increased amount of snow accumulation as a consequence of global warming.

ACKNOWLEDGMENTS

I thank the officers and the crew of RV *Polarstern* for continuous support during the expedition. Numerous people have also contributed in field and analytical work, which is greatly appreciated. Support from NATO Collaborative Research Grant CRG 890452 is greatly appreciated. I thank my colleagues for constructive discussions, particularly S. F. Ackley and an anonymous reviewer for constructive criticism. Contribution No. 387 of the Alfred-Wegener-Institute for Polar- and Marine Research.

REFERENCES

Bryan K., F. G. Komro, S. Manabe, and M. J. Spelman, Transient climate response to increasing atmospheric carbon dioxide, *Science*, *215*, 56–58, 1982.

Casarini, M. P., and R. Massom, (Eds.), *Winter Weddell Sea Project; sea ice observations, leg 1: June-September 1986*, Cambridge, University of Cambridge. Scott Polar Research Institute, 1987.

Clarke, D. B., and S. F. Ackley, Sea ice structure and biological activity in the Antarctic marginal zone, *J. Geophys. Res.*, *89*, 2087–2095, 1984.

Eicken, H., and M. A. Lange, Development and properties of sea ice in the coastal regime of the southeastern Weddell Sea, *J. Geophys. Res.*, *94*, 8193–8206, 1989.

Gordon, A. L., and B. A. Huber, Southern ocean winter mixed layer, *J. Geophys. Res.*, *95*, 11655–11672, 1990.

Gow, A. J., S. F. Ackley, K. R. Buck, and K. M. Golden, Physical and structural characteristics of Weddell Sea pack ice, *CRREL Rep. 87-15*, 75, 1987.

Hoffert, M. I., Climatic change and ocean bottom water formation: are we missing something?, in *Climate–Ocean-Interaction*, edited by M. E. Schlesinger, pp. 295–317, 1990.

Kottmeier, C., and R. Hartig, Winter observations of the atmosphere over Antarctic sea ice, *J. Geophys. Res.*, *95*, 16551–16560, 1990.

Lange, M. A., Basic properties of Antarctic sea ice as revealed by textural analyses of ice cores, *Ann. Glaciol.*, *10*, 95–101, 1988.

Lange, M. A., and H. Eicken, Sea ice thickness distribution in the northwestern Weddell Sea, *J. Geophys. Res.*, *96*, 4821–4837, 1991a.

Lange, M. A., and H. Eicken, Textural characteristics of sea ice and the major mechanisms of ice growth in the Weddell Sea, *Ann. Glaciol.*, 1991b, In press.

Lange, M. A., S. F. Ackley, P. Wadhams, G. S. Dieckmann, and H. Eicken, Development of sea ice in the Weddell Sea, *Ann. Glaciol.*, *12*, 92–96, 1989.

Lange, M. A., P. Schlosser, S. F. Ackley, P. Wadhams, and G. S. Dieckmann, ^{18}O concentrations in sea ice of the Weddell Sea, Antarctica, *J. Glaciol.*, *36*, 315–323, 1990.

Lytle, V., K. Jezek, P. Gogineni, S. Ackley, and M. Lange, Microwave properties of Antarctic sea ice (abstract), *EOS*, *71*, 100, 1990.

Manabe, S., and R. J. Stouffer, Sensitivity of a global climate model to an increase of CO_2 concentration in the atmosphere, *J. Geophys. Res.*, *85*, 5529–5554, 1980.

Marshall, H. P., The overwintering strategy of Antarctic krill under pack-ice, *Pol. Biol.*, *9*, 129–135, 1988.

Maykut, G. A., The surface heat and mass balance, *The Geophysics of Sea Ice*, edited by N. Untersteiner, *NATO ASI B146*, pp. 395–463, 1986.

Spindler, M., G. S. Dieckmann, and M. A. Lange, Seasonal and geographic variations in sea ice community structure of the Weddell Sea, Antarctica, *Antarctic Eco Systems. Ecological Change and Conservation*, edited by K. R. Kerry and G. Hempel, pp. 129–135, 1990.

Wadhams, P., M. A. Lange, and S. F. Ackley, The ice thickness distribution across the Atlantic sector of the Antarctic ocean in midwinter, *J. Geophys. Res.*, *92*, 14535–14552, 1987.

Weeks, W. F., and S. F. Ackley, Growth, structure and properties of sea ice, *The Geophysics of sea ice*, edited by N. Untersteiner, *NATO ASI B146*, pp. 49–164, 1986.

AD-P007 300

Greenland Sea Ice Anomalies During 1901–1984 and their Relation to an Interdecadal Arctic Climate Cycle

L. A. Mysak and D. K. Manak
Centre for Climate and Global Change Research, and Dept. of Meteorology, McGill Univ., Montreal, P.Q., Canada

R. F. Marsden
Dept. of Physics, Royal Roads Military College, F.M.O., Victoria, B.C., Canada

92-17982

ABSTRACT

Two ice data sets from the Greenland and neighboring seas have been analyzed to determine interannual and decadal time scale sea ice extent anomalies during this century. Sea ice concentration data on a 1° x 1° grid for 1953–1984 revealed the presence of a large positive anomaly in the Greenland Sea during the 1960s which coincided with the "Great Salinity Anomaly," a low-salinity water mass that traveled cyclonically around the northern North Atlantic during 1968–1982. The two anomalies propagated into the Labrador Sea with a typical travel time of 3–5 years.

Spring and summer ice-limit data obtained from Danish Meteorological Institute charts for 1901–1956 indicated the presence of heavy ice conditions in the Greenland Sea during 1902–1920 and in the late 1940s, and generally light ice conditions during the 1920s and 1930s. Only limited evidence of propagation of Greenland Sea ice anomalies into the Labrador Sea was observed, however. On the other hand, several large ice anomalies in the Greenland Sea occurred 2–3 years after large runoffs from northern Canada into the western Arctic Ocean. Similarly, a large runoff into the Arctic preceded the large Greenland Sea ice anomaly of the 1960s. These facts, together with recent evidence of "climatic jumps" in the Northern Hemisphere tropospheric circulation, suggest the existence of an interdecadal, self-sustained climate cycle in the Arctic which is described in terms of a negative feedback loop. In the Greenland Sea this cycle is characterized by a state of large sea ice extent overlying a layer of cool freshwater that does not convectively overturn, which alternates with a state of small sea ice extent and warm saline surface water that frequently overturns.

INTRODUCTION

The North Atlantic "Great Salinity Anomaly," a widespread freshening of the upper layer of the subpolar gyre waters during 1968–1982 [Dickson et al., 1988], is a climatic event which has received considerable attention in recent years. Although described as an advective event which could be traced around the subpolar gyre, the Great Salinity Anomaly (hereafter referred to as GSA) appeared to play a crucial role in the formation of large sea ice anomalies in the Greenland Sea [Malmberg, 1969; Vinje, 1970] and Labrador Sea [Mysak and Manak, 1989]. It also suppressed convection (and hence deep water formation) in different parts of the northwest Atlantic [Malmberg, 1969; Lazier, 1980]. Because of these factors, such anomalies could have profound effects on the thermohaline circulation and hence global climate [Broecker et al., 1985; Bryan, 1986; Aagaard and Carmack, 1989; Stocker et al., *this volume*].

Mysak and Manak [1989; hereafter referred to as MM] noted that coincident with the passage of the GSA from the

Greenland Sea into the Labrador Sea, was the movement of areal sea ice extent anomalies (computed from the Walsh and Johnson [1979] sea ice concentration data) from one region to the other. The propagation speed of the ice anomalies was estimated by MM to be 3.2 cm s^{-1}, which compares favorably with the overall propagation speed of the GSA around the subpolar gyre, namely 2–3 cm s^{-1} [Dickson et al., 1988]. In this note we first present a more detailed analysis of the cyclonic propagation of both positive and negative sea ice extent anomalies from the Greenland Sea into the Labrador Sea over the period 1953–1984.

Next, a brief report is given on a search for earlier large sea ice anomalies in the Greenland–Labrador Sea region using a gridded version of the Danish Meteorological Institute (DMI) ice-limit data for the period 1901–1956 [Kelly, 1979]. Salinity time series from the Faroe–Shetland Channel for the period 1902–1982 [Dickson et al., 1988], surface air temperature records for the Arctic region [Kelly et al., 1982] and the Koch index for Icelandic ice conditions [Lamb, 1977] suggest that large sea ice extent anomalies may have prevailed in the Greenland Sea during the first two decades of this century.

Finally, we present recently published data showing hydrological and atmospheric variations during the 1950s and 1960s which help to shed light on (i) the initial formation of the GSA in the Greenland Sea during the mid-1960s and (ii) the possible feedback effect of the GSA on climate in the 1970s. Collectively, these data suggest the existence of a negative feedback loop that could sustain interdecadal Arctic climate oscillations.

Dickson et al. [1975] documented the existence of a high pressure anomaly cell during winter over Greenland between the late 1950s and the late 1960s, and proposed that the associated wind anomalies in this region resulted in more fresh water (and hence sea ice) being transported in the East Greenland Current towards Iceland during the early 1960s. Walsh and Chapman [1990b], on the other hand, showed that sea level atmospheric pressure fluctuations in the Arctic itself may have enhanced the export of sea ice (fresh water) from the Arctic into the Greenland Sea in the 1960s. We shall argue that an ice buildup in the Arctic (and hence in the Greenland Sea) could be first due to increased runoff from North America into the Arctic Ocean during the early 1960s.

THE SEA ICE DATA

The sea ice distribution data used in Section 3 were obtained from John Walsh of the University of Illinois. The data consist of monthly sea ice concentration grids (with a 1° x 1° latitude spacing) for the years 1953–1984, inclusive. At each grid point (see Figure 1a) the ice concentration (fraction of a 111 x 111 km^2 grid area covered by ice) is given in tenths, and from these monthly values areal sea ice extent anomalies were calculated as described in MM (section 2) to remove the 32-year climatological annual cycle. The monthly areal sea ice extent anomalies for each of the five subregions shown in Figure 1a were used in cross-correlation and CEOF (complex empirical orthogonal function) analyses.

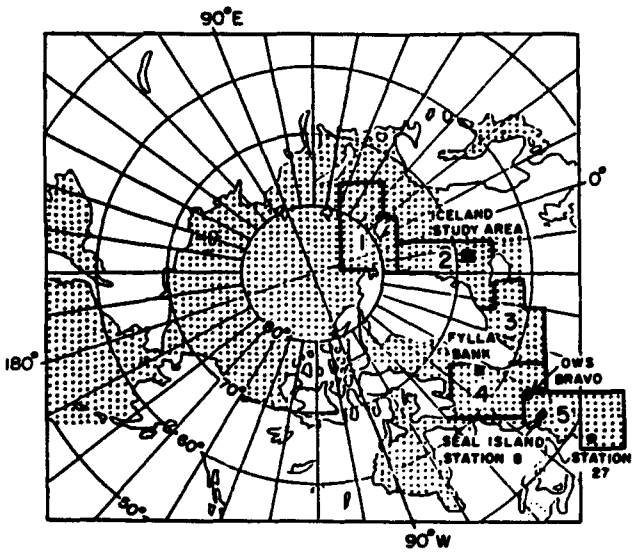


Figure 1a. The division of the Greenland–Labrador Sea region into 5 subregions, with center-to-center spacing of 1500 km. The numbers of the subregions increase in the direction of the cyclonic circulation in the subpolar gyre. The dots (1° x 1° latitude spacing) represent the sea ice concentration grid developed by Walsh and Johnson [1979]. Temperature and salinity data from the 5 hydrographic stations shown in subregions 2, 4 and 5 have been used to track the Great Salinity Anomaly in the Greenland and Labrador Seas [Dickson et al., 1988].

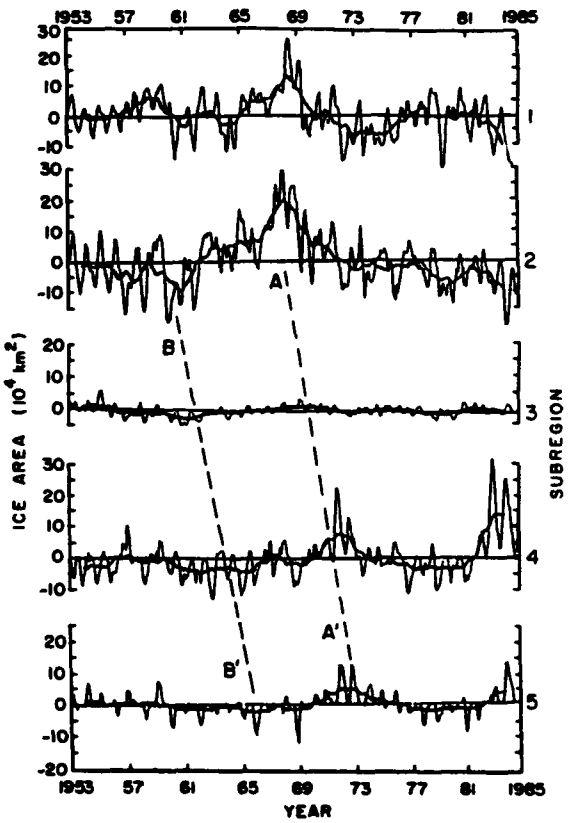


Figure 1b. The 3-month and 25-month running means of the monthly anomalies of areal sea ice extent (MM) for subregions 1 to 5 of the Greenland–Labrador Sea region (see Figure 1a). The dashed lines with negative slope indicate the propagation of ice anomalies from subregion 2 through to subregion 5.

The ice data used to study sea ice anomalies during the first half of the century were obtained from circumpolar ice-limit data for the spring and summer months, digitized onto the Walsh 1° x 1° latitude grid (Figure 1a) from a chart series produced by the Danish Meteorological Institute (DMI). A description of the data set and the digitization procedure is given by Kelly [1979]. The data set consists of estimated ice limits for the months April to August, inclusive, for the years 1901–1939 and 1946–1956, a total of 50 years. An ice/no ice indicator (1 = ice, 0 = no ice) is given within each grid square; the ice limit approximates the 3 or 4/10 ice concentration isopleth used in earlier studies [e.g., Walsh and Johnson, 1979; MM]. A "quick look" atlas [Manak and Mysak, 1988] was compiled of the April and July ice-edge limits in the Greenland and Labrador sea regions for the years 1901–1939 and 1946–1956 inclusive.

PROPAGATION OF SEA ICE ANOMALIES FROM GREENLAND SEA INTO LABRADOR SEA

Figure 1b shows the 3-month and 25-month running means of the monthly areal sea ice extent anomalies for the five subregions shown in Figure 1a. The time series for subregions 1 and 2 show that the dominant 1968 peak which is associated with the salinity minimum of the GSA in the Greenland Sea, as well as several smaller peaks and troughs, are in phase, especially for the 25-month running mean curves. In subregion 3, there is a broad relative maximum centered at around 1970 which is the downstream and hence delayed signal of the 1968 peak in subregion 2. In subregions 4 and 5 there are large positive anomalies occurring approximately in 1971 and 1972, respectively, which suggest a further advance of this anomaly into the Labrador Sea and then southward along the northeast coast of Newfoundland. The direction of travel of the "1968" anomaly is consistent with the hypothesis that it is advected by the near-surface currents which move cyclonically around the subpolar gyre. The slope of the dashed straight line AA' passing through all the peaks for subregions 2 to 5, gives an estimate of about 3 km day^{-1} for the average speed of propagation of the 1968 anomaly. Other small anomalies also propagated from subregion 2 to subregion 5, such as the trough in subregion 2 in 1961, which appears in subregion 3 in 1962, in subregion 4 in 1963–64 and in subregion 5 in 1965 (see dashed line BB').

To determine whether there is a continuous movement of all anomalies from the Greenland Sea into the Labrador Sea during the period 1953–1984, cross-correlations between the 25-month smoothed anomaly time series in Figure 1b were calculated as a function of lag with respect to subregion 2 [Mysak et al., 1990, Figure 4]. The maximum correlation values were generally above the 95% significance level, and from these values a distance versus lag curve was plotted [Mysak et al., 1990, Figure 5]. From the latter figure an estimate of 2.7 + 0.29 cm s^{-1} (2.3 ± 0.25 km day^{-1}) is obtained for the average speed of travel of the longer-term ice anomalies, which is comparable to the average current speed of the subpolar gyral circulation, namely 2–3 cm s^{-1}.

The results of the cross-correlation analysis were compared with those of a COEF analysis of the monthly sea ice concentration anomaly data for subregions 1 to 5 [Mysak et al., 1990, section 4]. In the lowest frequency band (period of about 4 years), 67% of the spectral power density is phase-locked into the first mode of this band which was also found to propagate from the Greenland Sea into the Labrador Sea with a mean speed of 4.9 ± 2.5 cm s^{-1}. Clearly, the lower bound of this estimate (2.4 cm s^{-1}) is comparable to that found above (2.7 ± 3 cm s^{-1}) from the cross-correlation analysis, and confirms the propagation of the ice anomalies as a low-frequency event.

The relationship between sea ice anomalies and (negative) salinity anomalies in the Greenland–Labrador Sea region has been discussed by Marsden et al. [1991] and Mysak et al. [1990, section 5]. Malmberg [1969] showed that anomalously low surface (upper 200 m) salinities in these regions increase the stability of the water column to prevent deep convection during winter, even at the water freezing point (-1.8°C). Thus the formation of sea ice during winter is enhanced since no warm, saline Atlantic water is brought up to the surface, which explains the presence of the large ice anomalies during the passage of GSA through the Greenland and Labrador Seas. For the longer period 1953–1980, Marsden et al. [1991] showed that the lag correlations between surface salinity and sea ice anomalies at several of the hydrographic stations in Figure 1a have a common structure for the case where salinity leads sea ice. These results are consistent with the concept of stability enhancement of sea ice formation.

Examination of the ice-limit maps in Manak and Mysak [1988], which were derived from Danish Meteorological Institute (DMI) ice charts for the period 1901–1956, revealed large ice anomalies in the Greenland Sea during 1902, 1911, 1915, 1934 and 1952 [Mysak et al., 1990, section 6]. However, only limited evidence was found in this spring–summer data set for the cyclonic propagation of sea ice anomalies from the Greenland Sea into the Labrador Sea. The best example of this was seen in the April 1902 and 1907 pair of maps, and it is consistent with the cyclonic propagation of a large negative salinity anomaly in the subpolar gyre seen later in the Faeroe–Shetland Channel during 1908–1910 [see Figure 1 in Dickson et al., 1988].

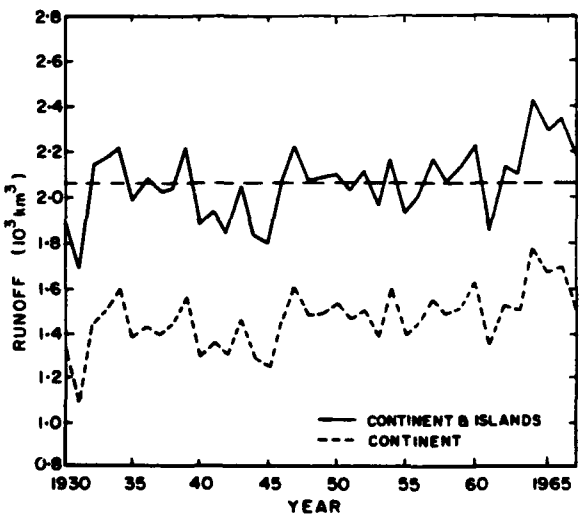


Figure 2. Annual runoff from the North American continent into the Arctic basin. (Redrawn from Lawford [1988].) For the total runoff (solid curve), the mean and standard deviation are 2.06 (horizontal dashed line) and 0.15 respectively.

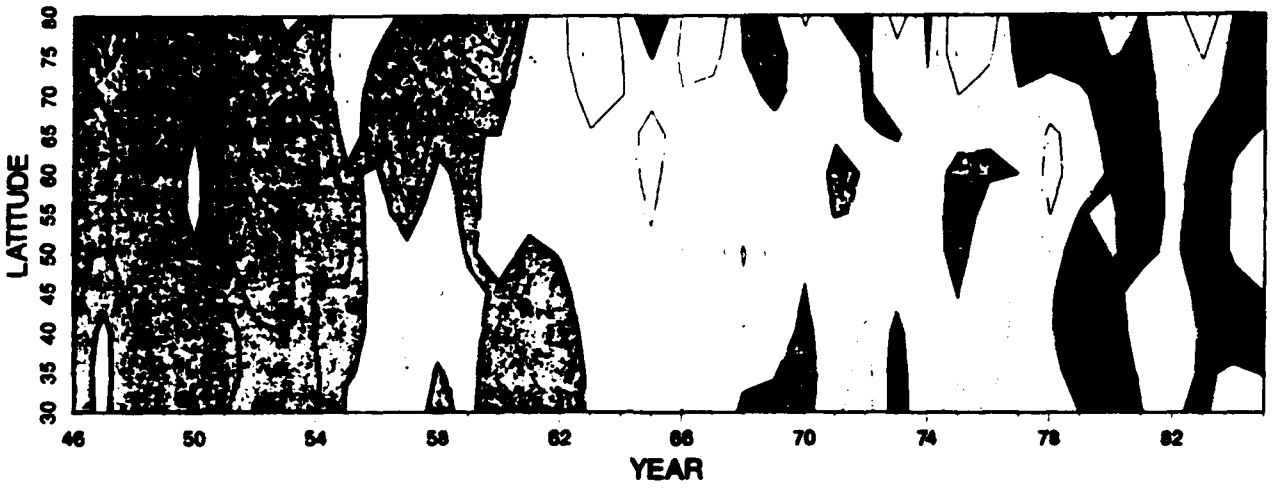


Figure 3. Variation by year and latitude of the summer (June, July, August, September) zonally average 50 kPa height anomaly. Contour interval, 1 dam. Shaded areas denote positive anomalies, whereas clear areas denote negative anomalies. (From Knox et al. [1988].) Similar plots were also obtained for the other seasons.

RUNOFF AND ATMOSPHERIC PRESSURE VARIABILITY

The large Greenland Sea ice anomalies of 1934 and 1952 [Figure 14 in Mysak et al., 1990] occurred two to three years after relatively large runoffs from North America into the Arctic, which in turn were preceded by relatively rapid increases in runoff during 1931–1932 and 1945–1947 (Figure 2). This phenomenon, together with the dramatic runoff increase during 1961–1964 (Figure 2), strongly suggests that large-scale hydrological events in northern Canada may be the precursors of large ice and (negative) salinity anomalies in the Greenland Sea. The large runoff duriag 1964–1966 (Figure 2) would have resulted in extensive sea ice formation in the Beaufort Sea during ring 1965–1967 [Manak and Mysak, 1989], and such a large sea ice anomaly would then follow the drift of the Beaufort Gyre and Transpolar Drift [Walsh and Chapman, 1990b, Figure 3] and exit into the Greenland Sea through Fram Strait. The estimated transit time for such ice movement is 2–3 years [Mysak et al., 1990, section 7]. The effect of Eurasian runoff on sea ice in the central Arctic appears to be minimal, however, in creating anomalies like the GSA [Mysak et al., 1990].

The origin of the three large runoffs shown in Figure 2, which are roughly 15–20 years apart, may be traced to "climatic jumps" in the Arctic tropospheric circulation which appear to occur just prior to these anomalous runoffs [Knox et al., 1988; Walsh and Chapman, 1990a]. Associated with the change in sign of the 50 kPa height anomalies around 1961–1962 (Figure 3), for example, was a subsequent increase in precipitation in the Canadian high Arctic [Bradley and England, 1978]. This presumably led to the large 1964–1966 runoff seen in Figure 2.

As a final issue, one must ask "what is the origin of the climatic jumps and associated precipitation increases?" We propose that this is due to an increase in cyclogenesis north of Greenland [Mysak et al., 1990, section 7] which could be caused by an increased inflow through Fram Strait of warm West Spitsbergen Current (WSC) water from the Greenland and Norwegian Seas. This would result in an increased ocean-to-atmosphere heat transfer north of Greenland and hence more active cyclogenesis in the Arctic especially during winter. Conversely, should the inflowing WSC be colder than normal due to reduced convective overturn (and more extensive sea ice) in the Greenland Sea, then Arctic cyclogenesis would be reduced, as would precipitation and hence runoff and sea ice formation in the western Arctic.

PROPOSED ATMOSPHERE–CRYOSPHERE–HYDROSPHERE NEGATIVE FEEDBACK LOOP

The above sequence of atmospheric, hydrological, oceanic and sea ice events which occurred in the 1960s, together with the apparent secondary "climate jump" around 1976–1978 (Figure 3), suggests that a multi-component feedback loop may be operative in the Arctic and Greenland Sea which results in interdecadal climate oscillations. Following the diagramatic approach of Kellogg [1983], we show in Figure 4 a 10-component feedback loop linking most of the various processes described in this paper. A plus (minus) sign between two boxes A and B, say, means that an increase in A would cause an increase (decrease) in B. Upon tracing around this loop in the clockwise direction (the direction of cause-and-effect), we note that the product of the pluses and minuses is negative. Thus Figure 4 represents a reversing or negative feedback loop [Kellogg, 1983]. Therefore, in the absence of other strongly damping factors, a perturbation transferred from any one component in the loop to the next can theoretically result in a reversal of the sign of the initial perturbation.

In Mysak et al. [1990] it is estimated that the period (which is 2X the loop circuit time) of the proposed Arctic climate cycle is about 20–30 years. Thus if this interdecadal cycle is real, then the sea ice extent in the Greenland Sea should be extensive, the salinity should be relatively low and convective overturning should be reduced during the late 1980s and early 1990s. Remarkably, at the recent 1990

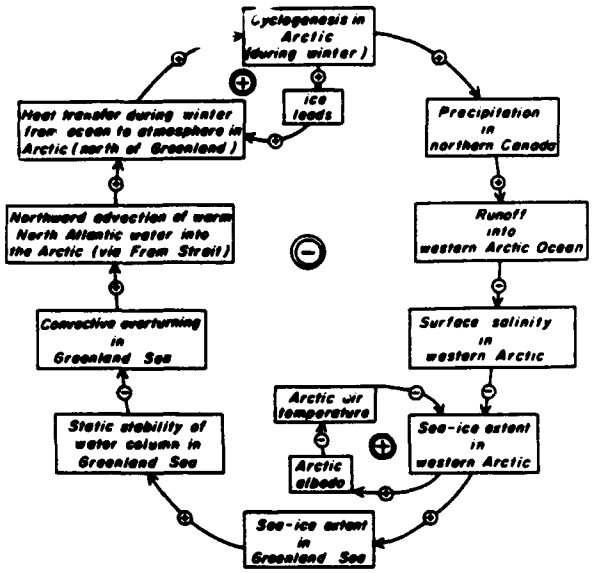


Figure 4. Possible negative feedback loop linking Arctic cyclogenesis, precipitation, runoff, salinity, sea ice extent, oceanic stability, convective overturning, poleward oceanic heat transport and heat flux into the atmosphere in the Arctic. A simpler version of this loop (without sea ice and oceanic advection) was proposed by Lawford [1988] to characterize large-scale air/sea interactions in the North Pacific. The lower small positive feedback loop involving Arctic air temperature is the familiar ice-albedo feedback mechanism which could assist in cooling of the troposphere if ice extent increases. The upper small positive feedback loop involving ice leads results in the intensification of cyclogenesis if the area of ice leads increases.

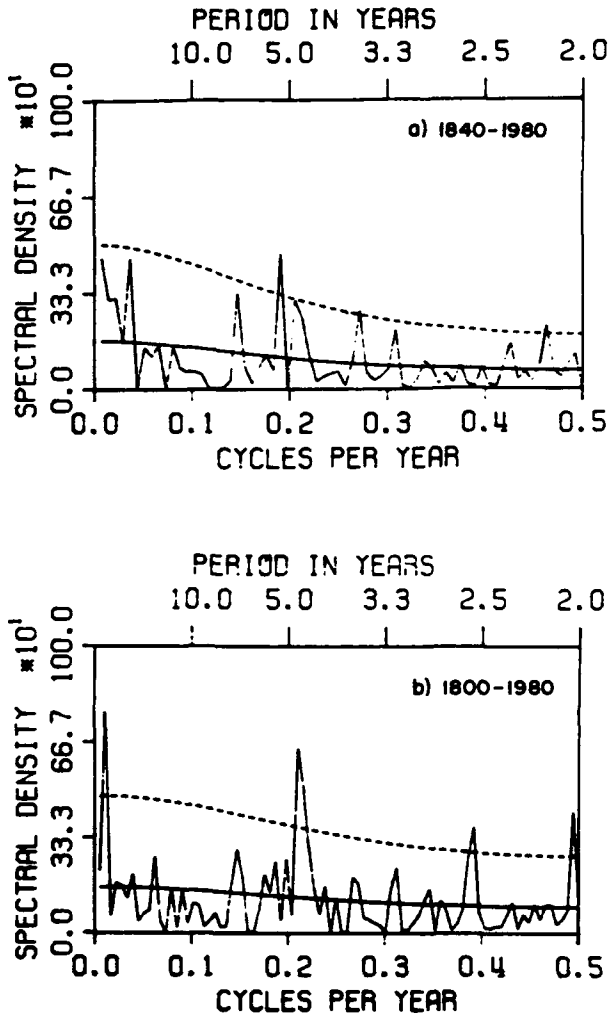


Figure 5. Periodogram (power spectrum) of the Koch ice index fluctuations [Lamb, 1977] for the years (a) 1840-1980 and (b) 1800-1980. The spectra have dimensions of (number of weeks)^2/cpy. In each case the dashed curve represents the 95% confidence limit and the solid curve, the red noise spectrum (based on the first order autoregression coefficent for two degrees of freedom).

International Conference on the Role of the Polar Regions in Global Change, a number of papers [summarized in Mysak et al., 1990] presented preliminary results which are consistent with these speculations.

To search for earlier evidence of the interdecadal cycle, Koch's ice severity index for Iceland [Lamb, 1977] was examined. This index, defined as the number of weeks per year when ice affected the coast of Iceland, is a reasonable measure of the ice cover of a large area of the North Atlantic sector. The power spectrum of the associated ice index fluctuations for 1840–1980 shows a low-frequency (interdecadal) peak (at a 27-year period) which is just below the 95% confidence limit (Figure 5a). The most prominent peak which is above the 95% limit occurs at a period of 5.2 years, which is comparable to the time scale of the North Atlantic Oscillation. Further, because of strong interannual fluctuations in the ice index during 1800–1840 [see Figure 10 in Mysak et al., 1990], this high-frequency peak is intensified (and slightly shifted to 4.8 years) in the spectrum for the longer data record 1800–1980, which we note shows no significant interdecadal peak. Instead, there now emerges a significant very low-frequency peak at about 88 years.

CONCLUDING REMARKS

We have proposed that the GSA and associated sea ice anomalies in the Greenland Sea may be a manifestation of an interdecadal signal which links various high-latitude processes in the atmosphere–hydrosphere–cryosphere part of the climate system. Curiously enough, Royer [1989] recently noted the existence of a 20- to 30-year fluctuation in the sea surface temperature in the northeast Pacific, north of 50°N. We are tempted to speculate that this may also be a signal of the interdecadal oscillation proposed here.

In the modern terminology of thermohaline circulation theories [e.g., Broecker et al., 1985], we suggest that the surface Greenland Sea water vacillates every 10–15 years between a cool, low-salinity icy state (with reduced convective overturning—the so-called halocline catastrophe) and a warm, saline low-ice state (with frequent, deep convective overturning). Further, the transport of these respective waters into the Arctic causes the atmospheric circulation there to oscillate between a state of weak and strong cyclogenesis. It is worth noting that our proposed interdecadal cycle is highly nonlinear, with the increases in runoff and sea ice extent for example, being much more rapid than the return to normal or below normal conditions (e.g., Figures 3 and 1b). This asymmetric property of the interdecadal cycle also characterizes longer-term climate cycles, such as the 10^5-year ice ages and the 10^3-year fluctuations recently described during the past interglacial [Broecker et al., 1985].

Clearly, future work on this cycle is needed. It would be worthwhile to examine and monitor new hydrological, atmospheric, sea ice and hydrographic data to determine, for example, whether there have been large annual runoffs into the Arctic in the late 1980s and whether extensive sea ice coverage and reduced convective overturning are indeed occurring in the Greenland Sea during the 1990s. Secondly, it would be of interest to develop simple models of the interdecadal cycle in order to gain further insight into the processes and mechanisms involved. A number of such modeling approaches are outlined in Mysak et al. [1990], where it is also suggested how global climate general circulation models may be improved in the Arctic regions in order to simulate interdecadal variability.

ACKNOWLEDGMENTS

We thank Ann Cossette for typing this paper and Ursula Seidenfuss for drafting assistance. LAM is grateful for financial support received from AES, NSERC, FCAR and ONR; RFM completed part of the work presented here while a sabbatical visitor to the Climate Research Group (now Centre for Climate and Global Change Research) at McGill, and is also grateful for the support of ARP award RR15 from the Canadian Department of National Defence.

REFERENCES

Aagaard, K., and E. C. Carmack, On the role of sea ice and other fresh water in the Arctic circulation, *J. Geophys. Res.*, *94*, 14485–14498, 1989.

Bradley, R. S., and J. England, Recent climatic fluctuations of the Canadian high Arctic and their significance for glaciology, *Arctic and Alpine Res.*, *10*, 715–731, 1978.

Broecker, W. S., D. M. Peteet, and D. Rind, Does the ocean–atmosphere system have more than one stable mode of operation?, *Nature*, *315*, 21–26, 1985.

Bryan, F., High-latitude salinity effects and interhemispheric thermohaline circulations, *Nature*, *323*, 301–304, 1986.

Dickson, R. R., H. H. Lamb, S. A. Malmberg, and J. M. Colebrook, Climatic reversal in the northern North Atlantic, *Nature*, *256*, 479–482, 1975.

Dickson, R. R., J. Meincke, S. A. Malmberg, and A. J. Lee, The "Great Salinity Anomaly" in the northern North Atlantic 1968–1982, *Prog. Oceanog.*, 20, 103–151, 1988.

Kellogg, W. W., Feedback mechanisms in the climate system affecting future levels of carbon dioxide, *J. Geophys. Res.*, *88*, 1263–1269, 1983.

Kelly, P. M., An Arctic sea ice data set, 1901–1956, World Data Center -A for Glaciology (Snow and Ice), *Glacial Data Rep GD-5*, pp. 101–106, Boulder, CO, 1979.

Kelly, P. M., P. D. Jones, C. B. Sear, B. S. G. Cherry, and R. K. Tavakol, Variations in surface air temperatures: Part 2. Arctic regions, 1881–1980, *Mon. Wea. Rev.*, *110*, 71–83, 1982.

Knox, J. L., K. Higuchi, A. Shabbar, and N. E. Sargent, Secular variation of Northern Hemisphere 50 kPa geopotential height, *J. Climate*, *1*, 500–511, 1988.

Lamb, H. H., *Climate: Present, Past and Future*, Vol. 2, Methuen, London, 1977.

Lawford, R. G., Towards a framework for research initiatives involving the impacts of climatic variability and change on water resources in the Canadian Prairies, in *The impact of climate variability and change on the Canadian Prairies*, Symposium/Workshop Proceedings, 1987 September 9–11, edited by B. L. Magill and F. Geddes, pp. 275–306, Alberta Department of the Environment, Edmonton, 1988.

Lazier, J. N. R., Oceanographic conditions at Ocean Weather Ship BRAVO 1964–1974, *Atmosphere–Ocean*, *18*, 227–238, 1980.

Malmberg, S. A., Hydrographic changes in the waters between Iceland and Jan Mayen in the last decade, *Jokull*, *19*, 30–43, 1969.

Manak, D. K., and L. A. Mysak, Atlas of April and July Arctic ice edge limits, 1901–1956, *Climate Res. Group Rep. 88-12*, Dept. Meteorol., McGill Univ., Montreal, 1988.

Manak, D. K., and L. A. Mysak, On the relationship between Arctic sea ice anomalies and fluctuations in northern Canadian air temperature and river discharge, *Atmosphere–Ocean*, *27*, 682–691, 1989.

Marsden, R. F., L. A. Mysak, and R. A. Myers, Evidence for stability enhancement of sea ice in the Greenland and Labrador Seas, *J. Geophys. Res.*, *96*, 4783–4789, 1991.

Mysak, L. A., and D. K. Manak, Arctic sea-ice extent and anomalies, 1953–1984, *Atmosphere–Ocean*, *27*, 376–405, 1989.

Mysak, L. A., D. K. Manak, and R. F. Marsden, Sea-ice anomalies in the Greenland and Labrador Seas during 1901–1984 and their relation to an interdecadal Arctic climate cycle, *Climate Dynamics*, *5*, 111–133, 1990.

Royer, T. C., Upper ocean temperature variability of the northeast Pacific Ocean: Is it an indicator of global warming?, *J. Geophys. Res.*, *94*, 18175–18183, 1989.

Stocker, T. F., D. G. Wright, and L. A. Mysak, A coupled, zonally averaged atmosphere–ocean model: variability of the thermohaline circulation, *this volume*, 1991.

Vinje, T. E., Sea ice observations in 1968, *Arbok norsk Polarinst.*, *1968*, 95–100, 1970.

Walsh, J. E., and W. L. Chapman, Short-term climate variability of the Arctic, *J. Climate*, *3*, 237–250, 1990a.

Walsh, J. E., and W. L. Chapman, On the Arctic contribution to upper-ocean variability in the North Atlantic, *J. Climate*, *3*, 1462–1473, 1990b.

Walsh, J. E., and C. M. Johnson, An analysis of Arctic sea ice fluctuations, *J. Phys. Oceanogr.*, *9*, 580–591, 1979.

Seasonal Mean Ice Motion in the Arctic Basin

R. Colony
Polar Science Center, University of Washington, Seattle, Washington, U.S.A.

ABSTRACT

Each year about 15% of the surface ice cover in the Arctic Basin is exported through the Fram Strait and into the North Atlantic. The net annual balance of sea ice is maintained by the often competing processes of in situ thermodynamics, ice advection, and ice divergence, each process having a marked seasonal cycle. The seasonal mean field of motion is also the agent for large scale transport of ice, salt, sediment, and pollutants.

The seasonal fields of ice motion are studied using observations taken over the past 100 years. The basic data base includes the trajectories of beset ships, manned research stations, remote autonomous meteorological stations, and satellite-linked buoys. In all, more than 250 station years of data are used in the analysis.

The mean velocity fields are analyzed using a statistical interpolation scheme which minimizes the variance of the difference between the estimated velocity and the true velocity. It can be shown that this procedure also gives an optimal estimate of the velocity gradient. The mean seasonal fields of velocity, vorticity, divergence, and shear are shown.

Topological features of the mean fields are described. Here the approach considered the velocity field as a transformation, mapping ice from one location into another location. The mathematical properties of this transformation are studied.

AD-P007 301

92-17983

A Coupled, Zonally Averaged Atmosphere–Ocean Model: Variability of the Thermohaline Circulation

Thomas F. Stocker
Centre for Climate and Global Change Research, and Department of Meteorology, McGill University, Montreal, PQ, Canada (now at: Lamont-Doherty Geological Observatory, Columbia University, Palisades, New York, U.S.A.)

Daniel G. Wright
Department of Fisheries and Oceans, Bedford Institute of Oceanography, Dartmouth, N.S., Canada

Lawrence A. Mysak
Centre for Climate and Global Change Research, and Department of Meteorology, McGill University, Montreal, PQ, Canada

ABSTRACT

Two experiments with a recently developed zonally averaged climate model which includes the ocean's thermohaline circulation are performed. The first experiment simulates a global thermohaline circulation in which deep water is formed in the North Atlantic, flows as a deep current into the Pacific basin and then upwells. The water is returned as a near-surface flow through the Indian Ocean into the South Atlantic [Gordon, 1986]. The present model reproduces a global deep circulation under present-day forcing and shows that the zonal atmospheric water vapor transport is of importance.

The second experiment studies the effect of glacial meltwater runoff at different latitudes on the thermohaline circulation, meridional heat flux and surface air temperature. Depending on the strength and position of the forcing anomaly, severe cooling can be observed in high northern latitudes. The mechanism may provide further insight into the Younger Dryas climate event.

INTRODUCTION

During the last few years several studies have focused on the dynamics and variability of the ocean circulation to understand climatic change. In particular, the thermohaline circulation has been recognized as a key part in the interactions of the atmosphere, cryosphere and hydrosphere. About 50%, i.e., 2 to 3 PW (1 PW = 10^{15} W), of the global meridional heat transport is carried through the world ocean. Unlike in the atmosphere, transport in the ocean is mainly due to the mean meridional overturning, or thermohaline circulation, as confirmed by various general circulation models [e.g., Bryan, 1987]. Such studies also demonstrate the variability of the thermohaline circulation [Bryan, 1986; Marotzke et al., 1988; Manabe and Stouffer, 1988]. A common result was the presence of multiple equilibria under identical forcing. This clearly calls for the implementation of more sophisticated oceanic components in climate models.

A two-dimensional climate model suitable for annual-mean studies was recently developed by Stocker et al. [1990]. The purpose of this paper is to present its application to two well-known problems of our climate history. The first concerns the global thermohaline circulation that is believed to operate like a conveyor belt causing a continuous flow of water masses through all ocean basins. Gordon [1986] proposes that the water, upwelling mainly in the Pacific, is returned as a thermocline flow through the Indian into the South Atlantic ocean, in order to feed North Atlantic deep water formation. This hypothesis is tested and confirmed with the model running in an ocean-only mode.

The second problem focuses on the Younger Dryas cooling event around 10700 B.P., that has been linked to changes in the rate of deep water formation [Broecker et al.,

1985]. With the coupled model, whose atmospheric part consists of an idealized surface energy balance, we investigate the effect of anomalous fresh water input due to ice sheet melting on the ocean–atmosphere climate.

The following section describes the model; then the Pacific–Atlantic thermohaline circulation is presented; the results of the deglaciation experiment are discussed; and the conclusions are presented.

BRIEF MODEL DESCRIPTION

The climate model is designed for paleoclimatic studies on time scales exceeding decades. Integration over many thousands of years can be carried out because the model simulates only zonally averaged, annual-mean fields of the ocean's meridional overturning, ocean temperature and salinity, and atmospheric surface temperature.

The oceanic part of the model [Wright and Stocker, 1991] is based on the zonally averaged balance equations for momentum, mass, energy and salt content. Temperature T and salinity S satisfy the time-dependent advection–diffusion equations using constant diffusivities with values of 10^3 m^2 s^{-1} (horizontal) and 4×10^{-5} m^2 s^{-1} (vertical). The ocean dynamics is purely buoyancy-driven by surface heat and salt fluxes. During spin-up from rest, T and S at the surface are restored to prescribed values. Once a steady state is obtained, mixed boundary conditions are used, i.e., temperature is still restored as before, whereas the steady-state salt flux is kept fixed henceforth. The ocean model shares some similarities with the one of Marotzke et al. [1988], with the most significant difference being a realistic value (10^{-4} m^2 s^{-1}) for the vertical eddy diffusivity in the momentum equations.

The atmospheric part of the climate model is a quasi-stationary surface energy balance model similar to that of Sellers [1969]. This allows a first assessment of the influence of the thermohaline circulation on surface air temperature. The model balances the diffusively parameterized meridional sensible and latent heat fluxes with the radiative fluxes at the top of the atmosphere and the ocean-to-atmosphere heat flux. The latter includes radiative, latent and sensible heat fluxes. The various parameterization constants are all representative of the present climate, symmetrized about the equator and held fixed.

THERMOHALINE CIRCULATION OF THE ATLANTIC AND PACIFIC

To simulate a global thermohaline circulation, the ocean model is extended to two basins of 120° and 60° angular width, connected at 55°S, where an open boundary allows for fluxes of mass, energy and salt between them [Stocker and Wright, 1991]. The Pacific basin extends from 55°S to 50°N, the Atlantic from 55°S to 80°N, and the calculations are performed on a coarse grid of 15 (horizontal) x 10 (vertical) points. The model is spun up using realistic restoring sea surface temperatures and salinities.

Figure 1 shows the meridional overturning stream function in the two ocean basins after 7000 years. Deep water is formed at a rate of 16 Sv in the North Atlantic only. The Atlantic bottom water flows south, and about 6 Sv are exported into the Pacific. The rest is upwelling in the Atlantic and joins the thermocline return flow from the Pacific. In the Pacific about 10 Sv are overturned, the main part of

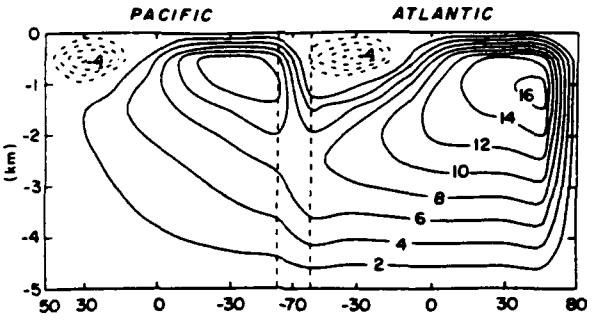


Figure 1. Contours of the meridional overturning stream function in Sv (1 Sv = 10^6 m^3 s^{-1}) after a 7000-year spin-up. Realistic surface forcing causes a global thermohaline circulation with main deep water formation in the North Atlantic and upwelling in the Pacific.

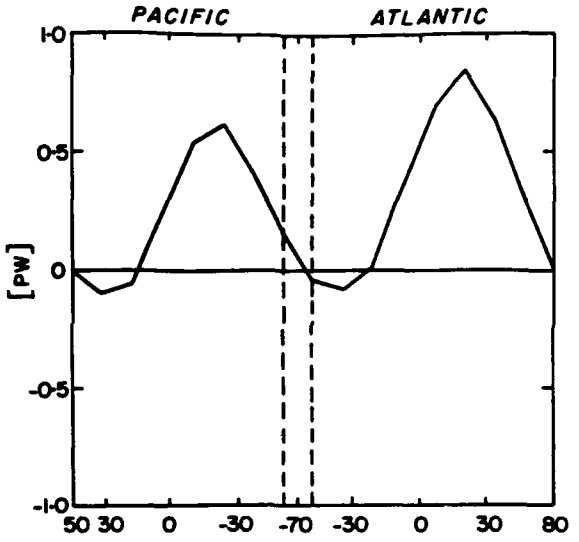


Figure 2. The oceanic meridional heat flux integrated across the respective basin for the steady state of Figure 1. Heat transport in the Pacific is mainly south (0.6 PW) whereas it is north in the Atlantic (0.8 PW).

which originates from Atlantic bottom water. 6 Sv are returned as a shallow flow through the circumpolar current region (vertically dashed) into the Atlantic. In addition to this global circulation, two weak (4 Sv) and shallow cells in the South Atlantic and the North Pacific are observed. The meridional oceanic heat flux of this steady state is given in Figure 2. In the Atlantic the heat flux is mainly northward with a maximum of 0.8 PW (0.4 PW across the equator), whereas in the Pacific it is to the south peaking at 0.62 PW (0.3 PW across the equator). It is found that this global thermohaline circulation is maintained by a net freshwater transport through the atmosphere from the Atlantic to the Pacific in qualitative agreement with data [Baumgartner and Reichel, 1975]. When the forcing is switched to mixed boundary conditions, the circulation is found to be stable [Stocker et al., 1990; Stocker and Wright, 1991].

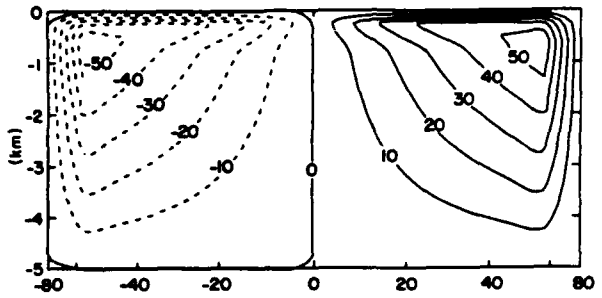


Figure 3. Global thermohaline circulation (in Sv) of a hypothetical world ocean covering 70% of the earth's surface resulting from the coupled climate model after 18,000 years of integration.

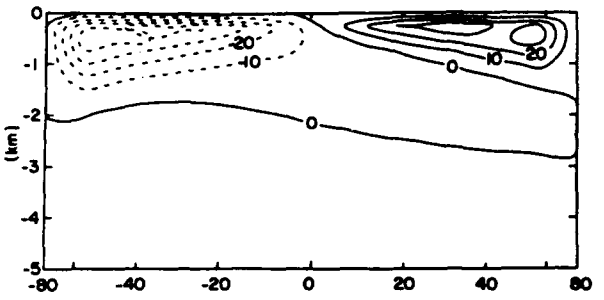


Figure 4. The deep circulation weakens and shallows after 20,000 years of anomalous freshwater input of 0.63 m yr^{-1} to the northern hemisphere.

YOUNGER DRYAS EXPERIMENT

We now present an experiment performed with the *coupled* climate model described earlier. The Younger Dryas climate event and its precursors Bølling and Allerød, which are observed in various proxy-data records [Broecker et al., 1985] around the North Atlantic basin, produced a significant reduction of the oxygen isotope ratios. This is usually interpreted as a regional atmospheric cooling of the order of 3°C to 5°C that lasted for 2000 to 3000 years. Broecker et al. [1985] suggest that a possible mechanism to explain the cooling is the change of deep water production rate in high latitudes caused by an excess of runoff from melting ice caps.

The idealized climate model consists of a world ocean of 5000 m depth, extending from 80°S to 80°N and with an angular width of 252° corresponding to an ocean covering 70% of the earth's surface. The numerical grid comprises 15 (horizontal) x 20 (vertical) points. The ocean-only model was spun up from rest for 3000 years after which time it was coupled to the atmospheric energy balance model. During adjustment over another 15,000 years, the model steadily reduced global energy imbalance to -5.3×10^{-3} W m^{-2}.

The annual average climate produced by the coupled model is symmetric about the equator and reasonably close to present-day conditions. Surface air temperatures vary from -5°C (at 67°) to 28.3°C (at 0°), and heat is taken up by the ocean at latitudes lower than 25° with a maximum equatorial value of -50 W m^{-2} and released at high latitudes at a rate of 35 W m^{-2}. Figure 3 shows the thermohaline circulation at t=18,000 years. In this hypothetical world ocean deep water is formed at high latitudes in both hemispheres at a rate of 57 Sv. The return flow upwells in mid and low latitudes and brings cooler water to the surface. The global meridional heat flux peaks at about 38° with 5.2 PW; a maximum of 2.4 PW is carried through the ocean at 25°.

Starting from this equilibrated climate a deglaciation experiment is performed. A steady fresh water flux anomaly equivalent to a runoff anomaly of 0.63 m yr^{-1} is located at 15°N for 1000 years and then moved to 52°N for another 1000 years. This mimics the disappearance of 30×10^6 km^3 continental ice sheets within 2000 years and the northward shift of meltwater runoff. While this volume is realistic, the retreat, however, occurred in stages lasting about 7000 years [Denton and Hughes, 1981]. The chosen short period of meltwater release compensates somewhat for the fact that, in reality, the flux anomaly influences the much narrower basin of the Atlantic. In a recent study [Stocker and Wright, 1991] we investigated the effect of realistic runoff anomalies on the deep circulation of the Atlantic–Pacific basin system presented in the preceding section.

Figure 4 exhibits the thermohaline circulation of the world ocean at t=20,000 years, just before the end of the

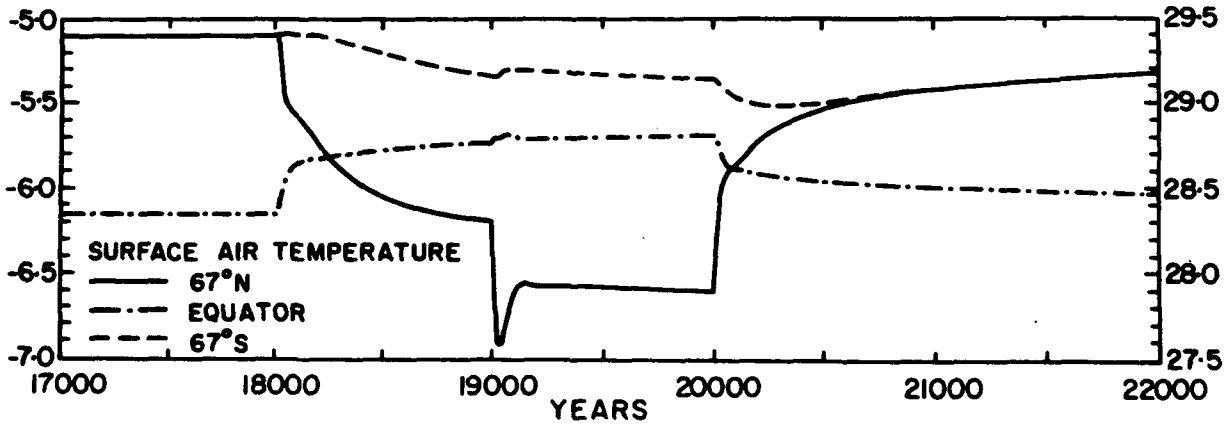


Figure 5. Time series of surface air temperature at 67°N (solid), 0° (dash-dotted) and 67°S (dashed). The constant anomaly is turned on at 15°N and t=18,000 years. At 19,000 years it is moved north to 52°N and operates until t=20,000 years, when it is switched off.

deglaciation. The deep circulation in both hemispheres has shallowed and the total overturning dropped to 43 Sv and 36 Sv in the southern and northern hemispheres, respectively. As the equatorial upwelling is reduced and the water comes from shallower depths, the heat loss of the equatorial atmosphere to the ocean is reduced. In turn, the downwelling northern waters release less heat to the atmosphere. The global meridional heat transport is reduced in the northern hemisphere by about 0.3 PW with climatic effects primarily in the northern high latitudes (see below). After the fresh water anomaly is turned off (at t=20,000 years) the climate slowly approaches the original state.

We now examine the air temperature history (Figure 5) that would be recorded by an observer at 67°N (solid), at the equator (dash-dotted) and at 67°S (dashed) during this deglaciation event. Only moderate variations of 0.47°C at the equator and -0.25°C at 67°S are registered. The shift of the runoff at t=19,000 years is hardly evident at all. A different situation, however, occurs at 67°N where the maximum temperature change is -1.8°C after an immediate onset of the cooling. At the time the source is moved to 52°N a cold spell occurs lasting for only 130 years. At the termination (t=20,000 years) an instant warming followed by an exponential approach to the original temperature is recorded. Five hundred years after the termination of the flux anomaly surface air temperatures have come close to their original values. The adjustment in the ocean, however, will last for several thousands of years until eventually the structure of Figure 3 is reassumed.

A second experiment has been performed [Stocker et al., 1990] where a doubled anomaly was applied. Here, the thermohaline circulation in the northern hemisphere breaks down and reverses. The low latitudes and the southern hemisphere now experience a warming, whereas the air temperature at 67°N drops by as much as 7°C.

CONCLUSIONS

The zonally averaged, coupled climate model of Stocker et al. [1991], that consists of a prognostic ocean part reproducing the thermohaline circulation and a diagnostic atmosphere part for the surface energy balance, has been applied to two problems. In the ocean-only mode we presented evidence to support the hypothesis of Gordon [1986], that Pacific upwelling and North Atlantic deep water formation form part of a global thermohaline circulation. Interocean water exchange is not a consequence of basin asymmetries but is caused by an excess of evaporation in the Atlantic and a corresponding excess of precipitation in the Pacific. It is this mechanism that maintains both the observed surface salinity contrast between the basins and the global circulation pattern.

A deglaciation experiment was performed with the coupled model by applying a steady fresh water flux at 15°N for 1000 years. This weakened the northern hemisphere overturning, and an atmospheric cooling of 1.2°C occurred in high northern latitudes. Upon moving the source north, further cooling was observed. In the southern hemisphere, on the other hand, changes do not exceed 0.5°C. The observed temperature changes in this simple model are significantly lower than the values inferred from the oxygen isotope records, provided the entire signal is interpreted as a proxy for temperature. This discrepancy may be due to several reasons.

First, the model presented here is only a crude approximation of reality: the anomaly would act on a narrower basin (about a fourth of the width) and over a longer period of time (about four times). The specific flux anomaly per unit area was therefore realistic. Second, the atmospheric feedback consists only of a thermodynamic part; the hydrological cycle and its variability are not included here. Third, it may well be that only a fraction of the oxygen isotope ratio signal can actually be attributed to a temperature change (R. G. Fairbanks, personal communication). The rest would be due directly to glacial meltwater with typically low values of $\delta^{18}O$. The model results presented here are certainly consistent with this observation. We hope that the ongoing investigation will provide further quantitative insight into the Younger Dryas climate event.

ACKNOWLEDGMENTS

TFS was supported by grant 82.613.0.88 of the Swiss National Science Foundation. DGW was visiting the Centre for Climate and Global Change Research during 1989–1990. LAM acknowledges research grants from the Canadian Natural Sciences and Engineering Research Council and Atmospheric Environment Service.

REFERENCES

Baumgartner, A., and E. Reichel, *The World Water Balance*, 179 pp., Elsevier, 1975.

Broecker, W. S., D. M. Peteet, and D. Rind, Does the ocean-atmosphere system have more than one stable mode of operation? *Nature*, *315*, 21-26, 1985.

Bryan, F., High-latitude salinity effects and inter-hemispheric thermohaline circulations, *Nature*, *323*, 301-304, 1986.

Bryan, F., Parameter sensitivity of primitive equation ocean general circulation models, *J. Phys. Oceanogr.*, *17*, 970-985, 1987.

Denton, G. H., and T. J. Hughes, *The Last Great Ice Sheets*, 484 pp., Wiley, 1981.

Gordon, A. L., Interocean exchange of thermocline water, *J. Geophys. Res.*, *91*, 5037-5046, 1986.

Marotzke, J., P. Welander, and J. Willebrand, Instability and multiple equilibria in a meridional-plane model of the thermohaline circulation, *Tellus*, *40A*, 162-172, 1988.

Manabe, S., and R. J. Stouffer, Two stable equilibria of a coupled ocean–atmosphere model, *J. Climate*, *1*, 841-866, 1988.

Sellers, W. D., A global climatic model based on the energy balance of the earth–atmosphere system, *J. Appl. Meteorol.*, *8*, 392-400, 1969.

Stocker, T. F., D. G. Wright, and L. A. Mysak, Experiments with a zonally-averaged atmosphere–ocean model: Structure and variability of the global thermohaline circulation and its influence on surface air temperatures, *Centre for Climate and Global Change Research Report, 90-4*, McGill University, 1990.

Stocker, T. F., and D. G. Wright, A zonally averaged ocean model for the thermohaline circulation. Part II: Inter-ocean circulation in the Pacific–Atlantic basin system, *J. Phys. Oceanogr.*, 1991, In press.

Wright, D. G., and T. F. Stocker, A zonally averaged ocean model for the thermohaline circulation. Part I: Model development and flow dynamics, *J. Phys. Oceanogr.*, 1991, In press.

AD-P007 302

Tidal Water and Ice Dynamics in the Arctic Ocean

A. Yu. Proshutinsky
Arctic and Antarctic Research Institute, Leningrad, U.S.S.R.

92-17984

ABSTRACT

To model the tides of the Arctic Ocean, one uses a two-dimensional non-linear model for water, which takes into account the effects of astronomical factors, the Atlantic and the Pacific Oceans, the earth's tides, the effects of loading and self-gravitations, and a non-linear model of ice drift, which allows internal stresses in the ice cover. At the interface of two media, the friction, proportional to the second power of the difference between the water and ice velocities, is prescribed.

The calculations of the propagation of diurnal (K1, 01) and semi-diurnal (M2, S2) waves of the tidal potential are given. The accuracy of the modeling was estimated at 94 points at the coast. Mean square root errors in calculating the amplitude were 0.054, 0.023, 0.013 and 0.014 m, and 26°, 15°, 28° and 30° for the phase of the M2, S2, K1, O1 waves, respectively. It is shown that semi-diurnal oscillations are generated by waves penetrating from the Atlantic Ocean and by the local resonance in some areas. The diurnal oscillations are generated by tide-forming forces in the ocean itself and they attenuate under conditions of anti-resonance.

Due to friction in the ocean, about 262 x 10^{16} erg s^{-1} of energy is dissipated. The maximum amount of energy is spent in the North Sea (16%), the White Sea (14%), Baffin Bay (13%), the Barents Sea (11%), and the Arctic Seas (7%).

The drifting ice does not have a strong influence on the transformation of tidal waves. Stationary ice leads to a decrease of the oscillation amplitude and delays the phases. The residual tidal currents and the ice drift can form zones of constant compression and divergence of the ice cover in the areas of maximum tidal dynamics.

The periodic ice convergence and divergence may result in the formation of young ice and subsequent ridging and thus serve as a mechanism for the ice mass generation in the ocean. According to preliminary estimates about 4 x 10^{11} m^3 of ice grows annually and forms pressure ridges due to this mechanism.

In the Arctic Ocean semidiurnal tides with tidal ages of 2 to 3 days prevail. Tidal amplitude ranges from 10 meters or more in the Mezen Bay in the White Sea to a few centimeters in the East Siberian Sea [Dvorkin, 1970; Atlas of Oceans, 1980]. Litke [1844] was the first to explore the nature of semidiurnal variations in the sea level of the Arctic Ocean. He considered tides to be caused by a wave of Atlantic origin. Empirical maps of the Arctic Ocean tides have been produced by many researchers [Harris, 1911; Fjeldstad, 1918/25; AUSNOO, 1958]. Litke's idea about the semidiurnal variations in sea level has been justified not only in these studies but also in the analytical investigations using a classical approach to studying tides [Goldsbrough, 1913; Lineykin; Sretensky, 1937].

The first numerical hydrodynamical model presenting the Arctic and Atlantic Oceans in the shape of a channel was developed by Defant [1924]. In the course of numerical experiments he established that the semidiurnal tide in the Arctic Ocean is caused by Atlantic tides, and that the diurnal tides are formed directly in the Arctic Ocean itself by astronomical forces. Further studies of polar ocean tides have advanced mainly by using improved numerical models

describing its various regions [Tiron, 1937; Nekrasov, 1962; Kagan, 1968; Dvorkin et al., 1972; Godin, 1980].

Including the Arctic Ocean in the models of global oceanic tides [Tiron, 1966; Hendershott, 1977; Schwiderski, 1980] positively influenced the quality of calculations in the Atlantic Ocean, although the modeling accuracy did not increase in the polar regions. The local Arctic Ocean models approximating its surface area by grids with spatial steps of 75 to 37 km [Kowalik and Untersteiner, 1978; Kowalik, 1981; Proshutinsky and Dvorkin, 1987; Polyakov and Proshutinsky, 1988; Gjevik and Straume, 1989] showed a higher calculation accuracy. However, each of the local models had certain restrictions. For example, in Gjevik and Straume [1989], no account was taken of ice cover; and in Kowalik [1981] ice cover was considered but tide-forming astronomical forces were not, the dynamics of the M2 wave only was treated, and so on.

In this paper, we use the shallow water theory and we take into account all the known models to estimate the dynamics of tidal movements of water and ice for four harmonics of tidal potential (M2, S2, K1, O1).

The model includes both water and ice motions:

$$\frac{d\vec{u}}{dt} + f\vec{u} = -gm\nabla(\alpha\zeta - \beta\zeta^{+}) + Am^2\nabla^2\vec{u} - \frac{1}{\rho_w H}(\vec{\tau}_B + \vec{\tau}_i S), \quad (1)$$

$$\frac{\partial\zeta}{\partial t} = -m^2 div\left(\frac{\vec{u}}{m}H\right), \quad (2)$$

$$\frac{d\vec{u}_i}{dt} + f\vec{u}_i = -gm\nabla\zeta + \frac{\vec{\tau}_i}{\rho} + F_i \quad (3)$$

$$\frac{\partial S}{\partial t} = -m^2 div\left(\frac{\vec{u}_i}{m}S\right), \quad (4)$$

$$\vec{u} = (u,v);\ \vec{u}_i = (u_i, v_i),\ \frac{\partial}{\partial t} + m\frac{\partial}{\partial x} + m\frac{\partial}{\partial y} = \frac{d}{dt}$$

where $\vec{u}$ and $\vec{u}_i$ are the vectors of mean vertical flow speed and ice drift; t is the time; $H=h+\zeta$; ζ is the displacement of sea level from the undisturbed state; h is the ocean depth; g is the acceleration due to gravity; f is the Coriolis parameter; ζ^{+} is the value of equilibrium tide; α is the factor considering load effects and self-attraction of oceanic tides (not taking into account the changes in tidal phases); $\beta = 0.69$ is the Love reduction factor allowing for effects of the solid earth tide; m is the scale coefficient to correct distortions in a stereographic projection; $\vec{\tau}_B$ and $\vec{\tau}_i$ are the stresses at ocean bottom and ice boundary, respectively;

$$\vec{\tau}_B = K_B\rho_w\vec{u}|\vec{u}|;$$
$$\vec{\tau}_i = K_i\rho_w|\vec{u} - \vec{u}_i|(\vec{u} - \vec{u}_i)$$

K_B and K_i are the friction coefficients at ocean bottom and ice boundary, respectively;

$$\vec{F}_i = \eta m^2\nabla^2\vec{u} + \gamma m^2\nabla div\vec{u} - m\nabla P,$$

$$P = -Kpmdiv\vec{u}_i \text{ if } div\vec{u}_i < o,$$

$$P = 0 \text{ if } \vec{u}_i \geq 0$$

η and γ are the coefficients of the bulk and shear viscosity in the ice cover; P is the pressure due to ice stress; A is the horizontal turbulence water friction coefficient;

$$\rho = \rho_i h_i S,\ A = 10^2\,H\ m^2/s,$$

$$K_B = 2.6 \times 10^{-3},\ K_i = 5.5 \times 10^{-3}$$

$$\eta = \gamma = 10^4\ m^2/s,\ K_p = 10\eta$$

ρ_i and h_i are the density and thickness of ice, respectively. The following sticking condition is accepted on the coastline G_1

$$\vec{u}|_{G_1} = 0;\ \vec{u}_i|_{G_1} = 0 \quad (5)$$

At open boundary G_2 the mean speed vector is considered to be a known function of coordinates and time

$$\vec{u}|_{G_2} = \vec{u}(x,y,t) \quad (6)$$

The average transport through this boundary is

$$\Phi dt \int_{G_2} u_n dG = 0$$

$$u_n = u\sin\alpha_1 + v\cos\alpha_1$$

α_1 - is an angle between n and x-axis,

where n is a normal to open boundary G_2.

For ice cover the condition of free flow is assumed at the open boundary

$$\frac{\partial\vec{u}_i}{\partial n}|_{G_2} = 0 \quad (7)$$

The state of rest is used for initial conditions for water and ice and the ice concentration is considered to be given. To solve Equations 1–4 with initial and boundary (Equations 5–7) conditions, a semi-implicit finite-difference scheme with central Lax–Wendroff differences has been used. The water surface of the Arctic Ocean on the stereographic projection map was approximated by a square grid with 55.6-km grid spacing.

It is necessary to mention that the model described by Equations 1–7 differs from the model in Gjevik and Straume [1989] by taking into account ice cover, and from the models in Kowalik [1978] and Kowalik and Untersteiner [1978] by considering tide-generating forces, load effects, and self-attraction of oceanic tides and earth's tides. In addition,

unlike the above models, the present model treats the entire water surface of the Arctic Ocean, including Baffin Bay and the straits of the Canadian Arctic Archipelago. At the open boundary of the model region the mean current velocities obtained earlier for all waves by the Arctic Ocean model [Proshutinsky and Dvorkin, 1987; Polyakov and Proshutinsky, 1988] have been prescribed. Calculating tidal movements continued until a regular regime was established wherein the full energy of the system remained unchangeable from cycle to cycle. The stationary fluctuation regime, i.e., the constancy of full system energy, was reached after 20 tidal cycles.

Modeling accuracy was estimated by comparison with 94 coastal stations. Root-mean-square errors of calculating the amplitudes of waves M2, S2, K1 and O1 were 0.054, 0.023, 0.013 and 0.014 m respectively; those of phases were 26, 30, 28 and 30 degrees respectively. The calculation results turned out to be the closest to observational data on the Scandinavian coast, the southeastern part of the Barents Sea, and on the islands of the North European basin. Less accurate are the calculations for water surface of the Arctic seas. On the one hand this could be attributed to the fact that harmonic constants of Arctic Ocean tides are unstable, having seasonal variations due to changing ice cover area on the sea surface [Dvorkin, 1970]. In this case "variability" of the harmonic constants is comparable to modeling errors for a number of stations on the Arctic coast. On the other hand, observational data also have certain errors since the harmonic analysis is mostly based on short-term observational series and the amplitude of tidal sea level variations, as a rule, is small compared to the value of storm surge sea level oscillations.

The tidal maps of semidiurnal waves M2 and S2 (Figure 1a,b) are similar in general. The phase difference of these waves amounts to 50°–80° and restricts the age of semidiurnal tides to 2–3 days. The phase differences of waves K1 and O1 is 15°–45°, which corresponds to the age of diurnal tides of 1–2 days. In connection with the fact that previous studies were devoted mainly to investigating the peculiarities of formation of the semidiurnal M2 wave, we shall compare the results of this study with those by other authors for this tidal harmonic.

The location of amphidromic systems in the North European basin agrees with the results obtained in Nekrasov [1962], Kagan [1968], Zahel [1975], the Atlas of Oceans [1980], Schwiderski [1980], and Gjevik and Straume [1989]. The calculation results in Baffin Bay are close to Godin's [1980] empirical maps. Unlike the previous studies, we succeeded in obtaining the amphidromic system in the Amundsen Gulf whose existence was predicted by Godin [1980].

The pattern of cotidal lines, and coordinates of amphidromic points in the Arctic seas corresponds on the whole to the results obtained in Tiron [1966], Schwiderski [1980], Kowalik [1981], and Gjevik and Straume [1989]; however, it would be a mistake to require that the results agree with different authors. The results of numerical experiments showed that the differences in approximating ocean depths, its coastline and conditions at the open boundary are responsible for the differences in tidal distributions rather than other factors in the model equations. The largest discrepancy between tidal maps of the M2 wave is observed by different authors in the Barents Sea. Goldsbrough [1913] showed that the periods of free oscillations are close to the periods of semidiurnal harmonics of tide-generating forces. The rate of resonance amplification of the tide can be determined as the amplitude ratio between the model and equilibrium tides. For the southeastern part of the Barents Sea this ratio at the frequency of the M2 wave is equal to 58, and for S2 to 45.4.

Calculating tide movements in the Arctic Ocean without taking into account the White Sea leads to considerable redistribution of tidal energy not only in the Barents Sea but in adjacent areas as well. For instance, in the Kara Sea semidiurnal tide amplitudes double in this case and the locations of amphidromic points change. All this testifies to the local resonance of semidiurnal sea level oscillations in the southeastern part of this sea. Therefore small differences in the approximation of depths or coastline between one model and another may lead to considerable differences in the cotidal charts obtained.

The local resonance on these frequencies is revealed also in other regions of the Arctic Ocean. Among them are the water surfaces of the Baidaratskaya Bay in the Kara Sea, the Khatanga Gulf in the Laptev Sea, the region north of the New Siberian Islands, Wrangel Island, and a number of straits of the Canadian Arctic Archipelago. The amplification factors of the diurnal tides in the Arctic Ocean are less than unity over the largest part of the water surface (Arctic seas, the central part of the Arctic Basin). Thus the antiresonance conditions are observed in the diurnal tidal band; therefore diurnal motions of water and ice in the Arctic Ocean are relatively weak.

To clarify the features of tide formation in the Arctic Ocean, consider the budget of tide energy. The balance equation of tide energy is easily obtained by multiplying Equation 1 by uH and Equation 2 by $g\zeta$. After adding these equations, and some transformations, we obtain in area Q

$$\frac{d}{dt}\iint_Q [H\frac{u^2+v^2}{2} + \frac{g\zeta^2}{2}]dQ = g\iint_Q \beta(uH\frac{\partial\zeta^+}{\partial x} + vH\frac{\partial\zeta^+}{\partial y})dQ +$$

$$g\int_{G_2} \zeta u_n H dG + A\int_{G_2} H\frac{\partial}{\partial n}\frac{u^2+v^2}{2}dG - \iint_Q R(u^2+v^2)dQ -$$

$$\iint_Q R_1(u_1+u_2)dQ - A\iint_Q H[(\frac{\partial u}{\partial x})^2 + (\frac{\partial u}{\partial y})^2 + (\frac{\partial v}{\partial x})^2 + (\frac{\partial v}{\partial y})^2]dQ +$$

$$A\iint_Q H[\frac{\partial^2}{\partial x^2}\frac{u^2+v^2}{2} + \frac{\partial^2}{\partial y^2}\frac{u^2+v^2}{2}]dQ; \qquad (8)$$

$$R = K_B H(u^2+v^2)^{0.5}; \; R_1 = K_i H(\Delta u^2+\Delta v^2)^{0.5};$$

$$\Delta u = u-u_i; \; \Delta v = v-v_i, \; u_1 = u\Delta u, \; u_2 = v\Delta v$$

In Equation 8, the term on the left-hand side characterizes the rate of changing the full energy of tide movements. The first, second and third terms on the right-hand side are responsible for the energy flux into the Arctic Ocean due to astronomical factors, wave energy transfer through the open boundary, and horizontal transfer of kinetic energy through the open boundary of the model, respectively. The last term

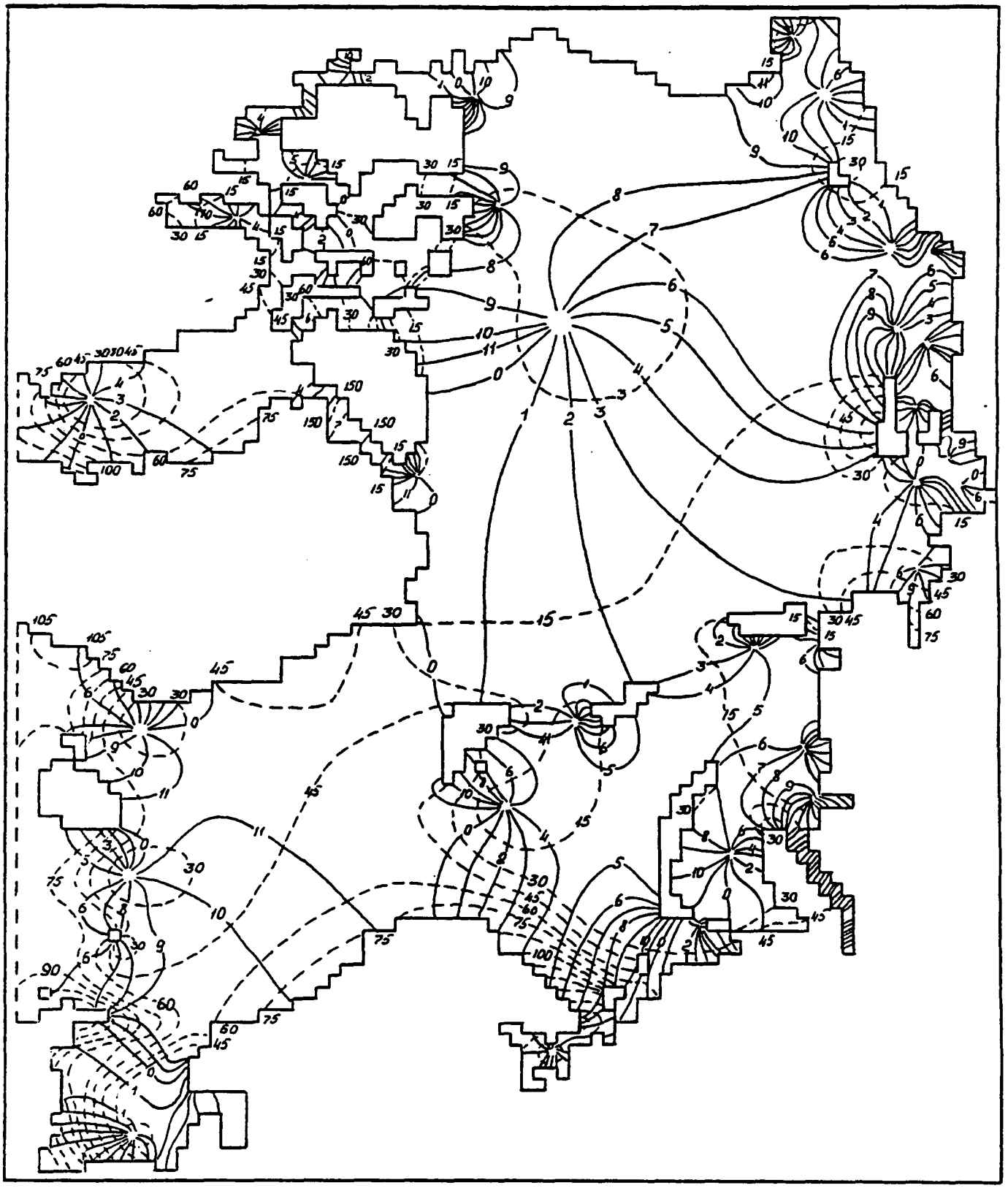


Figure 1a. Phase lags (continuous) and amplitudes (broken) of M2 tides. Zero phase corresponds to transit at the Greenwich Meridian. Phases are divided by 30 degrees (constituent hours); amplitudes in cm.

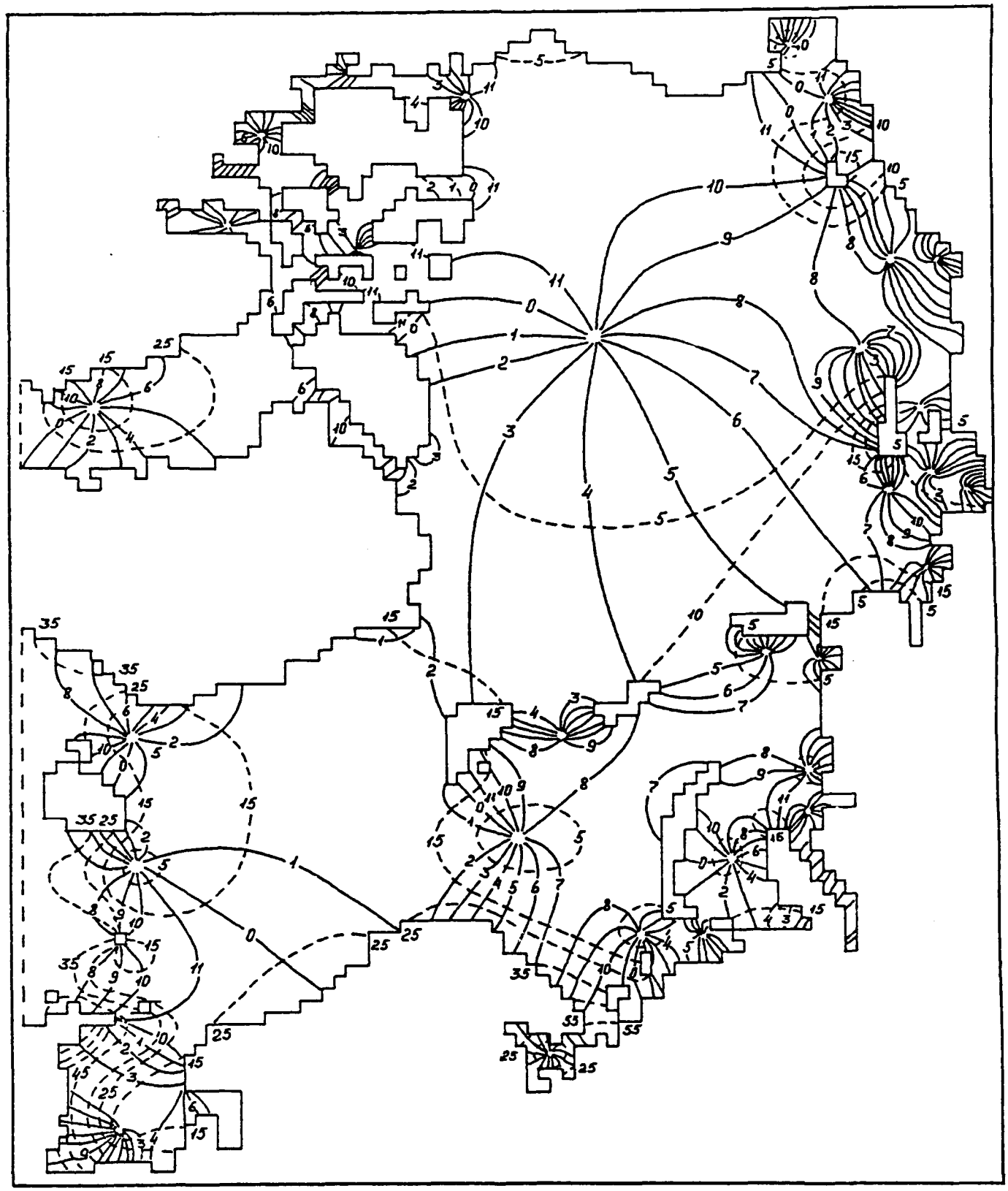


Figure 1b. Phase lags (continuous) and amplitudes (broken) of S2 tides. Zero phase corresponds to transit at the Greenwich Meridian. Phases are divided by 30 degrees (constituent hours); amplitudes in cm.

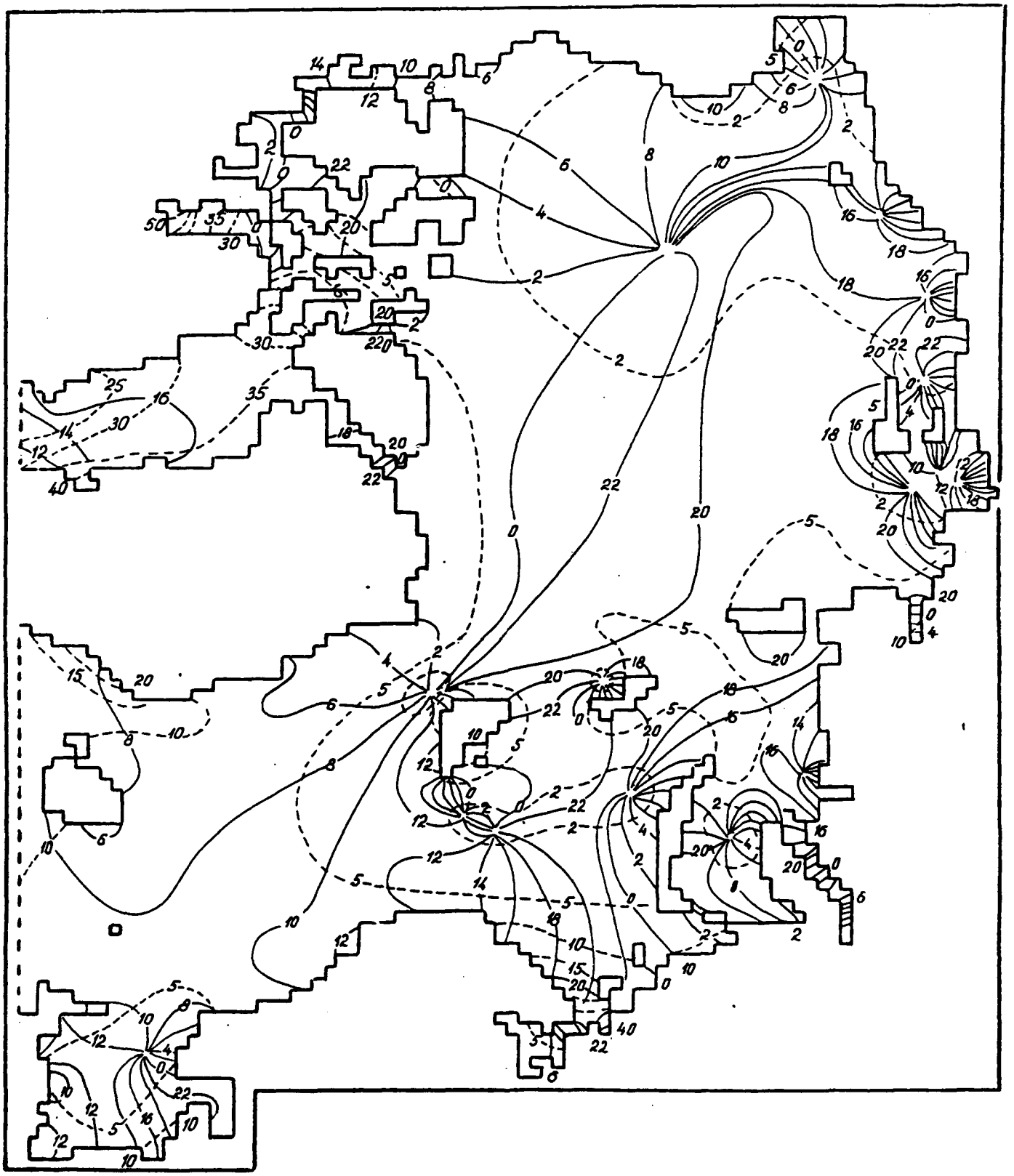


Figure 2a. Same as Figure 1 but for K1 tides. Phase lags are divided by 15 degrees (constituent hours).

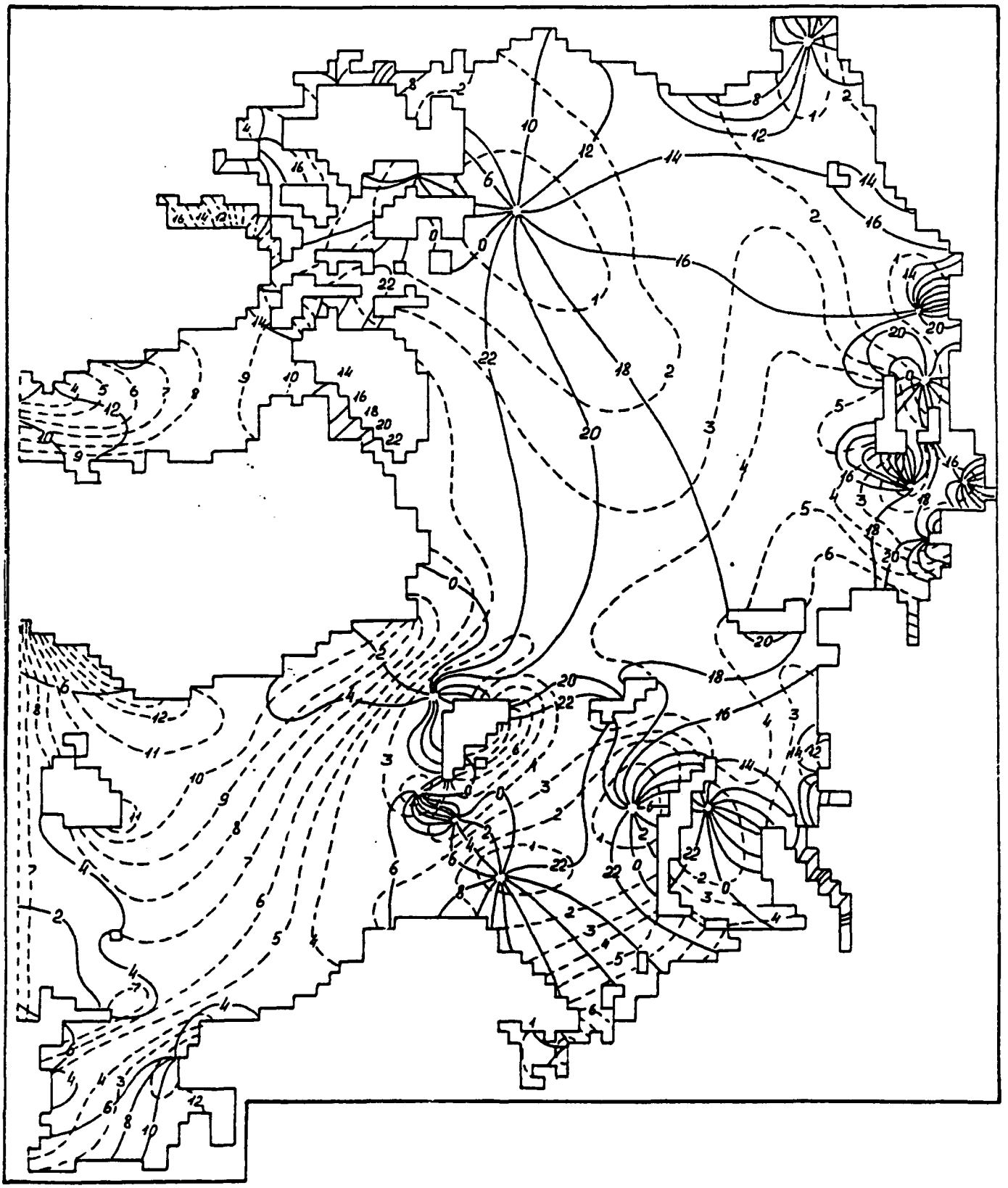


Figure 2b. Same as Figure 1 but for O1 tides. Phase lags are divided by 15 degrees (constituent hours).

of the tide energy balance equation is interpreted as kinetic energy losses due to horizontal inhomogeneity of the tidal flow field.

Analysis of the budget of the Arctic Ocean tide energy and the diagram of certain tide wave distributions (Figures 1 and 2) allows a number of conclusions to be made. In particular, semidiurnal tides are actually determined by the wave of Atlantic origin. Input of astronomical energy at semidiurnal frequencies is one and a half orders of magnitude less than energy income through the open boundary. Diurnal tides, in contrast, are caused almost entirely by the influence of astronomical forcing in the Arctic Ocean. Input of tidal energy through the open boundary is important only for K1.

In the Arctic Ocean about 280 x 10^{16} erg s^{-1} of tidal energy dissipates due to friction forces. In this case in the North Sea about 16% is dissipated, in the White Sea - 14%, Baffin Bay - 13%, the Barents Sea - 11%, and in the Arctic Seas about 7% of the tide energy coming into the Arctic Ocean. The relationship between energy losses for friction at the ocean bottom and ice boundary, and for horizontal turbulent exchange strongly changes from region to region. Drifting ice exerts no considerable influence on tidal waves. Tidal energy losses due to ice friction are an order of magnitude less than those for bottom and turbulent friction. In winter, when energy losses from ice friction grow due to increasing internal ice stresses and formation of the coastal fast ice cover, then tidal amplitudes, tidal current and ice drift velocities decrease, and phases of tidal waves lag compared to times when ice or freely drifting ice cover are absent.

Considerable ice movement due to tidal forces can be expected in the regions of intense tidal movements. In these areas there exists the so-called "residual" tidal ice cover drift caused by both residual tidal currents (due to spatial inhomogeneity of the Reynolds stresses because of non-linear advection in Equation 1), and proper ice drift connected with non-linear effects of internal forces in ice fields. Residual ice drift can lead to ice removal from Arctic Seas with rates of 2–3 cm s^{-1}, which coincides with the estimates made by Kowalik [1981]. In addition, residual tidal drift can result in the formation of regions with constant stresses and the appearance of channels in the ice cover which are preserved for a long time.

Periodic stresses and openings of the ice cover can serve as the mechanism of ice formation in the Arctic Ocean. Assuming that during ice opening in channels and polynyas a young ice cover is formed at an average rate of 3 cm day^{-1}, and during contraction of ice fields this ice is converted into ice ridges, then according to preliminary estimates only due to tidal ice movements caused by the M2 wave, the ice formation in the Arctic Ocean increases by 4 x 10^{11} m^3 yr^{-1}.

REFERENCES

Atlas of Oceans, The Arctic Ocean (in Russian), 202 pp., GUNIO MO USSR, 1980.

AUSNOO (Arctic U.S. Naval Oceanographic Office), *Oceanographic Atlas of the Polar Seas, Part 2*, 200 pp., Washington, DC, 1958.

Defant, A., Die Gezeiten des Atlantischen Ozeans und des Arktischen Meeres, *Ann. Hydr. Marit. Met., Jahrg., 52*, 8–9, 153–166, 177–184, 1924.

Dvorkin, E. N., Tides, in *Soviet Arctic* (in Russian), pp. 191–197, M. Nauka, 1970.

Dvorkin, E. N., B. A. Kagan, and G. P. Klescheva, Simulation of the tidal motions in the Arctic seas, *Izv. AN USSR, Physics of Atmosphere and Ocean, 8*, 298–306, 1972.

Fjeldstad, J. E., Contributions to the dynamics of free progressive tides waves, *Sci. Res. Norweg. North Polar Exped. "MAUD," 4*(3), 3–80, 1918–1925.

Gjevik, B., and T. Straume, Model simulations of the M2 and K1 tide in the Nordic Seas and the Arctic Ocean, *Tellus, 41A*, 73–96, 1989.

Godin, G., Cotidal charts for Canada, 91 pp., Manuscript Rep. Ser. 55, 1980.

Goldsbrough, G. R., The dynamical theory of tides in a Polar Basin, *Proc. London Math. Soc., 14*, 31–66, 1913.

Harris, R. A., *Arctic Tides*, 103 pp., U.S. Coast and Geodetic Servey, Washington, DC, 1911.

Hendershott, M. C., Numerical models of ocean tides, in *The Sea*, pp. 47–65, Wiley Interscience, New York, 1977.

Kagan, B. A., Hydrodynamical models of the tidal motions in the sea (in Russian), 219 pp., L. - Hydrometeoizdat, 1968.

Kowalik, Z., and N. Untersteiner, A study of the M2 tide in the Arctic ocean, *Deutsche Hydr. Zeitsch., 31*, 216–229, 1978.

Kowalik, Z., A study of the M2 tide in the ice-covered Arctic Ocean, *Modelling, Identification and Control, 2*, 201–223, 1981.

Lineykin, P. S., To the theory of tides in the basins and channels (in Russian), *Geophysics*, YII, 1, 5–47.

Litke, F., About the tides in the North Great Sea and Icing Sea - Notes of Hydrographical Department Marine Ministry (in Russian), Part 2, pp. 353–376, 1844.

Nekrasov, A. V., The calculation and building the tidal map of M2 waves in the Norwegian and Greenland seas by Hansen's method (in Russian), *Trans. Leningrad Hydromet. Inst., 16*, 49–57, 1962.

Polyakov, I. V., and A. Yu. Proshutinsky, The eigenoscillations of the Arctic Ocean sea level (in Russian), *Meteorologia and Hydrologia, 11*, 91–99, 1988.

Proshutinsky, A. Yu., and E. N. Dvorkin, Simulations of the tidal movements in the Arctic ocean (in Russian), *Theses of Papers of the 3rd Congress of Soviet Oceanologists*, Section of Physics, pp. 104–105, L. - Hydrometeoizdat, 1987.

Schwiderski, E. W., Ocean tides. Part II: A hydrodynamical interpolation model, *Marine Geodesy, 3*, 219–255, 1980.

Sretensky, L. N., About the motion of free tidal wave inside the Polar Basin (in Russian), *Izv. AN USSR, Ser. geograph. and geophys., 3*, 383–402, 1937.

Tiron, K. T., Tides in the Arctic Basin, *Second International Congress, Theses of Papers*, p. 373, M. Nauka, 1966.

Zahel, W., A global hydrodynamic numerical 1 - model of the ocean tides: The oscillation system of the M2-tide and its distribution of energy dissipation, *Ann. Geophys., 33*, 31–40, 1975.

AD-P007 303

Laboratory Studies of Exchange Between a Polar and a Subpolar Basin

Kenneth Hunkins
Lamont-Doherty Geological Observatory of Columbia University, Palisades, New York, U.S.A.

92-17985

ABSTRACT

Experiments on the exchange of a freshwater surface layer between two basins in a rotating tank demonstrate the contrasting roles of wind and buoyancy forces. Buoyancy-driven exchange occurs primarily in narrow boundary currents along the walls. Wind-driven exchange has a complex flow pattern with net transfer controlled by the sign of wind stress curl. Freshwater is transferred from the basin with positive curl to the one with negative curl. These results are related to freshwater flow from the Arctic Ocean to the Greenland Sea in which the southward flow of freshwater under buoyancy forces may be either increased or decreased by wind stress depending upon the sign of the curl. At present there is a negative stress curl over the Arctic Ocean which leads to a deep surface layer and no deep convection while opposite conditions in the Greenland Sea tend to remove the surface layer and allow deep convection.

INTRODUCTION

Regional climate is strongly influenced by the meridional circulation of atmosphere and ocean which transports heat from low to high latitudes. Although the transport is carried about equally by air and water, the ocean circulation is more localized with convective sinking occurring only in a few small areas. Thus the meridional circulation of the ocean may be more sensitive to interruption than that of the atmosphere. The Greenland Sea is one of the areas where surface waters are cooled in winter to sink through a nearly neutrally stable water column to great depths from which they flow equatorward. This descending leg of oceanic convective circulation can only exist when the stability of the water column is weak enough to allow surface waters of increased density in winter to penetrate downward. If a continuous surface layer of sufficiently low density were to be formed in the Greenland Sea the stability might be too great for penetrative convection to occur.

The Arctic Ocean is at a higher latitude and has more severe winter conditions than the Greenland Sea, but no deep convection takes place there due to the surface layer of low salinity, and hence low density, which effectively forms a lid preventing deep convection. This lens of low salinity water over the Arctic Ocean is fed principally by the runoff of rivers entering from Eurasia and has its greatest thickness at the center of the Beaufort Sea.

In contrast the Greenland Sea has a surface layer which is thickest around the edges, with thinning near the center where the deep homogeneous layer may be exposed to the atmosphere through a "window." Since formation of deep water in the Greenland Sea is considered to be an important factor in the present moderate climate which northern Europe enjoys, the effect of shutting down the penetrative convection in this ocean is of considerable interest. In numerical experiments with a global atmosphere–ocean circulation model it has been shown that a cessation of deep water formation in the Greenland Sea would lead to more severe winters and deterioration of climate in northern Europe [Rind et al., 1986]. It has been suggested on the basis of paleoclimatic evidence from marine and terrestrial records that abrupt reorganizations of the convective circulation of the coupled atmosphere and ocean in the past resulted in the Younger Dryas cooling of ~10–11 ky B.P., an event which cannot be related to orbital changes in solar insolation [Broecker and Denton, 1989].

In this paper we focus on only one aspect of the complex question of climate change due to the interactions of ocean and atmosphere in polar regions. The behavior of a low-

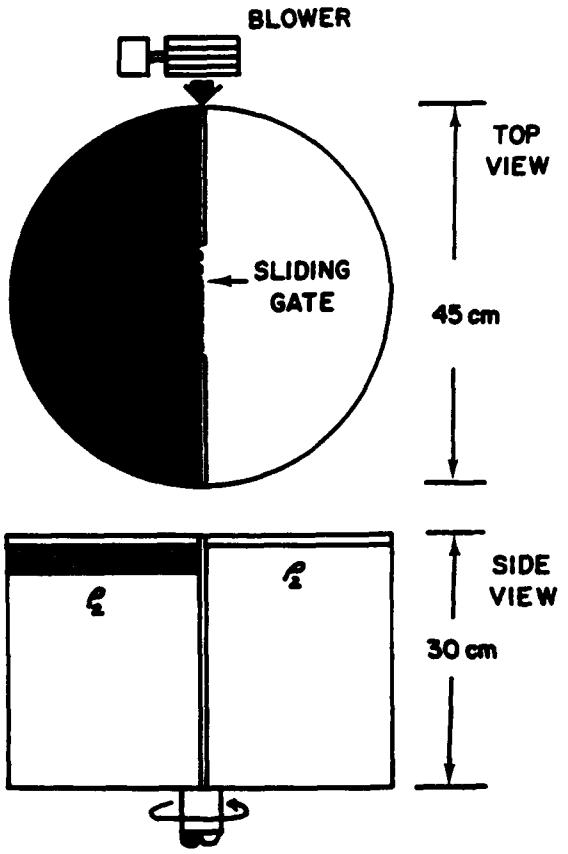


Figure 1. Sketch of rotating laboratory tank.

density surface layer is studied as it changes in thickness with time and location under the driving forces of gravity and wind. This problem was approached experimentally using a rotating tank divided by a wall with a gap as a highly idealized representation of a polar and a subpolar sea connected by a broad strait.

EXPERIMENTAL TECHNIQUE

A cylindrical lucite tank with an inside diameter of 45 cm and height of 30 cm was divided by radial walls into two basins (Figure 1). A gap at the center of the wall could be closed by a sliding gate. The tank was rotated on a turntable driven by a 3/4-h.p. electrical motor through a Graham variable-speed transmission and toothed rubber belt. Rotation for all experiments was at a rate of 0.25 revolutions per second and in a counterclockwise direction, simulating the northern hemisphere. A saline layer about 18 cm deep was first introduced into the tank and spun up to solid rotation. Since the sliding gate did not reach bottom, pressure was equalized between the two basins. Next a layer of freshwater which had been dyed blue was carefully floated on the surface of one of the basins, hereafter called the polar basin. The upper layer was 1 1/4 to 2 1/2 cm in thickness, much less than the thickness of the deep layer, so the experiments corresponded to reduced gravity dynamics on an f-plane. Winds were simulated in some of the runs with a small turbine fan which provided a well-defined jet of air about 10 cm in width. The air stream was directed with its axis along the radial walls so there was a wind shear of opposite sign in each basin. These were lock exchange experiments in which adjustment of the fresh layer was observed visually and photographically after initial removal of the sliding gate.

Run No.	H_1 (cm)	H_2 (cm)	ρ_1 (kg m^{-3})	ρ_2 (kg m^{-3})	R (cm)	Wind Dir.
3-90	18.0	2.5	998.2	1025.0	3.86	None
4-90	17.8	2.3	998.2	1025.0	3.70	Easterly
5-90	18.3	1.25	998.2	1025.0	2.73	Westerly

Table 1. Laboratory runs.

Buoyancy-Driven Exchange

In the first experiment, a layer of freshwater 2 1/2-cm thick was initially retained in the polar basin by the sliding gate (Table 1, Run 3-90). Upon removal of the gate the freshwater layer, marked by dye, flowed into the subpolar basin as a narrow boundary current along the right-hand wall (Figure 2). After following the radial wall to the rim the nose of the current turned to flow along the outer wall of the tank, still keeping the wall on its right-hand side. During these early stages of the experiment the width of the current was comparable to the baroclinic radius of deformation, 3.86 cm. In later stages the freshwater boundary current expanded in width, eventually covering the subpolar as well as the polar basin. A comparable experiment with similar results was performed by Wadhams et al. [1979] in a different wall geometry and considered by them to be a model for the East Greenland Current which gave evidence for the importance of buoyancy forcing in the dynamics of that current. Another feature of this run was the thinning of the freshwater layer along the wall which was anti-symmetric to that wall along which the "East Greenland Current" flowed. This thinning is evidence of inflow of deep water into the polar basin as a subsurface boundary current and may be considered an analog of the intrusion of the West Spitsbergen Current into the Arctic Ocean.

These observations are in qualitative agreement with theories for geostrophic adjustment after removal of a dam in a channel [Gill, 1976; Hermann et al., 1989]. In these theories adjustment is accomplished by Kelvin and Poincaré waves with inertial overshoots occurring in the case of large amplitudes. In the steady state this type of current can be analyzed, under conditions of geostrophic balance, to show that volume transport is given by

$$V = \frac{1}{2}\frac{g'H^2}{f}$$

where $g'=g(\rho_2-\rho_1)/\rho_2$ is reduced gravity, g is gravitational acceleration, ρ_1 and ρ_2 are upper and lower layer density, H

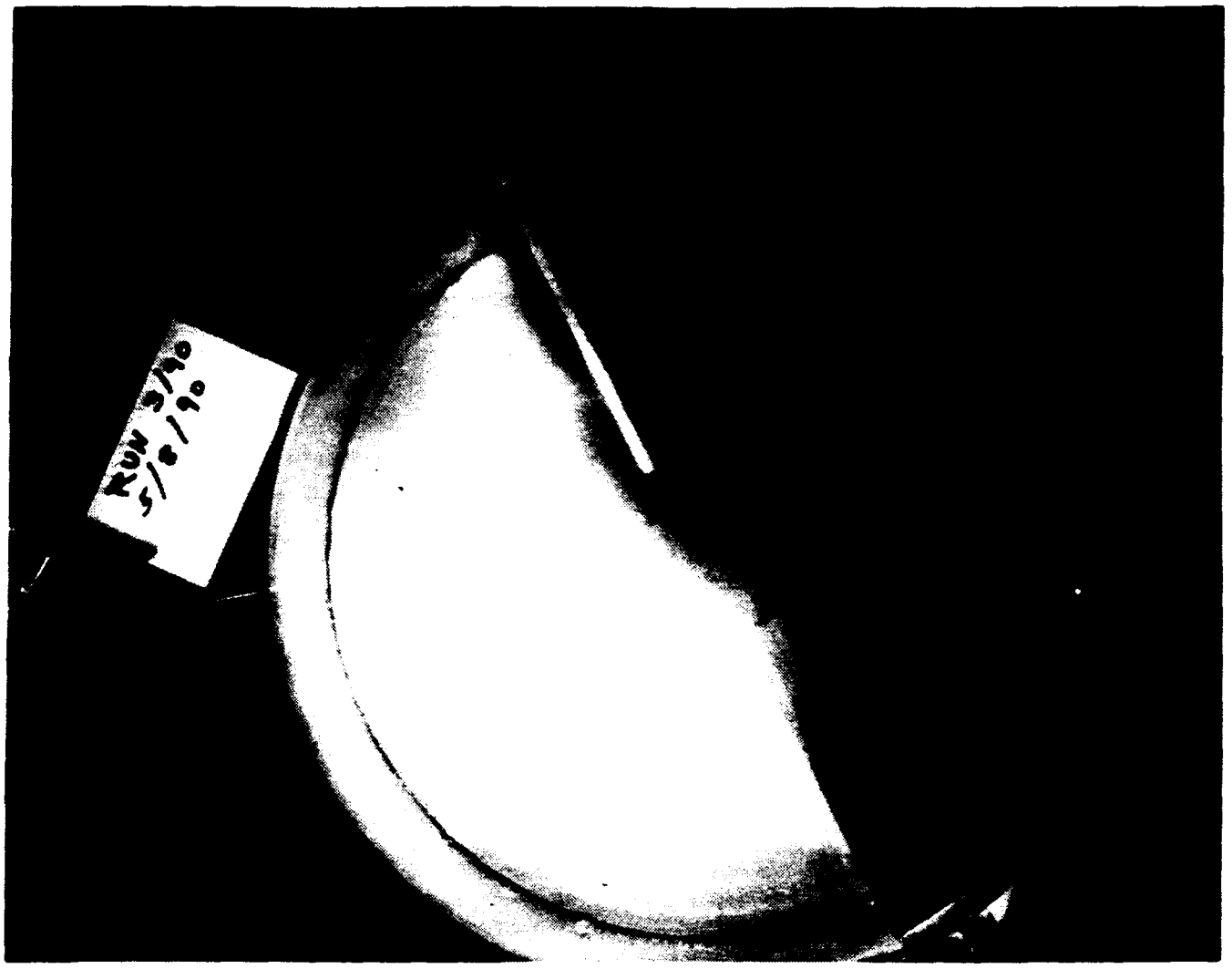


Figure 2. Run 3-90. Pure buoyancy-driven exchange. Freshwater layer intrudes into subpolar basin as a narrow boundary current along right-hand wall.

is upstream depth of the layer and f is the Coriolis parameter. This expression gives results which compare favorably with observational evidence when applied to the East Greenland Current [Manley and Hunkins, 1987].

In this pure buoyancy-driven run the freshwater layer was confined to a narrow boundary current in the subpolar basin and did not spread over the entire basin until late in the experiment when the buoyancy driving force was exhausted and friction became important. In a hypothetical frictionless experiment with a continuous source and sink of freshwater there would presumably be no spreading of freshwater into the interior of the subpolar basin.

Wind-Driven Exchange

Results were strikingly different when wind stress was added to buoyancy forcing. In the first wind-driven run (Figure 3, Run 4-90) the air stream was directed so that the polar basin was on the right-hand side when looking along the axis in the direction toward which the air was blowing. This simulates idealized Polar Easterlies which produce anticyclonic shear in the polar basin and cyclonic shear in the subpolar basin (Figure 4). The fan was turned on one minute before the gate was removed. A circular anticyclonic gyre developed quickly in the freshwater layer of the polar basin as evidenced by the dark-colored circle indicating greater thickness. Freshwater was trapped in this gyre and there was little exchange with the subpolar basin. Buoyancy forces tend to drive freshwater from the polar to the subpolar basin but in this run wind forcing opposes that tendency. The upper layer increased in depth at the center of the polar gyre and was $7\frac{1}{2}$-cm deep at a time 3 minutes after the gate was withdrawn. This was a threefold increase in layer depth.

In the final run (5-90) similar conditions were maintained except that the wind direction was reversed. This is not at all a realistic situation since we do not expect the atmospheric circulation system to reverse, even during glacial periods, but it does serve to explore the full range of wind effects. In

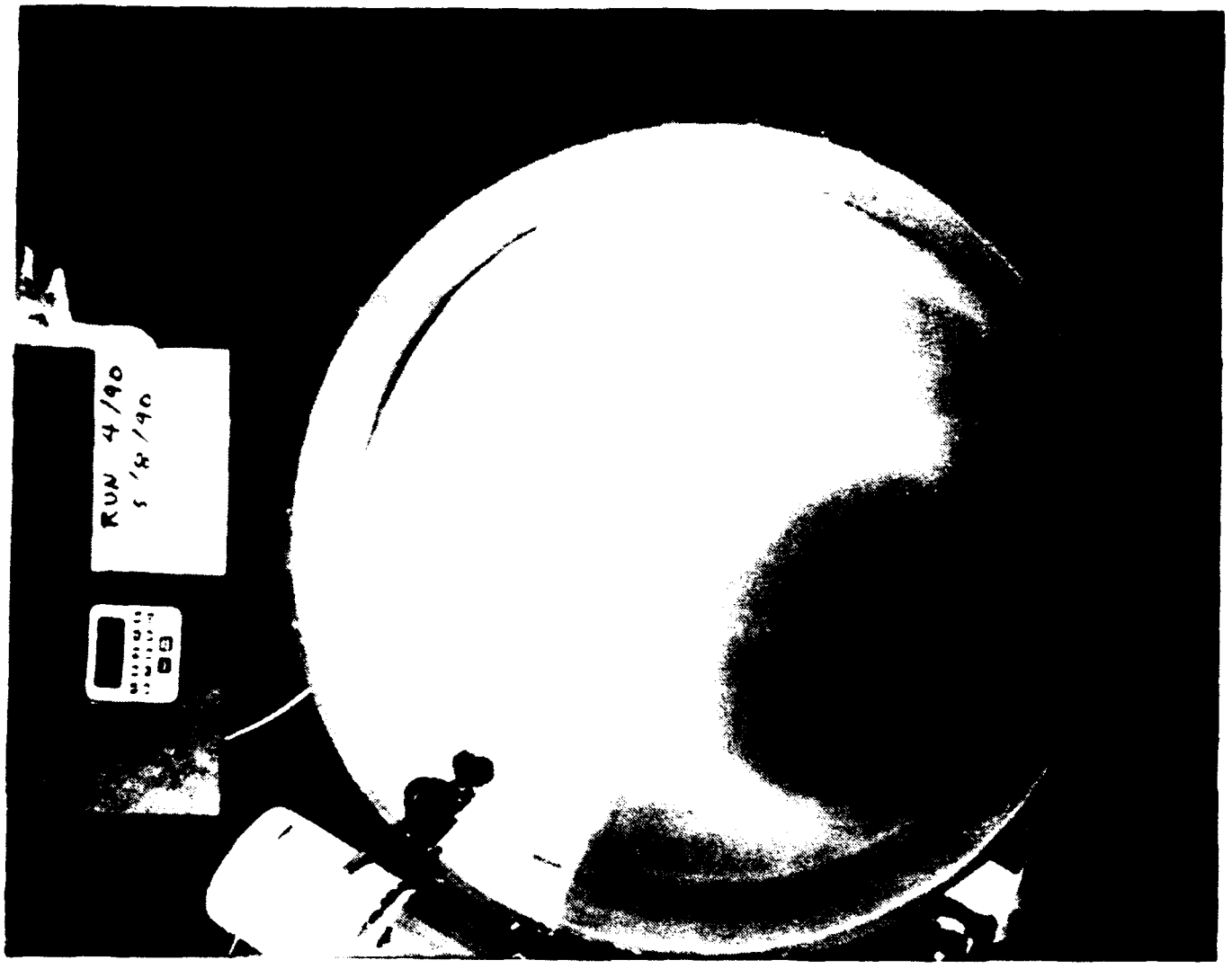


Figure 3. Run 4-90. Combined wind- and buoyancy-driven flow. Polar Easterlies. Anticyclonic wind shear over the polar basin creates an anticyclonic lens of freshwater. There is little intrusion into the subpolar basin.

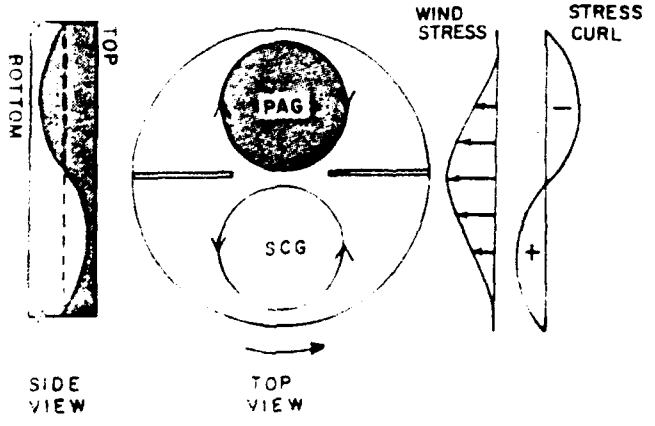


Figure 4. Sketch of results with simulated Polar Easterlies (Run 4-90). Freshwater layer thickens near center of polar basin and there is little exchange between basins.

this case a cyclonic wind stress was present over the polar basin and an anticyclonic stress over the subpolar basin. Now buoyancy and wind forcing both tend to transport freshwater from the polar to subpolar basin. Under this reversed wind stress a cyclonic gyre developed in the polar basin with a rapid thinning of the freshwater layer near the center of that basin. Freshwater flowed into the subpolar basin both as a right-hand boundary current driven by buoyancy as in the first run without wind and also as a tongue entering near the center of the gap which then moved anticyclonically around the subpolar basin. The freshwater layer was efficiently transported from the polar to the subpolar basin in this complex exchange. Four minutes after removal of the gate transfer of freshwater was virtually complete with a lens of freshwater now in the subpolar basin and only the clear deep layer in the polar basin (Figure 5).

Surface Layer Dynamics

From the horizontal equations for momentum and continuity, an equation may be derived which describes the

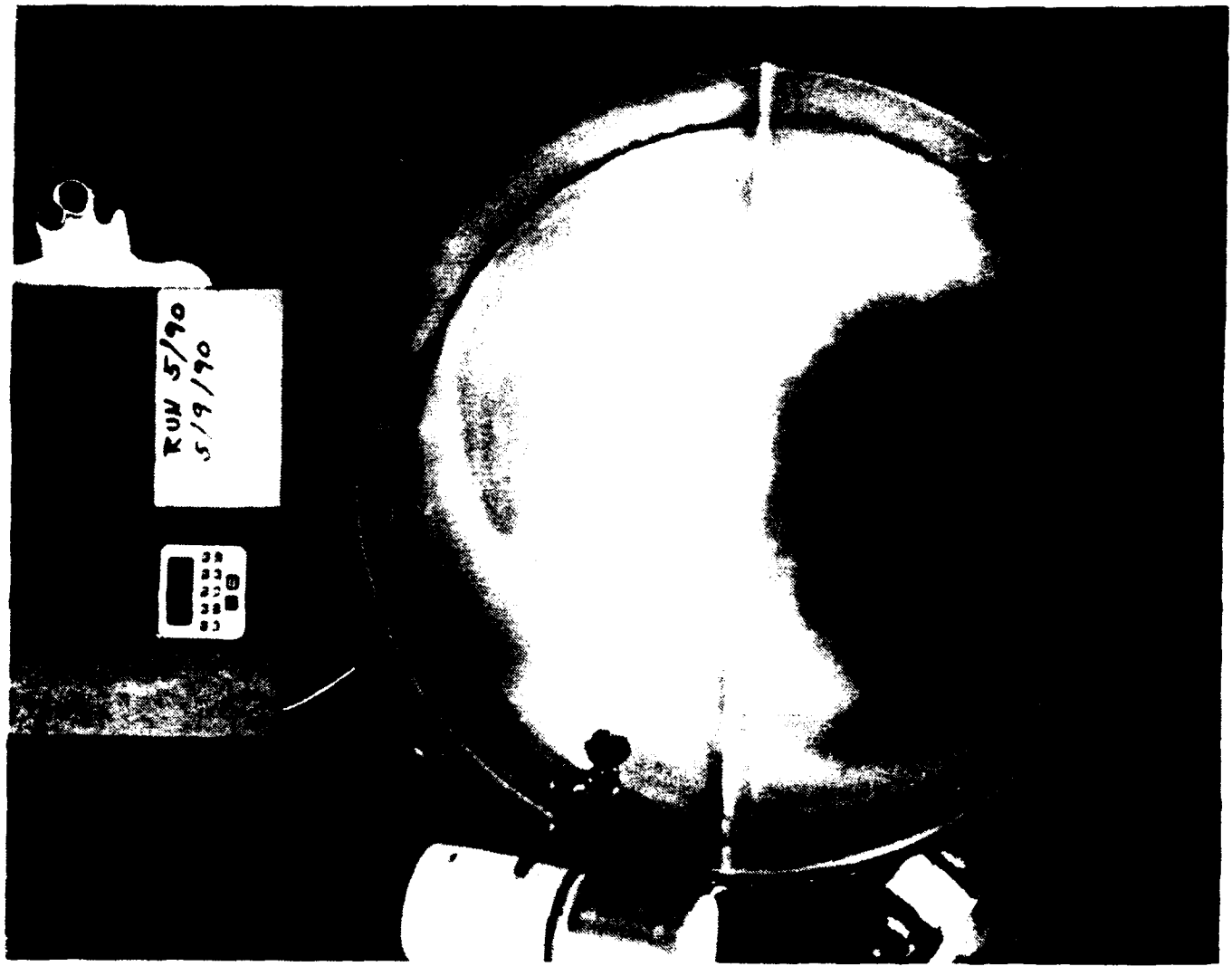


Figure 5. Run 5-90. Combined wind- and buoyancy-driven flow. Polar Westerlies. Cyclonic wind shear over the polar basin and anticyclonic shear over the subpolar basin. After four minutes the freshwater layer has been completely transferred to the subpolar basin where it forms an anticyclonic gyre.

changes in thickness of a homogeneous upper layer under the influence of gravity and wind stress. Scaling arguments may then be used to reduce this equation to a thickness-tendency equation which becomes equivalent to the Ekman pumping relation under certain limiting approximations.

Under the assumptions of nearly geostrophic motion and reduced gravity, the potential vorticity equation for a slab-like upper layer over an infinitely deep lower layer may be written in terms of layer thickness, h, as dependent variable,

$$[(g'/f)\frac{\partial}{\partial t} - (g'/f)^2(\frac{\partial h}{\partial y}\frac{\partial}{\partial x} - \frac{\partial h}{\partial x}\frac{\partial}{\partial y})][\frac{\partial}{\partial x}(h\frac{\partial h}{\partial x}) + \frac{\partial}{\partial y}(h\frac{\partial h}{\partial y})] - f\frac{\partial h}{\partial t} = \frac{1}{\rho_1}(\frac{\partial \tau_y}{\partial x} - \frac{\partial \tau_x}{\partial y}) \quad (1)$$

where τ_x and τ_y are components of surface wind stress and the other symbols have their usual meaning. If equation (1) is scaled in terms of a characteristic horizontal dimension L, a characteristic layer depth H_0, a time scale T and stress scale τ_0 the result is the dimensionless equation

$$[(R/L)^2\frac{\partial}{\partial t} - fT(R/L)^4(\frac{\partial h}{\partial y}\frac{\partial}{\partial x} - \frac{\partial h}{\partial x}\frac{\partial}{\partial y})][\frac{\partial}{\partial x}(h\frac{\partial h}{\partial x}) + \frac{\partial}{\partial y}(h\frac{\partial h}{\partial y})] - \frac{\partial h}{\partial t} = (\frac{\tau_0 T}{\rho_1 f L h_0})(\frac{\partial \tau_y}{\partial x} - \frac{\partial \tau_x}{\partial y}) \quad (2)$$

where the variables are now understood to be scaled. $R = \frac{1}{f}\sqrt{g'H_0}$ is the baroclinic radius of deformation. The ratio R/L is a Rossby number which for the model described here as well as for the Arctic Ocean is much less than one except near boundaries. Under these conditions the stretching term dominates the LHS of equations (1) and (2) and must balance the stress curl on the RHS. In the interiors of the basins dimensional equation (1) thus reduces to the Ekman pumping relation,

$$\partial h,\partial t) = \frac{1}{\rho_1 f}\text{curl}\,\tau \qquad (3)$$

Note that although the upper layer is considered to be much deeper than the Ekman layer, vertical pumping at the base of the Ekman layer serves to change the thickness of the entire upper layer. The mean rate of change in thickness using typical oceanic parameters is about 30 m yr^{-1}. Changes in layer thickness depend only on the curl of wind stress. This result corresponds qualitatively with the laboratory experiments in which a thickening anticyclonic lens develops in the region of negative stress curl and a thinning cyclonic layer develops in the positive curl region. A more complete mathematical description of the experiment, including details of the transfer of freshwater from one basin to another, would require a solution of equation (1) with all terms included, but this is outside the scope intended here. The approximation represented by equation (3) demonstrates the general importance of the curl of the wind field to the dynamics of the mixed layer.

DISCUSSION

Present mean atmospheric conditions over the Arctic Ocean are dominated by high pressure over the Beaufort Sea with associated anticylonic winds. This is a system with negative stress curl which produces a gyre in the surface layer effectively locking a reservoir of freshwater into the polar basin. This layer prevents deep water formation in the present Arctic Ocean. However, in the Greenland Sea mean winds possess a positive stress curl resulting in a thinning of the surface layer and intermittent exposure of deep water to the atmosphere, one of the essential conditions for deep convection. In these simple terms, the laboratory model rationalizes present conditions in these two oceans.

Assuming that a change to a warmer global climate would lead to less temperature contrast between polar and temperate latitudes, and in turn reduced intensity of atmospheric circulation, there would in that case be a reduced tendency to retain freshwater in the Arctic Ocean and an increase in the thickness of the mixed layer in the Greenland Sea. This effect needs careful consideration in attempts to model climatic changes associated with the global interaction between the atmosphere and the ocean.

ACKNOWLEDGMENTS

This research was supported by the Office of Naval Research under contract N00014-90-J-11.

REFERENCES

Broecker, W., and G. Denton, The role of ocean–atmosphere reorganizations in glacial cycles, *Geochim. Cosmochim. Acta*, *53*, 2465–2501, 1989.

Gill, A., Adjustment under gravity in a rotating channel, *J. Fluid Mech.*, *77*, 603–621, 1976.

Hermann, A., P. Rhines, and E. Johnson, On linear Rossby adjustment in a channel: beyond Kelvin waves, *J. Fluid Mech.*, *205*, 469–502, 1989.

Manley, T., and K. Hunkins, Current regimes across the East Greenland Polar Front at 78°40' North latitude during summer 1984, *J. Geophys. Res.*, *92*, 6741–6753, 1987.

Rind, D., D. Peteet, W. Broecker, A. McIntyre, and W. Ruddiman, The impact of cold North Atlantic sea surface temperatures on climate: Implications for the Younger Dryas cooling (11–10k), *Climate Dyn.*, *1*, 3–33, 1986.

AD-P007 304

Mathematical Modeling in Studies of Arctic Ocean Circulation

N. Yu. Doronin and A. Yu. Proshutinsky
Arctic and Antarctic Research Institute, Leningrad, U.S.S.R.

92-17986

ABSTRACT

A hierarchy of mathematical models adapted to certain physical phenomena of the Arctic Ocean has been developed. The density structure of the Arctic Ocean water is characterized by a well-marked stratification. This allows us to describe it by means of models with a discrete stratification. In this context a two-dimensional model of the upper 200 m of the ocean can be considered as the "lowest" level of a hierarchy of models. With the help of this model, coupled with the ice drift model, seasonal oscillations of sea level, and variability of barotropic water circulation in the annual cycle, affected by wind, atmospheric pressure and river runoff, were studied. The same model is used to successfully predict level oscillations and ice drift up to 6 days in advance.

The multi-layer models are suggested as models of the second level. For example, energy concentration in the upper layer of the ocean, the main property of baroclinicity, is well simulated in the two-layer version. The advantage of these models as compared with those of the first level, is that the depth of the interface is given as a solution. The diagnostic two-layer model is quite simple to use on small computers. The prognostic two-layer model allows one to estimate the time when the water circulation becomes stationary in the ocean of real depth.

The diagnostic three-dimensional ocean model with a continuous stratification is suggested as the third level model. The elliptical equation relative to denivelation of the free surface is the governing equation of the model. The estimation of the terms of the motion and continuity equations indicates the need to introduce geostrophic corrections for non-linear effects and a horizontal turbulent exchange when calculating vertical current velocity.

Tidal motions in the ocean are simulated by means of a joint non-linear model of water and ice motion, taking into account astronomical factors, the earth's tides, effects of loading and self-gravitation, and viscous-elastic interaction of the ice cover. On the basis of these models, the formation features of the diurnal O, K and semi-diurnal M and S harmonics of the tidal potential are studied and the irregularities of the ice cover during the tidal period are calculated.

The water dynamics of the Arctic Ocean are extensively modeled, but, as was noted at a meeting in Cambridge, investigations in this direction are behind field programs [AOMM, 1983]. All the works in modeling can be divided into three groups by regions: circulation models of the North European Basin; models of the Arctic Basin; and simulations of arctic marginal seas.

Large-scale dynamics of the North European Basin were calculated mainly as a part of the World Ocean circulation [Marchuk and Sarkisyan, 1988], but there are some numerical experiments for particular seasons based on the results of hydrographical surveys [Bub and Popov, 1989; Nikiforov et al., 1989].

The majority of the works are connected with the simula-

tion of Arctic Basin circulation. There are simplified models, which are directed to illustrate processes qualitatively [Felzenbaum, 1958; Gudkovich and Nikiforov, 1963; Campbell, 1969; Hart, 1975]; models to reconstruct velocity fields using observed T,S-fields [Ponomaryev and Gazova, 1981; Proshutinsky, 1988; Treshnikov and Baranov, 1978]; and the most advanced approximations, based on primitive equations [Hibler and Bryan, 1987; Semtner, 1987].

A separate group consists of the models developed for the marginal arctic seas [Kudryavtsev, 1970; Doronin, 1989].

Most of the studies, though, are still in the pilot study stage. Modeling as a tool of detailed regional analysis has not been particularly pursued. It is not possible yet to develop a general mathematical model of the Arctic Ocean water dynamics allowing for all the diversity of determining factors and the full scope of their effects. It is more reasonable, though, to develop a hierarchy of models, each describing a certain physical process or an area where the process is most pronounced.

We present an approach to the development of a series of related models describing the main features of the Arctic Ocean water dynamics and sea level changes. The Reynolds approximation is assumed as an equation describing fluid dynamics

$$\frac{d\vec{V}}{dt} + 2\vec{\omega} \times \vec{V} = -\frac{1}{\rho}\vec{\nabla}P + \vec{\nabla}\varphi + \vec{F} \qquad (1)$$

where φ is the potential of the conservative mass force, while F denotes non-conservative forces (friction), with other notation as commonly accepted.

The general circulation in the ocean is represented by a statistical ensemble of its large-scale motions. Slow currents occurring throughout the entire water column belong to its low frequency end. These motions have a spatial scale of 10^6–10^7 m and a temporal scale of 10^0–10^2 years. The same spatial scale is characteristic of the main quasi-stationary surface currents; these currents also have a high temporal variability. The currents together with long-period motions display distinct seasonal variations. For the motions of the indicated scales Equation (1) can be simplified by neglecting certain terms

$$2\vec{\omega} \times \vec{V} = -\frac{1}{\rho}\vec{\nabla}P + \vec{\nabla}\varphi + \vec{F}_1 \qquad (2)$$

where F_1 describes vertical shear eddy viscosity only. The class of the models describing the low-frequency spectrum of the ocean general circulation is based on Equation (2). The equations differ by the way they approximate a pressure gradient ∇P.

(1) If baroclinicity is neglected, we obtain a barotropic model of the steady-state ocean circulation. By means of eddy operations over the X and Y components of Equation (2) the problem is reduced to that of an elliptic equation relative to sea level deleveling

$$\nabla^2\zeta + 2\alpha J(H,\zeta) + \frac{2\alpha H}{f}\beta\frac{\partial\zeta}{\partial x} = \frac{2\alpha}{\rho g H}\mathrm{curl}\,\vec{\tau} + \frac{2\alpha\beta}{\rho g f}. \qquad (3)$$

where H is the ocean depth; J is the Jacobian; f is the Coriolis parameter; φ is latitude; ζ is a displacement of sea surface from its undisturbed position; g is the acceleration due to gravity; $a = f/2k$, k is the coefficient of vertical turbulent mixing and τ is wind stress at the surface.

This equation reflects a balance between the wind stress curl at the surface and eddy friction at the bottom. Obviously, such an approximation is highly idealized; it can be used only for the solution of a few problems related to climate.

Numerical experiments show that there can be year-to-year variations in positions of the centers of anticyclonic gyres in the Arctic Basin and cyclonic circulation in the North European Basin, as well as in the location of the Trans-Arctic Current. The Trans-Arctic Current weakens during that part of the year when the kinetic energy in the upper layer of the ocean is at its minimum; simultaneously a cyclonic gyre is formed in the Canadian Basin, and the center of the anticyclonic gyre is displaced towards the Siberian Shelf.

(2) The irregular vertical mass distribution is schematically accounted for in the models with discrete stratification. For instance, two-layer models directly account for the major baroclinic effect manifested in the kinetic energy concentration in the upper ocean. These models of the ocean circulation are based on equations which are united into systems by conditions of speed and stress continuity at the interface between the layers with different density. The models of this class have certain merits for the study of climatic or seasonal changes of major ocean structural zones. Figure 1 shows that sea level increases due to the wind caused by the Arctic High. Observational data confirm sagging of the interface between the surface and North Atlantic Water Masses also caused by the Arctic High winds. The North Atlantic upwelling along the continental slope in the marginal seas is caused by the sea level drop due to storm surges over the arctic sea shelf.

(3) The diagnostic model based on Equation (2) accounting for the continuity of the fluid stratification can be used for qualitative and quantitative analysis of the 3-D current field by the density distribution. The governing equation of the model is

$$\Pi = \frac{2\alpha}{\rho_0 g}\mathrm{curl}\,\vec{\tau} + \frac{2\alpha\beta}{\rho_0 g f}\vec{\tau}_x - \nabla^2 q^H - 2\alpha J(H,q^H) - \frac{2\alpha}{f}$$

$$q^H = \int_0^H \rho\,dz,\quad Q = \int_0^H dz\int\rho\,dz, \qquad (4)$$

where τ is the wind stress. If wind is neglected we can estimate the thermohaline water circulation. The estimates of the variability of thermohaline motions in the Arctic Ocean are obtained by means of sea level, which can be considered as an integral index. Figure 2 shows that the mean long-term location of the sea level surface does not change, i.e., there is a dome-shaped sea level increase in the eastern Arctic Ocean, while in the western Arctic Ocean there is a sagging of the surface. A year-to-year variability is expressed by the changes of the current speed and displacement of the circulation centers from their mean location.

The high-frequency region of the spectrum of large-scale motions is formed by synoptic processes with spatial scales of 10^4–10^5 m and temporal scales of 10^0–10^2 days; in this

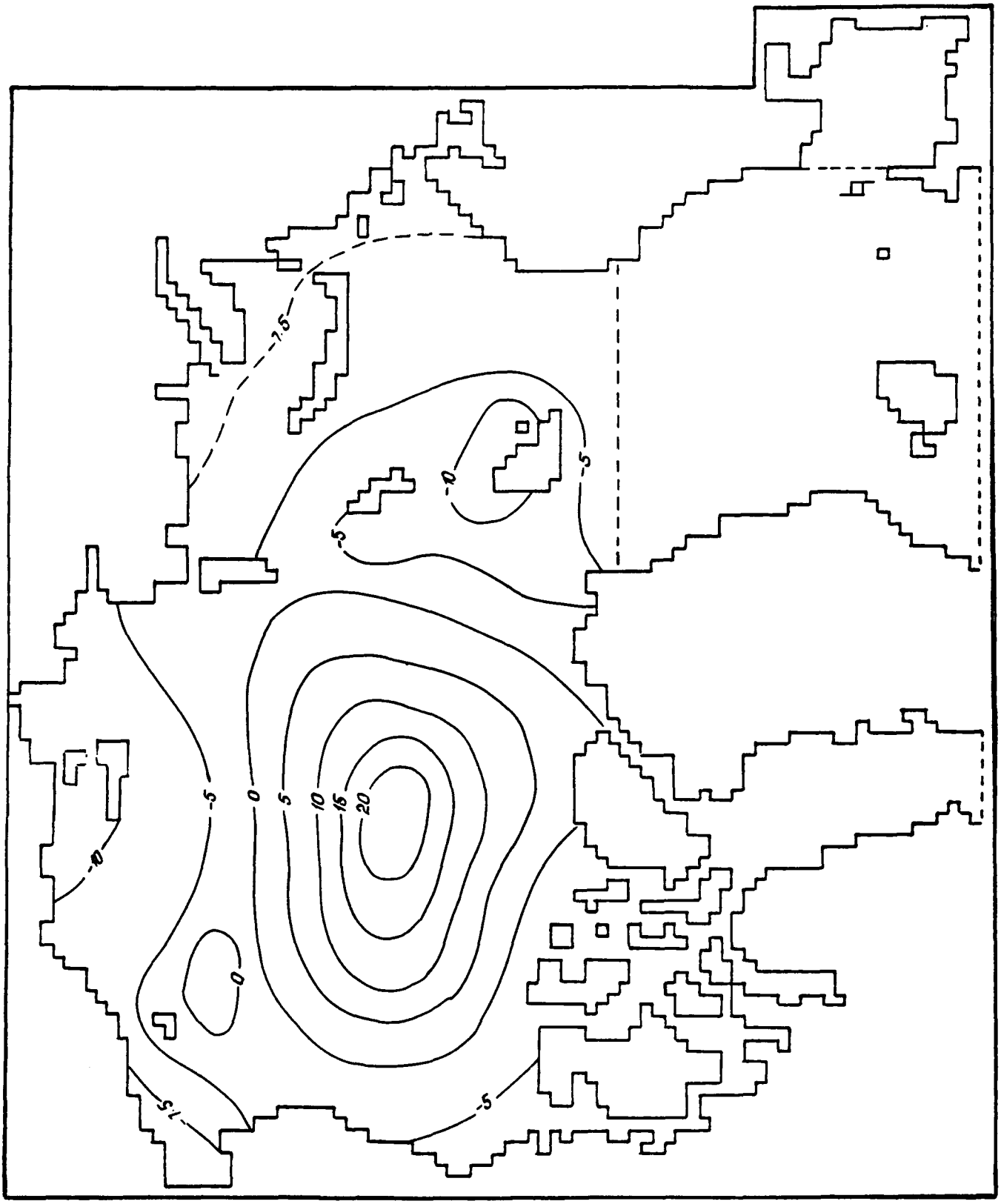


Figure 1(a). The topography of the Arctic Ocean free surface in centimeters for an average climatic February. Results of two-layered ocean model.

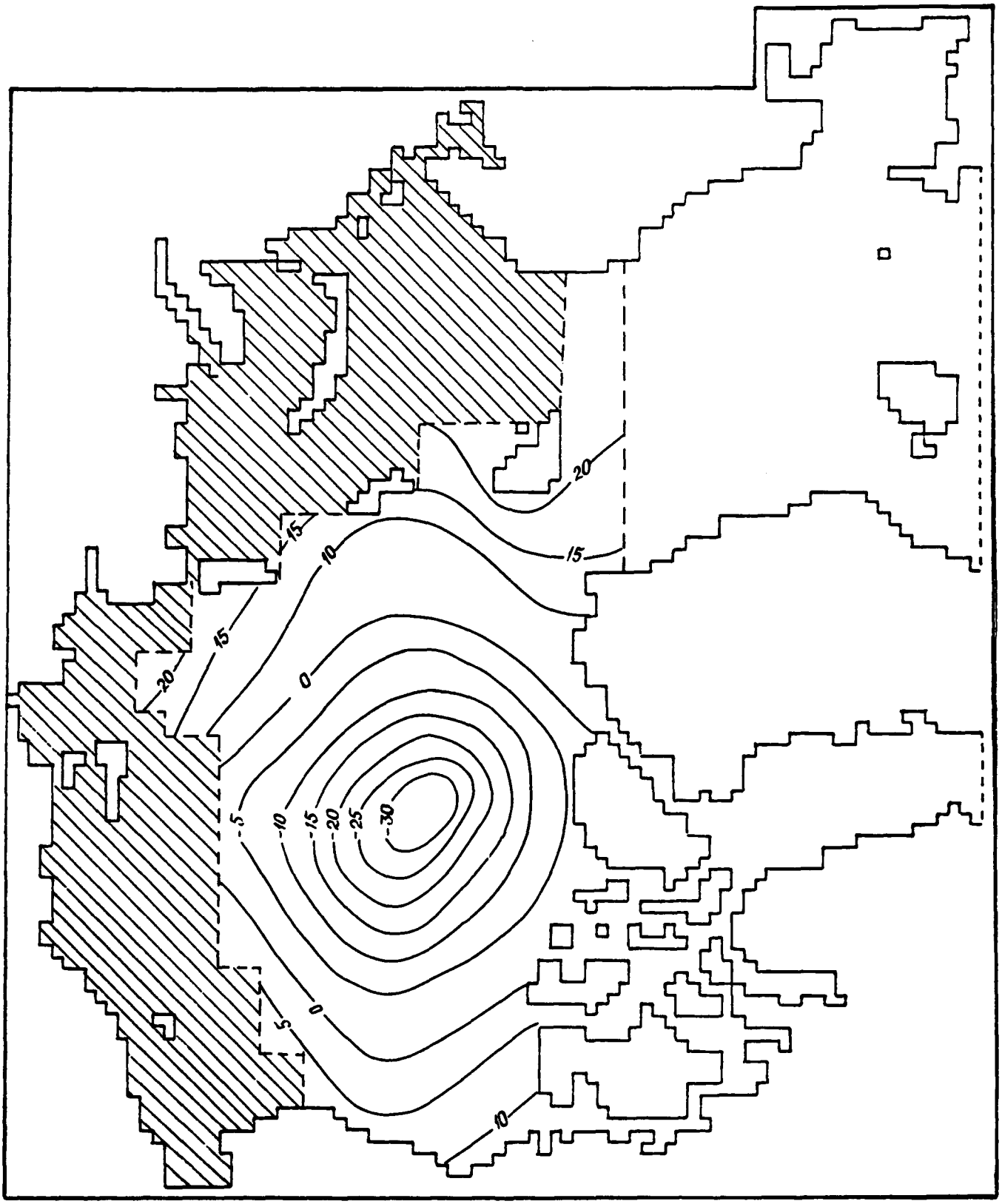


Figure 1(b). The topography of the interface between the Surface and North Atlantic waters in meters for an average climatic February. Results of two-layered ocean model.

case the non-stationary part of Equation (1) cannot be neglected. This is also true of shorter period tidal motions. Equation (1) can be simplified by parameterization of friction forces and by neglecting the density stratification or by its vertical averaging. Here we use a model built in the framework of the shallow-water theory. The following model is proposed to study the Arctic Ocean synoptic dynamics, tides and sea ice drift

$$\frac{d\vec{U}}{dt} + 2\vec{\omega} \times \vec{U} = -g\vec{\nabla}\zeta + A\nabla^2\vec{U} + \frac{1}{\rho}\vec{\nabla}P_a + \frac{1}{\rho(H+\zeta)}(\vec{\tau}^S + \vec{\tau}^B), \quad (5)$$

$$\frac{d\zeta}{dt} = -\mathrm{div}(H\vec{U}), \quad \vec{U} = \frac{1}{H+\zeta}\int_0^{H+\zeta}\vec{U}\,dz, \quad (6)$$

$$\frac{d\vec{U}_i}{dt} + 2\vec{\omega} \times \vec{U}_i = -g\vec{\nabla}\zeta + \frac{1}{\tilde{\rho}_i}(\vec{\tau}_i^{\,S} + \vec{\tau}_i^{\,H}) + \vec{F}, \quad (7)$$

$$\frac{\partial s}{\partial t} = -\mathrm{div}(S\vec{U}_i), \quad \tilde{\rho}_i = \rho_i H_i S, \quad (8)$$

where U_i is the sea ice drift speed; r_1 the sea ice density; τ^S, τ^B, τ_i^S, τ_i^H are the frictions at the interfaces, F is the interaction force between ice floes, H_i is the thickness of ice and S is the ice concentration.

The model (Equations 5–8) can also be used for the estimation of the time needed for barotropic motion generation in the real ocean, for the study of the seasonal variations of sea level and ice drifts, not taking into account melting and growth of sea ice. Numerical experiments have shown the spatial structure and sea level temporal changes to be determined by the strength and location of the Arctic High and Icelandic Low. In cold months (from November to April), when the Arctic High is well developed, the sea level increases in the center of the anticyclonic gyre, storm surges become stronger along the arctic sea coast, and runoff decreases. All of these result in an observed sea level drop at the stations on the Siberian coast.

In the warm months, when the Arctic High weakens, the anticyclonic circulation also grows weak, the sea level under the anticyclone drops, storm surges along the coast decrease, runoff is enhanced, and sea level increases along the Siberian coast. The estimation of the contributions of different elements has shown that the wind forcing is responsible for 50–80%. This forcing displays significant seasonal variations as well as a strong dependence on sea ice presence in the area.

It is interesting to note that the topography of the sea level field in the Arctic Ocean calculated only on the basis of air pressure and wind data for cold months would be similar to that formed by thermohaline factors. Let us discuss in this connection a possible mechanism for water circulation and sea level changes in the Arctic Ocean. The calculations show that winter ocean currents can be estimated using wind and pressure fields. In summer these factors are no longer important, and no barotropic circulation forms. The observations, however, indicate that the major pattern of water and sea ice motions in the Arctic Basin remain the same. We can therefore suggest that from April to November the atmosphere controls Arctic Ocean dynamics, and the observed currents would contribute to the readjustment of the density field. In the second half of the year the atmospheric effect

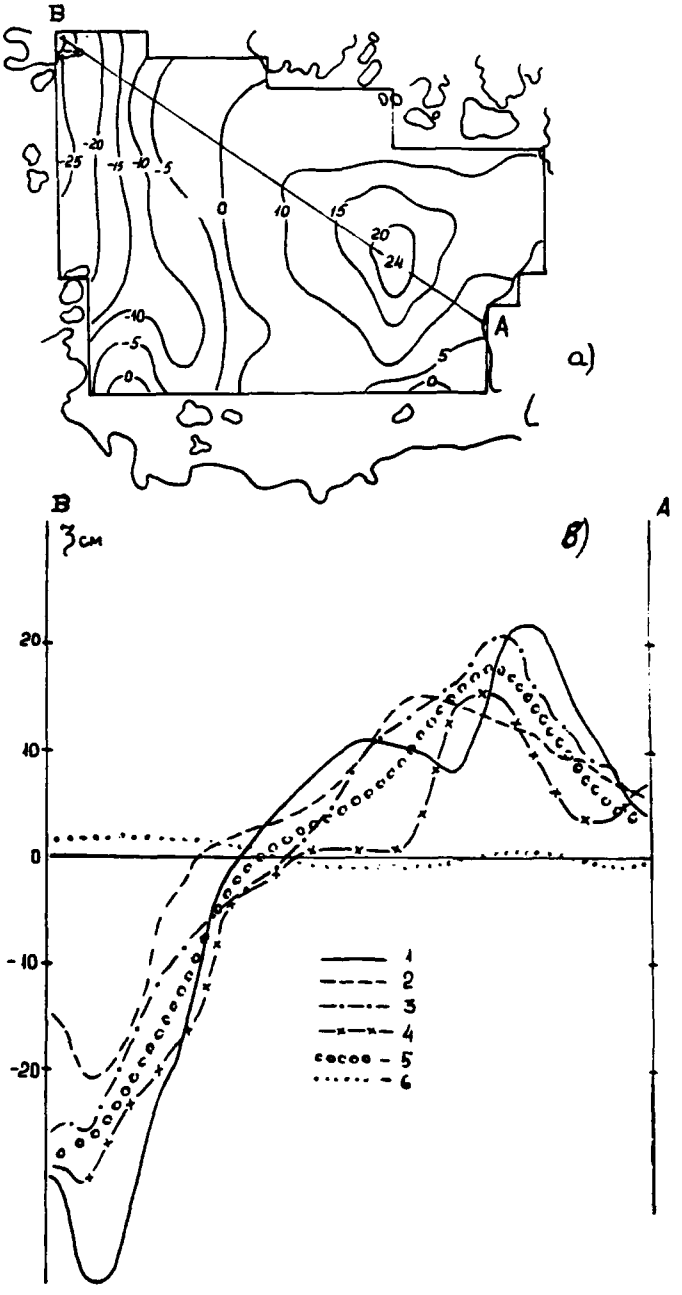


Figure 2. The free surface topography in the Arctic Ocean: (a) in the plane, as a result of thermohaline ocean circulation calculations by mean long-term data; (b) along line AB from Alaska (A) to Spitsbergen (B) as a result of the thermohaline ocean circulation calculations for 1973 (1), 1974 (2), 1975 (3), 1976 (4) years, by model (Equations 5–8) results winter (5), summer (6).

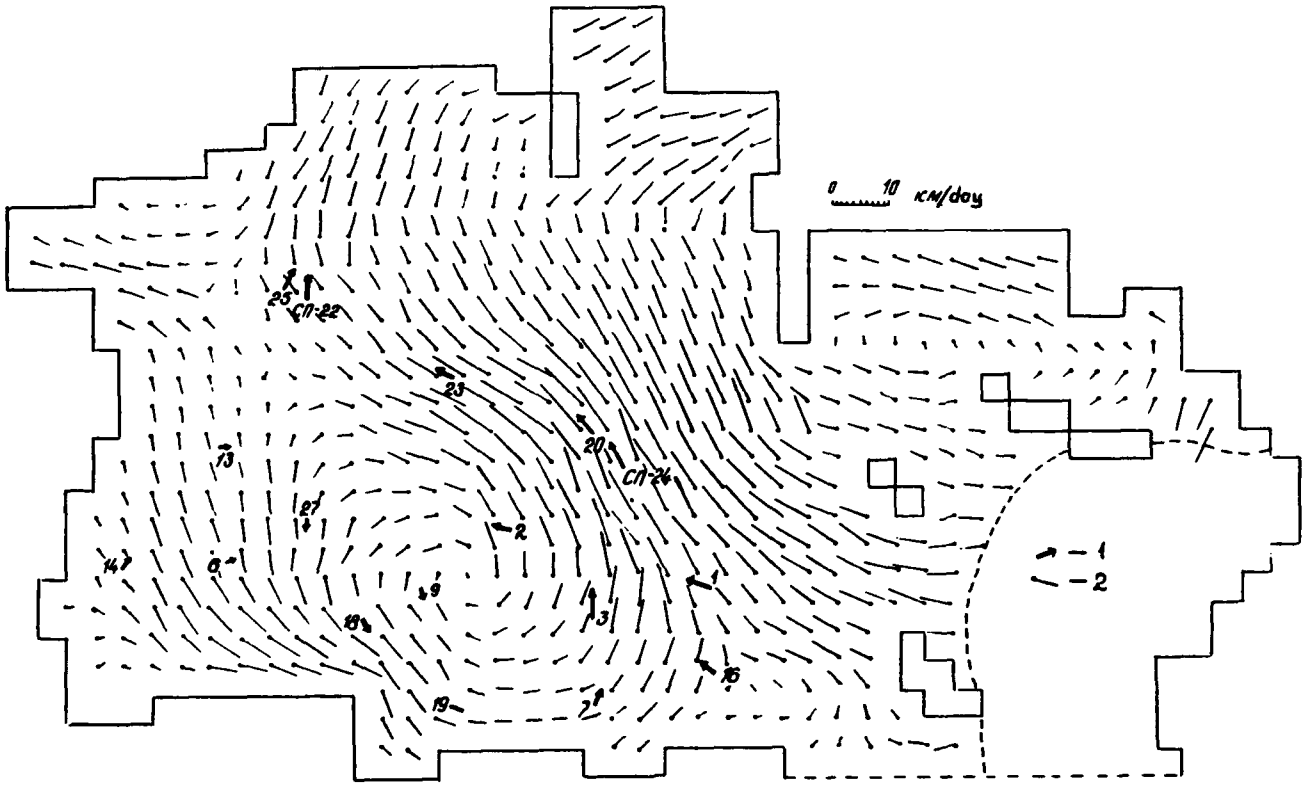


Figure 3. Model calculated ice drift (Equations 5–8) for 1–5 July, 1979. By observational data (1), by modeling (2).

grows weaker and the water circulation is driven by barotropic factors. The horizontal distribution of the mass field observed in the Arctic Basin in spring seems to be due to the barotropic effects.

The proposed model (Equations 5–8) is primarily used for the calculation of synoptic motions of water and sea ice (Figure 3). It is also appropriate for operational support of arctic navigation and can be used for the forecasts of storm surges level oscillations five days in advance. The model forecasts during three navigation seasons (1987–1989) had a skill score during the first three days of 82% on average, while the forecasts for the fourth and fifth days can be regarded as recommendations for the estimation of the trend (the growth or decrease of sea level). If wind stress data and pressure gradients are excluded from the model, while tidal forces are added to the model equations, we can get a system of equations suitable for prediction and estimation of water and sea ice tides [Polyakov and Proshutinsky, 1988].

The development and practical use of numerical hydrodynamic forecasts requires that the model be supported by full-scale experiments. Observations should be adequately planned for both model calibration and verification. So the model development strategy should include the whole cycle of "model–experiment–model."

Let us now dwell a little on the problem area which includes both further development of models and the results of the study of Arctic Ocean hydrology by numerical models. The first task would include the development of a program of full-scale observations and their implementation along the following lines:

- to determine actual transport of water masses, heat, and salt across all the Arctic Ocean outlets;
- to make hydrographic surveys in the Arctic Ocean year-round;
- to monitor currents, sea level changes, sea ice drift and meteorological elements in the ocean for the calibration and verification of numerical models.

All these tasks can be resolved on the basis of international cooperation and combined efforts of different countries.

There are certain areas in the Arctic Ocean which merit special attention. The background circulation in the North European Basin is cyclonic; there is also a cyclonic gyre to the northeast of Jan-Mayen. This area has been extensively studied lately, since it is here that conditions are extremely favorable for the development of deep convection which is believed to be related to bottom water formation. One of the most timely problems of polar oceanography is the development of the theory and numerical models of deep and bottom water formation in the Greenland Sea to determine its quantitative characteristics.

The anticyclonic gyre in the Lofoten Basin of the Norwegian Sea has been studied lately. The anticyclonic quasi-geostrophic rotation there is related to the expressed sagging of isopicnal surfaces. The area of the gyre seems to be a certain condenser of potential energy which can be released when the coming flow weakens and accumulated when the Norwegian Current becomes more intense. A more detailed study is desirable, as its results might greatly contribute to better modeling of the North European Basin processes.

The dynamics of deep and bottom waters in the Arctic Ocean are less studied. It is believed that deep and bottom currents in the North European Basin might have velocities comparable with those in the upper layer [Alekseev et al., 1989; Bub and Popov, 1989]. What mechanisms cause it are not clear yet. "Overflows" of deep and bottom waters are particularly important not only in the North European Basin, but also in other areas of the World Ocean. These are overflow of the Greenland Sea bottom waters to the Norwegian Sea and Arctic Basin. There is also water overflow from the American Basin to the Eurasian Basin and so on. The mechanism of the phenomenon is not known yet.

Special studies of the interaction process in the system of atmosphere–ice–ocean occurring in the so-called sea-ice marginal zones should be organized.

REFERENCES

Alekseev, G. V., P. V. Bogorodsky, A. S. Tsvetukhin, and A. I. Shuvalov, Investigation of Norwegian Sea circulation using instrumental current measurements, *Problemy Arktiki i Antarktiki*, *64*, 83–87 1989.

Arctic ocean modelling meeting, Cambridge, June 1982, *Rep. SCOR Group 58, No 57*, 85 pp., Bergen, Norway, June 1983.

Bub, A. F., and A. V. Popov, Structure and circulation of water masses in the Northern part of Greenland Sea, *Problemy Arktiki i Antarktiki*, *64*, 88–97, 1989.

Campbell, W. J., The wind driven circulation of ice and water in a Polar Ocean, *J. Geophys. Res.*, *70*, 3279–3301, 1969.

Doronin, N. Yu., Numerical modeling of the Kara Sea steady-state circulation, *Trudy AANII*, *414*, 37–44, 1989.

Felzenbaum, A. I., Theory of the steady-state sea ice drift in the central Arctic Basin, *Problemy Severa*, *2*, 16–46, 1958.

Gudkovich, Z. M., and Ye. G. Nikiforov, Experimental investigations of Arctic Basin steady-state currents, *Trudy AANII*, *254*, 129–154, 1963.

Hart, J. E., The flow of two layer fluid over topography in a Polar Ocean, *J. Phys. Oceanogr.*, *5*, 678–685, 1975.

Hibler, W. D., and K. Bryan, A diagnostic Ice–Ocean model, *J. Phys. Oceanogr.*, *17*, 987–1015, 1987.

Kudryavtsev, N. F., Stationary wind currents in a shallow stratified sea, *Trudy AANII*, *395*, 138–144, 1970.

Marchuk, G. I., and A. S. Sarkisyan, *Numerical Modeling of the Ocean Circulation*, 301 pp., Nauka, Moskva, 1988.

Nikiforov, Ye. G., N. Yu. Doronin, and A. V. Popov, Three-dimensional circulation in the area of Greenland Deep (diagnostic calculations), *Problemy Arktiki i Antarktiki*, *64*, 98–110, 1989.

Polyakov, I. V., and A. Yu. Proshutinsky, Periods of eigen-oscillations of the Arctic Ocean sea level, *Meteorologia i Hydrologia*, *11*, 91–99, 1988.

Ponomaryev, V. I., and L. A. Gazova, Diagnostic model of the Arctic Basin water and sea ice circulation, *Meteorologia i Hydrologia*, *3*, 54–61, 1981.

Proshutinsky, A. Yu., Modelling of seasonal variations of the Arctic Ocean sea level, *Meteorologia i Hydrologia*, *2*, 57–65, 1988.

Semtner, A. J., A numerical study of sea and ice ocean circulation in the Arctic, *J. Phys. Oceanogr.*, *17*, 1077–1099, 1987.

Treshnikov, A. F., and G. I. Baranov, *Circulation Structure of the Arctic Ocean Waters*, 158 pp., Hydrometeoizdat, Leningrad, 1978.

Air–Sea Interaction and Penetrating Winter Convection in the Greenland Sea

G. V. Alekseyev
The Arctic and Antarctic Research Institute, Leningrad, U.S.S.R.

ABSTRACT

Since 1984 research vessels of the Arctic and Antarctic Research Institute have carried out continuous studies in the central Greenland Sea, where the development of winter convection, penetrating down to the bottom, is possible [Nansen, 1909]. At the present time more than 20 oceanographic surveys have been made in this area, with 10 surveys conducted in winter (January–April). Penetrating convection events were observed in March 1984, 1988 and 1989. The strongest event was observed in March 1984, a somewhat less extensive event occurred in March 1989 (considered in detail in this work) and a relatively weak one occurred in winter 1988. The analysis of distributions of thermodynamic characteristics of water masses in the convection area allowed us to define major features of seasonal and inter-annual changes of vertical water structure, and to single out necessary conditions and stages of the penetrating convection development, which generally agree with the existing understanding [Gordon, 1978; Killworth, 1983], but which were supplemented by the indication of a specific role of atmospheric processes over the Greenland Sea. Quantitative estimates of the possible volume of bottom and deep waters forming in the penetrating convection events were made. The climate-forming role of this process and the possibility of forecasting it are discussed.

Multiyear Variability of Atmospheric Circulation Shifts Over the North Pacific and a Method to Forecast Ice Cover on the Okhotsk and Bering Seas

A. M. Polyakova
Pacific Oceanological Institute, Far Eastern Branch U.S.S.R. Academy of Sciences, Vladivostok, U.S.S.R.

ABSTRACT

Typical atmospheric processes were revealed by the motion of cyclones and anticyclones above the North Pacific. All the variability of synoptical situations could be separated into 6 types. Study of the multiyear variability of these typical processes showed the existence of rather complicated periodical fluctuations repeating every 4–5 to 30 years. The transition from one process to another takes place rather unevenly. For instance, all the types readily change to the North Western type (43%), but very rarely to the Okhotsk–Hawaii type. The same synoptical uninterrupted situation can last up to 2 months.

According to the concepts of ocean–atmosphere interactions we have found some clear relationships between the repeating typical processes and the ice cover of Far Eastern Seas. Regression equations were determined for the ice cover forecast for the Okhotsk Sea for January to April and for the Bering Sea for April and May. In these periods both seas have the maximum ice cover. The accepted equations appear to meet all the standard requirements. Checking was done on independent two year material. It turned out that the method worked for 88–96% of the time, its reliability was 79–96%, and its effectiveness was 31–38%.

Sea Surface Temperature Anomalies in the North Pacific, Their Connection With Atmospheric Processes in Transitional Seasons and Ice Variability in the Bering and Okhotsk Seas

K. A. Rogachev
Pacific Oceanological Institute, Far Eastern Branch of the USSR Academy of Sciences, Vladivostok, U.S.S.R.

A. F. Lomakin
Far Eastern Hydromet Institute, Vladivostok, U.S.S.R.

ABSTRACT

The formation of sea-surface temperature anomalies (SSTAs) in the North Pacific have been examined for some decades. It was shown that in extreme years SSTAs have produced changes in the thermal contrast between ocean and continent.

In transitional seasons (spring and fall) surface temperature contrasts between ocean and continent (for example between the Aleutian Low and the Siberian High) were small. Hence, a small SSTA can determine ocean–continent surface contrasts and the time lag of transitional seasons.

The timing and shift of the onset of winter in the middle and high latitudes depends on the value of these contrasts. Thus, in the present study the time lag of the transitional seasons is considered to be one of the main climatic elements.

In extreme years the sea ice cover in the Bering and Okhotsk Seas changes significantly. In warm years (as determined by SSTA) the ice-covered area in the Bering Sea is less than 30%. Since there is a difference in the position of ice sources between the Bering and Okhotsk Seas, a different ice dynamic occurs in the Okhotsk Sea.

A Statistical Study of Atmosphere–Sea Ice Interactions in the Southern Ocean

E. Breitenberger and G. Wendler
Geophysical Institute, University of Alaska Fairbanks, Fairbanks, Alaska, U.S.A.

ABSTRACT

By regulating the heat exchange between ocean and atmosphere, sea ice strongly forces the atmospheric circulation. In turn, atmospheric conditions distinctly control the growth and decay of the sea ice cover.

Using weather grids and satellite-derived sea ice data for the Southern Ocean, we have undertaken a statistical investigation of these interactions. Our approach has been to examine the correlations between various indices of the circulation and sea ice for different spatial and temporal lags.

Our results indicate large variability in the magnitude, sign, and lag of ice–atmosphere interaction. Since there are considerable noise and autocorrelation in the data, it seems that only the strongest interactions can be unambiguously determined. Interactions are particularly pronounced in the Ross Sea and Weddell Sea, which are the principal areas of ice production in the Antarctic. These interactions exhibit strong seasonal dependence, but do not seem to conform to simple models of ice–atmosphere interaction. Many other sectors of the Southern Ocean show correlations between atmosphere and ice, but these correlations are generally of marginal statistical significance. On the whole, we find strong interactions in the Ross and Weddell sectors, with strong seasonal dependence, but little statistically significant interaction elsewhere.

AD-P007 305

92-17987

The Impact of Snow and Sea Ice Variations on Global Climate Change

Tamara Shapiro Ledley

Department of Space Physics and Astronomy, and the Earth Systems Institute, Rice University, Houston, Texas, U.S.A.

ABSTRACT

Recent work with a coupled energy balance climate–sea ice model has shown that sea ice has a large impact on the energy fluxes between the ocean and the atmosphere and thus on climate, especially in the polar regions. In this study the impact of the addition of snowfall on sea ice and its effect on climate is examined. The results show that the addition of snow introduces three major competing effects. The first effect is that the snow acts as an insulator, keeping the ice warm and thus thin. This would seem to produce a warming effect on the climate. The second is that snow has a lower volumetric specific heat than ice causing it to cool during the winter and warm during the summer more rapidly than ice. The third is that snow has a higher albedo than ice. This causes a reduction in the absorbed solar energy by the entire earth–atmosphere system and thus a cooling of the climate. The results described here indicate that the albedo effect is dominant, so that the addition of snow cools the climate.

INTRODUCTION

The exchange of energy between the ocean and atmosphere is a major factor in determining atmospheric temperature. This exchange is altered by the existence of snow and sea ice on the ocean surface because sea ice insulates the relatively warm ocean from the cold winter atmosphere, and has a significantly higher surface albedo than open ocean.

The net impact of snow and sea ice on surface energy exchange depends on its latitudinal extent and characteristics such as thickness, impurities, and the area of open ocean within the ice pack (leads). Previous work with a coupled energy balance climate–thermodynamic sea ice model (CCSI model) showed that the amount of leads during the winter [Ledley, 1988a,b], and meridional sea ice transport [Ledley, 1990a,b, 1991] can have significant effects on climate.

Ledley [1988a,b] showed that variations in the small wintertime lead fraction produced a dramatic impact on the ocean–atmosphere energy exchange, and thus on temperature. This was because the energy exchange between the ocean and the atmosphere can be two orders of magnitude greater over open ocean than over sea ice during the winter. The effect on climate was largest in the polar regions; however, through meridional energy transport, it extended globally.

Further investigations [Ledley, 1990a,b, 1991] showed that sea ice transport also plays an important role in shaping climate in that it produces a thinning of the sea ice in the poleward-most zones which, through its impact on the maximum summertime lead fractions and ice-free conditions, produces significantly warmer conditions compared to when sea ice transport is neglected.

In the above studies the impact of sea ice and sea ice variations alone were examined. However, snow can have a significant influence on the seasonal variation of sea ice [Ledley, 1985b], and thus on ocean–atmosphere energy exchange and temperature. The mechanisms that cause this influence are (1) snow also acts as an insulator, keeping the sea ice relatively warm and thin during the winter and thus easier to melt away; (2) snow has a lower volumetric specific heat than ice causing it to cool and warm more rapidly than ice; and (3) snow generally has a higher albedo than sea ice, reflecting more solar radiation and thus producing thicker sea ice.

In this study the impact of snow on sea ice, and its subsequent influence on ocean–atmosphere energy exchange and climate is examined. The relative importance of the

competing effects of the insulating of sea ice by snow, the lower volumetric specific heat of snow compared to ice, and the higher albedo of snow as compared to ice, and their impact on global climate is described.

THE CCSI MODEL

The CCSI model is a coupled energy balance climate–thermodynamic sea ice model that treats four distinct regions of the climate system, each of which is represented by a single layer. These regions include the air over land, the air over ocean, a mixed layer ocean, and a ground layer. The model computes 336 time steps per year and employs a 10° latitudinal grid, with land–sea resolution in each zone distributed in accordance with current land–sea distribution.

The CCSI model prognoses the future air layer temperatures by computing the energy balance of each layer. The energy fluxes that are included in this calculation are the horizontal heat transports, meridional and zonal; short and long wave radiative fluxes; and the sensible and latent heat fluxes.

The thermodynamic sea ice model that is used in the CCSI model is that described by Ledley [1985a,b] and is based on the models of Semtner [1976] and Maykut and Untersteiner [1971]. It is a three-layer thermodynamic model that includes conduction within the ice, penetration of solar radiation into the ice layers, and surface energy balances.

The formation of new sea ice on open ocean and the opening and closing of leads are computed following the techniques of Ledley [1987]. In this parameterization a minimum lead fraction of the total ice/ocean area to be occupied by leads during the winter is specified. Also included is the transport of sea ice into equatorward latitude zones.

The snowfall rate is determined as a function of precipitation rate, which is specified as a constant for all latitudes and times; and of the temperature, which determines the fraction of the precipitation that falls as snow. The purpose of using the constant precipitation rate is to isolate the effect of snow on sea ice and climate variations, without the complications of variable precipitation rates.

THE EXPERIMENTS

There are two sets of experiments that are performed with the CCSI model. In the first set, the albedos of snow, α_s, and ice, α_i, are set as follows:

$$\alpha_s = \begin{cases} 0.84 & T_{air} \le 260°K \\ 0.84 - 0.0065\,(T_{air} - 260) & 260°K \le T_{air} < 280°K \\ 0.71 & 280°K < T_{air} \end{cases}$$

$$\alpha_i = \begin{cases} 0.71 & T_{air} \le 260°K \\ 0.71 - 0.01\,(T_{air} - 260) & 260°K \le T_{air} < 280°K \\ 0.51 & 280°K < T_{air} \end{cases}$$

In the second set of experiments the albedo of snow is set equal to that of ice. The purpose here is to examine how the properties of snow affect sea ice variations, ocean–atmosphere interactions, and climate.

In each set of experiments the precipitation rate is set to a constant rate at all latitudes, and the simulations are made for 20 years. The precipitation rates specified are (1) 0 m yr^{-1}, (2) 0.1 m yr^{-1}, (3) 0.2 m yr^{-1}, (4) 0.4 m yr^{-1}, (5) 0.8 m yr^{-1}. Here we will examine the results when the precipitation rate is specified at 0.2 and 0.4 m yr^{-1}. In these cases repeating seasonal cycles are produced.

Precipitation	85°N	75°N	65°N	55°S	65°S	75°S
a) $\alpha_s > \alpha_i$		Mean Snow Thickness				
0.0 m yr^{-1}	0.00	0.00	0.00	0.00	0.00	0.00
0.2 m yr^{-1}	0.66	0.16	0.04	0.02	0.07	0.22
0.4 m yr^{-1}	0.80	0.28	0.09	0.04	0.10	0.24
b) $\alpha_s = \alpha_i$		Mean Snow Thickness				
0.2 m yr^{-1}	0.21	0.09	0.03	0.01	0.06	0.19
0.4 m yr^{-1}	0.35	0.17	0.07	0.02	0.08	0.21

Table 1. Mean Snow Thickness at Year 20 in m. (The simulation was carried out for 20 years. These results are for the last year.)

Precipitation	85°N	75°N	65°N	55°S	65°S	75°S
a) $\alpha_s > \alpha_i$		Sea Ice "Volume"				
0.0 m yr^{-1}	2.85	1.33	0.34	0.01	0.35	1.37
0.2 m yr^{-1}	2.40	1.25	0.42	0.01	0.27	0.72
0.4 m yr^{-1}	2.76	1.28	0.43	0.01	0.26	0.79
b) $\alpha_s = \alpha_i$		Sea Ice "Volume"				
0.2 m yr^{-1}	2.01	0.97	0.23	0.01	0.18	0.61
0.4 m yr^{-1}	1.64	0.76	0.18	0.01	0.20	0.68

Table 2. Sea Ice "Volume" at Year 20 in m. (The sea ice "volume" is defined as: sea ice thickness x (1 - lead fraction).)

IMPACT OF SNOW ON SEA ICE THICKNESS

Table 1 shows the mean annual snow thickness in each of the latitude zones that has snow on sea ice for each of the precipitation scenarios. As expected, the snow thickness increases as the precipitation rate increases; however, when the albedo of the snow is set equal to the albedo of the sea ice the snow thickness in each case decreases dramatically.

Table 2a shows the impact of increasing the snow thickness on the sea ice "volume" when $\alpha_s > \alpha_i$ (sea ice "volume" is defined as the sea ice thickness times one minus the lead fraction). The effect of adding a relatively small amount of snow is to decrease the sea ice thickness in all but the zones near the ice edge. The thinning of the ice is due to the insulating properties of the snow on the ice. When snow is added to the bare ice, the ice remains warmer, grows more slowly, melts more readily, and is therefore thinner than when there is no snow.

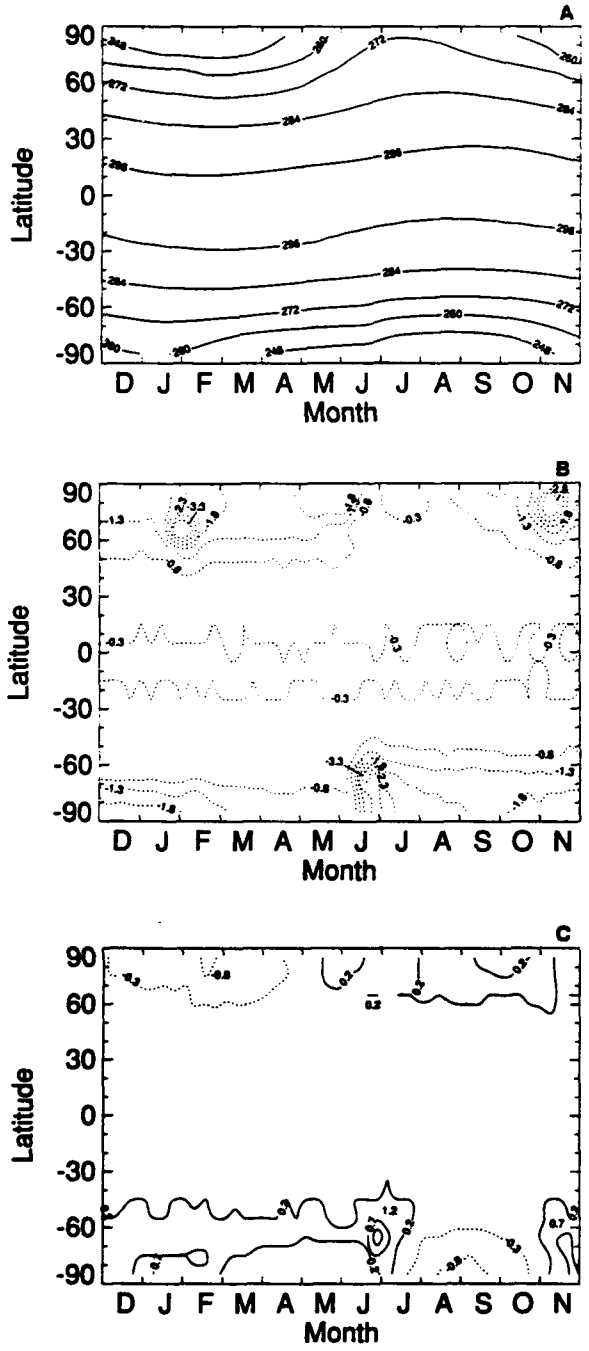


Figure 1.(a). The seasonal cycle of surface air temperature over ocean and sea ice in °K when snow is neglected, and (b & c) the change in the seasonal cycle of surface air temperature in °K when precipitation is added at a rate of 0.4 m yr^{-1} when (b) the albedo of snow is greater than that of ice, $\alpha_s > \alpha_i$ and (c) the albedo of snow is equal to that of ice, $\alpha_s = \alpha_i$. Note that decreases in temperature are denoted by dotted contours and increases by solid contours.

The higher albedo of the snow surface, which causes a reduction in absorbed solar radiation, offsets this warming of the ice to some extent, but does not eliminate it. As a result when the snow thickens enough and temperatures do not get much above the freezing point, melting is reduced and sea ice begins to get thicker. This can be seen quite dramatically by comparing the mean sea ice thicknesses in Tables 2a and 2b for a precipitation rate of 0.4 m yr^{-1}. The only difference between these two sets of sea ice thicknesses is the albedo of the snow. When $\alpha_s > \alpha_i$ (Table 2a) the sea ice is thicker at almost all latitudes than when $\alpha_s = \alpha_i$ (Table 2b). In addition, when examining the effect of increasing precipitation from 0.2 to 0.4 m yr^{-1} the sea ice thickens at almost all latitude zones when $\alpha_s > \alpha_i$; but when the albedo effect is neglected the sea ice continues to thin in the northern hemisphere, and thickens only to a small extent in the southern hemisphere. The thickening in the southern hemisphere may be due to the lower thermal inertia of snow compared to ice.

IMPACT OF SNOW ON SURFACE AIR TEMPERATURES

Figure 1 shows the seasonal variation of surface air temperature over ocean and sea ice as a function of latitude when no snow is specified (Figure 1a) and the effect of adding precipitation at the rate of 0.4 m yr^{-1} when $\alpha_s > \alpha_i$ (Figure 1b), and when $\alpha_s = \alpha_i$ (Figure 1c).

The addition of snow with its higher albedo leads to cooler temperatures (Figure 1b). The largest decreases in temperature occur at 75°N - October–November, 65°N - January–February, and 65°S and 75°S - June, and correspond to decreases in the periods of ice-free conditions.

These temperature changes are superimposed on a year-round decrease in surface air temperature on the order of 1.5°K, that varies from a maximum during the winter to a minimum during the summer in both hemispheres. The winter decrease in surface air temperature, when snow is added, is the result of lower volumetric specific heat of the snow as compared to ice. This causes snow surface temperatures to cool more during the cooling phase of the seasonal cycle. During the warming phase the snow temperatures warm faster than the ice, but this is offset by the increase in the surface albedo which causes a decrease in absorbed solar radiation and thus a cooling. The cooler snow surface temperatures cause the surface air temperature to decrease.

When the higher albedo of snow is neglected (Figure 1c) the rapid cooling of the snow as compared to ice during the winter also produces a decrease in surface air temperatures; however, this cooling is restricted to the winter and early spring and is on the order of 0.5°K. During the rest of the year there are small increases in temperature in the polar regions on the order of 0.2°K. These result partially from the more rapid warming of the snow as compared to ice during the spring and summer, the larger amounts of absorbed solar radiation due to the lower snow albedo than when $\alpha_s > \alpha_i$ (Figure 1b) and the increased periods of ice-free conditions.

SUMMARY

In summary, the addition of snow to the sea ice surface insulates the sea ice, because of the lower thermal diffusivity of snow as compared to ice. This causes the sea ice to remain relatively warm and, as a result, relatively thin. It would seem that this would result in warmer climate conditions. However, the higher surface albedo of snow as compared to sea ice causes a large reduction in the absorbed short wave radiation at the surface. This causes a reduction in the melting of sea ice during the summer, and larger growth rates during the winter, which produces a reduction

in the energy fluxes from the ocean to the atmosphere, and thus causes a cooling of the atmosphere. This cooling is enhanced during the winter because the snow has a lower volumetric specific heat compared to ice, which allows the snow surface to become colder than the ice surface under the same conditions.

This work has shown that the albedo effect is the more important of the three properties of snow affecting sea ice (the change in albedo, the lower volumetric specific heat of snow compared to ice, and the insulating effect of snow on ice). As a result the addition of a constant precipitation rate resulting in a snow cover on sea ice produces a cooling effect in the polar regions.

ACKNOWLEDGMENTS

This work was supported in part by two grants from the National Science Foundation, ATM-8904437 and DPP-8922415. This material is also based in part upon work supported by the Texas Advanced Technology Program under grants 3639 and 003604009. Computer time for this project was supplied by the National Center for Atmospheric Research.

REFERENCES

Ledley, T. S., Sensitivity of a thermodynamic sea ice model with leads to time step size, *J. Geophys. Res.*, *90*, 2251-2260, 1985a.

Ledley, T. S., Sea ice: Multi-year cycles and white ice, *J. Geophys. Res.*, *90*, 5676-5686, 1985b.

Ledley, T. S., Development of a new sea ice growth and lead parameterization, *Climate Dynamics*, *2*, 91-100, 1987.

Ledley, T. S., For a lead-temperature feedback in climate variations, *Geophys. Res. Lett.*, *15*, 36-39, 1988a.

Ledley, T. S., A coupled energy balance climate–sea ice model: Impact of sea ice and leads on climate, *J. Geophys. Res.*, *93*, 15919-15932, 1988b.

Ledley, T. S., The warming effect of meridional sea ice transport on climate, *Sea Ice Properties and Processes*, Proceedings of the W. F. Weeks Sea Ice Symposium, edited by Stephen F. Ackley and Wilford F. Weeks, pp. 256-258, *CRREL Monograph 90-1*, 1990a.

Ledley, T. S., Meridional sea ice transport and its effect on climate, *Ann. Glaciol.*, *14*, 141-143, 1990b.

Ledley, T. S., The climatic response to meridional sea ice transport, *J. Climate*, *4*, 147-163, 1991.

Maykut, G. A., and N. Untersteiner, Some results from a time dependent thermodynamic model of sea ice, *J. Geophys. Res.*, *76*, 1550-1575, 1971.

Semtner, A. J., A model for the thermodynamic growth of sea ice in numerical investigations of climate, *J. Phys. Oceanogr.*, *6*, 379-389, 1976.

AD-P007 306

92-17988

Energy Exchange Over Antarctic Sea Ice in Late Winter

G. König-Langlo
Alfred-Wegener-Institute, Bremerhaven, Germany

B. Ivanov and A. Zachek
AARI, Leningrad, USSR

ABSTRACT

In September and October 1989 during the "Winter Weddell Gyre Study" energy balance measurements were performed from the Soviet ice-breaker *Akademik Fedorov*. The average radiation balance of the sea ice surface turned out to be zero, i.e., short-wave radiation gains were fully compensated by long-wave radiation losses. Due to turbulent fluxes of sensible and latent heat the atmosphere received about 25 W m^{-2} energy from the ice/ocean system. Since no significant ice melting or freezing was observed, the latter must originate mainly from warm deep water which is entrained into the oceanic mixed layer.

INTRODUCTION

Sea ice covers only 4% of the earth's surface but it is nevertheless believed to play an important role in the climate system through its coupling with the ocean and the atmosphere. For a review see Walsh [1983].

Thus a hierarchy of sea ice models has been developed [e.g., Maykut et al., 1971; Hibler, 1979; Lemke et al., 1990]. They all use parameterization schemes for the exchange between ice, atmosphere and ocean. For the antarctic regions there is very little in situ data to verify and improve these models. Especially in remote areas, such as the Weddell Gyre, and during strong ice conditions at the end of winter, nearly no field observations exist.

The multinational Winter Weddell Gyre Study 1989 (WWGS89) offered a good opportunity to take surface measurements in the antarctic sea ice belt during the period of maximum ice extent. The data collected may help to improve the parameterization schemes describing the physical processes which control the sea ice development as well as its interaction with the ocean and the atmosphere. Subsequently we present some observational results of the surface heat and radiation balance of the Weddell Sea ice area.

CRUISE

The WWGS89 was carried out by the research vessels *Akademik Fedorov* (Leningrad) and *Polarstern* (Bremerhaven). Both ships operated for about six weeks in the sea ice–covered Weddell Gyre.

The energy balance measurements were performed on the *Akademik Fedorov*. The ship reached the rather sharp ice edge (60°20'S, 34°25'W) on 18 September 1989 (see Figure 1). The ice edge was well pronounced. Within several meters the ice cover changed from 0% to nearly 100% 50 cm of thick first-year ice.

Heading southeast, some multi-year ice floes of up to 200-cm thickness were observed. After crossing the polar circle (24 September, 20°W) and heading eastward to Maud Rise, first-year ice with thicknesses between 60–100 cm was dominant. West of Maud Rise the ice thickness dropped to 30–40 cm for about 50 km. This coincided with a shallow mixed layer of only 40 m depth and a mixed layer temperature 0.2°C above freezing. This local phenomenon can be interpreted as an orographic effect of Maud Rise.

After several days of measurements near Maud Rise *Akademik Fedorov* stopped on 6 October for a 12-day drifting station. During this period the ship drifted together with the ice more than 100 km from 65°46'S, 1°50'W to 65°21'S, 4°8'W. First-year ice of 60 cm thickness was mainly observed. Heading northward *Akademik Fedorov* left the ice on 24 October (58°3'S, 25°15'W).

With some exceptions during the last few days of the cruise the ice coverage was always well above 90%. The observed cracks and leads were frequently filled with thin new

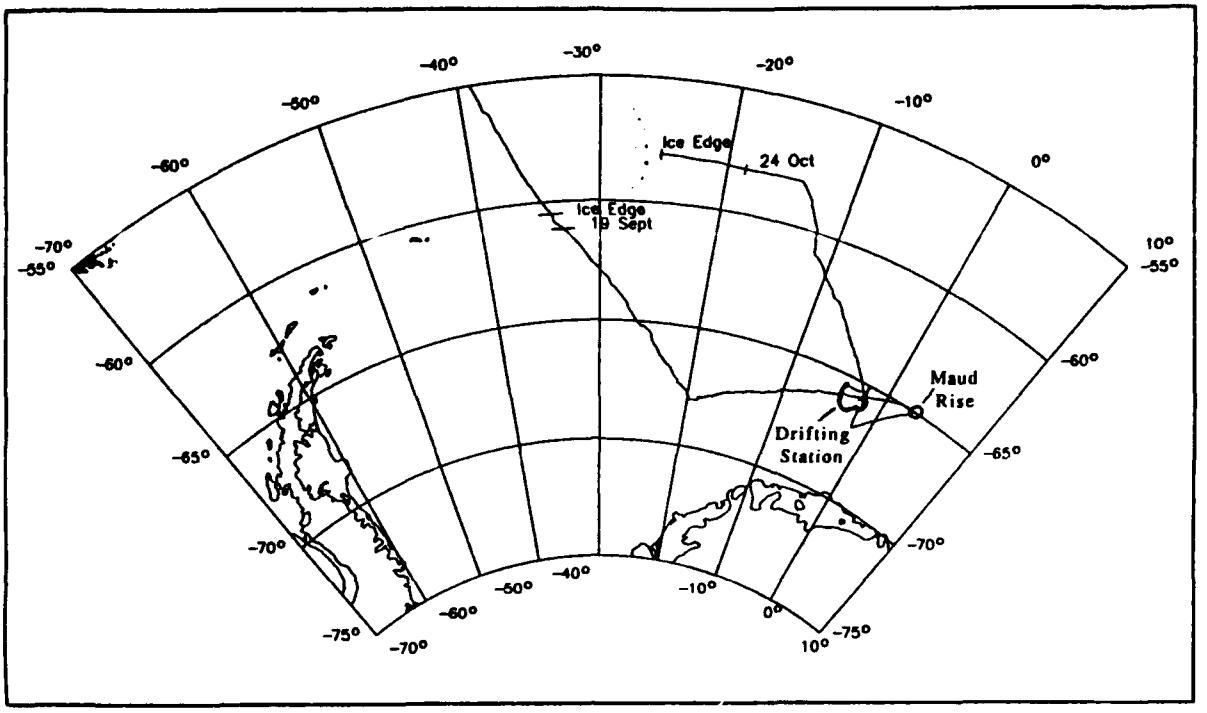


Figure 1. Cruise of *Akademik Fedorov*.

ice and nilas. Ice ridging was low to moderate. The sea ice was always covered by snow with a depth of about 20 cm. Except in newly opened cracks and leads no significant ice formation or melting was observed until the end of the drifting station.

Weather conditions were quite variable. The air temperature was always below freezing (minimum=-24°C, mean=-12°C), and the wind speed ranged between 1–21 m s^{-1} (mean=10 m s^{-1}). From the ice edge to the drifting station westerly winds prevailed. Later on winds from east and south were more common. Frequently the sky was totally overcast and snow fell several times.

The cruise can be divided into three parts. Along the first part from the ice edge to the drifting station *Akademik Fedorov* stopped every 30 or 60 miles for a 2- to 6-hour hydrological station and experiments on the ice. During the two weeks drifting station, part two, ice work was done continuously. The last part from the drifting station to the ice edge was organized similarly to part one.

INSTRUMENTATION

The following components of the surface energy balance were measured:

- •global radiation ($K\Downarrow$)
- •reflected solar radiation ($K\Uparrow$)
- •downward long-wave radiation ($L\Downarrow$)
- •upward long-wave radiation ($L\Uparrow$)
- •turbulent flux of sensible heat (H)
- •turbulent flux of latent heat (LE)

Additionally weather and ice observations were carried out routinely. To achieve accurate and reliable data all components were measured using different methods and instruments wherever possible.

Short-wave Radiation. The global radiation ($K\Downarrow$) was measured with three redundant pyranometers (CM11, Kipp + Zonen). During the drifting station the reflected solar radiation ($K\Uparrow$) was determined directly using a fourth CM11 instrument mounted on a sledge 500 m away from *Akademik Fedorov*. In all other cases $K\Uparrow$ was calculated using $K\Downarrow$, albedo values obtained periodically from a hand-held albedometer and ice observations. The absolute error of the mean short-wave balance can be expected to be less than 3 W m^{-2} according to the small scatter of the redundant instruments, the rather low global radiation and rather high albedo.

Long-wave Radiation. The downward long-wave radiation ($L\Downarrow$) was measured with a pyrgeometer (Eppley PIR) and an instrument (P2-30) developed recently in Leningrad. A built-in filter compensation and heating prevents the P2-30 from being affected by hoar-frost. With a measuring angle less than 180° a second P2-30 and an infrared thermometer (KT4) determined the upward long-wave radiation ($L\Uparrow$) while the ship was in motion. Furthermore a second Eppley PIR supplied $L\Uparrow$ data during the drifting station. Comparing these data derived from quite different instruments, the mean deviation was less than 3 W m^{-2}.

Radiation Balances. The German net pyrradiometer of the type Schulze–Lange mounted on the ship provided the total downward radiation ($Q\Downarrow=K\Downarrow+L\Downarrow$). This instrument was mounted on a sledge during the drifting station and measured additionally the upward radiation balance ($Q\Uparrow=K\Uparrow+L\Uparrow$). The Soviet net pyrradiometer BP_1 also fixed on the radiation sledge determined the radiation balance ($Q^*=Q\Downarrow+Q\Uparrow$) directly.

Q^* could therefore be estimated from several independent instruments (Figure 2). The good agreement is expressed by the low standard deviation of 3 W m^{-2}. Adding all errors of the single radiation components $K\Downarrow$, $K\Uparrow$, $L\Downarrow$ and $L\Uparrow$ leads to much greater uncertainties in Q^*. Due to the high albedo and frequently overcast sky the errors in the

downward components were often compensated by the errors of the upward components.

Despite the fact that the net pyrradiometers offered reasonable radiation balances, all derived quantities like $L\Downarrow=Q\Downarrow-K\Downarrow$ show systematic errors and were excluded from analysis.

Turbulent Fluxes. While the ship was in motion the turbulent fluxes were estimated continuously on the basis of an algorithm established by Ivanov and Makshtas [1986] based on the Monin–Obukhov method. During the drifting station and at some hydrographic stations additionally a small gradient tower and a sonic anemometer–thermometer (Kaijo Denki DAT 300) erected on the ice were used. The mean difference between tower data and sonic data was less than 30%. The error for the mean turbulent fluxes was assumed to be within the same order.

RESULTS

From the radiative and turbulent fluxes the surface energy balance

$$B = K\Downarrow + K\Uparrow + L\Downarrow + L\Uparrow + H + LE$$

was computed. Positive values indicate a gain, negative values a loss of energy at the surface. The component B comprises all energy fluxes below the surface, i.e., B depends on changes in heat storage of the ice, phase changes and energy supplied by the ocean. Figure 3 shows some time series from the first part of the cruise.

The surface gained energy mainly by the short-wave balance ($K^*=K\Downarrow,+K\Uparrow$). The long-wave balance ($L^*=L\Downarrow,+L\Uparrow$), generally negative, significantly depended on cloud coverage. Thus the radiation balance (Q^*) did not follow the daily cycle as strictly as K^*. Generally, the mean short-wave gain was about compensated by the mean long-wave loss.

When Q^* distinctly exceeded +50 W m^{-2} the turbulent fluxes transported most of this energy into the atmosphere, thus preventing ice melting or ocean warming. The analogous mechanism for cases with Q^* lower than -50 W m^{-2} was less pronounced. Due to the reduced turbulence under stable atmospheric conditions the surface radiation loss could not be compensated by the atmosphere. Thus the mean surface energy balance was negative. Figure 4 shows the same data as Figure 3 but averaged over 17 days of part I of the cruise.

An energy imbalance of B=-24 W m^{-2} corresponds to a sea ice growth of about 12 cm within 17 days. But no significant ice formation was observed. The same imbalance over the same period could decrease the mean ice temperature within the order of 10°C. But no significant changes in heat storage of the ice were observed. Thus B can be interpreted as primarily energy supplied by the ocean.

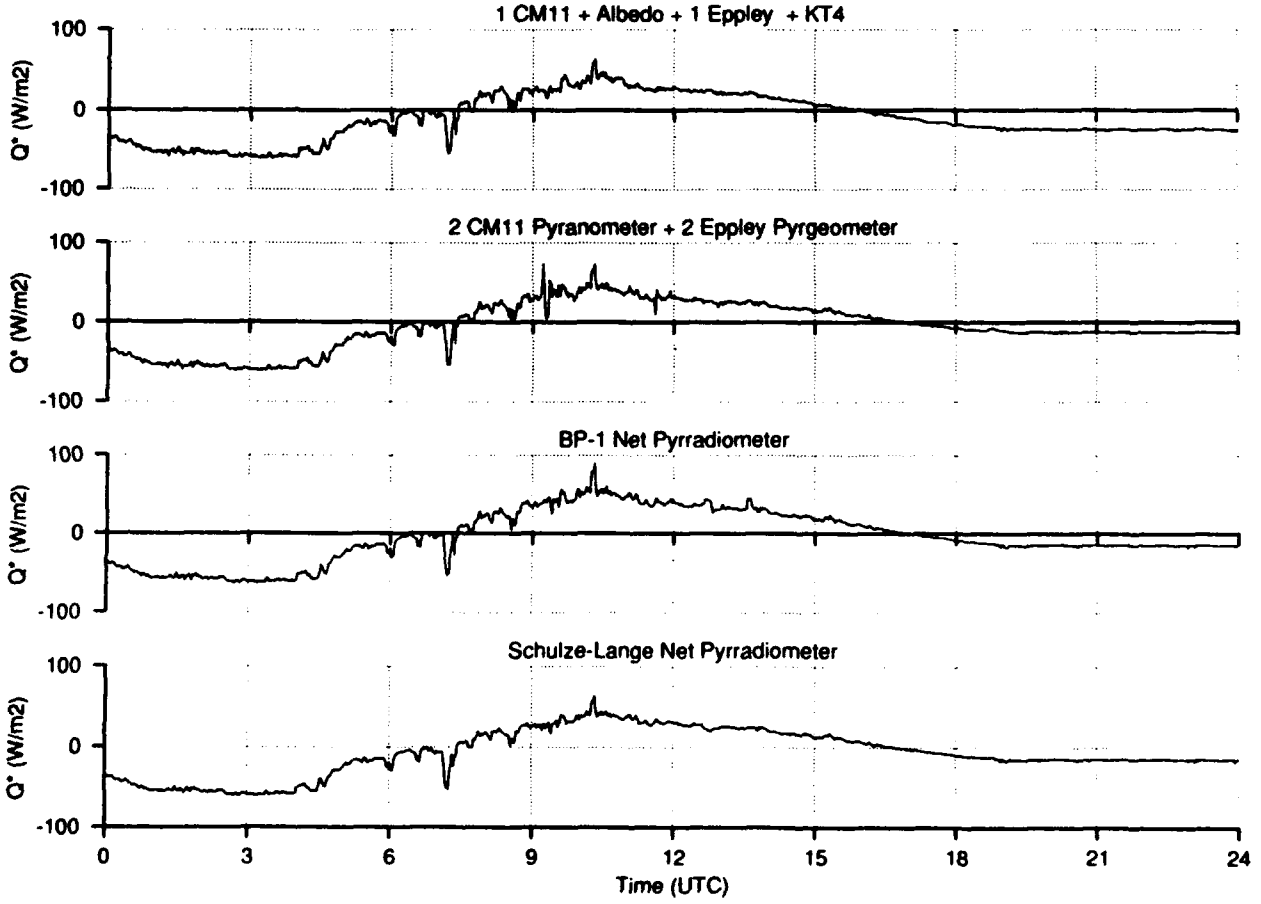


Figure 2. Example of radiation balances from 12 October measured with four different instrument systems.

Similar data analyses were carried out also for parts II and III of the cruise. Figure 5 shows the daily averaged values.

The data obtained during the drifting station are quite similar compared to the data described above. Again K* and L* are nearly equal but opposite. The surface energy balance is slightly more negative because of stronger turbulent fluxes. During the 9 days analyzed from the drifting station the ice thickness was constant at 60 cm. The energy imbalance of B=-34 W m^{-2} could readily change it by about 10 cm. But the observations indicated no ice thickness change. Thus B can be interpreted as a heat flux from the ocean. Only during the last part of the cruise was the surface energy balance positive, indicating the arrival of spring.

DISCUSSION

The results described above can be compared with data from the *Michail Somov* expedition in 1981 and the *Polarstern* cruise in 1986.

Energy balance measurements were made north of Maud Rise from 20 October to 14 November on *Michail Somov*. The last days of the *Akademik Fedorov* cruise covered the same area during the same time of the year as the *Somov* expedition. But in the mean *Akademik Fedorov* activities were more concentrated on the interior of the Weddell Gyre and took place about one month earlier.

Andreas and Makshtas [1985] reported albedo values typically between 50–60%. On the *Akademik Fedorov* generally higher values were observed (Figure 5). Obviously the albedo is less in spring than in late winter when surface melting is uncommon and cracks and leads are covered with thin ice.

The long-wave radiation balance (L*) measured in 1981 accounts for a mean loss of 10–15 W m^{-2}. On the *Akademik Fedorov* the loss was about two times larger, reflecting the fact that the sky was not as predominantly overcast as was observed in 1981. Under clear sky conditions the ratio of L⇓ to L⇑ ranged between 0.65–0.75. Due to the very clean and dry air these values are 10–15% lower than similar data from the Arctic Basin.

In the austral winter 1986 *Polarstern* activities were concentrated on oceanographic work along the Greenwich Meridian. Gordon and Huber [1990] reported a mean bulk mixed layer temperature 0.08°C above the freezing point leading to a mean heat flux to the ice of 22 W m^{-2}. This value fits quite well with the data obtained from the surface energy balance measurements on *Akademik Fedorov*.

Values for the oceanic heat flux found in the literature range between 2–20 W m^{-2}. Sea ice models such as that of Lemke et al. [1989] show that this uncertainty has only a minor effect on sea ice extent but a major effect on sea ice volume. Regarding the observations described above, 20 W m^{-2} seems to be more realistic than 2 W m^{-2}. Our result

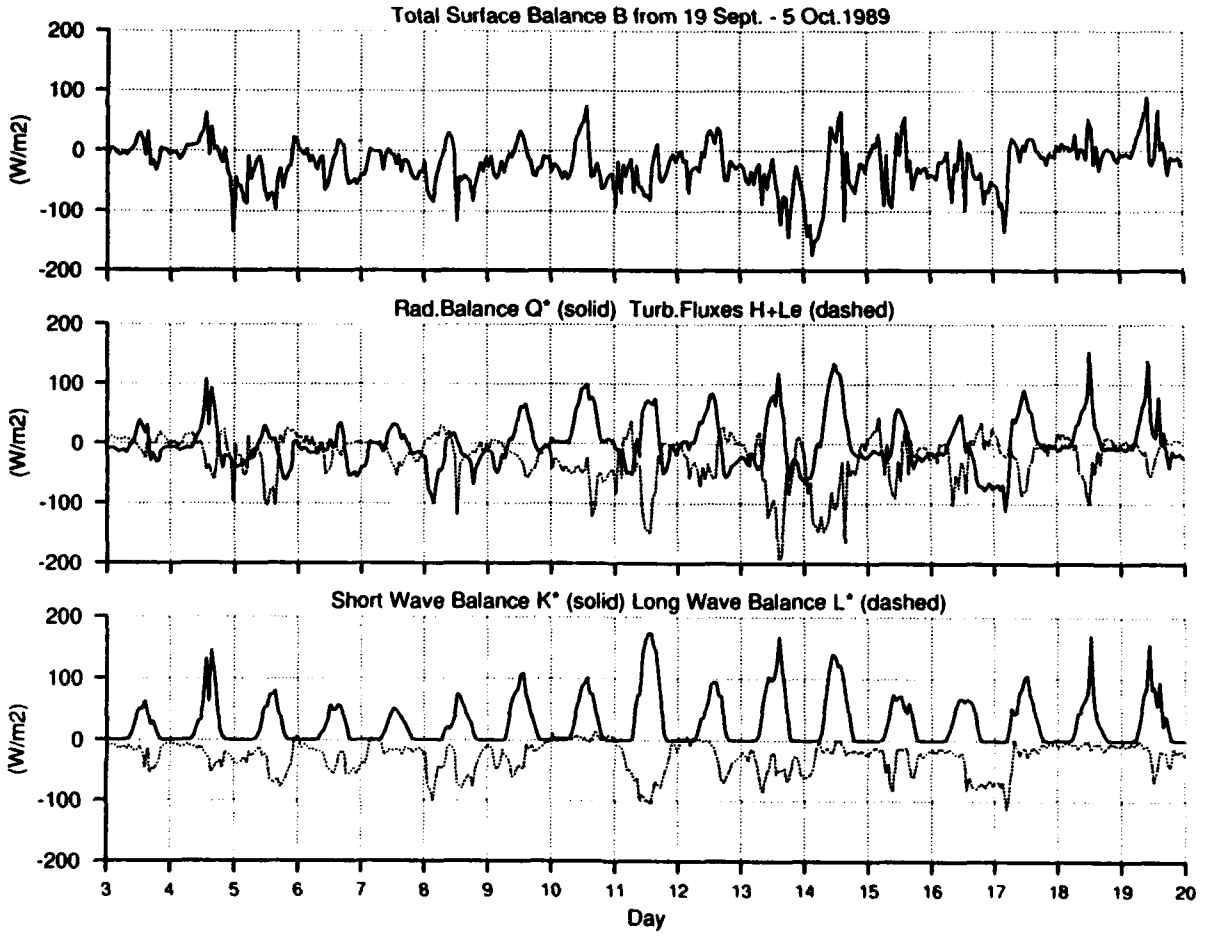


Figure 3. Time series of some components of the energy balance measurements made during part I of the cruise.

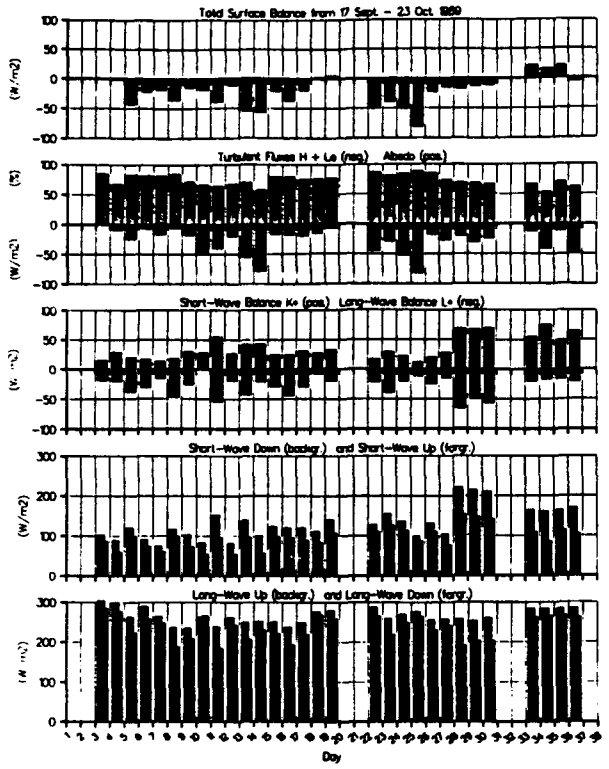


Figure 4. Mean energy balance components during part I of the cruise.

agrees with the annual heat flux of 19 W m^{-2} that Gordon and Huber [1990] derived from an analysis of a depression of oxygen saturation under the sea ice found in 1986.

CONCLUSION

Zero ice production and zero mean radiation balance can be regarded as a special feature of late winter in the area where the measurements took place.

The instantaneous radiation imbalances can amount to ±100 W m^{-2} (see Figure 3) but they are largely compensated by turbulent heat fluxes. A mean oceanic heat flux larger than 20 W m^{-2} seems to be more realistic than smaller values often used in numerical models.

Until now energy balance measurements have been carried out in the Weddell Gyre in late winter and in spring. Observations during ice formation seasons are still needed to achieve a better understanding of the physical processes controlling one of the most sensitive components of our climate system.

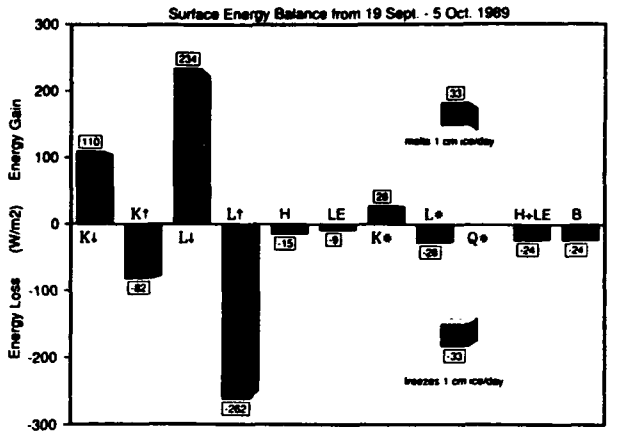


Figure 5. Daily averaged components of the energy balance for all three parts of the cruise.

ACKNOWLEDGMENTS

The data collection and analysis was supported by the Alfred-Wegener-Institute for Polar- and Marine Research (Bremerhaven, FRG) and the Arctic and Antarctic Research Institute (Leningrad, USSR). We thank all members of these institutes who made this joint expedition as successful and enjoyable as it was.

REFERENCES

Andreas, E. L., and A. P. Makshtas, Energy exchange over antarctic sea ice in the spring, *J. Geophys. Res.*, *90*, 7199–7212, 1985.

Gordon, A. L., and B. A. Huber, Southern ocean winter mixed layer, *J. Geophys. Res.*, *95*, 11655–11672, 1990.

Hibler, W. D., A dynamic thermodynamic sea ice model, *J. Phys. Oceanogr.*, *9*, 815–846, 1979.

Ivanov, B., and A. P. Makshtas, On the estimation of surface air parameters over sea ice by observation from moving vessel, *AARI Proceedings*, *406*, 139–145, 1986.

Lemke, P., W. B. Owens, and W. D. Hibler, A coupled sea ice–mixed layer–pycnocline model for the Weddell-Sea, *J. Geophys. Res.*, *95*, 9513–9525, 1990.

Maykut, G. A., and N. Untersteiner, Some results from a time dependent thermodynamic model of sea ice, *J. Geophys. Res.*, *76*, 1550–1575, 1971.

Walsh, J. E., The role of sea ice in climate variability: Theory and evidence, *Atmos. Ocean.*, *21*, 229–242, 1983.

The Partition of Thermal Energy in the Summertime Sea Ice–Ocean System

Michael Steele
Polar Science Center, Applied Physics Lab/University of Washington, Seattle, Washington, U.S.A.

ABSTRACT

The relative roles of bottom, side, and top melting on sea ice floes are investigated in a coupled sea ice–ocean numerical model. A new state parameter for sea ice, the mean caliper diameter, is defined in order to measure the lateral extent of ice floes. Observed distributions of this quantity in the Arctic will be presented. In this simple model, the ice cover is assumed to be composed of floes of a single thickness and diameter. As melting proceeds (due to atmospheric forcing), the diameter and thickness both decrease, which leads to a decrease in the areal coverage of ice. Several parameterizations for bottom and side melting are compared.

The results show that side wall melting is significant only for small floes of less than several hundred meters in diameter. Larger floes melt mostly from top and bottom surfaces. The standard ice–ocean models in use today parameterize these processes by dividing the atmospheric thermal forcing that enters the ocean through leads equally between bottom and side wall melting, which leads to overestimates of the amount of open water during the summer. This will in turn affect the amount of first-year ice that grows during the ensuing winter.

The model is a first step in assessing the partition of thermal energy in the sea ice–ocean system. Climatic variation of the atmospheric thermal input is likely to affect the three sea ice state parameters (thickness, diameter, and concentration) independently. Each parameter has different implications for exchange processes such as air–ocean heat transfer.

Ice Thickness and Vertical Heat Flux in the Arctic Ocean

J. S. Wettlaufer
Polar Science Center and Geophysics Program, University of Washington, Seattle, Washington, U.S.A.

N. Untersteiner
Department of Atmospheric Sciences, University of Washington, Seattle Washington, U.S.A.

ABSTRACT

Ice thickness and extent are controlled by the heat balances at the upper and lower surfaces of the ice. Observations of the surface heat balance suitable for driving and validating sea ice models are relatively abundant, while the scarcity of observations of the heat exchange at the ice–ocean interface has made that process a frequently invoked tuning parameter in numerical simulations of the sea ice cover. In a water column capped by a layer of ice, the heat flux, F_w, is generally either zero or directed upward. A downward heat flux is possible only when the far-field mixed layer is at or very near the freezing point, and a layer of low salinity water forms at the ice bottom (either from surface drainage or bottom melting). Since the early studies of the overall heat balance of the Arctic Basin (e.g., by Mosby and Tomfeev) it has been thought that F_w is synonymous with the heat lost by the Atlantic water along its circuit around the Arctic Basin. Badgley [1966] estimated that number to be 2 W m^{-2}, a value later supported by calculations with a thermodynamic ice model. While this value per se may still be approximately correct, the source of that heat flux is in question because: (a) it is not clear how much of the Atlantic water entering through Fram Strait is recirculated and exits into the Greenland Sea without traveling around the Arctic Basin; (b) the cooling of the Atlantic water may, at least in part, be the result of cold water entrainment along the Eurasian shelf; and (c) the estimated F_w in the central Arctic may not originate from the Atlantic water but from radiational heat stored in the upper ocean during summer and returned to the surface during autumn and winter.

In view of the importance of these questions for ice cover modeling under different climatic scenarios, it will be necessary to make year-round observations of F_w in several key locations. The technology to make such observations by automatic data buoys is available. A field study of F_w in the autumn of 1989 north of Svalbard is used to illustrate the need to overcome the scatter of point observations caused by the effects of ice morphology and sporadic events in the mixed layer.

AD-P007 307

Perennial Water Stratification and the Role of Basal Freshwater Flow in the Mass Balance of the Ward Hunt Ice Shelf, Canadian High Arctic

Martin O. Jeffries
Geophysical Institute, University of Alaska Fairbanks, Fairbanks, Alaska, U.S.A.

92-17989

Abstract

A pronounced perennial water stratification in Disraeli Fjord behind the Ward Hunt Ice Shelf on the north coast of Ellesmere Island is described. The ice shelf acts as a hanging dam at the mouth of the fjord and minimizes mixing between inflowing meltwater runoff and the seawater. Consequently, a 41-m-deep layer of low salinity water, interposed between a 2- to 3-m-thick fjord surface ice layer and deeper seawater, is impounded behind the ice shelf. Highly negative $\delta^{18}O$ values and high tritium activity in the low salinity water indicate it is derived primarily from snow-meltwater. Highly negative $\delta^{18}O$ values and high tritium values in a 5-m-thick basal ice layer in Hobson's Choice Ice Island, which broke off the East Ward Hunt Ice Shelf in 1982-83, might be evidence that basal accretion from freshwater flowing out of Disraeli Fjord below the ice shelf occurred prior to the calving. Using the known chronology of tritium occurrence in precipitation since 1952 and the measured levels in the basal ice, mean basal accretion rates of 96–141 mm yr^{-1} (water equivalent, w.e.) are calculated. The record of ablation and accumulation at the surface of the East Ward Hunt Ice Shelf for the period 1966–1982 shows an accumulated loss at the surface of 1.26 m (w.e.) at a mean annual rate of 74 mm yr^{-1}. Therefore, despite many consecutive warm summers with considerable surface melting and runoff, the calculated basal accretion exceeds the surface loss and the ice shelf has increased, or at least maintained, its thickness. The thickening has been possible because of the feedback system created by the location of the ice shelf across the mouth of the fjord, the resultant water stratification and the outflow of freshwater below the ice shelf.

INTRODUCTION

The north coast of Ellesmere Island in the Canadian High Arctic is the location of the most extensive ice shelves in the northern hemisphere. They originated about 3000–4000 years ago as multiyear landfast sea ice and from the seaward advance of grounded glaciers, which thickened further by a combination of surface snow and ice accumulation and basal accretion of fresh, brackish and sea ice. It is known that the ice shelves were once much more extensive than they are today when only relatively small, individual ice shelves occupy fjords and embayments after a significant period of disintegration this century [Koenig et al., 1952; Jeffries, 1987]. The causes of the massive disintegration are uncertain, but it is noteworthy that it occurred during a period when, according to the nearby Agassiz ice core record, the summers have been the warmest in 1000 years [Koerner and Fisher, 1990].

In numerous fjords and embayments where it is known there were once ice shelves there are now extensive areas of multiyear landfast sea ice (MLSI) as much as 25 years old and with undeformed thicknesses of 10 m. Structurally the MLSI comprises fresh, brackish and sea ice layers which are a proxy record of basal ice accretion and sub-ice water salinity variations, particularly frequent and widespread year-round water stratification of low salinity water layers interposed between the base of the MLSI and the underlying

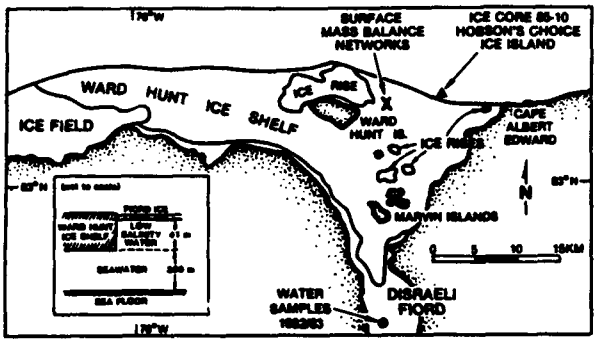


Figure 1. Map of the Ward Hunt Ice Shelf showing (1) its position across the mouth of Disraeli Fjord; (2) the location where water samples were obtained from the fjord in May 1982 and 1983; (3) the area from which Hobson's Choice Ice Island calved in 1982-83 and the approximate site of ice core 85-10; and (4) the location of the mass balance networks where measurements of surface melting and accumulation have been made since the 1960s. To the west of Disraeli Fjord the far western part of the ice shelf is firmly attached to the icefield, but between the ice field and the fjord the ice shelf is separated from the shore by a moat. The insert is a diagrammatic representation of the water stratification in the fjord where a surface layer of low salinity water is impounded behind the ice shelf to a depth equivalent of the ice shelf draft.

seawater [Jeffries and Krouse, 1988; Jeffries et al., 1989]. Under these conditions, double-diffusive ice growth processes, i.e., frazil/platelet ice growth in supercooled low salinity water layers, may lead to basal accretion rates exceeding surface ablation rates, i.e., a positive mass balance [Jeffries and Krouse, 1988; Jeffries et al., 1989].

Paradoxically, despite many consecutive warm summers in recent years the MLSI along the north coast of Ellesmere Island has been thickening steadily due to unusual feedback relationships between the ice and the ocean. This paper presents evidence for a similar phenomenon at the Ward Hunt Ice Shelf, the largest remaining ice shelf on the north coast of Ellesmere Island.

BACKGROUND

The Ward Hunt Ice Shelf has an area of about 440 km^2, a thickness of 40–50 m and lies across the mouth of Disraeli Fjord where it is anchored in place by islands and ice rises (Figure 1). The ice shelf has been a major source of ice islands (tabular icebergs). A massive calving in 1961-62 removed almost 600 km^2 of ice, about half the ice shelf [Hattersley-Smith, 1963]. The most recent calving event occurred in 1982-83 when about 40 km^3 of ice, including Hobson's Choice Ice Island, broke off the East Ward Hunt Ice Shelf (Figure 1) [Jeffries and Serson, 1983].

The ice shelf extends only about 10 km south of the Marvin Islands into Disraeli Fjord (Figure 1). The remainder of the 30-km-long fjord is covered year-round by 2- to 3-m-thick multiyear lake ice. The growth of lake ice rather than sea ice at the fjord surface can be attributed to the extreme stratification in the fjord where >40 m of low salinity water interposed between the thin surface ice and underlying seawater was discovered in the 1960s [Hattersley-Smith and Serson, 1967; Keys, 1978]. Keys [1978] subsequently concluded that meltwater flowing into the fjord from the surrounding land each summer was being impounded behind the ice shelf, which, acting as a hanging dam, minimized mixing between the freshwater and seawater thereby creating a perennial layer of low salinity water with a depth equivalent to the draft of the ice shelf (Figure 1).

Keys [1978] also reported frazil/platelet ice formation in the freshwater just above the halocline due to supercooling by the underlying seawater, a process called double-diffusive ice formation, and suggested that if the freshwater was flowing out of Disraeli Fjord below the ice shelf, such ice formation could contribute to basal accretion onto the ice shelf. Past accretion of brackish and sea ice from brackish and seawater respectively at the base of the southern and western parts of the ice shelf has been confirmed by ice core analysis [Lyons et al., 1971; Jeffries et al., 1988]. Ice core evidence for basal ice accretion from freshwater, and by implication basal freshwater flow, has been found only in the eastern ice shelf [Jeffries et al., 1988, 1991].

Prior to the initiation of annual measurements of surface ablation and accumulation in 1966 at mass balance stake networks on the East Ward Hunt Ice Shelf (Figure 1) there had been a net loss of the order of meters of ice due to melting at the surface since at least the beginning of the 20th century [Hattersley-Smith and Serson, 1970]. A continued net loss of ice was documented during the 1960s and 1970s, but, in the absence of any data on basal processes, it was not known whether the surface measurements were evidence of an actual reduction in ice thickness [Hattersley-Smith and Serson, 1970; Serson, 1979]. The melting and ice losses at the surface of the Ward Hunt Ice Shelf this century are consistent with other records of a mild climatic interval this century in the Canadian High Arctic [e.g., Koerner and Fisher, 1990]. As a consequence of the many consecutive warm summers, ice that had accumulated during previous, cooler climatic intervals has been lost [Jeffries et al., 1991].

This paper presents evidence for the continued ice shelf-induced, perennial stratification of Disraeli Fjord and examines the relationship between bottom ice accretion and surface ice losses in order to demonstrate how accretion from freshwater flowing out of the fjord beneath the ice shelf might be contributing to the thickening of the ice shelf despite the warm summer climate.

METHODS

In May 1982 and 1983, at a location in Disraeli Fjord about 5 km south of the ice shelf (Figure 1), water temperatures were measured with reversing thermometers attached to a Knudsen bottle, which collected water samples for later measurements of salinity, $^{18}O/^{16}O$ ratios and tritium activity. In September 1985, a 42-m-long, 100-mm-diameter ice core was obtained from the surface to the base of the thickest, shelf ice portion of Hobson's Choice Ice Island using a CRREL-type ice coring auger. The Specific Electrolytic Conductivity (SEC), $^{18}O/^{16}O$ ratios and tritium activity of melted core samples were subsequently measured. A full explanation of the history of surface ablation–accumulation measurements and procedures is given by Hattersley-Smith and Serson [1970].

For the fjord samples, the SEC of each water sample was measured, followed by the SEC of Standard Seawater (P95), using a conductivity meter. The practical salinity of the water samples is based on the ratio (R15) of the sample SEC to that of the Standard Seawater SEC. According to conven-

tion the salinity values are expressed as pure numbers. For the ice core samples, the SEC was measured without reference to Standard Seawater, since the level of dissolved impurities was too low to express meaningfully as salinity values.

The $^{18}O/^{16}O$ ratios were measured using a mass spectrometer. The oxygen isotopic composition is expressed as $\delta^{18}O$, the fractional difference in parts per thousand (per mil, o/oo) between the isotope abundance ratio ($^{18}O/^{16}O$) of the unknown sample and a standard (V-SMOW: Vienna–Standard Mean Ocean Water). The measurement accuracy of the $\delta^{18}O$ values is ±0.1 o/oo. V-SMOW represents the mean oxygen isotopic composition of the world's oceans and has a $\delta^{18}O$ value of -0.07 o/oo. On the other hand, the $\delta^{18}O$ values of precipitation are considerably more negative than those of seawater. For example, in early June the snowpack in the study area has a mean $\delta^{18}O$ value of -31.3 o/oo [Jeffries and Krouse, 1987].

The tritium activity was measured by direct liquid scintillation counting without prior enrichment. Tritium activity is expressed in Tritium Units (TU) where 1 TU represents one tritium atom per 10^{18} hydrogen atoms. The measurement accuracy of the tritium values is ±8 TU. Prior to 1952, precipitation tritium values were in the range 0–25 TU, but with the initiation of atmospheric thermonuclear bomb testing in 1952 precipitation tritium values increased two to three orders of magnitude, reaching a peak in 1963 [Gat, 1980].

LATE WINTER OCEANOGRAPHY OF DISRAELI FJORD

The salinity and $\delta^{18}O$ profiles (Figure 2) show that water in the fjord is highly stratified, with two distinct layers: (1) immediately below the 3-m-thick fjord surface ice cover there is a 41-m-deep layer of low salinity water (salinity range, 1.07 to 6.52) with highly negative $\delta^{18}O$ values ($\delta^{18}O$ range, -28.7 o/oo to -24.5 o/oo); and (2) a deeper layer of seawater (salinity range, 31.34 to 34.8) with $\delta^{18}O$ values close to zero ($\delta^{18}O$ range, -3.6 o/oo to 0.23 o/oo). Across the halocline, within a depth interval of 1 m, from 41 m to 42 m, salinity increases abruptly from 6.52 to 31.34 and $\delta^{18}O$ increases abruptly from -24.5 o/oo to -3.6 o/oo.

The highly stratified temperature profile is not illustrated, but the minimum temperatures in the low salinity and seawater layers are -0.52°C (41 m) and -1.7°C (45 m) respectively, and the temperature decrease across the halocline is 1.02°C, from -0.52°C (41 m) to -1.54°C (42 m). The stratification is also evident in the tritium profile; the low salinity layer has very high tritium values, from 127 TU to 215 TU, while the seawater layer has relatively low tritium values, from 0 TU to 39 TU (Figure 3).

The salinity and $\delta^{18}O$ values of the two water layers in Disraeli Fjord show that a layer of freshwater remains impounded in the fjord behind the ice shelf, interposed between the fjord surface ice and a deeper layer of seawater. The high tritium values and highly negative $\delta^{18}O$ values in the freshwater layer indicate that it is derived primarily from snow-meltwater. Since the water samples were obtained prior to the onset of snowmelt, the low salinity surface layer must be derived from previous years' meltwater runoff. Thus, the fjord remains perennially stratified.

BASAL ACCRETION AND SURFACE ABLATION ON THE EAST WARD HUNT ICE SHELF

The tritium activity levels and the $\delta^{18}O$ values in ice core 85–10 from Hobson's Choice Ice Island are illustrated in

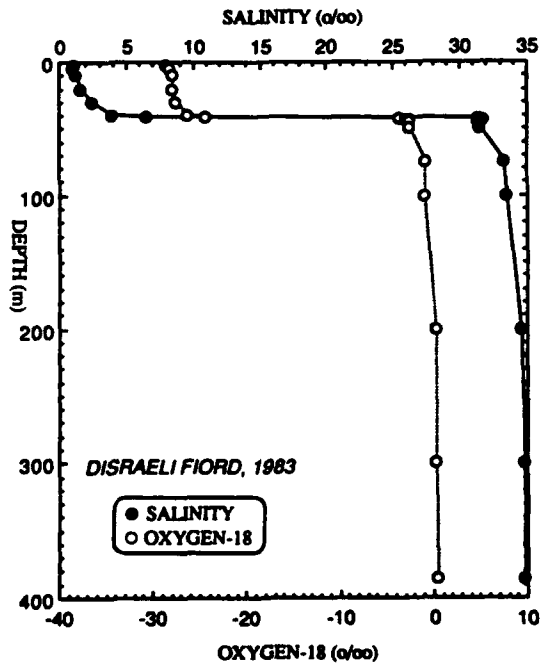


Figure 2. Salinity and $\delta^{18}O$ profiles in Disraeli Fjord, May 1983 showing the 41-m-deep layer of low salinity water at the surface of the fjord overlying deeper seawater.

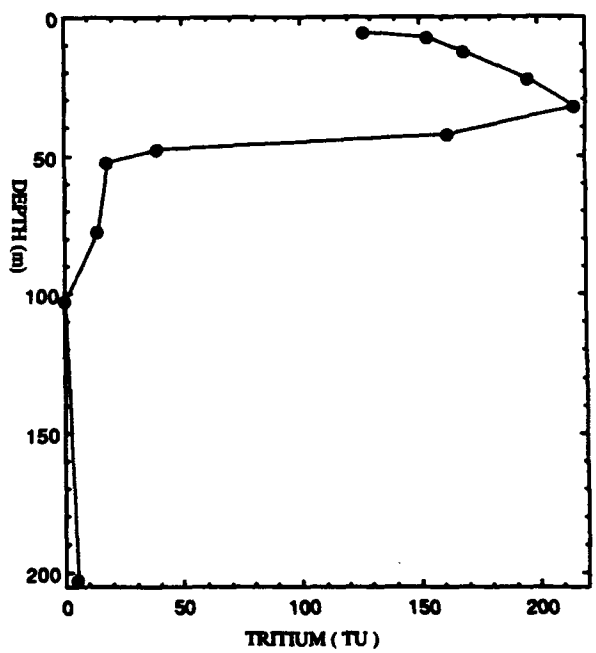


Figure 3. Tritium profile in Disraeli Fjord, May 1982 showing high, anthropogenic tritium levels in the surface low salinity layer in contrast to the low tritium levels in the deeper seawater.

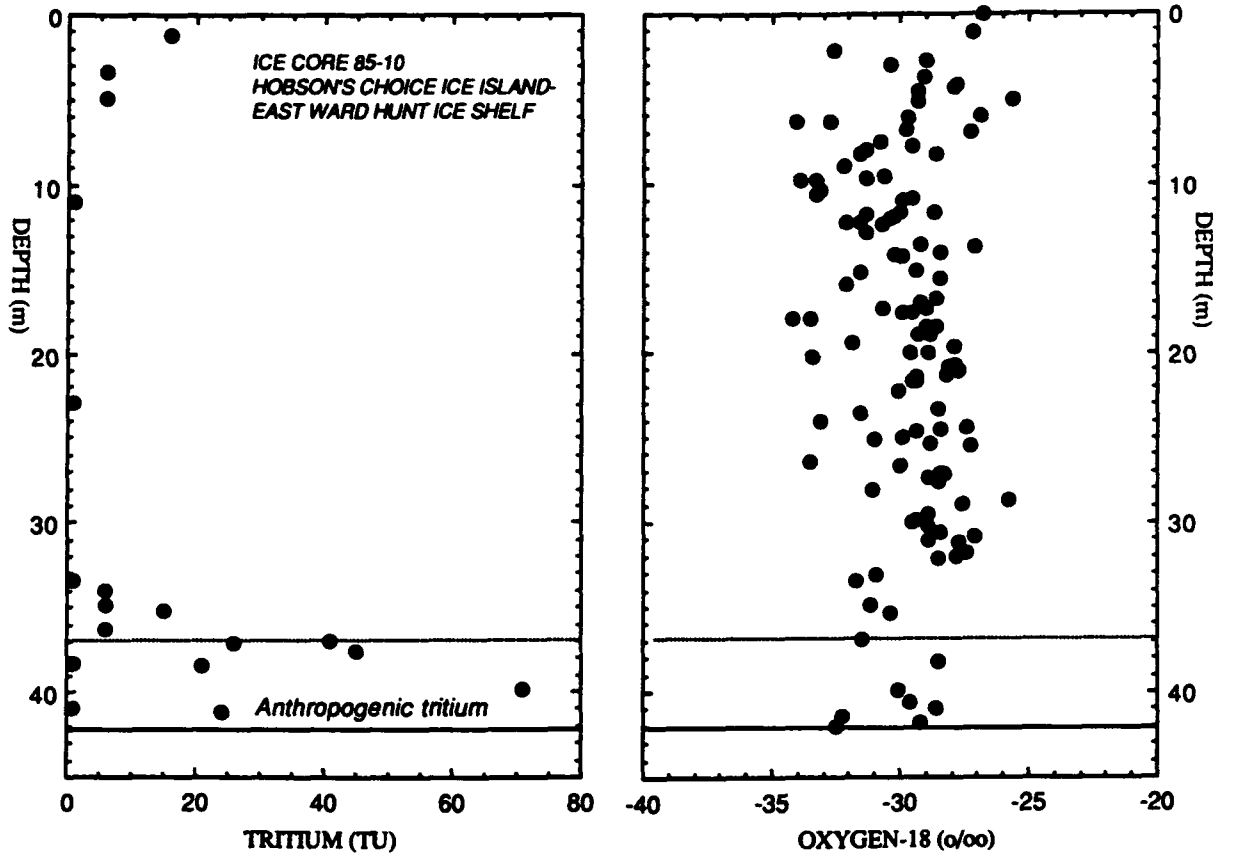


Figure 4. Tritium (left) and $\delta^{18}O$ (right) profiles in ice core 85-10 from Hobson's Choice Ice Island-East Ward Hunt Ice Shelf. The 5-m-thick ice layer with high tritium values at the base of the ice shelf is identified. The scatter in the $\delta^{18}O$ values is attributed to natural variability, since the scatter far exceeds the measurement accuracy (±0.1 o/oo) of each data point.

Figure 4. From the surface to the base of the shelf ice portion there are highly negative $\delta^{18}O$ values (mean, -29.6 o/oo; range -34.2 o/oo to -25.7 o/oo). There are considerable variations in the tritium activity. From the surface to a depth of 37 m tritium activity falls within pre-bomb, natural background levels, but the lowermost, 5-m-thick layer has high, anthropogenic levels of tritium, with a peak of 71 TU at 40 m (Figure 4a). The SEC values are not illustrated, but they show that all the ice has a very low level of dissolved impurities and a mean salinity <0.01 o/oo [Jeffries et al., 1988, 1991].

The ice core $\delta^{18}O$ values alone are evidence of ice derived directly and/or indirectly from precipitation. Structural analysis of the uppermost 37-m layer has shown that it comprises accumulated iced-firn, slush ice and lake ice resulting from the melting and refreezing of snow [Jeffries et al., 1991]. No structural data are available for the lowermost 5-m ice layer. However, the combination of high tritium levels and highly negative $\delta^{18}O$ values strongly suggests that it accreted at the base of the ice shelf from a layer of freshwater, with a significant snow-meltwater component, flowing below the ice shelf prior to the ice island calving in 1982-83. Disraeli Fjord is the most probable freshwater source [Jeffries et al., 1988; 1991].

The high tritium activity indicates the lowermost 5 m of ice must post-date 1952. Assuming a conservative basal ice density of 830 kg m^{-3} and that the ice began to accrete as early as 1952, a minimum mean annual basal accretion rate of 141 mm yr^{-1} (w.e., water equivalent) since 1952 is calculated. Assuming the same ice density, but that the 40 m tritium maximum (71 TU) represents 1963, when peak atmospheric tritium values occurred, a minimum mean annual basal accretion rate of 96 mm yr^{-1} (w.e.) since 1963 is calculated.

The record of ablation and accumulation variations at the mass balance networks on the East Ward Hunt Ice Shelf (Figure 1) for the period 1966–1988 is presented in Figure 5. There have been a few years with a positive balance, but these have been far exceeded by the many years of ablation. Consequently, there has been a cumulative loss of ice. Between 1966 and 1982 (the last measurement prior to the calving of Hobson's Choice) cumulative losses amounted to 1.26 m (w.e.) with a mean annual ablation rate of 74 mm yr^{-1}.

DISCUSSION

It is evident that there has been a significant amount of basal ice accretion on the East Ward Hunt Ice Shelf in recent years. Furthermore, this has occurred as melting has removed ice from the surface. If it is assumed that the mean annual surface ablation rate (74 mm yr^{-1}) calculated in the previous section applies to the entire post-1952 period, then mean annual basal accretion may have exceeded mean annual surface ablation by about a factor of 1.9 from 1952 to 1982; or by a factor of 1.3 from 1963 to 1982. The data thus suggests that the East Ward Hunt Ice Shelf has actually

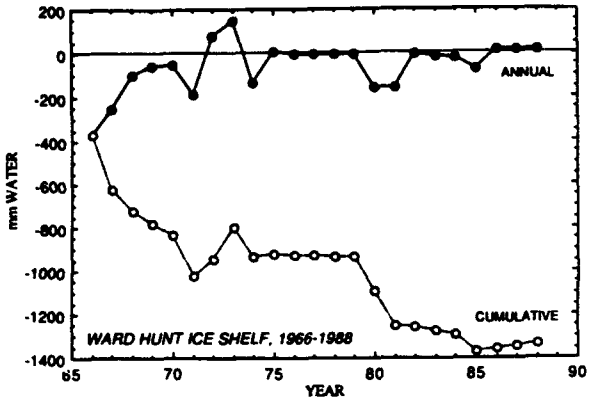


Figure 5. Interannual variations in surface ablation and accumulation, and cumulative losses at the mass balance networks on the East Ward Hunt Ice Shelf, 1966–1988. Each point represents the mean value of measurements made at a number of aluminum stakes set in the ice. The data are from Hattersley-Smith and Serson [1970], Serson [1979] and from my own records.

been slowly thickening in recent years despite surface ice losses. However, because the calculated annual rates of basal accretion and surface ablation are for unequal time intervals, and the basal accretion rates are subject to uncertainties, the possibility of a small negative mass balance cannot be eliminated.

The possible increase of the ice shelf thickness has occurred during a period of many consecutive warm summers. In a sense, it has been those warm summers and the resultant meltwater runoff into Disraeli Fjord that have been the cause of this apparent paradox of a positive mass balance during a mild climatic interval. The runoff has been held back behind the surviving ice shelf, which acts as a hanging dam and reduces mixing between the meltwater and seawater to maintain the perennial water stratification in the fjord. A slow outflow of freshwater below the ice shelf has then evidently contributed to basal ice accretion.

The magnitude of the stratification and the freshwater reservoir in Disraeli Fjord makes it the most plausible source of freshwater and basal ice accretion. The possibility that the basal accretion is very local and confined only to the area of the ice shelf from which Hobson's Choice Ice Island calved is discounted, since there is no known source of freshwater in this area sufficient to penetrate below the ice shelf and remain as a discrete layer from which basal accretion could occur.

Thus far, the discussion of mass balance has considered only the surface and base of the ice shelf, without reference to its lateral extent. If the calving of ice from the ice shelf front is taken into account, then the situation is somewhat different. There has been some growth of multiyear landfast sea ice at the ice shelf front since the massive calving of 1961-62, and it can be regarded as incipient ice shelf, but the MLSI is neither as thick nor as extensive as the lost shelf ice. Neither has the amount of ice that has accreted on the base of the ice shelf been of sufficient volume to make up for the massive ice losses. Thus, when ice calvings are considered, the Ward Hunt Ice Shelf has had a negative mass balance in recent years.

Nevertheless, the process of basal accretion of freshwater below an ice shelf during a time of warm summers and increased meltwater runoff from the adjacent land is significant and indicates that the effects of climatic ameliorations need not be entirely negative at high latitudes. Viewed from the perspective of global climatic change and its predicted amplification in the polar regions, the feedback situation at the Ward Hunt Ice Shelf and Disraeli Fjord offers an example of the resilience of the ice–ocean system in the face of environmental change and demonstrates that responses will vary according to time and place.

CONCLUSION

Disraeli Fjord on the north cost of Ellesmere Island in the Canadian High Arctic remains highly stratified year-round. Meltwater runoff from the surrounding catchment is impounded at the fjord surface to a depth of 41 m, roughly equivalent to the draft of the Ward Hunt Ice Shelf, which lies across the mouth of the fjord. The ice shelf acts as a hanging dam and minimizes mixing between seawater in the fjord and the inflowing meltwater. This unusual example of ice–ocean interaction creates a feedback system in which freshwater flowing out of the fjord contributes to basal accretion on the ice shelf at rates apparently in excess of surface ablation rates. The paradox of a slowly increasing ice shelf thickness during a period of many consecutive warm summers demonstrates that (1) responses to the predicted amplification of global climatic change at high latitudes may vary temporally and spatially, and (2) for floating ice of any type, a knowledge of basal processes is absolutely necessary if the response of the ice to environmental change is to be completely understood. This applies particularly to the antarctic ice shelves where the role of basal melting and/or basal accretion in the mass balance of the antarctic ice sheet is almost completely unknown.

ACKNOWLEDGMENTS

The assistance and support of the following organizations and individuals is greatly appreciated: The Polar Continental Shelf Project, Energy, Mines and Resources Canada; The Canadian Defence Research Establishment Pacific (DREP, Arctic Acoustics Section); Gulf Canada; Dome Petroleum; PetroCanada; The Arctic Institute of North America and the Department of Geography, University of Calgary; The U.S. Department of Energy, Morgantown Energy Technology Center; The Geophysical Institute, University of Alaska Fairbanks (Dr. S.-I. Akasofu, Director, and Dr. Bill Sackinger); Jim Poplin, Exxon Production Research Company; Dr. Roy Krouse, University of Calgary. Special thanks to Harold Serson who made available the original Ward Hunt Ice Shelf ablation and accumulation data record and who has contributed greatly to the success of my work since 1982.

REFERENCES

Gat, J. R., The isotopes of hydrogen and oxygen in precipitation, in *Handbook of Environmental Isotope Geochemistry, Vol. I, The Terrestrial Environment*, edited by P. Fritz and J. Ch. Fontes, pp. 21–47, Elsevier Scientific Publishing Co., Amsterdam, 1980.

Hattersley-Smith, G., The Ward Hunt Ice Shelf: recent changes at the ice front, *J. Glaciol.*, *4*, 415–424, 1963.

Hattersley-Smith, G., and H. V. Serson, Ice-dammed bodies of water in northern Ellesmere Island, Extended abstract, International Union of Geodesy and Geophysics, International Association of Scientific Hydrology, General Assembly of Bern, 1967.

Hattersley-Smith, G., and H. V. Serson, Mass balance of the Ward Hunt Ice Rise and Ice Shelf: a 10 year record, *J. Glaciol.*, *9*, 247–252, 1970.

Jeffries, M. O., The growth, structure and disintegration of arctic ice shelves, *Polar Record*, *23*, 631–649, 1987.

Jeffries, M. O., and H. R. Krouse, Snowfall and oxygen isotope variations off the north coast of Ellesmere Island, N.W.T., Canada, *J. Glaciol.*, *33*, 195–199, 1987.

Jeffries, M. O., and H. R. Krouse, Salinity and isotope analysis of some multiyear landfast sea ice cores, northern Ellesmere Island, Canada, *Ann. Glaciol.*, *10*, 63–67, 1988.

Jeffries, M. O., and H. V. Serson, Recent changes at the front of the Ward Hunt Ice Shelf, *Arctic*, *35*, 542–544, 1983.

Jeffries, M. O., W. M. Sackinger, H. R. Krouse, and H. V. Serson, Water circulation and ice accretion below Ward Hunt Ice Shelf (northern Ellesmere Island, Canada) deduced from salinity and isotope analysis of ice cores, *Ann. Glaciol.*, *10*, 68–72, 1988.

Jeffries, M. O., H. R. Krause, W. M. Sackinger, and H. V. Serson, Stable isotope ($^{18}O/^{16}O$) tracing of fresh, brackish and sea ice in multiyear landfast sea ice, Ellesmere Island, Canada, *J. Glaciol.*, *35*, 9–16, 1989.

Jeffries, M. O., H. V. Serson, H. R. Krouse, and W. M. Sackinger, Ice physical properties, structural characteristics and stratigraphy in Hobson's Choice Ice Island and implications for the growth history of the East Ward Hunt Ice Shelf, Canadian High Arctic, *J. Glaciol.*, 1991, In press.

Keys, J., Water regime of Disraeli Fjord, Ellesmere Island, *DREO Report No. 792*, Canada, Department of National Defence, Research and Development Branch, Defence Research Establishment Ottawa, 1978.

Koenig, L. S., K. R. Greenaway, M. Dunbar, and G. Hattersley-Smith, Arctic ice islands, *Arctic*, *5*, 67–103, 1952.

Koerner, R. M., and D. A. Fisher, A record of Holocene summer climate from a Canadian high-Arctic ice core, *Nature*, *343*, 630–631, 1990.

Lyons, J. B., S. M. Savin, and A. J. Tamburi, Basement ice, Ward Hunt Ice Shelf, Ellesmere Island, Canada, *J. Glaciol.*, *10*, 93–100, 1971.

Serson, H. V., Mass Balance of the Ward Hunt Ice Rise and Ice Shelf: an eighteen year record, *Technical Memorandum No. 79-4*, Department of National Defence, Research and Development Branch, Defence Research Establishment Pacific, 1979.

The Influence of the Hydrologic Cycle on the Extent of Sea Ice with Climatic Implications

K. G. Dean and J. P. Gosink
Geophysical Institute, University of Alaska Fairbanks, Fairbanks, Alaska, U.S.A.

T. Weingartner and D. Musgrave
Institute of Marine Science, University of Alaska Fairbanks, Fairbanks, Alaska, U.S.A.

ABSTRACT

Analysis techniques and models are being developed to provide a basis to investigate the role of the hydrologic cycle on the extent of sea ice throughout the Arctic Basin and hence its net influence on regional as well as global climate. A predicted global climatic warming may have a pronounced effect on the Arctic environment including a decrease in the extent of sea ice. This will affect the fluxes of heat and moisture transferred from the ocean to the atmosphere in the region, as well as the arctic marine ecosystem. Rivers are an important source of thermal energy and fresh water to this marine environment. The magnitude of the influence of the rivers is being assessed in a limited region offshore of Alaska and Canada (Mackenzie River). This region was chosen for logistical reasons and because of the availability of supporting field data.

Two numerical models are being developed to assess the effect of the hydrologic cycle on the break-up and formation of sea ice, and to evaluate the associated heat and moisture fluxes at the atmosphere–ocean–sea ice interface. A break-up model will simulate the river discharge as a fresh water plume which provides sensible heat to the nearshore sea ice–ocean environment, and affects the radiation budget of the sea ice by significantly altering its albedo. The second model is a mixed-layer model of the oceanic salinity–temperature regime to predict the initial formation of the sea ice cover as a function of late summer oceanic stratification and autumn meteorological conditions.

Satellite imagery, hydrologic field measurements and meteorological data will be used for the calibration and testing of the models. The satellite imagery provides information on the extent of sea ice, its rate of retreat, surface temperature of ice and river discharge, ice and water albedo and the trajectory of the discharge plume. Hydrologic data include discharge rates, water temperature, concentration of suspended sediments and salinity. Meteorological data include air temperature, humidity, solar energy, wind velocity and wind direction. After calibration, it is expected that the models will provide a useful tool for the assessment of the effect of extrapolated changes in hydrologic regime upon the coastal regions of the Arctic.

Water Mass Formation at High Latitudes

S. Hakkinen and G. L. Mellor
Princeton University, Princeton, New Jersey, U.S.A.

ABSTRACT

Water mass formation in the high latitude ocean is studied using a three-dimensional, coupled ice–ocean model and the Mellor–Yamada 2.5 level turbulence closure scheme. The snow–ice system is represented by a 3-level model. The coupled model is forced by specified strong winds and surface cooling.

In the Greenland Sea marginal ice zone, convection can take place via ice edge upwelling, which can bring warm and saline waters to the surface. Influence of the ice cover and of the topography in pre-conditioning and selecting the location of deep convection are found to be relevant. In ice-covered areas such as in the Eurasian Basin, the upwelling type of ventilation of deeper water masses is not possible even though its deep water renewal rate is comparable to the Greenland Sea renewal rates. Here, two other deep water sources and their relative importance are considered: the effect of eddies separating from the West Spitsbergen Current and the effect of salty shelf waters.

AD-P007 308

Tracing Upper Waters in the Arctic Ocean

E. Peter Jones
Department of Fisheries and Oceans, Bedford Institute of Oceanography, Dartmouth, Nova Scotia, Canada

Leif G. Anderson
Department of Analytical and Marine Chemistry, University of Goteborg, Goteborg, Sweden

92-17990

ABSTRACT

We report results from the 1987 F.S. *Polarstern* cruise to the Nansen Basin that begin to address questions regarding how global climate change might affect the Arctic. Before the effects of global change can be assessed, the sources of upper waters must be determined and their circulation patterns mapped. In surface water, total carbonate concentrations distinguish between a northern fresh water component, whose origin is river runoff, and a southern freshwater component, whose origin is sea ice meltwater. Below the surface layer, the halocline in the Nansen Basin has the same unique nitrate–oxygen characteristic, "NO," as the lower halocline in more central regions. The earlier speculation that this water forms in the Barents–Kara Sea region is confirmed. We hypothesize that some of this water must flow east and north from this region to central regions, eventually following the Polar branch of the Transpolar Drift and exiting through Fram Strait. Some can be traced in a general way flowing west directly to Fram Strait where the Polar and Siberian branches meet and flow into the Norwegian–Greenland Sea.

INTRODUCTION

In one important scenario, the Arctic Ocean could play a role in global climate change through changes in fresh water outflow that would change global thermohaline circulation by influencing deep convection in the North Atlantic [Aagaard and Carmack, 1989]. Many oceanographers believe, however, that while the Arctic Ocean climate will be driven by global changes, the Arctic Ocean itself will not have a major influence on global climate. Given the large changes predicted in the Arctic regions by global simulations [e.g., Hansen et al., 1988] and how these changes will affect large and economically important areas surrounding the Arctic Ocean, the problem of Arctic climate change is significant.

The major questions for the Arctic Ocean are: What processes contribute to its present cold and dry climate and how might a changing climate affect these processes? We are just beginning to address the first question and so far can only speculate on the second. Before we can predict (via models) what changes may occur as a result of global processes, we must improve our understanding of the Arctic Ocean hydrography.

The Arctic Ocean, in contrast to most world oceans, does not have large open borders for easy exchange of water with the global ocean (Figure 1). Its main exchange with other oceans is through Fram Strait, where water of Atlantic origin flows in and Arctic Ocean water flows out. In addition, some surface water of Pacific origin enters through Bering Strait over a very shallow sill and some Arctic Ocean Surface Water exits through the Canadian Archipelago.

A second critical characteristic of the Arctic Ocean is its ice cover, more or less constant in central regions and seasonal near the coasts. River runoff is particularly significant in the formation of this ice. Without this source of fresh water, the Arctic Ocean ice cover could be much reduced [e.g., Stigebrandt, 1981]. Ice formation and transport are closely intertwined with heat and salt budgets, which are a major factor in driving ocean circulation and hence in determining of climate. In an open Arctic Ocean, heat and moisture fluxes that are now impeded by ice cover would almost certainly occur on a considerable scale.

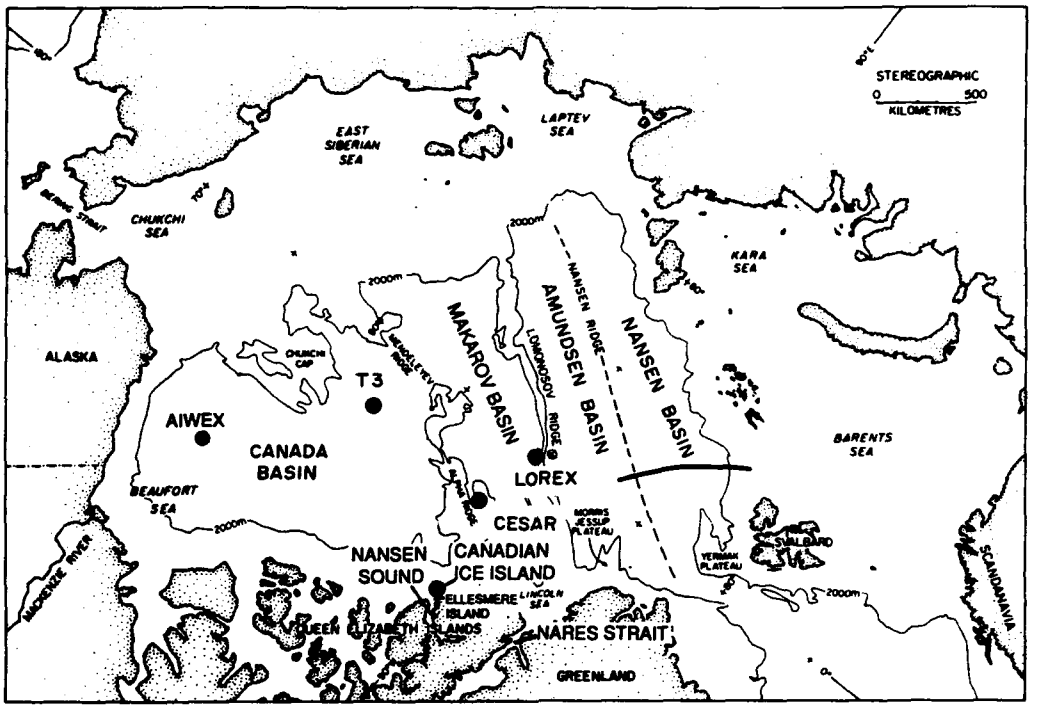


Figure 1. The Arctic Ocean showing Ice Camps at which modern oceanographic measurements have been made. The historic cruise of F.S. *Polarstern* crossed the Nansen Basin approximately along 35°E to 86°N.

A third critical characteristic of the Arctic Ocean is its density structure. Fresh water from rivers and brine production during ice formation over the continental shelves play a large role in determining the density structure. The continental shelves are unusually large for an ocean basin, comprising about one-third of the total area of the Arctic Ocean and including nearly all of the area that undergoes seasonal variation in ice cover. Shelf processes produce the strong density gradient and many of the chemical characteristics of the upper waters of Arctic Ocean. Shelves are one of the dominating influences on the climate of the Arctic Ocean. There is, for example, enough heat in the relatively warm Atlantic layer under the halocline to melt the surface ice, but this water is isolated from the surface by the strong density gradient which prevents such mixing.

RESULTS AND DISCUSSION

The water mass characteristics of the upper waters of the central Arctic Ocean (above 700 m) have been described by several authors [e.g., Kinney et al., 1970; Moore et al., 1983; Jones and Anderson, 1986; Anderson et al., 1990] and are briefly summarized as follows. In the central Arctic Ocean near the North Pole in the Amundsen and Makarov Basins and in the Canada Basin, these waters can be divided into a surface mixed layer, upper halocline water, lower halocline water and the Atlantic layer (Figure 2).

The origins of the water in the surface mixed layer have not been ascertained unambiguously. From ice drift patterns we presume the surface mixed layer in much of the central region to be water from the Bering Sea (ultimately of Pacific origin) that contains sea ice meltwater and runoff from Siberian rivers. On the Eurasian side, especially in the Nansen Basin, the surface mixed layer likely contains Atlantic water mixed with sea ice meltwater and river runoff [Rudels, 1989]. Where the boundary lies between these has not yet been determined. The upper halocline water in central regions is also of Pacific origin but modified in the Chukchi–East Siberian–Laptev Sea region [Jones and

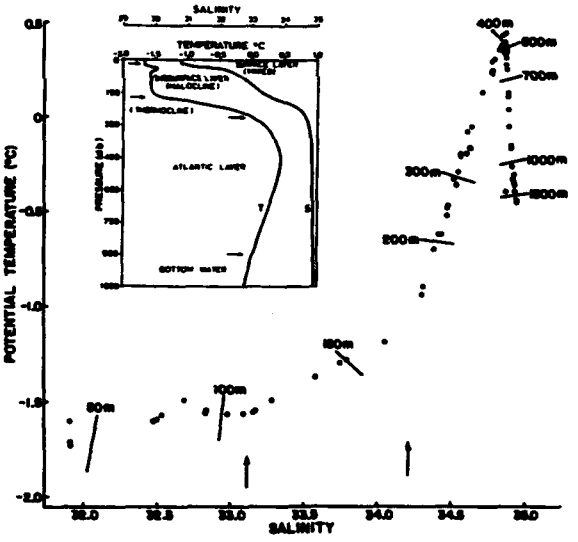


Figure 2. Temperature vs. salinity at the CESAR Ice Camp [after Jones and Anderson, 1986] with insert showing typical temperature and salinity profiles from the central Arctic Ocean [after Melling and Lewis, 1982]. High values of total carbonate from river runoff are associated with the surface layer. The nutrient maxima (silicate, phosphate, nitrate, carbonate) and oxygen minimum are associated with the upper halocline at S = 33.1 and the NO minimum is associated with S = 34.2. Relatively high temperatures characterize the Atlantic layer.

Anderson, 1986]. It has a prominent nutrient maximum at a salinity of 33.1. The lower halocline water, of Atlantic origin modified in the Barents–Kara–Laptev Sea region [Jones and Anderson, 1986], has a salinity near 34.2 and is identified by a minimum in NO. The Atlantic layer is identified by a temperature maximum ranging from above 2°C along the northern Barents Sea shelf break to values near 0.5°C in the central Arctic Ocean. This temperature maximum pattern has been explained by the cyclonic circulation of the Atlantic layer with the loss of heat to waters above and below within the Arctic Ocean [e.g. Aagaard et al., 1985].

The surface layer circulation has been inferred from tracking ice drift [e.g., Colony and Thorndike, 1984]. The sea ice drift pattern clearly resolves two general features: a large anticyclonic gyre over the Canadian Basin (the Beaufort gyre), and the Transpolar Drift, which begins in the Beaufort gyre, crosses over the North Pole, and leads into Fram Strait [e.g., Gordienko and Laktionov, 1969; Colony and Thorndike, 1984; Pfirman et al., 1989]. Below the surface layer, we have a moderately good idea of where the water comes from but we know only vaguely how it moves [e.g., Moore et al., 1983; Perkin and Lewis, 1984; Aagaard et al., 1985; Jones and Anderson, 1986].

The circulation of the surface and upper waters of the Arctic Ocean can be traced using the differing chemical constituents and concentrations in the water masses themselves. Measurements of chemical constituents in the Arctic Ocean using modern techniques have been obtained from ice camps [e.g., Moore et al., 1983; Jones and Anderson, 1986; Anderson and Swift, 1990]. In 1987, the German icebreaker, F.S. *Polarstern*, completed the first full depth, multi-tracer oceanographic section across the Nansen Basin in the Arctic Ocean [Anderson et al., 1989]. These ice camp and icebreaker measurements form the basis of the following discussion.

The distributions of temperature, salinity, total carbonate (normalized to a salinity of 35 in order to remove effects due to salinity changes, $C_t(35) = 35C_t/S$), and NO are shown in sections of the upper 500 meters along the most easterly stations of the cruise track (Figure 3). NO is a conservative property defined by Broecker [1974] as being the sum of the oxygen concentration and nine times nitrate concentration ($NO = [O_2] + 9*[NO_3^-]$). The temperature section shows the near-freezing surface water and the warm core of inflowing water of Atlantic origin. These same features are also reflected in the salinity section. The normalized total carbonate shows a general tendency of increasing values from the south to the north, with a distinct maximum in the northern surface water. The NO section shows a general trend of decreasing values towards the surface. Superimposed on the general trend are two NO minima around 150 meters depth north of 83°N–84°N.

The high normalized total carbonate values to the north of the section can only be explained by inputs of Siberian river water [Anderson and Dyrssen, 1981; Anderson et al., 1990]. These higher values are an indication that the Transpolar Drift describes the flow of the surface water below the ice layer and that it includes Siberian river runoff as the main fresh water source. Furthermore, the lower total carbonate concentrations south of 84°N–85°N indicate that the river runoff into the Kara Sea (and to a lesser degree also into the Barents Sea) enters the Nansen Basin well east of our investigation area. This also means that the surface water south of 84°N–85°N in our section is of rather local origin, formed from Atlantic water passing through Barents Sea and mixing with sea ice melt water in the northern Barents Sea and southern Nansen Basin. It is also possible that Atlantic water, while mixing with sea ice melt water, penetrates into the Kara Sea and then enters the Nansen Basin without mixing with any river runoff.

The two minima in the NO section near a depth of 150 m have very nearly the same concentrations and are therefore treated as being part of the same water mass. This minimum NO water mass is spread further to the south than the high total carbonate surface layer. The minimum NO values, about 400 mM, found in this water mass are very close to those of the lower halocline at ice station CESAR, [Jones and Anderson, 1986]. Jones and Anderson [1986] hypothesized that the lower halocline water is formed in the Barents and Kara Seas, distinguishing it from the upper halocline water which is formed in the Chukchi and East Siberian Seas.

Our findings in the Nansen Basin are consistent with the hypothesis regarding the formation areas for the upper and lower halocline water in two respects [Jones and Anderson, 1986]. First, the low NO water is found more to the south and through a much larger part of the section than is the water containing significant river runoff. This indicates that at least part of the formation area is limited to a region of the Barents and Kara Seas where no river runoff signal exists. Second, there was no sign of any nutrient maximum in water with salinity near 33.1, the indicator of the upper halocline water, at any station in the Nansen Basin section. This observation together with the presence of upper halocline water in the Beaufort gyre [Kinney et al., 1970; Moore et al., 1983; Jones and Anderson, 1986] and in the western part of Fram Strait [Anderson and Dyrssen, 1981] denotes a merging of two branches of the Transpolar Drift. The existence of these branches is not readily apparent from sea ice drift in the surface water, which shows a fairly uniform general flow towards Fram Strait [Colony and Thorndike, 1984], although earlier work [Gordienko and Laktionov, 1969] suggested various branches feeding into the Transpolar Drift just north of Fram Strait.

The absence of any sign of water with a nutrient maximum at a salinity near 33.1 shows that the upper halocline water in the Beaufort gyre and the flow of upper halocline water towards Fram Strait occur to the north of the Nansen Basin section. This is a further indication that the upper halocline water is formed well to the east of this region, likely, as earlier postulated, in the Chukchi–East Siberian Sea region. Since the Nansen Basin section did not extend far enough north to detect the upper halocline water, a clear boundary cannot be specified. One can suggest, however, that the boundary is in the region somewhat to the north of the Nansen–Gakkel Ridge, since even though the Nansen–Gakkel Ridge rises only to a depth of about 3000 m, there is evidence that the currents above it up to the surface are bathymetrically driven [Anderson et al., 1989].

The absence of water with low NO south of station 340 can be explained by the flow of this water from the formation area. The water in the Barents Sea that would form the lower halocline water of the central Arctic Ocean does not exit north between Svalbard and Franz Josef Land, but

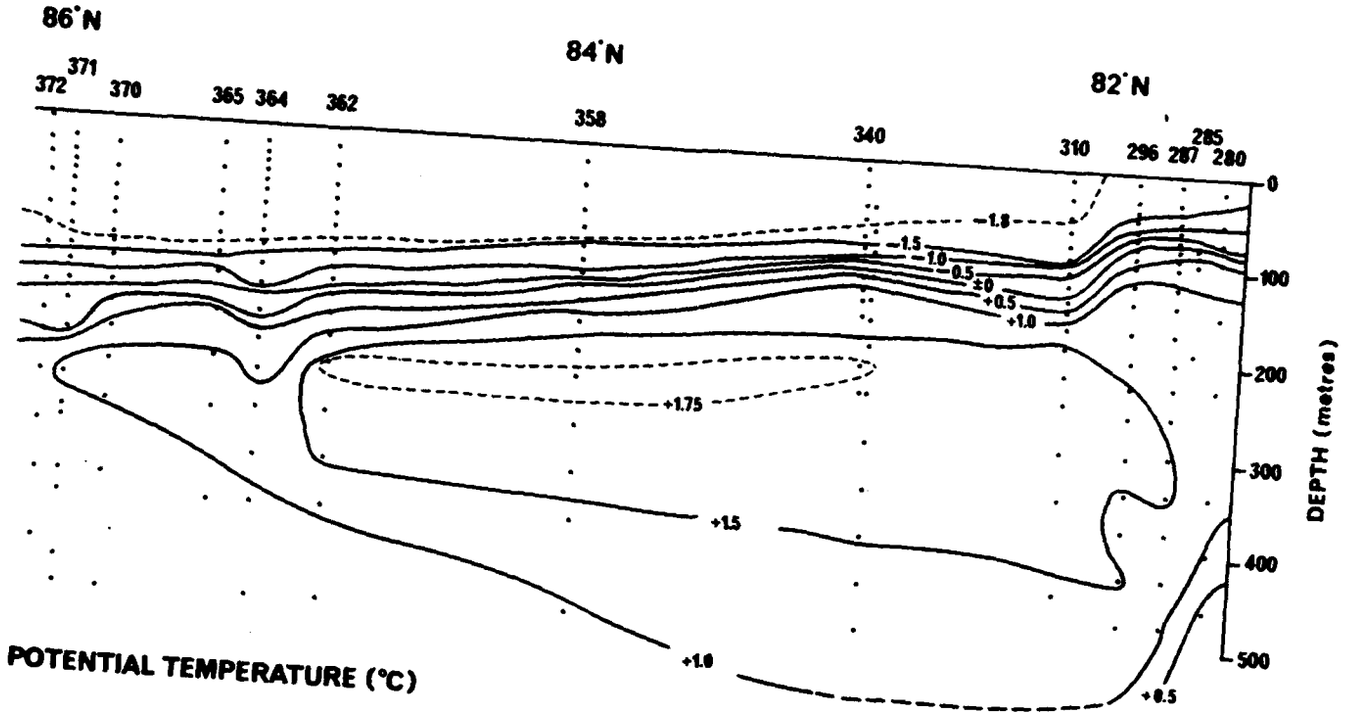


Figure 3(a). Sections of the top 500 m along the eastern stations indicated in Figure 1: Potential Temperature.

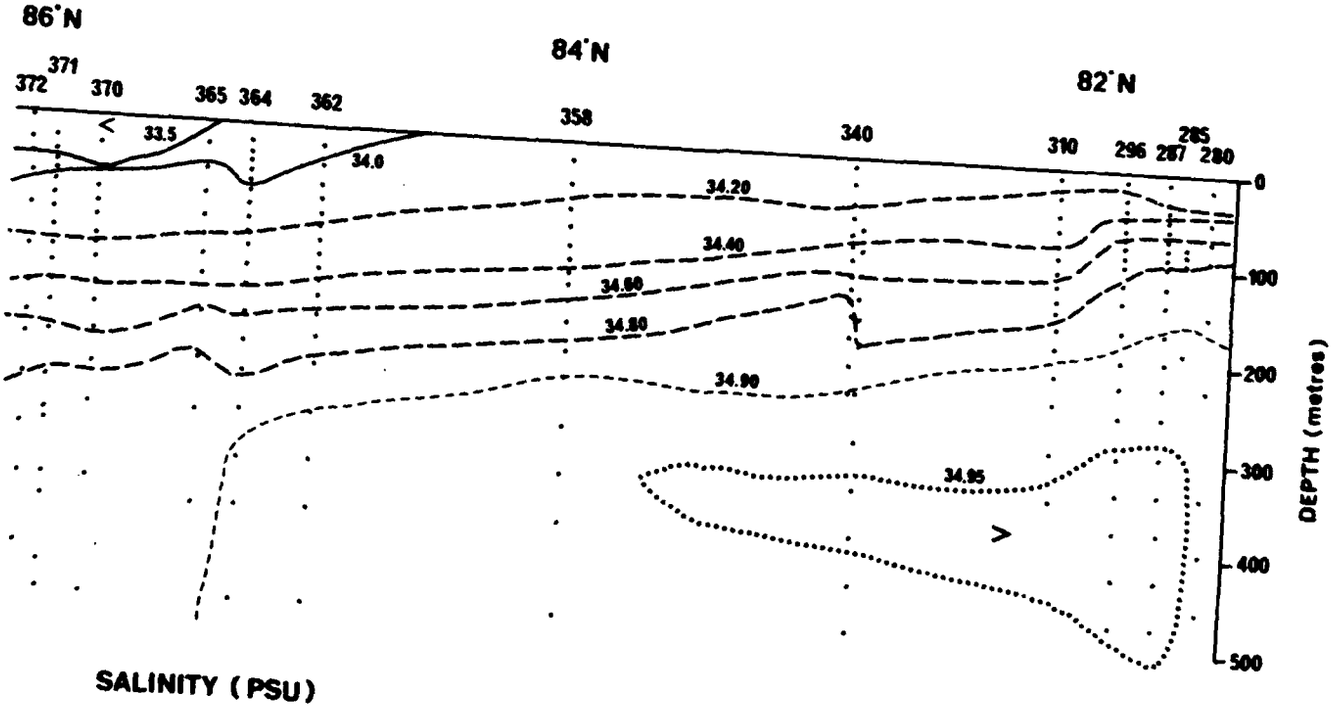


Figure 3(b). Sections of the top 500 m along the eastern stations indicated in Figure 1: Salinity.

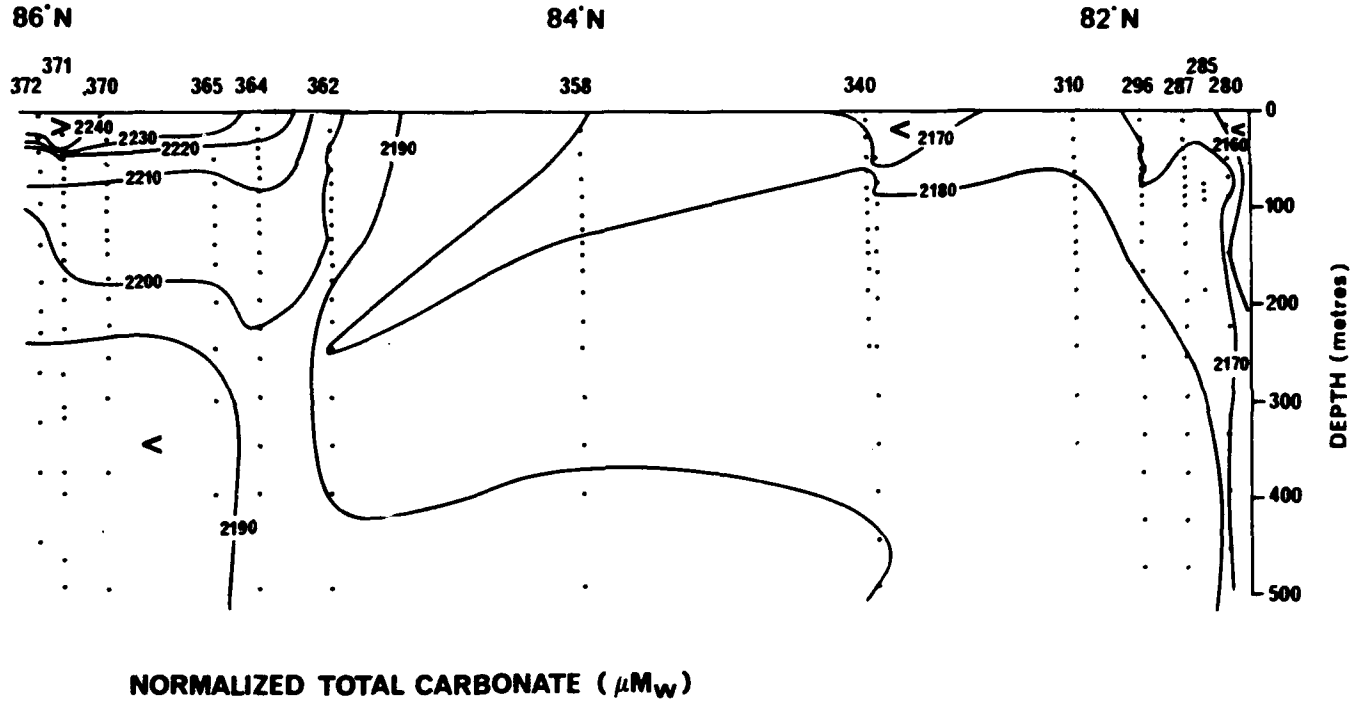


Figure 3(c). Sections of the top 500 m along the eastern stations indicated in Figure 1: Normalized Total Carbonate, $C_t(35)$.

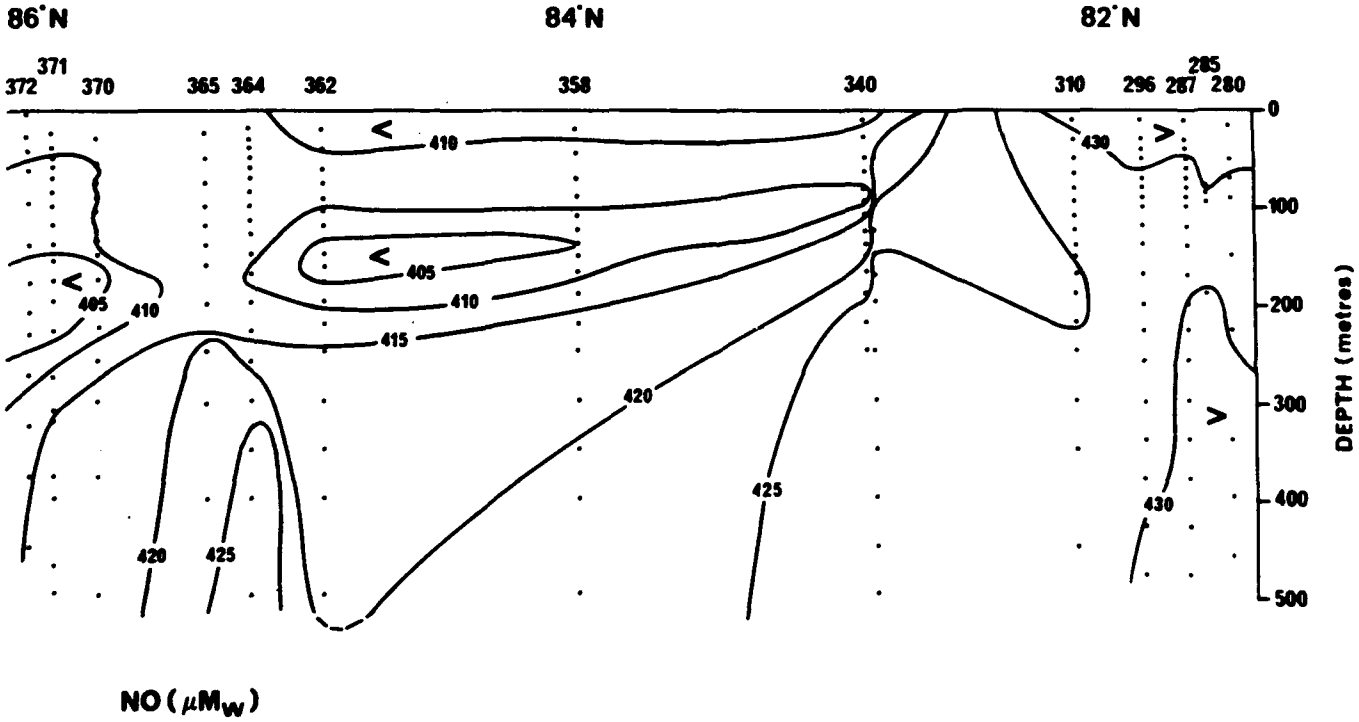


Figure 3(d). Sections of the top 500 m along the eastern stations indicated in Figure 1: NO.

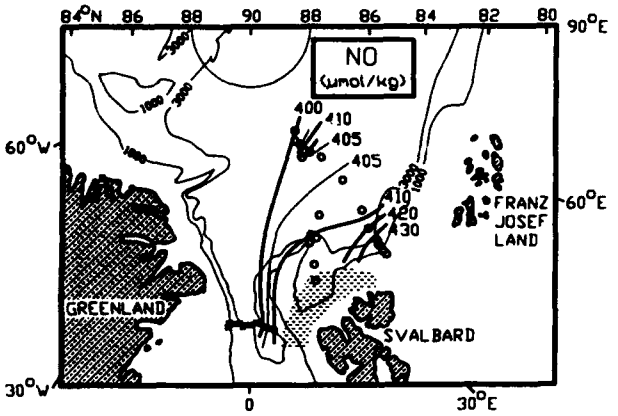
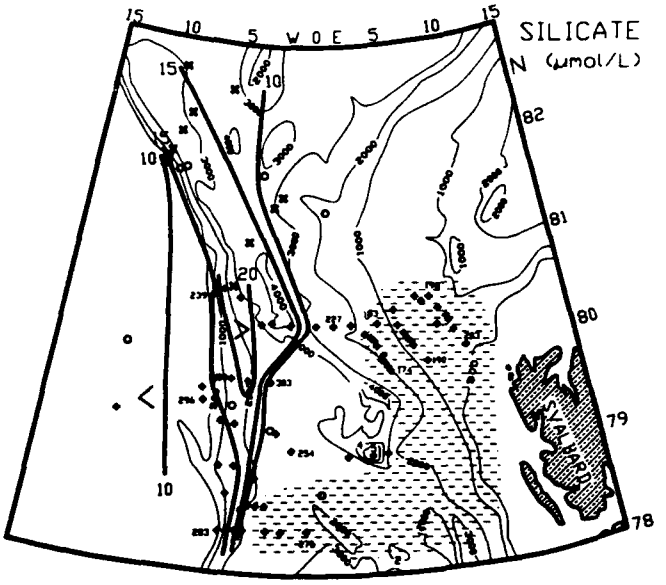


Figure 4. Distribution of NO along the salinity surface 34.4. The open circles denote stations from the 1987 Polarstern Nansen Basin cruise and x's denote stations from the MIZEX-84 Polarstern cruise. The shaded area indicates the outcropping of the salinity surface.



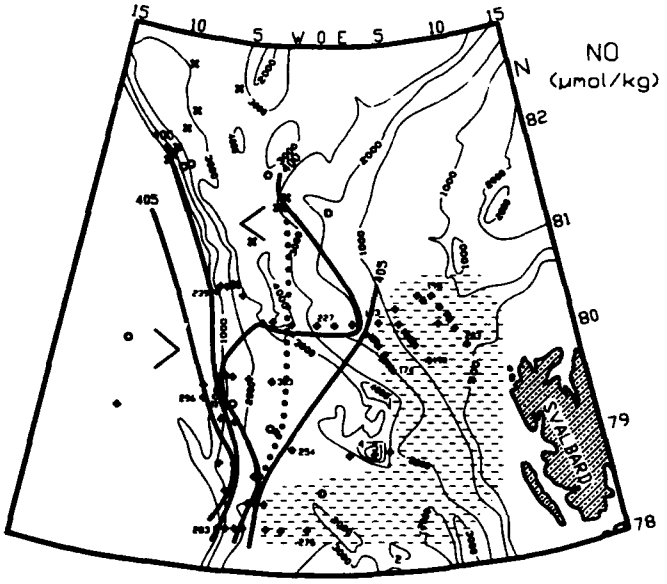


Figure 5. Water from the upper halocline (indicated by the silicate maximum on the S = 33.1 salinity surface) and the lower halocline (indicated by the NO minimum on the S = 34.2 salinity surface.

flows to the east towards the Kara Sea. This picture is consistent with the conclusions by Midttun [1985] who showed that the cooled, high salinity bottom water in the eastern Barents Sea moves eastward into the Kara Sea and further to the north along the Saint Anna Trough. At some stage, there must be a division in the sub-surface low NO water. Some low NO water would flow east and/or north with the Atlantic layer to coincide with the Transpolar Drift and the anticyclonic Beaufort Sea gyre. This Beaufort Sea gyre low NO water in fact distinguishes the lower halocline water observed at the CESAR and LOREX ice camps in the central Arctic Ocean and is separated from the surface layer by the upper halocline water. Some low NO water with S = 34.4 appears to flow west to follow the Transpolar Drift immediately under the surface layer.

Low NO waters with both salinities were observed in Fram Strait in a section near 81°N taken during the MIZEX 84 where they come together and flow out in the East Greenland Current. The observation in northern Fram Strait of low NO water from two sources is consistent with the view of the origin and flow of low NO water described above. The flow pattern of low NO water with S = 34.4 is illustrated by a plot of NO values along the 34.4 salinity surface in south western Nansen Basin (Figure 4). As the data are sparse, the shape of the isolines cannot be taken as more than an indication of the current pattern, but the general picture is consistent with the ice drift in this region. The flow of the upper and lower halocline water from the central Arctic Ocean, as traced by a silicate maximum on the S = 33.1 surface and a NO minimum on the S = 34.2 surface, occurs on the western side of Fram Strait (Figure 5). While the chemical signals for these water masses are clear, exactly how the water arrives at Fram Strait from the central Arctic Ocean has not yet been determined.

ACKNOWLEDGMENTS

We wish to acknowledge the scientific personnel and crew of F.S. *Polarstern* for valuable cooperation during the ARKTIS IV/3 expedition and personnel at the Alfred Wegener Institute for Polar and Marine Research for additional logistic support. L.G.A. acknowledges the Swedish Natural Science Research Council for financial support.

REFERENCES

Aagaard, K., and E. C. Carmack, The role of sea ice and other fresh water in the Arctic circulation, *J. Geophys. Res.*, *94*, 14485–14498, 1989.

Aagaard, K., J. H. Swift, and E. C. Carmack, Thermohaline circulation in the Arctic Mediterranean Seas, *J. Geophys. Res.*, *90*, 4833–4846, 1985.

Anderson, G. C., and J. H. Swift, Arctic Internal Waves Experiment (AIWEX) hydrographic data, *SIO Reference 90-10*, Scripps Institution of Oceanography, University of California, La Jolla 92093, 1990.

Anderson, L., and D. Dyrssen, Chemical constituents of the Arctic Ocean in the Svalbard area. *Oceanologica Acta*, *4*, 305–311, 1981.

Anderson, L. G., E. P. Jones, K. P. Koltermann, P. Schlosser, J. H. Swift, and D. W. R. Wallace, The first oceanographic section across the Nansen Basin in the Arctic Ocean, *Deep-Sea Res.*, *36*, 475–482, 1989.

Anderson, L. G., D. Dyrssen, and E. P. Jones, An assessment of the transport of atmospheric CO_2 into the Arctic Ocean, *J. Geophys. Res.*, *95*, 1703–1711, 1990.

Broecker, W. S., "NO", A conservative-mass tracer, *Earth Planet. Sci. Lett.*, *23*, 100–107, 1974.

Colony, R., and A. S. Thorndike, An estimate of the mean field of Arctic Sea Ice motion, *J. Geophys. Res.*, *89*, 10623–10629, 1984.

Gordienko, P. A., and A. F. Laktionov, Circulation and physics of the Arctic Basin waters, In *Annals of the International Geophysical Year, XLVI Oceanography*, pp. 94–112, Pergamon Press, 1965.

Hansen, J., I. Fung, A. Lacis, D. Rind, S. Lebedeff, R. Ruedy, and G. Russell, Global climate changes as forecast by Goddard Institute for Space Studies three-dimensional model, *J. Geophys. Res.*, *93*, 9341–9364, 1988.

Jones, E. P., and L. G. Anderson, On the origin of the chemical properties of the Arctic Ocean halocline, *J. Geophys. Res.*, *91*, 759–767, 1986.

Kinney, P., M. E. Arhelger, and D. C. Burrell, Chemical characteristics of water masses in the Amerasian Basin of the Arctic Ocean, *J. Geophys. Res.*, *75*, 4097–4104, 1970.

Melling, H., and E. L. Lewis, Shelf drainage flows in the Beaufort Sea and their effect on the Arctic Ocean pycnocline, *Deep-Sea Res.*, *29*, 967–985, 1982.

Midttun, L., Formation of dense bottom water in the Barents Sea, *Deep-Sea Res.*, *32*, 1233–1241, 1985.

Moore, R. M., M. G. Lowings, and F. C. Tan, Geochemical profiles in the central Arctic Ocean: Their relation to freezing and shallow circulation, *J. Geophys. Res.*, *88*, 2667–2674, 1983.

Perkin, R. G., and E. L. Lewis, Mixing in the West Spitsbergen Current, *J. Phys. Oceanogr.*, *14*, 1315–1325, 1984.

Pfirman, S., J. C. Gascard, I. Wollenburg, P. Mudie, and A. Abelmann, Particle-laden Eurasian Arctic sea ice; observations from July and August 1987, *Polar Res.*, *7*, 59–66, 1989.

Rudels, B., The formation of Polar Surface Water, the ice export and the exchanges through the Fram Strait, *Progr. Oceanogr.*, *22*, 205–248, 1989.

Stigebrandt, A., A model for the thickness and salinity of the upper layer in the Arctic Ocean and the relationship between the ice thickness and some external parameters, *J. Phys. Oceanogr.*, *11*, 1407–1422, 1981.

AD-P007 309

92-17991

The Arctic Ocean Eigen Oscillations

A. Yu. Proshutinsky and I. V. Polyakov
The Arctic and Antarctic Research Institute (AARI), Leningrad, U.S.S.R.

ABSTRACT

The spectral task on the eigen oscillations of the Arctic Ocean level was solved using numerical integration of tidal Laplace equations without friction as the nonstationary boundary-value problem. The adiabatic conditions were prescribed at the boundaries. Free oscillations were induced by an arbitrary initial perturbation in the level field.

The spectra of free oscillations of the Arctic Ocean have significant maxima of spectral density at the periods of 30.38, 23.70, 17.30, 13.91, 12.55, 11.03, and 8.10 hours. The zoning of the Arctic Ocean was made on the basis of differences in the spectra of free oscillations in some of its areas, the results of zoning being consistent with common representations of the geographical subdivision of the Arctic Ocean into basins, seas, and bays. The possibility of resonance amplification of shelf waves and double Kelvin waves in the areas with significant bottom topography irregularities was revealed. The resonance nature of the surge level oscillations caused by rapidly shifting cyclones was proven. The experimental studies confirmed the hypothesis of the resonance mechanism of tidal motions in the marginal seas of the Arctic Ocean.

Many studies have been made of the free surface positions of the Arctic Ocean (AO). At present the level regimes of many coastal areas are sufficiently well studied; for some regions methods have been developed for calculating in advance and forecasting fluctuations of the level induced by tides and storm surges. The results of these methods, however, do not always allow us to explain and hence predict the anomalous oscillations of the level, to reveal the nature of level regimes differing in various AO areas. We will attempt to answer many unsolved questions using a resonance hypothesis of excitation of level fluctuations at some frequencies of the real spectrum.

The process of generation of motions in the ocean by an external force can be defined as an effect of a complex forcing on the system with many degrees of freedom. The ocean response to this disturbance can be represented as a superposition of free and forced fluctuations with which coincidence or closeness of resonance occurs. For instance, Adams and Buchwald [1969], Garret [1974], and Robinson [1964] indicated the possibility of an increase in resonance of the level oscillations in the synoptical frequency range. The suggestion of the coincidence of free oscillation periods with the components of tide-generating forces allowed Farrell [1874] to explain the observed distribution of semidiurnal tides in the North Atlantic, and Harris [1904] to construct a cotidal map of the World Ocean tides. The periods of eigen oscillations calculated by different methods for the systems of the Atlantic–Indian oceans [Platzman, 1978], the Fundy–Man Gulfs [Garret, 1974], the Ligurian Sea [Papa, 1977], the entire World Ocean [Platzman, 1978; Gotlib and Kagan, 1981] (without the Arctic Ocean) indicate possible support for the ideas of Farrell. Thus the determination of the periods of eigen oscillations of the Arctic Ocean will probably allow us to explain the nature of some features of the level dynamics in the region to better understand the physics of tidal- and surge-induced oscillations of the level.

To calculate the eigen oscillations of the North European and Arctic Basins with the marginal seas we used the method developed by Papa [1977] and Gotlib and Kagan [1981].

Let us consider this approach with those changes which have been made taking into account the specific task for the area under study.

For the case when the eigen oscillations in the basin are excited by an arbitrary perturbation in the absence of friction forces, the following equation system and boundary conditions can be applied:

$$\frac{\partial \vec{W}}{\partial t} = L\vec{W}, \tag{1}$$

$$\vec{u} \cdot \vec{n}\,|_{S_1} = 0, \quad \zeta|_{S_2} = 0 \tag{2}$$

$$\vec{W}|_{t=0} = \vec{W}_0 \tag{3}$$

where $\vec{W}$ is a vector function with components $(\vec{u},\zeta)$; $\vec{W}_0$ is the initial disturbance in the flux field $\vec{u} = (u,v)$ and free ocean surface ζ;

$$L = -\begin{pmatrix} f\vec{k}\times & g(H+\zeta)\nabla \\ \nabla & 0 \end{pmatrix}$$

where H is the non-disturbed sea depth, ∇ is the Hamiltonian operator, f is the coriolis parameter, $\vec{k}$, $\vec{n}$ are single vectors, directed respectively vertically upward and along the normal toward the solid contour S_1 of the area under consideration, and S_2 is the open ocean boundary. The condition of the level at the open boundary being equal to zero, assuming adiabatic processes inside the area, also signifies the existence of a zero amplitude line at the open boundary for all free oscillations in the basin under study. This condition leads to the loss of the low-frequency spectrum range of free oscillations, which should be present in the investigated basin as an element of the World Ocean.

To solve equations 1–3 numerically, the AO water area on the stereographic projection map was covered by a grid with constant steps along the X and Y coordinate axes of 55,555 m.

The u, v, ζ variables were calculated in point with a spacing of a half grid step (Richardson grid). Spatial derivatives of the system (1) were substituted by central finite-difference analogs. To preserve the antisymmetry property for a finite-difference analog L_h of the operator L, the terms containing the Coriolis parameter were approximated by averaging four neighboring points with weights $f/(H+\zeta)$. For example, in u-point for v-component of $\vec{u}$-vector the value is taken of the type

$$v_0 = \frac{1}{8}\sum_{i=1}^{4}\left(1 + \frac{H_0+\zeta_0}{H_i+\zeta_i}\cdot\frac{f_i}{f_0}\right)v_i$$

To decrease dissipation of the numerical scheme in the work of Gotlib and Kagan [1981] it is suggested that, when substituting those terms which contain time derivatives by a difference analog, that four rather than two expansion terms be used in the Taylor series of values. Substituting the time derivations with a difference analog in equation 1 we obtain the difference scheme

$$\vec{W}_{i,k}(t+\Delta t) = \vec{W}_{i,k}(t) + L_h\vec{W}_{i,k}(t)\Delta t +$$

$$L_h\vec{W}_{i,k}(t)\frac{\Delta t^2}{2} + L_h\vec{W}_{i,k}(t)\frac{\Delta t^3}{6}$$

where Δt is the time step. The inequality

$$\Delta t \le \frac{\sqrt{3}}{2}\Delta x\,(2gH_{max})^{-1/2}$$

is a sufficient condition for the stability of this scheme, where H_{max} is maximum ocean depth.

The time step for the model of the Arctic Ocean was 150 s. The initial conditions of the task are fulfilled by prescribing an arbitrary disturbance in the fields of flux and level. The quantity of numerical values of the level used to obtain the spectra of free oscillations in the Arctic Ocean was 1000, with a one-hour interval. The numerical spectra of the ocean eigen oscillations are constructed for 147 points of the area. Some points are at coastal level recording sta-

T hours	Kara Sea 77.27°N 82.10°E	Chukchi Sea 68.08°N 172.30°W	Arctic Basin 88.11°N 30.00°E	No. Europ. Basin 74.00°N 7.20°E
30.48			0.05	0.20
29.09	0.10	0.06		
26.67			0.06	
23.70	0.10			0.45
21.33			0.11	
20.65	1.00			0.59
19.39		0.32		
18.82			0.07	
17.78		0.16		
17.30			0.08	1.00
16.84	0.65			
16.41		0.25	0.07	
14.88			0.15	
14.55	0.20			
13.91		0.18	0.21	
12.80	0.05			
12.55			0.23	
11.64		0.18		
11.43	0.05			
11.03			1.00	
10.85	0.86	1.00		
10.32			0.05	
10.00	0.24		0.20	
9.41	0.08			
9.28		0.06		
9.01			0.05	
8.65	0.75		0.09	
8.53				0.25
7.53	0.11			

Table 1. Periods (T) of the eigen oscillations of sea level in the Arctic Ocean with the relative amplitudes $\setminus f(h,hmax) \ge 0.05$.

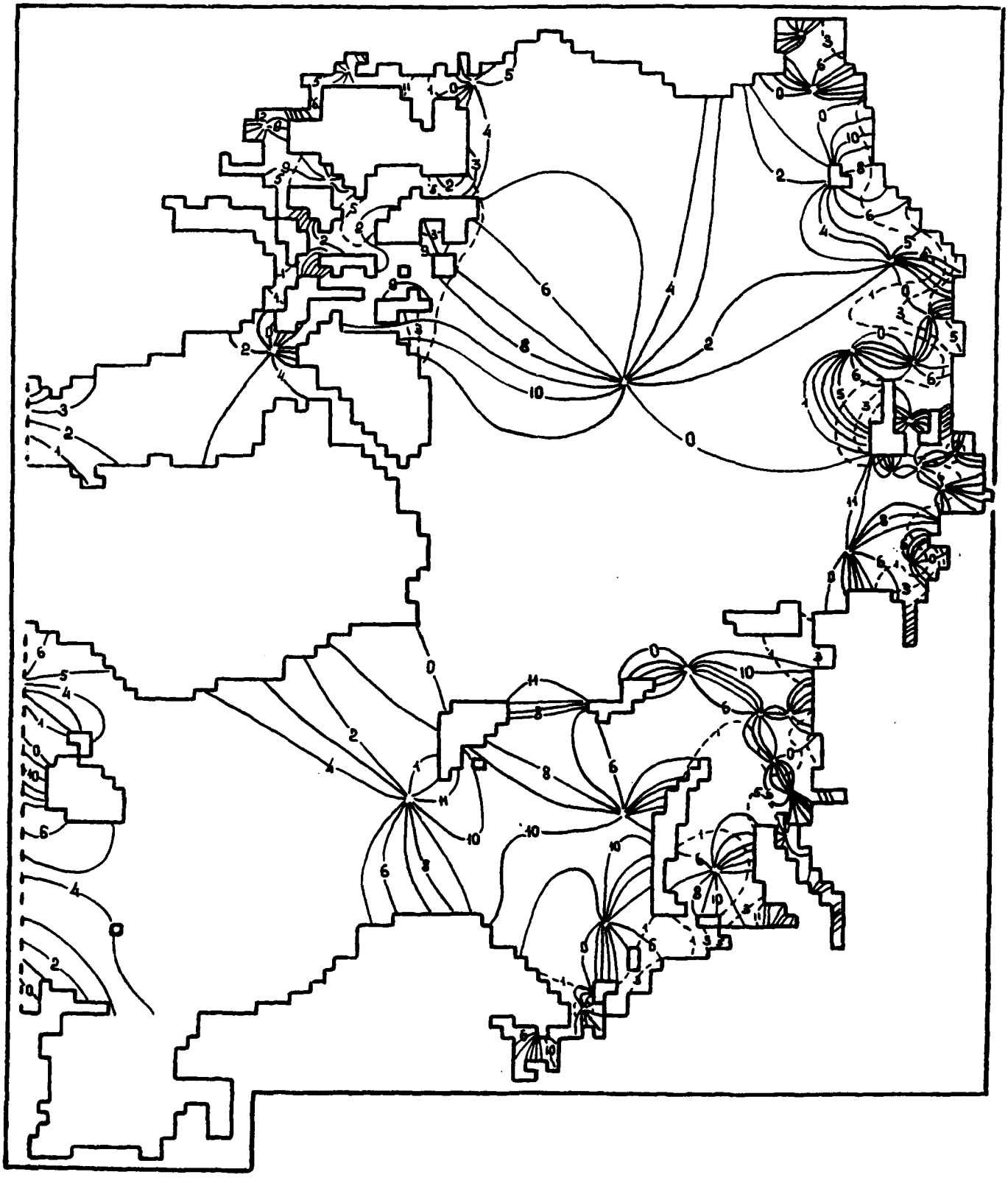


Figure 1. The scheme of the eigen oscillation phases (1) and amplitudes (2) with a period of 12.55 h. Phases are normalized by 30 degrees, amplitudes by the standard deviation over the region of oscillation amplitudes.

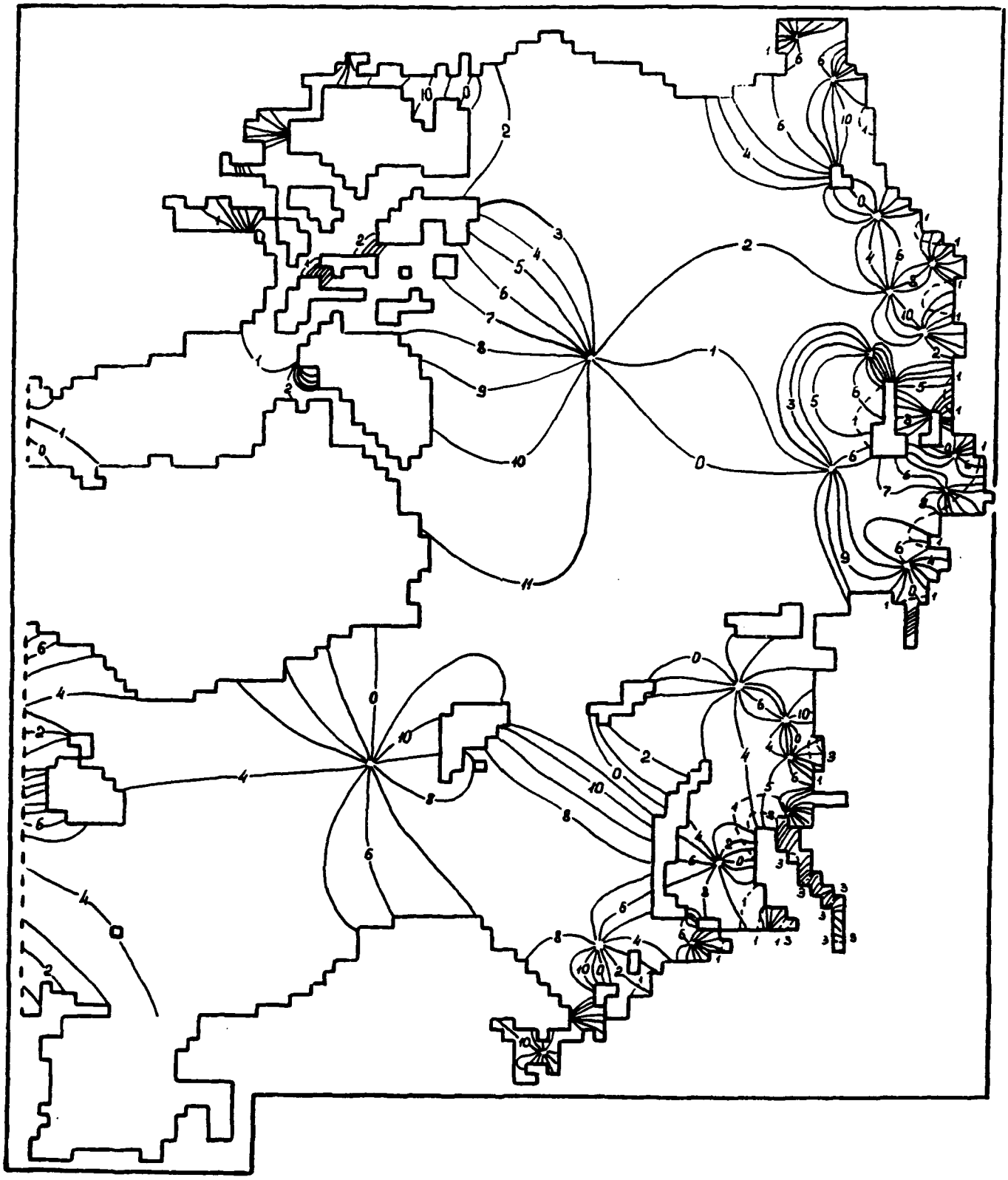


Figure 2. The same as in Figure 1, but for a period of 12.31 h.

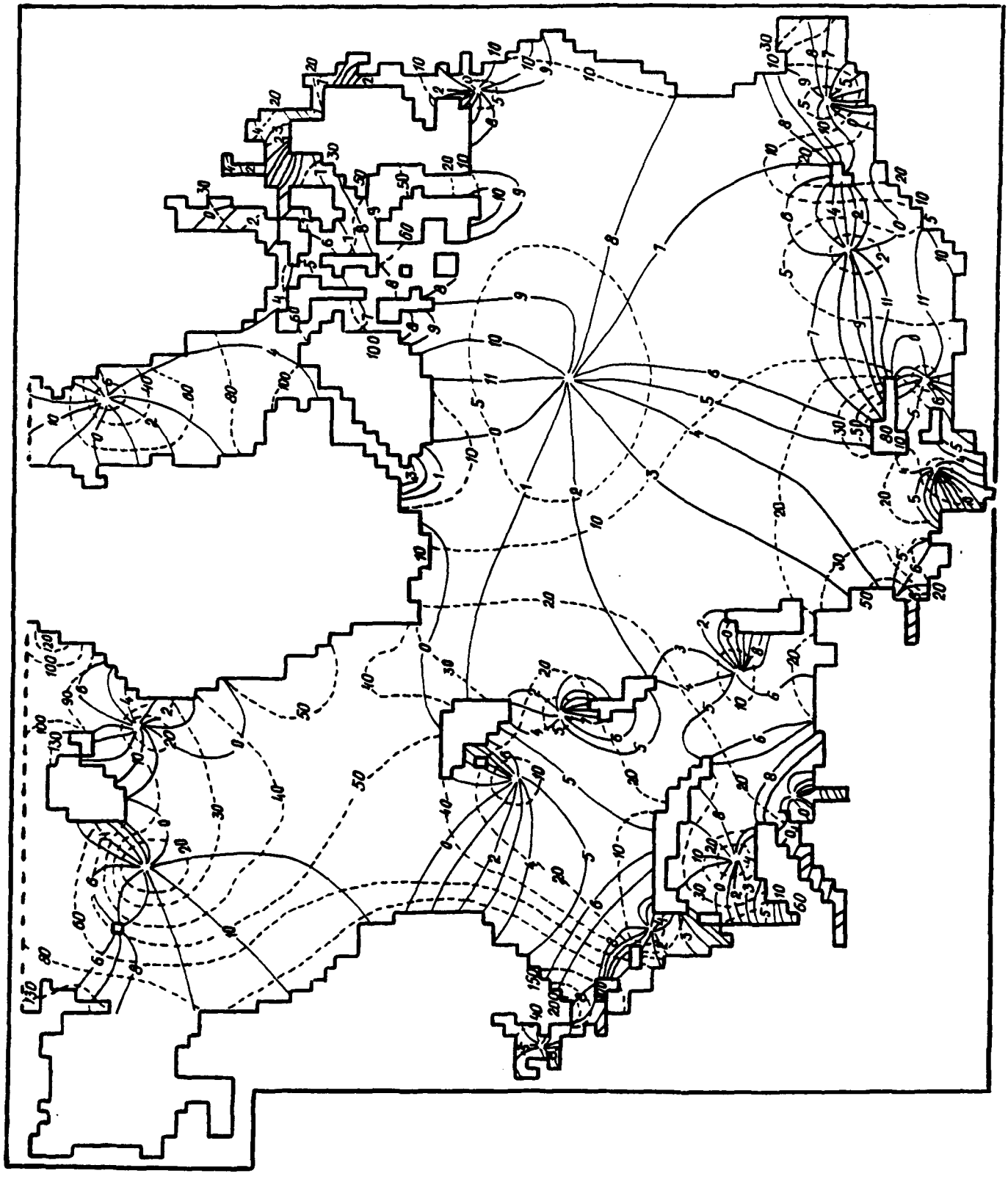


Figure 3. The scheme of the M2 tidal wave propagation. Phases are normalized by 30 degrees, amplitudes in cm. Results of the linear model.

tions, 67 points for a regular network covering the ocean area with a 400-km interval, and the rest of the spectra characterize two polygons of different scales in regions with significant irregularities of sea bottom topography.

Analysis of the spectra indicated that each of the areas, along with free oscillation modes common for the entire ocean, has its own characteristic frequencies. The collected data allowed us to divide the Arctic Ocean area into zones according to this feature. More generally, zones with similar free oscillation characteristics coincided with geographical subdivisions of the AO (basins, seas, bays). This is quite understandable, as eigen frequency oscillations are governed by bottom topography, coastal configurations, and basin dimensions.

Among significant energy modes common for all ocean areas one can single out the oscillations with 30.48 h, 23.70 h, 20.65 h, 17.30 h, 13.91 h, 12.55 h, 11.03 h, 8.10 h.

Table 1 gives characteristics of the spectrum of free level oscillations for various AO regions. It follows that for the North European Basin the mode with the oscillation period of 17.30 h is the main one in terms of energy; for the Kara sea, 20.65 h; for the Chukchi Sea, 10.32 h; and for the Arctic Basin, 11.03 h.

In a semi-diurnal band of frequency spectra for most of the arctic seas the energy contributions of oscillations with periods from 11.03 h to 12.80 h are small.

In the frequency domain near the diurnal harmonics of the tidal potential, the most pronounced are the modes with periods of 20.65 h and 23.70 h. The energy of these oscillations for all areas of the AO except the North European Basin is also insignificant.

Spatial structures of the level fields reflect two eigen oscillation modes close to a semi-diurnal period, presented in Figures 1 and 2. For comparison, Figure 3 shows the scheme of propagation of the M2 tidal wave in the AO, calculated by the linear model

$$\frac{\partial \vec{u}}{\partial t} + f_1 \vec{u} = -g(H+\zeta)\nabla\zeta - \frac{r}{(H+\zeta)^2}\vec{u}\cdot|\vec{u}|, \qquad (4)$$

$$\frac{\partial \zeta}{\partial t} + \mathrm{div}\,\vec{u} = 0, \qquad (5)$$

$$\vec{u}\cdot\vec{n}\,|_{s_1} = 0, \quad \zeta|_{s_2} = \zeta(x,y,t), \qquad (6)$$

$$(\vec{u},\zeta)|_{t=0} = 0, \quad f_1 = \begin{pmatrix} 0 & -2\omega\sin\varphi \\ 2\omega\sin\varphi & 0 \end{pmatrix} \qquad (7)$$

The denotations are the same.

The solution obtained for equations 4–7 for a semi-diurnal tide in the AO (Figure 3) induced by the Atlantic Ocean was compared with the observation data from 94 points. Mean absolute error in the calculation of the wave amplitude M2 was 4 cm, and that of the phase was 30 degrees.

It can be seen from comparison of Figures 1, 2 and 3 that the schemes of cotidal lines and relative isoamplitudes (ratio of the level oscillation amplitude in a given point to the root square one for the entire ocean) at the frequencies near the frequency of the main moon semi-diurnal wave M2 have many common features. First of all, there are amphidromic systems in the Canadian Arctic, Spitsbergen area, the White, Kara, Laptev, East Siberian and Chukchi seas. The agreement of relative amplitudes in some of the areas is also noted.

It is interesting to note that in Figures 1 and 2 there are some significant differences not only in the character of wave propagation, but also in the values of relative amplitudes with a comparatively small difference in the periods of free oscillations (only 0.24 h).

It appears that a resonance is possible in or close to these frequencies. Let us attempt to analyze the degree of closeness of different AO areas to the resonance at some frequencies. As an example, Table 2 gives relative amplitudes (or coefficients of amplification) of those places where observations of well-pronounced tides have been made.

As can be seen from Table 2, in a semi-diurnal frequency band for all denoted areas, amplification of oscillations is characteristic. In some cases this amplitude is of resonance character, as the amplitudes at closer frequencies differ more than ten times. It should be mentioned that the calculations, being to a large extent idealized, did not take into account friction forces. However, as shown in Table 2, the model results allow us with known approximation to determine the features of the level oscillations regime in different AO areas, or to predict them in the areas with observation gaps.

As can be seen from Tables 1 and 2, the eigen frequencies of the AO on the whole are far from the frequencies of the main harmonics of the tidal potential. For example, the frequencies close to the frequency of a diurnal tide in the seas of the Siberian shelf are characterized by anti-resonance conditions. Possibly due to this, with other conditions being the same, diurnal tidal level oscillations are actually not observed anywhere in the AO.

The description of the ocean level oscillations in the vicinity of areas with significant depth variations was constructed on the basis of analysis of spatial–temporal spectra of computed series of free level oscillations in the points forming the polygons in the area of the Lomonosov Ridge and the land slope of the Laptev Sea. As an example, Figure 4 shows the section of a spatial–temporal section by the plane of wave numbers at the 64.3-h period in the land slope area. It can be seen that the wave energy is transferred in the direction of more dense isolines of the relative eddy f/H, leading to the relative isolation of the shelf and deep sea. The multi-mode structure of the wave field can be seen in the presence of two maxima of spectral density, corresponding to the waves with 690- and 505-km lengths. Usually such patterns of wave energy transfer are attributed to the shelf wave propagation. The spectral analysis of the series of free oscillations in the Lomonosov Ridge area showed the existence of Kelvin double waves. This result suggests that resonance is one of the possible mechanisms of generation and amplification of long waves in the areas of significant bottom topography irregularities.

The estimates obtained for the periods of free level oscillations in the marginal seas of the Siberian shelf were used in the studies of the role of resonance in the excitation of

Periods hours	Mezensky Guba	Baydaratskaya Guba	Hatangski Gulf	Novosibirskie Island	Wrangel Island
26.67	8.2	13.5	1.1	1.5	1.4
23.70	6.4	19.1	0.1	0.1	0.7
22.86	16.0	27.3	0.8	0.3	0.6
21.33	29.8	11.3	0.2	0.4	1.8
15.24	1.1	5.4	6.0	14.8	3.3
13.91	3.8	0.7	11.4	4.6	2.0
13.62	2.3	1.0	11.6	5.0	2.7
12.80	4.8	5.3	3.9	6.3	0.9
12.55	0.3	3.0	1.0	2.9	0.9
12.31	8.9	4.9	5.6	1.6	2.4
11.64	2.7	4.0	2.0	6.2	2.7
11.03	9.6	10.2	5.8	6.9	0.8
7.20	5.6	1.0	0.1	5.1	1.3

Table 2. Coefficients of amplification eigen oscillations of sea level of the Arctic Ocean.

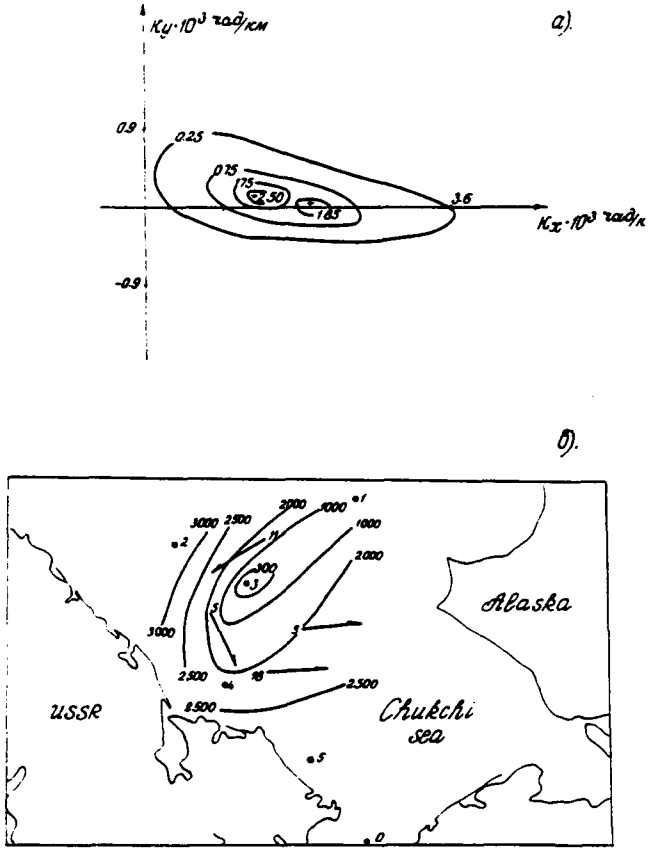


Figure 4. (a) The section of a spatial–temporal spectrum by the plane of wave numbers for the 64.3-h period for the Laptev Sea slope area. The normalized spectral value 1.0 is equivalent to 10 cm^2 hr^{-1}. The direction along the slope is parallel to the X-axis. The crosses correspond to the points of spectral density maxima. (b) The chart of level oscillations spectral density for a 12.5-h period. Chukchi Sea, July–August 1988. The positions of sea level oscillation gauges are shown by dots. The arrows show the direction of M2 tidal wave propagation. The figures near the foot of the arrows are wave phase velocities, cm s^{-1}.

significant surge oscillations. An analytical solution of the task on storm surges in a one-dimensional channel of constant depth, given by Murty [1984], was used, as well as a numerical solution of the task (1)–(2) with an undisturbed initial state of the vector $\vec{W}$ and addition to the right-hand side of equation (1) of the forcing vector, presented as a superposition of the simplest harmonic components.

The study indicated that surge oscillations can be the result of a resonance energy transfer from rapidly shifting cyclones. Also, when the cyclone speed coincides with the velocity of propagation of free long waves on the shelf, the wave field is formed by a small number of level oscillation harmonics and the main surge maximum can be the result of seiche oscillations.

Stationary deep cyclones generate surges having complex polymodal structure. The values of amplitudes of forced level oscillations are mainly governed by the intensity of dynamic atmospheric processes. The atmospheric effect on the ocean in these situations can lead to the formation of local sources of resonance amplification of level oscillations.

The comparison of calculated and experimental data with the character of level surface changes at the shelf of the arctic seas is made from the results of polygon observations of the level variations in the Chukchi Sea in summer of 1988. The map of the distribution of the spectral density of level oscillations for a 12.5-h period (Figure 4) fully confirms the conclusion based on numerical computations about the location of the center of the amphidromic system of the AO eigen vector with a 12.55-h period in the area point 3. The estimates of spatial–temporal spectra of synchronous parts of level series allowed us to obtain data on the direction of shifting of long-wave formations (denoted by arrows in Figure 4). These results are also in good agreement with the existing understanding of the dynamics of free long waves in the area under study. In addition, a known hypothesis of the resonance nature of the semidiurnal tides in the Chukchi Sea is experimentally confirmed.

REFERENCES

Adams, J. K., and V. T. Buchwald, The generation of continental shelf waves, *J. Fluid Mech.*, *35*, 815–826, 1969.

Farrell, W. O., *Tidal Researches*, p. 237, London, 1874.

Harris, R. A., Manual of Tides, part IVB: Cotidal lines of the World, *U.S. Coast and Geodet. Surv. Rept. App.*, *5*, pp. 315–400, 1904.

Garret, C. J. R., Normal modes of the Bay of Fundy and Gulf of Main, *Can. J. Earth Sci.*, *11*, 549–556, 1974.

Gill, A. E., and E. H. Schumann, The generation of long waves by the wind, *J. Phys. Oceanogr.*, *4*, 83–90, 1974.

Gotlib, V. Yu., and B. A. Kagan, About resonance generation of semi-diurnal tides in the World Ocean (In Russian), *Izv. Ak. Nauk, Phisica atm. and ocean*, *17*, 502–512, 1981.

Murty, T. S., *Storm Surges - Meteorological Ocean Tides*, 900 pp., Dept. of Fisheries and Oceans, Ottawa, 1984.

Papa, L., The free oscillations of the Ligurian sea computed by the NH-method, *Dtscr. Hydrog. Z.*, *30*, 81–90, 1977.

Platzman, G. W., Two-dimensional free oscillations in natural basins, *J. Phys. Oceanogr.*, *2*, 117–138, 1972.

Platzman, G. W., Normal modes of the Atlantic and Indian Oceans, *J. Phys. Oceanogr.*, *5*, 201–221, 1975.

Platzman, G. W., Normal modes of the World Ocean, Part I, Design of a finite-element barotropic model, *J. Phys. Oceanogr.*, *8*, 323–343, 1978.

Robinson, A. R., Continental shelf waves and the response of sea level to weather systems, *J. Geophys. Res.*, *69*, 367–368, 1964.

Transport of Atmospheric CO_2 to the Bottom Water of the Weddell Sea

L. G. Anderson
Dept. of Analytical and Marine Chemistry, University of Goteborg and Chalmers University of Technology, Goteborg, Sweden

ABSTRACT

Production of bottom water in the Weddell Sea mainly occurs as a result of processes taking place on the large shelf areas in the south/southwest. Water with increased salinity is formed during the production and aging of sea ice. Over the southern shelf, this water sinks toward the bottom and, due to the topography, part of it flows southward in under the ice shelf. Here it exchanges heat with the shelf ice resulting in both melting of shelf ice and freezing of seawater, the net result being a decrease in both salinity and temperature of the seawater, commonly noted as Ice Shelf Water (ISW). The ISW flows at some locations, due to topography, northward into the deep Weddell Sea, where it mixes with surrounding waters and interleaves at the resulting density surface. Much of the resulting waters have high enough density to reach all the way to the bottom.

The atmospheric CO_2 reaching the bottom water is thus incorporated in the surface water prior to sea ice production, that is during the productive season. The production decreases the partial pressure of CO_2 which drives a flux from the atmosphere into the surface water. The organic matter leaves the surface layer and decays mainly on the sediment surface and in deeper waters.

Data from the Swedish Antarctic Project (SWEDARP) 1988/89 will be presented covering four sections across the shelf break as well as from stations in the Filchner depression, down to the ice shelf. Total carbonate, including the dissolved atmospheric CO_2, will be affected by several biogeochemical processes during the transport from the surface down into the deep Weddell Sea. Total carbonate is therefore corrected for biological production and decay using oxygen, and for calcium carbonate precipitation and dissolution by total alkalinity and calcium. The resultant corrected total carbonate (C_t-corr) clearly shows the increased atmospheric CO_2 concentration with time. The increase of C_t-corr in the ISW compared to the pre-industrialized Warm Deep Water indicates the saturation degree of the surface water to be close to 100% when it was shielded from the atmosphere. A potential temperature versus C_t-corr diagram verified the mixing pattern of the different water masses in the area.

On Small Climatic Effects of Air Invasion in Polar Regions: The Influence on Atmospheric Pressure and Heat Flux

I. P. Semiletov
Pacific Oceanological Institute, Far Eastern Branch, Academy of Sciences of the U.S.S.R., Vladivostok, U.S.S.R.

ABSTRACT

The possibility of decreasing atmospheric pressure by air invasion in the downwelling zone of the ocean is discussed. The boundary condition for the solution of the baric tendency equation on the atmosphere–ocean interface is derived. It is shown that atmospheric pressure may decrease about 0.1–10 Pa day^{-1} for gas invasion and downwelling rates of 0.001–0.1 cm c^{-1}, due to active gas–water exchange without regard for heat and water vapor transfer. This calculation was based on a model of the diffusion boundary layer. It was used for the total solution of the baric tendency equation. These estimates were made for the region of formation of Antarctic Bottom Water. This factor, with regard to the quasi-stationary condition of the process, provides a significant contribution to the formation of atmospheric depressions, sub-antarctic depressions and some depressions in high latitudes of both hemispheres.

The heat effect of N_2, O_2 and CO_2 solutions in polar sea regions is considered. It is shown that, for example, the heat flux with CO_2 solution (~20 mol m^{-2} yr^{-1}) corresponds to 12 Cal cm^{-2} year. This flux and the flux from the earth's interior (~47 Cal cm^{-2} yr^{-1}) are the same order of magnitude. In winter, this factor is one positive member of the heat balance for the polar surface layers.

AD-P007 310

92-17992

Determination of Net Atmospheric Heat Transfer, Ice Production, and Salt Rejection from the Chukchi Polynya Using AVHRR Thermal Imagery

J. E. Groves and W. J. Stringer
Geophysical Institute, University of Alaska Fairbanks, Fairbanks, Alaska, U.S.A.

ABSTRACT

Digital analysis of AVHRR (Advanced Very High Resolution Radiometer) thermal infrared band imagery has yielded sea ice surface temperatures which were used to calculate daily net surface heat loss and accompanying ice production and salt rejection from strips of thin ice within the Chukchi Polynya. These results are in agreement with published estimates of heat loss, ice production and salt rejection from the open water surface of the St. Lawrence Island polynya and of Whaler's Bay north of Svalbard and from thin ice in the central Arctic.

INTRODUCTION

Polynyas are mesoscale areas of open water or thin ice in sea ice–covered regions. Although polynyas cover only 3–4 percent of the surface area of the Arctic, they are responsible for up to 50% of its oceanic and atmospheric heat transfer [IAP[2], 1989]. This transfer takes place at the surface of thin ice, as well as open water. Smith et al. [1990] state that many polynyas are active sites for salt concentration and may therefore affect both the local water density structure as well as influence larger-scale water mass modification at distances removed from the polynya site. Ice surface temperature analysis of internal structure and ice thickness within polynyas is a critical step in the quantitative calculation of surface heat transfer to the atmosphere, ice production and salt rejection within polynyas which will advance understanding of the quantitative effect that polynyas may have in global change processes.

There are two types of polynyas [Smith et al., 1990]: latent heat polynyas and sensible heat polynyas. Latent heat polynyas occur in regions where the sea water is at the freezing point. Heat loss to the atmosphere leads to ice formation rather than to additional cooling of the water column. Therefore in order for a polynya to form, the ice which forms must be physically removed from the region by some combination of winds and currents. Sensible heat polynyas occur where sea water is above the freezing point and sufficient oceanic heat is available to the water surface to prevent ice from forming. The upward heat transfer can occur through vertical mixing of heat from deeper water or through upward advection of heat by upwelling. Smith et al. [1990] identify those polynyas which form off south-facing coasts in the Bering and Chukchi Seas as latent heat polynyas.

Several studies have focused on the use of remote sensing methods for determining sea ice thickness. Kuhn et al. [1975] describe the use of airborne infrared imagery for this purpose in the northern Bering Sea. Eppler and Farmer [1991] describe the use of 33.6 Ghz passive microwave for detecting formation of ice within polynyas. Maykut [1986] outlines theoretical considerations for calculation of ice thickness if the sea ice surface temperature, the surface air temperature, and the freezing temperature of the water are known.

Martin and Cavalieri [1989] estimated heat flux ranging from 55–290 W m^{-2} from the surface of Whaler's Bay, an open water polynya located off the north coast of Svalbard. Schumacher et al. [1983] estimated a heat flux of 535 W m^{-2} from the surface of the St. Lawrence Island polynya. These authors used sea surface temperature and coastal weather station data for their calculations. Maykut [1986] estimated the heat flux from thin ice (<5 cm) as 494 W m^{-2} in the central Arctic.

Martin and Cavalieri [1989] calculated the seasonal volume of sea ice production and salt rejection generated in the earliest stages of freeze-up based on the estimated heat loss from the surface of an open water polynya as ranging from 9–44 km^3 and 0.09 to 9.6 x 10^{11} kg respectively for the Siberian Shelf polynyas.

We have used AVHRR thermal infrared imagery to distinguish between thin ice and open water in polynyas [Groves and Stringer, 1991], determine polynya area [Stringer and Groves, 1991], and provide data to enable ice thickness calculations [Groves and Stringer, 1991]. Here, we have used these sea ice surface temperatures measured for very thin ice to approximate the amount of heat transfer to the atmosphere and the ice volume and salt generation in the thin ice stage of the process of freeze-up of the Chukchi Polynya.

The Chukchi Polynya (Figures 1,2), which forms in the Chukchi Sea off the northwest coast of Alaska between Cape Lisburne and Icy Cape [Stringer and Groves, 1988, 1991], was chosen as a site to study the feasibility of using AVHRR TIR imagery for ice thickness calculations [Groves and Stringer, 1991]. During the period selected, the polynya extended 125 km south from Icy Cape, and its greatest width was 20 km. Water depths in this region range between 15 and 25 meters. The polynya displayed the striping parallel to the coast which is typical of many polynyas. This striping is generally thought to be caused by the episodic freezing of the sea surface as the polynya opened under the influence of wind and reflects differences in ice thicknesses and ice surface temperature within the polynya.

METHODOLOGY

An exceptionally cloud-free period on the Chukchi Coast between Barrow and Pt. Hope, when we could be sure the freshly generated polynya surface was free of snow cover, was identified for March 12 through March 21, 1987. Nine AVHRR computer-compatible image tapes (CCTs) from the polar-orbiting NOAA-09 and NOAA-10 satellites were ordered from the National Environmental Satellite, Data, and Information Service's National Climatic Data Center in Washington, DC (NESDIS). The nine CCTs were analyzed at the Alaska Data Visualization and Analysis Laboratory (ADVAL) located at the Geophysical Institute, University of Alaska Fairbanks. Temperature calibration for each CCT was accomplished using the method described by Lauritson et al. [1979].

The thickness of thin ice can be estimated by its relative gray scale as evaluated by an observer's eye. Four categories of thin ice are listed by the World Meteorological Organization [WMO, 1970]: dark nilas <5 cm; light nilas 5–10 cm; gray ice 10–15 cm; and gray white ice 15–30 cm. For the visual and near-infrared bands of AVHRR imagery, gray levels also arise from relative amounts of reflected solar radiation. However, care must be exercised when making thickness estimates based on these gray values because of the calibration which may have been applied to the images. Regardless of calibration, dark striping indicates open water or very thin ice and very light gray or white striping indicates thicker ice. There is excellent agreement among the visual and thermal infrared imagery on the boundaries of ice thickness variation within the polynya.

Vector wind and air temperature measurements on a three-hour interval were obtained for March 12 through 21, 1987 from Local Climatological Data sheets for Kotzebue and Barrow [National Climatic Data Center, 1987]. We calculated mean daily vector winds and air temperatures based on the 24-hour period immediately preceding the satellite pass. Figure 3 displays mean daily temperatures at Barrow and Kotzebue. Barrow temperatures were used for calculations. Figure 4 displays the mean daily wind vectors at Barrow.

Ice thickness calculations were made from Maykut's [1986] theoretical model:

$$H_M = \frac{K_{iM}(T_F - T_O)}{C_t(T_O - T_a)}$$

where H_M = cumulative ice growth in a 24-hr period, K_{iM} = 419.9 cal cm^{-1} day^{-1} °C^{-1}, T_F = -1.8°C, C_t = 50 cal cm^{-1} day^{-1} °C^{-1}, T_O = ice surface temperature in °C, and T_a = air temperature in °C.

The ice surface temperature analysis yielded a discrete series of bands stepping from -6.0°C to -29.0°C in increments of 2°C. This work is reported in Groves and Stringer [1991]. The ice thicknesses of the discrete series for the first three bands extending seaward from the fast ice is given in Table 1. Areas of each thickness category were calculated from the imagery for each of the discrete series of temperature bands for each image (Table 1). Figure 2 shows the most conspicuous of the discrete series in shades of gray for the Chukchi Polynya on March 15.

Ocean-to-atmosphere heat flux was calculated using a standard model [Martin and Cavalieri, 1989]:

$$F_{net} = F_S + F_L + F_B$$

where F_{net} is the total heat flux, F_S is the sensible heat flux, F_L is the outgoing long wave radiation, and F_B is the long wave backscatter from clouds.

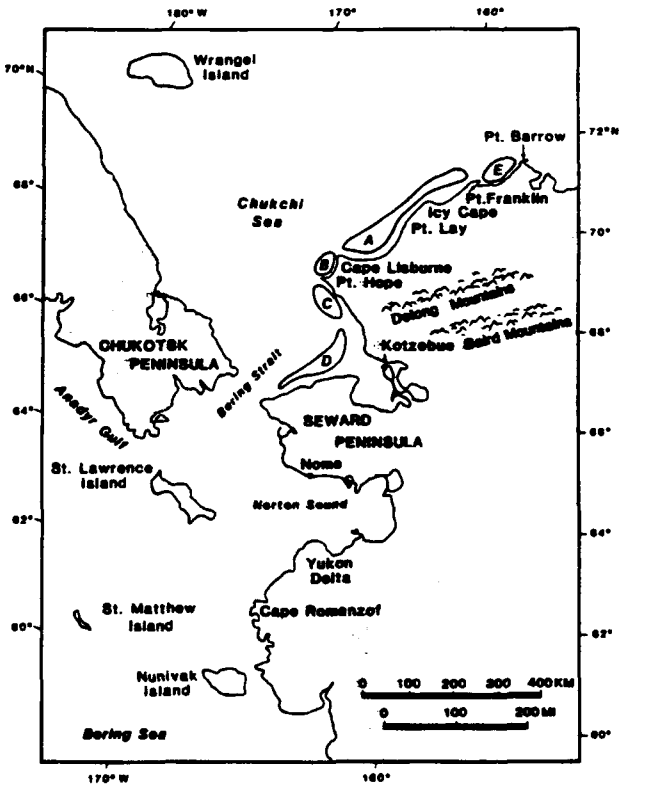


Figure 1. Location of polynyas along the Chukchi Coast of Alaska. (A) Chukchi Polynya; (B) Cape Lisburne Polynya; (C) Cape Thompson Polynya; (D) Kotzebue Sound Polynya; (E) Peard Bay Polynya.

The long wave and the long wave backscatter radiation, F_L and F_B, are calculated from the Stephan–Bolztman law,

$$F = e\sigma T^4$$

where σ = the Stephan–Bolztman constant (5.67×10^{-8} W m^{-2} $°K^{-4}$). For F_L, e, the emissivity, is assumed to be 0.98, and T(°K) is the temperature of the sea ice surface. For F_B, e is assumed to be 0.78 (for a condition of no cloud cover), and T(°K) is the air temperature.

The sensible heat flux, F_S, is calculated by the equation:

$$F_S = C\rho_{air}c_pU_{10}(T_{air}-T_{seaice})$$

where ρ_{air} is the air density 1.3 kg m^{-3}, C is the heat transfer coefficient (2.0×10^{-3}), U_{10} is the 10-m air velocity, T_{air} is the 10-m air temperature, T_{seaice} is the sea ice surface temperature, and c_p, the specific heat of air at constant pressure,

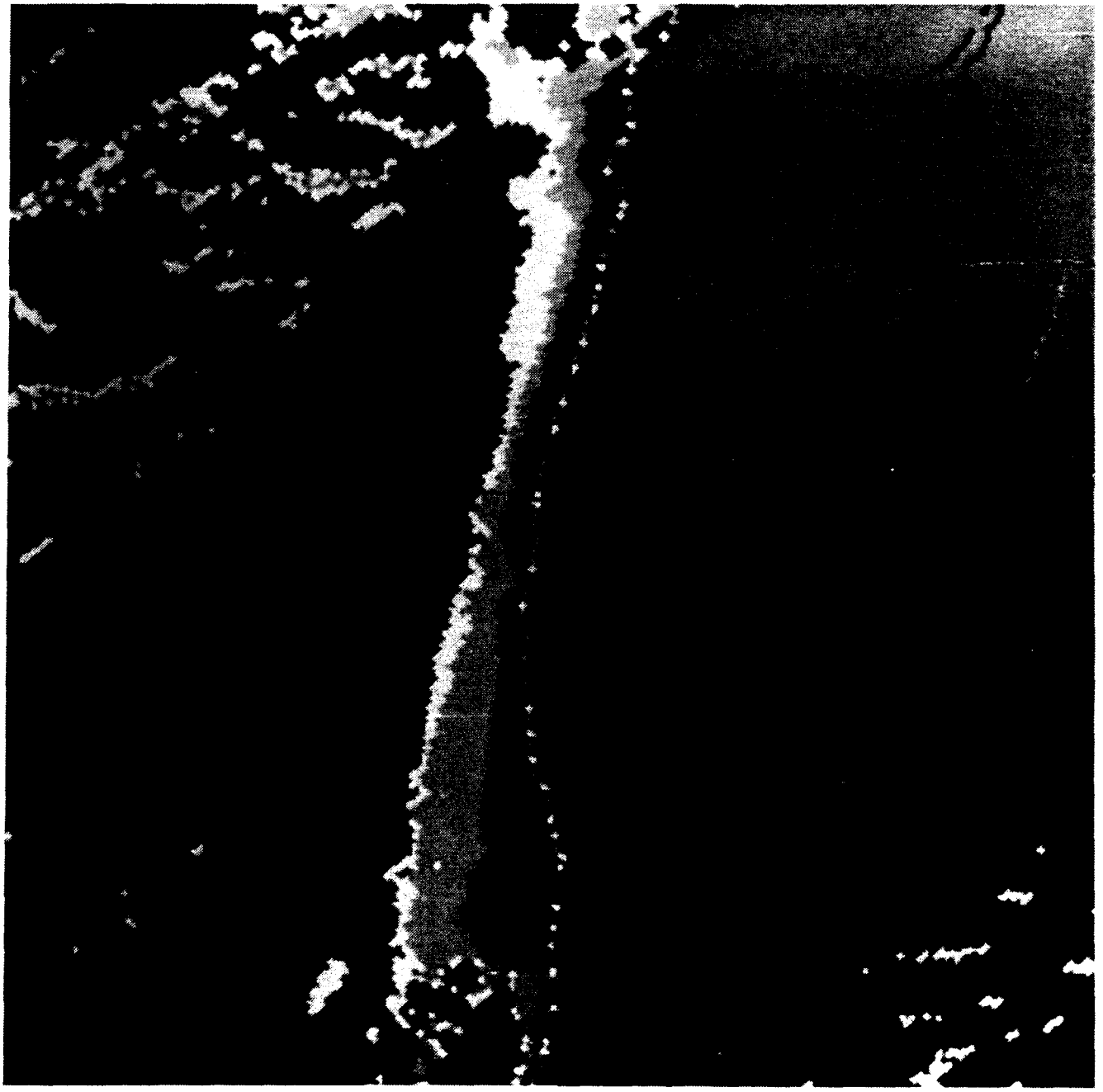


Figure 2. The Chukchi Polynya as it appeared on March 15, 1987 on the AVHRR Thermal Infrared band. This image has been enhanced to reveal the internal structure of the polynya. The four strips chosen have median values of -7.6°C (black), -10.2°C, -12.9°C, and -15.5°C (white). The gray region surrounding the polynya which comprises pack ice, fast ice, and land, is unenhanced. The gray tone of the unenhanced region represents temperatures ≤ -18°C.

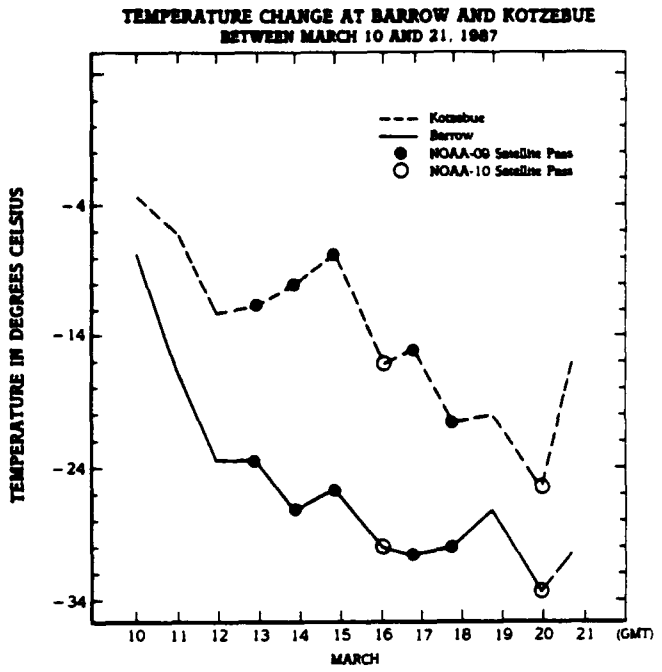


Figure 3. Air temperatures at the Synoptic Weather Stations at Barrow and Kotzebue near the time of each satellite pass.

= 1004 J deg^{-1} kg^{-1}. The 10-m daily average air velocity, U_{10}, is given in Table 1.

The rate of ice growth, dh/dt, is calculated from the formula:

$$dh/dt = F_{net}/\rho_{ice}L$$

where dh/dt is the freezing rate in m s^{-1}, ρ_{ice} = 0.92 x 10^3 kg m^{-3}, and L, the latent heat of fusion, is 3.34 x 10^5 J kg^{-1}.

Net heat transfer from each identified band of thin ice was calculated by multiplying the net heat transfer per square meter for each band by the area of the band.

Salt flux was calculated as given in Martin and Cavalieri [1989]:

$$S_F = \rho_{ice}\,(dh/dt)\,(s_w - s_{ice})$$

where S_F = salt flux in kg day^{-1}, ρ_{ice} = density of ice = 0.92 x 10^3 kg m^{-3}, s_w = salinity of sea water = 31.8 ‰, and s_{ice} = salinity of sea ice = 9.8‰. Coachman et al. [1975] report 31.0–32.5‰ for the Chukchi Sea in August. We use the average 31.8‰. We calculate s_{ice} using the formula: s_{ice} = 0.31 (s_w). Table 2 lists daily generated ice volume and salt flux.

Total salt rejection is calculated as follows:

$$S_T = \rho_{ice}\,(V_T)\,(s_w - s_{ice})$$

DATE OF AVHRR SATELLITE PASS (GMT)	POLYNYA STRIP	TEMPERATURE IN °C		10-METER WIND VELOCITY m sec^{-1}	BAND AREA km^2	ICE THICKNESS cm	NET HEAT TRANSFER W m^{-2}	HEAT TRANSFER FROM EACH BAND W x 10^{-11}	RATE OF ICE GROWTH m day^{-1}	ICE VOLUME km^3
		Sea Ice Surface	Air							
March 13,14*	1	-6	-24.5	3.1	220	2	262	0.58	0.07	1.6 x 10^{-2}
	2	-8.1			548	3	237	1.3	0.07	3.6 x 10^{-2}
	3	-10.2			612	5	211	1.3	0.06	3.6x 10^{-2}
March 15	1	-6	-29.2	4.0	984	2	365	3.6	0.10	10 x 10^{-2}
	2	-8.1			2353	3	335	7.9	0.09	22 x 10^{-2}
	3	-10.2			4385	4	305	13	0.09	38 x 10^{-2}
	4	-12.4			7687	5	273	21	0.08	59 x 10^{-2}
March 16	1	-8.1	-26.8	3.7	1051	3	294	3.1	0.08	8.7 x 10^{-2}
	2	-10.2			880	5	265	2.3	0.07	6.6 x 10^{-2}
	3	-12.4			806	6	234	1.9	0.07	5.3 x 10^{-2}
March 17	1	-10.2	-30.4	5.2	853	4	385	3.3	0.11	9.2 x 10^{-2}
	2	-12.4			1801	5	346	6.2	0.10	17.5 x 10^{-2}
	3	-14.6			3180	7	308	9.8	0.09	
March 18	1	-10.2	-30.6	3.4	672	3	298	2.0	0.08	5.6 x 10^{-2}
	2	-12.4			1405	5	270	3.8	0.08	11.0 x 10^{-2}
	3	-14.6			2735	6	242	6.6	0.07	18.6 x 10^{-2}
March 19	1	-12.4	-30	5.1	512	4	395	2.0	0.11	5.7 x 10^{-2}
	2	-14.6			1026	6	357	3.7	0.10	
	3	-16.5			1475	7	324	4.8	0.09	
March 21	1	-16.5	-33.3	7.0	368	8	384	1.4	0.11	
	2	-19.3			786	10	322	2.5		
	3	-21.6			1815	15	272	4.9		

Table 1. Surface heat transfer and rate and volume of ice production calculated using AVHRR-derived sea ice surface temperature of thin strips within the Chukchi Polynya. *Denotes two consecutive AVHRR satellite passes approximately 1 hour and 40 minutes apart. One occurred just before midnight on March 13 (GMT) and the second just after midnight. No significant change in polynya area was observed in this short time.

DATE	ICE VOLUME* ($x10^{-2}$ km^3)	SALT PRODUCTION* ($x10^5$ kg)
March 13, 14	8.9	18
March 15	129	260
March 16	20.5	31
March 17	26.8	54
March 18	16.3	33
March 19	5.7	12

Table 2. Daily ice and salt production within the Chukchi Polynya. *Ice volume and salt production per day for ice thickness ≤ 5 cm .

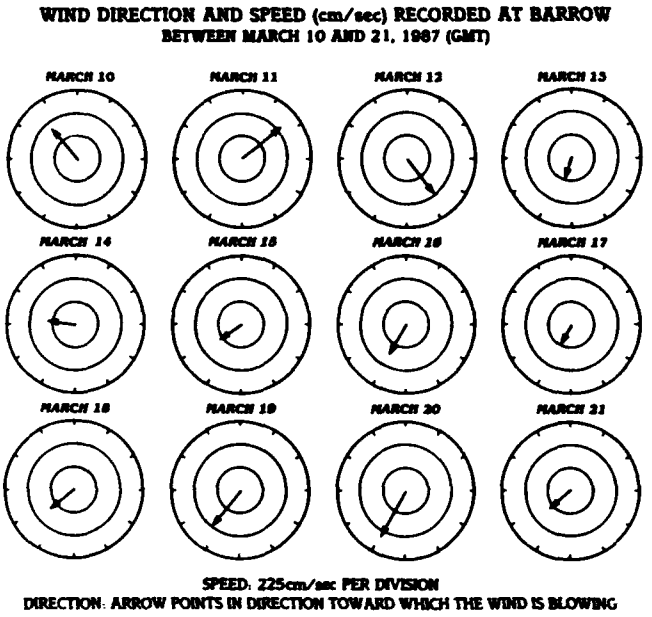


Figure 4. Daily modal wind direction at Barrow.

where V_T is the total ice volume generated, and S_T is the total salt production.

RESULTS

Calculations of ice thickness following Maykut [1986], and of heat transfer, rate of ice growth, and salt rejection following Martin and Cavalieri [1989], are given in Table 1. Daily ice and salt production are given in Table 2.

Total ice volume and salt rejection for the season defined as November through March are estimated by multiplying the mean freezing rate (0.09 m day^{-1}) by a "monthly median polynya area" of 600 km^2 [Stringer and Groves, 1988, 1991], for the Chukchi Polynya, which accounts for those periods during the month when the polynya is closed. Total seasonal ice generation for the five-month period is 8.1 km^3. Total seasonal salt rejection is 1.9×10^{11} kg. Martin and Cavalieri [1989] report seasonal ice production of 9–44 km^3 and seasonal salt rejection of 0.09 to 9.6×10^{11} kg for the Siberian Shelf polynyas.

The highest net heat transfer per square meter (185 W m^{-2}) and the highest net heat transfer over the polynya surface area for ice <5 cm (26×10^{11} W m^{-2}) occur on March 15 when the polynya is largest. The net heat transfer per square meter values in Table 1 are in general agreement with published values. These are 494 W m^{-2} for sea ice <5 cm [Maykut, 1986], from 55–290 W m^{-2} for the open water within Whaler's Bay [Martin and Cavalieri, 1989], and 535 W m^{-2} for the St. Lawrence Island Polynya [Schumacher et al., 1983].

CONCLUSIONS

(1) Calculations of net heat transfer per square meter of polynya surface area and of net heat transfer from polynya surface area as a whole suggest that when ice cover is thin and polynya area is extensive, heat transfer from the Chukchi Polynya is as significant as that from the Siberian Shelf Polynyas.

(2) Ice volume production and salt rejection values are given which are of the same order of magnitude as those reported by Martin and Cavalieri [1989] for the Siberian Shelf polynyas. The Chukchi Polynya could be as important as a source of salt for the water masses of the Chukchi Sea as the Siberian Shelf polynyas are for water masses of the Arctic Ocean.

ACKNOWLEDGMENTS

This study was funded in part under Contract #59 ABNC-00045 by the Minerals Management Service, U.S. Department of the Interior, through an interagency agreement with the National Oceanic and Atmospheric Administration, U.S. Department of Commerce as part of the Outer Continental Shelf Environmental Assessment Program.

REFERENCES

Eppler, D. T., and L. D. Farmer, Texture analysis of radiometric signatures of new ice forming in arctic leads, *IEEE Trans. Geosci. Rem. Sensing*, 2, 233–241, 1991.

Groves, J. E., and W. J. Stringer, The use of AVHRR thermal infrared imagery to determine sea ice thickness within the Chukchi Polynya, *Arctic*, 1991, In press.

International Arctic Polynya Program IAP[2], Arctic Oceans Sciences Board, Institute of Marine Science, University of Alaska Fairbanks, Fairbanks, AK 99775-1080, 1989.

Kuhn, P. M., L. P. Sterns, and R. O. Ramseier, Airborne infrared imagery of arctic sea ice thickness, *NOAA Technical Report ERL 331-APCL 34*, U.S. Department of Commerce, NOAA, Environmental Research Laboratories, Boulder, Colorado, May 1975.

Lauritson, L., G. J. Nelson, and F. W. Porto, Data extraction and calibration of TIROS-N/NOAA radiometers, *NOAA Technical Memorandum NESS 107*, 73 pp., November 1979.

Local Climatological Data, U.S. Department of Commerce (NOAA) National Climatic Data Center, Asheville, North Carolina, 28801, 1987.

Martin, S., and D. J. Cavalieri, Contributions of the Siberian Shelf polynyas to the Arctic Ocean Intermediate and Deep Water, *J. Geophys. Res.*, *94*, 12725–12738, 1989.

Maykut, G. A., *The Surface Heat and Mass Balance, Geophysics of Sea Ice*, edited by N. Untersteiner, pp. 395–463, NATO Advanced Science Institutes Series B, Physics, Vol. 146, Plenum Press, New York, 1986.

Schumacher, J. D., K. Aagaard, C. H. Pease, and R. B. Tripp, Effects of shelf polynyas on flow and water properties in the northern Bering Sea, *J. Geophys. Res.*, *88*, 2723–2732, 1983.

Smith, S. D., R. D. Muench, and C. H. Pease, Polynyas and leads: An overview of physical processes and environment, *J. Geophys. Res.*, *95*, 9461–9479, 1990.

Stringer, W. J., and J. E. Groves, A study of possible meteorological influences on polynya size, Geophysical Institute, University of Alaska Fairbanks, NOAA-OCS Contract No. ABNC-60041, November 1988.

Stringer, W. J., and J. E. Groves, Location and areal extent of polynyas in the Bering and Chukchi Seas, *Arctic*, 1991, In press.

WMO Sea-Ice Nomenclature, No. 259, TP. 145, Secretariat of the World Meteorological Organization, Geneva, Switzerland, 1970.